

AWARD NUMBER: W81XWH-13-1-0050

TITLE: Development of Ultrasound to Measure In-vivo Dynamic Cervical Spine
Intervertebral Disc Mechanics

PRINCIPAL INVESTIGATOR: Brian D. Snyder, MD, PhD

CONTRACTING ORGANIZATION: Beth Israel Deaconess Medical Center, Boston
Boston, MA 2215. US

REPORT DATE: JULY 2019

TYPE OF REPORT: Final Report

PREPARED FOR: U.S. Army Medical Research and Materiel Command
Fort Detrick, Maryland 21702-5012

DISTRIBUTION STATEMENT: Approved for Public Release;
Distribution Unlimited

The views, opinions and/or findings contained in this report are those of the author(s) and should not be construed as an official Department of the Army position, policy or decision unless so designated by other documentation.

REPORT DOCUMENTATION PAGE				Form Approved OMB No. 0704-0188	
Public reporting burden for this collection of information is estimated to average 1 hour per response, including the time for reviewing instructions, searching existing data sources, gathering and maintaining the data needed, and completing and reviewing this collection of information. Send comments regarding this burden estimate or any other aspect of this collection of information, including suggestions for reducing this burden to Department of Defense, Washington Headquarters Services, Directorate for Information Operations and Reports (0704-0188), 1215 Jefferson Davis Highway, Suite 1204, Arlington, VA 22202-4302. Respondents should be aware that notwithstanding any other provision of law, no person shall be subject to any penalty for failing to comply with a collection of information if it does not display a currently valid OMB control number. PLEASE DO NOT RETURN YOUR FORM TO THE ABOVE ADDRESS.					
1. REPORT DATE JULY 2019		2. REPORT TYPE Final report		3. DATES COVERED 26 Dec 2012 – 26 Mar 2019	
4. TITLE AND SUBTITLE Development of Ultrasound to Measure In-vivo Dynamic Cervical Spine Intervertebral Disc Mechanics				5a. CONTRACT NUMBER W81XWH-13-1-0050	
				5b. GRANT NUMBER	
				5c. PROGRAM ELEMENT NUMBER	
6. AUTHOR(S) Brian Snyder E-Mail: Brian.Snyder@childrens.harvard.edu				5d. PROJECT NUMBER	
				5e. TASK NUMBER	
				5f. WORK UNIT NUMBER	
7. PERFORMING ORGANIZATION NAME(S) AND ADDRESS(ES) Beth Israel Deaconess Medical Center 330 Brookline Avenue, Boston, MA Medical College of Wisconsin 8701 W Watertown Plank Rd, Milwaukee, WI 53226				8. PERFORMING ORGANIZATION REPORT	
9. SPONSORING / MONITORING AGENCY NAME(S) AND ADDRESS(ES) U.S. Army Medical Research and Materiel Command Fort Detrick, Maryland 21702-5012				10. SPONSOR/MONITOR'S ACRONYM(S)	
				11. SPONSOR/MONITOR'S REPORT NUMBER(S)	
12. DISTRIBUTION / AVAILABILITY STATEMENT Approved for Public Release; Distribution Unlimited					
13. SUPPLEMENTARY NOTES					
14. ABSTRACT We developed a unique dual ultrasound system that can non-invasively measure Intervertebral Disc (IVD) deformation and mechanical compliance ex-vivo and in-vivo. The system is capable of providing real-time images of IVDs and dynamic vertebral motion during simulated tasks. Vertebrae motion and IVD deformation were measured by tracking the bony surface profiles in consecutive US images. Classical Voigt model and finite element model were built to investigate the "transfer function" human cadaveric spine functional spine units to account for the differential elasticity during compression or tension. As a portable, low cost imaging modality, the dual ultrasound system quantified cervical spine IVD displacement and the mechanical compliance of a functional spinal unit (FSU) in response to applied forces. This technology allowed in-vivo evaluation of cervical spine mechanical behavior in dynamic environments where MRI and CT cannot be used.					
15. SUBJECT TERMS NONE LISTED					
16. SECURITY CLASSIFICATION OF:			17. LIMITATION OF ABSTRACT	18. NUMBER OF PAGES	19a. NAME OF RESPONSIBLE PERSON
a. REPORT	b. ABSTRACT	c. THIS PAGE			USAMRMC
U	U	U	UU	228	19b. TELEPHONE NUMBER (include area code)

Table of Contents

2. Keywords	5
3. Overall Project Summary.....	6
4. Key Research Accomplishments	7
1.1 Dual US System Capable of Measuring Cervical Vertebra Motion in Response to Static and Dynamic Loads Applied to Human C-Spine Ex-vivo and In-vivo.....	7
1.2 Validation of Dual US System Ex-vivo Using Human Cadaver C-Spines Mounted in Multi-Axial Servo Hydraulic Testing Machine Subjected to Physiologically Relevant Forces and Moments	9
1.3 Relationship Between “Health” of IVD Measured on Static MRI Images vs. Mechanical Compliance of FSU Measured by US	12
1.4 Custom Cervical Collar to Maintain Dual US Probes in Proper Alignment for Imaging Anterior and Posterior C-Spine Anatomic Landmarks In-vivo	15
1.5 Using US to Measure C-Spine Motion and IVD Deformation In-vivo to Evaluate Mechanical Properties of the C-Spine During Simulated Conditions With and Without Headgear	16
1.6 Analytic Models Developed from Ex-vivo Simulations to Specify Permissible Load Amplitudes, Load Rates, and # of Cycles for Different Loading Modes	19
2.1 US System Development and Validation (Continuation of Aim 1, Task 1 & 2).....	23
2.2 Ex-vivo Hydration vs IVD Compliance and Cervical Spine Health and Integrity (Task 4 & 6)	25
2.3 In-vivo Ultrasound Test in Simulated Environment (Task 7)	27
2.4 FE Model Validation and Modification (Task 11) and Simulating Operation Loading Conditions (Task 12).....	33
3.1 Cervical Design and Production	53
3.2 In-vivo Dual US Test in Repetitive Jumps	54
3.3 In-vivo US Test in Simulated Environment.....	57
3.4 Fatigue Experiments on Cervical Spine Disc Segments.....	59
3.5 Developing a Finite Element Model of Intervertebral Disc.....	64
4.1 Combining US/MR Data and Calculating 3D Kinematics of C-Spine.....	70
4.2 In-vivo Dual US Imaging of Cervical Spine During Repetitive Jumps.....	74
4.3 Fatigue Testing on Cervical Spine Disc Segments	77
4.4 Development of a Finite Element Product to Predict Spine Fatigue Using the Experimental Data	89
5.1 Long-Term Movement Analysis of Vertebra in Ultrasound Image Sequence	105
5.2 In-vivo Ultrasound Imaging of C-Spine and The Effects of Helmet Weights and Muscle Activation.....	111

5.3	Ongoing Study of In-vivo Ultrasound Imaging of C-Spine in MARS	118
6.1	IRB Protocol for USAARL Subject Enrollment Center	128
6.2	Consent Form and Flyer for Subject Enrollment.....	135
6.3	Consent Form for Subject Enrollment	136
6.4	Evaluation of Mass Properties of Helmet	147
6.5	Development of Mass Attachment Device to Recreate Vertical (z-axis) Offset Helmet Configurations.....	149
6.6	Technology to Image Spine Using Single 3D US System.....	150
5.	Conclusion	153
6.	Publications, Abstracts, and Presentations.....	154
	Publications.....	154
	Conference Abstracts	155
	Conference Presentations.....	156
	Dissertations.....	157
7.	Inventions, Patents and Licenses	157
8.	Reportable Outcomes.....	158
9.	Other Achievements.....	158
10.	References.....	159
11.	Appendices.....	163

1. Introduction

Neck pain is a common complaint in the general population and is strongly associated with reduced quality of life for individuals and family. Mean prevalence of neck pain is 23.3% in the general population [1]. National surveys and meta-analysis of the literature indicated a higher overall prevalence of neck pain in females than males [1,2], though it is still controversial to conclude that there are gender differences in the onset and remittance of neck pain. Laborers and military personnel exposed to repetitive loads and vibrations are at highest risk [3,4]. Structural defects such as disc herniation or endplate fracture can be revealed by traditional imaging technologies such as plain radiography, computed tomography (CT) and magnetic resonance imaging (MRI). However, understanding the pathophysiology and mechanism of progression of acute and chronic degenerative intervertebral disc (IVD) disease induced by repetitive, dynamic loads typically encountered in the work environment remains challenging since the etiology of these injuries are not evident in static images. CT and MRI evaluations of C-spine kinematics under dynamic conditions simulating work environments are impractical owing to the size and power required for these imaging modalities.

Ultrasound (US) provides a practical, cost-effective alternative for imaging soft tissue. Especially for evaluating musculoskeletal pathoanatomy, the ability to capture the dynamic real-time motion of internal musculoskeletal structures such as joint and tendon movement was demonstrated. For spine studies, it has been previously proved US can image change of IVD height [5]. Key landmarks in the musculoligamentous internal architecture of the c-spine were compared between US to MRI on human [6]. Other studies identified the IVD of the human thoracic and lumbar spines [7] and pathoanatomy of IVD ex-vivo [8]. US has been used to measure the compliance of lumbar spine FSUs by measuring the change in IVD height after submerging a subject in a water bath and applying longitudinal traction [9,10].

Compared to US imaging, other dynamic assessment methods are less portable and have to be implemented in a lab environment because of space and power supply requirements. Motion capture system is safe but unable to provide the anatomy of the human directly. Numerous studies have quantitated the error caused by skin sliding and task movement dependent [11-13]. Among all dynamic measurements, bi-plane fluoroscopy provides the most precise evaluation of kinematics of C-spine, but the radiation exposure to the human subject's brain and thyroid region is a deep concern to human participants, clinicians, and researchers. Furthermore, the range of activities of the human participant is limited because the fluoroscopy systems are immobilized.

Our overarching goal is to demonstrate that clinical US can provide a portable imaging modality capable of quantifying cervical spine motion and IVD deformation, in real time, for individuals working in extreme dynamic environments. We hypothesize that time sequences of US imaging signals can be used to characterize the deformation of C-spine functional spinal units in response to applied displacements and loads.

2. Keywords

Dual ultrasound; In-vivo cervical spine kinematics; Intervertebral disk

3. Overall Project Summary

Understanding the pathophysiology of degenerative C-spine IVD disease remains a challenge since mechanisms of injury are not evident in static X-ray, CT, or MR images. Methods to evaluate C-spine kinematics are difficult to implement in workplace environments. To circumvent these problems we developed hardware and software using B-mode US to derive the mechanical behavior of cervical FSUs that we validated *ex-vivo*. By combining dynamic US image profiles of C4-6 with a 3D C-spine model derived from subject specific MRIs, we evaluated C-spine kinematics *in-vivo* of subjects engaged in repetitive jumping to simulate a physiologically relevant extreme loading activity.

Ex-vivo experiments: MR images were obtained on 5 cadaveric C2-T1 specimens (53-61yrs) to measure IVD heights, cross-section areas, and Pfirrmann grade. Specimens were subjected to compressive CREEP and cyclic axial loading. Elastic and damping coefficients were calculated assuming a Voigt model. C4-5 FSU kinematics were derived from concurrent dual US image profiles of the anterior and posterior vertebral anatomy superimposed onto a 3D C-spine model constructed from corresponding MR images. The changes in IVD height were automatically tracked using a custom-made multi-frame tracking algorithm using Radio Frequency environment.

In-vivo experiments: With IRB approval, 10 subjects jumped repetitively from a step for 4 mins wearing weighted helmets. Dual B-mode US images of C4-6 motion were captured in real-time using a custom collar to hold the sonically coupled US probes in fixed orientation to access anterior and posterior vertebral profiles. in motion capture lab to jump repetitively from 0.8 ft step @ 0.5Hz x4min while wearing a helmet with and without 2.5 lbs additional weight. We measured head to torso displacement, impact on landing, FSU kinematics and muscle EMG.

C4-5 kinematics were calculated by projecting sequential dual US image profiles onto a C4-6 virtual model created from subject specific MRIs. IVD kinematic was evaluated using automated motion tracing algorithm.

Key findings

Ex-vivo: C4-C5 FSU elastic modulus ranged 10.3 to 76.0 MPa; the damping coefficient ranged 0.5 to 4.5 MPa*s. Pfirrmann grade correlated with elastic modulus (Pearson coefficient = 0.93).

In-vivo: Axial strain correlated with muscle activity in weighted (Pearson = 0.7) and unweighted (Pearson = 0.3) groups. Additional helmet weight increased C4-5 axial strain and muscle fatigue ($p < 0.05$). And over time, increased muscle activation was required to maintain same IVD strain. The addition of an eccentrically placed weight, paracervical muscles fatigued more rapidly, which contributed to increased FSU strain. This indicates the importance of dynamic muscle activity in dampening the effect of applied loads. FSU deformation is limited at 70% strain. This indicates that strain cannot further increase because it is starting loading facet and endplate. At higher strain, EMG signal showed large variances. This can indicate that muscles are not acting in the same manner between individuals that can implicate effect of muscle strength on dampening spinal loads and potential protective role on IVD degeneration.

Conclusion:

We demonstrated that dual B-mode US provides low cost, portable, non-ionizing radiation imaging system capable of accurately measuring real time dynamic FSU deformation in

simulated work environments. B-mode US is capable of accurately tracking vertebral motion under clinically relevant physiologic conditions. Our study had some limitations: first, 2D FSU deformation was measured in sagittal plane. Second, *Ex-vivo* validation studies may not correspond to *in-vivo* accuracy. The sample sizes were limited in both ex-vivo and in-vivo experiments. We conclude that US can characterize dynamic behavior of C-spine FSU at higher frame rates than MRI and CT, and dynamic material properties can be measured by US and related to anatomy and IVD integrity and hydration. Para-cervical muscles serve to dampen loads applied to C-spine, thereby protect IVD from excessive deformation. As muscles fatigue, protective effect is lost, and increased deformation may contribute IVD “fatigue failure” over repetitive loading in extreme work environments. This could further provide information to improve the work procedure as well as exercise regimens to protect C-spine from excessive loading in different tasks in dynamic environments.

4. Key Research Accomplishments

Year 1: Further develop ultrasound (US) system to measure cervical spine kinematics and inter-vertebral disc (IVD) strain; validate using human cadaveric cervical spines. Use ex-vivo simulations on cadaver C-spines to develop and validate finite element model (FEM) of human cervical spine.

1.1 Dual US System Capable of Measuring Cervical Vertebra Motion in Response to Static and Dynamic Loads Applied to Human C-Spine Ex-vivo and In-vivo

We collaborated with the commercial US system manufacturer Terason (Burlington, MA) to develop the hardware and software for this unique dual ultrasound system (Figure 1-1).

Hardware development: A block diagram of the dual ultrasound system’s hardware configuration is shown in Figure 1-2. One of the T3200 US devices serves as the master to synchronize signal and data acquisition from the second US “slave” device. A "synchronous acquisition" mode was developed by Terason to accomplish this: the master US system sends out a sync pulse to the slave US system every time it takes an image frame such that both the master and slave systems collect the image frames synchronously. The dual system has a scanning frame rate of 64 frames per second. Binary radio frequency (RF) data output is streamed to a solid-state hard drive at the dual ultrasound scanning frame rate. To provide synchronized video output, compact external frame grabbers capture the video output (DVI format, 30 frames per second) from each of the Terason T3200 US systems to archive the data in lossless compression format.



Figure 1-1: Dual ultrasound system allows simultaneous imaging of the anterior and posterior C-spine.

Software Development: Workflow to process the stereophotogrammetric images and calculate the 3D vertebral body motion and IVD deformation is outlined in Figure 1-3. The user specifies a region of interest (ROI) corresponding to the bony profiles of the vertebral body that is then applied to each subsequent image frame. The overall motion of the centroid of that bone profile is calculated by averaging the displacement of all the pixels contained within that bony profile. After the RF stream is recorded on the SSD, a custom C-based software program converts the RF stream to RF data frame sequences. We developed a motion tracking program based on “A Parallelizable Real-time Motion Tracking Algorithm with Applications to Ultrasonic Strain Imaging” (J Jiang, TJ Hall, Phys. Med. Biol. 2007) to compare two consecutive US images and map the lateral (perpendicular to US beam) and axial (parallel to US beam) displacement of pixels comprising the bony profiles of the vertebrae using a block matching algorithm. To discretize the data, kernels corresponding to a width (lateral) and length (axial) of 0.90 mm and 1.20 mm, respectively are moved over the RF signal from sequential image frames with 33% axial and lateral overlap. A quadratic fit to the cross-correlation function is used to detect sub-sample motion. A user specified region of interest corresponding to the bony profile of the cervical vertebrae is illustrated in Figure 1-3. This region is then tracked on sequential images to determine the average displacement of each pixel contained within that profile. The overall displacement of the centroid of the bone profile (corresponding to the spinous process of C5 in Figure 1-3) is then graphed over time.

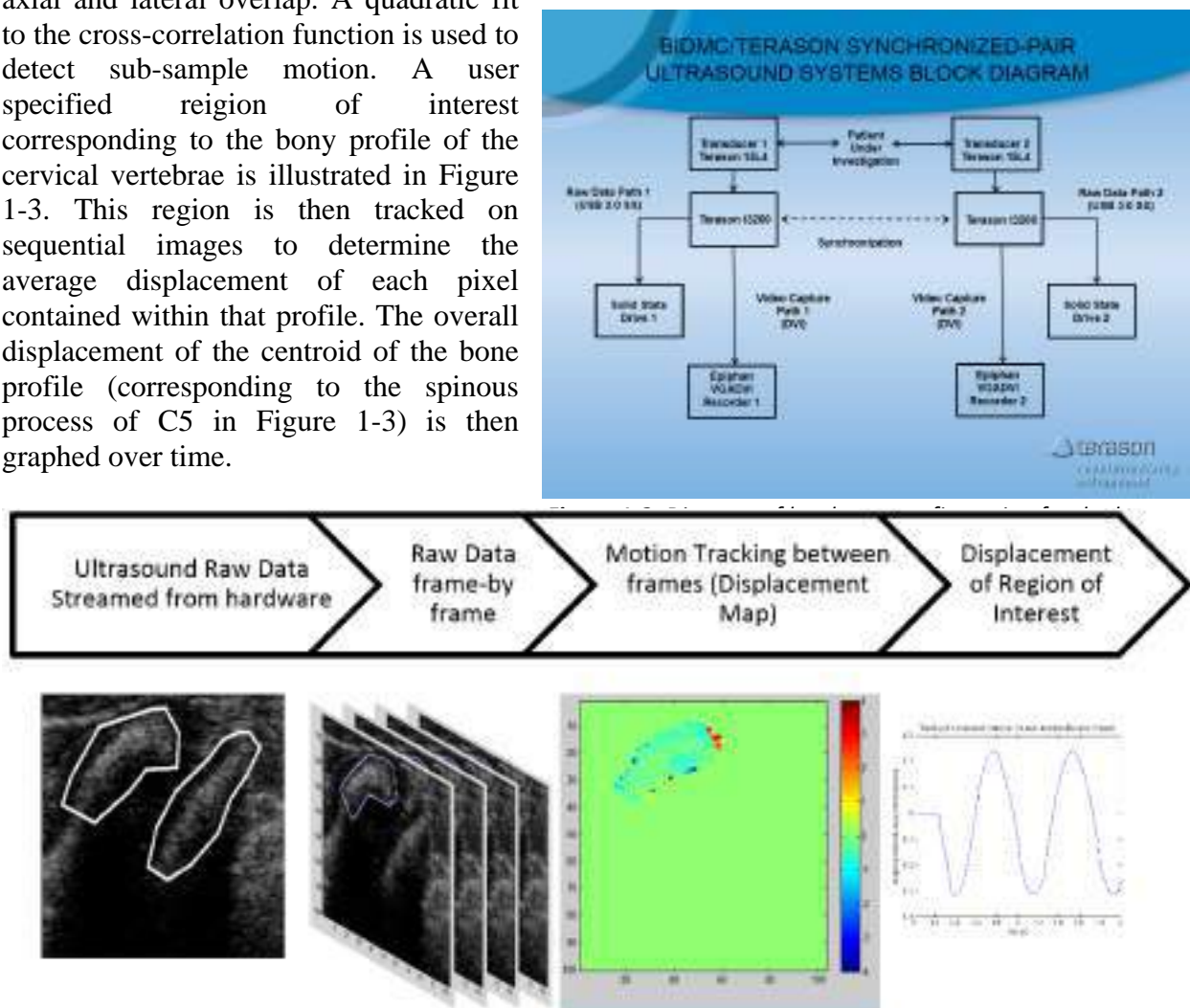


Figure 1-3: Workflow for processing dual US images and calculating vertebral displacement from sequential images. Spinous processes of contiguous cervical vertebrae C5 and C6 illustrated.

1.2 Validation of Dual US System Ex-vivo Using Human Cadaver C-Spines Mounted in Multi-Axial Servo Hydraulic Testing Machine Subjected to Physiologically Relevant Forces and Moments

A. Comparison of IVD deformation measured via dual US system vs direct measurements

Two 15L4 ultrasound probes (linear transducer, Terason, Burlington, MA), oriented at a known fixed angle to one another, were synchronized to acquire B-mode US images of the anterior and posterior profiles of a dynamically loaded *ex-vivo* human C6-7 FSU excised from a 56 year old male (Figures 1-4 and 1-5).

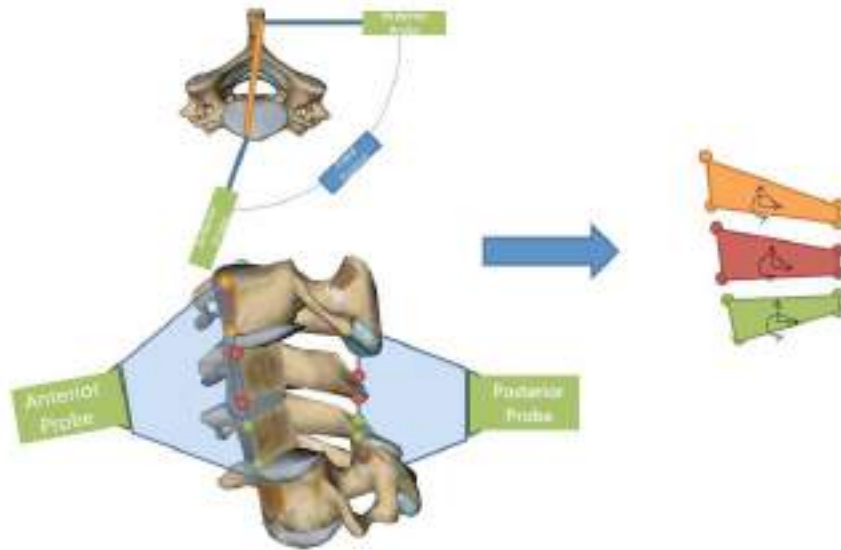


Figure 1-4: Stereographic US imaging of cervical spine and simplified rigid body representation of C4-C7.

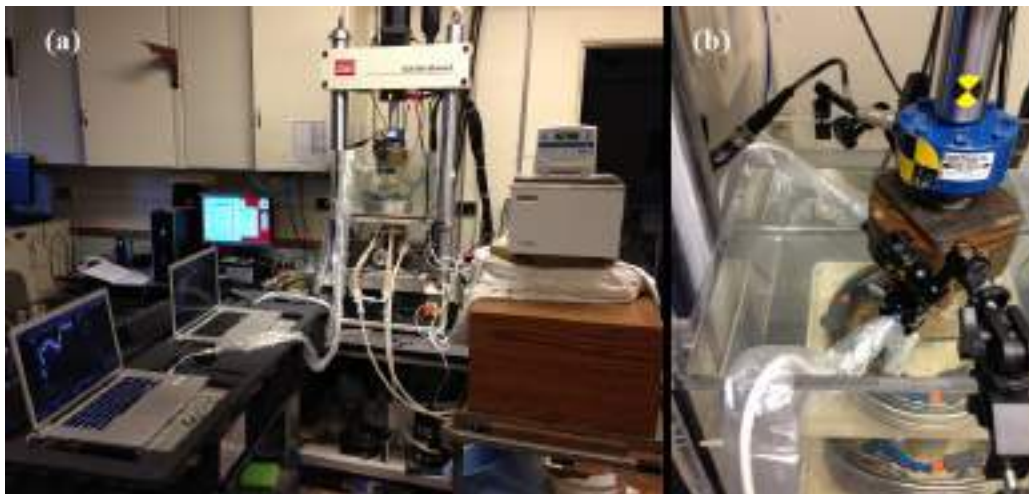


Figure 1-5: Human cadaveric C6-7 FSU mounted in MTS servohydraulic load frame immersed in a saline bath and imaged using the dual ultrasound system in real time. (a) Experimental set-up; (b) Orientation of ultrasound probes relative to specimen.

Adjacent vertebral bodies of the C6-C7 FSU were rigidly mounted in an MTS material testing system (MTS System Corporation, MA). The entire specimen was submerged in 0.9% saline

bath at 37°C to replicate physiological conditions. The anterior US probe was oriented to image the anterior margins of the vertebral bodies and IVD, and the posterior US probe was oriented to image the margins of the spinous processes (Figure 1-5b). The FSU was subjected to dynamic compressive and distractive loads (-90 N to +90 N @ 1-8 Hz). After the user specifies the ROI corresponding to the profiles of the vertebral body and spinous process on the initial image frame, the code is fully automated to calculate the displacement of these anatomic structures over time. The processing time of the algorithm using RF data is 5 minutes for each 10-second sequence of US image frames, compared to 30 minutes using the video-based algorithm. The calculated displacements are highly reproducible, and manual correction between consecutive US frames is not needed for the RF-based analysis.

The real time, IVD deformation deduced from the stereographic US images was compared to IVD deformations measured directly using the in-line linear variable displacement transformer (LVDT) of the MTS system. Overall there was good correspondence between the IVD deformations measured using either anterior or posterior anatomic landmarks (Figure 1-6) compared to IVD deformation measured directly by the LVDT. The asymmetric deformation of the IVD in compression vs. distraction implies that the IVD is stiffer in compression than tension.

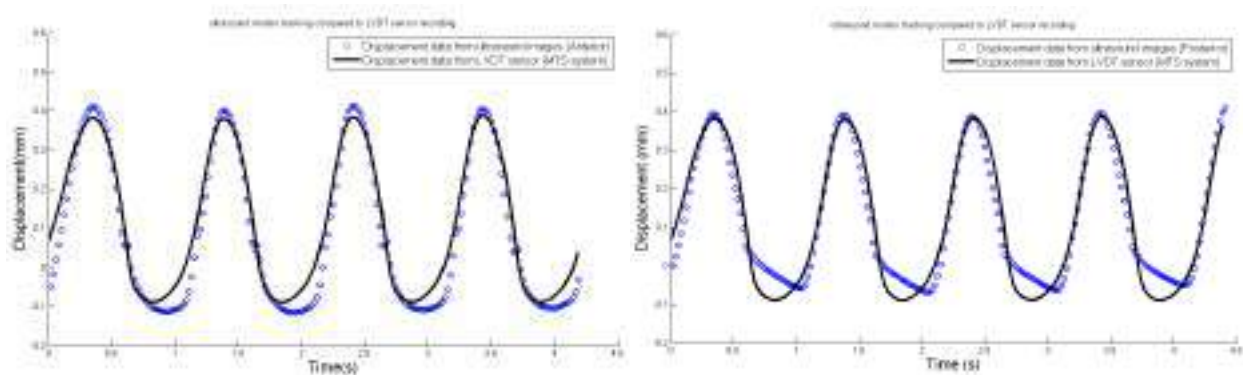


Figure 1-6: Representative C6-7 IVD displacement data for FSU subjected to sinusoidal compressive and distractive force (-90 N to +90 N @ 1 Hz). Black line shows IVD displacement measured by LVDT. Blue circles correspond to IVD displacement deduced from the anteriorly positioned US probe (left) and posteriorly positioned US probe (right).

C6-7 IVD deformations deduced by ultrasound using the RF algorithm were highly correlated with IVD deformations measured directly by the LVDT (Table 1-1, Figure 1-7). Compared to the video-based tracking algorithm implemented previously (Table 1-1, Figure 1-8), the performance of RF based tracking algorithm demonstrated improved performance for applied frequencies > 4 Hz, and US measures of IVD deformation using the RF algorithm accounted for ~92% of the variation in the IVD deformation measured directly for frequencies up to 6 Hz and 77% of the variability in deformation at 8 Hz ($R^2 = 0.77$), a significant improvement over the video-based tracking algorithm ($R^2 = 0.30$).

Table 1-1: Coefficients of determination (R^2) for RF-based and video-based IVD deformation compared to direct

Goodness-of-fit(R^2)		
Frequency (Hz)	Raw data-based	Video-based
1	0.95	0.97
2	0.96	0.92
4	0.85	0.80
6	0.91	0.56
8	0.77	0.30

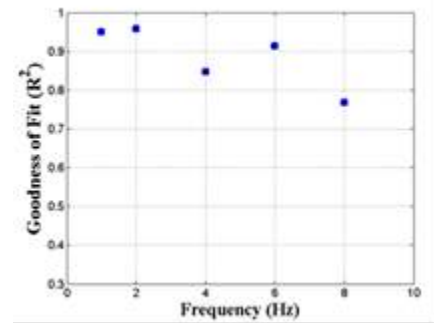


Figure 1-7: Coefficients of determination from Table 1 plotted as a function of applied frequency.

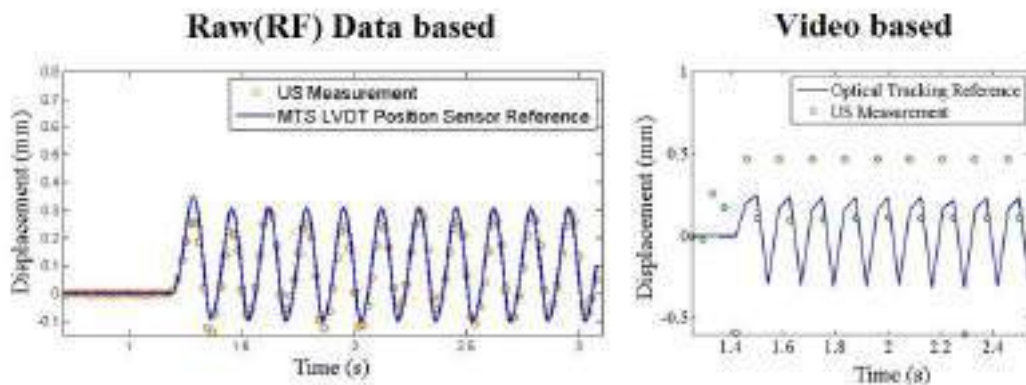


Figure 1-8: Representative C6-7 IVD deformation deduced from US using RF algorithm and video-based algorithm compared to deformation measured directly via in-line LVDT for applied -90 N to +90 N sinusoidal force @ 6 Hz. Blue line is LVDT displacement and red circles are displacements deduced from US images. The RF data based motion tracking are highly consistent with LVDT measurements at 6 Hz.

Compared to the video-based tracking algorithm used in our previous work, the RF-based algorithm has better performance with respect to image processing time, reproducibility, and accuracy particularly at higher frequencies (6-8 Hz). Based on data from USAARL, the cervical spines of soldiers driving in armored vehicles are exposed to vibrations at frequencies of approximately 5-6 Hz and up to 8 Hz in helicopters. Therefore, to be able to analyze the dynamic motion of the C-spine of soldiers participating in military operations, the scan rate of the system was optimized to 64 Hz (i.e. 64 frames per second). The improvements to our hardware and software now allow us to track C-spine motion at frequencies up to 8 Hz with $> 75\%$ confidence.

B. Preliminary studies of 3D kinematics using dual US stereographic imaging of C-spine

We evaluated the ability of the dual ultrasound stereographic imaging system to derive 3D kinematics of a C-spine FSU by applying a pure 1 N-m flexion moment to the C6-7 FSU. Ultrasound images were taken of the superior and inferior facets and spinous processes (Figure 1-9) and used to calculate the Euler angle between contiguous vertebrae, each represented by a plane triangular rigid body (Figures 1-10 and 1-11). The calculated instantaneous center of rotation was at the middle column of the vertebra so that in flexion, the anterior IVD compressed and posterior IVD distracted. The IVD was stiffer in compression than tension.



Figure 1-9: Lower vertebral body of the FSU mounted in PMMA and attached to a plate fixed on a tripod. Four hydraulic pistons rigidly attached to the PMMA allow the application of force couples that induced pure flexion-extension or lateral bending moments to the FSU. Dual US probes were oriented to image the facet joints and spinous processes of the C6-7 FSU.

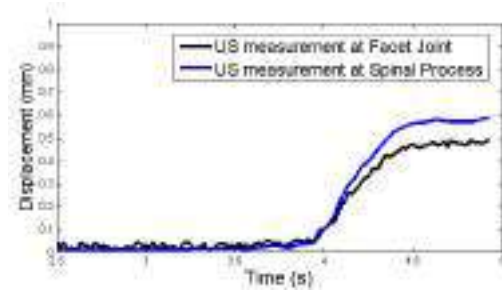


Figure 1-10: Displacement measured at facets and spinous processes by US during applied flexion moment.

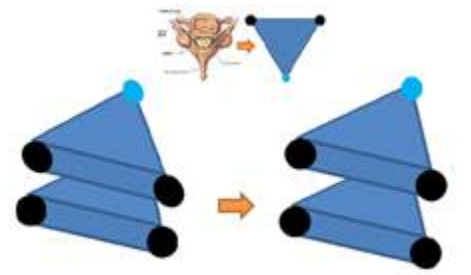


Figure 1-11: Rigid body motion of FSU represented by triangular shaped vertebrae. Animated model using stereographic ultrasound images to generate Euler angles.

1.3 Relationship Between “Health” of IVD Measured on Static MRI Images vs. Mechanical Compliance of FSU Measured by US

The feasibility of using US to measure the functional performance of cervical spine FSUs was evaluated by plotting the static and dynamic deformation of the IVD measured by US as a function of the applied load. A single US probe was oriented in the anterior “window” between the sternocleidomastoid muscle and carotid artery of human cadaveric cervical spine specimens obtained from elderly individuals (ages 73-91 years). The C4-5 and C5-6 FSUs were evaluated as these levels are most commonly affected by degenerative disc disease, presumptively as a consequence of chronic overloading. Consistent, standardized anatomic landmarks corresponding to the intersection of the anterior vertebral body cortical shell with the vertebral body endplate adjacent to the IVD were identified and this profile tracked on all subsequent US images of the FSU.

Static and dynamic compliances measured directly and by US are summarized in Table 1-2. The static compliance of the FSU was calculated as the slope of the deformation of the IVD in response to statically applied compressive and distractive forces of 20 lbs to C4-5 and C5-6 (Figure 1-12). A simplified linear approximation of the dynamic compliance was calculated using linear regression to the non-linear data set to evaluate and compare the static compliance to the dynamic compliance (Figure 1-13). Damping, which represents the lost work during each load cycle, was calculated from the area between the loading and unloading trajectories of the force-displacement curve. There was significant variation among the specimens, but the mean compliance for the C4-5 FSU measured statically and dynamically by US was 2.98×10^{-3} mm/N

and 4.59×10^{-3} mm/N respectively. The mean compliance for the C5-6 FSU measured statically and dynamically by US was 4.27×10^{-3} and 5.70×10^{-3} mm/N respectively. For this small number of specimens (due to lack of power), we could not demonstrate significant differences between the static or dynamic compliance of C4-5 and C5-6, nor demonstrate an effect of age using 1-way ANOVA. Considering the elderly ages of these specimens, this result is not inconsistent with our previous finding that C4-5 is more compliant than C5-6 in younger aged specimens. The static compliance measured by applying a 20-lb compressive and distractive load was positively correlated the with dynamic compliance measured directly ($R = 0.6$) and by US ($R = 0.9$) for a dynamic displacement of 1 mm @ 1 Hz, suggesting that although this static test ignores the viscoelastic behavior of the IVD, it might be a useful clinical examination to predict the overall dynamic mechanical behavior of the FSU.

Table 1-2: Compliance and damping coefficient derived for C4-5 and C5-6 FSU levels from each specimen.

Age	IVD level	Static Compliance (mm/N)	Dynamic Compliance (mm/N)	Area Estimate (N·mm)	Pfarrmann Grading
91	C4-5	3.37E-03	3.68E-03	9.08	4
	C5-6	2.25E-03	2.00E-03	9.98	4
81	C4-5	2.25E-03	2.28E-03	18.48	4
	C5-6	7.42E-03	1.10E-02	18.78	4
81	C4-5	5.62E-03	1.09E-02	29.36	4
	C5-6	6.29E-03	8.06E-03	28.7	5
73	C4-5	6.74E-04	1.51E-03	91.84	5
	C5-6	1.12E-03	1.72E-03	62.05	5

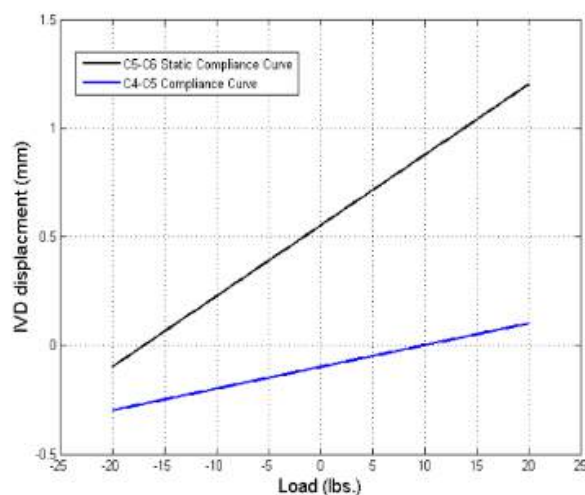


Figure 1-12: Representative static displacement-load curves for C4-5 (black) and C5-6 (blue) FSUs to determine static compliance (slope).

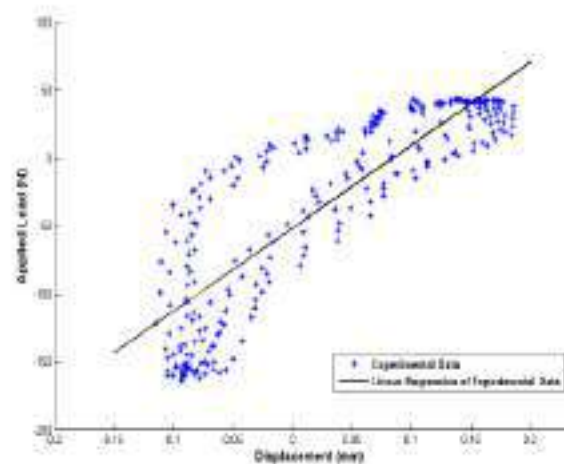


Figure 1-13: Representative dynamic load vs displacement data for C4-5 and C5-6 FSUs. Line fit to the non-linear data to derive linear elastic estimate of dynamic compliance.

The integrity of cadaveric C-spine IVD was also evaluated from MRI T2-images using Pfirrmann scale. Not unexpectedly, most IVDs were degenerated because of the advanced ages

of the specimens (grade 4 or 5). For this limited number of specimens, the linear elastic approximations of static and dynamic compliance of the C4-5 and C5-6 FSUs were affected by the integrity of the IVD as measured by Pfirrmann grade (1-way ANOVA, $p < 0.05$). The damping coefficient was unaffected by the Pfirrmann grade. This finding is consistent with the observation that the “health” and integrity of the IVD affects the mechanical performance of the FSU and that our US system may provide a cost-effective clinical tool to evaluate the integrity and performance of the IVD by applying low amplitude traction and compressive loads to the head and neck *in-vivo*.

Recognizing the deficiencies of modeling the dynamic mechanical properties of the cervical spine FSU using a linear approximation, we collaborated with our subcontractor at Medical College of Wisconsin to generate more sophisticated non-linear models that better fit the dynamic force-displacement data and account for the differential elastic and viscoelastic response during cyclic loading in tension and compression (Figure 1-14). Focusing on the C4-5 FSU, this differential mechanical behavior is evident as the specimen is initially loaded to 50 N in tension (A-B), followed by tensile unloading (B-C), then compressive loading to 150 N (C-D) followed by unloading and “recoil” (D-A). The unloading path did not follow the loading path, consistent with Mullin’s effect. Also, the IVD strain “softened” in tension and compression as the peak strain increased with progressive loading cycles. The stiffness during tensile and compressive loading was approximately 300 kN/m and 800 kN/m. The force-displacement data was converted to stress-strain data based on the following equations:

$$\text{Stress} = \frac{\text{Force}}{\text{Area}} \quad (1.1)$$

$$\text{Strain} = \frac{\Delta \text{Length}}{\text{Original length}} \quad (1.2)$$

The average cross-sectional area of C4-5 disc was assumed to be 400 mm² (Pooni, Hukins et al. 1986) and the average disc height was assumed to be 3.3 mm (Pait, Killefer et al. 1996). The corresponding stress-strain response is shown in Figure 1-15.

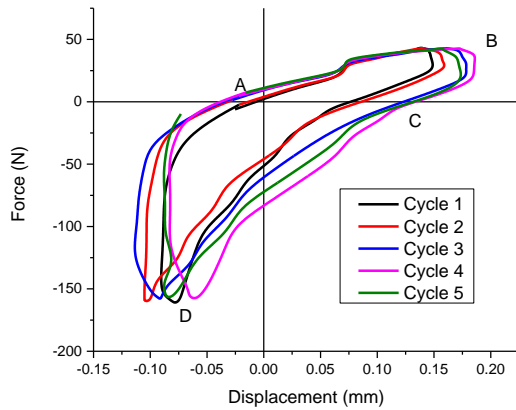


Figure 1-14: Force-displacement curve for C4-5.

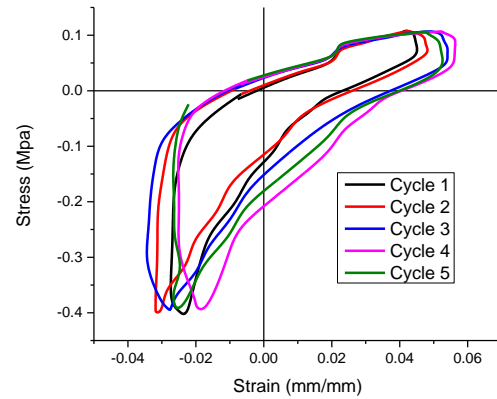


Figure 1-15: Stress-strain curve for C4-5 segment.

The next phase in the analysis was to arrive at an appropriate nonlinear mathematical function (material model) representing the observed stress-strain responses. For this purpose, the coefficients in the nonlinear function were optimized using a generic algorithm C++ toolbox (Sastry and Goldberg 2007). The optimization scheme involved the evaluation of the “fitness of error,” defined as the difference between the experimental response and the model response in

one cycle over the entire loading-unloading sequence. The “fitness of error” is given in Equation 1.3. The lower the fitness, the better the agreement between the experimental data and analytical model. Six nonlinear material models (finite element) were identified and calibrated to minimize the error. The model that best correlated with the experimental data was used.

$$\text{Fitness}, f(X_1, X_2, \dots, X_n) = \sqrt{\frac{\sum_i^n (F_i^{\text{exp}} - F_i^{\text{eval}})^2}{n}} \quad (1.3)$$

where X_i = variables to optimize; n = number of data points; F_i^{exp} = experiment data; and F_i^{eval} = evaluated m

This “Three Network Model” represented the differential material properties of the FSU/IVD complex. In the model, the IVD material is represented using three distinct structural domains that capture the experimentally observed non-linear, time-dependent (and expected temperature-dependent) response at both small and large strains. The governing constitutive equation for the Three Network Model is given in Equations (1.4-1.6). The optimized fit to the experimental data after convergence is presented in Figure 1-16. The final converged “fitness of error” was 9.8 N. The goodness-of-fit (r-squared value) associated with this was 0.98.

$$\sigma_A = \frac{\mu_A}{J_A^e \lambda_A^e} \frac{L^{-1}(\lambda_A^e / \lambda_L)}{L^{-1}(1 / \lambda_L)} \text{dev}[b_A^e] + \kappa(J_A^e - 1) \quad (1.4)$$

$$\sigma_B = \frac{\mu_B}{J_B^e \lambda_B^e} \frac{L^{-1}(\lambda_B^e / \lambda_L)}{L^{-1}(1 / \lambda_L)} \text{dev}[b_B^e] + \kappa(J_B^e - 1) \quad (1.5)$$

$$\sigma_C = \frac{1}{1+q} \left\{ \frac{\mu_C}{J_C^e \lambda_C^e} \frac{L^{-1}(\lambda_C^e / \lambda_L)}{L^{-1}(1 / \lambda_L)} \text{dev}[b_C^e] + \kappa(J_C^e - 1) + q \frac{\mu_C}{J_C^e} \left[I_1 b_C^e - \frac{2I_2}{3} I - (b_C^e)^2 \right] \right\} \quad (1.6)$$

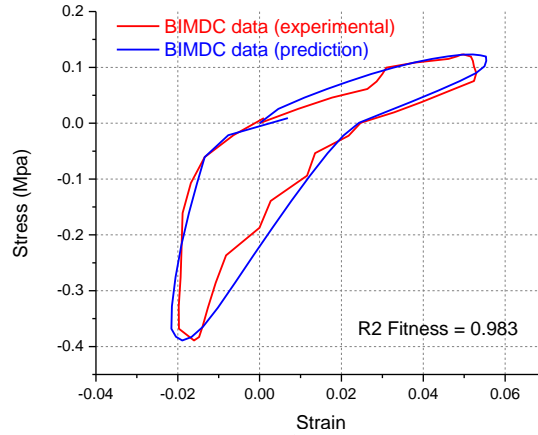


Figure 1-16: Final optimized fit.

1.4 Custom Cervical Collar to Maintain Dual US Probes in Proper Alignment for Imaging Anterior and Posterior C-Spine Anatomic Landmarks In-vivo

A cervical collar, comprised of a modified motocross EVS RS-Evolution (Rancho Dominguez, CA) race collar was developed (Figure 1-17). The collar holds the dual Terason 15L4V US probes against the subject’s neck in the proper orientation to acquire posterior and anterior image projections of the C-spine *in-vivo*. Two articulating arms (Ultraflexx) allow the

contact force against the subject's neck to be adjusted so as to obtain consistent US images. A Tethertools mini-clamp locks each US probe in its final position. The probes and cervical collar did not inhibit neck motions (rotation, flexion and extension) with and without the subject wearing a standard issue Army helmet (Figure 1-18). Dual ultrasound images of anterior vertebral body and posterior spinous process at C4 and C5 levels are shown in Figure 1-19.



Figure 1-17: Custom cervical collar for maintaining position of dual US probes. Anterior probe (left); posterior probe (right).



Figure 1-18: Dual US system on subject wearing army helmet.

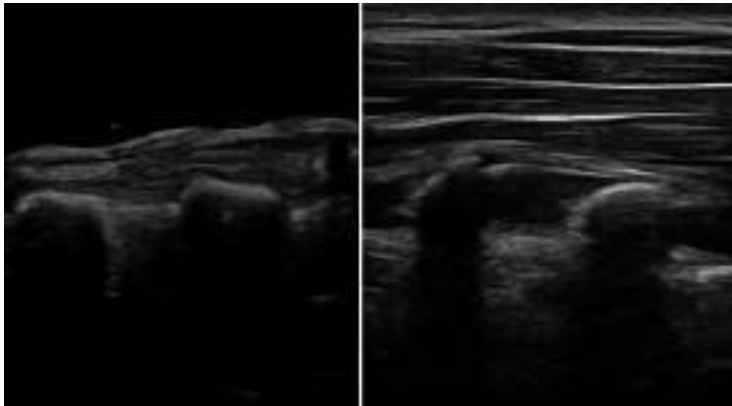


Figure 1-19: B-mode US images acquired from anterior (left, vertebrae body) and posterior (right, spinal processes).

1.5 Using US to Measure C-Spine Motion and IVD Deformation In-vivo to Evaluate Mechanical Properties of the C-Spine During Simulated Conditions With and Without Headgear

In order to derive a transfer function for the mechanical behavior of the cervical spine *in-vivo* in a consistent and reproducible way, a system similar to standard cervical spine traction used by physical therapists to treat neck pain is being developed that can apply cyclic loads to the head and neck over a range of frequencies up to 8 Hz. This system will allow us to conduct a parametric analysis of the effect of varying load amplitudes and frequencies on the elastic and damping coefficients of individual FSU's *in-vivo*. The system is composed of a weighted helmet and a solenoid-based load actuator driven by a programmable DC power supply that applies a variable traction force to the weighted helmet via a pulley/cable system (Figure 1-20). Load transducers mounted in the helmet (in contact with the head) and a force plate on the ground measures the force applied to the head/neck and torso of the subject while sitting or standing.

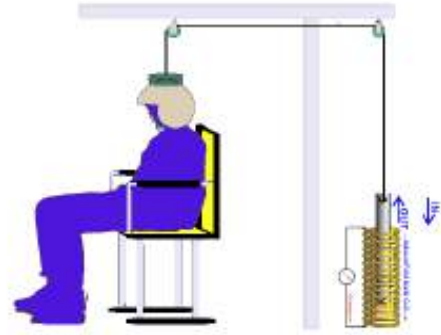


Figure 1-20: Schematic of cyclic load application system to head/neck of subject while sitting or standing in load frame.

The design concept was tested using cadaveric cervical spine specimens (Figure 1-21) and compared to data generated using a servo-hydraulic test system (Instron 8811, Norwood, MA). The applied force was measured with load cell in series with the spine. A 1 Hz square wave with 20-lb load amplitude was applied to the entire cadaveric cervical spine, C1-T1, while the deformation at the C4-5 and C5-6 FSUs were measured in real time using an optical tracking system and dual US probes. The resultant load-displacement curves for the cadaveric C-spine were similar for the solenoid-based traction system and the Instron servohydraulic system (Figure 1-22), however the solenoid-based transducer was unable to dampen the initial impulse of the applied weight to the spine, as evident by transient spikes at initial application of force.

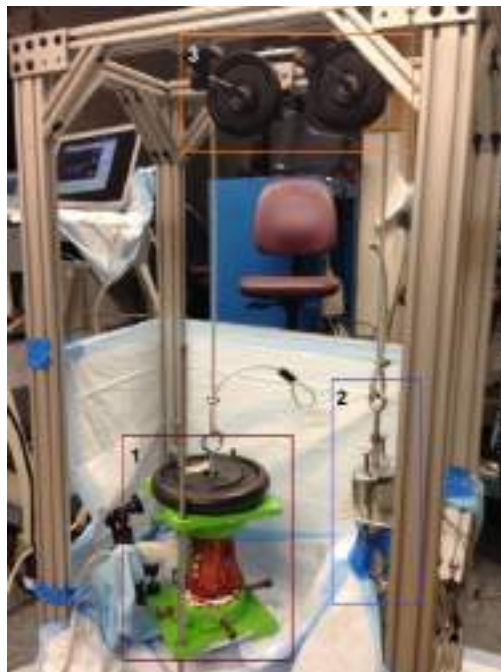


Figure 1-21: The prototype load frame system. Spine specimens are mounted in the frame and a fixed weight [Box 1] is rigidly mounted to the atlas vertebra, C1, to provide a constant compressive force to the entire C-spine. A solenoid-based load actuator (Magnetic Sensor Systems, Van Nuys, CA) [Box 2] driven by programmable DC power supply (Genesys, TDK-Lambda, NJ) applies a variable traction force to the fixed weight via pulley/cable system [Box 3] so that a known, variable, cyclic load can be applied to the spine while the resulting displacement of the FSUs are measured by US and optical tracking (reflected markers shown on spine [Box 1]).

The deformation between C4 and C6 measured by the US probe was affected by bulging of the IVD and soft tissues during compressive loading as evidenced by the dicrotic wave form observed consistently during compression at the “valley” of the cyclic displacement curve for both the servo-hydraulic and solenoid-based load actuators. However, the deformation of C4-6 measured by the US probe in distraction was also affected by high frequency vibrations induced by the traction impulse applied to the spine by the solenoid actuator (Figure 1-22).

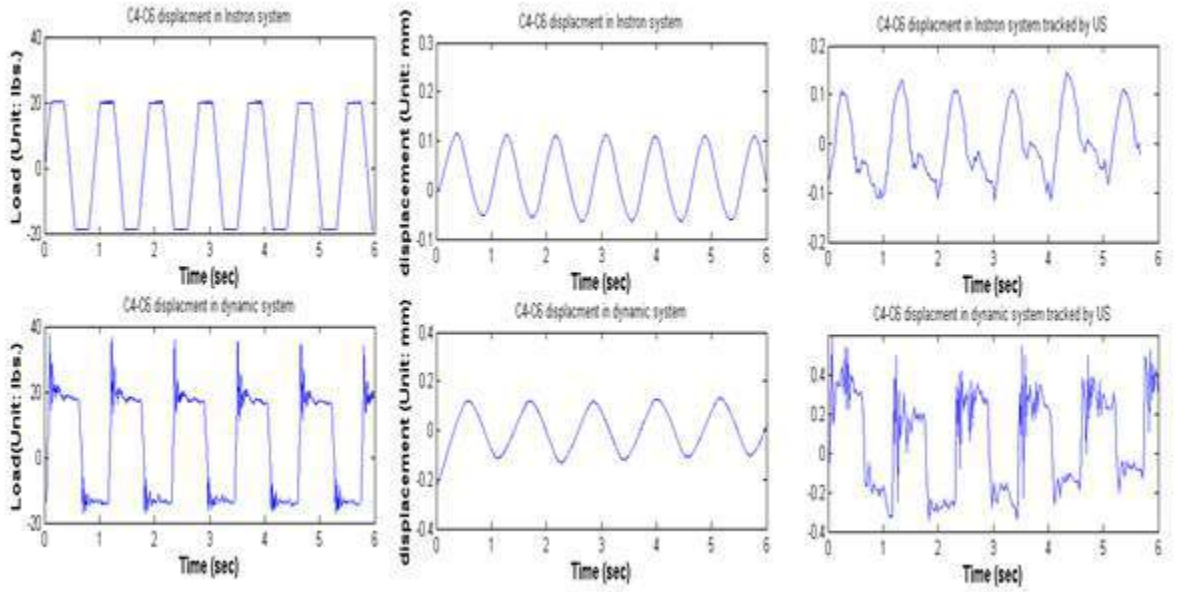


Figure 1-22: Comparison of load and displacement values measured directly and using US for C4-C6 using Instron vs. solenoid-based traction system for cadaver specimens.

We also tested the solenoid-based traction system on ourselves. A 10-lb load was applied to the neck, cyclically alternating between distraction and compression (Figure 1-23). To ensure that the central axis of the head and neck were collinear with the applied uniaxial force, a 5-point latch & link restraint system was used to fix the torso of the sitting subject in the load frame along the line of action of the cable. So that load is safely applied to the neck, the subject wears a well-padded, tight fitting helmet with an attached 10 lb. weight that applies a constant compressive load to the spine which is then “unloaded” by the application of an increasing traction force generated by the solenoid-based load actuator via a cable attached to the weight. A load cell interposed between the weight and the helmet measures the resultant force applied to the neck in real time (iLoad Mini, Loadstarsensor, Fremont, CA). For this preliminary trial, a square-wave function was used to apply a 0 to 20 lb traction force via the solenoid to cyclically load the neck between -10 to +10 lbs. The dual US system was used to measure the resulting dynamic motion of the C4-5 and C5-6 FSUs. The anterior US probe imaged the anterior profile of the C4-5-6 vertebral bodies and interposed discs, and the posterior US probe imaged the profiles of the corresponding spinous processes.

Preliminary test data is shown in Figure 1-24. Similar to the cadaver test, the initial impulse applied to the head/neck by the traction load generated by the solenoid actuator created undesirable high frequency vibrations at the initiation of the applied step loads. These transmitted vibrations were reflected in the measured C4-C5 displacements. These high frequency vibrations will be addressed by interposing a spring to dampen the initial load

impulse. Alternatively, a pneumatic powered load actuator might allow more controlled load application than the solenoid-based actuator.



Figure 1-23: (left) Solenoid powered traction system for applying cyclic loads *in-vivo*: a programmable DC power supply is used to power a solenoid that applies a variable traction force via two fixed pulleys to a fixed weight attached to the top of the helmet; (middle) front view; (right) a side view demonstrating restraints and dual ultrasound probes positioned on the subjects neck anteriorly and posteriorly in a fixed orientation.

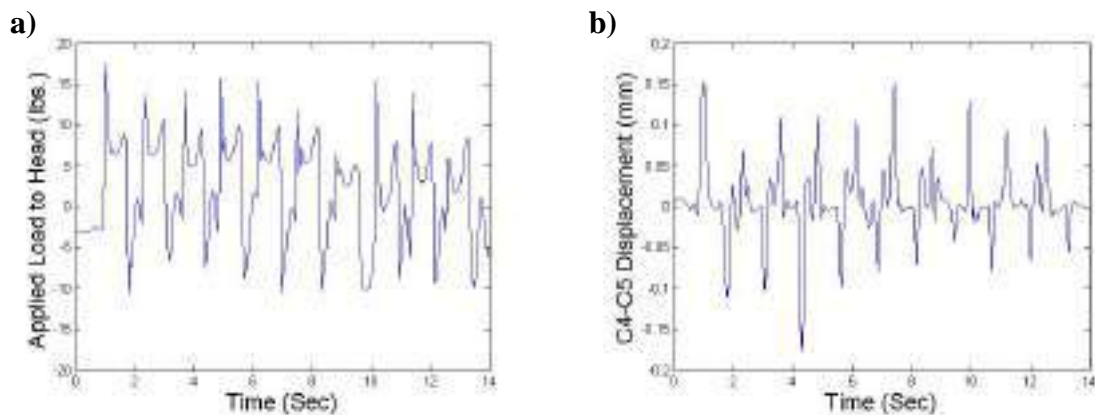


Figure 1-24: (a) Cyclic tensile/compressive step load applied to head; (b) Resultant C4-C5 displacement measured by US.

1.6 Analytic Models Developed from Ex-vivo Simulations to Specify Permissible Load Amplitudes, Load Rates, and # of Cycles for Different Loading Modes

A finite element model of C4-C7 developed from CT scans of cadaveric human C-spine has been developed (Figure 1-25). The osteo-ligamentous material properties assumed for each of the elements were ascertained from the literature. The model was then subjected to pure flexion and extension moments similar to the experiments performed in task 3. The overall rigid body motions of the vertebrae and deformations of the IVD and interposed ligaments were extracted from the displacement map. Predicted responses were within the mean \pm one standard deviation of the experimental data (Figure 1-26). The resultant motion of the FSU's and deformation of the IVD in flexion and extension are shown (Figure 1-27). These results suggest that this model can be interfaced with the force-displacement data generated from the *in-vivo*

traction-compression loading and FSU displacements measured by the dual US system as part of 44e5 to calculate local osteo-ligamentous strains and IVD deformation in response to applied external loads.

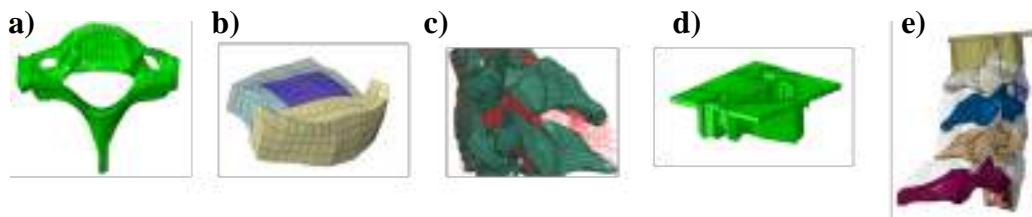


Figure 1-25: Finite element representations of subaxial cervical vertebra. (a) top view; (b) axial view of intervertebral disc; (c) sagittal view of facet joints; (d) loading device; (e) sagittal view of the C4-C7 spinal column with loading device at the superior end.

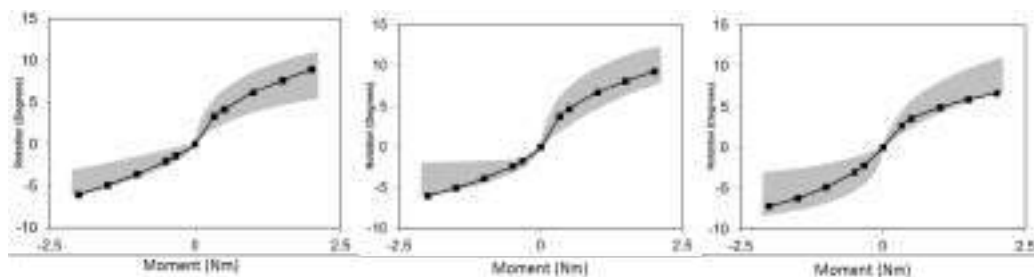


Figure 1-26: Moment-rotation kinematics of C4-C5-C6 motion segments subjected to physiological flexion-extension moments.

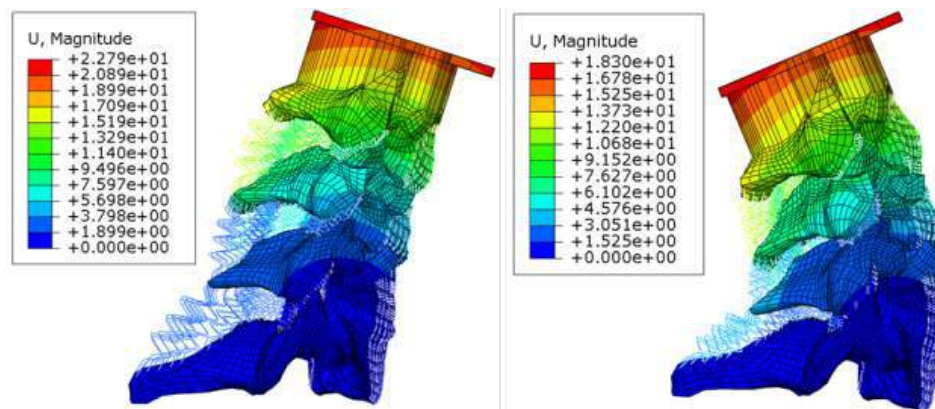


Figure 1-27: Displacement heat map of C4-C5-C6 motion segments subjected to physiologic flexion moment (left) and extension moment (right). Color scale represents the magnitude of deformations represented by the elements.

The FEM of the cervical spine was updated to be more relevant to the military population. It has improved geometry, uses a finer mesh, has an increased number of elements and includes an additional spine segment. These refinements will improve the capability of the FEM to simulate different types of loadings and expand the model's responsiveness making it more suitable to carry out parametric studies.

The geometry of the cervical spine FEM was updated using data from the Global Human Body Model Consortium. In the previous FEM, the nodes at the inferior margin of the C7 vertebrae were constrained. The T1 vertebra was added to the updated model to better represent the foundation of the cervical spine. The updated model (C4-T1) is based on anthropometric specifications for a mid-size male (175 lbs), in contrast to the previous generic model generated from a female cadaver. Since this model was developed for use in LS-DYNA software, it needed conversion to the ABAQUS solver to perform stress analysis. As the two finite element software packages have different built-in material models and element types, the conversion tasks included: input deck compatibility, element type compatibility, and material model compatibility. The previous FEM consisting of 18731 mesh elements and 24086 nodes was improved to have a finer mesh consisting of 65316 elements and 48302 nodes (Figure 1-28). The finely meshed IVDs at C4-5, C5-6, C6-7 and C7-T1 better mimic the actual geometry (Figure 1-29). Tie constraints between the bony endplates of the vertebrae and cartilaginous endplate of the discs were added to all segments.

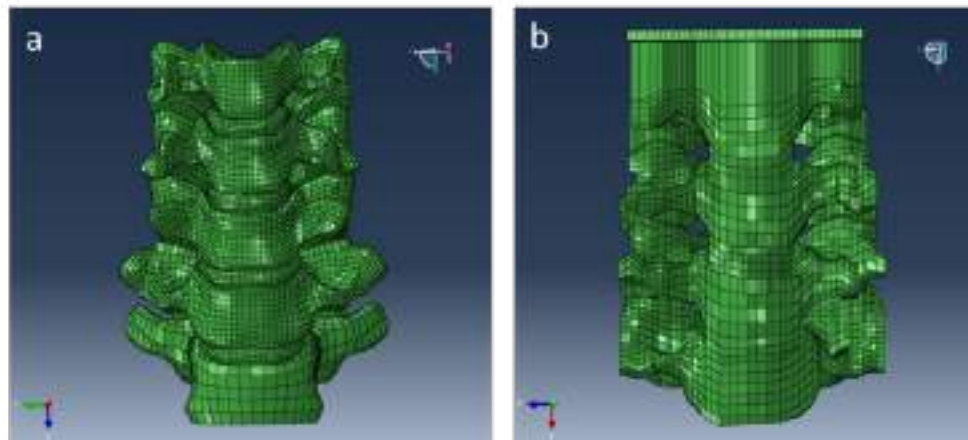


Figure 1-28: Coronal views of (a) updated C4-T1 FEM and (b) previous C4-C7 FEM.

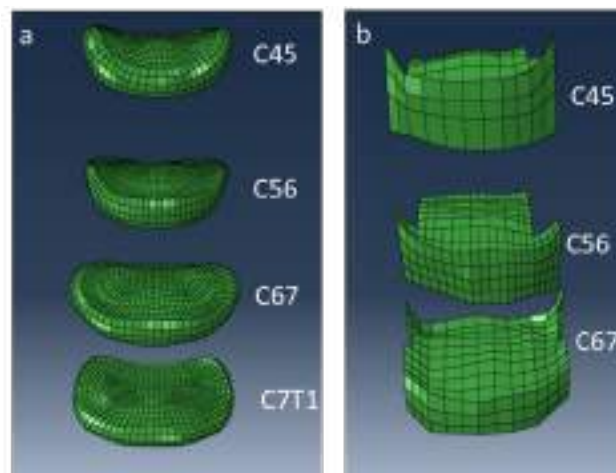


Figure 1-29: Geometry of IVD for (a) updated C4-T1 FEM and (b) previous C4-C7 FEM.

In addition, elements corresponding the ligaments and soft tissue connections that provide stability to the cervical spine FSUs were added (Figures 1-30 and 1-31). For the anterior

longitudinal ligament, a total of 324 connector elements were used between C4 to C7 (12 elements wide and 27 elements long). Elements representing the interspinous ligaments, facet joint capsule and ligamentum flavum are now included in the updated FEM.

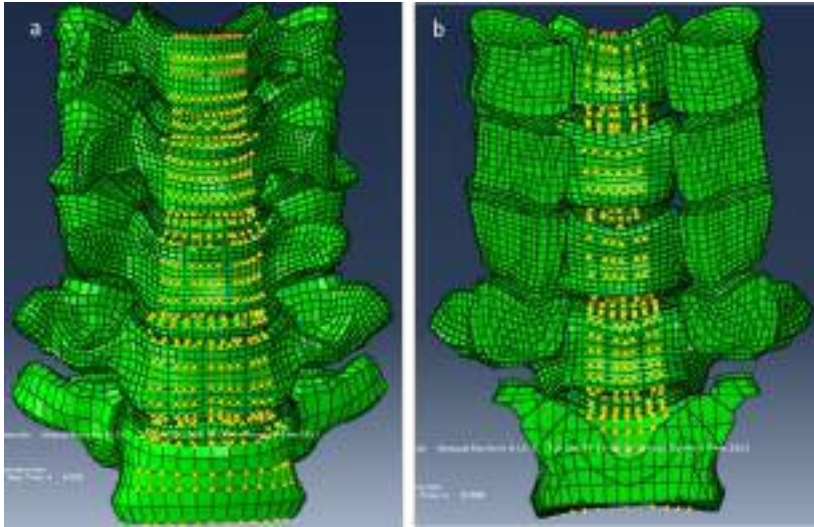


Figure 1-30: Ligament attachments to the updated model shown by sectioning C-spine in coronal plane. (a) Anterior longitudinal ligament; (b) Posterior longitudinal ligament.

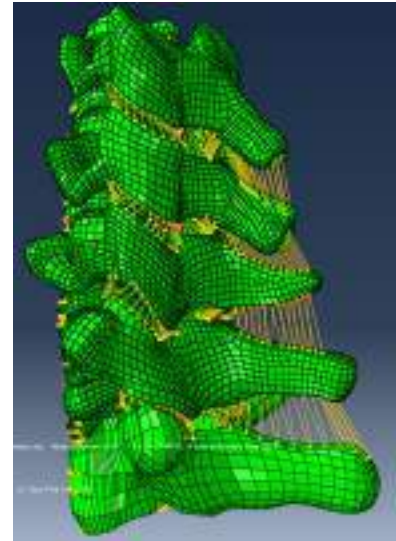


Figure 1-31: Updated model showing the facet joint capsule, interspinous ligament and ligamentum flavum.

A rectangular plate was attached to the superior endplate of the C4 vertebrae using mesh manipulation software (ANSA). The plate helps in the application of pure moments by applying a force couple along anterior and posterior edges of the plate. The plate can be also be used to simulate other experimental load scenarios and the mass imposed by a helmet.

During the next quarter the finite element analysis will proceed as follows:

1. Subject the updated model to experimental *ex-vivo* and *in-vivo* load conditions.
2. Extract internal parameters such as stresses, strains and strain energy densities in various regions of the disc from the abacus solver, from stress analysis outputs.
3. Use outputs extracted in step two and include experimental output conditions: incorporate the US-measured deformation/strain fields over the fatigue period, simulating cyclic loading conditions, to a fatigue solver.
4. From the fatigue solver, determine the 'life span' of the spine for the inputted experimental condition, described in step one.
5. Exercise the finite element stress analysis and fatigue solver models to different parametric conditions such as the effect of added mass and locations that may be off-center from the center of gravity/mass of the neck to predict the 'life span' under these conditions.

Year 2: Apply US system in-vivo to evaluate static and dynamic mechanical behavior of C-spine during running, jumping and simulated operational conditions. Apply acquired in-vivo data as load/displacement boundary conditions to FEM of C-spine.

2.1 US System Development and Validation (Continuation of Aim 1, Task 1 & 2)

A blockmatching algorithm was used to compare two consecutive US images and map the lateral (i.e. perpendicular to U/S beam) and axial (parallel to U/S beam) displacement of pixels forming the image profiles of the vertebrae. This algorithm was previously validated using *ex-vivo* cadaver cervical spines. However during real time *in-vivo* tracking of cervical vertebrae, new challenges emerged that did not occur in the cadaver test: it was difficult to maintain the dual ultrasound probes in the standardized fixed position in direct acoustic contiguity with the vertebrae during dynamic flexion/extension motion. The previous methods failed to correct signal drift, which was accumulated during long duration US tracking. Accuracy of FSU kinematics especially during high frequency motion was limited.

Based on the work of Rahimi et al. [14], we developed a mathematical model suitable to correct signal drift during tracking of vertebrae during long duration ultrasound imaging. This method relaxes the restriction that only temporally adjacent ultrasound frames are compared (known as frame-to-frame tracking) to calculate the relative interval motion of the vertebra. It allows high-quality, non-sequential measurements to be used in-lieu of poor quality, sequential measurements. When estimating the position of vertebrae, the motion tracking method accounts for the change in position between the current frame and the previous frame, as well as other previous spatially related image frames tracking the position of the vertebra. This expanded set of high quality US images is now used to analyze the ultrasound radio frequency (RF) data.

The accuracy and precision of US measurements of vertebral motion were validated using a PMMA phantom to track rigid body motion over a range of frequencies. A PMMA block was secured to the actuator piston of a servohydraulic materials testing machine to which 1mm sinusoidal displacements were applied over a range of frequencies for 20 seconds (1000 frames). The block was fully immersed in a water bath to allow acoustic coupling to the US probe. The applied displacement was compared between direct measurements from the linear voltage differential transformer (LVDT) in line with the actuator and that derived using a single US device and the motion tracking software (Figure 2-1).

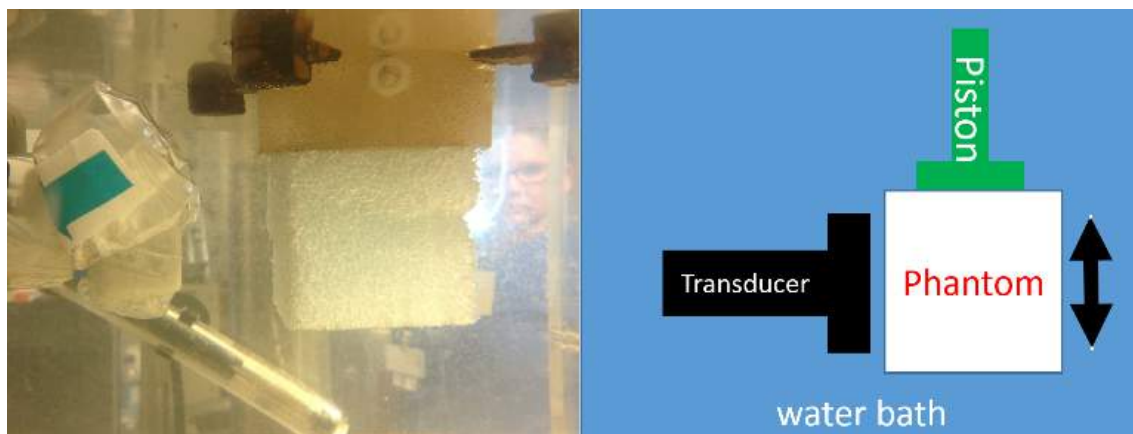


Figure 2-1: US imaging of PMMA phantom secured to actuator piston of materials testing machine. Measurements were compared between derived displacements using tracking algorithm and LVDT.

Six different regions of interest (ROIs) on the phantom were chosen to evaluate the precision of the tracking algorithm. For applied frequencies 1-8 Hz, the mean absolute error (MAE) between translational motion measured using the US tracking system and the LVDT ranged from 0.0227 to 0.0508 mm (Figure 2-2). The overall average MAE of US measurements was 0.041 mm. No drift was observed during the course of scan (1000 frames). Accuracy was not significantly affected by motion frequency. Assuming typical IVD deformation of 0.8 mm under 150 N load, this corresponds to a 6.3% precision error in the US measured strain.

Software using the new tracking algorithm has been integrated into dual US package. The software has graphic user interface (Figure 2-3), which allows the operator to analyze the relative displacements of cervical vertebrae and the deformation of intervertebral discs (IVD). The program is written on C++ under open source framework and the executive files are compatible with different systems (tested in PC and Mac), which makes the dual ultrasound system (US) usable as a stand-alone system to acquire cervical spine motion data to calculate kinematics and IVD deformation.

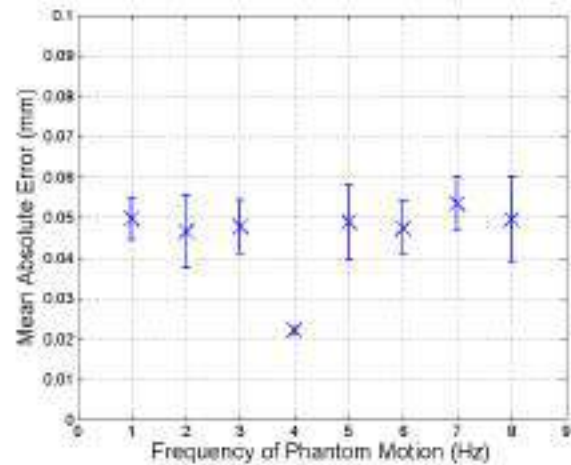


Figure 2-2: The mean absolute error between US and LVDT measurements of phantom motion as function of applied frequency.

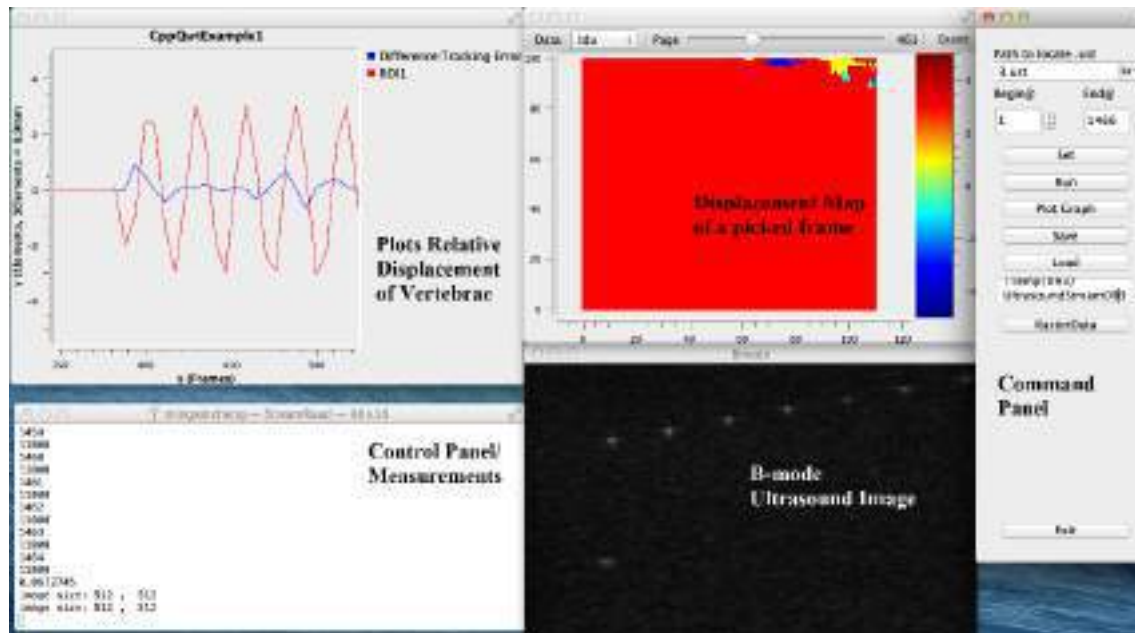


Figure 2-3: Graphic user interface (GUI) of tracking software which allows users to analyze displacement of objects. (top left) Displacement curve; (top middle) displacement map between frame pairs. Since we are applying this program to track a rigid phantom, all points inside phantom show the same displacement. (bottom middle) B-mode image of phantom; (bottom left) measurements/image details.

2.2 *Ex-vivo Hydration vs IVD Compliance and Cervical Spine Health and Integrity (Task 4 & 6)*

Methodology to measure the mechanical properties of single and contiguous FSUs using intact cadaver specimens C2-C7 was developed. Previous *ex-vivo* experiments were conducted on isolated cervical spine FSU's which fail to replicate physiological conditions, especially the lordotic curvature of C-spine.

Contiguous segments C2-C7 from an 84-year-old male were used to develop the protocol. The posterior skin was retained to provide acoustic coupling for the dual US probes. The trachea and anterior skin were removed, but paracervical muscles and ligament were retained to maintain the tensile and compressive properties of the connective soft tissue envelope. The C2 and C7 vertebral bodies were potted in liquid plastic. Using minimally invasive technique, uniaxial, 5 mm diameter titanium pedicle screws were placed into the vertebral bodies, just anterior to the transverse process, under fluoroscopic guidance. To maintain the cervical lordosis, a slightly bent, 5 mm diameter stainless steel interconnecting rod was secured in the tulip head connectors of contiguous pairs of pedicles screws, rigidly secured with set screws. Our method was slightly modified from pedicle screw placement protocol. The pedicle screws were placed in the vertebral bodies in an anterior-posterior (A-P) position to better control (limit) flexion/ extension motion of "instrumented" FSU's during cyclic mechanical testing. By using variable lengths of interconnecting rods secured to different pedicle screw levels, different combinations of FSU's could be fixed or mobilized. The specimen was mounted in material testing system (Instron 8511, Norwood, MA) and loaded from 20 lbs of compression to 20 lbs of tension. Fluoroscopic images captured the position of the vertebral bodies during different loading conditions (Figure 2-4). Dual US transducers were positioned anteriorly and posteriorly to image the IVD and vertebral bodies anteriorly and spinous processes posteriorly. There was no movement between the fixed FSUs during compression and tension (Figure 2-5), while the "empty" pedicle screws did not interfere with the motion of the mobile FSUs.

The stiffness and damping coefficients of the C4-C5 FSU (most common level of degenerative disease) were correlated with qualitative grading (Pfirrmann scale) of the IVD on MRI images (Figure 2-6**Error! Reference source not found.**). The ability of the dual US system to measure the biomechanical properties of the FSU was further validated by tracking the deformation of the C4-C5 FSU in real time during a standard creep test. Five fresh frozen, cadaveric human cervical spines, C2-T1, ages 54 - 67 years (Medcure, Portland, OR) were defrosted, the trachea, esophagus, and skin were removed. The surrounding para-cervical muscles and adipose tissue were retained. Each spine was subjected to 150 N compressive creep test. Using minimally invasive technique, uniaxial, 5 mm diam. titanium pedicle screws were placed into the vertebral bodies under fluoroscopic guidance. Steel rods were used to fix C2-C4 FSUs and C5-T1 FSUs. The deformation of the C4-C5 IVD was measured by the dual US system



Figure 2-4: Cadaver testing with dual US and C-arm X-ray.

and correlated with the real-time applied load.

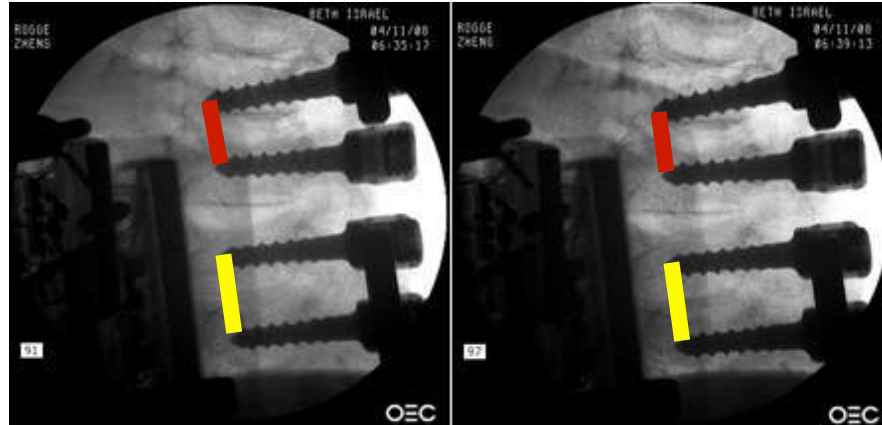


Figure 2-5: X-ray images of 20 lbs of tension (red) and 20 lbs of compression (yellow). Black shadows are US transducers. Relative motion occurred between mobile FSU levels (red bar length change = 0.1435 mm), while no motion occurred between fixed FSU levels (yellow bar length change = 0.029 mm, image resolution of X-ray is 0.3mm).

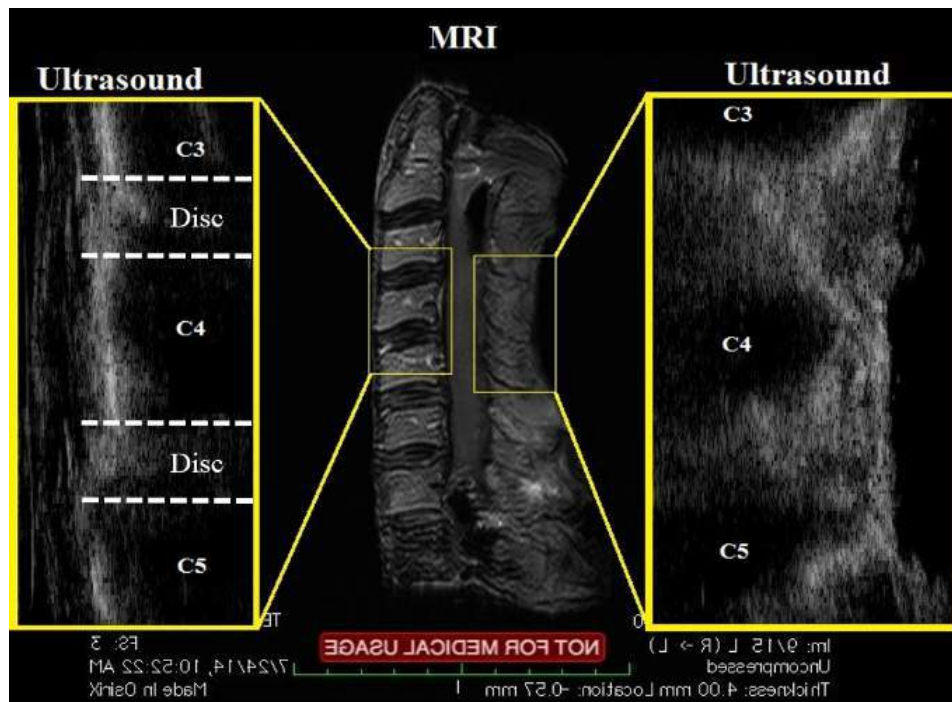


Figure 2-6: Ultrasound B-mode images are compared to MRI sagittal images of cadaveric C-spine. US provides a magnified window of FSUs in cadaver. One US probe acquired anterior vertebrae body while the other imaged posterior spinal processes.

Stiffness and damping coefficients of C4-C5 FSU were derived assuming a standard Voigt model comprised of an elastic spring and a viscous damper connected in parallel. Multivariate Linear Regression was used to calculate the stiffness of the elastic spring and the damping coefficient of viscous damper. These derived mechanical properties were compared to the structural integrity of the IVD measured on T₂ weighted MRI images of each FSU based on the Pfirrmann grading system, which is the clinical standard for evaluating the “health” of the IVD.

Grade 1 is healthy hydrated disc that shows homogeneous brightness on T₂ MRI image while black, collapsed, dehydrated IVD on T₂ MRI image is graded 5.

Table 2-1: Material properties of C4-C5 FSU measured by dual ultrasound system.

2.3 In-vivo Ultrasound Test in Simulated Environment (Task 7)

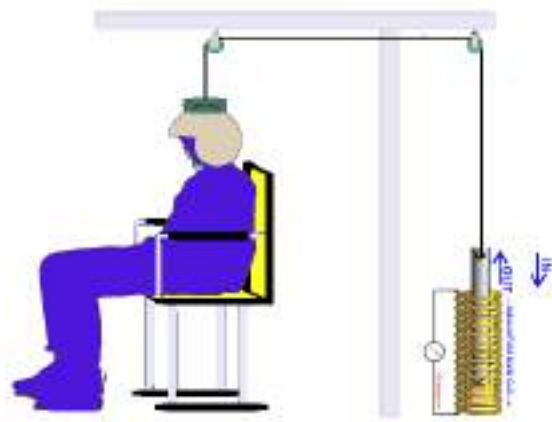




Figure 2-8: Solenoid powered traction system for applying cyclic loads in-vivo.

To ensure that the loading axis of the head and neck were collinear with the applied uniaxial force, a 5-point latch & link restraint system was used to fix the torso of the sitting subject to the load frame along the line of action of the cable. We tested the solenoid-based traction system on ourselves by performing static and dynamic analysis of the compliance of C4-C5.

The geometry of the vertebrae is assumed to remain constant during the course of the test.

The surface contours of the cervical vertebrae imaged by the dual ultrasound probes can be depicted as a simplified 2D rigid-body (Figure 2-9). A global Cartesian coordinate system is fixed relative to the torso. The anterior and posterior motion of the C4-C5 FSU is represented by two vectors \vec{r}_A (vertebral body endplate motion) and \vec{r}_P (posterior element motion). The deformation of the C4-C5 IVD is estimated from the average displacement of these two vectors, while the flexion/extension angle of C4-C5 is estimated by calculating their vector cross-product:

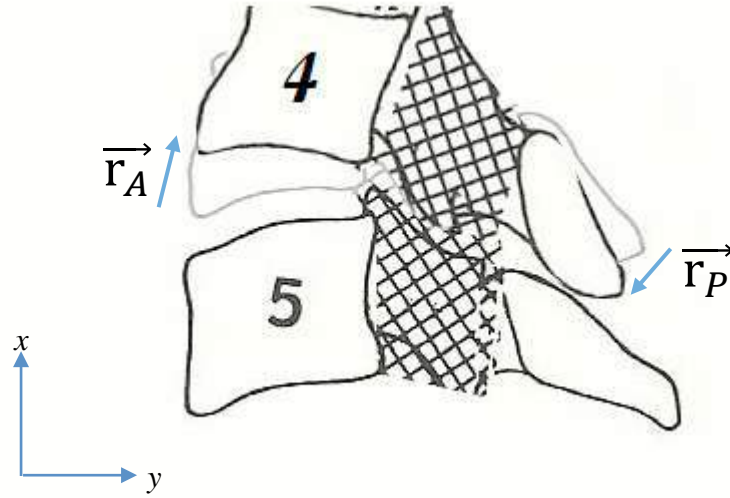


Figure 2-9: Simplified rigid body representation of cervical spine and coordinate system. The anterior profile of the vertebral body and IVD is imaged by the anteriorly positioned US probe, while the facet joint (cross-hatched region) and spinous process is imaged by the posteriorly positioned US probe ($\sim 60^\circ$ relative to the anteriorly positioned probe).

$$Displacement = \frac{|\vec{r}_A| + |\vec{r}_P|}{2}$$

$$Angle = \arctan \frac{r_{Ay} + r_{y0}}{r_{Ax} + r_{x0}} + \arctan \frac{r_{Py} + r_{y0}}{r_{Px} + r_{x0}}$$

where $r_{Ax}, r_{Ay}, r_{Px}, r_{Py}$ are the components of \vec{r}_A, \vec{r}_P in the superior-inferior (X) and anterior-posterior (Y) directions, respectively in the loaded configuration and r_{x0} and r_{y0} are the components of these vectors in the unloaded configuration.

Static Testing: A static force from -10 lbs (compression) to +15 lbs (traction) was applied incrementally to the cervical spine using our controlled traction system (Figure 2-10). The dual US system measured the resultant C4-C5 FSUs displacement and angular motion (Figure 2-10). The static compliance was derived from the slope of the displacement vs. load curve deduced by linear regression (Figure 2-11).

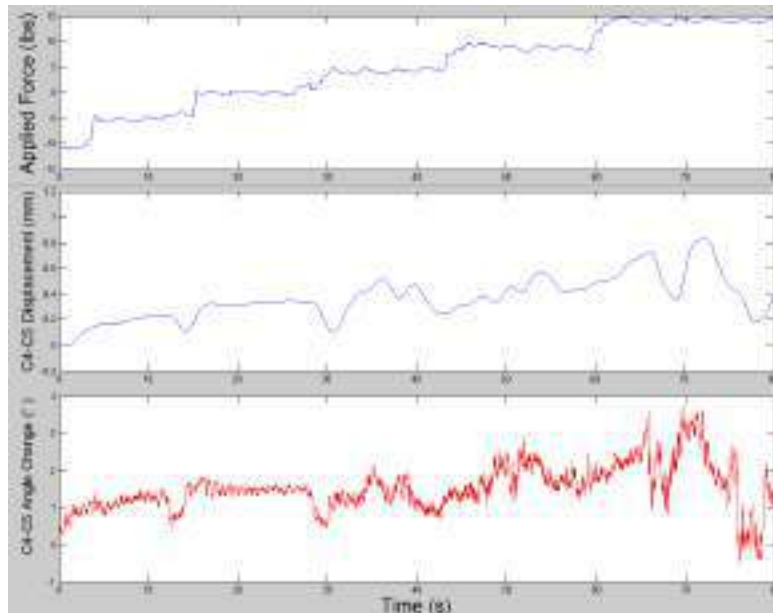


Figure 2-10: Sequential step loads applied to the head and neck with resultant C4-C5 displacement and flexion/extension angle measured by US. The morphology of load-time curve and displacement-time curve demonstrated that the IVD displacement at C4-C5 correlated with the applied axial force. The resultant angular deformation implies that the applied axial force also exerts a moment on the cervical spine, a consequence of either the natural cervical spine lordosis, misalignment between the line of action of the applied load and the neutral axis of the cervical spine or voluntary muscle contraction by the subject

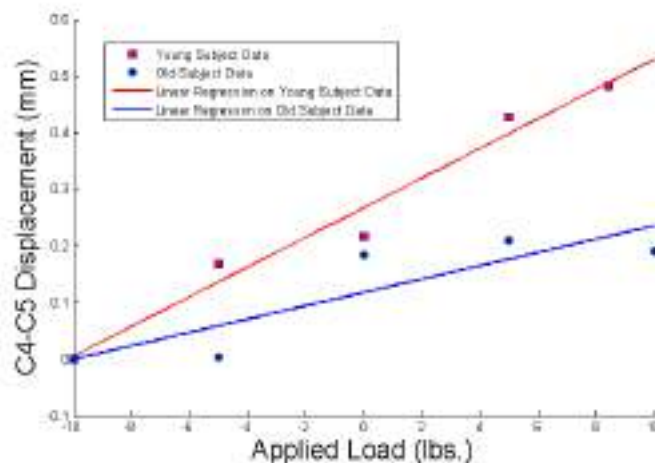


Figure 2-11: Elastic compliance of C4-C5 FSU using solenoid-based traction device to apply static incremental loads $R^2 = 0.97$ (red, 25 y/o subject), 0.76 (blue, 56 y/o subject). FSU tended to be more compliant for the younger human subject (0.00589 mm/N) compared to older subject (0.00265 mm/N).

Dynamic Testing: The feasibility of using US to measure the dynamic mechanical properties of cervical spine FSUs was explored by cyclically loading the neck between 0 to +20 lbs. The applied load was a square-wave function (Figure 2-12a), the resultant displacement was highly non-linear (Figure 2-12b) exhibiting two distinct phases during loading and unloading: 1) there

was little FSU displacement during the application and release of the traction load impulse; 2) there was creep deformation during the phase that the applied load was held constant. Analysis in the frequency domain facilitated derivation of the dynamic compliance, while the damping effect was calculated from the area under the displacement-load curve which physically represents the work lost in each cycle.

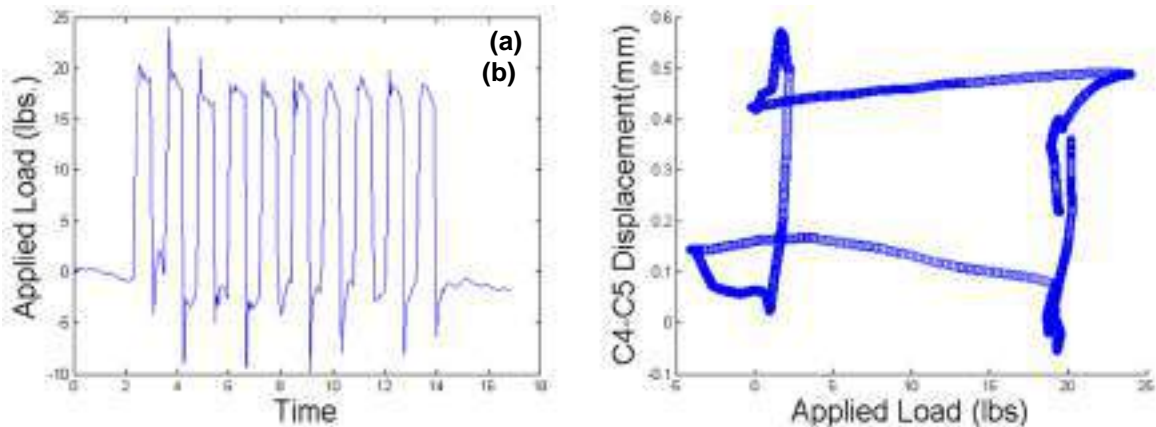


Figure 2-12: (a) Cyclic tensile step load applied by solenoid actuator; (b) Resultant C4-C5 FSU deformation measured by dual US system.

Dynamic frequency analysis demonstrated the relative power spectra of applied loads and displacements (Figure 2-13). The highest peak in the frequency spectrum corresponded to the load and displacement at the applied frequency of the square wave and was used to filter out higher frequency “noise”. Dynamic compliance was derived from the ratio of the C4-C5 FSU deformation in response to the applied load at the applied frequency. The 25 y/o subject had a more compliant C4-C5 FSU than the 56 y/o subject at all frequencies, but the compliance decreased at higher frequencies. The compliance of the C4-C5 FSU for the 56 y/o subject changed little as a function of the applied frequency (Table 2-2**Error! Reference source not found.**). The damping coefficient was more affected by frequency than age (Table 2-3).

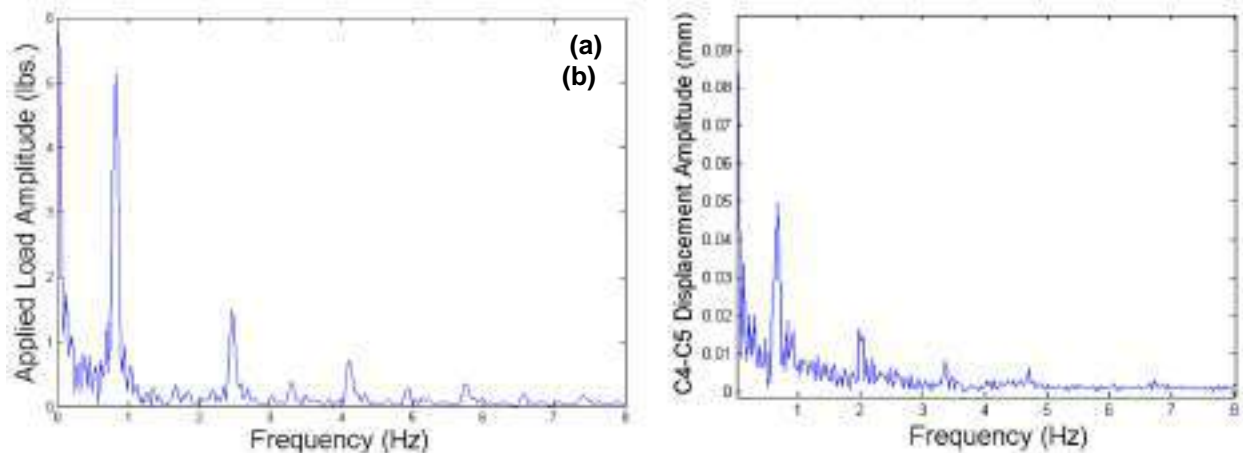


Figure 2-13: (a) Frequency analysis of applied load waveform (b) C4-C5 displacement measured by dual US in frequency domain.

Table 2-2: Dynamic compliance as a function of applied frequency and age

Frequency of load applied to neck	Dynamic Compliance (mm/N)		
	1 Hz	2Hz	3Hz
Younger Subject	0.0306	0.0242	0.0098
Older Subject	0.0111	0.0147	0.0123

Table 2-3: Work loss as a function of applied frequency and age

Frequency of load applied to neck	Work Loss Area Estimate (N × mm)		
	1 Hz	2Hz	3Hz
Younger Subject	39.28	64.81	75.03
Older Subject	42.95	64.23	127.13

While this data is preliminary and limited to the PI and his graduate student, it demonstrates the promise of the proposed dynamic actuator to apply static and dynamic loads to the C-spine in a controlled, parametric fashion while simultaneously measuring the resulting deformation of C-spine FSUs using the dual US system thereby allowing calculation of the mechanical properties of the cervical spine *in-vivo* that dictate its functional performance. Differences in the transport of water through the poroelastic matrix of the IVD (which will be investigated further using diffusion-based MRI) may account for the apparent effect of age and applied frequency on the compliance of the FSU. Additionally, reflexive contraction of the paracervical muscles to dampen forces applied to the cervical spine at higher loading frequencies could also account for the observed decrease in compliance and increase in energy dissipation at higher applied loading frequencies. EMG measurement of the activation of the paracervical muscles will elucidate this further.

These preliminary data identified a significant shortcoming of the solenoid actuator to apply cyclic distraction/compression loads at frequencies and amplitudes that will facilitate derivation of a universal transfer function for the mechanical behavior of the cervical spine FSUs *in-vivo* in a consistent and reproducible fashion or allow the application of different load profiles (sinusoidal, square wave, triangle, combinations thereof) that simulate the forces and moments applied to the head and neck of mounted troops during military maneuvers. Therefore we have developed a new system that uses a pneumatic powered load actuator that will allow more controlled cyclic load applications (Figure 2-14**Error! Reference source not found.**).

In this new design, the force is applied vertically through the seat that the subject is seated, transferred up the spine to the head and neck, which is secured in a helmet rigidly fixed to an adjustable cross-bar. At the point of attachment of the helmet to the cross-bar, there is a safety clutch that “breaks” for any applied load exceeding 25 lbs of tension or compression (Figure 2-14B). Four co-axial linear bearing attached to the seat ensure precise up/down vertical movement without binding (Figure 2-14C). The maximum extension of the actuator is limited by a separate position sensing system. To safeguard against the risk of irregular air flow to the actuator, two redundant valves were added with an electronic PSI regulator. Additional safety features include an emergency “stop” switch that can be activated by either the subject or technician. Validation of the system and a full safety evaluation is being conducted using a Crash dummy (Humanetics, Plymouth, MI), an established test device in accordance with the USA Code of Federal

Regulations. The dummy (Figure 2-15) has two 6-axis load cells on the top and bottom of its simulated C-spine, which provide real time load data applied to the neck. Preliminary studies on the break-away device were performed. The break-away device consists of 4 sets of commercially available wire break-away connectors (DCD Design, British Columbia, Canada), that break when the applied load exceeds the strength of internal wire. Repetitive loading studies that applied hyper-extension and hyper-compression to the dummy's spine demonstrated that the device released at -245.0 ± 9.1 N (≈ 50 pounds) compressive load for a maximum applied flexion moment of 9.1 ± 3.4 Nm and 291 ± 28 N (≈ 60 pounds) for a maximum applied extension moment of 14.1 ± 8.5 Nm (Table 2-4). This exceeds our design criteria of 25-30 lbs maximum load to be applied to the spine elements, so customized wires from manufacturer will be used to attain this safety standard.

Cyclic loading of the dummy was attempted at different frequencies (1-5 Hz). At frequencies higher than 2 Hz the pneumatic actuator was unable to apply a symmetric load-displacement curve; the rate of the applied load to lift the seat and dummy was slower than the rate of unloading. This is a result of the difference in the rate of pressurizing and depressurizing the pneumatic actuator. To compensate, we will use dead weights equivalent to the weight of the subject and the seat to "tare" the system, so that the pneumatic actuator only applies ± 25 lbs. Cadaveric torsos with attached cervical spines C2-C7 will also be tested in this device prior to any *in-vivo* human tests to further establish the capabilities of the system to measure cervical spine FSU kinematics and IVD deformation. These data will be compared to similar tests conducted on isolated cervical spines using the Instron servohydraulic test system.

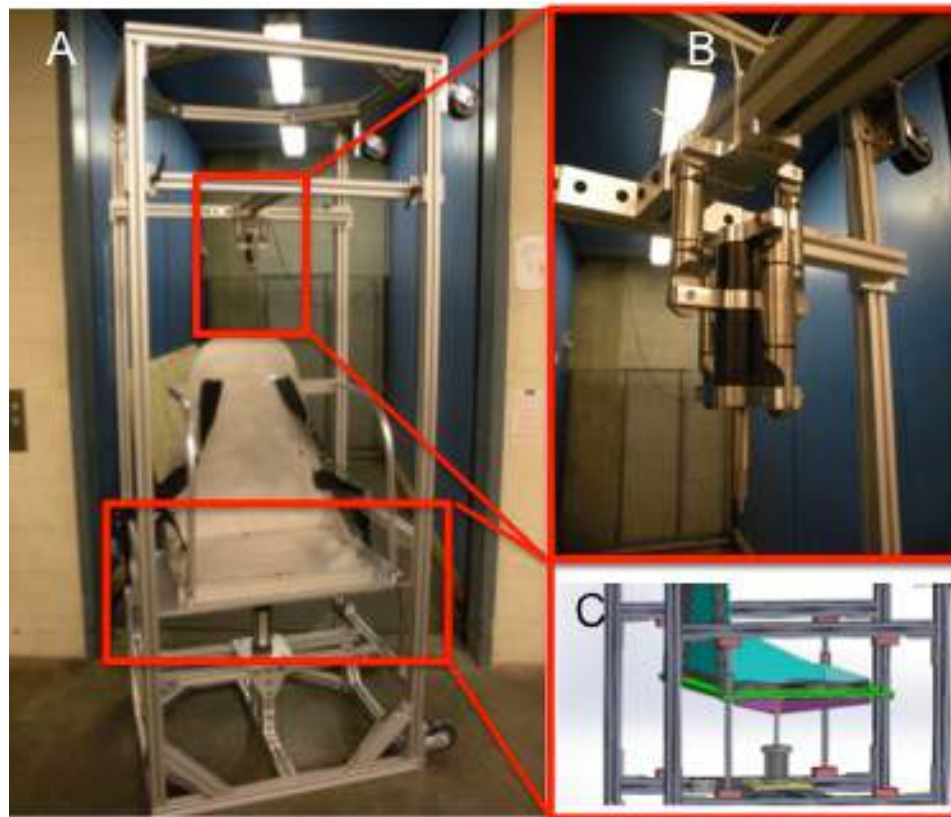


Figure 2-14: (A) front view of the updated design; (B) safety device release when applied force exceeds limit; (C) Lateral view of linear bearings and actuator placement.



Figure 2-15: lateral view of the dummy in spine cyclic loading system and its Cartesian coordinates system.

Table 2-4: Force and moment applied to neck when safety device breaks away.

		Extension		Compression	
		Average	Std. Dev.	Average	Std. Dev.
Upper Neck (C1)	<i>x-Axis Force (N)</i>	66.6	8.7	-67.9	6.1
	<i>y-Axis Force (N)</i>	11.2	8.8	-7.5	1.3
	<i>z-Axis Force (N)</i>	272.3	28.8	-232.2	13.4
	<i>x-Axis Moment (Nm)</i>	1.0	0.8	-0.3	0.1
	<i>y-Axis Moment (Nm)</i>	-1.7	3.1	-3.3	1.1
	<i>z-Axis Moment (Nm)</i>	0.7	0.4	-0.7	0.2
Lower Neck (C7)	<i>x-Axis Force (N)</i>	61.2	9.4	-53.0	9.7
	<i>y-Axis Force (N)</i>	15.0	5.2	-6.6	1.0
	<i>z-Axis Force (N)</i>	290.9	27.9	-245.0	9.1
	<i>x-Axis Moment (Nm)</i>	1.8	1.1	-0.7	0.2
	<i>y-Axis Moment (Nm)</i>	14.1	8.5	-9.1	3.4
	<i>z-Axis Moment (Nm)</i>	1.0	1.0	-0.5	0.0

2.4 FE Model Validation and Modification (Task 11) and Simulating Operation Loading Conditions (Task 12)

Finite element (FE) modeling for prediction of fatigue-related material property changes in cervical spine soft tissues is ongoing. N-code (HBM, Southfield, MI), was used to determine fatigue in the disc and it was able to reproduce fatigue in terms of number of cycles for a prescribed compressive load. However the formulation for calculation of stress-number of cycles (SN) curve used is N-code is suitable for metals than for soft tissues as it is directly calculated from initial stiffness of the material, hence it is difficult to validate the results. Considering the observations, conclusions and challenges from the previous exercise a unique method of FE modeling was developed during the last quarter. The new method consists of coupling of MATLAB (The Mathworks Inc., Natick, MA) and LS Dyna (Livermore Software Technology, Livermore, CA) to carry out fatigue simulations. This method was based, in part, on Qasim et al. 2012 [15] and Qasim et al. 2014 [16], who adopted a similar technique using Fortran in ADINA (ADINA R&D Inc., Watertown, Massachusetts).

Methodology: The computational algorithm which was used to model material property changes in cervical spine soft tissues related to repetitive axial compressive loading was outlined in Figure 2-16. Fatigue experiments with varying force amplitude and frequency were performed on bone-disc-bone segments at an interval of 10,000 cycles, up to 50,000 cycles. Quantified changes in intervertebral disc properties included: cycle-by-cycle compressive stiffness, intervertebral disc height, viscoelasticity, and tensile/compressive stiffness. The experimental results were used as input to the FE model as change in material properties due to fatigue.

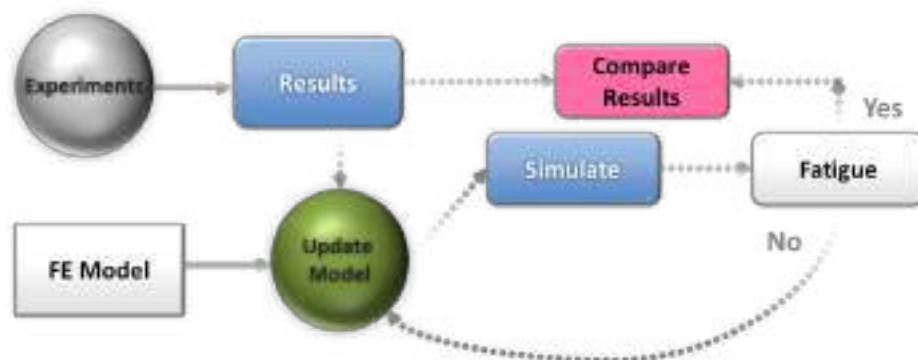


Figure 2-16: Schematic representation of vertebral disc segment under repetitive loading in a saline bath.

A FE model of a single cervical spine segment was developed. The IVD model consists of annulus fibrosus, nucleus pulposus, and superior and inferior endplates. The IVD model was discretized and programed with element-specific material properties with a script in MATLAB. This process changing of material property values to model fatigue-related changes based on element-specific loading conditions after each cyclic loading procedure. The procedure consists of first performing a computational set of fatigue cycles in LS Dyna, then using a MATLAB script to alter element-specific material properties of the soft tissues using von Mises stress as the decision parameter, followed by the next fatigue cycle simulation in LS Dyna. Changes in IVD material properties are based on experimental results and will include scaling factors for the rate and magnitude of applied repetitive compressive loads. The degraded material properties will be incorporated for elements with von Mises stress higher than the average. This report highlights experimental results from cervical spine segment testing to quantify fatigue-related material

property changes and discretization of the finite element model, along with the experiments and FE fatigue modeling done before.

Experiments: Experiments performed during the three quarters of last year are described below. Based on results from the previous set of experiments, the experimental protocol was updated. The experiments can be considered to be performed in three parts during the year and the protocol adopted during quarter 4, yielded best results and will be used for the future experiments.

Part 1: The experiments were performed to understand the effect of pure moment tests, viscoelastic tests in between fatigue tests and the inclusion of saline bath. Pure moment testing was first used to measure the bending response of cervical segments. Testing consisted of the static application of pure moments at 0.33 Nm, 0.5 Nm, 1 Nm, 1.5 Nm and 2 Nm under flexion-extension and lateral bending [17]. Following pure moment testing, the segment was mounted on an anvil of MTS Systems, Eden Prairie, MN, which was immersed in a saline bath maintained at 34°C. The segment was allowed to acclimate in the water bath for 1 hour. Stress relaxation testing was then performed to quantify viscoelasticity of the segment. The specimen was compressed by 5% of the disc height and allowed to relax under the constant deformation. Stress relaxation testing was also performed prior to and following all fatigue sets. A Maxwell material model under fixed compressive strain was used to quantify viscoelasticity during the stress relaxation testing. Segments were then exposed to cyclic loading between 0 and -150 N for 1000, 10,000 and 20,000 cycles at a frequency of 2 Hz and pure moment and viscoelastic testing was performed between each fatigue set. The fatigue sets were performed at an interval of 24 hours.

Part 2: In this set of experiments five segments were tested under a cyclic compressive force of 0-150 N at 2 Hz up to 50000 cycles in two sets, in combination of 10,000-40,000 or 20,000-30,000 fatigue cycles. From the conclusion of experiments in previous quarter, it was observed that the pure moment tests affected the mechanical response of segments; therefore the pure moment tests were not performed prior to fatigue testing. Fatigue experiments were performed using the same MTS machine, the anvil of which was surrounded by a chamber saline bath, maintained at 35 °C. During testing, the segment was mounted on the anvil and allowed to acclimate in the water bath for 1 hour. A cyclic palpation of 10 cycles for 100 N was performed to precondition the ligaments and tissues. Stress relaxation testing was then performed to assess viscoelasticity of the segment. The specimen was compressed by 100 N force and was allowed to relax under the constant deformation. A quasi-linear viscoelastic material model [18] was used to fit the stress relaxation data and the material parameters were obtained. After viscoelastic testing the spine segment was again allowed to rest in the saline bath for 30 mins. Segments were then exposed to cyclic loading between 0 and -150 N for first set of fatigue cycles at a frequency of 2 Hz, and the axial force and displacement were measured with respect to time. The details of segments tested are tabulated in Table 2-5. After the first set of fatigue tests the segment was allowed to settle again for 30 minutes in the saline bath and then again viscoelastic test at the same strain (as done before fatigue test) was done. Further, after allowing the segment to settle for 30 minutes the pure moment test was performed on the segment. After the first set of fatigue loading the segment was again refrigerated and again the same protocol was followed when second set of fatigue tests were done.

Table 2-5: Details of segments tested under fatigue during quarter 3.

S. N.	PMHS	Age (yrs)	Sex	Mass (Kg)	FSU	Initial Height (mm)	Disc Area (mm ²)	Cycles Set 1	Cycle Set 2
1	HS-798	58	Male	57.61	C2-C3	7.824	274.961	10000	40000
2	HS-795	54	Male	107.05	C4-C5	9.809	355.028	10000	40000
3	HS-798	58	Male	57.61	C4-C5	8.457	407.961	20000	30000
4	HS-796	63	Male	56.7	C4-C5	5.404	211.459	30000	20000
5	HS-800	58	Female	79.83	C4-C5	6.485	447.486	10000	40000

Part 3: In this set of experiments the conclusion from the previous two sets of experiments was used pure moment test was completely removed from the protocol and all the fatigue sets were performed on bone disc bone segments, simultaneously with in 15 to 20 hours approximately. Four bone disc bone spine motion segments without posterior elements obtained from the cervical spines of human donors were fixed at cranial and caudal extents using polymethylmethacrylate (PMMA) (Table 2-6). Specimens were exposed to a protocol that included fatigue loading for 5 sets of 10,000 cycles with tension-compression and viscoelastic assessments prior to the first and after each 10,000-cycle fatigue set. Fatigue testing was performed with specimens submerged in a physiologic saline bath with temperature maintained at 34°C and consisted of repetitive compression applied using the piston of an electrohydraulic testing device (MTS Systems, Eden Prairie, MN) between 0 and 150 N at 2 Hz using a sine wave function. Tension compression tests were performed at a quasi-static speed of 0.1 mm/s to 10% strain. The viscoelastic test involved compressing the specimen to 10% strain and allowing it to relax under the constant deformation. Disc height was measured from x-rays obtained after each fatigue set and was computed based on the average of three readings obtained at consistent locations in the disc. Axial force was measured at 100 Hz during the entire test using a uniaxial load cell attached to the piston. The segment was allowed to relax in the saline bath for 15 minutes after each 10,000-cycle fatigue set prior to the the initiation of the next test. The schematic representation of the experimental setup is provided in Figure 2-17**Error! Reference source not found..**

Table 2-6: Details of segments tested under fatigue during quarter 4.

S. N.	PMHS	Age (Yrs)	Sex	Mass (Kg)	FSU	Initial Height (mm)	Disc Area (mm ²)
1	HS 799	64	Female	48.1	C6-C7	8.13	318
2	HS-799	64	Female	48.1	C4-C5	6.05	283
3	HS-799	64	Female	48.1	C2-C3	7.47	195
4	HS-798	58	Male	57.61	C6-C7	7.78	442

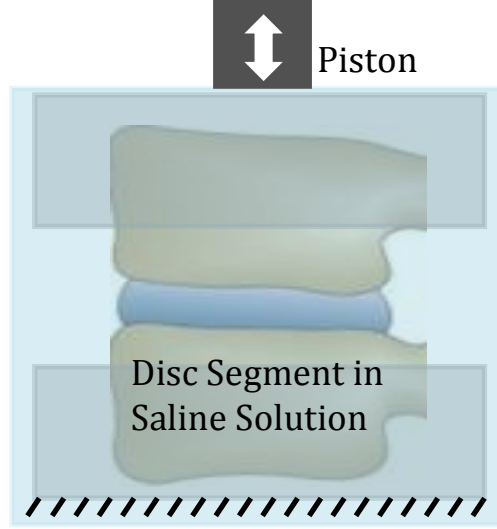


Figure 2-17: Schematic representation of vertebral disc segment under repetitive loading in a saline bath.

Quasi Linear Viscoelastic Model: A quasi-linear viscoelastic (QLV) material model [18] was used to fit the stress relaxation data and allow for the quantification of discrete material property constants to describe the viscoelastic behavior. The QLV theory models the viscoelastic response of a material as a stress relaxation function formed using a series of discrete linear sections. The instantaneous stress resulting from a ramp strain is given as:

$$\sigma(t) = G(t) \times \sigma^e(\varepsilon) \quad (2.1)$$

where $\sigma(t)$ is the stress at any time t , $\sigma^e(\varepsilon)$ is the stress corresponding to an instantaneous strain, $G(t)$ is the reduced relaxation function representing the stress of the material divided by the stress after the initial ramp strain. The complete stress history at any time t is then the convolution integral:

$$\sigma(t) = \int_{-\infty}^t G(t-\tau) \times \frac{\partial \sigma^e(t)}{\partial \varepsilon} \frac{\partial \varepsilon}{\partial \tau} \quad (2.2)$$

where G is the reduced relaxation function, $\frac{\partial \sigma^e(t)}{\partial \varepsilon}$ represents the instantaneous elastic response, and $\frac{\partial \varepsilon}{\partial \tau}$ is the strain history. The reduced relaxation function proposed by Toms et al. 2002 [19] is:

$$G(t) = ae^{-bt} + ce^{-dt} + ge^{-ht} \quad (2.3)$$

where, a , b , c , d , f , g are all constants. The instantaneous stress response is assumed to be represented through the nonlinear elastic relationship:

$$\sigma^e(\varepsilon) = A(e^{B\varepsilon} - 1) \quad (2.4)$$

where, A and B are constants. Assuming that t starts at 0 instead of negative infinity, and substituting the strain history and the instantaneous stress response into the QLV model to obtain the stress history from t_0 (time at peak strain) to t (end of stress relaxation curve) we get:

$$\sigma(t > t_0) = \int_0^{t_0} \left\{ ae^{-b(t-\tau)} + ce^{-d(t-\tau)} + ge^{-h(t-\tau)} \right\} e^{B\gamma\tau} d\tau \quad (2.5)$$

Integrating and applying the limits we obtain:

$$\sigma(t > t_0) = AB\gamma \left[\frac{ae^{-bt} e^{(b+B\gamma)t_0}}{b+B\gamma} + \frac{ce^{-dt} e^{(d+B\gamma)t_0}}{d+B\gamma} + \frac{ge^{-ht} e^{(h+B\gamma)t_0}}{h+B\gamma} \right] - AB \left[\frac{ae^{-bt}}{b+B\gamma} + \frac{ce^{-dt}}{d+B\gamma} + \frac{ge^{-ht}}{h+B\gamma} \right] \quad (2.6)$$

This analytical form is used to optimize the QLV material parameters in MATLAB.

Results: The results from the aforementioned experiments is summarized as follows.

Part 1: Piston stroke (relative strain / piston displacement for respective cycle) and segmental stiffness was calculated from the force-displacement response measured for each cycle. For the first 1,000 cycles the piston stroke was well as stiffness was almost constant, which indicated that segmental axial stiffness for that specimen remained approximately unchanged during the 1,000 cycles. Stiffness gradually increased with repetitive compressive loading during the 10,000 cycles, more dramatically after the first 500 cycles. Following the 10,000 cycles, segmental stiffness again decreased during the initiation of the 20,000-cycle set as shown in Figure 2-18. To investigate the effects of the pure moment protocol and saline bath on fatigue, two segments were tested without saline solution, but included pure moment testing before and after fatigue sets. Increased segmental stiffness was evident during the tests but occurred considerably earlier in these tests conducted without saline bath. Those specimens demonstrated considerable stiffness change during the first 1,000 cycles (~27%) (Figure 2-19 **Error! Reference source not found.**) that was not evident in the prior tests that included saline. However, stiffness change between tests was considerably lower, presumably because of the large change during the first 1,000 cycles.

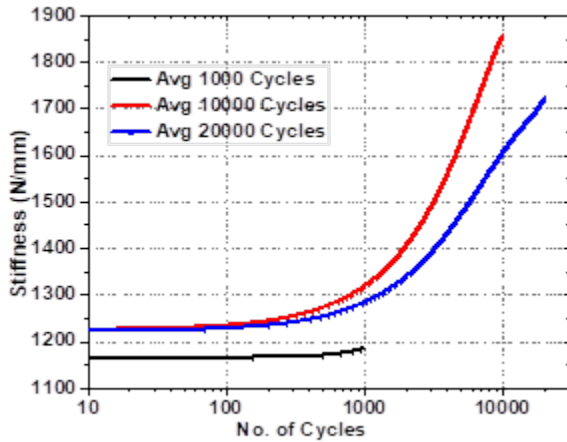


Figure 2-18: Average stiffness for 1st set of segments.

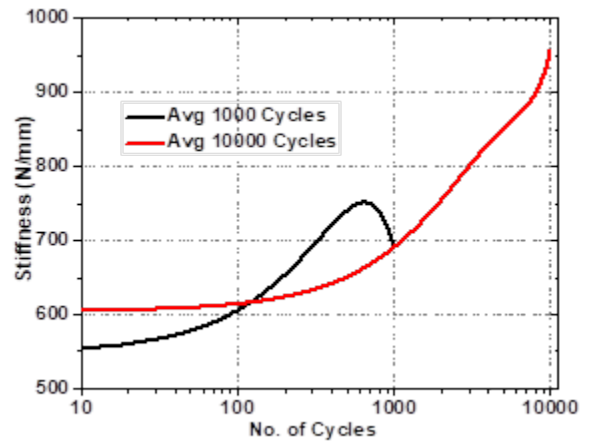


Figure 2-19: Average stiffness for 2nd set of segments.

Two additional segments were tested without saline bath or pure moment testing. Similar to the tests above, a greater and earlier stiffness change was observed during the first 1,000 cycles (Figure 2-20 **Error! Reference source not found.**). Likewise, 12 and 16% increase in stiffness as demonstrated between the end of the 1,000-cycle set and the beginning of the 10,000-cycle set. It was likely due to dehydration of the specimen that occurred when not in the saline bath,

which leads to an accelerated decay in soft tissues that manifests biomechanically as increased stiffness.

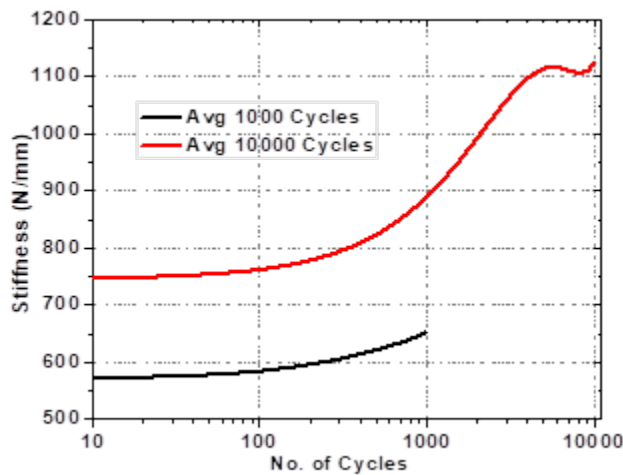


Figure 2-20: Average stiffness for 3rd set of segments.

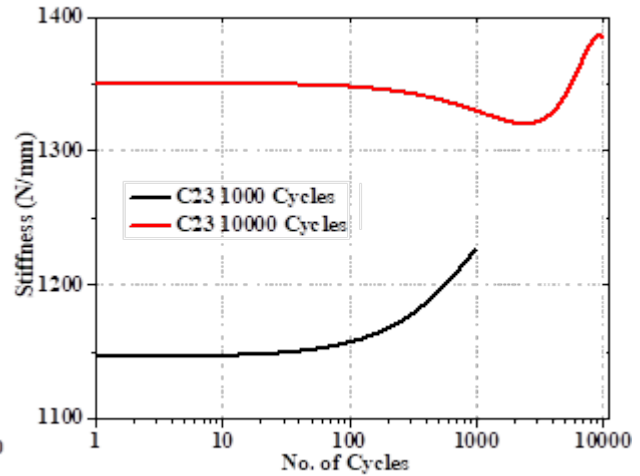


Figure 2-21: Stiffness for segment tested w/o pure moment.

The final segment was tested in saline bath without the pure moment, and the segment responded with a limited change in axial stiffness during the first 1,000-cycle set and limited change (10%) between the 1,000 and 10,000 cycle sets. Based on the findings, the testing protocol was adjusted to limit pure moment testing between fatigue sets, while maintaining the saline bath for all fatigue cycles. Specimens fatigue tested in saline demonstrated a modest change in stiffness (4%) during the first 1,000 cycles, which is more in line with expectations. However, specimens tested without saline demonstrated over a 20% change in stiffness during the first 1,000 cycles. Likewise, exclusion of the pure moment protocol resulted in limited test-to-test changes (13%) between 1,000 and 10,000 cycles. When testing included the pure moment protocol, mean test-to-test changes were somewhat greater (15%).

Part 2: As observed during the tests of previous quarter the compressive displacement required to achieve 150N for the segments was reduced with increasing number of fatigue cycles. It can be observed that the relative strain decreased with respect to the number of cycles and was observed to be between 1-4% (Figure 2-22) for all the segments tested up to 50,000 cycles. It can be observed that the relative strain curve behavior did not change a lot for the first and second fatigue set, except the initial strain was more during first fatigue set as compared to second. The absolute strain of the segments was observed to increase up to 10-20% (Figure 2-23**Error! Reference source not found.**), suggesting that there is about 8 to 18% residual strain in the segments. The absolute strain was observed to be a function of number of applied cycles for first 10,000 cycles, whereas the slope of the absolute strain is observed to be almost constant for each interval of 10,000 cycles. As the segments were allowed to relax after the fatigue test, it was observed to regain some of its lost height and the residual strain was reduced. However the segments never regained their original heights.

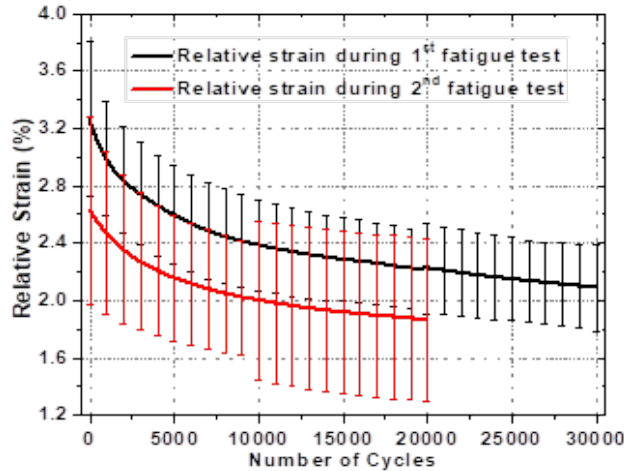


Figure 2-22: Relative strain response of the segments.

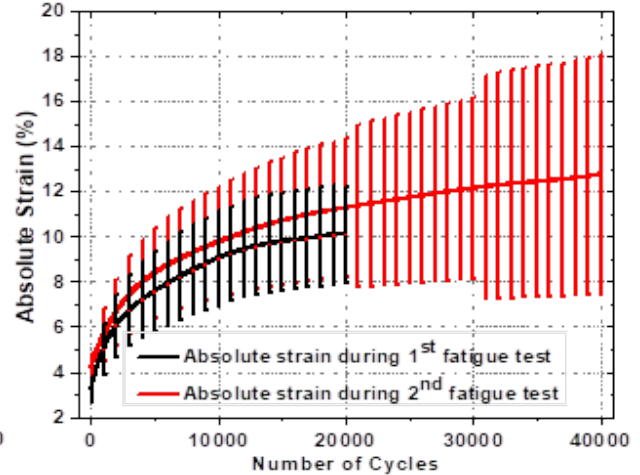


Figure 2-23: Absolute strain response of the segments.

The stress relaxation response in terms of stress with respect to time showed that before any fatigue the segment showed least stress for the strain. But further for the same amount of strain the stress in the segment after the fatigue tests was observed to increase (Figure 2-24). It was observed that after the second fatigue test, the stress was considerably higher; suggesting that the fatigue test stiffened the segment. The asymptote of the curve was also shifted and took more time to show the steady response. After first and second fatigue tests pure moment test was performed on each segment in flexion extension and lateral bending at 0.3, 0.5, 1, 1.5 and 2 Nm. After the first fatigue test the range of motion of the segments is on higher side as compared to Wheeldon et al. 2006 [17] (Figure 2-25 **Error! Reference source not found.**). The average increase in the range of motion between the first and second fatigue cycle is about 28% in flexion.

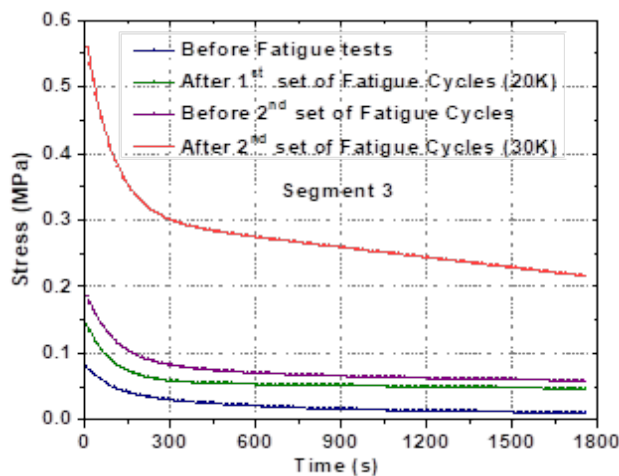


Figure 2-24: Viscoelastic response for segment 3 before and after fatigue test.

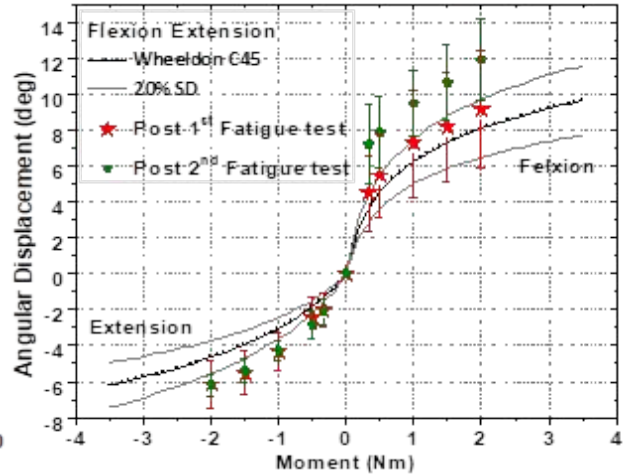


Figure 2-25: Pure moment response of in flexion and extension.

The heights of the discs were also measured from the x-rays and averages of three measurements were taken at right, left and center of the IVD and the average was taken. The average and percentage change in the disc heights are tabulated in Table 2-7. The percentage change in disc height was observed to be comparable with absolute strain, except segment 3

which showed more decrease in height. It was perhaps due to error in height measurement or injury which would be clear from MRI scans. The disc heights are reduced mainly due to dehydration of the soft tissue and if the tissue is allowed to relax in a water bath it again regains its height up to a certain extent.

Table 2-7: Heights of the segments before and after fatigue tests.

S. N.	Initial Height (mm)	Cycles Set 1	Height after fatigue set 1	Decrease %	Cycles Set 2	Height after fatigue set 2	Decrease %
1	9.824	10000	9.123	7.14	40000	7.437	18.48
2	9.809	10000	9.336	4.82	40000	8.97	3.92
3	9.457	20000	9.071	4.08	30000	6.596	27.28
4	8.404	30000	7.207	14.24	20000	6.962	3.39
5	7.485	10000	6.399	14.51	40000	5.579	12.81

It was difficult to compare results with sets having different fatigue cycles. So the next set of experiments were designed to avoid removal of the segment from the water. In this experimental protocol, posterior elements were removed, and all tests were performed in a flow without removing the segment for the saline bath.

Part 3: In the resented set of experiments four segments were tested under a cyclic compressive force of 0-150 N at 2 Hz up to 50,000 cycles at an interval of 10,000 cycles. The cyclic force response for one of the segments for 10,000 cycles is plotted in Figure 2-26 **Error! Reference source not found.**, whereas the zoomed-in image shows the force plot with respect to time for two cycles. The force response of all the segments was observed to be smooth sine wave with no abnormal peak or trough, which would suggest damage to segment.

It was observed that the absolute strain i.e. the strain with respect to the initial height of the disc, during fatigue increased with an increasing number of fatigue cycles. The absolute strain and the height with respect to each cycle was calculated for all four segments and is plotted in Figure 2-27. It can be observed that the absolute strain and/or the disc height loss, was maximum during the first 10,000 cycle fatigue set. As the number of cycles increased, the IVD demonstrated a more stable response and the absolute strain during the fourth and fifth fatigue set was almost identical. For segment 2 it was observed that during the third fatigue set there was a sudden increase in absolute strain or decrease in height, which represents that there must have been some failure and it is also validated by the viscoelastic test which shows sudden increase in force post third fatigue set. Results for testing of

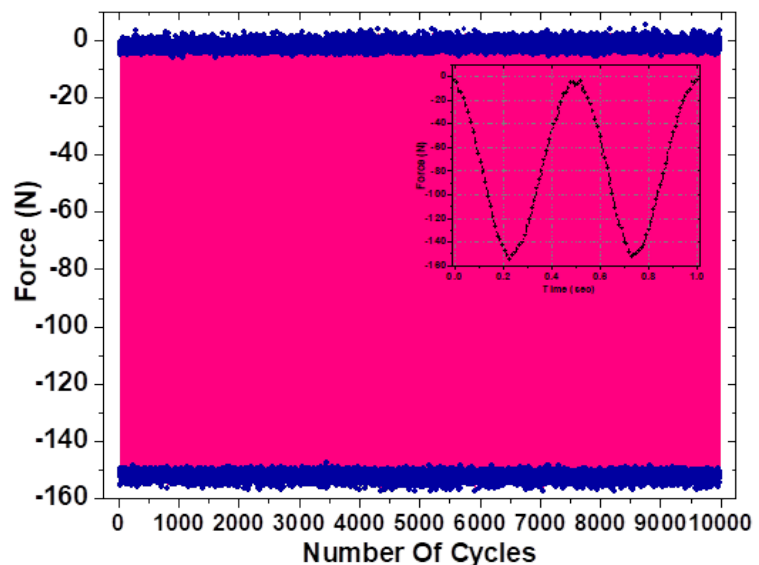


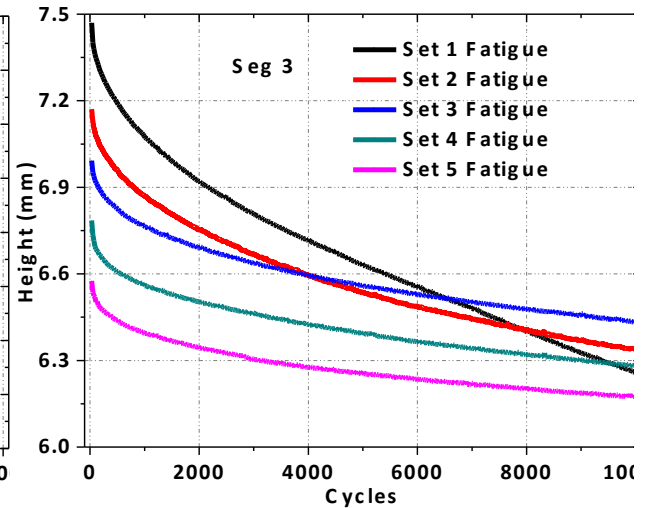
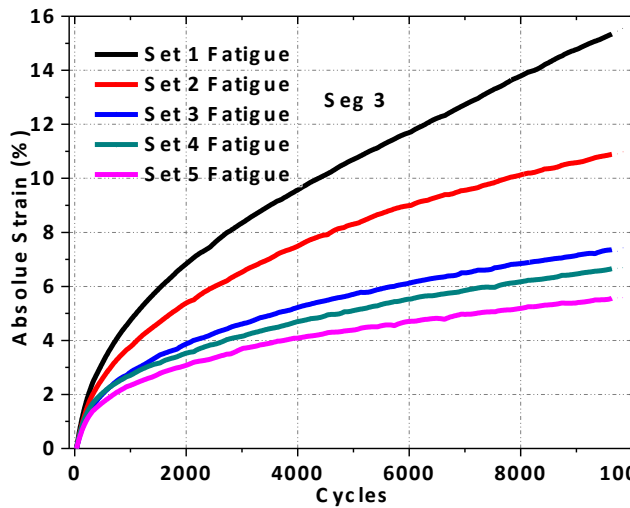
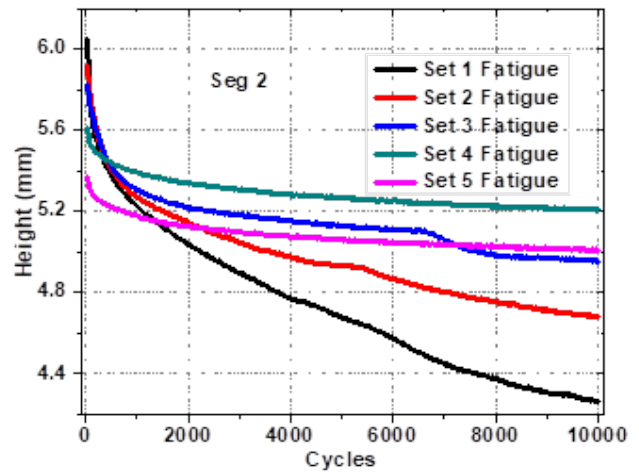
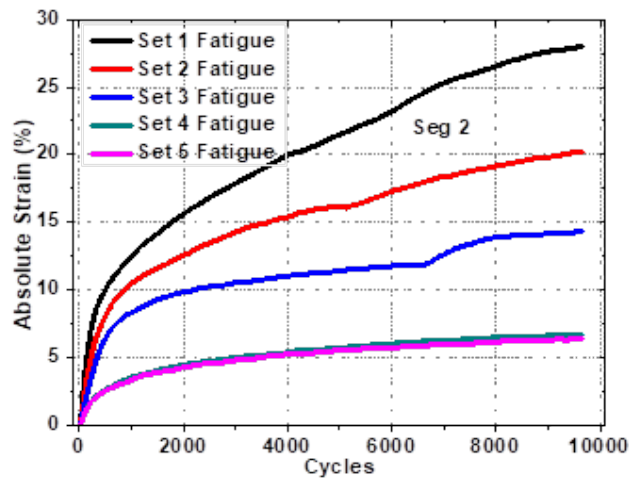
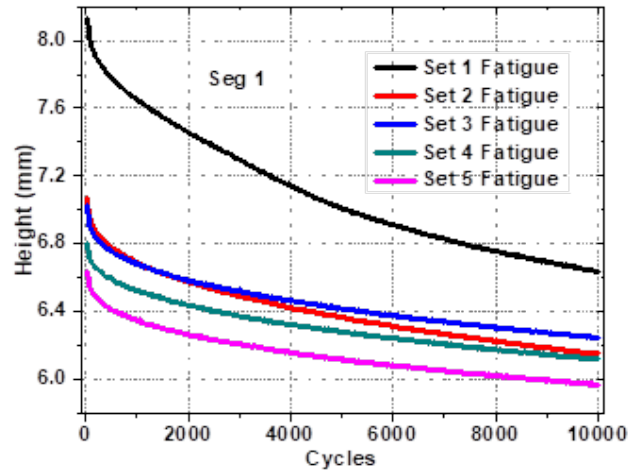
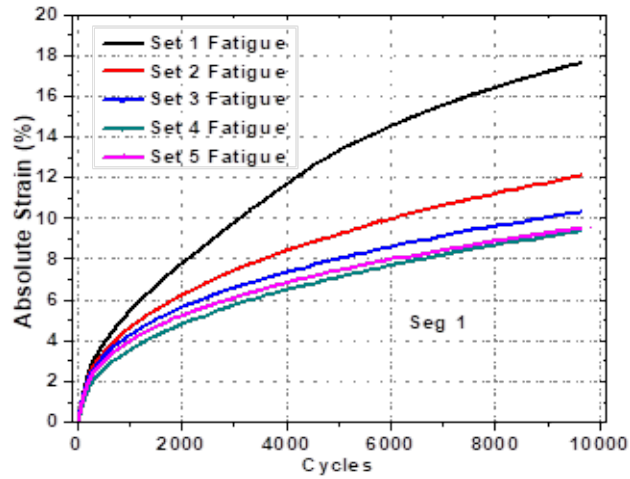
Figure 2-26: Cyclic force response of the segment.

that segment were only included up to the time of failure. Dissection of that segment is currently planned and will detail specific structures that failed during the fatigue loading. Segment 4 was the only exception to this behavior of gradual drop in absolute strain curves and showed increase during second, third and fourth fatigue sets. The average curves of absolute strain and height loss for all the segments (last figure in Figure 2-27) clearly shows the difference between the fatigue sets. As the segments were allowed to relax after the fatigue test, it was observed to regain some of its lost height and the residual strain was reduced. However the segments never regained their original heights (Table 2-8**Error! Reference source not found.**).

Intervertebral disc heights were measured from the x-rays before and after the fatigue tests. Averages of three measurements were taken at right, left and center of the IVD. The average and percentage disc height losses are tabulated in Table 2-8**Error! Reference source not found.**. Disc height loss was maximum during the first fatigue set averaging 5.5%. The height loss further reduced with the fatigue sets and there was least difference post fourth and fifth fatigue set disc height. The average disc height loss between set 1 and set 5 (i.e. after 50,000 cycles) is obtained as 14%, with 18% maximum for the segment 1 and 11% minimum for segment 2. It can also be observed from average height loss in Figure 2-27 that the curve profile for first two fatigue sets is similar and the curve profile for next three fatigue sets is similar. It shows that for the first two fatigue sets the disc demonstrates viscoelastic properties, whereas for the next three sets the disc shows only elastic response with decrease in height. The disc heights are reduced mainly due to dehydration of the soft tissue and if the tissue is allowed to relax in the water bath it again regains its height up to a certain extent. Thus if a considerable permanent change in disc height is obtained it can be used as failure parameter, however that percentage needs to be determined with more experiments.

Table 2-8: Heights of the segments before and after fatigue tests.

	Seg1	Loss (%)	Seg2	Loss (%)	Seg3	Loss (%)	Seg 4	Loss (%)	Avg Loss (%)
Initial	8.13		6.05		7.47		7.78		
Post Fatigue 1	7.07	0.13	5.92	0.021	7.35	0.016	7.38	0.05	0.055
Post Fatigue 2	7.03	0.006	5.83	0.015	7.17	0.024	7.24	0.02	0.016
Post Fatigue 3	6.8	0.033	5.6	0.04	6.99	0.025	7	0.033	0.033
Post Fatigue 4	6.65	0.022	5.37	0.04	6.78	0.030	6.82	0.026	0.03
Post Fatigue 5	6.64	0.0015	5.37	0	6.57	0.030	6.62	0.03	0.015
		0.18		0.11		0.12		0.15	0.14



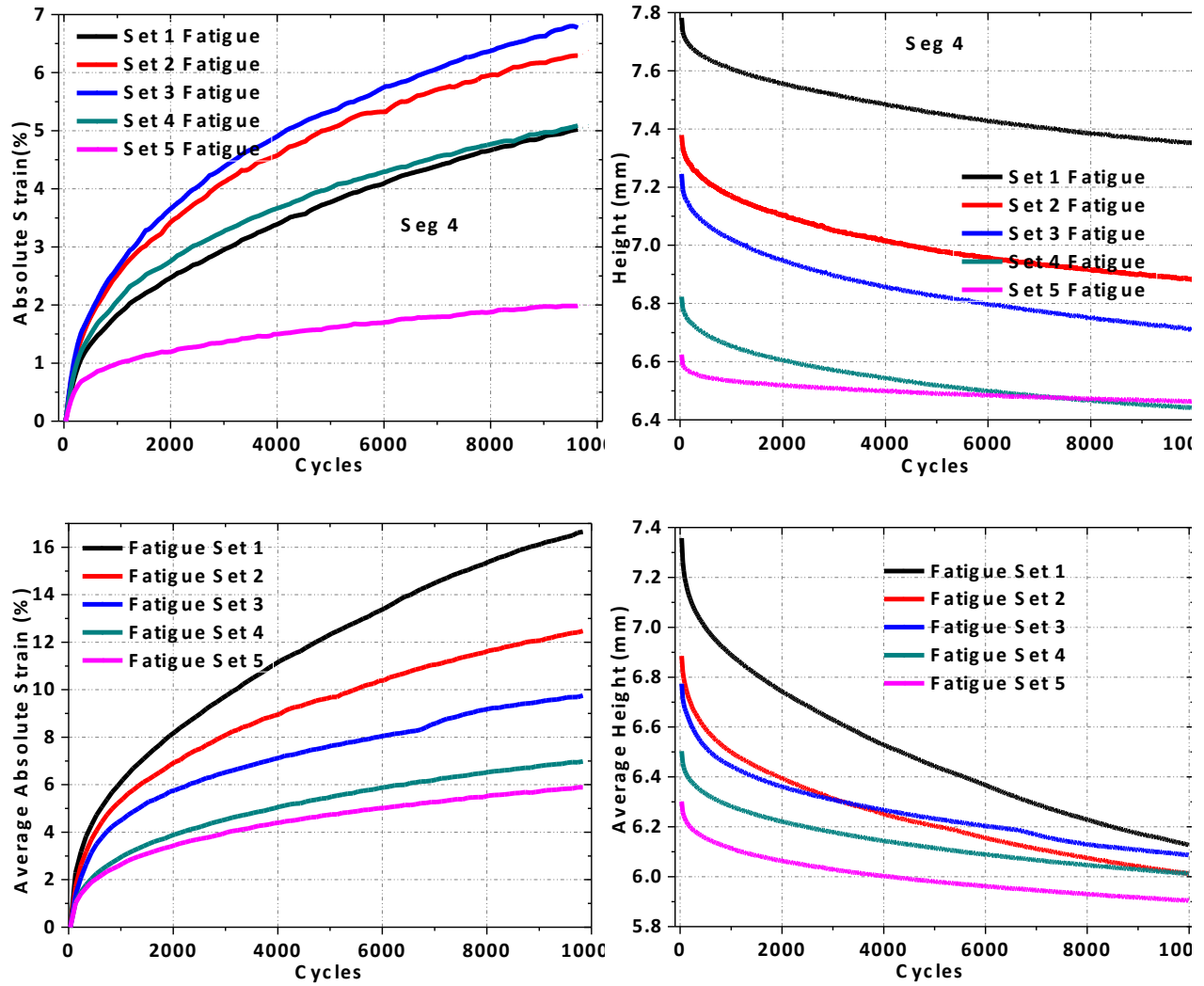


Figure 2-27: Absolute strain and decrease in height response of the segment.

Viscoelasticity: Before first and after each fatigue set a stress relaxation viscoelastic test was performed on each segment and quasi linear viscoelastic material parameters were extracted for each using Equation (2.6). The parameters were optimized with the experimental curve using a MATLAB function `fminsearch`. The stress relaxation response in terms of stress with respect to time is plotted in Figure 2-28.

Figure 2-28: Viscoelastic response for all segments after fatigue sets. . It can be observed that for segment 2 and 4, before any fatigue the segment showed least stress for the strain caused by 10% strain load, but further for the same amount of strain the stress in the segment after the fatigue two fatigue sets was observed to increase, whereas segment 1 and segment 3 showed mixed behavior. The asymptote of the curve is also shifted and takes more time to show the steady response.

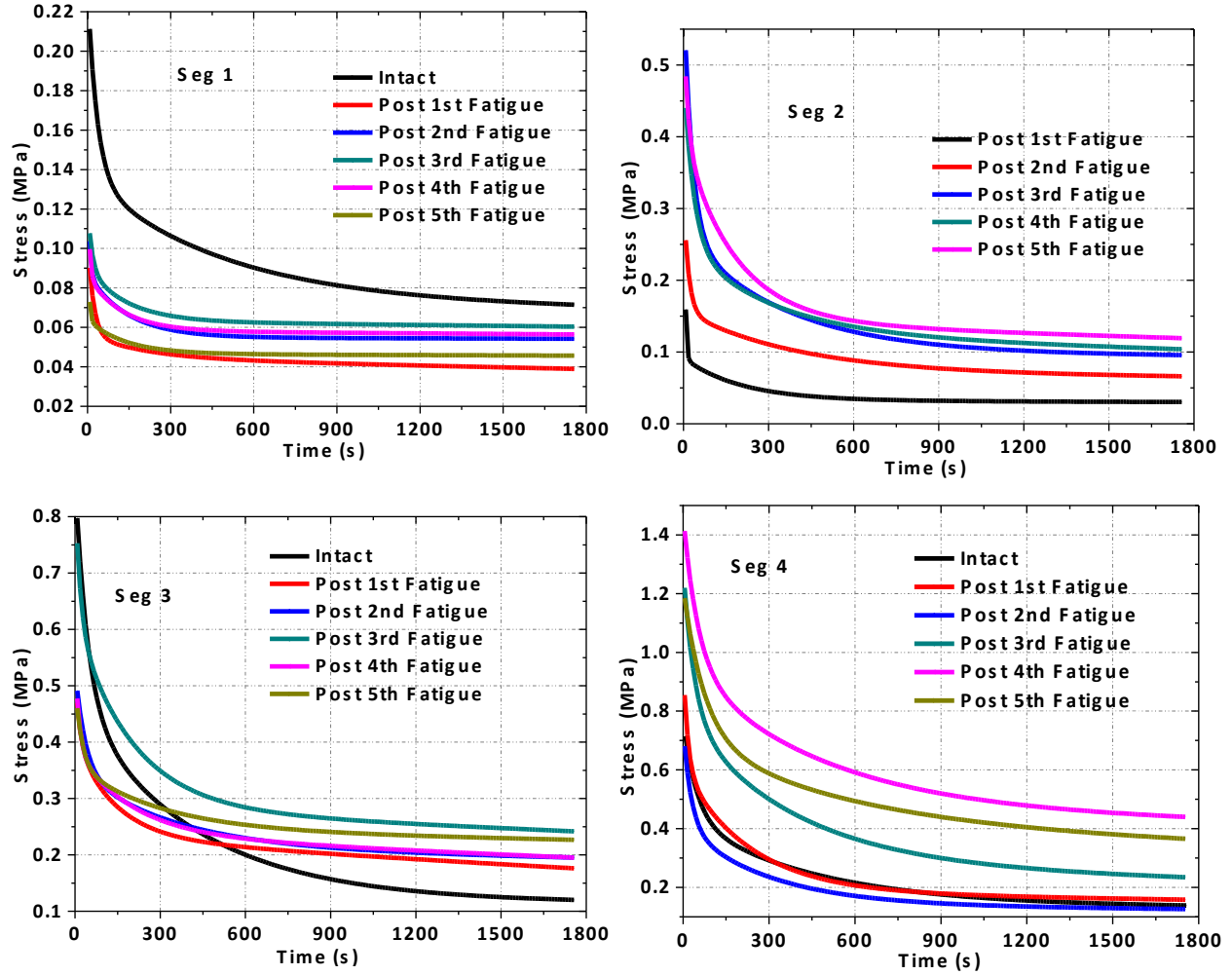


Figure 2-28: Viscoelastic response for all segments after fatigue sets.

The quasi-linear viscoelastic material parameters for all the tests are tabulated in Table 2-9. It can be observed from Table 2-9 that the stress response constants A and B are observed to increase after the fatigue test whereas the relaxation constants (a, b, c, d, g & h) are observed to decrease with a couple of exceptions due to experimental results. It denotes that the relaxation constants work over a time interval. Constants a & b represent the initial slope of the curve or the first time interval c & d represent the second, whereas g & h represent the later part of the curve. Thus it can be inferred that the increase in stiffness constants and decrease in the relaxation constants show the stiffening of the intervertebral disc, and the change in the time relaxation constants result in shifting of the asymptote.

Table 2-9: Quasi linear viscoelastic parameters before and after fatigue tests.

Seg #	Fatigue	Quasi Linear Viscoelastic Material Parameters							
		A	B	a	b	c	d	g	h
1	Intact	0.0086	9.34	0.24	0.03	0.18	0.002	0.22	3.17E-05
	Post 1 st Set	0.045	8.96	0.035	0.052	0.01	0.005	0.04	7.67E-05
	Post 2 nd Set	0.008	8.95	0.143	0.16	0.15	0.007	0.266	7.12E-06
	Post 3 rd Set	0.0067	8.98	0.13	0.069	0.14	0.007	0.34	2.49E-05
	Post 4 th Set	0.015	8.6	0.096	0.16	0.106	0.008	0.23	1.76E-05
	Post 5 th Set	0.025	7.95	0.087	0.21	0.075	0.0073	0.21	1.07E-05
2	Intact								
	Post 1 st Set	0.01	9.93	0.14	0.06	0.098	0.0025	0.084	5.71E-05
	Post 2 nd Set	0.02	10.086	0.2	0.034	0.11	0.003	0.07	3.65E-05
	Post 3 rd Set	0.028	9.37	0.22	0.03	0.13	0.003	0.13	0.00011
	Post 4 th Set	0.0025	12.9	0.046	0.067	0.097	0.005	0.056	0.000103
	Post 5 th Set	0.01	10.8	0.082	0.28	0.03	0.005	0.017	3.77E-05
3	Intact	0.029	9.61	0.166	0.023	0.16	0.0024	0.0554	1.68E-05
	Post 1 st Set	0.04	8.94	0.11	0.02	0.074	0.002	0.12	2.13E-05
	Post 2 nd Set	0.02	8.99	0.22	0.029	0.19	0.0023	0.3	5.09E-05
	Post 3 rd Set	0.01	10.84	0.072	0.059	0.13	0.005	0.11	9.01E-05
	Post 4 th Set	0.012	9.35	0.17	0.07	0.22	0.005	0.35	0.00011
	Post 5 th Set	0.015	9.45	0.12	0.044	0.12	0.003	0.25	4.60E-05
4	Intact	0.024	10.89	0.12	0.022	0.12	0.0022	0.06	3.96E-05
	Post 1 st Set	0.0003	15.58	0.1	0.0622	0.17	0.0043	0.077	9.01E-05
	Post 2 nd Set	0.026	8.82	0.9	0.036	0.86	0.0033	0.46	6.51E-05
	Post 3 rd Set	0.01	12.272	0.23	0.026	0.26	0.0026	0.15	1.14E-04
	Post 4 th Set	0.003	13.92	0.2	0.02	0.2	0.0021	0.2	5.01E-05
	Post 5 th Set	0.05	10.662	0.23	0.013	0.15	0.0018	0.2	9.29E-05

Stiffness: The increase in stiffness for the four disc segments and average stiffness for all the segments during fatigue is illustrated in Figure 2-29. It can be observed that during first three sets there was not much change in stiffness of the disc, whereas fourth and fifth sets showed a high increase in stiffness. This behavior is observed due to decrease in disc height and loss in viscous behavior. Loss in viscosity can also lead to functional losses and thus failure of the soft tissue.

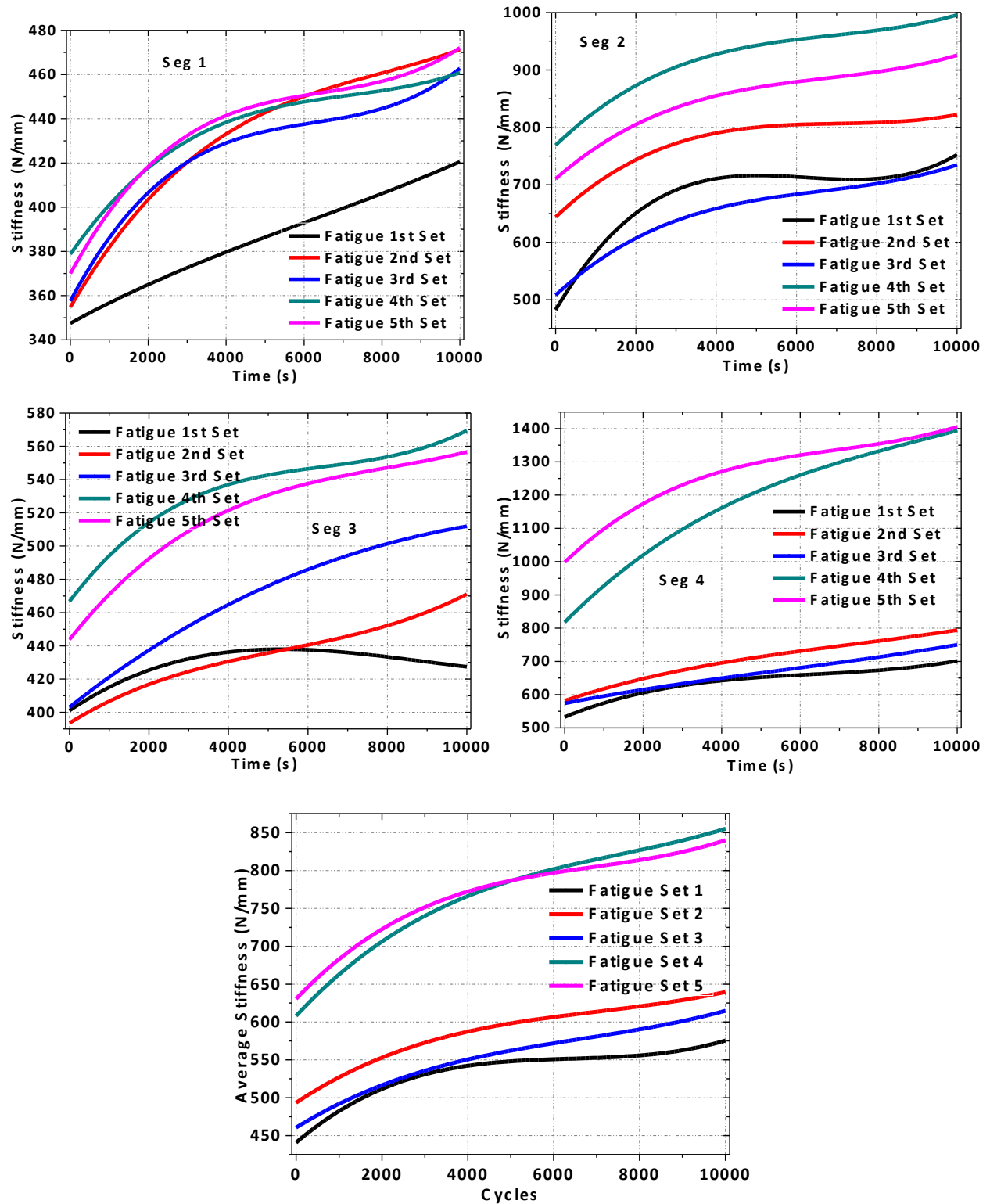
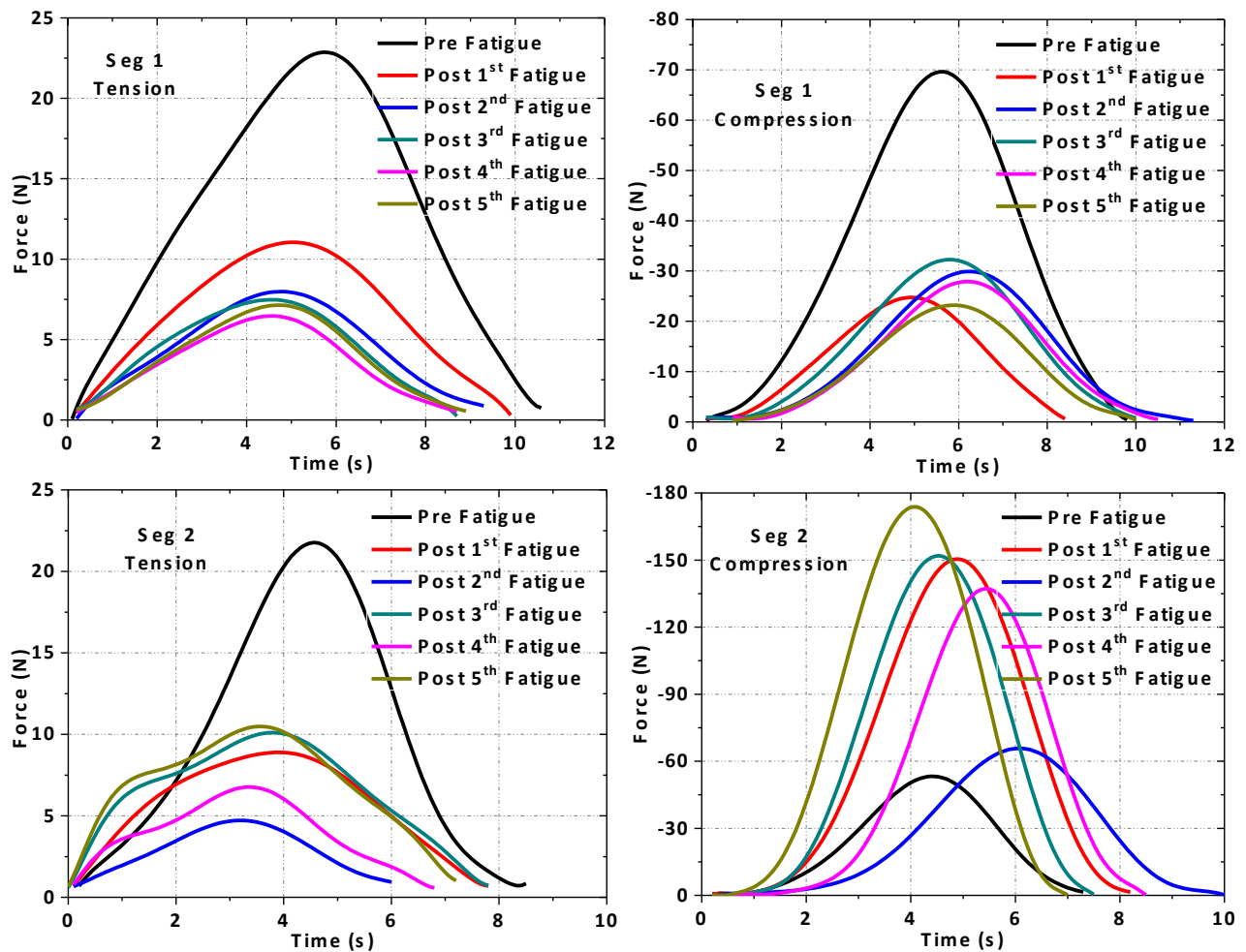


Figure 2-29: Stiffness response for all segments during fatigue sets.

Tension Compression: The tension and compression curves from the tests along with average curves are shown in Figure 2-30. It can be observed that the discs showed less stiff behavior in tension with increase in fatigue, whereas it shows stiffer behavior in compression. Again this behavior was observed due to decrease in disc height and loss in viscous behavior. The behavior could also be indicative of progressive yielding-type behavior of the annular fibers [20], resulting in annular laxity. Increased annular laxity could contribute to lost disc height and would have a mechanical signature of decreased tension stiffness as the laxity is taken up in during the early stages of tension, and increased compressive stiffness, as the decreased disc height results in more bulk mass of the disc resisting compression earlier in the compressive response. The tension compression results will be converted to stress strain plots and will be fitted with desired material models to obtain material parameters which will be used for updating the finite element model.



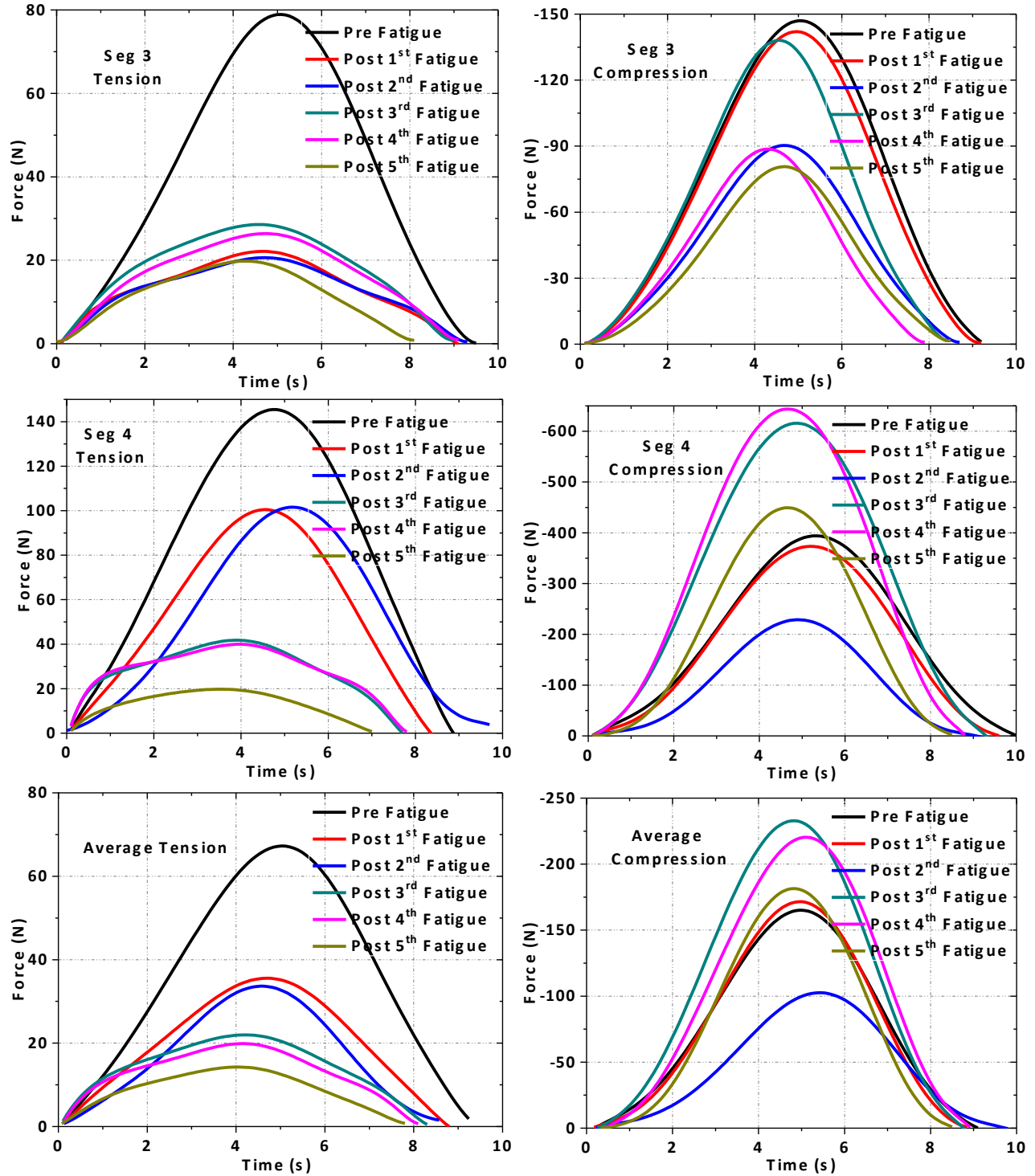


Figure 2-30: Tension and compression response for all segments post fatigue sets.

Finite Element Modeling: Finite element modeling of soft tissues under fatigue is a very difficult task and it has never been done before. During this study various attempts were made to develop a finite element model which could replicate fatigue. The efforts of finite element modeling are also divided in three parts as follows.

Part 1: In the first attempt, a finite element model of the spine segment in LS Dyna was obtained and a freshly implemented module in LS Dyna was used:

(*FREQUENCY_DOMAIN_RANDOM_VIBRATION)

which incorporates location, direction and range of frequencies for the random excitation, exposure time and SN curve. As per experiments, cyclic load was applied to the spine segment as shown in Figure 2-31, for segment C6-7, all the surface nodes of vertebra C7 were constrained in x, y and z direction and a cyclic load of 150 N was applied on the cortical bone of C6. LS dyna performs modal analysis as the first step, and the natural frequencies and mode shapes were determined. Based on all the above data LS Dyna determines cumulative damage ratio, expected fatigue life and irregularity factor as the fatigue parameters. While defining the boundary conditions for fatigue, the loading was defined in the frequency domain using power spectral density analysis (PSD). Therefore, the FFT of the force-time curve was calculated and the load was applied in frequency domain as PSD. The frequency range for the modal analysis as well as the number of modes over which fatigue will be distributed has to be defined.

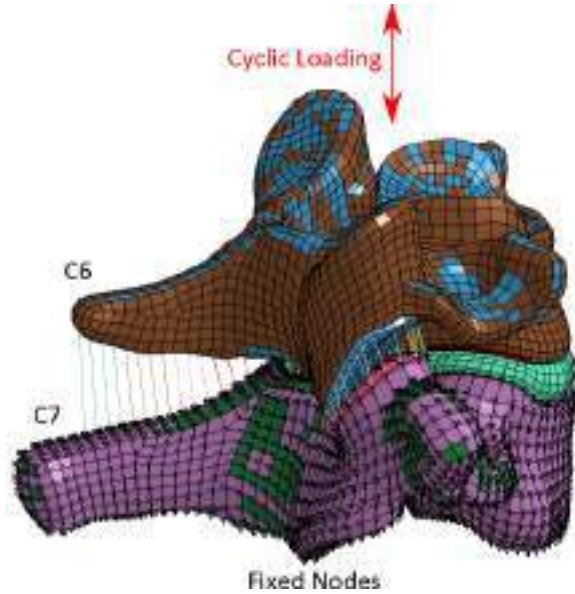


Figure 2-31: Boundary conditions (C6-7 vertebral segment).

The results were obtained in terms of mode shapes and natural frequencies for the segment C6-7. The mode shapes for the lower frequencies were the normal modes such as flexion-extension, bending and rotation. However for higher frequencies the intervertebral disc showed unrealistic mode shapes, in which the disc deformed to such an extent that it penetrated into the vertebral bone, making the model unstable for higher frequencies.

To correct that, the material properties and the boundary between the parts (nucleus, annulus, annulus fibrosus and the endplates) had to be modified. And it was discovered that only high strength material can be used for this kind of analysis in LS Dyna. Soft tissues or hyper elastic materials are unable to replicate fatigue using this method in LS Dyna.

Part 2: Further, another software ‘n code’ (HBM-nCode Inc., Southfield, MI) was used to determine fatigue in discs. N-code is software which is developed for industrial fatigue analysis applications. It accepts material properties (elastic modulus, Poisson’s ratio, yield stress, etc.) and fatigue properties in terms of SN or EN Curve are generated from them. A loading simulation analysis for unit load has to be provided from the Finite Element software (LS Dyna in our case). The loading conditions (random vibrations or sinusoidal vibration), number of loading cycles and loading force can be adjusted in N-code, and the output is obtained as damage sustained and life of the object. So, the segment C4-C5 was separated from the spine model and the boundary conditions were applied as in the experiments. The inferior vertebra (C5) was fixed and the superior vertebra (C4) was applied with a sinusoidal force of 1 N for 0.5 sec (1 cycle). The result of the FE simulation was used as input in the n code for fatigue analysis.

The snapshot of glyphs used for fatigue analysis is shown in **Error! Reference source not found.** The FE Input glyph represents the result of FE simulation (unit compressive load in 0.5 sec), the second glyph 'EN analysis' performs the EN analysis and thus requires EN curve for each part on which fatigue analysis has to be performed. The n-code software is meant for the fatigue analysis of metals, and the SN or EN curve is developed for each part from the material properties of the part. Hence only the material properties of only the IVD were used as obtained from the experiments (elastic modulus = 10 MPa and Poisson's ratio = 0.45). The third glyph shows the output of the fatigue analysis in terms of 'damage' and 'life' of the material which are inversely equal.

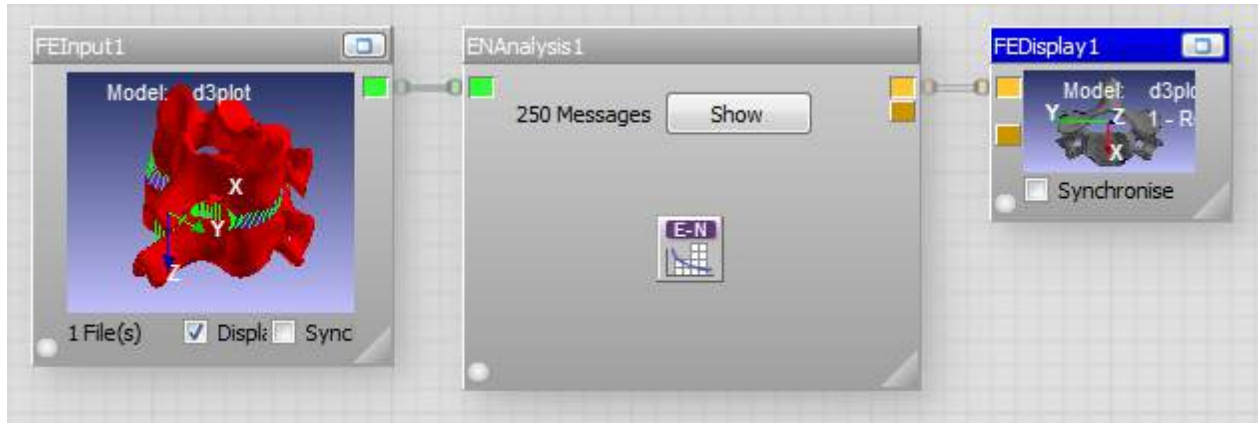


Figure 2-32: Glyph snapshot of n-code used for fatigue analysis.

The analysis was performed for 50,000 cycles at a compressive force of 150 N. The damage and life observed for IVD (Inter vertebral disc) is plotted in Figure 2-33. It was observed that for the loading condition, the life interpreted for IVD is interpreted more than $6E7$ cycles; the damage is observed to be very small at the inferior end of the disc. Also during the experiments, the segments didn't show any visible damage after 50,000 fatigue cycles. Further the fatigue analysis was performed in n-code with higher force and the life contour plots for the IVD are shown in Figure 2-34 and Figure 2-35 for 500 N and 1000 N force. It was observed that with increase in force, the life of the tissue is observed to reduce to 2,146 cycles and 190 cycles for 500 N and 1000 N force respectively. As compared to literature these values were too small.

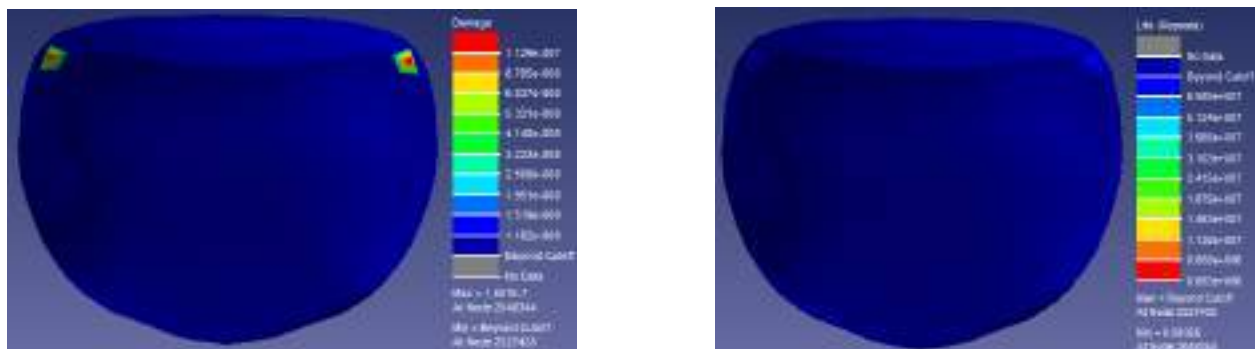


Figure 2-33: Damage and life of the IVD for 50,000 cycles and 150 N force.

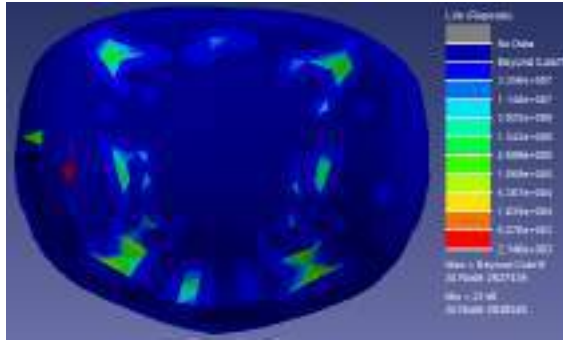


Figure 2-34: Life of the IVD for 50,000 cycles and 500 N force.

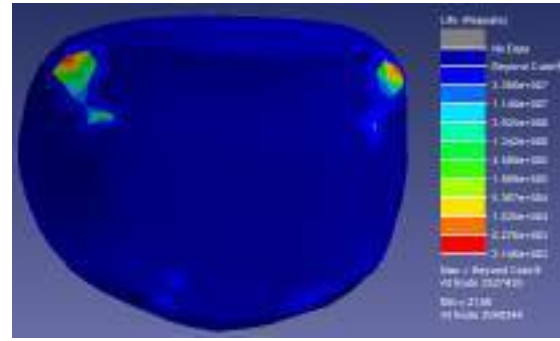


Figure 2-35: Life of the IVD for 50,000 cycles and 1000 N force.

The superior side of the discs was observed to have more damage as compared to the inferior side. Though the model showed exponential decrease in life with increase in the load, the software is built for to predict the fatigue in metals and the potential of it to produce fatigue in soft tissue accurately is still questionable. Also for this case the fatigue with higher force will have to be investigated experimentally. Hence, though n code represented some kind of fatigue in the soft tissue, it still needs better understanding and experimental validation to correctly predict the life of intervertebral disc.

Part 3: For recent protocol, the finite element model was obtained as discussed in previously. The elements were further renumbered so that all the parts have serial element IDs. A MATLAB algorithm was further developed to note the IDs of nucleus and annulus and material IDs with the same ID as that of part IDs were created. The material IDs were then referred to the corresponding element ID, and the discretized model for disc was created. Figure 2-36 shows the finite element model with annulus and nucleus modeled with discrete parts. The model was applied with boundary conditions and loading.

Another MATLAB algorithm was developed, which can execute the model in loop and read the results and update the model after a corresponding execution. To illustrate, once the first execution is done the algorithm will read through the von Mises stress output file. The elements with more than average stress will be sorted out and the material properties for those elements will be updated from a lookup file which will be based on the material properties calculated from tension compression tests during fatigue. The final fatigue simulation will show the elements with most stress and degraded material properties. The objective here will be to develop a material data base for degraded material properties of disc and determining the location is highest stress or failure using those material properties. The assumption made here is that the one

cycle simulation in LS Dyna demonstrates same results as of 10,000 cycles experimentally. This is done as time required for each simulation is more than 10 hours and increasing the number of cycles will increase the simulation time considerably. The simulations are being done and the results will be provided in the next deliverable.

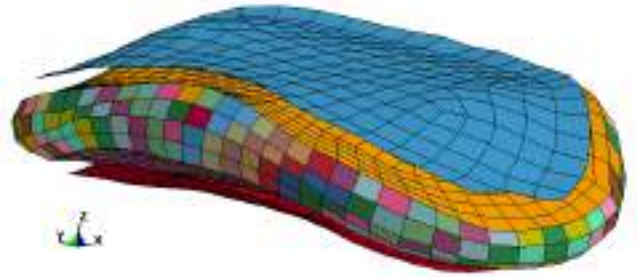


Figure 2-36: FE model of cervical spine intervertebral disc with different material for each annulus element.

Year 3: Continue to conduct in-vivo testing on military personnel to define C-spine kinematics during simulated operational conditions. Use FEM to specify load limits and number of load cycles that can be applied to C-spine repeatedly during operational conditions.

3.1 Cervical Design and Production

In-vivo FSU deformation measurement by dual US was challenging without a proper design of cervical collar over the years. As a planar imaging method, US required relatively fixed imaging windows and angles during the examination. In our previous *ex-vivo* validation experiments, the overall mean absolute error of US measurements was 0.041 mm for applied frequencies 1-8 Hz. Assuming typical IVD deformation of 0.8 mm under 150 N load, this corresponds to a 6.3% precision error in the US measured strain. However, the large range of neck motion brought issues of stabilizing ultrasound transducer on human volunteer during *in-vivo* experiments: on one hand, loose contact between transducer and neck skin caused miss of vertebrae image, and affected accuracy of FSU deformation measurement; on the other hand, using devices such as orthotic collar guaranteed quality of dual US imaging, but the range of neck motion was limited.

A flexible neoprene fabric cervical collar (Figure 3-1) was developed to mount ultrasound probes in effort to provide reliable US measurement of *in-vivo* FSU deformation on volunteers in activities (ex. jumping or cyclic neck compression/tension). Tensile adhesive gel (Parker Laboratories, Fairfield, NJ) maintained probe-to-skin contact over the testing period. In current study protocol, human subjects perform six 4-minute jumping trials with a motorcycle helmet. Subjects were able to extend and flex neck with the ultrasound devices and helmet mounted. Compared to previous collars, US imaging generally maintained equivalent quality as the trials with a rigid orthotic collar, which only

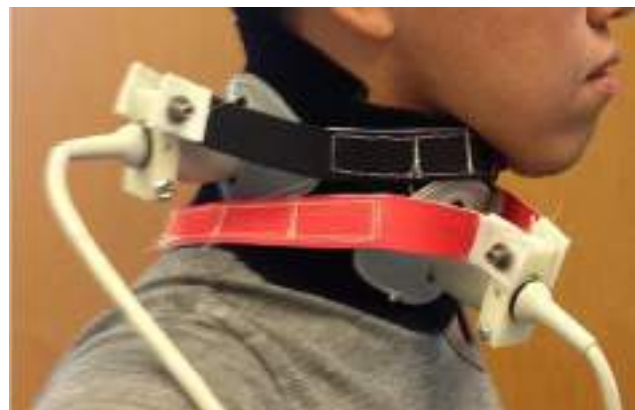


Figure 3-1: The flexible neck collar has two openings for US probes to image vertebral bodies anteriorly and laminae posteriorly. On the outer surface, the fabric strip provides mating sites for other fabric strips. The US probes were fastened on their tail end by multiple elastic bands. The flexibility of neoprene allows the subject to perform jumping, flexion/extension to a certain degree without loss of US images.

provides flexibility to neck motion in superior- inferior direction.

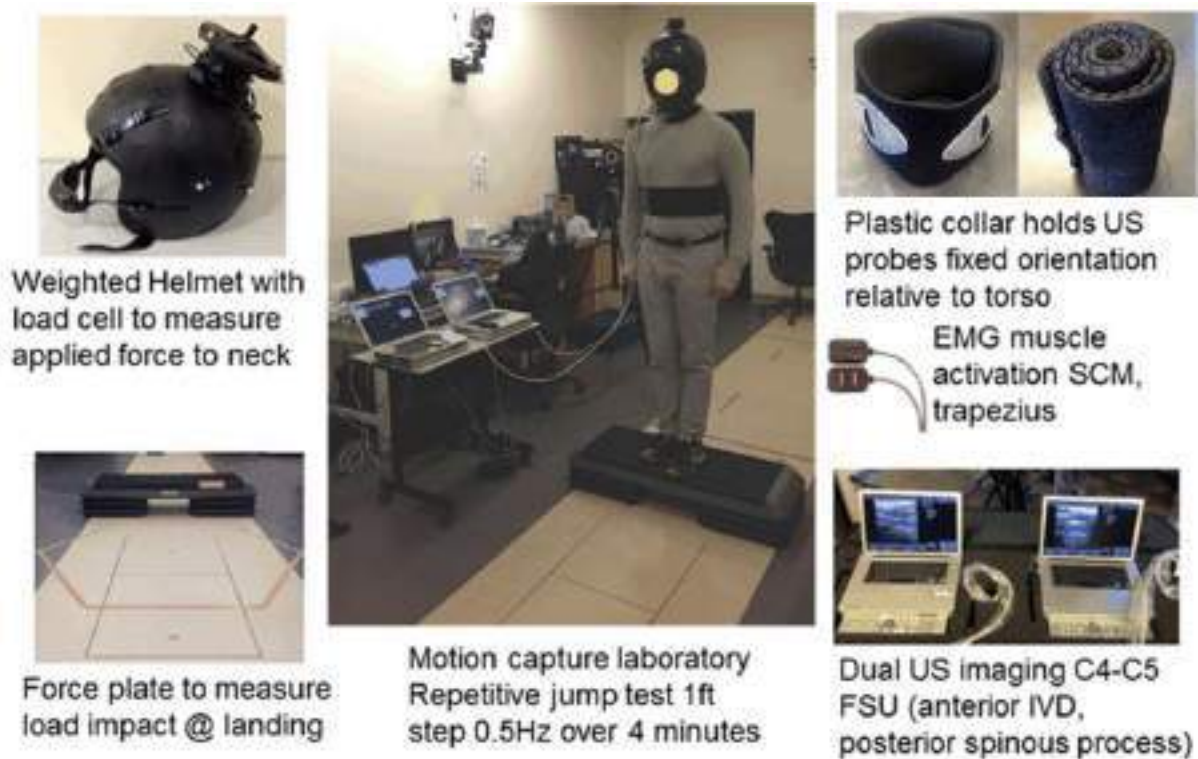


Figure 3-2: Human volunteer performing repetitive jumping task with a geared helmet. Impact to head and impact during landing were measured by load cell and force plate. The resultant C4-C5 FSU deformation was imaged by dual ultrasound system during jumping. Para-cervical muscles (SCM, upper trapezius) activation were measured by non-invasive surface EMG.

3.2 In-vivo Dual US Test in Repetitive Jumps

The aim of study is to measure the effect of para-spinal muscle activation of deformation of FSU/IVD during repetitive jumping (simulated tasks) by using dual US system. Eight human subjects were recruited under IRB approval by Committee on Clinical Investigation at BIDMC. We hypothesized reflexive contraction of the para-cervical muscles helped to dampen the extra force transmitted to the cervical spine, but prolonged and recurrent jumping may result in muscle fatigue with increased load applied to the IVD and a change of dynamic compliance of the FSU/IVD. IVD integrity was evaluated in T2-weighted Magnetic Resonance (MR) Images for all subjects in BIDMC Radiology. Subject repetitively jumped on/off 0.8 feet step at 0.5 Hz landing with both feet on force plate while maintaining upright posture for 4 minutes, wearing a helmet to simulate military head gear (Figure 3-2).

The motorcycle helmet subject wore during jump activities weighted 4 lbs with an additional 2.5-lb weight to mimic night vision goggle and communication unit. Seven passive reflective optical markers were placed on the helmet and torso to track relative displacements of head relative to the first thoracic vertebrae by Vicon Motion Capture System (10 MX-T40 cameras, Vicon Industries Inc., Hauppauge, NY). C4-C5 FSU superior-inferior deformation was measured

by a dual US system consisting of two Terason t3200 systems (Terason, Burlington, MA) synchronized to collaboratively capture US images with 15L4 linear arrays (4-15 MHz). A surface electromyography (sEMG) system (Bagnoli Desktop System, Delsys, Natick, MA) was used to evaluate para-cervical muscle activities by collecting sEMG of upper trapezius and sternocleidomastoid muscles. The compressive applied load by extra weight and landing force profile were measured by a miniature load cell (iLoad Mini, Loadstar Sensors, Fremont, CA) embedded in helmet and a grounded force plate (Figure 3-3).

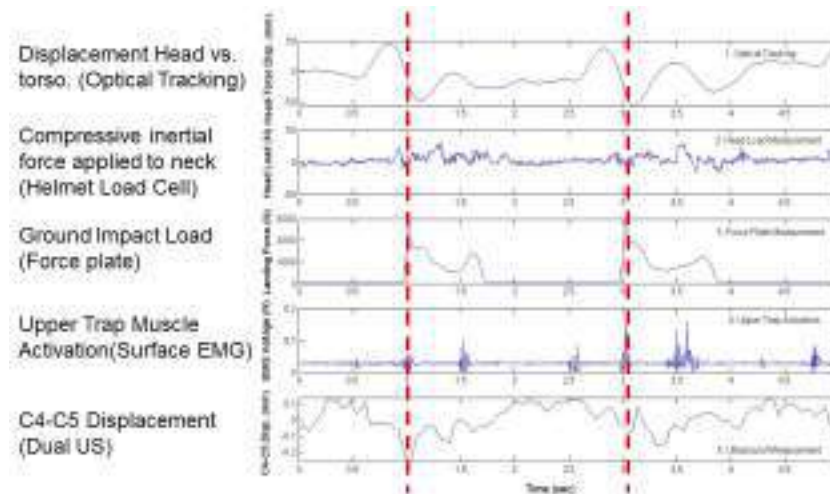


Figure 3-3: Synchronized measurements over 5 seconds (2 jumps) with un-weighted helmet. Head displacement, load applied to head, impact force profile, IVD deformation measured by dual US, and para-cervical muscle activation measured by sEMG synchronized in time. Impact force measured by force plate reaches maximum during landing (red dashed lines).

The number of times that EMG signal exceeded a set threshold (0.1V/1kAmp & 1V/10kAmp for upper trapezius and SCM respectively) were used to evaluate the intensity of EMG activation times in a period. The para-cervical muscle activities were compared between volunteers who have regular strength training vs. endurance training (swimming). The volunteer who participated in the weight training program (Figure 3-4 A and B) had greater muscle activation signals compared the volunteer who did endurance training (Figure 3-4 D and E). However, fatigue became apparent sooner in the weight training volunteer as indicated by muscle activation decreasing over time (Figure 3-4 C and F). For the weight training volunteer, fatigue occurred faster (slope = -0.17 s^{-1}) compared to the endurance training volunteer (slope = -0.012 s^{-1}).

During jump tests, C4-C5 FSU was repetitively compressed and then recovered after each landing. Amplitude of FSU deformation, defined by the difference between minimum and maximum displacements, was shown as double arrow in Figure 3-5. Mean of the amplitudes (length of double arrows) over time is used to characterize FSU motion levels in different time periods.

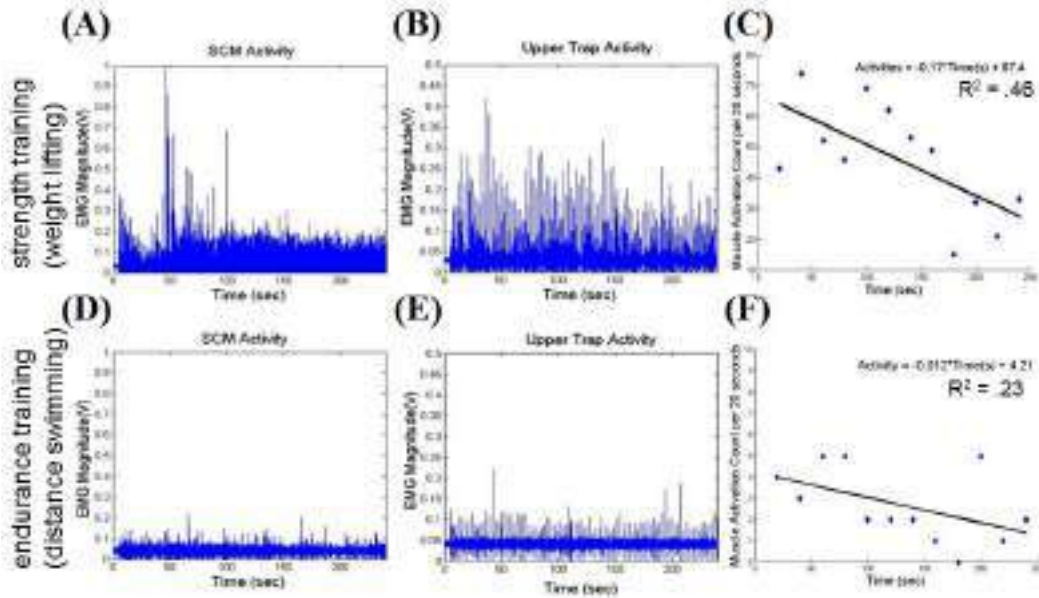


Figure 3-4: Muscle activation for volunteers who have regular strength training (A-C) vs. regular endurance training (D-F).

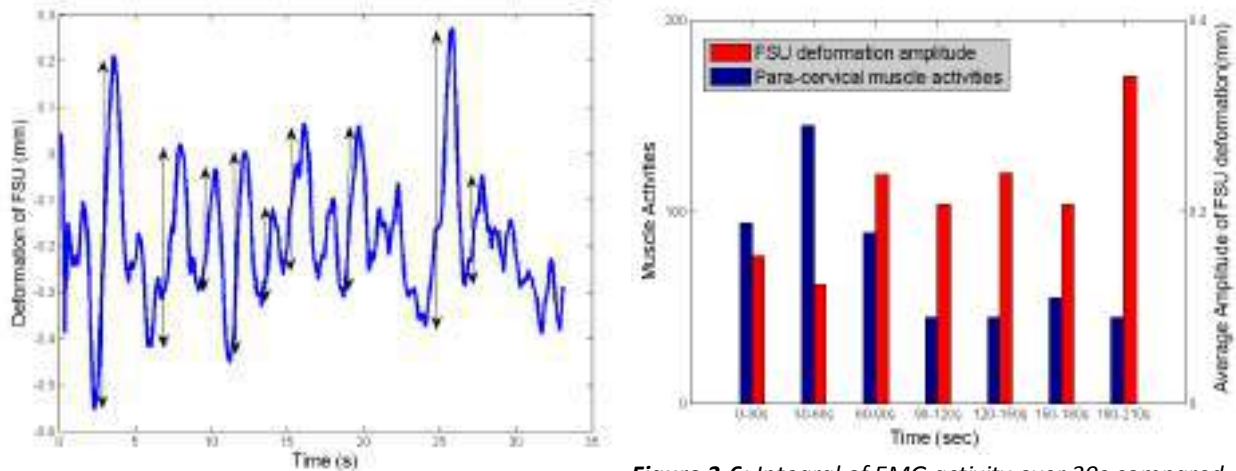


Figure 3-5: C4-C5 FSU compression and re-expansion during the jump tests. The amplitude of FSU motion is illustrated by the double arrows.

Figure 3-6: Integral of EMG activity over 30s compared to corresponding mean FSU deformation. Initially, muscle activation stiffens FSU and is manifested by attenuating IVD deformation. However, muscle fatigue reduces dampening of the load transmitted to IVD.

Due to muscle fatigue, para-cervical muscle activities decreased over time, when FSU deformation amplitudes gradually increased (Figure 3-6). The jump tests suggest that para-cervical muscles are capable of stiffening the FSUs and minimizing the magnitude Intervertebral Disc (IVD) deformation. However, over the course of jump test, muscle fatigue was noted, and the para-cervical muscles are less capable of dampening transmitted load to IVD and deformation increases. Plotting amplitude of FSU deformation as a function of muscle activities shows an inverse correlation between FSU deformation and muscle activation (Figure 3-7).

Our preliminary data demonstrated IVD deformation inversely correlated with muscle activity, emphasizing the importance of dynamic stiffness imparted by muscle activation. Passive measurement of FSU kinetics and kinematics were not able to incorporate the muscle effect and reflect in-vivo performance during activities. Our previous study showed that a larger fraction of the compressive impulse was transmitted to the C4-C5 IVD when a subject wears a helmet compared to not wearing additional head gear when performing jumping from a height using single US. In future, we will use our current experimental data to understand the difference of kinematics and muscle dampening effect when compressive impact was applied to head between using an unweighted helmet vs. a weighted helmet.

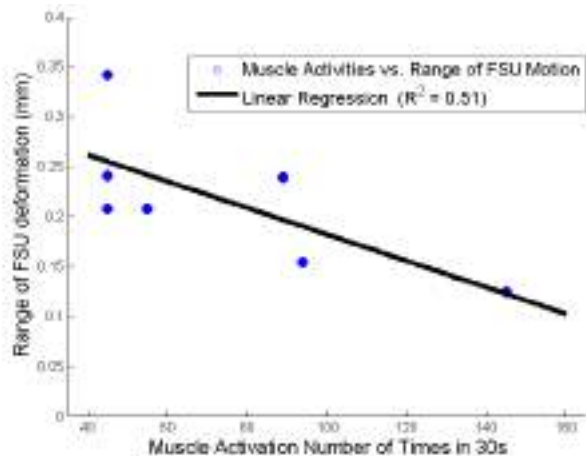


Figure 3-7: Amplitude of FSU deformation as function of muscle activities. Linear regression shows an inverse correlation ($R^2 = 0.51$).

3.3 *In-vivo US Test in Simulated Environment*

In order to derive a transfer function for the mechanical behavior of the cervical spine *in-vivo* in a consistent and reproducible way, we developed a system (Figure 3-8) that applies cyclic distraction/compression loads at frequencies and amplitudes that will facilitate derivation of a universal transfer function for the mechanical behavior of the cervical spine FSUs *in-vivo* in a consistent and reproducible fashion and allow the application of different load profiles (sinusoidal, square wave, triangle wave, or combinations thereof) that simulate the forces and moments applied to the head and neck of mounted troops during military maneuvers.

To provide controllable, safe forces to spine, the neck loading system incorporated adjustable counter-weights which tared the weight of human subject of different weights and a safety force break-away force (Figure 3-9). This update allowed the system to be driven by light-duty actuators as well as manual lifting. A pivot study using the system was performed to evaluate effect of voluntary neck muscle activation on C-spine properties. The actuation was done by lifting or pushing down the seat by hand. A miniature load cell on helmet was used to measure the transmitted load. The resultant deformation of C4-5 FSU was

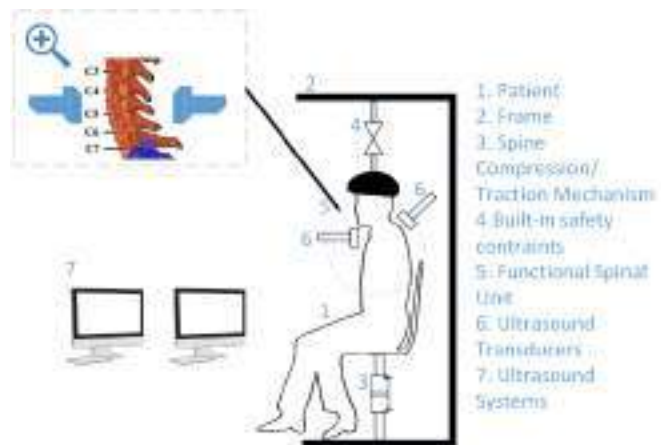


Figure 3-8: Schematic of system that applies cyclic load to head/neck of subject while sitting or standing in load frame. Under control with built-in safety constraints (4), a selected compression/traction pattern (3) is applied vertically through the seat that the subject (1) is seated upon. The load is transferred up the spine to the head and neck which is secured in a helmet rigidly fixed to an adjustable cross-bar. Dual US (7) simultaneously measures the deformation of selected FSU (5) in real time.

imaged by dual ultrasound system during different frequencies.

Cyclic loading at 4 different frequencies (0.5, 1.0, 1.5, 2.0 Hz) were applied to the helmet of a human volunteer seated in the C-spine cyclic loading system. Examination of Figure 3-10A demonstrates that even though a cyclic tensile tension-compression load is applied to head, the deformation of IVD tended to be compressive only. This reflects 1) creep deformation; 2) the rate of relaxation/re-expansion of IVD is much slower than the rate of applied external load; and 3) tensile load is resisted mainly by muscles and ligaments, while the compressive load is resisted primarily by IVD. Furthermore, examination of Figure 3-10B demonstrates that the volunteer contracts the para-cervical muscles, the deformation of FSU is considerably dampened.

Together, these results support the observation from the jump tests that para-cervical muscles are capable of dampening the load applied to the IVD and that as these muscles fatigue, more load will subsequently be transferred to IVD, contributing to fatigue and “wear”. The conclusion from these test results suggest that a combination of strength and endurance para-cervical muscles will protect our troops from cervical spine degeneration.

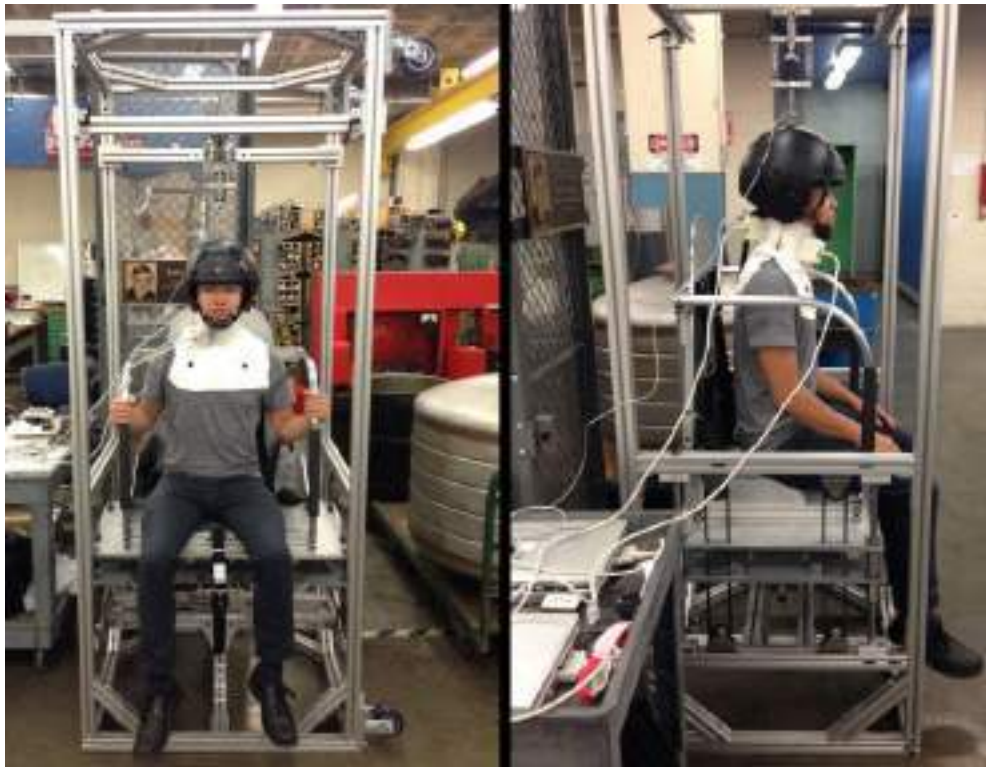


Figure 3-9: Modified frame with taring weights underneath the seat which enable seat lifting to be done by manual power. The volunteer is seated in a neutral position and wears a cervical collar mounted with dual US probes at fixed orientations with respect to the neck.

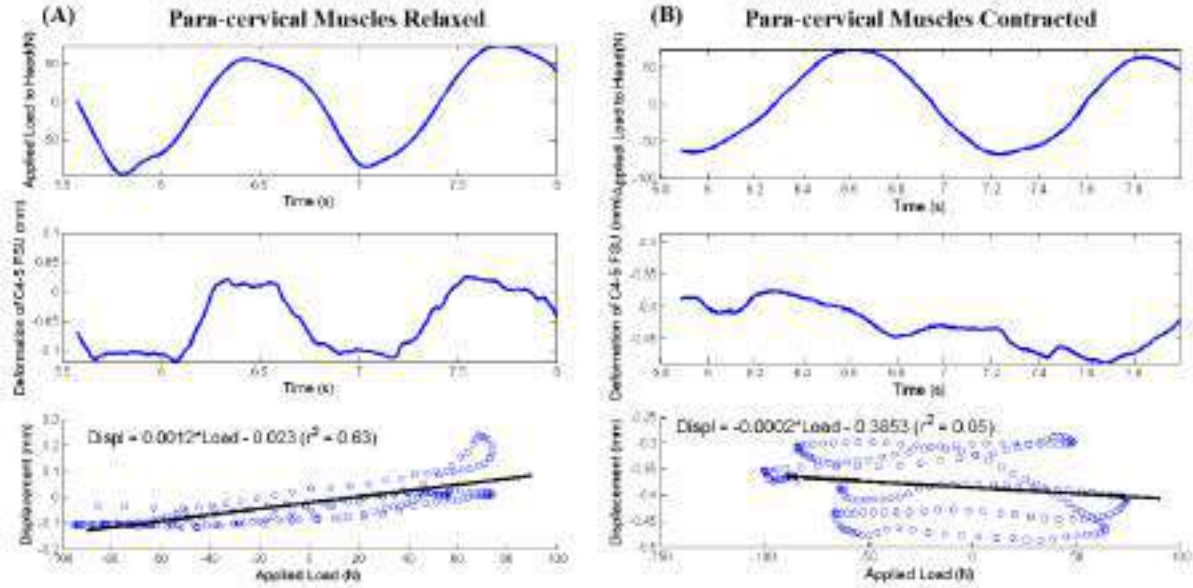


Figure 3-10: Representative result of dynamic testing at 1 Hz. Applied load to head over time (top row); resultant C4-C5 FSU deformation over time (middle row); displacement as a function of applied load to represent the transfer function (bottom row).

3.4 Fatigue Experiments on Cervical Spine Disc Segments

Experiments were performed on 3 more disc segments based on the previously mentioned protocol, and a finite element model of disc with and without nucleus, which can be applied with different fatigue conditions is developed in Abaqus software. The finite element model is developed with a hyper-viscoelastic material for the annulus and linear elastic materials for nucleus and end plates. The loading is applied in two steps, one single compression at 2 or 4 Hz, and second direct cyclic fatigue loading, which extrapolates the response after every 500 cycles.

The direct cyclic algorithm uses a modified Newton method in conjunction with a Fourier representation of the solution and the residual vector to obtain the stabilized cyclic response directly. In direct cyclic loading the elastic stiffness serves as the Jacobian matrix throughout the analysis, the equation system is solved only once. Therefore, the direct cyclic algorithm is less expensive to use than the full Newton approach to the solution of the nonlinear equations, especially when the problem is large like in case of fatigue.

The results for 8 disc segments tested at 2 Hz and 4 Hz each, are compared below. The results from finite element model are also compared to the experimental data.

Experiments: In this set of experiments, the fatigue tests were performed on three bone disc segments, simultaneously. Two segments were tested under 150 N compressive load at 2 Hz and one segment was tested at 4 Hz and same compressive load. The results were combined with the results of the previous segments and the average from a total of 16 disc segments are presented.

Magnetic resonance imaging (MRI) of all the disc segments was performed to ensure that there were no prior discontinuities in the spine and that the discs were representative of a healthy population. Pfirrmann scores (Pfirrmann et al. 2001) were determined from the MRI scans and all the segments with scores less than 3, determining a normal to slightly diseased specimen,

were selected. The posterior elements and facets of the segment were removed as per the protocol explained in the previous reports. Details of the disc segments tested are presented in Table 3-1.

Table 3-1: Details of segments tested under fatigue.

Seg. #	PMHS	Age (yrs)	Sex	Mass (kg)	FSU	Initial Disc Height (mm)	Disc Area (mm ²)	Frequency (Hz)	Pfirschmann Grades
1	HS-799	64	F	48.1	C6-C7	5.7366	318	2	2
2	HS-799	64	F	48.1	C4-C5	4.614	283	2	3
3	HS-799	64	F	48.1	C2-C3	5.3404	195	2	2
4	HS-798	58	M	57.6	C6-C7	6.4266	442	2	2
5	HS-795	54	M	107	C6-C7	4.5694	614	2	4
16	HS-821	59	M	106	C2-C3	5.8418	311	2	
18	HS-823	31	F	138	C4-C5	5.42	223	2	
19	HS-823	31	F	138	C6-C7	5.27	282	2	
Avg		53		80.4		5.4	333.5		
7	HS-800	58	F	79.83	C2-C3	4.5294	193	4	
8	HS-795	54	M	107	C2-C3	6.2124	325	4	2
9	HS-801	65	F	83.01	C2-C3	6.0146	227	4	2
11	HS-801	65	F	83.01	C6-C7	3.9666	627	4	
12	HS-797	67	M	99.79	C2-C3	4.4708	209	4	
13	HS-820	47	M	75	C6-C7	4.576	699	4	
14	HS-820	47	M	75	C4-C5	4.632	319	4	
17	HS-823	31	F	138	C2-C3	3.85	232	4	
Avg		54		92.6		4.8	354		

Results: The piston stroke (i.e. the displacement of the piston) due to 150 N load amplitude was measured for all eight segments at 2 Hz and 4 Hz, and the average curves are plotted in Figure 3-11 and Figure 3-12 respectively. The piston stroke was observed to decrease with increasing number of fatigue cycles. It was further reduced with increasing fatigue sets, i.e. the piston displacement for 1st fatigue set was highest and was least for 5th fatigue set, for both the frequencies. This shows that as compressive displacement of the disc decreases, the disc becomes rigid with increasing fatigue. The piston displacement was also higher at 2 Hz as compared to 4 Hz for all five fatigue sets, showing that at 4 Hz the disc exhibits strain rate hardening effect, whereas at 2 Hz the water in the disc gets enough time to move, causing more strain. The piston displacement for 5th fatigue set at 2 Hz was also higher than the piston displacement for 1st fatigue set at 4 Hz, showing a clear distinction between disc response at 2 Hz and 4 Hz. At 4 Hz the piston displacement was almost constant after the first fatigue set, showing that the stiffness of the disc remained constant after the first fatigue set.

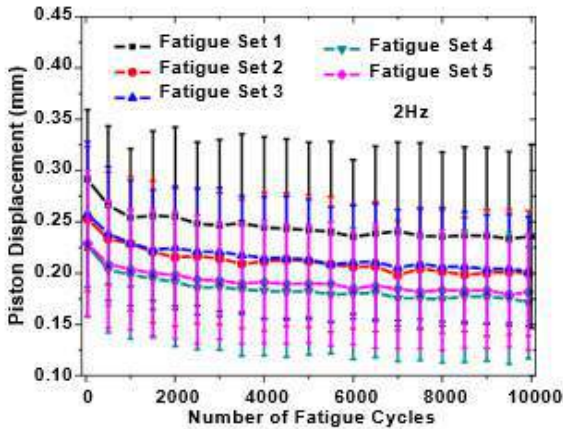


Figure 3-11: Average piston displacement for 5 sets at 2 Hz.

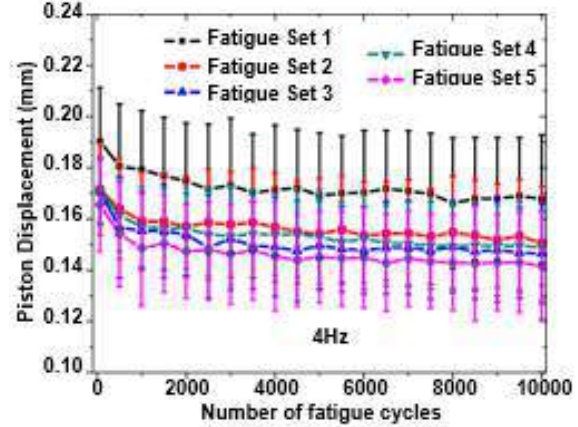


Figure 3-12: Average piston displacement for 5 sets at 4 Hz.

Height loss due to fatigue was calculated with two sets of data. First, height loss from fatigue data was calculated as the difference between initial and final position of the piston for each fatigue set. This height loss represents the reduction in height during fatigue. Second, height loss was calculated from x ray measurements before fatigue, and after the IVD was allowed to relax post fatigue. IT represents the effective height loss, as the disc was allowed to relax post fatigue. Both height losses for all 5 fatigue sets are compared in Figure 3-13 and Figure 3-14 for 2 Hz and 4 Hz respectively. The height loss from fatigue as well as x-ray measurements are observed to be maximum during first fatigue set for both the frequencies, and was comparatively higher at 2 Hz. This was again due to the strain rate hardening effect at 4 Hz. The height loss calculated from x- rays was however almost the same with increase in fatigue for both the frequencies. This implies that the height loss might not necessarily dependent on frequency, but it depends on the number of cycles and magnitude of loading. From this it can be concluded that relaxation time for a person exposed at 2 Hz and 4 Hz fatigue loading could be same.

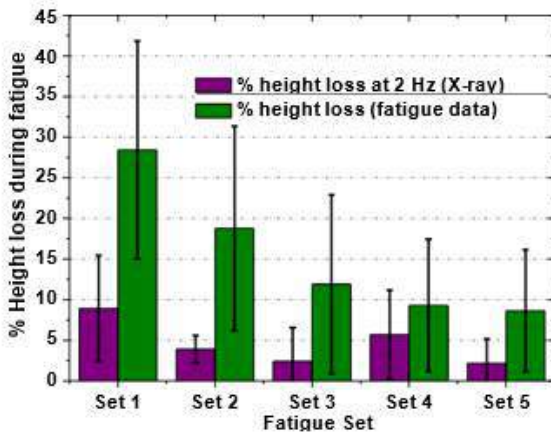


Figure 3-13: Height loss for 5 sets at 2 Hz.

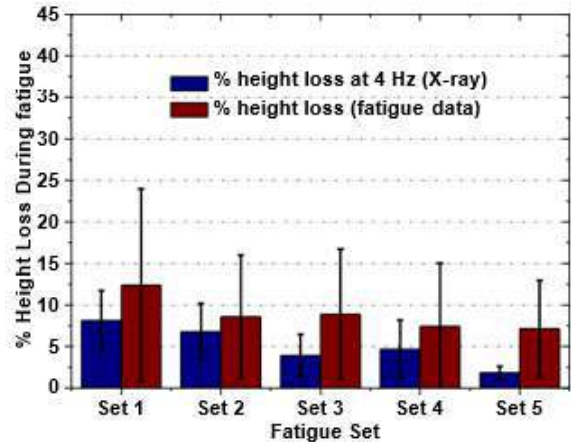


Figure 3-14: Height loss for 5 sets at 4 Hz.

The stiffness of the IVD was calculated as the ratio of force to displacement for every cycle. From Figure 3-15 the stiffness of the discs tested at 2 Hz can be observed to increase with fatigue. The stiffness for 2nd and 3rd fatigue set was higher than 1st fatigue set and the behavior was almost identical. Whereas the 4th and 5th fatigue sets show even stiffer and identical

behavior. For the segment tested at 4 Hz it can be observed from Figure 3-16 that the stiffness increased after the 1st fatigue set and was almost constant for remaining four fatigue set, suggesting some damage in terms of discharge of fluid in nucleus and steady material properties after the 1st fatigue set. It still needs to be verified with some imaging technique. The overall stiffness of the segments tested at 4 Hz was higher as compared to the segments tested at 2 Hz.

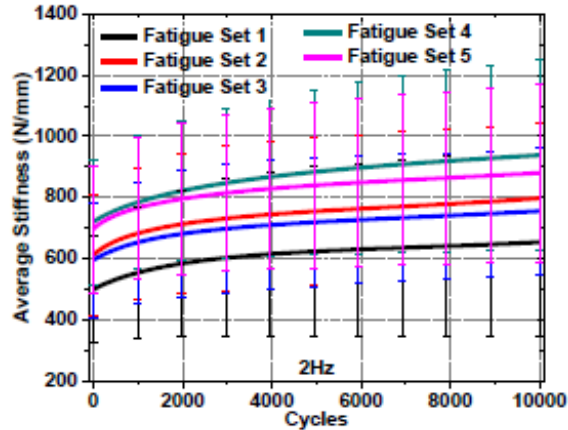


Figure 3-15: Average stiffness for 5 sets at 2 Hz.

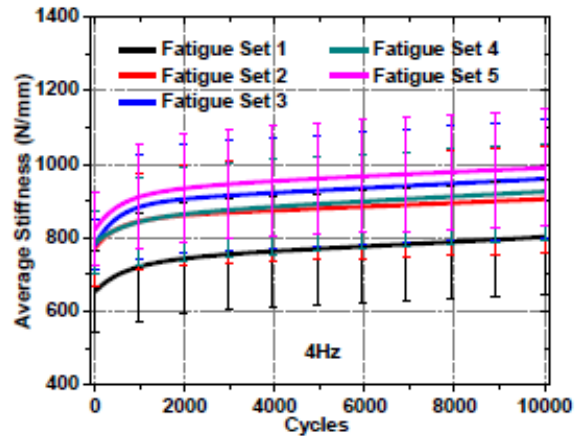


Figure 3-16: Average stiffness for 5 sets at 4 Hz.

In Figure 3-17 and Figure 3-18, the average stress versus strain plots from the static compression tests of all five segments are shown. The stiffness of the segments fatigued at 2 Hz was similar post first two fatigue sets. The stiffness increased further for the next three fatigue sets. This shows that at 2 Hz the disc is palpated during the first two fatigue sets and, during the 3rd, 4th and 5th fatigue sets there is loss in viscoelasticity and thus increase in stiffness. The disc segments fatigued at 4 Hz showed constant stiff behavior after the first fatigue set. Suggesting that viscoelasticity loss is maximum during the first fatigue set and if there is a damage, it will be initiated during the first fatigue itself. The increase in stiffness of segments was almost similar for both the frequencies, though the height loss in segments tested at 4 Hz is not as much.

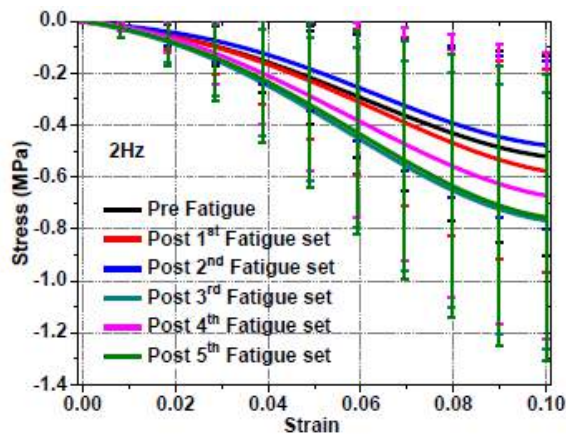


Figure 3-17: Stress-strain plots for static compression test pre and post 5 fatigue sets (2 Hz).

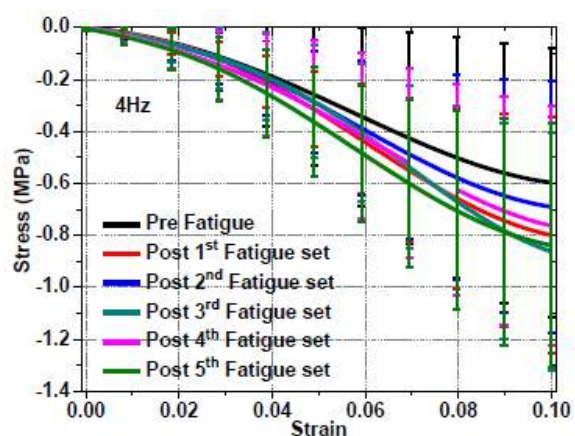


Figure 3-18: Stress-strain plots for static compression test pre and post 5 fatigue sets (4 Hz).

In the viscoelastic tests 10% strain was applied to the disc and the stress was allowed to relax for 30 minutes. The stress relaxation curves from the viscoelastic tests for segments tested at 2

Hz and 4 Hz are plotted in Figure 3-19 and Figure 3-20 respectively. The viscoelastic properties of the discs fatigued at 2 Hz did not change much for the first two fatigue tests. However the initial and final stiffness increased, and the toe region of the stress relaxation curve shifted to the right post 3rd, 4th, and 5th fatigue sets, suggesting a loss in viscosity. The viscoelastic response after the first fatigue test at 10% strain from the segments tested at 4 Hz was similar to that observed from the piston displacement, stiffness, and static compression plots. The viscoelastic material parameters for average viscoelastic curves pre and post fatigue are tabulated in Table 3-2.

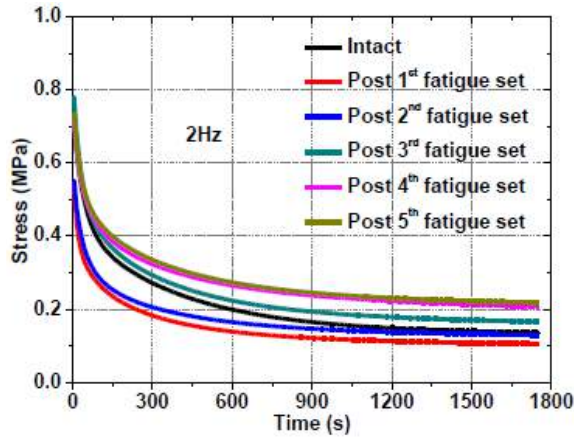


Figure 3-19: Average stress relaxation curve pre and post 5 fatigue sets (2 Hz).

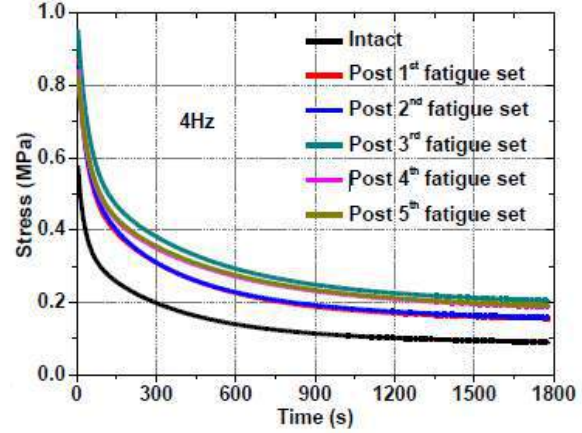


Figure 3-20: Average stress relaxation curve pre and post 5 fatigue sets (4 Hz).

Table 3-2: Average quasi-linear viscoelastic material parameters.

	A	B	a	b	c	d	g	h
Frequency	2Hz							
Intact	0.0032	1.2497	0.3320	0.0245	0.2998	0.0025	0.1613	5.5E-5
Post 1 st Fatigue	0.0009	1.4965	0.2744	0.0342	0.2525	0.0033	0.1708	8.0E-5
Post 2 nd Fatigue	0.0007	1.5625	0.2858	0.0543	0.2999	0.0037	0.2354	3.3E-5
Post 3 rd Fatigue	0.0093	0.9119	0.3188	0.0287	0.3438	0.0029	0.2008	4.4E-5
Post 4 th Fatigue	0.0096	1.0099	0.3185	0.0210	0.2755	0.0025	0.2982	6.3E-5
Post 5 th Fatigue	0.0103	0.9518	0.2770	0.0202	0.2654	0.0026	0.2895	7.8E-5
Frequency	4Hz							
Intact	0.0033	1.2065	0.3070	0.0380	0.2841	0.0034	0.1026	6.8E-5
Post 1 st Fatigue	0.0064	1.0749	0.2954	0.0310	0.2156	0.0028	0.1073	8.1E-5
Post 2 nd Fatigue	0.0045	1.1182	0.2321	0.0457	0.3156	0.0037	0.1289	6.8E-5
Post 3 rd Fatigue	0.0055	1.1620	0.4002	0.0172	0.2151	0.0019	0.1683	7.3E-5
Post 4 th Fatigue	0.0048	1.2257	0.3458	0.0233	0.2979	0.0022	0.1668	6.6E-5
Post 5 th Fatigue	0.0086	0.9625	0.3414	0.0238	0.2729	0.0024	0.2033	7.4E-5

Summary: Sixteen segments were fatigued at a 150 N compressive force at 2 Hz and 4 Hz loading frequencies for 5 sets of 10,000 cycles. Static tension-compression and viscoelastic stress relaxation tests were performed prior to testing and after each fatigue set. Average results for the

segments tested at 4 Hz showed strain rate hardening effect and thus were not strained as much as discs tested at 2 Hz.

The piston displacement and the disc height loss was maximum during the first 10,000 cycle fatigue set for both the frequencies. As the number of cycles increased, the IVD demonstrated a decreasing piston displacement for segments tested at 2 Hz, whereas the piston displacement was almost identical for the last four fatigue sets at 4 Hz. After the first fatigue set, the strain in all the 4 Hz sets was almost identical, suggesting some damage which needs to be further investigated using imaging. However the effective height loss from x-rays measured between two fatigue sets was observed to be similar for segments tested at 2 Hz and 4 Hz.

3.5 *Developing a Finite Element Model of Intervertebral Disc*

In the previous deliverable, a finite element model with homogeneous disc and end plates was developed in the Abaqus software, and the fatigue load was applied in two steps: 1) a uniform load of 150 N at 2 Hz was applied to the superior end plate, and the boundary condition at the inferior endplate was fixed in all degrees of freedom; 2) a direct cyclic loading step was applied to simulate 10,000 compression cycles based on the previous step history. Initially, the disc was modeled as a homogenous hyper-viscoelastic material termed “model A” below. Model A performed well for the prescribed boundary condition, so to accommodate a more realistic response, the model was further improved to represent a linear elastic material with a nucleus at the center, called “model B” below.

The finite element model was developed from a CT scan (Figure 3-21) of a 50th percentile male (25 years, 78 kg total body mass, and 183 cm stature). The model contained 676 quadratic shell elements and 845 hexahedral solid elements. The disc was modeled as hyper-viscoelastic material with the properties of the disc without fatigue obtained from the static compression test and viscoelastic stress relaxation. The end plates were modeled with a linear elastic material. In model B, the nucleus (35% of total volume of disc) was also modeled with a linear elastic material (Panzer 2006).

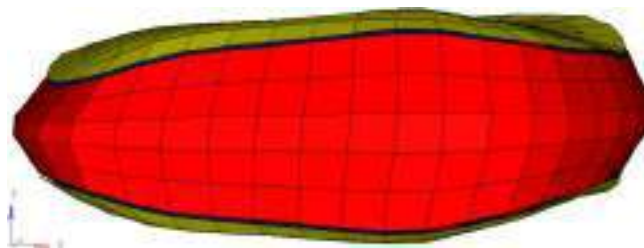
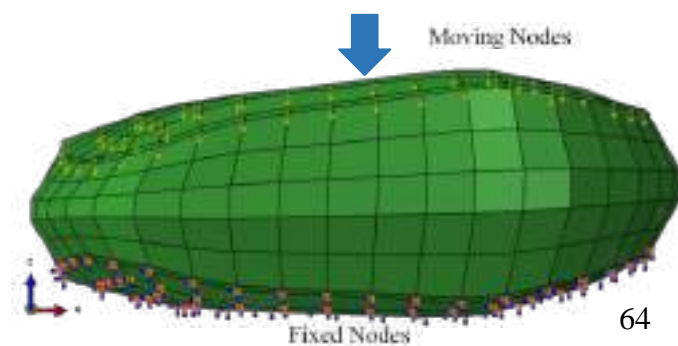


Figure 3-21: Developed disk FE model.

Boundary Conditions: A cyclic load at 2 Hz or 4 Hz frequency was applied to the developed FE model of the disc. As per the experiments, the cyclic load was applied to the disc segment as shown in Figure 3-22. All surface nodes of the inferior end plate were constrained in x, y, and z directions, and a cyclic load of 150 N was applied in z direction on the superior end plate. For the 2 Hz test, reconstruction of one cyclic simulation was performed as step 1. The next step of computation was the direct cyclic loading for 10,000 fatigue cycles.



Results:

Model A: Computation of Model A took about 1 hour using 64GB ram and an 8

core processor for the 2 Hz fatigue simulation. Figure 3-23 shows the von Mises stress distribution in the disc at the end of the step 2 (i.e. 10,000 cycles). The magnitude of the residual stress was present in the lateral parts of the disc. The displacement of the nodes during 10,000 cycles was compared to the piston stroke from experiments for the first 10,000 cycles (Figure 3-24). The experimental stroke and nodal displacements were comparable. The stroke was maximum during the first 1000 cycles, followed by a plateau showing the effect of viscoelastic properties in this first 1000 cycle period.

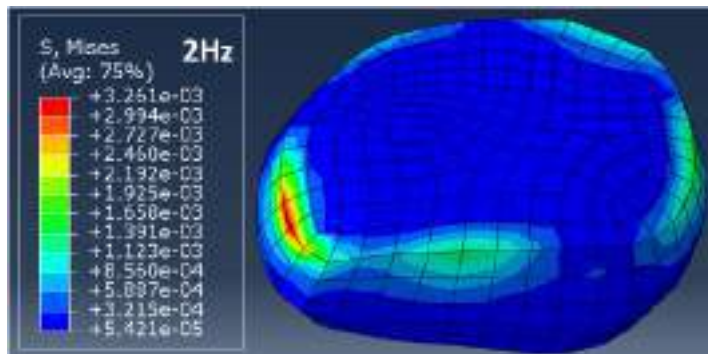


Figure 3-23: Von Mises (residual) stress (MPa) distribution post fatigue at 2 Hz.

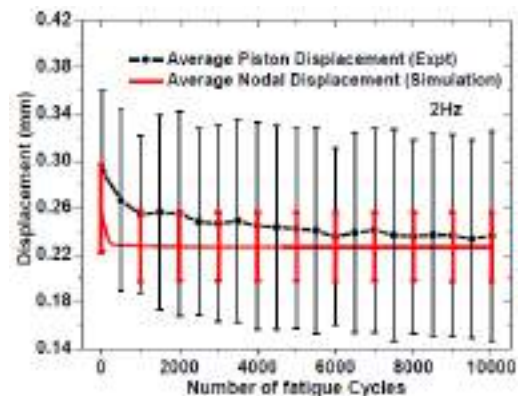


Figure 3-24: Comparison of piston stroke from experiments to the nodal displacements.

The FE model was then subjected to 4 Hz compressive load of 10,000 cycle. The nodal displacements were less at 4 Hz than at 2 Hz, demonstrating strain rate hardening in the intervertebral disc. The average displacements of all the nodes from simulations at 2 Hz and 4 Hz are shown in Figure 3-25. There was a discrepancy between nodal displacements at 4 Hz and the experimental stroke at 4 Hz, which can be attributed to the assumptions in the hyper elastic material model formulation in the Abaqus software.

It can be observed from the experimental data (Figure 3-15 and Figure 3-16) that the initial stiffness of the segments tested at 4 Hz is approximately 1.5 times greater than the stiffness of the segments tested at 2 Hz. Assuming that the stiffness of the segment also increases with the same ratio at 4 Hz, the results for simulation at 4 Hz are shown in Figure 3-26. The piston stroke and nodal displacement from simulation are in good agreement at this frequency.

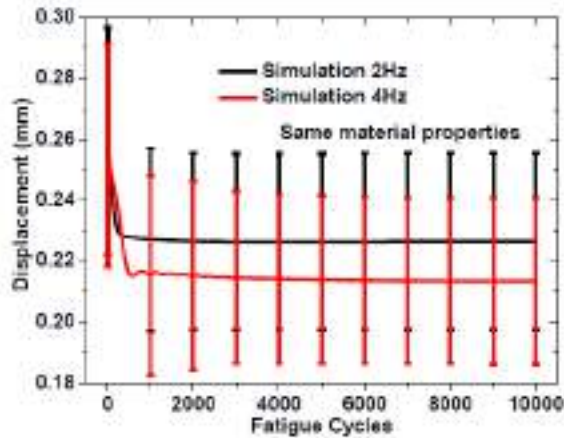


Figure 3-25: Comparison of nodal displacements at 2 Hz and 4 Hz.

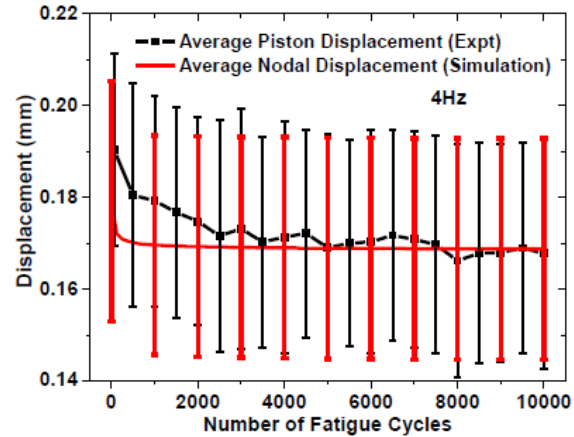


Figure 3-26: Comparison of piston stroke from experiments to FE nodal displacements.

Figure 3-27 shows the residual von Mises after 10,000 fatigue cycles at 4 Hz. The location of stress distribution was similar to 2 Hz, however the magnitude of the residual stress was greater in the 4 Hz condition. This suggest that stress and applied frequency are positively correlated.

Model B: Following the encouraging findings from the model A, in this subsequent model B, the center of the disc was modeled with an incompressible elastic material, more accurately simulating *in-vivo* nature. The nucleus was assumed to occupy 35% by volume of the disc and was modeled with material properties from Jones and Wilcox 2008.

The model was subjected to similar boundary conditions and the simulation took almost the same time (1 hour) using an 8 core and 64 GB ram machine. The simulations were carried out at 2 Hz and 4 Hz as in the experiments, and the nodal displacements were compared to experimental piston displacements. The nodal displacements from the simulation and a combined corridor for experimental piston displacement for both 2 Hz and 4 Hz frequencies are plotted in Figure 3-28. The nodal displacements from both the frequencies fit well within the experimental corridor, indicating improvement in the modeling process.

The residual von Mises stress, principal stresses in x-, y-, and z-directions, and pressure from fatigue were compared for the two simulations (i.e. 2 Hz and 4 Hz). It was observed from the

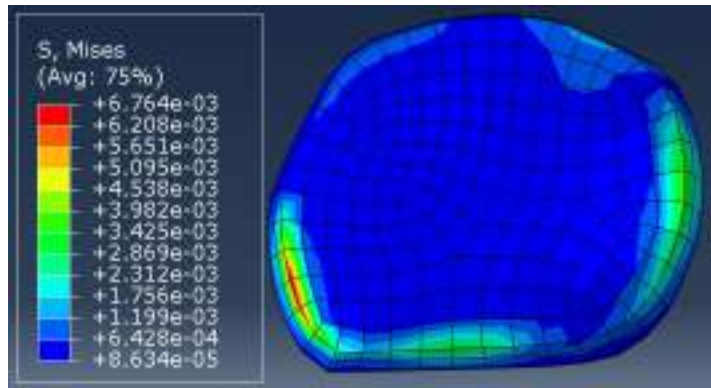


Figure 3-27: Von Mises (residual) stress (MPa) distribution post fatigue at 4 Hz.

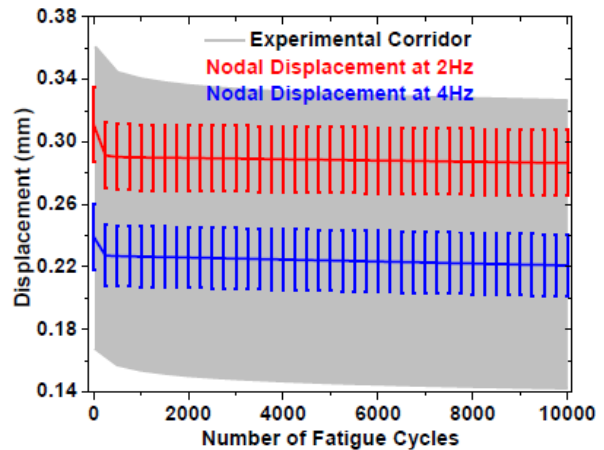


Figure 3-28: Comparison of piston stroke from experiments to nodal displacements from the simulations at 2 Hz and 4 Hz.

pressure that the nucleus was under maximum pressure causing it to reduce radially in the annulus. The maximum residual stress in the annulus occurred in the lateral direction while the nucleus was under the least stress. The principal stresses in the superior-inferior direction showed that both the annulus and nucleus were under similar magnitudes of stress, reflecting the applied load vector. From the von Mises stress, it was observed that the nucleus and annulus in the lateral directions were under maximum stress. The contour plots for both the frequencies for pressure, principal stresses, and von Mises stresses are shown in Figure 3-29 and Figure 3-30.

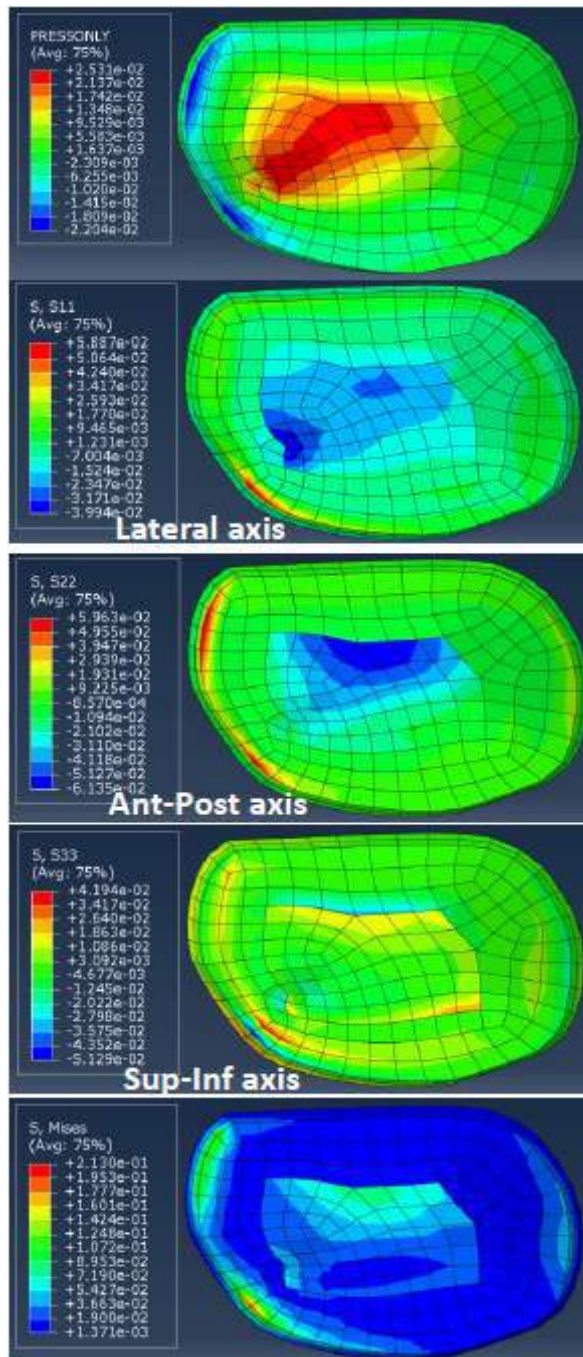


Figure 3-29: Contour plots of residual pressure, principal stress, and von Mises stress for cyclic loading at 2 Hz.

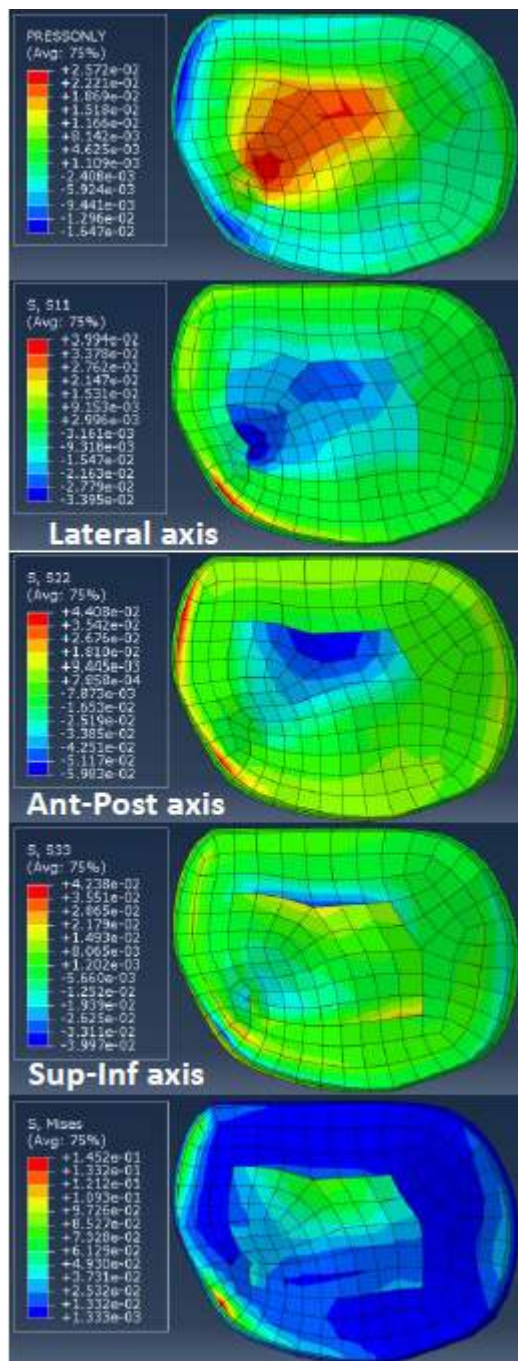


Figure 3-30: Contour plots of residual pressure, principal stress, and von Mises stress for cyclic loading at 2 Hz.

Summary: In this quarter, FE model of the intervertebral disc without nucleus (model A) and with nucleus (model B) was developed in Abaqus software. The boundary conditions and material properties used in the models were adopted from experimental data and literature. Model A showed good correlation with the experimental data. Model B with separations in its two components (i.e. the annulus and the nucleus) demonstrated differences in regional stress distributions during the fatigue loading process. The model was stiffer at 4 Hz than at 2 Hz, a phenomenon which validated the experimental observations. The peak principal stress

distributions in superior-inferior direction were on the superior regions in the simulation at 4 Hz, although the nodal displacements were not the greatest along the same direction. This demonstrates that with increasing frequency, there may be regional stress accumulations on the rostral side of the disc, with lesser transmission to the inferior region. These results suggest that a higher frequency of loading may be more injurious due to fatigue loading.

Year 4: Prove feasibility of measuring dynamic C-spine IVD deformation using dual US *in-vivo* in subjects engaged in repetitive jumping activities. Develop a vertebra registration method to track and overlay the volunteers' cervical spine MRI scan to ultrasound images by correlating anatomical landmarks. Construct finite element (FE) models of the IVD from the cyclic loading experiment to examine disc injury mechanism in response to physiological repetitive loading forces applied to the head and neck at different frequencies.

4.1 Combining US/MR Data and Calculating 3D Kinematics of C-Spine

To combine two sets of US FSU displacements and derive the cervical spine 3D kinematics and IVD strain mapping during the jump test, we developed an algorithm to register the US imaging planes in volunteers' cervical spine MRI scan comprised of the following steps:

1. Estimate feasible range of the corresponding US imaging slice in 3-D MR by placing fiducial optical markers on anatomical landmarks of subject and US transducers and correlating anatomical landmarks in the corresponding MRI image.
2. Recognize the anterior vertebra body-IVD-vertebra body and posterior laminae-interspinous ligament-laminae profiles in the slices over the feasible US orientation range by using a bone MR image enhancement algorithm.
3. Extract the vertebrae and laminar boundaries in US images by applying a semi-automated US phase bone localization algorithm.
4. Re-slice the MR C-spine images at different angles and search for the image of maximum profile likelihood (most similar) by minimizing the residuals of profile difference between MR and US.

US Imaging Plane Estimation: Optical markers were placed on US probes and anatomical landmarks on skin (C4/C6/T1 spinous process, sternal ends of clavicles, and thyroid cartilage notch) to find the relative positioning between US probes and C-spine (Figure 4-1). Each US probe has a 3-marker set that established the imaging plane in an absolute reference frame. Anatomical landmarks were identified in MR and palpated on the subject. Assuming the trunk posture remained steady, markers placed on thoracic T1 spinous process and clavicle sternal ends (left & right) were used as a rigid segment to map the MR images. Markers on C4, C6 spinous and thyroid cartilage notch were used to compensate the difference of C-spine curvature. The optical marker set on the US transducer defines the US imaging plane in the MR images. A range of angles were estimated to create the searching space to properly match the vertebra profiles between MR and US.

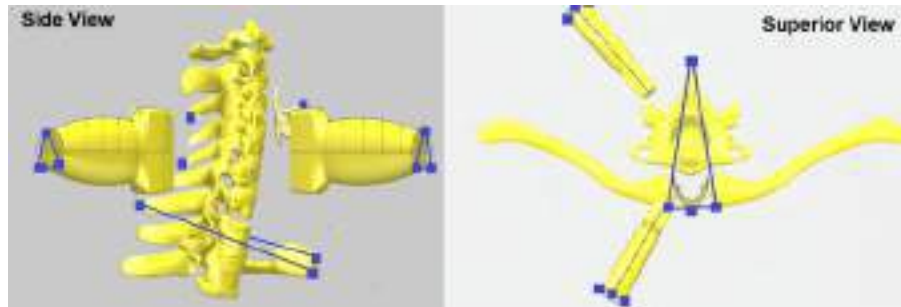


Figure 4-1: Optical markers (blue squares) were placed on human subjects and US probes. Selected anatomical landmarks include spinous processes of C4, C6, and T1, sternal end of clavicles, and thyroid cartilage.

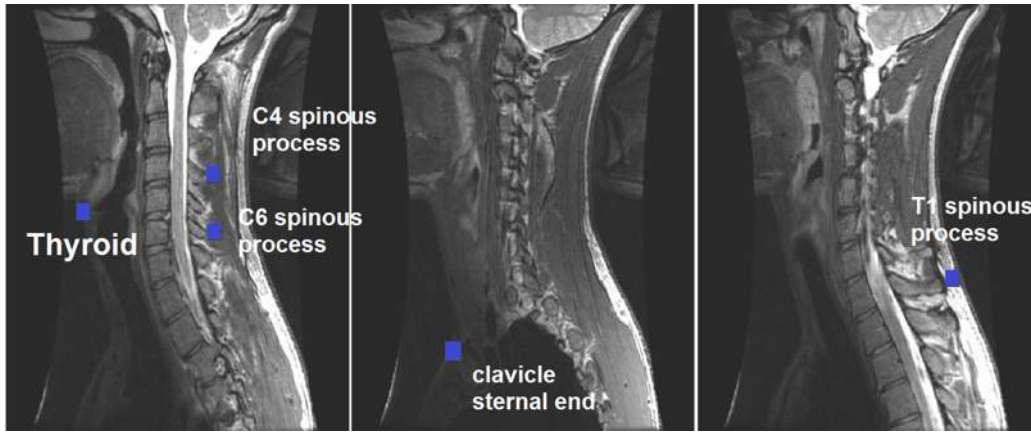


Figure 4-2: Anatomical landmarks were identified in corresponding MR scan slices.

Vertebra Profile Recognition in MR: C-spine MR scans were interpolated and re-sliced at different plane angles using an “ExtractSlice” algorithm developed by Teng. To recognize bone profiles in each slice, negative MR image was taken to increase the contrast between cortical bone/soft tissue and cortical/trabecular bone. The anterior and posterior bone profiles were extracted by outlining the emphasized cortical bone of vertebral bodies and laminae, which was later compared to their profiles in US images.



Figure 4-3: C-spine MRI image normal (left) and negative (right). The negative image enhances the contrast between compact bone/tissue and compact/spongy bone, which outlines the contour of vertebral bodies, spinous processes and laminar.

Vertebra Profile Extraction in US: The FSU profiles of vertebral bodies and laminar were outlined in US images. Using image phase information to derive symmetric features, a masked Log-Gabor filter is able to remove tissue layers, speckle noise, and highlight the contour of vertebral bodies/lamina surface for refining (Figure 4-4 and Figure 4-5). By using the internal US calibration factors, the contours sampled in image pixels were converted to physical length and compared to MR images.

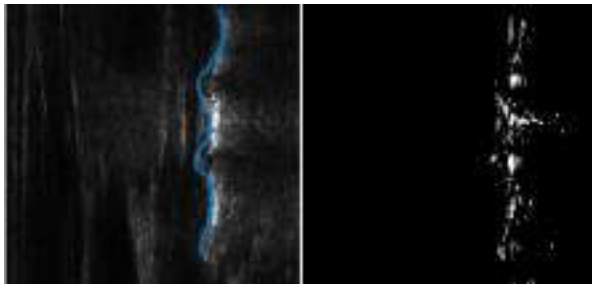


Figure 4-4: C4-C6 FSUs were imaged by US anteriorly (left), and the filtered image (right) localized the anterior surface of the vertebra and IVD.



Figure 4-5: C4-C6 FSUs were imaged by US posteriorly (left), and the filtered image (right) localized the surface of the laminar.

US Imaging Plane Localization: To match US image to its corresponding MRI slice, similarities between FSU profile curves in US and MR were characterized by point-to-point residuals calculation. The calculation was based on re-mapping of the profile curve in a local coordinate system where both superior endplates of C4 vertebrae in MR and US were selected as reference origin. Each point along the curve was represented as a 2-D vector. The averaged residual was calculated as the sum of the square root of all the square difference between points.

To find the best match US-MR image pair, averaged residuals were plotted as a function over the range orientation selection. The sample results in Figure 4-6 and Figure 4-8 show that the anterior and posterior ultrasound probes are orientated at 12° and 28° from the sagittal plane respectively, which coincides with our observation in optical tracking. It should be noted that the degree of freedom of a plane is 2, which means that 2 angles are needed to define a plane in space. For simplicity, Figure 4-6 and Figure 4-8 only show the search over a 1-D landscape

although the best match is found by searching the minimum residual in a 2-D landscape (Figure 4-7 and 4-9).

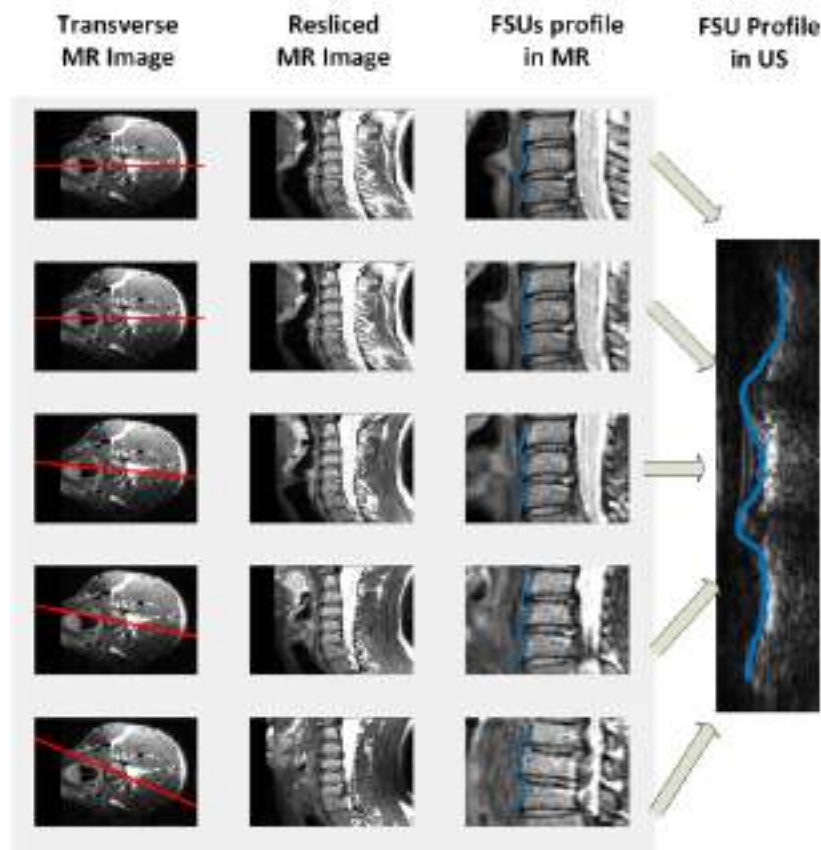


Figure 4-6: Workflow of registering an US image in a 3D MRI image. The MRI image was sliced at a range of pre-selected angles from fiducial optical marker data. The red line on transverse image portrays the slicing plane orientation. The FSU profile was outlined in the re-sliced image and compared to the US FSU profile. Similarity between profiles is characterized by the average residual between the curves.

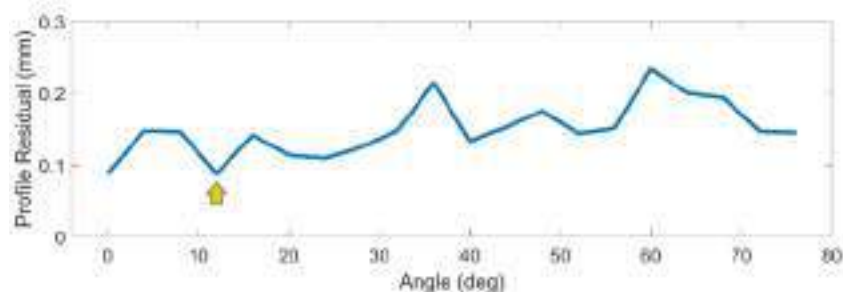


Figure 4-7: Residual between vertebral body-IVD-vertebral body profiles in MR and US as a function of imaging plane orientation angles.

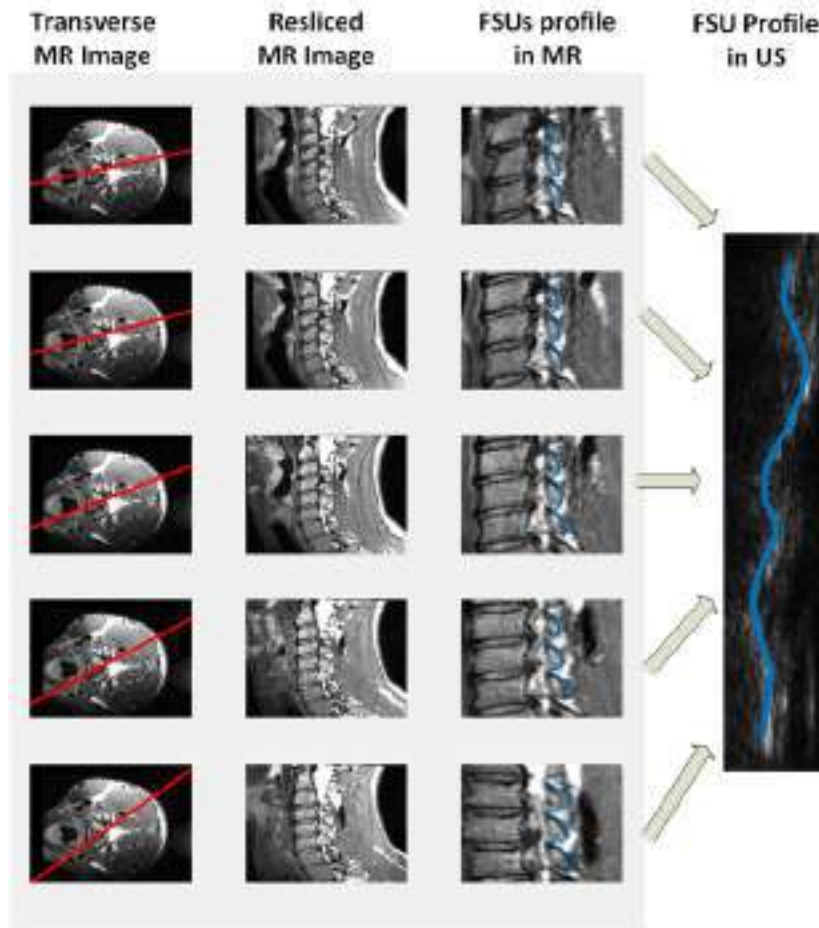


Figure 4-8: Registration workflow for aligning US posterior laminar image in 3D MR scan.

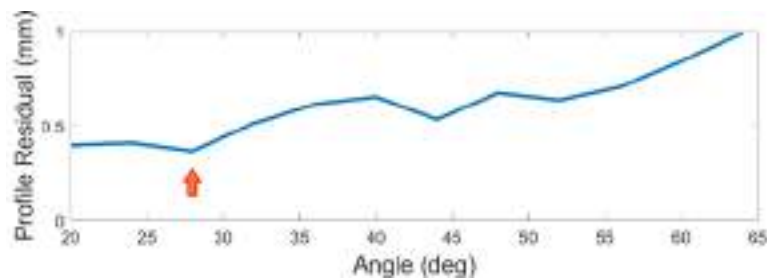


Figure 4-9: Residual between laminar-ligament-laminar profiles in MR and US as a function of imaging plane orientation angles.

4.2 *In-vivo Dual US Imaging of Cervical Spine During Repetitive Jumps*

After approval from Beth Israel Deaconess Medical Center Institutional Review Board, 9 adult subjects (ages 21-45 yrs, 7 males and 2 females) gave written consent to participate in this study. Sagittal T₂-weighted images of the cervical spine using a 3-Tesla MRI were obtained for each subject. B-mode clinical US was used to measure the height of C4-C5 and C5-C6 IVDs by placing the US probe along the anterior triangle of the neck, bounded infero-laterally by the

clavicular head of the sternocleidomastoid muscle, supero-laterally by the omohyoid and strap muscles and medially by the lateral border of the trachea (Figure 4-10). The trajectory of US probe was aimed towards the anterior margins of cervical FSUs C4 to C6. IVD height for C4-C5 and C5-C6 disk were measured from both MRI and US images using ImageJ software (Wayne Rasband, National Institute of Mental Health). US images visualize only the anterior profile of the IVD while MRI demonstrates the entire disk which is non-uniform in height extending from the anterior to posterior margin of the vertebral body.



Figure 4-10: A volunteer performed a repetitive jumping test wearing a weighted helmet to simulate night vision/communication unit gear. Impact to the head and trunk during landing was measured by interposed helmet load cell and force plate. Resultant C4-C5 FSU deformation was measured by dual US system in real time. Para-cervical muscle (SCM, upper trapezius) activation was measured by surface EMG.

Simulating Test Designs and Data Analysis: To simulate activities such as running/jumping while troops or laborers don protective headgear, subjects wore a helmet and repetitively jumped on and off a 0.8-foot step for 4 minutes while looking forward and landing on both feet (Figure 4-10). The impact at landing was measured using a force plate. The jump test was repeated 3x (with an 8-minute rest between trials) using a 4.5-lb unweighted helmet, then repeated 3x using a 6.5-lb weighted helmet to simulate the effect of additional gear such as a flashlight, communication equipment, and night vision goggles. The added weight was set along the mid-sagittal axis of the neck to increment the superior-inferior impact of the helmet on the head/neck during landing.

The axial and inertial loads applied to the C-spine during the jump test were studied by continuous US imaging of the anterior and posterior elements comprising contiguous FSUs C4-C6. A customized cervical collar held dual US transducers against the neck at fixed angles to image the vertebral body and IVD (anterior probe) and lamina/facet joint (posterior probe)

without restricting the flexion or extension motion of neck. Three wireless surface EMG pads (Trigno Lab, Delsys, Natick, MA) were placed on the left sternocleido-mastoid (SCM) and left/right upper trapezius to record para-cervical muscle activities.

Dual US images were collected at rate of 34 fps using a custom dual US system (Terason T3200, Teratech Corporation, Burlington, MA) with two 15L4 linear arrays (4-15 MHz). Scan depths were chosen between 4 cm and 5 cm, and focal depth was set on the anterior vertebrae bodies (2.1 cm and 3.5 cm) and posterior lamina/facet joint (2.1 cm and 3.5 cm) according to the body size of each individual.

The raw radio-frequency data for the US images were analyzed in an interactive algorithm that learns the appearance of a specified vertebra and tracks its position frame-by-frame. To track the vertebra, the user specifies a ROI in the first frame. Based on a naïve Bayes classifier, the algorithm extracts salient anatomic features corresponding to the anterior surface profile of the vertebral body and endplate using compressive sensing to learn the appearance of the vertebra. The position of the vertebra in the subsequent US frame is predicted by fast compressive tracking (FCT) [21] and compared to the actual position. The process can be corrected by the user if image quality is low (e.g. drift of probe or noise) and can adapt to changes in the US image appearance of the vertebra. A least sum of square difference, translational motion blockmatching tracker, validated in phantom and ex-vivo cadaveric experiment, is used to analyze the subsequent positions of opposing anterior vertebral endplates that represent the relative deformation of the interposed IVD for the corresponding FSU. During 4 minutes of jumping, IVD deformation was estimated over 8000 image frames.

Results of *In-vivo* Deformation of FSUs:

Static IVD Height Measurements MRI vs. US: Static mid-sagittal MR images of the cervical spine demonstrated significant variability in IVD height measured from anterior to posterior: mean C4-C5 IVD height at anterior border = 4.67 mm (SD = 0.99), midline = 5.68 mm (SD = 0.86), and posterior border = 3.72 mm (SD = 0.69). The mean C4-C5 IVD height measured by US = 4.72 mm (SD = 0.95). The C5-C6 IVD height measured by MRI was similar to C4-C5, mean IVD height at anterior border = 4.75 mm (SD = 1.02), midline = 6.17 mm (SD = 0.52), and posterior border = 3.75 (SD = 1.54). The mean IVD C5-C6 height measured by US = 4.84 mm (SD = 1.03). The mean of US derived IVD heights did not differ from those measured by MRI at the anterior or posterior borders, but US derived IVD heights were significantly smaller than the IVD measured by midline MRI.

Measurement of *In-vivo* Dynamic Deformation of FSUs: Representative C4-5-6 FSU kinematic motion over 1 second of a jump test sequence during landing is shown in Figure 4-12: (a) the landing impulse and recovery measured by the force plate during the jump approaches 3000 N; (b) activation of para-cervical muscles upon landing serve to dampen the applied and inertial forces generated by the head and helmet to the neck; (c) IVD deformation at impact approaches 1 mm of compression as measured by sequential US images of C4-C5 and C5-C6 FSUs.

A. Para-cervical Muscle Activity During Jumps

Baseline of EMG signal activity of paracervical muscles was determined by the maximum voltage generated when the subject was standing at rest while wearing the helmet. To evaluate

muscle activation above this baseline while jumping, the number of EMG signals exceeding this baseline voltage was integrated over sequential 30-second intervals (Figure 4-11). Para-cervical muscle activities were significantly lower when subjects were jumping with a weighted helmet compared to an unweighted helmet ($p < 0.05$).

B. FSU Deformation During Jumps

Since the C4-C5 IVD is most commonly affected by injury and degenerative disease [22], continuous, real-time, US measurements of the C4-C5 FSU deformation were calculated at the maximum compressive impulse amplitude for each jump and averaged over sequential 30 second intervals during the course of the 4-minute jump test. The additional 2.5-lb helmet weight significantly increased ($p < 0.05$) the IVD compressive deformation to ~2 mm during the course of the jump test (Figure 4-12). The initial IVD height measured from endplate-endplate distance was used to calculate the compressive strain; the average IVD compressive strain at impact increased from 23.3% to 33.95% with the additional 2.5 lbs added to the helmet. Linear regression revealed that the IVD compressive strain decreased with time over the course of the jump test ($R^2 = 0.67$) for the unweighted helmet, but that IVD deformation was unaffected by the duration of time for the weighted helmet ($R^2 = 0.007$).

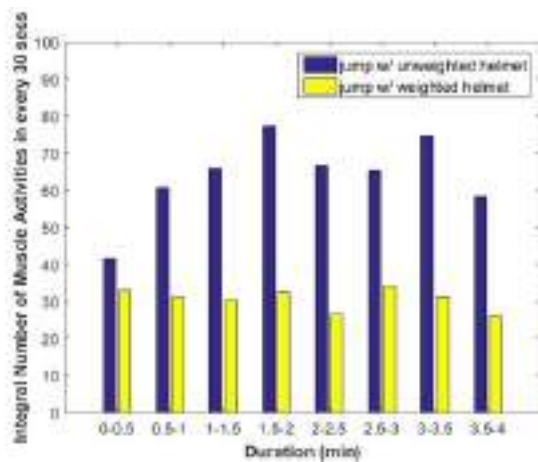


Figure 4-11: Number of EMG signals over baseline integrated over sequential 30 sec increments for subjects jumping with weight (yellow) and without weight (blue) added to the helmet.

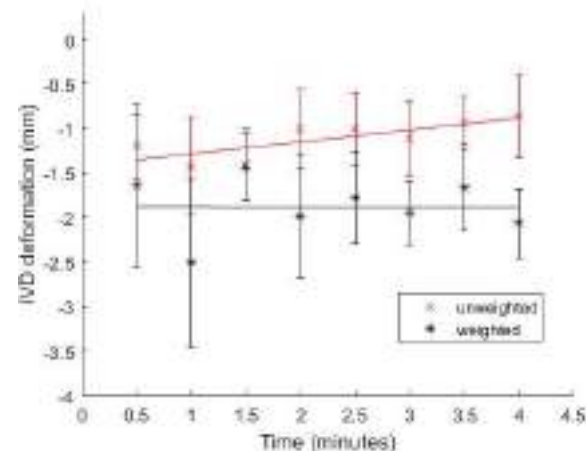


Figure 4-12: Averaged C4-C5 IVD deformation measured over sequential 30 sec intervals while jumping with and without additional 2.5 lbs weight on the helmet. Additional weight significantly increased the compressive IVD deformation at impact.

4.3 Fatigue Testing on Cervical Spine Disc Segments

A total of 37 cervical spine intervertebral disc segments were tested during the life of the study. Those segments were obtained from the cervical spines of 18 post mortem human subjects (PMHS) (10 males, 8 females) with a mean age of 55 ± 10 years. A majority of tests ($n = 27$) were conducted under the primary experimental protocol that consisted of 50,000 compressive cycles in five 10,000-cycle sets with intermittent assessments of disc mechanics. Fourteen of those tests were conducted at a frequency of 2 Hz, and thirteen of those tests were conducted at a frequency of 4 Hz. Ten tests were conducted using specimens obtained from C2-3, eight tests were conducted using specimens obtained from C4-5, and nine tests were conducted using specimens

obtained from C6-7. Eleven tests were conducted using disc segments obtained from male specimens, and sixteen tests were conducted using disc segments obtained from female specimens.

Four specimens were also tested to 50,000 cycles without intermittent testing. Two of those tests were conducted at 2 Hz, and two were conducted at 4 Hz. All four were tests were conducted using male specimens. Another four specimens were tested to beyond one million cycles. Three tests were conducted at 4 Hz and one at 7 Hz. Two male and two female specimens were used. Table 4-1 provides details of the tested specimens.

Test #	Segment	Cyclic Frequency	Compr. Magnitude	Sex	Age	Test Type
DCDM3272	C6-C7	2 Hz	150 N	F	64	5 sets of 10,000 cycles
DCDM3290	C4-C5	2 Hz	150 N	F	64	5 sets of 10,000 cycles
DCDM3308	C2-C3	2 Hz	150 N	F	64	5 sets of 10,000 cycles
DCDM3326	C6-C7	2 Hz	150 N	M	58	5 sets of 10,000 cycles
DCDM3344	C6-C7	2 Hz	150 N	M	54	5 sets of 10,000 cycles
DCDM3362	C6-C7	2 Hz	150 N	F	58	5 sets of 10,000 cycles
DCDM3384	C2-C3	4 Hz	150 N	F	58	5 sets of 10,000 cycles
DCDM3402	C2-C3	4 Hz	150 N	M	54	5 sets of 10,000 cycles
DCDM3420	C2-C3	4 Hz	150 N	F	65	5 sets of 10,000 cycles
DCDM3438	C4-C5	4 Hz	150 N	F	65	5 sets of 10,000 cycles
DCDM3456	C6-C7	4 Hz	150 N	F	65	5 sets of 10,000 cycles
DCDM3474	C2-C3	4 Hz	150 N	M	67	5 sets of 10,000 cycles
DCDM3492	C6-C7	4 Hz	150 N	M	47	5 sets of 10,000 cycles
DCDM3510	C4-C5	4 Hz	150 N	M	47	5 sets of 10,000 cycles
DCDM3528	C2-C3	2 Hz	150 N	M	47	5 sets of 10,000 cycles
DCDM3546	C2-C3	2 Hz	150 N	M	59	5 sets of 10,000 cycles
DCDM3564	C2-C3	4 Hz	150 N	F	31	5 sets of 10,000 cycles
DCDM3582	C4-C5	2 Hz	150 N	F	31	5 sets of 10,000 cycles
DCDM3600	C6-C7	2 Hz	150 N	F	31	5 sets of 10,000 cycles
DCDM3618	C4-C5	4 Hz	150 N	F	50	5 sets of 10,000 cycles
DCDM3636	C4-C5	2 Hz	150 N	F	41	5 sets of 10,000 cycles
DCDM3654	C6-C7	4 Hz	150 N	M	47	5 sets of 10,000 cycles
DCDM3672	C6-C7	4 Hz	150 N	F	60	5 sets of 10,000 cycles
DCDM3690	C4-C5	4 Hz	150 N	M	47	5 sets of 10,000 cycles
DCDM3708	C2-C3	2 Hz	150 N	M	47	5 sets of 10,000 cycles
DCDM3726	C2-C3	2 Hz	150 N	F	60	5 sets of 10,000 cycles
DCDM3744	C4-C5	2 Hz	150 N	F	60	5 sets of 10,000 cycles
DCDM3762	C2-C3	4 Hz	150 N	M	71	1 set of 50,000 cycles
DCDM3768	C6-C7	4 Hz	150 N	M	71	1 set of 50,000 cycles
DCDM3774	C4-C5	2 Hz	150 N	M	71	1 set of 50,000 cycles
DCDM3780	C2-C3	2 Hz	150 N	M	49	1 set of 50,000 cycles
DCDM3783	C6-C7	4 Hz	150 N	M	43	1 set to 1.5 million cycles
DCDM3785	C6-C7	4 Hz	225 N	F	63	1 set to 1.2 million cycles
DCDM3787	C6-C7	4 Hz	225 N	M	59	1 set of 1.7 million cycles

DCDM3788	C6-C7	8 Hz	225 N	F	60	1 set of 2.0 million cycles
----------	-------	------	-------	---	----	-----------------------------

Table 4-1: Cadaveric cervical FSU specimens tested for failure fatigue.

Experimental Protocol: All specimens were prepared and tested using a similar protocol. Cervical spine specimens were obtained from PMHS donors and sectioned into motion segments, consisting of two adjacent vertebrae with all connecting soft tissues including intervertebral discs, facet joints, and spinal ligaments. Posterior elements were then removed dorsal to the pedicles. Specimens were aligned such that the mid-disc plane was horizontal and fixed at the superior and inferior ends using polymethylmethacrylate (PMMA) to facilitate fixation to the testing apparatus. Specimens were maintained moist during preparation using saline solution. Intervertebral disc height was measured in multiple locations around the disc using either digital calipers or CT images obtained prior to testing. The superior fixation was attached to the piston of a custom-designed electro-hydraulic testing device (MTS Systems Corp., Eden Prairie, MN, USA), and the inferior fixation was attached to the loading frame through a load cell mounted on an x-y cross table (Figure 4-13). Specimens were then exposed to repetitive compression loading.



Figure 4-13: Experimental fatigue testing setup.

Twenty-seven cervical disc segments (C2-3, C4-5, and C6-7) were tested under a primary physiologic repetitive compression protocol (0 to 150 N) at either 2 Hz or 4 Hz frequencies [23]. Peak force of 150 N was used to represent repetitive compressive forces on the cervical spine during running. The mass of the head was multiplied by the vertical acceleration of the head during exhaustive running [24], which was approximately 150 N. Frequencies of 2 Hz and 4 Hz were chosen to represent running stride frequencies [25]. The fatigue testing protocol consisted of exposing cervical spine intervertebral disc segments to 50,000 compressive cycles over five 10,000-cycle sets. All testing was conducted with specimens submerged in physiologic saline at in vivo temperature (37°C). The physiologic saline mixture consisted of 0.5 g Cefepim / 25 L, 12.5 mg Amphotericin / 25 L, 5 mM Benzamidine, and 5 mM Ethylenediaminetetraacetic acid (EDTA) mixed with distilled water. Prior to fatigue testing and after each set, specimens were exposed to tension/compression preconditioning and a stress relaxation protocol to assess changes in tensile and compressive stiffness, and viscoelastic properties of the intervertebral disc. Including rest periods, specimens had approximately 60 min between 10,000 cycle sets.

Cyclic applied loads were force controlled between 0 N and the maximum compressive force shown in Table 4-1, which was 150 N for a majority of tests. Displacement of the cranial relative to the caudal vertebra was measured using the linear variable differential transducer (LVDT) in series with the MTS piston. Axial forces were measured using the load cell attached in series with the MTS piston. These biomechanical data were digitally collected at 1064 Hz during the entire protocol. Stiffness of the specimens was computed during the loading phase of each cycle as the slope of the applied force versus compressive displacement trace between 5% and 95% of the applied force.

Cyclic Loading Response: Specimens demonstrated a consistent response during the intermittent cyclic compressive loading protocol that was characterized by loss of intervertebral disc height and increased compressive stiffness of the disc segment. Mean (\pm standard error) stiffness response of the specimens is shown in Figure 4-14. Data are grouped by compressive loading frequency and spine region (upper vs. lower cervical spine). The upper cervical spine grouping

included only specimens from the C2-3 spinal level and the lower cervical spine grouping included specimens from C4-5 and C6-7 spinal levels. Between the beginning and end of each 10,000-cycle set, specimen groups demonstrated a mean increase in stiffness of between 8.8% (first set, upper cervical spine specimens, 2 Hz) and 51.2% (first set, lower cervical spine specimens, 2 Hz). Specimens from the upper cervical spine demonstrated a smaller average increase in stiffness from the first ten cycles of each set to the last ten cycles of each set ($16.9 \pm 3.9\%$) than specimens from the lower cervical spine ($29.6 \pm 9.6\%$). That change in stiffness was not different between 2 Hz and 4 Hz testing in the upper cervical spine. However, in the lower cervical spine 2 Hz testing produced a much larger average set-wise change in stiffness ($35.7 \pm 10.1\%$) compared to 4 Hz testing ($23.4 \pm 3.5\%$).

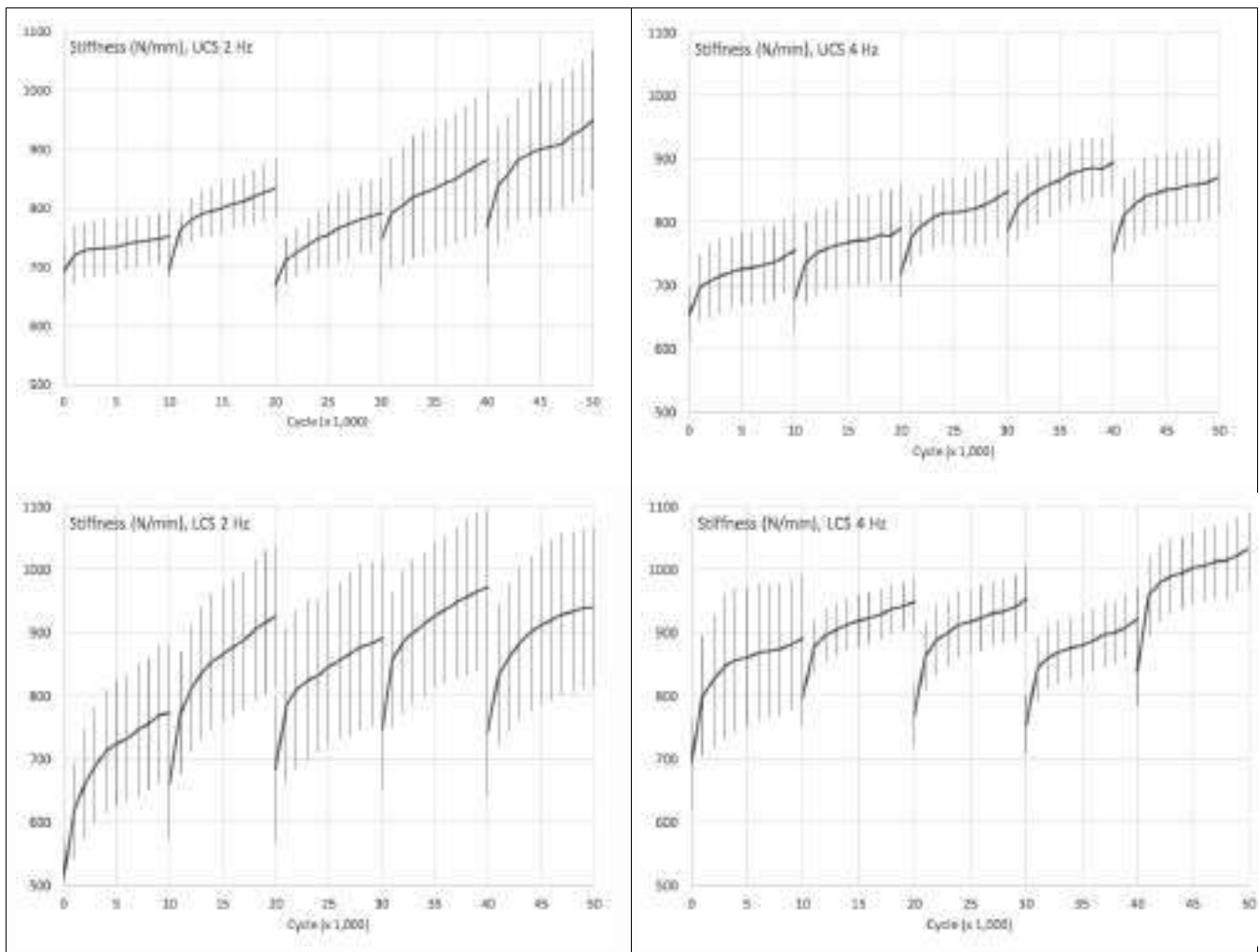


Figure 4-14: Stiffness response of intervertebral disc segments subjected to repetitive axial compressive loading under the intermittent loading protocol. Data are divided between 2 and 4 Hz frequencies (left and right columns) and upper and lower cervical spinal regions (upper and lower rows).

Specimen stiffness response during each 10,000-cycle set was modeled using a bilinear approximation (Figure 4-15) with linear regression analyses used to model the initial steep increase in stiffness associated with specimen conditioning and the more gradual increase in stiffness associated with fatigue of the intervertebral disc. Although there was some specimen-to-

specimen variation, the knee point of the differing rates of stiffness increase was approximately 1000 cycles. Accordingly, separate linear regression analyses were performed for cycles 0 to 1000 and cycles 1000 to 10,000. Given that the steep increase in stiffness during the initial response period was not sustained across the entire 10,000 cycle set, it was likely an artifact of the testing protocol that consisting of discrete sets with a period of rest prior to each set. The steep increase was therefore, likely related to preconditioning of the specimen after each rest period. Therefore, the analysis of stiffness response using linear approximation will focus on the second approximation, which describes the more gradual increase in stiffness during the last 9,000 cycles of each set, which likely is more representative of the fatigue response of the intervertebral disc. Metrics associated with the regression include the slope (N/mm per cycle) and the intercept, which is the point where the linear approximation crosses the zero cycle point for each 10,000 cycle set.

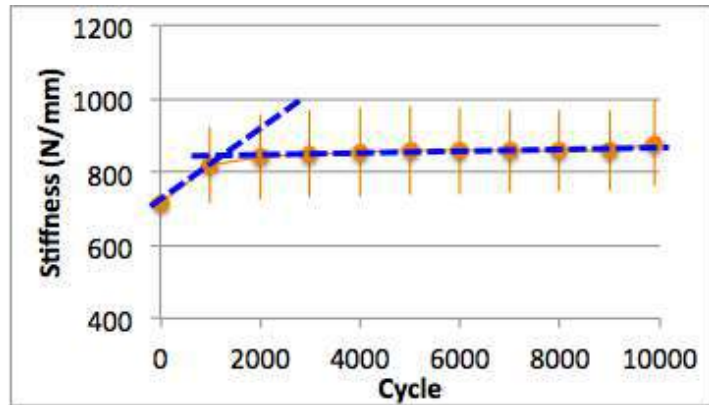


Figure 4-15: Bilinear approximation of stiffness data from the intermittent testing protocol. The first linear approximation represented cycles 0 to 1000, and the second approximation represented cycles 1000 to 10,000. Approximations were characterized as a slope and zero-crossing intercept for each region.

Table 4-2: Two-factor ANOVA *p*-values for slope and zero-cycle intercept of linear approximations for the stiffness response of disc segments during cycles 1000 to 10,000 of each set. Factors include cyclic testing rate (2 Hz vs 4 Hz) and cervical spine region (upper vs lower cervical spine). *P*-values less than 0.05 were considered statistically significant.

	Slope		Intercept	
	Rate	C-Spine Region	Rate	C-Spine Region
Set 1	0.1954	0.0305	0.2435	0.9031
Set 2	0.0709	0.1445	0.3159	0.4853
Set 3	0.1742	0.2834	0.4351	0.4548

Characterization of the change in stiffness during repetitive compressive loading was performed by

Set 4	0.1073	0.5393	0.9932	0.6852
Set 5	0.0906	0.7090	0.4879	0.4369

comparing the slope and intercept for the linear approximation of the stiffness response between 1000 and 10,000 cycles. Three statistical factors were apparent in this analysis (cyclic testing rate, spinal region, and set number). However, because of limitations with regard to the degrees of freedom related to the number of factor levels for the set variable ($n = 5$) combined with spinal region/level and rate variables in relation to the sample size for the number of specimens in some of the groups ($n = 5$), independent two-factor ANOVA analyses (rate and spinal region) were repeated for each set (Table 4-2). Accordingly, for the analysis of slope of the linear approximation, lower cervical spine specimens had significantly greater slope ($p < 0.05$) during the first set (Figure 4-16). Rate of cyclic loading demonstrated a non-significant trend ($p < 0.10$) of greater slope for 2 Hz testing during sets 2 and 5. There were no significant differences based on either cyclic testing rate or cervical spine region for the intercept of the linear approximation, although the intercept gradually increased from the first to the fifth sets, demonstrating a consistent increase in baseline stiffness of the specimens.

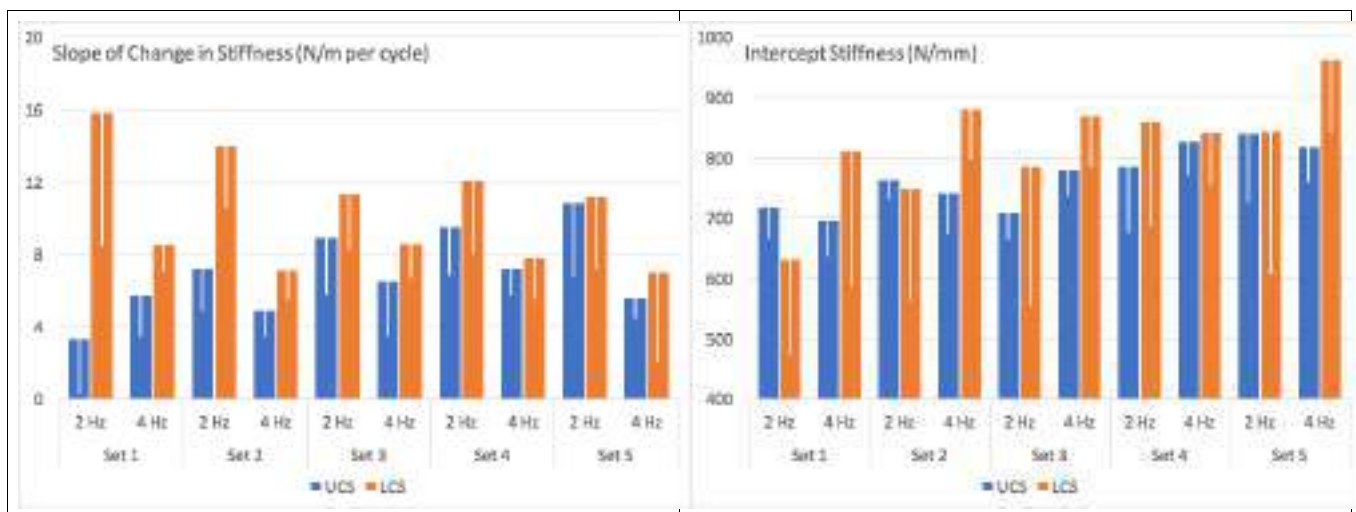


Figure 4-16: Slope (left) and intercept (right) of the linear approximation of cycles 1000 through 10,000 for sets 1-5 of the intermittent testing protocol. Blue bars represent mean and standard error data from upper cervical spine (C2-3) segments and orange bars represent lower cervical spine (C4-5 and C6-7) segments.

Changes in intervertebral disc stiffness described above were likely associated, at least in part, with loss of disc height due to dehydration of the components of the intervertebral disc. Accordingly, loss of disc height was calculated for all specimens following each 10,000-cycle set as the difference in disc height between the beginning and end of each set. As shown in Figure 4-17, disc height loss during the first three 10,000-cycle sets was much greater in the lower than the upper cervical spine, and greater for 2 Hz compared to 4 Hz testing. Most evident for 2 Hz testing was that the magnitude of intervertebral disc height loss was greatest during the first set and progressively decreased for sets two through four. Two-factor ANOVA was used to determine statistically significant differences ($p < 0.05$) in height loss based on cyclic testing rate and cervical spinal region. Independent ANOVA analyses were conducted for data from each of the five sets. Height loss was significantly dependent on testing rate during the first two sets of

the five-set intermittent protocol. Cyclic testing at 2 Hz resulted in greater height loss than 4 Hz testing. Height loss was also significantly dependent on spinal region ($p < 0.05$) during the first set and demonstrated a non-significant trend ($p < 0.10$) during the second set. Height loss was greater for lower cervical spine specimens (C4-5 and C6-7) than specimens obtained from the upper cervical spine (C2-3). Statistical p-values for these comparisons are presented in Table 4-3.

Intervertebral disc specimens regained a portion of the lost disc height during the period between each 10,000-cycle set. Disc height restitution was measured as the percentage of lost disc height that was regained during the first 15-minute rest period between each compressive loading set. In general, the magnitude of disc height restitution was not remarkably different between upper and lower cervical spine regions, or between 2 Hz and 4 Hz testing. One exception was that disc height restitution was significantly dependent upon cervical spinal region ($p < 0.05$) following the first 10,000-cycle set. This was due in large part to a very small magnitude of restitution at the C2-3 spinal level for 4 Hz testing, resulting from two specimens demonstrating increased disc height loss (i.e., decreased total disc height) during the rest period. With the exception of restitution following the first set, average disc height restitution for sets two through five was between 50% and 75% of the lost disc height during the previous compressive loading set. The magnitude of disc height restitution increased somewhat, although not significantly, from the second through the fifth sets.

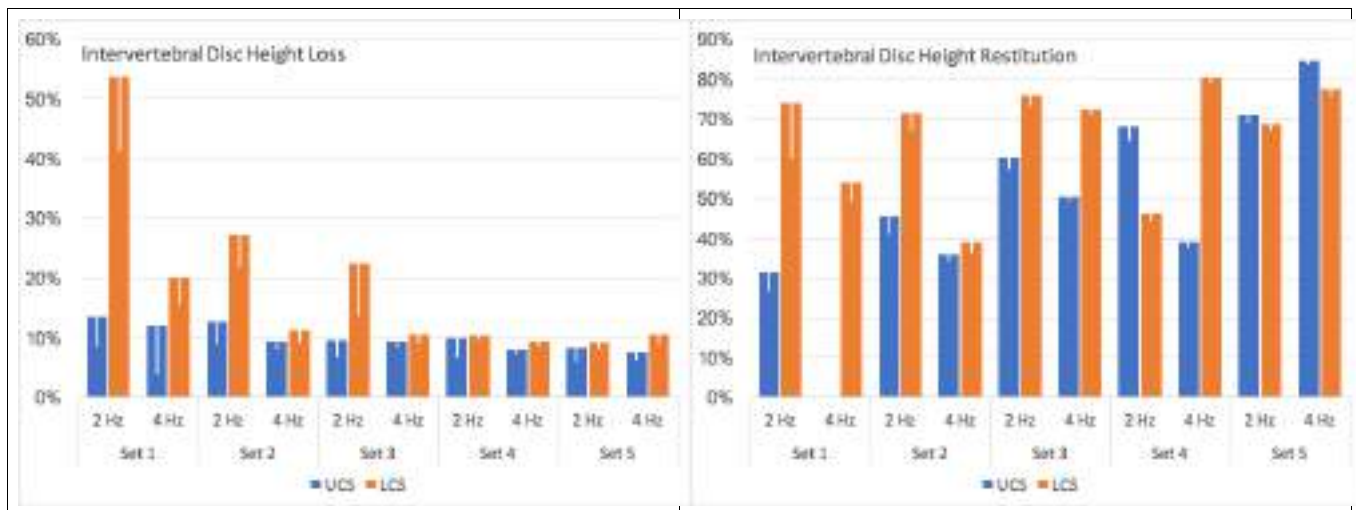


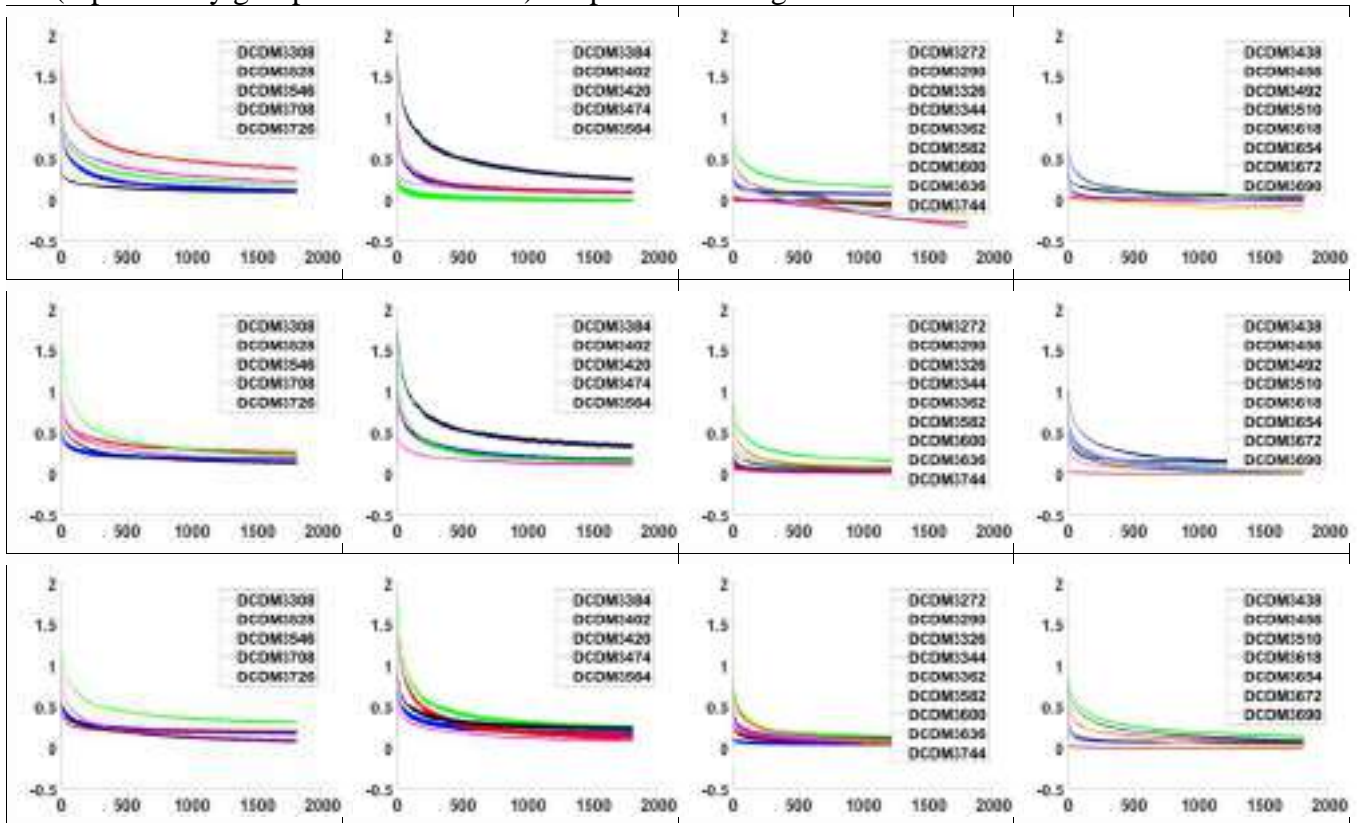
Figure 4-17: Intervertebral disc height loss during each 10,000-cycle set (left) and post-set disc height restitution (right) for sets 1-5 of the intermittent testing protocol. Blue bars represent mean and standard error data from upper cervical spine (C2-3) segments and orange bars represent lower cervical spine (C4-5 and C6-7) segments.

Table 4-3: Two-factor ANOVA p-values for intervertebral disc height loss during each 10,000-cycle set and disc height restitution following each set. Factors include cyclic testing rate (2 Hz vs 4 Hz) and cervical spine region (upper vs lower C-spine).

	Intervertebral Disc Height Loss		Disc Height Restitution	
	Rate	C-spine Region	Rate	C-Spine Region
Set 1	0.0391	0.0257	0.2129	0.0264

Set 2	0.0153	0.0748	0.1298	0.3603
Set 3	0.2268	0.2734	0.6612	0.1962
Set 4	0.3593	0.5027	0.5487	0.6219
Set 5	0.7220	0.2313	0.4397	0.7386

Viscoelasticity and Tension/Compression Stiffness: For the intermittent protocol, viscoelastic tests were conducted prior to testing and again following each 10,000-cycle set. The viscoelasticity assessment protocol consisted of a compression stress relaxation test that was conducted without removing the specimen from the environmental chamber. The protocol consisted of the following. Average intervertebral disc height was computed from five measurements obtained from x-rays of the specimen taken immediately prior to the viscoelastic test. Specimens were then preconditioned for ten cycles of tension and compression to 10% strain of the intervertebral disc height. The viscoelastic test then consisted of compressive displacement to 10% strain and hold for 30 minutes. Axial forces were measured during the 30-minute compressive hold period and characterized force relaxation of the intervertebral disc. Compressive forces were normalized using intervertebral disc cross-sectional areas measured from CT images to compute engineering stress. Stress relaxation plots for each of the specimens (separated by group in each columns) are provided in Figure 4-18.



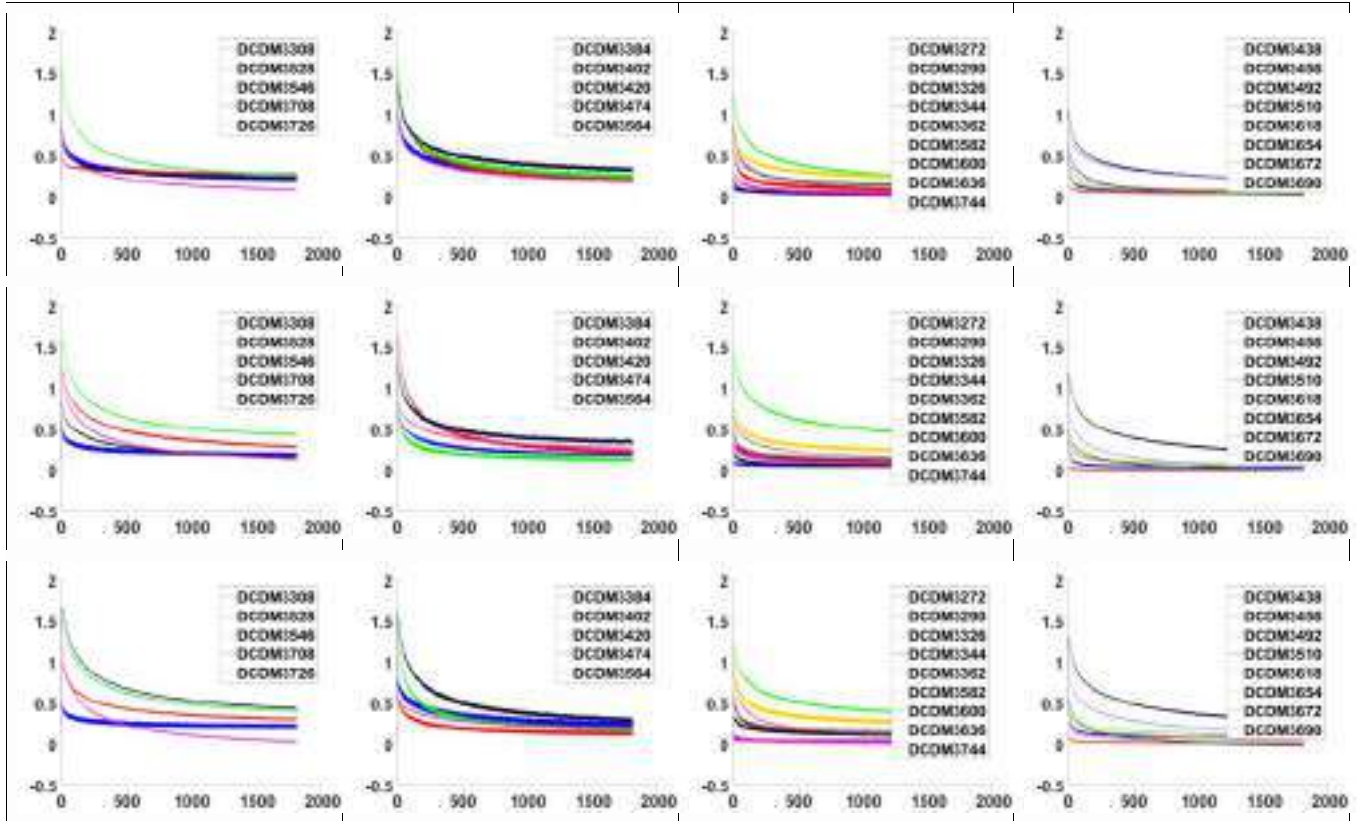


Figure 4-18: Stress relaxation of specimens prior to (top row) and following each 10,000-cycle set: post 10,000 cycles (2nd row), post 20,000 cycles (3rd row), post 30,000 cycles (4th row), post 40,000 cycles (5th row), post 50,000 cycles (6th row). The four groups are presented from the left to the right columns as 1) upper cervical spine, 2 Hz; 2) upper cervical spine, 4 Hz; 3) lower cervical spine 2 Hz; and 4) lower cervical spine, 4 Hz. The Y-axis is compressive stress in N/mm^2 and the X-axis is time in sec.

Cervical spine specimens demonstrated a predictable viscoelastic response characterized by a steep decrease in stress during the early phase of the displacement-hold protocol followed by a transition to a steady state or more gradual stress relaxation. However, there were no obvious trends in the viscoelastic response with regard to specimen group (upper/lower cervical spine or 2 Hz vs. 4 Hz) or the number of 10,000-cycle sets prior to viscoelastic assessment.

Intermittent Cyclic Compression Protocol: Twenty-seven cervical spine intervertebral disc segments were exposed to the intermittent cyclic compression testing protocol. Specimens were obtained from PMHS cervical spines (mean age: 55 ± 10 years) at levels C2-3, C4-5, and C6-7. Each specimen was subjected to 50,000 cycles of compressive loading between 0 N and 150 N at either 2 Hz or 4 Hz in 5 sets of 10,000 cycles. Between each set, specimens were allowed a rest period and assessments of tension/compression stiffness and viscoelasticity were performed. Specimens demonstrated increasing compressive stiffness during each 10,000-cycle set and across the entire 50,000 cycles. The magnitude of increase in stiffness was greater for specimens obtained from the lower cervical spine, than the upper cervical spine. Rate effects were not evident in the upper cervical spine, but testing at 2 Hz produced greater increases in stiffness than testing at 4 Hz in the lower cervical spine. The fatigue response of the intervertebral disc was modeled using a linear approximation. In general, specimens obtained from the lower cervical spine sustained a greater change in stiffness during repetitive compressive loading than

specimens obtained from the upper cervical spine. Likewise, testing at 2 Hz frequency produced greater changes in stiffness than testing at 4 Hz. This is likely related to fluid dynamics, with slower compressive rates permitting greater time for fluid flow out of the disc resulting in more rapid dehydration of the tissues and greater increase in stiffness. Zero cycle intercept of the approximation (i.e., baseline stiffness) increased from the first to the fifth sets. The increase in intercept stiffness was greater for 2 Hz testing and in the lower cervical spine, although differences did not attain statistical significance. Similar to the trends described above, disc height loss was greater during early compressive loading sets in the lower cervical spine and for the 2-Hz testing rate. Those differences were statistically significant ($p < 0.05$) during the first and second sets. Disc height restitution during the rest period in general was not different based on spinal level or testing rate and varied between 50% and 75% of the lost disc height during the previous compressive loading cycle. Although assessments of viscoelasticity were performed prior to testing and after each 10,000-cycle set, there were no clear trends for changes in the viscoelastic response of disc segments based on spinal region, cyclic compression rate, or set number. Nonetheless, some trends with regard to spinal level and testing rate were evident, although many did not attain statistical significance ($p < 0.05$). However, these findings provide an outline for future investigations that may be focused on high magnitude compressive loads to model head supported mass in military scenarios, higher frequencies to model different motor vehicle environments, or sex-based differences in fatigue properties.

Continuous Cyclic Compression Protocol: A secondary test series was conducted to complement the results of the intermittent protocol, described above. This series consisted of only four specimens and was focused on incorporating a continuous testing protocol, wherein specimens were subjected to 50,000 cycles of compression without intermittent rest periods following every 10,000 cycles. All other aspects of the testing protocol were identical between the intermittent and continuous protocols. The purpose was to provide data on whether changes in stiffness were consistent between a continuous and an intermittent testing protocol. As shown in the test matrix (Table 4-1), two specimens were obtained from the upper cervical spine, and two specimens were obtained from the lower cervical spine. Two specimens were tested at 2 Hz (one upper and one lower cervical spine) and two were tested at 4 Hz (one upper and one lower cervical spine) cyclic compression rates. Results of this comparison are presented in Figure 4-19, which demonstrates increased stiffness relative to the initial compressive stiffness after 1,000 and 50,000 cycles of compressive loading. While the limited sample size for the continuous protocol precludes statistical comparisons, trends are for the most part consistent between the intermittent and continuous protocols with no strong differences between the two test methods. This supports use of the intermittent cyclic compression employed for the majority of this study.

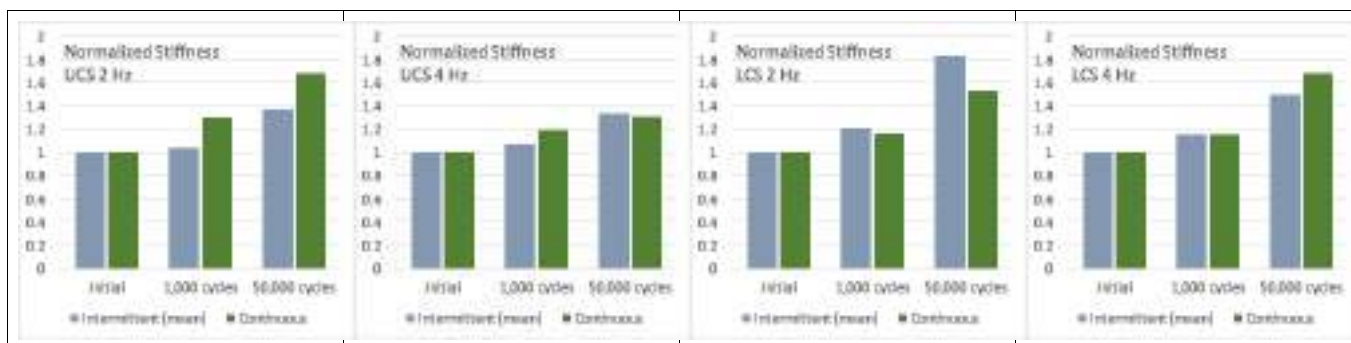
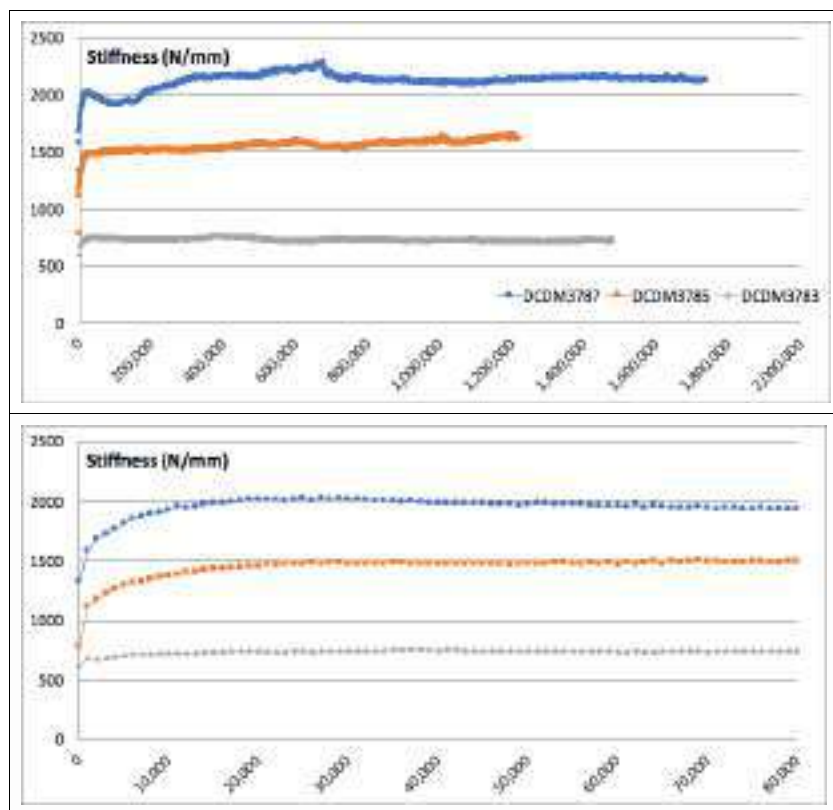


Figure 4-19: Comparison of stiffness increases for repetitive compression testing, comparing intermittent and continuous protocols. Stiffness values are normalized relative to the initial compressive stiffness of each specimen. Gray bars represent mean increase for specimens in each category (upper vs lower cervical spine, 2 Hz vs 4 Hz) under the intermittent protocol. Green bars represent the response of a single specimen under the continuous protocol.

Extended Fatigue Testing: In addition to the continuous protocol described above, another set of tests was conducted to determine whether extended exposure to repetitive compressive loading would produce mechanical evidence of injury in cervical spine disc segments tested under this experimental protocol. As shown in Table 4-1, specimens were exposed to between 1.2 and 2.0 million cycles of compressive loading. The first three specimens were tested at 4 Hz. The first specimen was loaded to 150 N, which was consistent with all earlier specimens in this study. The second and third specimens were loaded to 225 N to simulate a more severe loading scenario that might be consistent with head borne mass or more severe perturbations that might be experienced by military pilots. The difference between the standard loading magnitude for this study (150 N) and the more severe loading magnitude is clearly shown in Figure 4-20. As in prior specimens, the 150 N test (DCDM3783) resulted in a steep increase in stiffness over the first 1,000 cycles with an approximately steady state stiffness response following that point. Stiffness for that specimen increased approximately 20% between the initial and steady state stiffness values. However, specimens tested with greater compressive force demonstrated an elongated increase in stiffness occurring over approximately 20,000 cycles that led to a much greater stiffness change of between 62% and 98% than for the two specimens tested under this protocol. This is evident in the second (lower) plot shown in Figure 4-20.

According to data shown in Figure 4-20 and post-test examination of specimens, testing at these rates/magnitudes did not produce evidence of bony, endplate, or intervertebral disc injury.



Mechanical evidence of injury would likely include a dramatic and sustained change in stiffness for the specimen, which is clearly not evident in

the traces shown in Figure 4-20. The nonlinear change in stiffness for specimen DCDM3787 shown in Figure 4-20 is likely not indicative of failure as the stiffness change was not sustained and there was no evidence of bony or soft tissue injury for that specimen on post-test examination. The implication of these results is that the loading conditions incorporated in this study (2-4 Hz, 150-225 N) would not be expected to injure the cervical spine and extended exposures at those levels could be considered to be safe. However, these findings, of course, are subject to continued testing to provide stronger evidence.

Figure 4-20: Change in specimen stiffness for the extended fatigue testing protocol. Specimen DCDM3783 was tested with 150 N compressive loads and specimens DCDM3787 and DCDM 3785 were tested with 225 N compressive loads.

MRI Imaging: In addition to the standard pre-test CT scans that were performed to assess specimen quality and determine intervertebral disc height and cross-sectional area, MRI imaging was used on a limited number of specimens to collect preliminary data that might be used as a noninvasive methodology to assess changes in intervertebral disc integrity associated with progressive degradation. MRI scanning protocols were used in an attempt to identify intervertebral disc degeneration and changes in endplate perfusion [26] that might be used noninvasively to grade changes in intervertebral disc fatigue and could be used to determine exposure limits for individuals with significant occupational exposure to whole body vibrational environments. Unfortunately, mechanical changes in intervertebral disc highlighted in this report did not have an MRI correlate. This was likely associated with the relatively low level of changes brought on by these non-injurious loading scenarios. It remains likely that more severe loading scenarios could result in changes to the intervertebral disc that will be identifiable using MRI and correlated to quantitative MRI metrics. This will constitute a future direction for these studies.

Achievements and Deviations: The objective stated in the grant included performing fatigue testing on cadaveric cervical spine intervertebral disc segments under repeated axial loading using an intermittent protocol and establishing fatigue and failure envelopes. Accordingly, thirty-five intervertebral disc segments were subjected to repetitive compressive loading. Fatigue envelopes were characterized as the change in stiffness, loss of intervertebral disc height, and changes in viscoelasticity as a function of the number of loading cycles, spinal region, and cyclic compression rate. Statistically significant differences were not identified in a majority of cases, although trends were clear, as outlined in the sections above. Those trends included an effect of spinal region, indicating that different spinal levels may be more susceptible to fatigue-related mechanical changes to the soft tissues. An effect of loading rate was also evident, with lower rate testing producing greater changes in disc segment properties. Although only tested in a limited number of specimens, the effect of loading magnitude was also strong, with higher magnitude loads producing greater change in stiffness that occurred over an increased number of cycles. While a majority of specimens were exposed to 50,000 cycles of repetitive compressive loading, a subset of specimens were exposed to as many as 1.7 million cycles in an attempt to characterize the onset of failure under the types of loading conditions incorporated in this study. None of the specimens in that subset experienced mechanical evidence of failure or medical imaging evidence of injury. Therefore, although failure envelopes were not defined in this study,

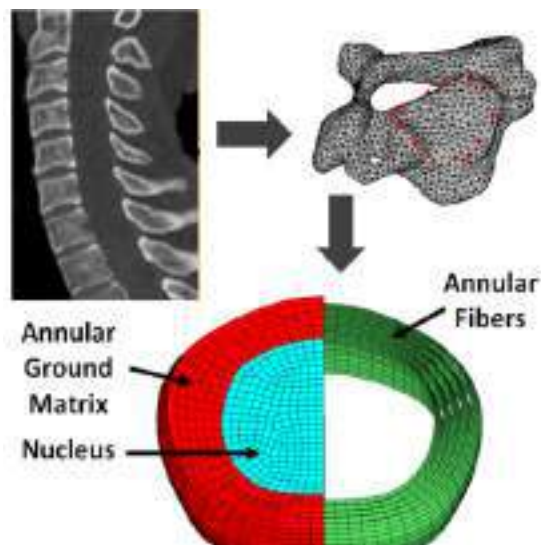
as described in the Specific Aim, findings of the extended fatigue testing protocol would imply that the types of loading incorporated in this study would generally be safe for occupants as the duration of loading for extended testing (i.e., continuous testing for 4+ days) far exceeded any reasonable exposure limit for occupational environments. However, results of the current study identified considerable effects of different loading conditions (i.e., rate and magnitude) that will change the magnitude of fatigue in the intervertebral disc, resulting in a higher risk of injury onset. These non-significant differences and trends deserve further attention.

While the study as described above followed the design outlined in the proposal in general, some deviations in the protocol were necessary to properly characterize fatigue of the intervertebral disc under repetitive compressive loading. A major deviation from the original proposal was that a majority of specimens were tested to 50,000 cycles as opposed to the 100,000 cycles that was outlined in Specific Aim 1. This change was made primarily for the sake of experimental expediency. Testing 50,000 cycles at 2 Hz resulted in approximately seven hours of cyclic compressive testing. However, in addition to that seven hours of testing was preparation time to mount the specimen to the apparatus and the intermittent protocol added approximately one hour prior to testing and between each set for specimen preconditioning, viscoelastic testing, and rest periods. Therefore, testing for each specimen at 2 Hz accounted for approximately 15 hours. For the intermittent protocol, our technicians were required to be present in the laboratory for a majority of the time to monitor the testing and set rest periods, preconditioning and viscoelastic tests. We felt it inappropriate to stop the testing at night and continue the next day so all of these tests were conducted continuously during a single day. However, we feel that the scientific consequences of this decision were limited. For example, Figure 4-20 clearly shows that specimen response for 150 N compressive loads, as were used during the intermittent protocol, had essentially plateaued prior to 10,000 cycles and the response of the specimens beyond 50,000 cycles was consistent with the steady state response prior to 50,000 cycles.

Another deviation from the proposal was the lack of pure moment testing between 10,000-cycle sets. Pure moment testing was eliminated from the final protocol to avoid exposing specimens to an extended period of time outside of the physiologic saline that was used for repetitive and viscoelastic testing. Pure moment testing requires a testing rig that was is not contained within an environmental chamber. The duration of each pure moment assessment is approximately one hour. Therefore, addition of the pure moment protocol would have considerably increased the likelihood of specimen dehydration and degradation associated with several hours of testing outside of the environmental chamber. This degradation would be an external variable that would confound specimen degradation associated with repetitive compressive loading. Characterizing specimen degradation associated with repetitive compressive loading the primary goal of these experiments.

4.4 Development of a Finite Element Product to Predict Spine Fatigue Using the Experimental Data

The finite element model of the C4-C5 intervertebral disc with associated superior and inferior end plates was developed from CT scans of specimens used in the experimental studies of this



project. The images were imported into a 3D slicer software and segmentation of vertebrae was performed using the threshold frequency of the bone. The segmentation image was exported in stereo-lithographic format and was processed using Altair Hypermesh software. A mapping technique was used to model the intervertebral disc, in which the vertices bounding the approximate location of the endplates were selected on the adjacent vertebral bodies [27]. Due to mesh correspondence, vertices selected on the vertebral bodies defined bony endplate boundaries only. The endplate boundaries were duplicated to simulate cartilaginous endplates at 0.1-mm thickness. All endplates were meshed with quadratic elements and a hexahedral mesh of the intervertebral discs was “dragged” from the top endplate to the bottom endplate. The parallel faces created between the two endplates were scaled to obtain the normal “bulge” shape of the disc (Figure 4-21).

The geometry represented the average area and disc height of C4-C5 segments tested at 2 Hz under the intermittent protocol (Table 1). The nucleus pulposus and annulus ground substance were modeled using solid hexahedral elements. The annular fibers were modeled with five pairs of concentric quadratic shell layers embedded in the ground substance [28]. The superior and inferior cartilaginous and bony endplates were modeled using shell elements. The element size was 0.5 mm, and the model was composed of 8,740 solid hexahedral elements and 18,636 quadratic shell elements. Compared to the existing cervical spine segment models, the current C4-C5 model has more than twice the number of elements [28]. The cross-sectional area at the center of the disc was 218 mm² in which nucleus contributed to 45% [29] of the area. Resolutions of pre-test MR images were inadequate to obtain accurate nucleus area. The disc heights from CT scans measured at the posterior-most, posterior-middle, middle, anterior-middle and anterior-most anatomical regions and input into the finite element model.

Material Properties: The material properties for the ground substance were obtained from experiments performed on disc segments before cyclic loading, whereas the material properties for the endplates, nucleus and annular fibers were obtained from literature. The annular ground substance was modeled as a hyper-viscoelastic material. The stress-strain data from tension-compression experiments was directly used as the input for the Aruda-Boyce hyper-elastic material (Figure 4-22). Viscous properties were introduced by the viscoelastic stress relaxation curve (Figure 4-23) from the experiments. The Poisson’s ratio for the ground substance was 0.4 [30,31]. The nucleus was modeled with an elastic modulus of 1 MPa [32,33]. The annular fibers were modeled as hyper-elastic material, and tension-only material properties were varied from the inner most to the outermost layer (Figure 4-24). The gradual change in the fiber angle with the radial position was included, with fiber angles $\pm 250^\circ$ in the outer layers to $\pm 450^\circ$ in the inner layers [34]. The bony endplates were modeled with an elastic modulus of 5,600 MPa and Poisson’s ratio of 0.3 [34], and uniform thickness of 1 mm [35]. The cartilaginous endplates were modeled with an elastic modulus of 24 MPa and Poisson’s ratio of 0.4 [27,29,30] and uniform thickness of 0.8 mm [34,36].

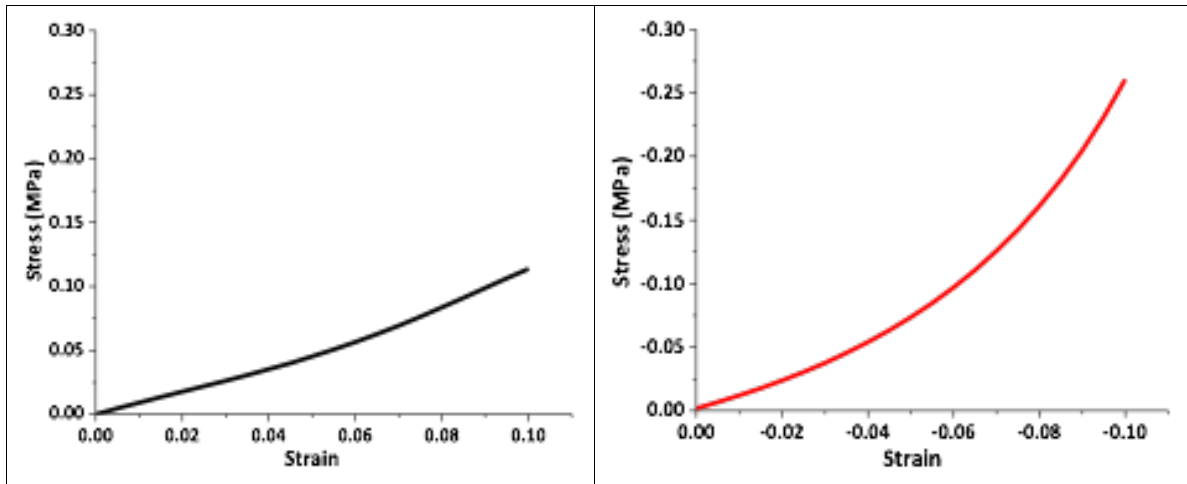


Figure 4-22: Annular ground matrix tensile (left) and compressive (right) properties.

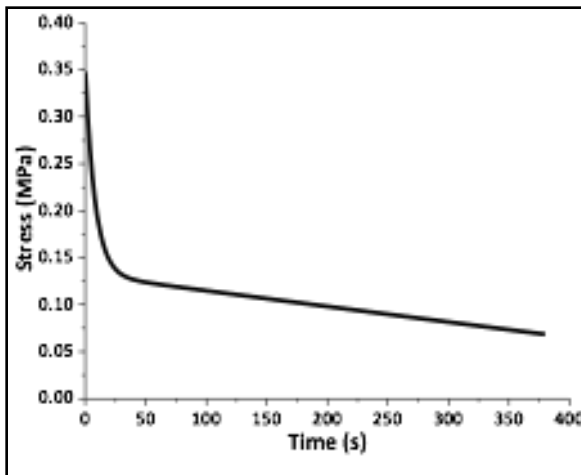


Figure 4-23: Annular ground matrix viscoelastic stress relaxation curve.

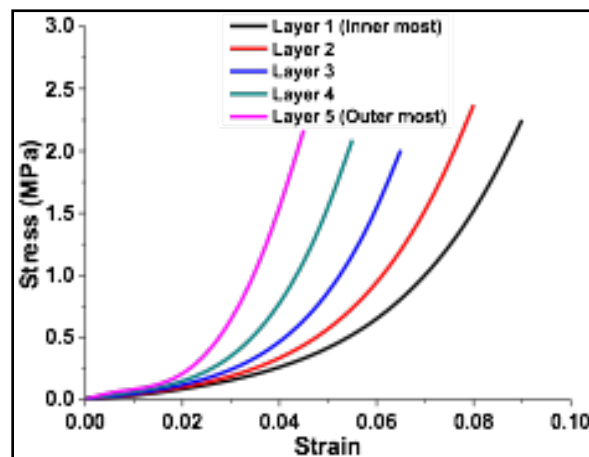
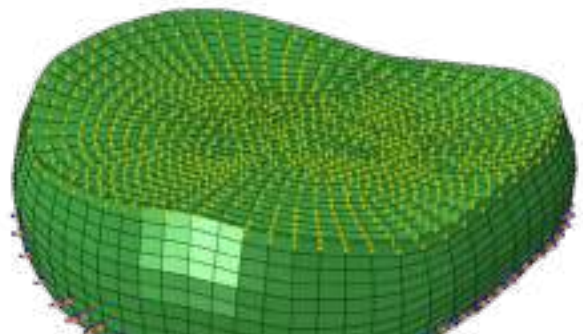


Figure 4-24: Annular fiber tensile properties.

A. Validation of Finite Element Model at 2 Hz and 150 N

Boundary Conditions: The bony and cartilaginous endplates had tied contacts. The cartilaginous endplate had shared nodes with the annulus and nucleus. Similarly, annular fibers had shared nodes with the ground substance. The inferior bony endplate was constrained in all six degrees-of-freedom and the superior bony endplate sustained the applied load. The cyclic load was applied in two steps: 1) a uniform load of 150 N at 2 Hz was applied to the superior end plate; and 2) a direct cyclic step simulating 10,000 compression cycles based on the previous step history (Figure 4-25**Error! Reference source**



ot found.). The results were output as displacements of the superior endplate over the entire 10,000 cycles and were compared with corresponding experimental data. The time history stress-analysis outputs included maximum and minimum principal stresses and strains, vector directions, von Mises stresses, and shear stresses.

Displacement of the superior endplate during the entire 10,000 cycles was compared to the piston stroke from experiments for 10,000 cycles (Figure 4-26). The simulation displacements were within the experimental mean plus/minus one standard deviation corridors. The displacement was greater during the initiation of the loading process and reduced exponentially in the first 2,000 cycles, followed by a plateau showing the effect of viscoelasticity in this first 2,000 cycle period. The loss in the height of the disc was compared to the height loss measured from pre- and post-cyclic test radiographs. The height from simulation was 0.14 mm as compared to height loss from experiments which was 0.4 mm. The decay modulus from the experimental displacement (0.014) and the simulation (0.0135) was in reasonable agreement ($n = 2$).

The von Mises stress distribution in the disc at the end of the step 2 (i.e. 10,000 cycles) is shown (Figure 4-27). The residual stress was maximum in the annulus and concentrated along the periphery. The residual von Mises stress in the nucleus was approximately one-tenth as in the

annulus and was concentrated along the outer circumference, presumably as the annulus constrained the bulging of the nucleus. As expected, the annular fibers had the least residual stress, concentrated in the innermost layer.

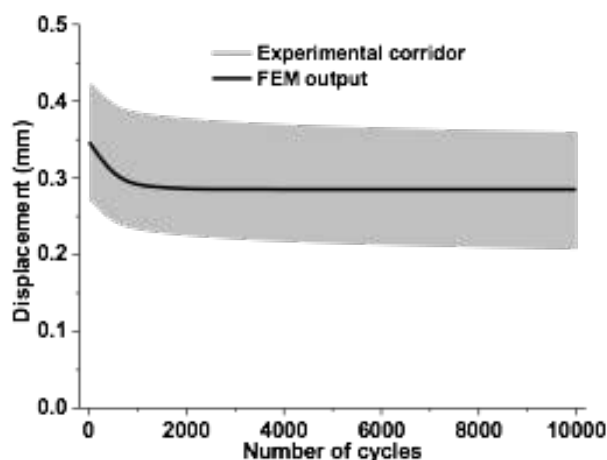
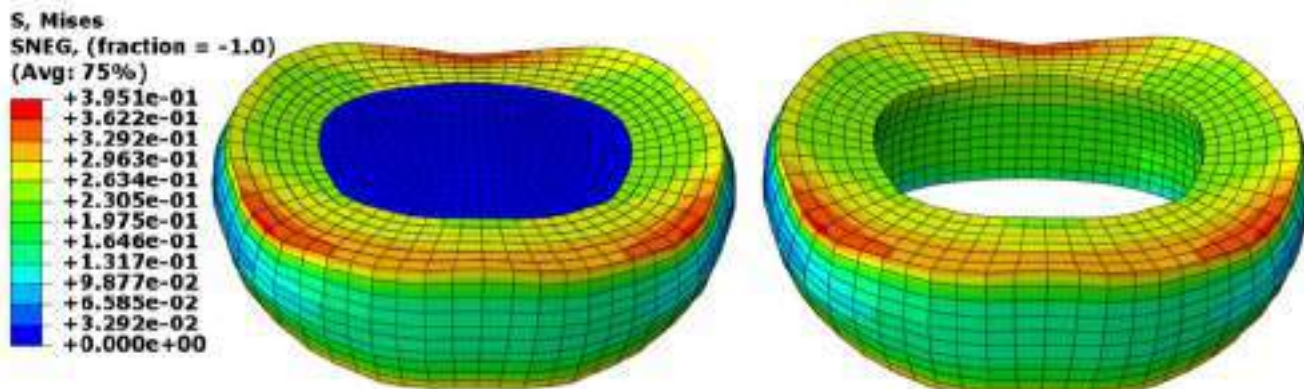


Figure 4-26: Comparison of the cyclic response from FEM with experimental corridor (shaded region) for 2 Hz and 150 N cyclic compressive loading.



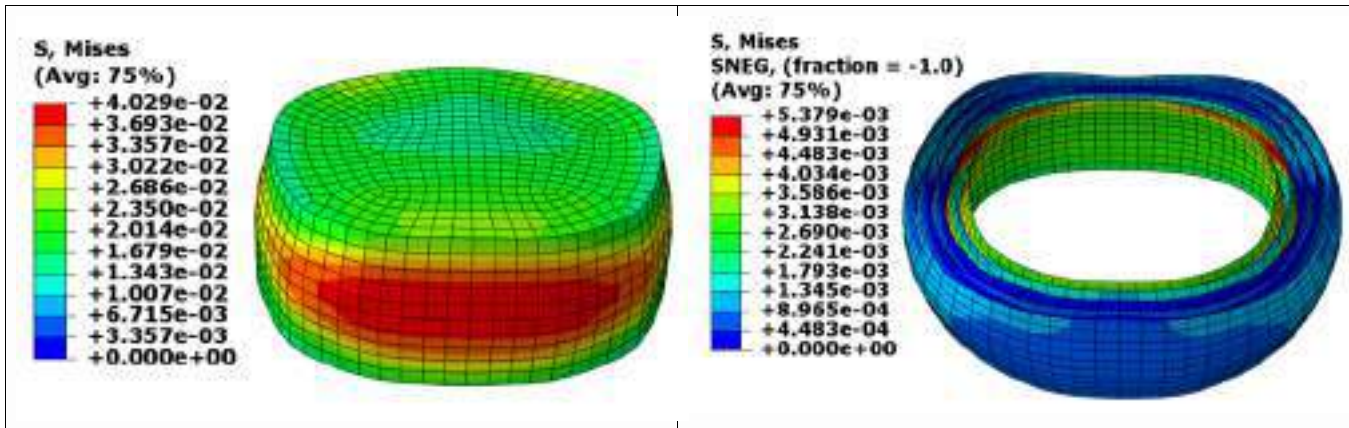
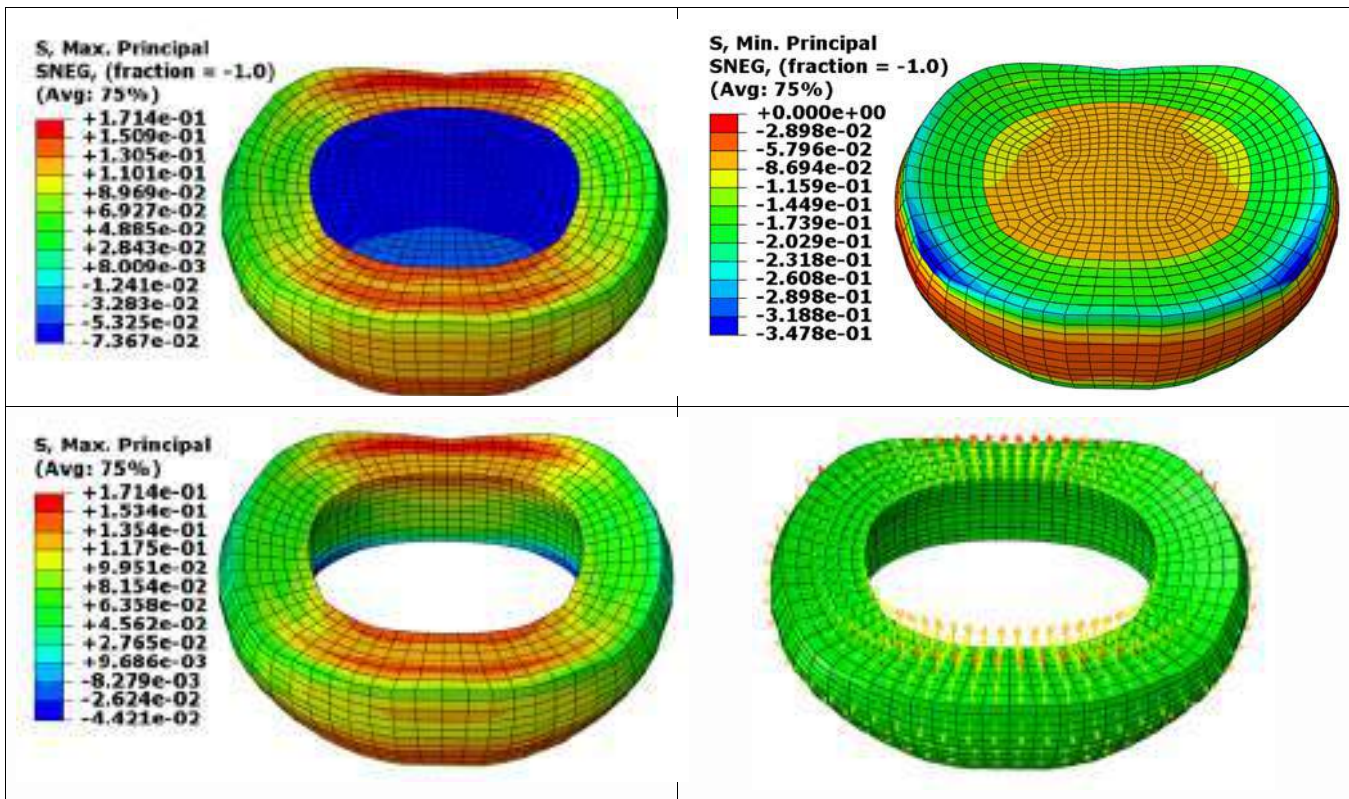


Figure 4-27: von Mises stress distribution (entire disc, annulus, nucleus and annular fibers).

The maximum (tensile) and minimum (compressive) principal stresses occurred in the annular ground matrix (Figure 4-28). The first row in Figure 4-15 shows the maximum (left figure) and minimum (right figure) principal stresses in the entire disc. The maximum principal stresses correspond to positive values and peak corresponds to red region in the left figure. The minimum principal stresses correspond to negative values and peak corresponds to blue region in the right figure. The peak minimum principal stresses were larger as compared to peak maximum principal stresses. The maximum principal stress was prominent in the anterior and posterior annular regions whereas the minimum principal stress was greater in the anterior region. The direction vectors of the principal stresses were inclined to the loading planes, indicating the development of shear stresses within the disc.



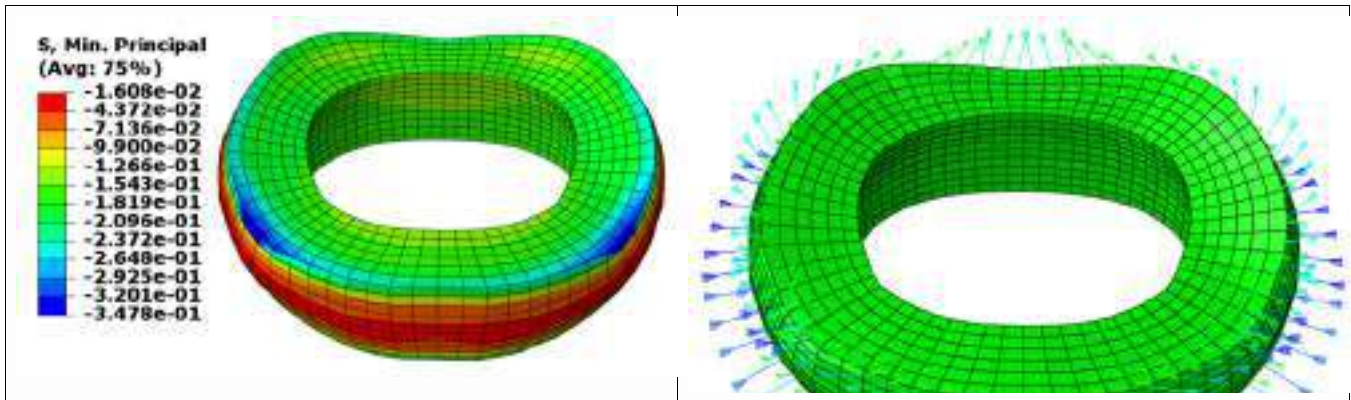


Figure 4-28: Maximum and minimum principal stress distribution (entire disc and annular ground matrix).

The principal stresses were lesser in the nucleus compared to the annular ground matrix. The maximum principal stresses in the nucleus were negative (i.e. only compressive) indicating the inability of the core of the nucleus to sustain tension (Figure 4-29). However, the annulus-nucleus boundary elements demonstrated shear based on directional vectors. This suggests that the mode of load transfer in this region of the disc is multi-modal.

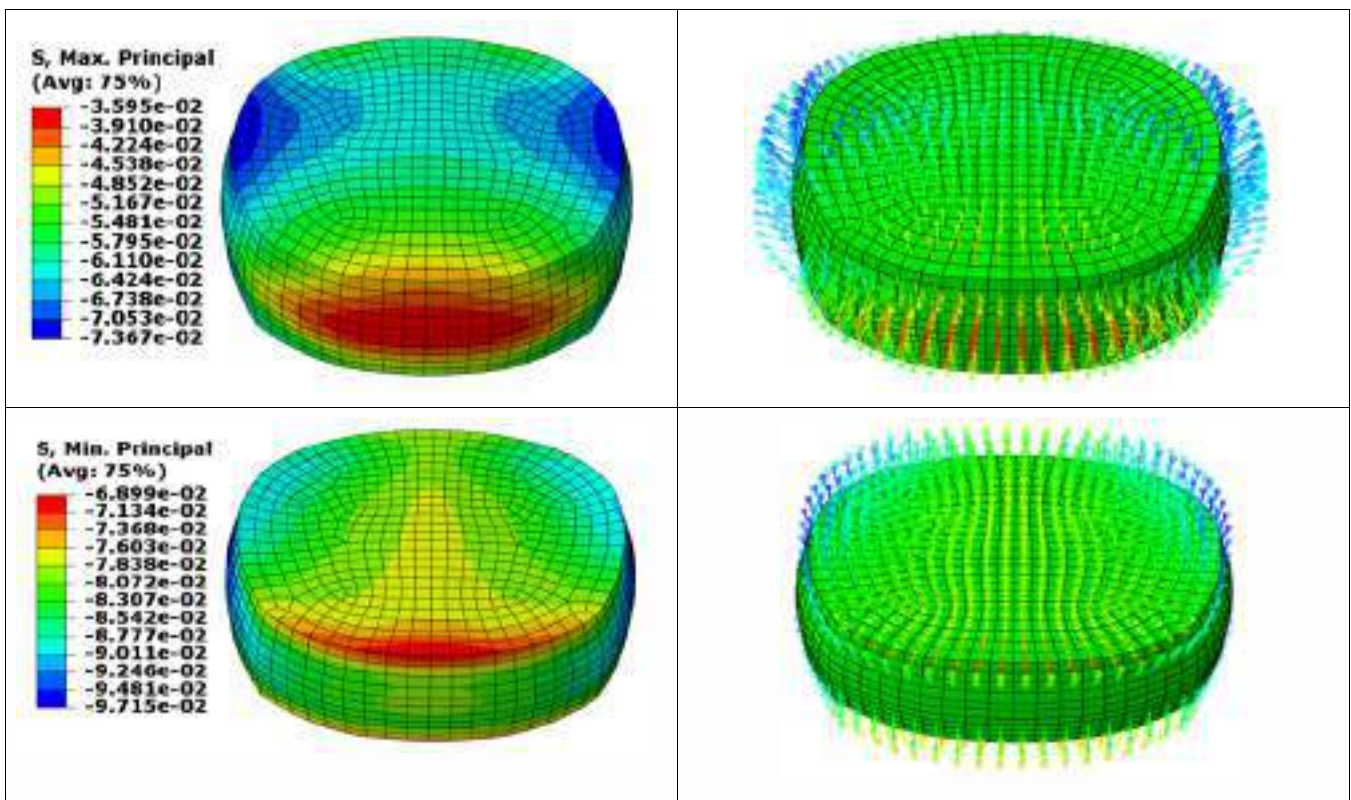


Figure 4-29: Maximum and minimum principal stress distribution (nucleus).

Tensile stresses in the annular fibers were low because of the compressive mode of loading (Figure 4-30). Along the inferior and superior ends, peripheral elements showed tensile stresses, and this was attributed to the bulging response of the disc. The compressive stresses did not exist in the annular fibers as they responded only to tensile forces.

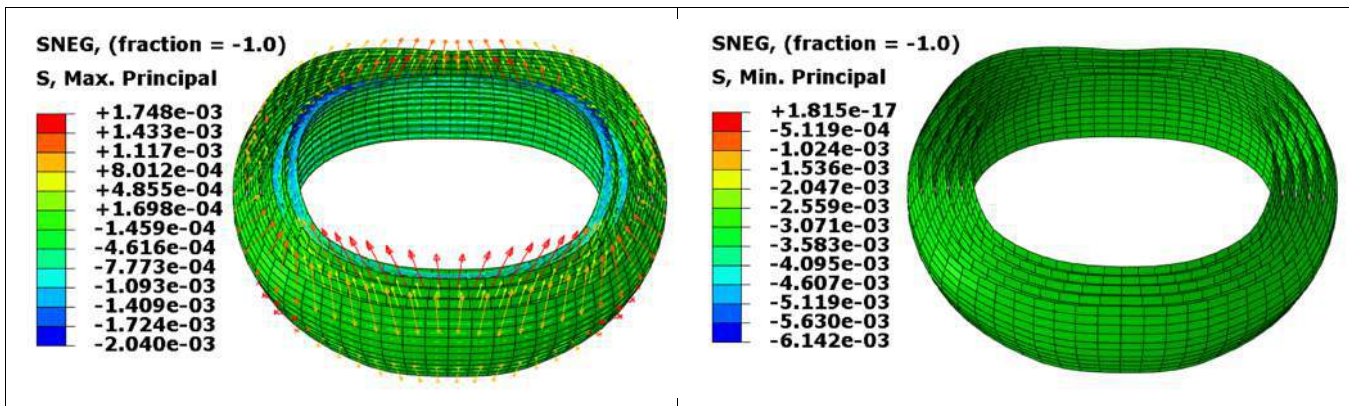


Figure 4-30: Maximum and minimum principal stress distribution (annular fibers).

Principal stresses were considerably lower than the von Mises stresses, indicating the role of the shear stress development during cyclic loading. This was also evident from direction vectors of the principal stresses. Shear stresses developed in the model in transverse, coronal and sagittal plane were compared (Figure 4-31). Transverse plane shear stress was almost one-half as compared to the other two anatomical planes. The development of shear stresses along the coronal and sagittal planes are attributed to the bulging of the annulus during compression. Also, shear stresses were greatest in the annulus ground substance.

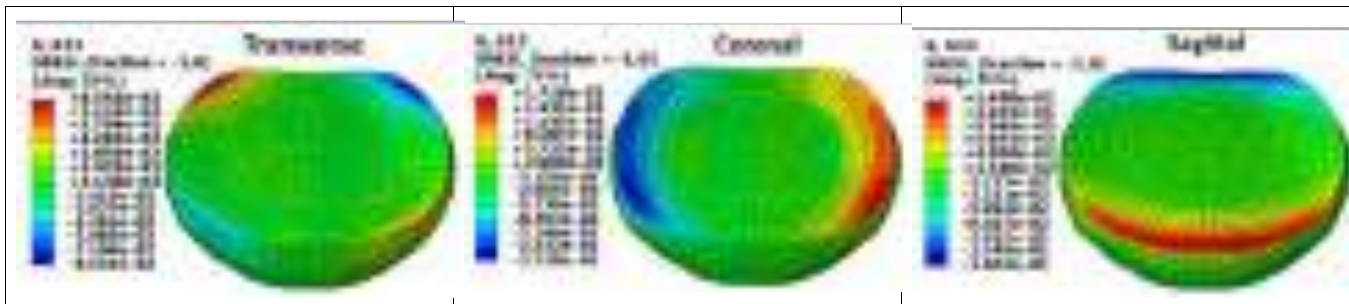


Figure 4-31: Shear stress distribution.

Principal strains were found to be maximum in the annulus ground substance and annular fibers. The maximum principal strains occurred in the radial direction, whereas the minimum principal strains occurred in the axial direction (Figure 4-32). The magnitude of minimum principal strain was higher as compared to maximum principal strain, similar to that of stresses. The inclined strain vectors suggest multi modal loading.

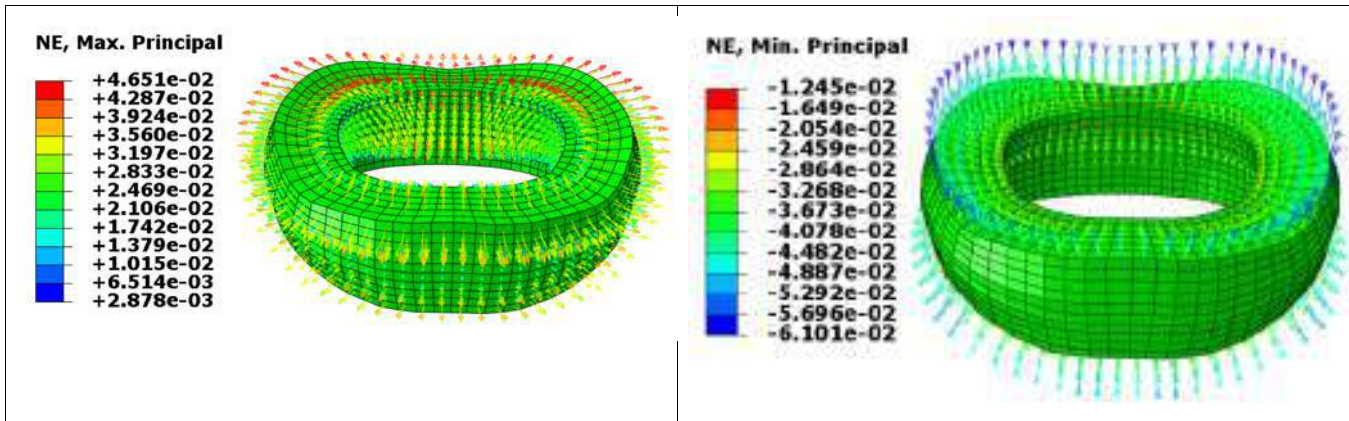


Figure 4-32: Maximum and minimum principal strain distribution (annulus ground matrix).

Force Variation: A parametric study was performed by varying the applied load on the developed and experimentally validated finite element model. Cyclic loads of 100 N and 200 N at 2 Hz were applied and results were compared with the 150 N and 2 Hz simulation, described above. Displacements of the superior endplate increased with increases in the applied force (Figure 4-33). Reduction in the displacement during first 2,000 cycles was also greater at higher loading magnitudes. Height loss increased with increasing loading magnitudes from 0.1 mm for 100 N to 0.17 mm for 200 N. However, the decay modulus remained relatively unchanged for the displacement plots: 0.012 for 100 N, 0.013 for 150 N, and 0.011 for 200 N loading magnitudes.

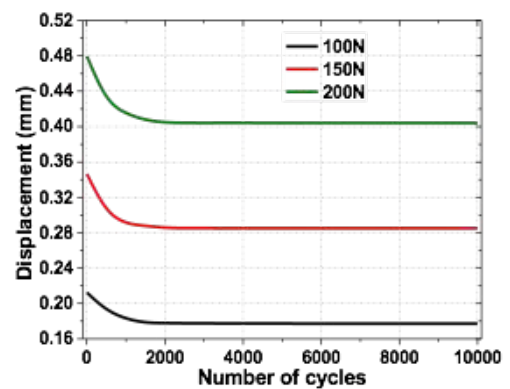
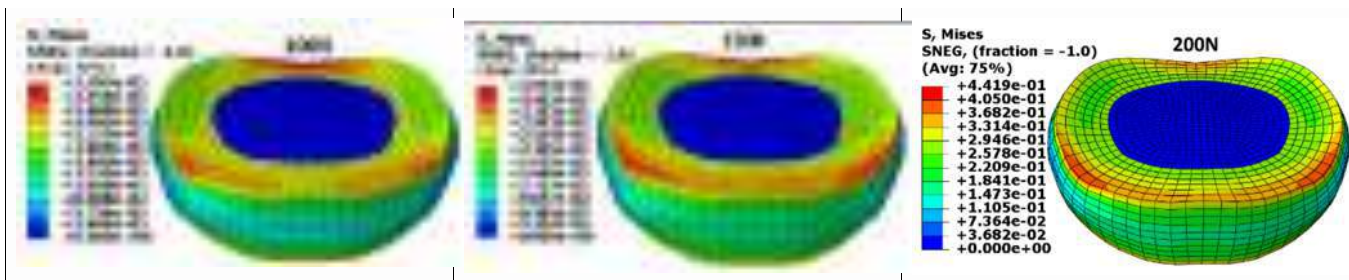


Figure 4-33: Comparison of displacement with variation in the magnitude of applied 2 Hz cyclic compressive force.

Stress-strain distributions were compared for the three loading magnitudes. The peak magnitudes of stresses and strains increased with increase in loading force (Figure 4-34). The first row in Figure 4-34 shows the von Mises stress. The maximum von Mises stress concentration shifted from the posterior to the anterior region. However as the magnitude of stress is increased with increasing force, the residual stress in every element was higher as compared to stress with lesser force.



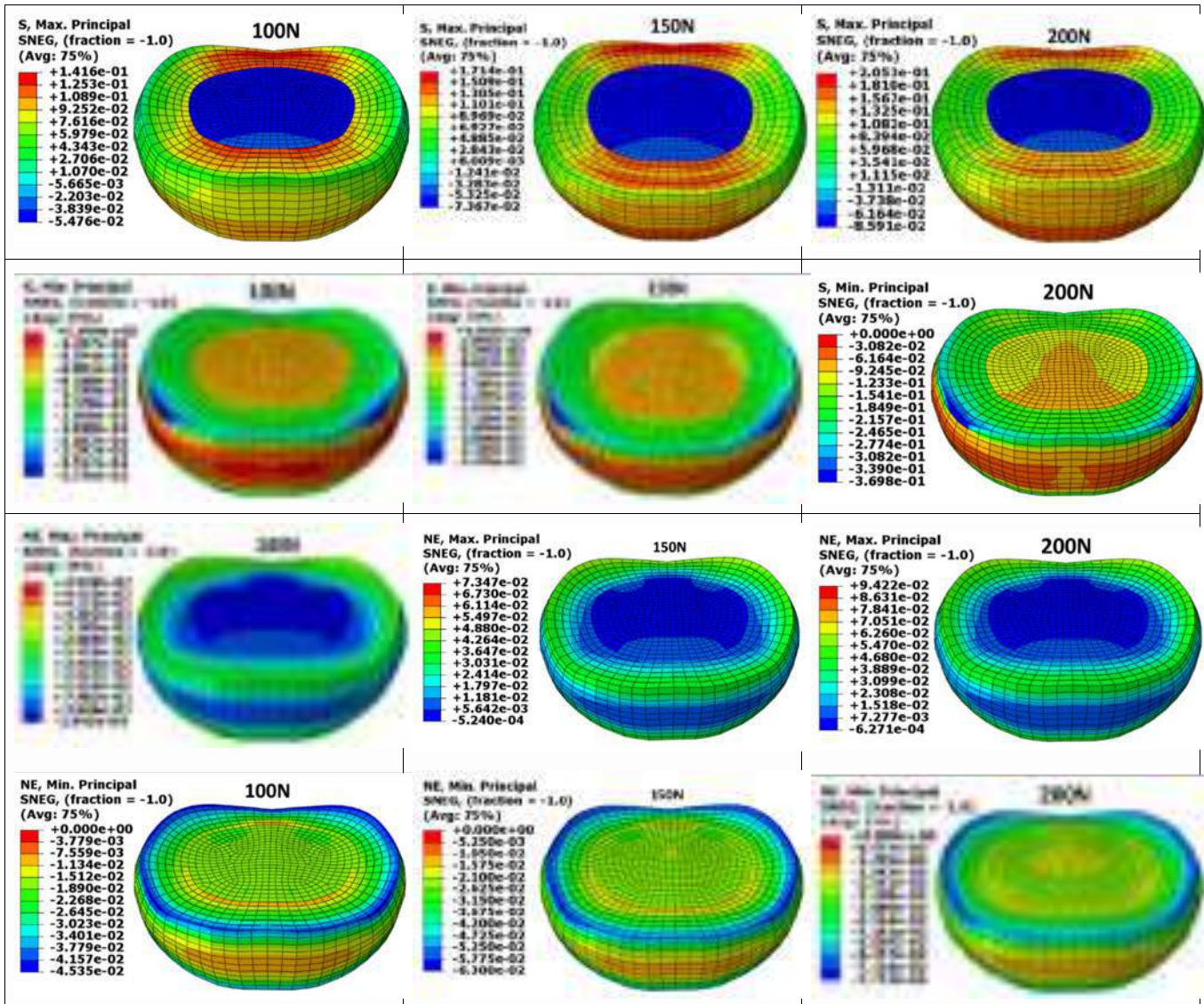


Figure 4-34: Comparison of stress and strain distribution for varying loads.

The second and third rows in Figure 4-34 show the maximum principal stress and minimum principal stress distributions, respectively. The magnitudes of stresses increased with increase in force level. The peak maximum principal stresses were observed in the annulus, radially distributed along the anterior and posterior regions. The peak maximum principal stresses were also in the annulus along superior-inferior ends of the anterior periphery.

The fourth and fifth rows in Figure 4-34 show the maximum principal strains and minimum principal strain distribution respectively. The maximum principal strain was slightly higher, probably as the annulus had negligible resistance in tension. The maximum principal strain was concentrated in the annulus ground substance and annular fibers (Figure 4-32). The minimum principal strain was along the annular outer periphery.

B. Validation of Finite Element Model at 4 Hz and 150 N

To validate the model for 4 Hz simulations, it was scaled from the 2 Hz model and material properties were used from tension/compression and viscoelastic tests for the disc segments tested at 4 Hz (Figure 4-35). Tension/compression and viscoelastic curves were almost identical to that

for the curves for segments tested at 2 Hz, showing good agreement with the mechanical properties of specimens from different human cadavers. Cross-sectional area of the model of was 300 mm² which was close to the average of the two segments tested at 4 Hz (297±26 mm²).

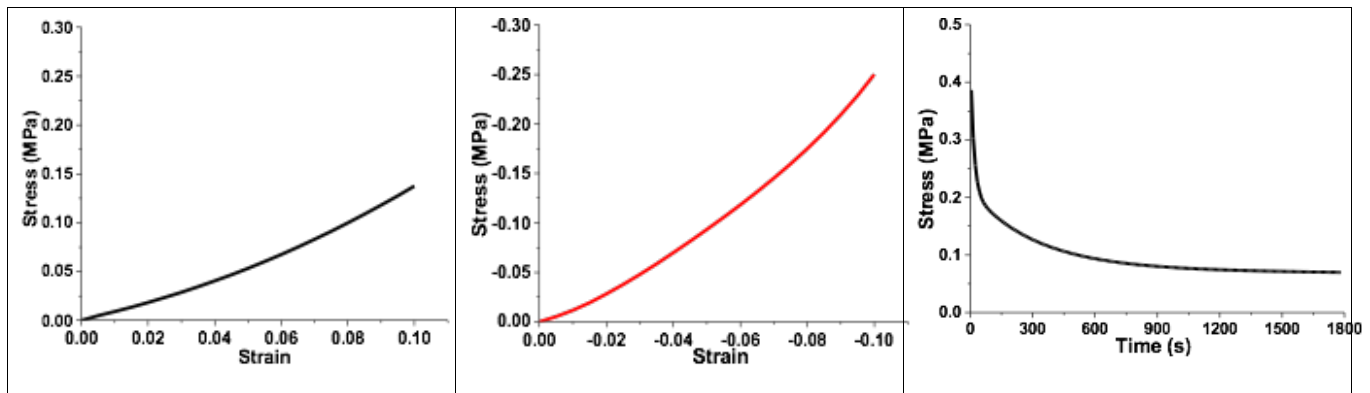


Figure 4-35: Annular ground matrix properties for tension (left) and compression (middle). Viscoelastic properties for the annular ground matrix are presented on the right.

Boundary Conditions: Boundary conditions were applied to the finite element model similar to that described previously for the 2 Hz model. Bony endplates and cartilaginous endplates had tied contacts. The cartilaginous endplate had shared nodes with the annulus and nucleus. Similarly, the annular fibers had shared nodes with the ground substance. The inferior bony endplate was constrained in all 6 degrees of freedom and the superior bony endplate sustained the applied load. The cyclic load was applied in two steps: 1) a uniform load of 150 N at 4 Hz was applied to the superior end plate; and 2) a direct cyclic step simulating 10,000 compression cycles based on the previous step history. The results were output as displacement of the superior endplate over 10,000 cycles and was compared with corresponding experimental data. The time history stress-analysis outputs included maximum and minimum principal stresses and strains, vector directions, von Mises stresses, and normal and shear stresses.

Validation: Displacement of the superior endplate during 10,000 cycles was compared to the piston stroke from experiments for 10,000 cycles for segments tested at 4 Hz (Figure 4-36). As observed in the experiments, displacement of the disc at higher frequency was lesser showing strain rate hardening. The simulation displacements were within the experimental mean plus minus one standard deviation corridors. The displacement was greater during the initiation of the loading process and reduced exponentially in the first 1,000 cycles, followed by a plateau showing the effect of viscoelasticity in this first 1,000-cycle period. Loss in disc height was compared to the height loss measured from pre- and post-cyclic test radiographs. Height loss from simulation was 0.1 mm as compared to height loss from

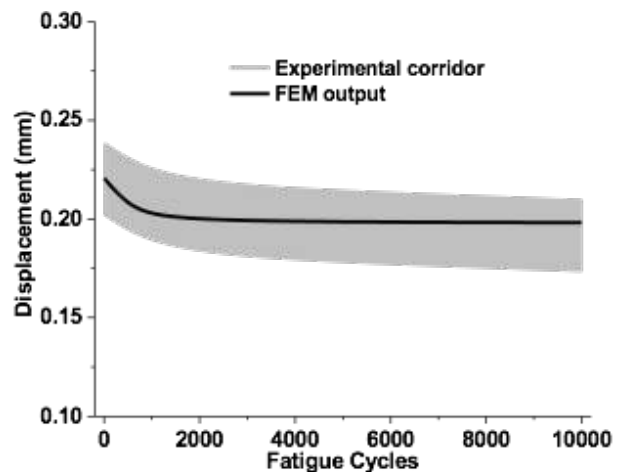


Figure 4-36: Comparison of the cyclic response of the FEM with the experimental corridor (shaded region) for 4 Hz and 150 N cyclic compressive loading.

experiments which was 0.08 mm. The decay modulus from the experimental (mean of two specimens) displacement (0.007) and the simulation (0.009) was in reasonable agreement.

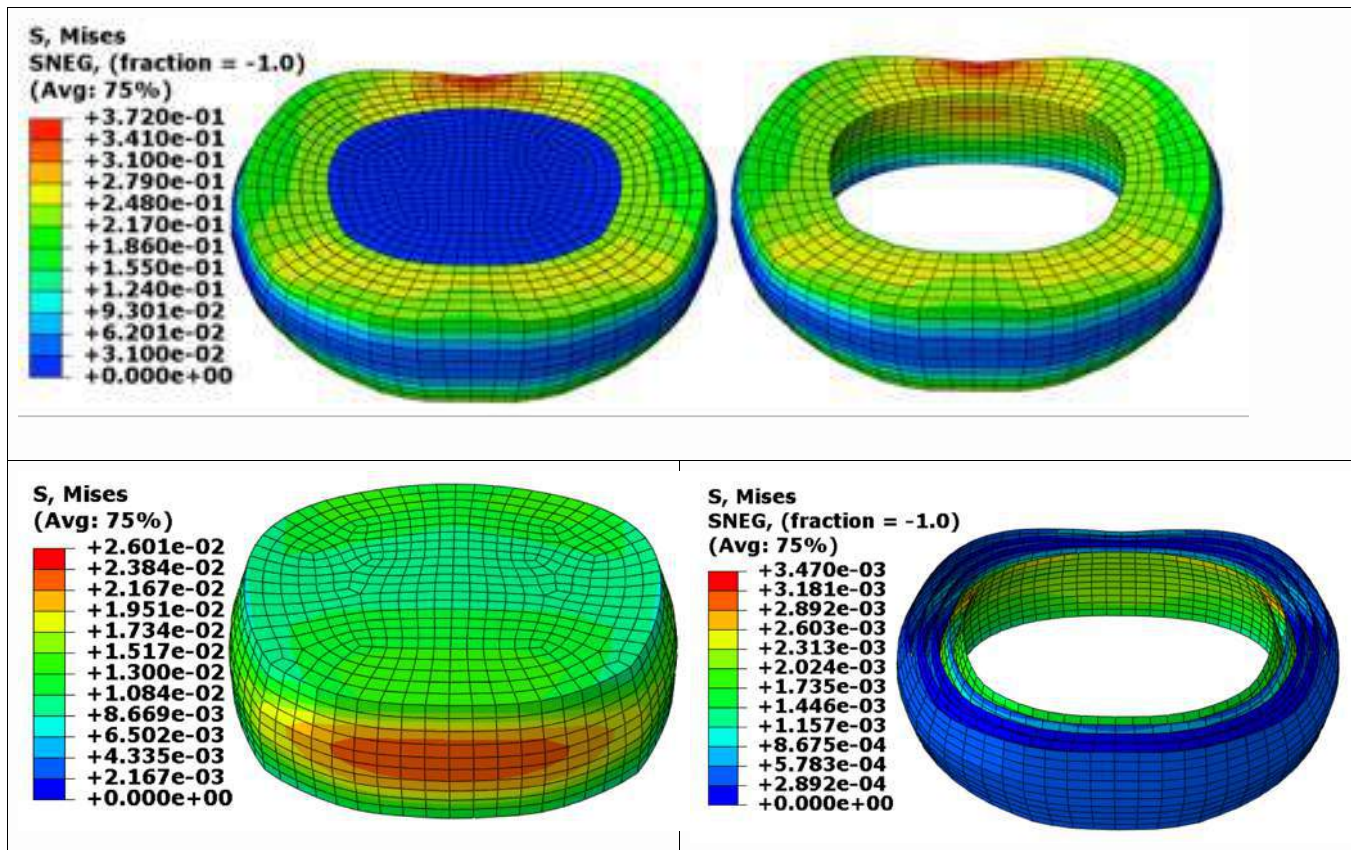
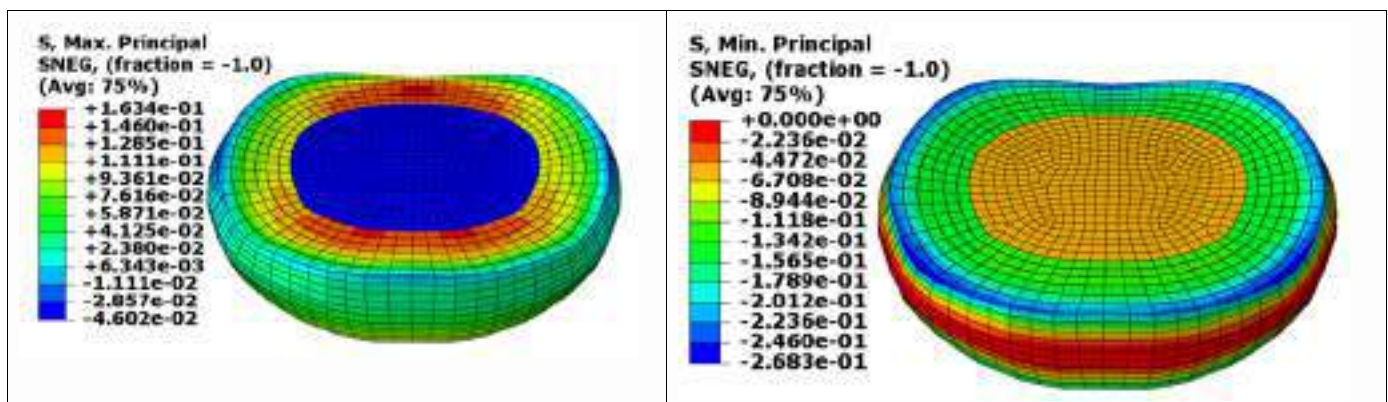


Figure 4-37: Von Mises stress distribution (entire disc, annulus, nucleus, and annular fibers).

The von Mises stress distribution in the disc at the end of the step 2 (i.e. 10,000 cycles) is shown (Figure 4-37). The stress distribution was greatest along the superior-inferior ends because the force didn't have enough time to get evenly distributed at higher frequency. The residual stress was maximum in the annulus and concentrated along the posterior end. The residual von Mises stress in the nucleus was much less as compared to as in the annulus and was concentrated along the annulus-nucleus boundary. As expected, the annular fibers had the least residual stress, concentrated in the innermost layer, similar to the previous 2 Hz model.



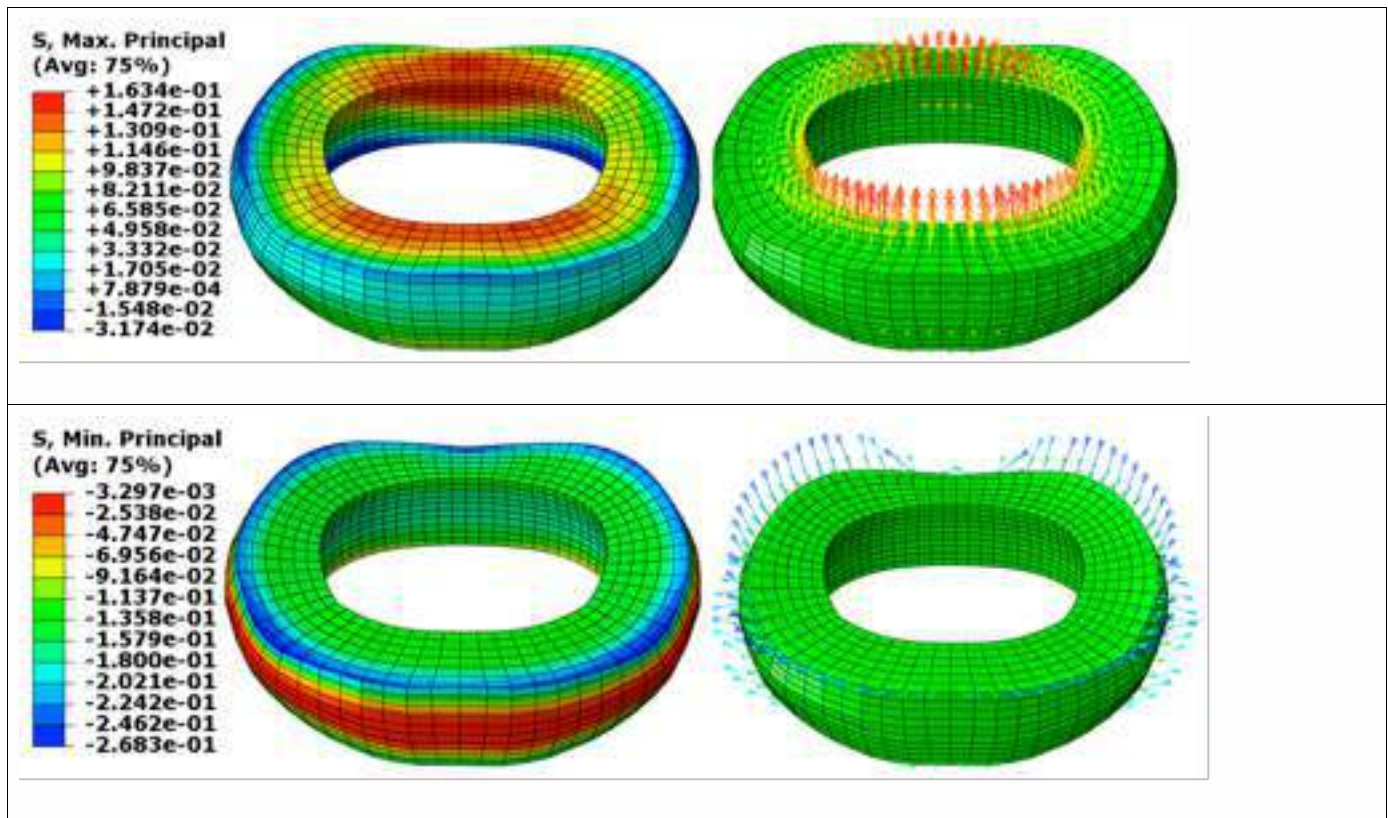


Figure 4-38: Maximum and minimum principal stress distribution (entire disc and annular ground matrix).

The maximum and minimum principal stresses occurred in the annular ground matrix (Figure 4-38). The compressive stresses were higher than tensile stresses in the disc. The maximum principal stress was greatest at the annulus-nucleus anterior-posterior boundary whereas the minimum principal stress was greater in superior-inferior annular periphery. The direction vectors of the principal stresses were inclined to the loading planes, indicating the development of shear stresses within the disc. The inclined direction vectors indicate introduction of shear stress in the elements.

The principal stresses were again lesser in the nucleus compared to the annular ground matrix. The maximum principal stresses in the nucleus were negative (i.e. only compressive) indicating the inability of the core of the nucleus to sustain tension (Figure 4-39). However, the annulus-nucleus boundary elements demonstrated shear based on directional vectors. This suggests that the mode of load transfer in this region of the disc is multi modal.

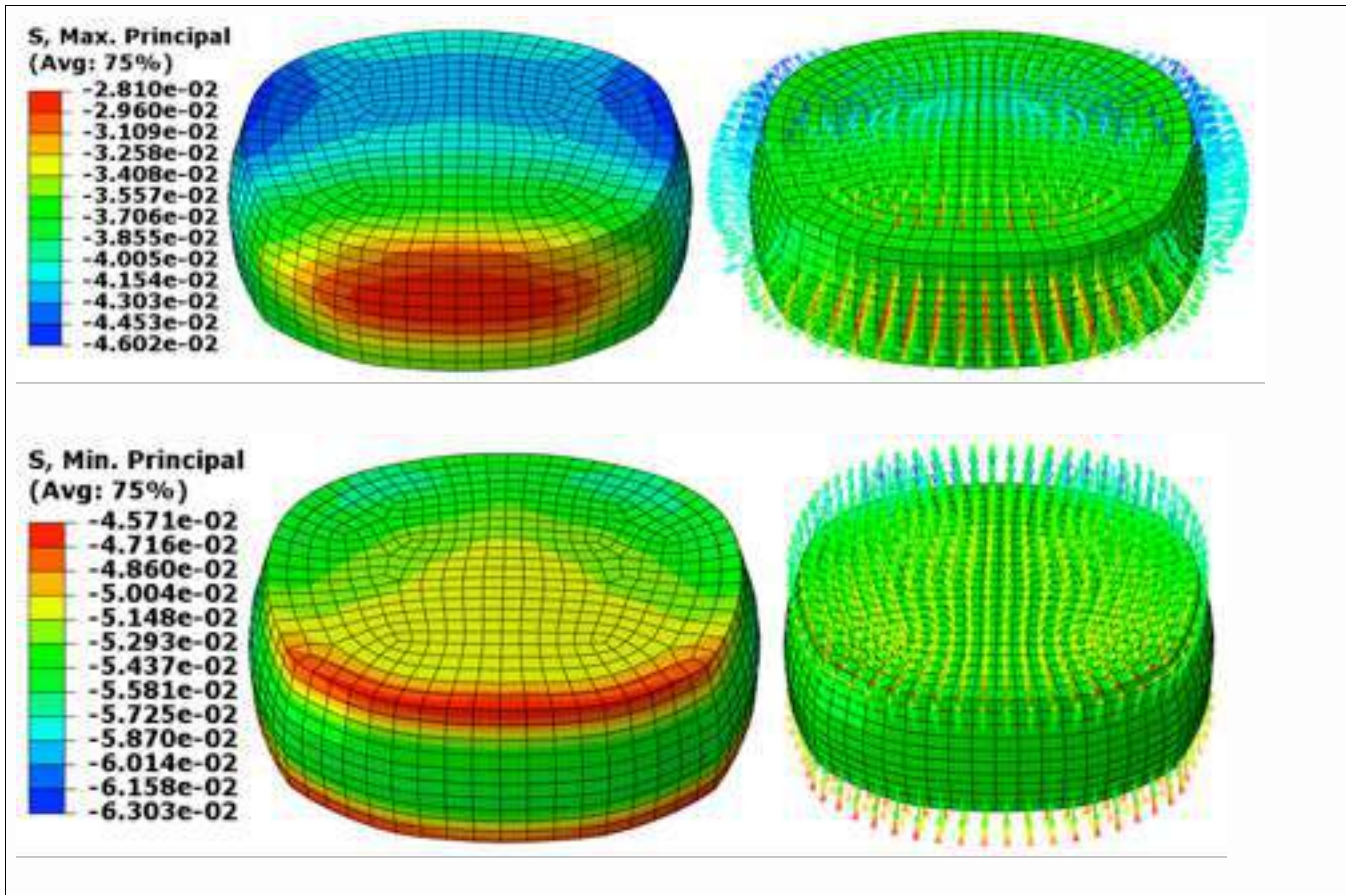


Figure 4-39: Maximum and minimum principal stress distribution (nucleus).

The stresses in the annular fibers were also low because of the compressive mode of loading. Along the inferior and superior ends (Figure 4-40), peripheral elements showed tensile stresses, and this was attributed to the bulging response of the disc. The compressive stresses did not exist in the annular fibers as they responded only to tensile forces.

The principal stresses were considerably lower than the von Mises stresses, indicating the role of the shear stress development during cyclic loading. This was also evident from direction vectors of the principal stresses. Shear stresses developed in the model in transverse, coronal and sagittal plane were compared (Figure 4-41). The shear stress along the transverse plane was almost one-half as compared to the other two anatomical planes. The development of shear stresses along the coronal and sagittal planes are attributed to the bulging of the annulus during compression. Also, the shear stresses were greatest in the annulus.

Principal strains were maximum in the annulus ground substance and annular fibers. The maximum principal strains occurred in the radial direction, whereas the minimum principal strains occurred in the axial direction (Figure 4-42). The inclined strain vectors suggest shear mode of transmission of the external loading.

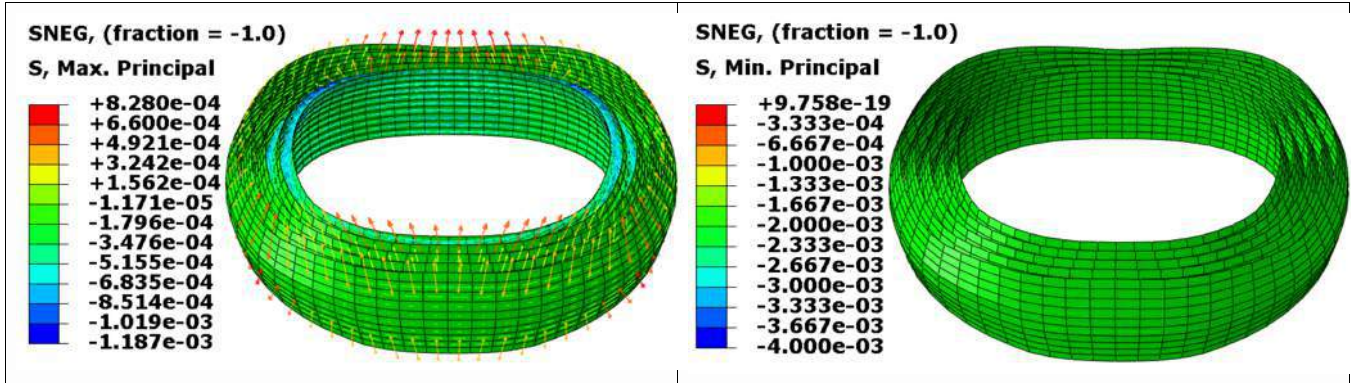


Figure 4-40: Maximum and minimum principal stress distribution (annular fibers).

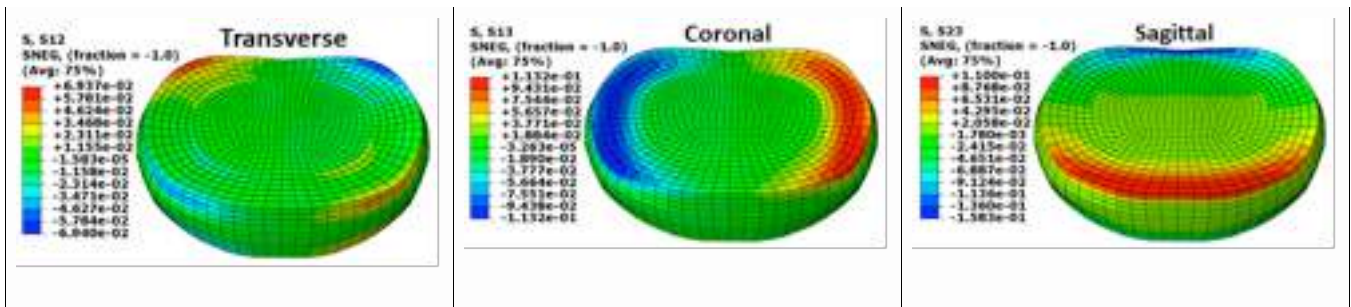


Figure 4-41: Shear stress distribution.

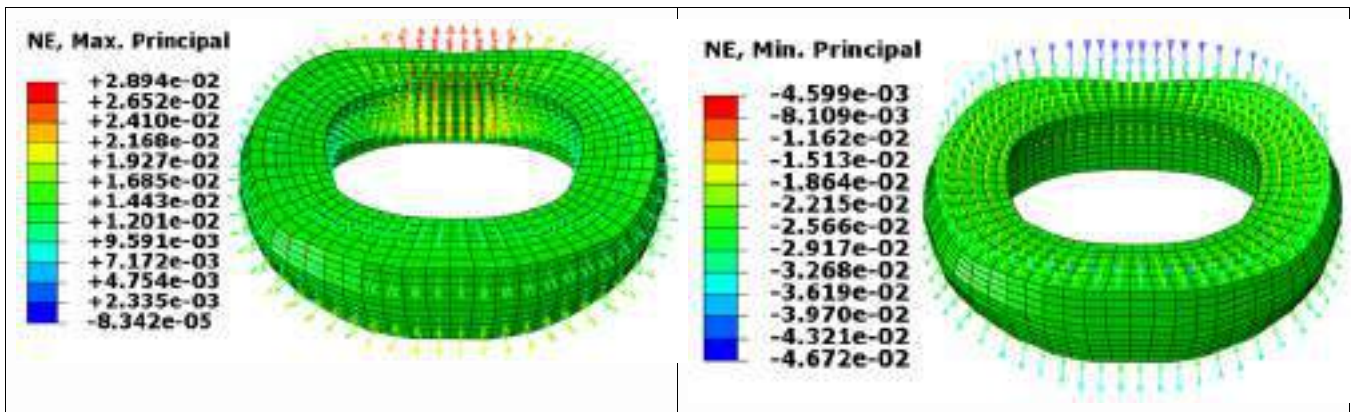


Figure 4-42: Maximum and minimum principal strain distribution (annulus ground matrix).

Force Variation: A parametric study was performed by varying the applied load on the validated finite element model. Cyclic loads of 100 N and 200 N at 4 Hz were applied and results were compared with the 150 N and 4 Hz simulation, described above. Displacements of the superior endplate increased with increase in the applied force (Figure 4-43). The reduction in the displacement during first 2,000 cycles was also greater for higher loading magnitudes. Height loss increased with increasing loading magnitudes from 0.05 mm for 100 N to 0.13 mm for 200 N. However, the decay modulus was found to change unlike the model validated at 2 Hz: 0.002 for 100 N, 0.007 for 150 N and 0.011 for 200 N loading magnitude.

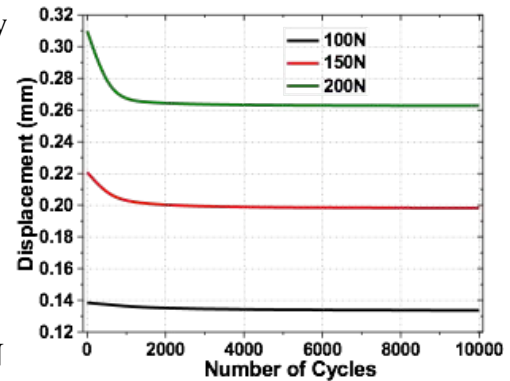


Figure 4-43: Comparison of displacement with variation in the magnitude of applied 4 Hz cyclic compressive force.

The stress-strain distributions were compared for the three loading magnitudes. The peak residual magnitudes of stresses and strains increased with increasing force (Figure 4-44). The first row in Figure 4-44 shows the von Mises stress. The maximum von Mises stress concentration was in the posterior regions. The magnitude of stress is increased with increasing force, as well the force transmission increased. At 100 N the stress distribution was only at the superior-inferior ends of the annulus, and there was almost negligible in the central periphery. This phenomenon can be attributed to the strain rate effect. At 4 Hz the tissue may not have ‘received’ enough time to get compressed, causing stresses to be accumulated in the superior inferior ends. However, with increasing force, as the compression was higher, the central peripheral elements of the annulus also showed increasing residual stress.

The second and third rows (Figure 4-44) represent the maximum and minimum principal stresses in the disc with increasing force. The maximum principal stresses can be observed at the annulus nucleus boundary and distributed radially with increasing force. The minimum principal stress was along the periphery and increased longitudinally with increasing force. This shows that the force transmission in the disc increased in the disc with increasing force. The peak maximum and minimum principal strains occurred along the cranial and caudal ends (third and fourth row of Figure 4-44). As discussed before, the vectors for the maximum principal strains were along the radial direction, whereas the vectors for the maximum principal strains were along the axial direction. This is caused due to the incompressible properties of the disc compression in one direction caused tension in other directions.

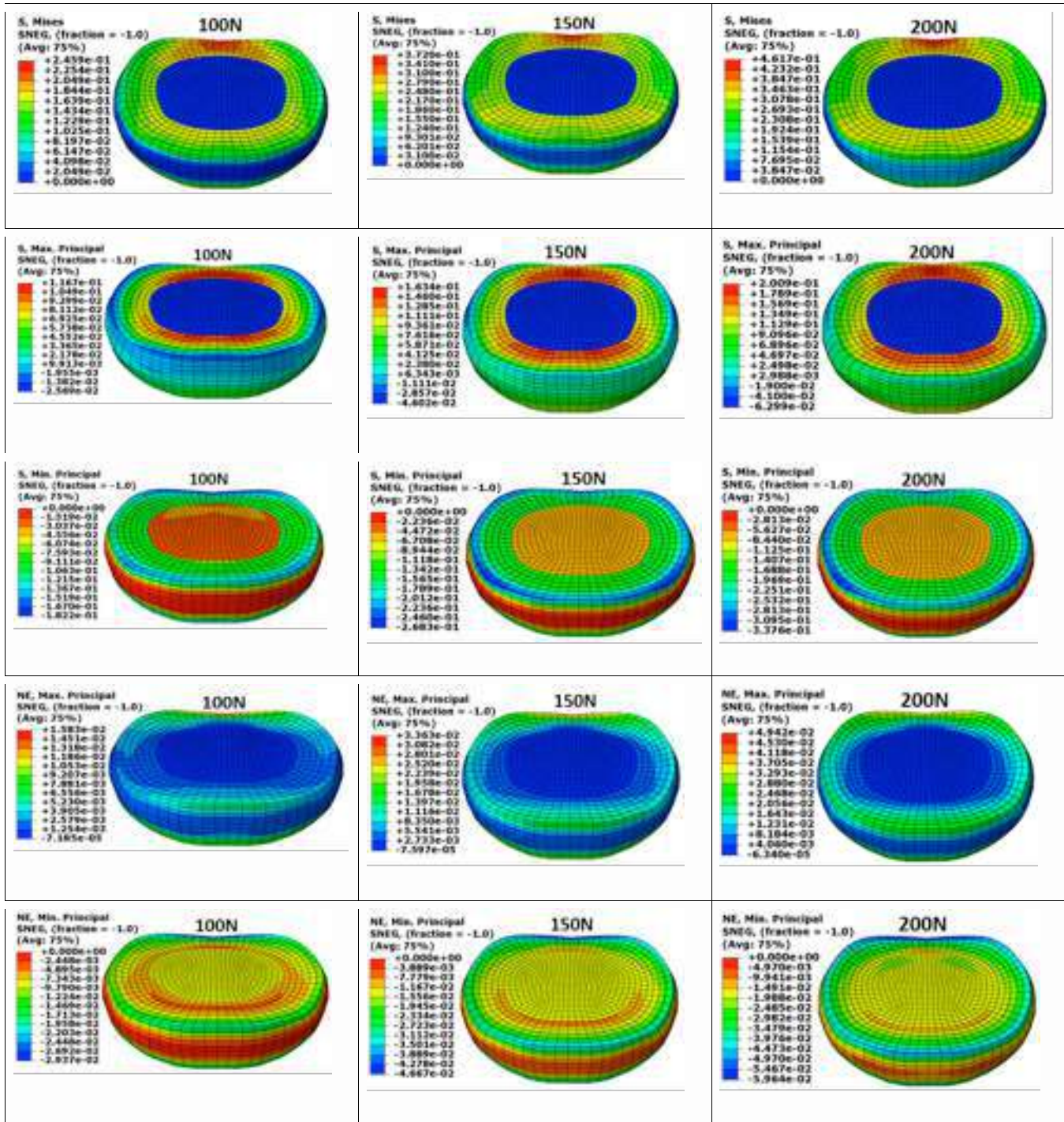


Figure 4-44: Comparison of stress and strain distributions for varying loads.

Year 5:

5.1 Long-Term Movement Analysis of Vertebra in Ultrasound Image Sequence

A. Error Accumulation in Displacement Estimation

High frame rate ($> 30\text{Hz}$) and long exposure times (> 1 minute) are requisite for analyzing in-vivo spine kinematics during activities such as running or jumping, which leads to the question of how to track large movements in hundreds of ultrasound data frames. Traditionally, displacement estimation in ultrasound imaging was made possible by matching the radio frequency (RF) speckle patterns between consecutive frames in the image sequence. The speckle patterns follow as the tissue deforms but will change eventually as the deformation continues over time. Therefore, estimating large displacement from nonconsecutive frames is usually avoided. Alternatively, large strains are tracked by a frame-by-frame summing method, which breaks a large deformation into a series of smaller steps and sums the displacement estimation of each step.

This framework, also referred as multi-compression in ultrasound elastography, will accumulate summing errors and error variances infinitely over time: each displacement estimation between consecutive frames contributes an error, so a large number of steps leads to a large number of noise-induced errors being summed. For the long-term tracking tasks, recent papers proposed methods to reduce drift and studied sources of error accumulation in ultrasound elastography [37,38]. Several methods were developed to reduce the drifting [39] by using larger steps, self-correction [40,41], or by building an observation model of the tissue biomechanics [42] without changing the step-by-step summing framework. In this report, we present and validate a drift reducing multi-frame tracking framework to analyze ultrasound RF data of long-term, large motion of vertebrae.

B. Multi-frame Algorithm and Displacement Estimation

In tissue elastography, a tissue region of interest (ROI) is divided into smaller packets which contain subsets of data samples in the region. The tissue deformation can be measured by tracking the displacements of each data packet, as shown in Figure 5-1. The displacement of the packets between two data frames is usually found by searching for the location of the maximum correlation. Due to the precision requirement from the correlation step, RF data frames are preferable than the clinical B-mode image because they provide a larger contrast between different packets in the same region. For ultrasound bone imaging, the displacements of the packets are restrained by the rigid body constraint, and especially for translational rigid-body motion, the displacements of all subset packet are equal to the displacement of the entire region. Therefore, the measurement of a vertebrae motion can be described by a 2-dimensional (2D) vector x .

Under the assumption that vertebra deformation is negligible, vertebrae are tracked as rigid objects in an ultrasound imaging RF sequence, denoted as $\{I(p)\}, p \in P$, where p is a unit data sample that belongs

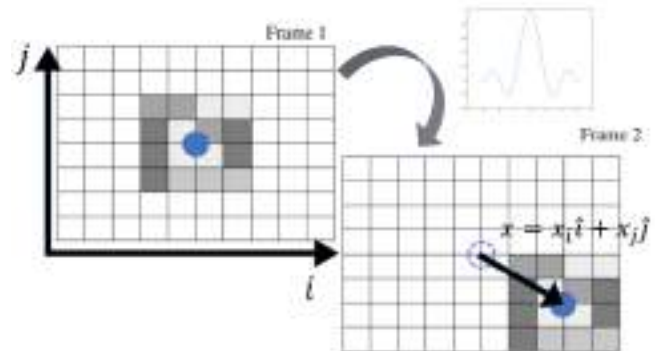


Figure 5-1: Speckle tracking in ultrasound RF data frames.

to vertebra region P in the RF data. The true position of a vertebra at the current frame number T is expressed as a 2D vector x_T^* , and the estimation of x_T^* is denoted as x_T . The goal of accurate tracking is to minimize the error between the true position and its estimation at the current frame. When the vertebra is in motion, the RF signal pattern of the vertebra changes because the vertebra is re-positioned in the field of view (FOV) of the ultrasound transducer. The vertebra RF pattern in the first frame of the sequence may be an inaccurate template to match the RF of the current frame. The conventional method solved this problem by computing displacements between temporally adjacent frames and summing the displacements to obtain the true position at the current frame. The displacements are usually computed by template block-matching or optical flow motion estimation methods.

The true 2D translational displacement of a vertebra P between two RF frames I_s and I_t , noted as $d_{s,t}^*$, is the difference of true positions, as shown in Equation 5.1. The number of RF data samples in vertebra P is denoted as $|P|$. The computed displacement estimation $d_{s,t}$ is a noisy version of $d_{s,t}^*$ with noise $\epsilon_{s,t}$, as shown in Equation 5.2. The traditional framework only compares the current frame with a previous frame. Provided that the initial true position x_0^* and its estimation x_0 are $(0, 0)$, in this frame-by-frame framework, position estimation x_T was obtained by summing displacements of adjacent frames. The error between the true position and its estimation at current frame is the summation of noise $\epsilon_{s,t}$ estimated from each frame pair, as shown in Equation 5.3. It suggested the errors accumulate infinitely if only one previous frame is selected for comparison.

$$d_{s,t}^* = x_s^* - x_t^* \quad (5.1)$$

$$d_{s,t} = d_{s,t}^* + \epsilon_{s,t} \quad (5.2)$$

$$x_T^* - x_T = \sum_{i=2}^T d_{i-1,i}^* + x_0^* - \sum_{i=2}^T d_{i-1,i} + x_0 = \sum_{i=2}^T \epsilon_{i-1,i} \quad (5.3)$$

To solve the problem of infinite error accumulation, Rahimi et al. proposed a method which took multiple previous frames, instead of the adjacent previous frame, to estimate position change to reduce drifting caused by accumulating errors [43,44]. For each current frame number T , the historical trajectory of motion was used to select a set of the closest neighboring previous frame numbers \mathcal{K} , as illustrated in the shaded region in Figure 5-1. Similarly as the conventional tracking, displacement is estimated between T and each frame in set \mathcal{K} , but due to the multiple frames chosen, there exist redundant displacement estimates which can be used to minimize position estimation error and improve the tracking robustness. The minimization problem was modeled as Equation 5.4 and approximated as a linear optimization problem in Equation 5.5.

$$\argmin_{x_T} \sum_{s \in \mathcal{K}} \left[\Lambda_{s,T}^{-1} (x_T - x_s - d_{s,T})^2 + \Lambda_{T,s}^{-1} (x_s - x_T - d_{T,s})^2 \right] \quad (5.4)$$

$$\sum_{s \in \mathcal{K}} (\Lambda_{s,T}^{-1} + \Lambda_{T,s}^{-1}) x_i - \sum_{s \in \mathcal{K}} (\Lambda_{s,T}^{-1} + \Lambda_{T,s}^{-1}) x_s - \sum_{\mathcal{K}} (d_{s,T} \Lambda_{s,T}^{-1} - d_{T,s} \Lambda_{T,s}^{-1}) = 0 \quad (5.5)$$

where $\Lambda_{s,t}$ is covariance of vertebra RF between frame I_s and I_t . The approximation of $\Lambda_{s,t}$ is derived in Equation 5.6.

$$\Lambda_{s,t} = \frac{1}{|P|} \sum_{p \in P} \left(I_s(p + d_{s,t}(p)) - I_t(p) \right)^2 [\nabla I_s(p)^T \nabla I_s(p)] \quad (5.6)$$

While sufficient information exists to solve all $x_t(t = 1 \dots T)$ uniquely in the frame-by-frame analysis, when multiple frames are chosen, redundant displacement estimates can be used to minimize the position error and improve tracking accuracy. In our multi-frame analysis, the algorithm solves Equation 5.5 for each RF frame recursively at each time T . We chose the image set by looking for the closest four frames in the historical trajectory, as illustrated in Figure 5-2.

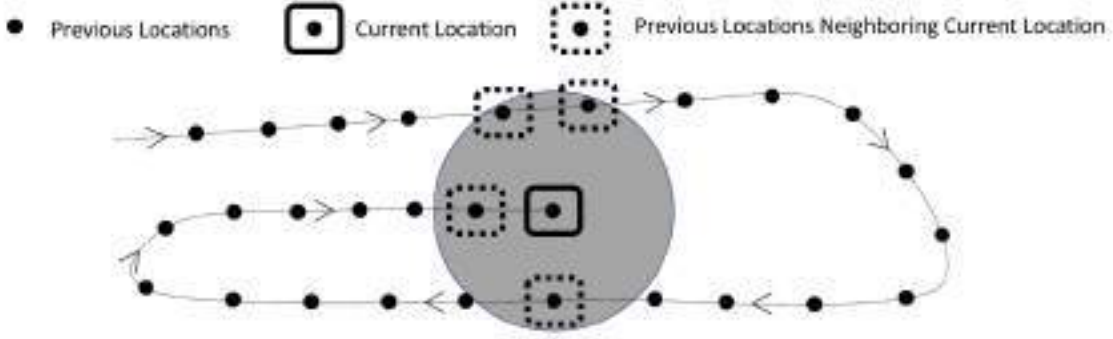


Figure 5-2: Object trajectory in cyclic motion with time increments. Black dots show previous locations in history and solid framed dots show current object location. Four previous frames were selected when the object tracked was neighboring current locations, as shown by the gray circle. Object displacements were estimated by calculating the normalized cross-correlation between all these frames with current frame, and the redundant information can be used to reduce error over the long-term

In our implementation, this multi-frame framework needs a motion estimator to compute $d_{s,t}(x)$; therefore, we selected 2D normalized cross-correlation (NCC) with subsample estimation to measure translational motion of vertebra. To focus on estimating displacements of the vertebra, their profiles in the first frame of ultrasound RF data were manually outlined as ROI. Because the acoustic echo signal from the vertebra surface is significantly stronger than the surrounding tissue or the ambient environment, the samples of vertebra were then further localized by thresholding a 2D moving average filtered image of the ROI. The dimensions of this tracking kernel in NCC matching, which is a subset of the RF data in the ROI around a grid point, are 3 lateral and 15 axial samples. For the purpose of fully validating tracking accuracy, no data point reduction was used in our experiments. Since most of the motion measured is in the low-resolution lateral direction of the ultrasound image, a quadratic fitting subsample estimation method was applied. If the vertebra is considered to be a rigid body, the displacement estimation of the vertebra cortical surface is derived by averaging over all the localized kernels which have a correlation coefficient over 0.85. Tracking algorithms were implemented on MATLAB 2016b (MathWorks, Natick, MA) to provide 2-dimensional translational displacement of the applied uniaxial vertebra motion. For a ROI that contains 3000 data samples, the average running time is 6.6 seconds per frame on one core of the central processing unit in an Intel Core i5 processor.

C. Data Acquisition and Experiment Design

To validate the accuracy of the multi-frame tracking method, precise axial motion was applied to a vertebra phantom, which was developed to replicate a perfect in-plane bone motion and exclude the factors such as tissue deformation. With the knowledge of ground truth data, the focus was to compare the accuracy of tracking long ultrasound image sequences with the multi-frame tracking and the traditional frame-by-frame methods.

The applied movement displacement, measured by a linear voltage displacement transformer (LVDT) and used as reference ground truth data, is compared to the tracking results from ultrasound RF data. Test specimens were mounted onto the piston of a material testing system Instron 8511 (Instron, Norwood, MA) and immersed in a water tank, as illustrated in Figure 5-3. The uniaxial displacement applied was measured by an internal LVDT with a sampling rate of 1000 Hz. This data was considered to be the ground truth. Ultrasound images and RF data were acquired by an ultrasonic system (Terason T3200, Terason Corp, Burlington, MA) with a Vermon 8IOL4 linear array (128 elements, center frequency: 3.6 MHz). The transmit focus length and imaging depth were set to 20 mm and 40 mm, respectively, at a data acquisition rate of 54 Hz. Time gain compensation were set to the same intermediate value. The start of each data acquisition was synchronized between the LVDT and ultrasound system. The projection angle was found by minimizing the square error between the LVDT sensor measurement and a projection of the 2D displacement of ultrasound tracking.

One vertebra phantom was fabricated by 3D printing, and a total of six vertebrae (C4, C5, and C6) were obtained from 2 fresh-frozen human cadaveric cervical spines. The levels were chosen because ultrasound can easily image these regions *in-vivo*. After defrosting at 4°C, the contiguous specimens were dissected into individual vertebrae. Para-cervical muscles and tissue were retained to mimic physiological condition and validate the tracking capabilities. A pedicle screw, normally used for spinal fusion surgery, was anchored on the vertebral body and used to connect the cadaveric vertebra to the alignment coupler which can mount to the piston of the Instron 8511 material testing system. Eighteen different imaging angles on one side of the phantom with equal angular increments (5°, 15°, ..., 165°, 175°) were used to generate different ultrasound vertebra phantom profiles. RF frame data were acquired in 5 different imaging angles of each cadaveric specimens (5°, 25°, 85°, 155° and 175° from the middle sagittal plane) to reflect the different bone surface profiles of important anatomical landmarks (anterior vertebral body, vertebral body, facet joint, lamina and spinous process).

Since the biomechanics properties of adjacent spinal segments were often evaluated by testing of passive motion *ex-vivo* [45,46] and *in vivo* [4,47], or assessing *in-vivo* functional abilities in repetitive active motion [48], sinusoidal cyclic loading waveforms at different frequencies and amplitudes were chosen to mimic passive applied motion. Using the same experimental platform, the vertebra phantom and cadaveric vertebrae were subjected to a total of 40 sets of sinusoid displacements movement all with integer value combinations of frequencies (1-10 Hz) and amplitudes (1-4 mm) for 10 seconds. On the vertebra phantom, this set of loading protocols was repeated over the 18 imaging angles. On the six cadaveric vertebrae, this set of loading protocols was repeated over the 6 anatomical landmark imaging angles. The LVDT in Instron testing system provided displacement measurement reference for tracking error estimation.

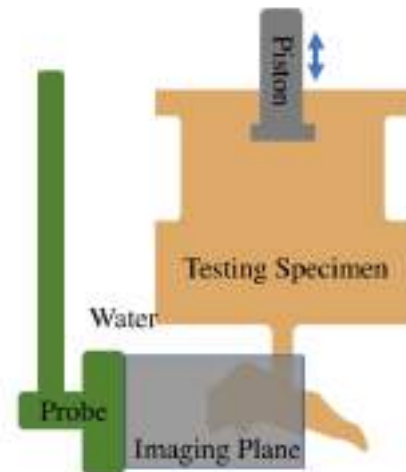


Figure 5-3: Specimen and alignment coupler mounted to the piston of Instron system. The piston drives specimen to move in a cyclic pattern. This motion of the specimen was captured by the US transducer in a water tank.

D. Data Analysis

To describe the overall speed of motion in one cycle and, we introduce the average absolute values of velocity $|\overline{v}|$, as approximated in Equation 5.7, which is proportional to the product of amplitude, A , and angular frequency, ω , or frequency of motion, f .

$$|\overline{v}| \approx \frac{\omega}{2\pi} \int_0^{T=\frac{2\pi}{\omega}} |\dot{y}_t| dt = \int_0^{T=\frac{2\pi}{\omega}} |A\omega \cos(\omega t)| dt = \frac{2}{\pi} A\omega = 4Af \quad (5.7)$$

where y_t is a sinusoidal waveform function of time t with amplitude A , angular frequency ω , and period of T .

Error variance is used to analyze the effects of test duration on the reliability of measurements. It is capable to assess accumulated displacement error over time and compare the performances between the frame-by-frame and multi-frame tracking of the vertebra phantom under cyclic sinusoidal motion. The error variances at a specific time were derived from the tracking results of 18 different bone profiles on the phantom under the same testing protocol, i.e., same frequency and amplitude. Since the increase of error variance over time indicates the decrease of measurement credibility, it provides a statistical time-dependent view of the error accumulation in the long-term.

E. Results

In order to quantify the overall effects of amplitude and frequency on the tracking of vertebra phantom, MSE in multi-frame tracking under a specific amplitude and frequency is evaluated for the 18 vertebra bone profiles on the phantom. The average value and standard deviation of MSE, reported in Figure 5-4, suggest that MSE in vertebra phantom tracking is dependent on the dynamic motion parameters. In each frequency group, the larger amplitude of vertebra phantom motion results in an increase of the MSE. Between the frequency groups, the higher frequency of vertebra phantom motion with the same amplitude also results in an increase of the MSE. Therefore, at the sinusoidal motion of 1 Hz and 1 mm amplitude, multi-frame tracking provides measurement with the lowest MSE of $1.31 \times 10^{-3} \text{ mm}^2$, in which the error percentage, approximated by RMSE divided by amplitude, is 3.6%. The largest MSE in tracking vertebra phantom motion of 10 Hz and 4 mm is $6.03 \times 10^{-1} \text{ mm}^2$, in which the error percentage is 19.4%. The standard deviation of MSE ranged from $7.33 \times 10^{-4} \text{ mm}^2$ (1

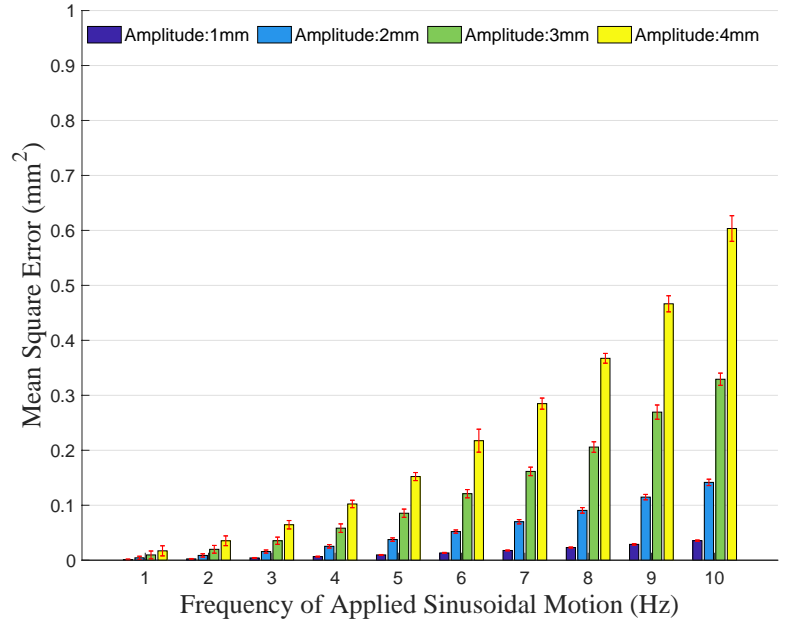


Figure 5-4: Displacement tracking errors for the multi-frame tracking of phantom, described by MSE, are dependent on the frequency and the amplitude of applied sinusoidal movement. Each bar represents average MSE of 18 independent tracking result of phantom image sequences, and the error bars show the standard deviations of MSE between vertebra profiles on phantom.

Hz, 1 mm) to $2.33 \times 10^{-2} \text{ mm}^2$ (10 Hz, 4 mm).

Similarly, to quantify the overall effects of amplitude and frequency on the tracking of cadaveric vertebrae, MSE in multi-frame tracking under a specific amplitude and frequency is evaluated for all 5 landmarks of the 6 cadaveric vertebrae. The average value and standard deviation of MSE, reported in Figure 5-5, suggest that MSE in cadaveric vertebrae phantom tracking is also dependent on the protocol motion parameters. Likewise, either higher motion frequency or larger amplitude will result in error increase in tracking. The lowest and largest MSE of using the multi-frame method to track cadaveric vertebrae are $1.87 \times 10^{-3} \text{ mm}^2$ (1 Hz, 1 mm, 4.32% error) and $6.80 \times 10^{-1} \text{ mm}^2$ (10 Hz, 4 mm, 20.6% error), respectively. The standard deviation of MSE ranges from $1.87 \times 10^{-3} \text{ mm}^2$ (1 Hz, 1 mm) to $2.30 \times 10^{-1} \text{ mm}^2$ (10 Hz, 4 mm).

When these results are compared to those in the tracking vertebra phantom, MSE in tracking cadaveric vertebra increased 28% for all testing protocols on average, and the standard deviation increased 620% on average. Changing the imaging orientation on specimens has a much larger effect on the error in tracking cadaveric vertebrae, so it has a much larger variance between trials. The major difference between the cadaveric vertebrae and vertebra phantom is that the vertebrae have soft tissue

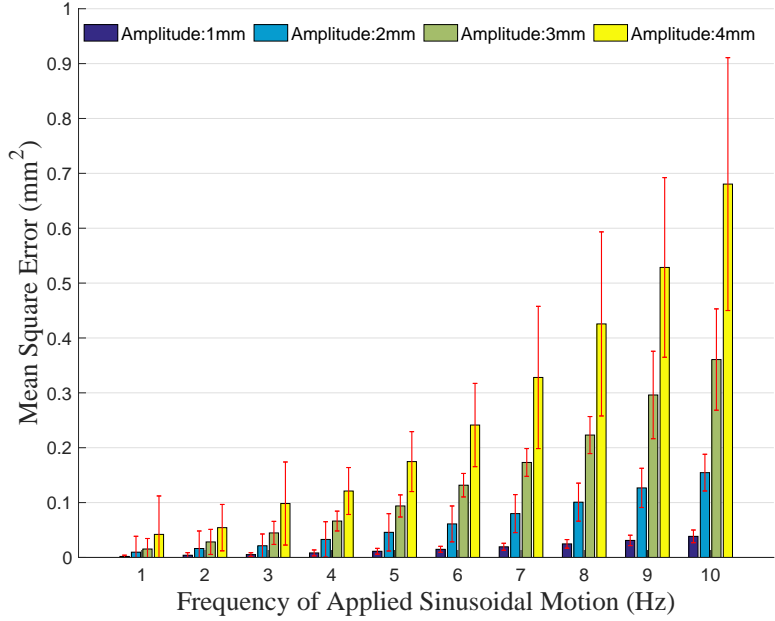


Figure 5-5: Displacement tracking error for the multi-frame tracking of cadaveric vertebra in MSE is also dependent on frequency and amplitude of the sinusoidal movement applied to cadaver specimens. Tracking assumed that vertebrae were rigid bodies and provided consistent RF speckle pattern as phantom. However, the retained tissue on the cadaver bone surface actually brought change to the image and increased the mean and standard deviation of MSE.

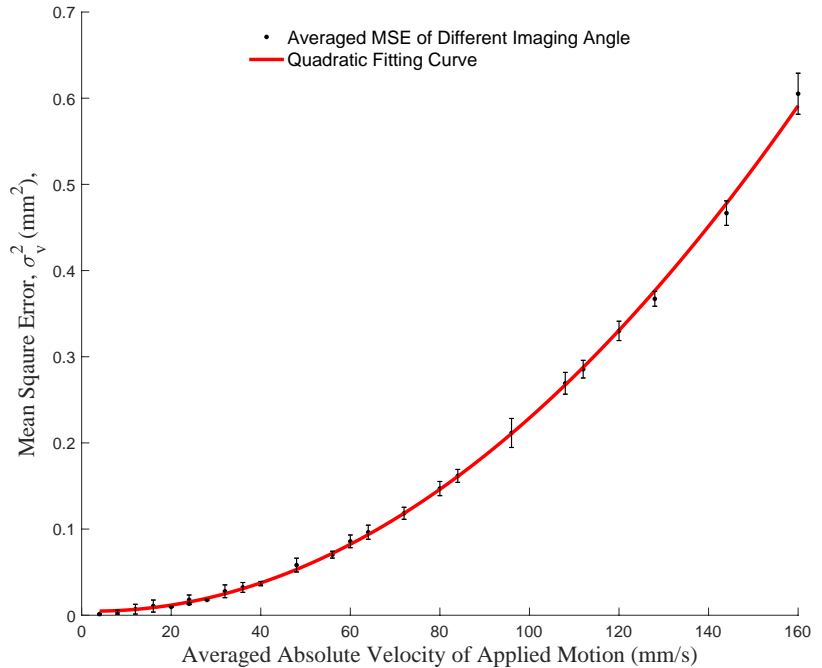


Figure 5-6: MSE of tracking a rigid phantom as a function of average absolute velocity of applied sinusoidal movement, denoted as v . Motion speed leads to larger motion frame to frame and introduces tracking errors. The R^2 of quadratic fitting model ($\sigma_v^2 = 2.34 \times 10^{-5} v^2 - 1.3580 \times 10^{-4} v + 0.005$) is 0.96.

covering on the bone surface, which will be discussed in next subsection.

To study the motion artifact, the average absolute velocity, is correlated with the MSE of phantom vertebra, as shown in Figure 5-6. MSE quadratically depends on average absolute velocity with coefficient of determination (R^2) of 0.96. The result indicates that multi-frame tracking provides robust measurements for low speed rigid body motion. At higher speeds, motion introduces artifacts to the rigid ultrasound image speckle pattern and there is a loss of RF signals correlation between frames.

Based on the assumption that artifacts from motion and tissue are independent, the error contribution from the tissue is decomposed by subtracting MSE of the motion artifact, as illustrated in Figure 5-7, from the total MSE of tracking cadaveric vertebra. As described earlier, the kernels of soft tissue were excluded from the ROI so that only movements of the bone surface region were tracked.

However, because of the concurrent tissue movement during the vertebral loading process, the retained tissue inconsistently changed the RF pulse signal pattern along its propagation path before the pulse approached the bone surface. Therefore, the average thickness of tissue above the bone surface positively correlates with the tracking accuracy with R^2 of 0.69 in a quadratic fitting model. The MSE contributed from the retained tissue was close to zero in cadaver specimens that have less tissue left on the surface (thicknesses less than 4 mm), while the mean and standard deviation increases dramatically in specimens that have greater tissue retained. These results indicate that tissue changed the bone surface speckle pattern and de-correlated signals between frames during tracking.

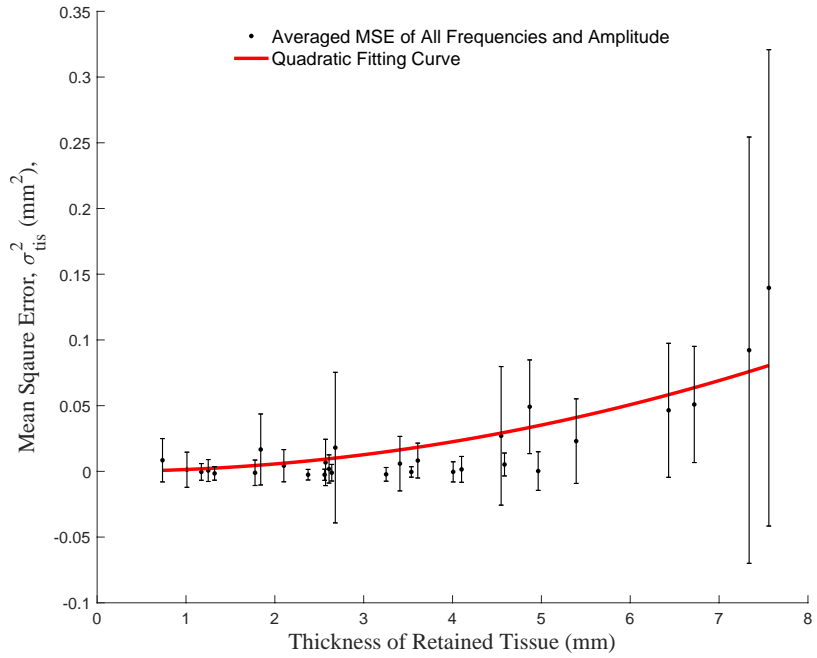


Figure 5-7: MSE introduced by tissue plotted as function of tissue thickness, denoted k . Each data sets represents the MSE of one specific image orientation of cadaver specimen averaged over all 4 amplitudes and 10 frequencies. The R^2 of the quadratic fitting model ($\sigma_{tis}^2 = 1.41 \times 10^{-3} k^2 + 1.11 \times 10^{-9}$) is 0.69.

5.2 In-vivo Ultrasound Imaging of C-Spine and The Effects of Helmet Weights and Muscle Activation

A. Intention of Repetitive Jump Study

From military reports [49], the weight of helmets approximately ranges from 3.3 to 6.5 pounds, which is further affected by the addition of headgear (e.g. night vision goggles). For personnel in extreme environments, e.g. aviators, the effect of helmet weight on the head rotation/acceleration, neck compression/shear motion is much amplified, which leads to neck

injuries [50]. Therefore, the intention of increased protection and the capability of soldier with the more advanced helmet may be compromised by increasing risk of neck injury and loss of experienced warriors in long term. Ultrasound is widely used as an imaging modality to measure the dynamic motion in liver, cardiac and obstetric care. Previous chapters have shown the development of methodologies of ultrasound to measure dynamic deformation of an FSU *ex-vivo* and *in-vivo*. The ability of ultrasound to measure the dynamic motion of the cervical spine of human subjects performing jumps with a helmet is of interest in this following series of experiments. The goal is to apply methods developed in previous chapters to understand the response of C-spine system in dynamic environments and also provide quantitative data of C-spine motion within these activities.

B. Experimental Methods

After approval from the Beth Israel Deaconess Medical Center Institutional Review Board, 10 adult subjects (21-45 years, 8 males and 2 females) gave written consent to participate in this study. Sagittal T₂-weighted images of the cervical spine using a 3-Tesla MRI were obtained for each subject. B-mode clinical US was used to measure the height of C4-C5 and C5-C6 IVDs by placing the US probe along the anterior triangle of the neck, bounded infero-laterally by the clavicular head of the sternocleidomastoid muscle, supero-laterally by the omohyoid and strap muscles, and medially by the lateral border of the trachea, using the neck-seal collar shown in Figure 5-8 (top right). The trajectory of ultrasound probe was aimed towards the anterior margins of cervical FSUs. C4 to C5 IVD height for C4-C5 disk were measured from both MRI and ultrasound images using ImageJ software (Wayne Rasband, National Institute of Mental Health). Ultrasound images visualize only the anterior profile of the IVD, while MRI demonstrates the entire disk, which is non-uniform in height extending from the anterior to posterior margin of the vertebral body.

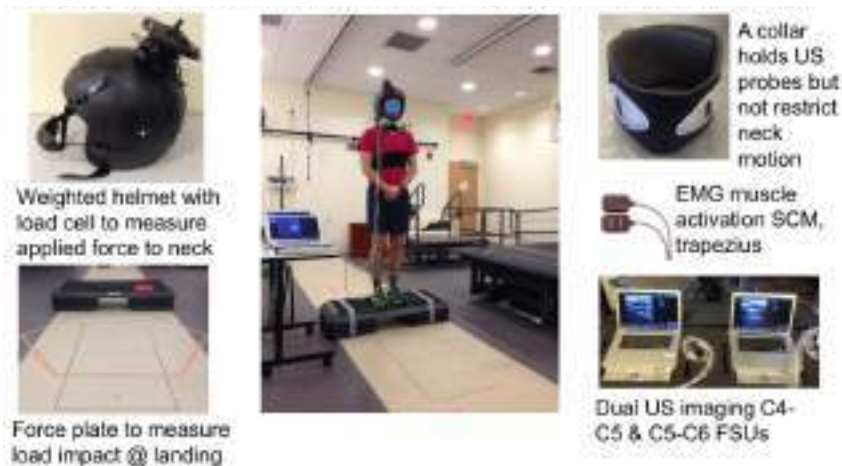


Figure 5-8: Human volunteer performing repetitive jumping with a geared helmet.

To simulate activities such as running/jumping while troops or laborers don protective headgear, subjects wore a helmet and repetitively jumped on and off a 0.8-foot step for 4 minutes (Figure 5-8) while looking forward and landing on both feet. The jump test was repeated 3 times (with an 8-minute rest between trials) using an unweighted helmet (4.0 lbs) and then repeated 3 times using a weighted helmet (6.5 lbs) to simulate the effect of additional gear such as a flashlight, a communication unit, or night vision goggles. The added weight was set along the

mid-sagittal axis of the neck to increment the superior-inferior impact of the helmet on the head/neck during landing. The helmet weights (4.0-6.5 lbs) are chosen based on the typical range of army helmets weights.

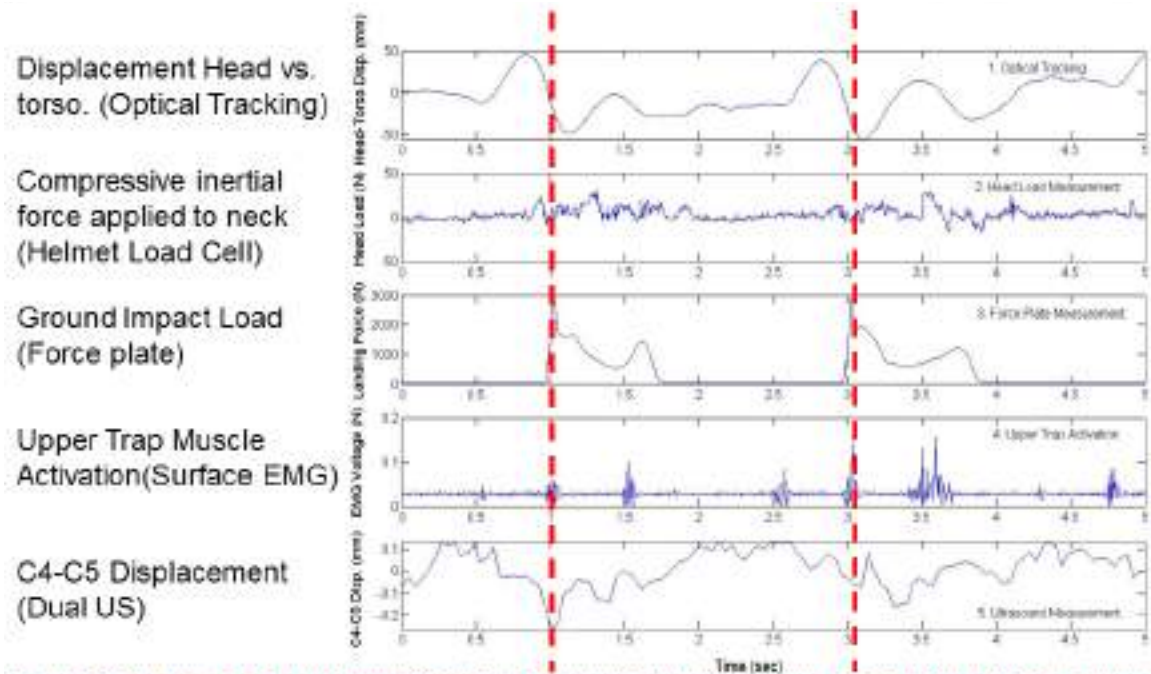


Figure 5-9: Measurements made on a subject performing repetitive jumping task.

In the experiments, 5 measurements were made on the human subjects as shown in Figure 5-9. Firstly, to track the head-torso displacements, 4 reflective optical markers were placed on the set positions of the helmets, and 3 reflective markers were placed on the two proximal ends of clavicle bone and the T1 spinous process. The positions of these markers were tracked by motion capture systems in the gait lab. Secondly, a miniature load cell was placed between the helmet and the additional weight to measure the impact of the weight. The head-torso displacements and helmet load cells are used to monitor if there is any abnormality in the system after the subject completed a jump trial. During the jumping, the impact at landing was measured using a force plate. The landing moments were marked by the time when the force plate measurement reached its maximum (vertical dash lines in Figure 5-9). The axial and inertial loads applied to the C-spine during the jump test were studied by continuous US imaging of the anterior elements comprising contiguous FSU C4-C5. The activities of para-cervical muscles during the jump test was measured by Trigno surface electromyography (sEMG) system with four-bar surface electrodes (Delsys Inc., Boston, MA). Palpation was made on the human subjects when they were shrugging their shoulders by two bilaterally placed sEMG electrodes on the upper trapezius. The skin was prepared for electrode placement by cleaning with 70% alcohol pads and/or shaving if needed.

In the jump tests, we are focused on the response of FSU to different applied loading and muscle fatigue. Due to the endurance differences between individuals in the 4-minute trials, subjects performed 25-59 jumps. To normalize the effect of the number of jumps, 10 progress groups, which are marked in percentage (10%-100%) is used to show the elapsed number of jumps finished. The compressive response of C4-C5 and the EMG signals are averaged among

the jumps in the same progress group. Furthermore, each subject performed 3 repetitive jump trials with or without the 2.5-lb weight on the helmet; the performance of C4-C5 FSU deformation from ultrasound and EMG were averaged among the 3 trials.

C. Data Analysis of EMG

The EMG data recorded at a sample rate of 1000 Hz during the jumping test were filtered by a hardware low-pass filter with cutoff frequency of 400 Hz. As shown in Figure 5-10, paracervical muscles are innervated to dampen the shock to the head through the spine at the moment of landing, which was gauged by a grounded load force plate. Between intense muscle contractions, the neck is either in a static or a tranquil state or has a slight movement when the subjects step back onto the jumping platform.

Figure 5-11 representatively shows that the pattern of EMG signals may be affected by the length of performing activities, which is the possible outcome of muscle fatigue. As reviewed by the literature [51,52], muscle fatigue leads to an increase in the overall mean of the EMG signal amplitudes, as well as an overall shift to the lower frequencies. Because of the short duration of muscle contraction during landing, the frequency pattern of EMG signals is dominated by the high-frequency, rapid-changed component in a short time. Therefore, a frequency-based analysis (e.g. the median frequency analysis) is not appropriate. This study quantitates the increasing amplitude of EMG action potentials by using an EMG signal power method. This method integrates the power in EMG spectrum from 1-400 Hz and used it as an indicator of the overall amplitude change and degree of muscle fatigue.

To characterize the muscle fatigue over time, an EMG signal power method was modified from the root-mean-square (RMS) EMG envelope analysis and applied in this study to account for the time-varied background noise. Traditionally, the RMS envelope extracts the square root of the EMG signals power over a duration of static tests and determines the envelope of the signals. However, due to the dramatic change of signals in the jumping tests, a common envelope extraction method, such as the Hilbert transform, is subject to the large signal

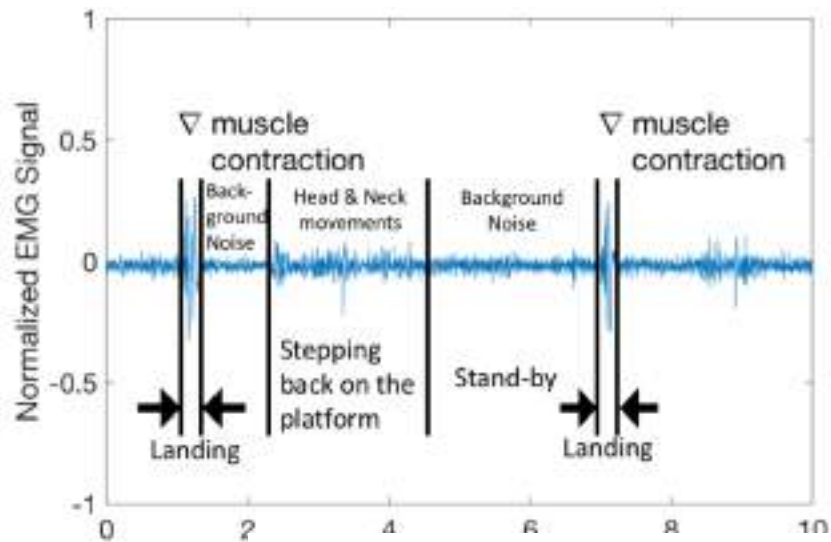


Figure 5-10: EMG signals are innervated muscles are innervated subject moves his/her

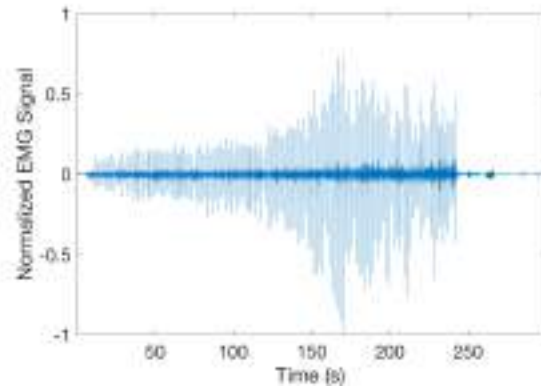


Figure 5-11: EMG signals amplitudes are dependent on the number of jumping performed, implying possible muscle fatigue.

oscillations. Therefore, the mean of EMG signal power is used without the RMS and envelope extraction in the current study. A 128-sample window of the EMG signals is chosen to be centered at the time when the measurements of grounded force plate reached their peak. The mean of landing EMG signal power is computed based on integrating the discrete spectral power density, $p(f)$, in which f is the signal frequency ranging from 1-400 Hz:

$$S_l = \sum_{f=1}^{400} p(f) \quad (5.8)$$

To exclude the time-varied background noise and the muscle action potential when the neck has no movement, 4 consecutive 128-sample windows were chosen when the subjects are in standby state. The mean of background EMG signal power is computed and averaged over the 4 windows:

$$S_{BG} = \frac{1}{4} \sum_{i=4}^4 \sum_{f=1}^{400} p_i(f) \quad (5.9)$$

The length of windows is chosen based on the width of landing peaks and for better performance of the Fourier transform. The difference in the mean power between the landing and background mean EMG signals are considered as the additional muscle activation when the landing is made. The signals are further converted to decibels and then normalized to the start of the jumping of every test, under the assumption that the subjects' muscle fatigue level is the same in the beginning of each test.

D. Reconstructed In-vivo Planar Motion of FSU

Figure 5-12 shows the merged measurements of FSU deformation and rotation angles which were derived from sequential ultrasound images with tracked vertebrae positions over 20 seconds. When the subject jumped off the step and landed on the ground, the impact was transmitted through the spine to the head and neck. In response, the FSUs are compressed, which are recorded in the lateral (x) direction in anterior and posterior imaging window, with concurrent shear displacements, which are mainly measured in the axial direction of anterior and posterior windows. The merged measurements derived from anterior and posterior imaging window and co-registration portrayed the FSU deformation in the superior-inferior and anterior-posterior axes, as well as the FSU rotation which represents flexion and extension in the midsagittal plane. During the landing, a large compressive pulse is seen in the superior-inferior direction, which refers to FSU compression. Meanwhile, the vertebrae in FSU move relatively to each other in a zig-zag pattern, which refers to a shear motion of FSU. The FSU flexes and changes the curvature of the C-spine to dampen the load. In between the landing, the subjects need to move back on the step, and the rotation when the subject looks down and steps back is also shown in the same plot.

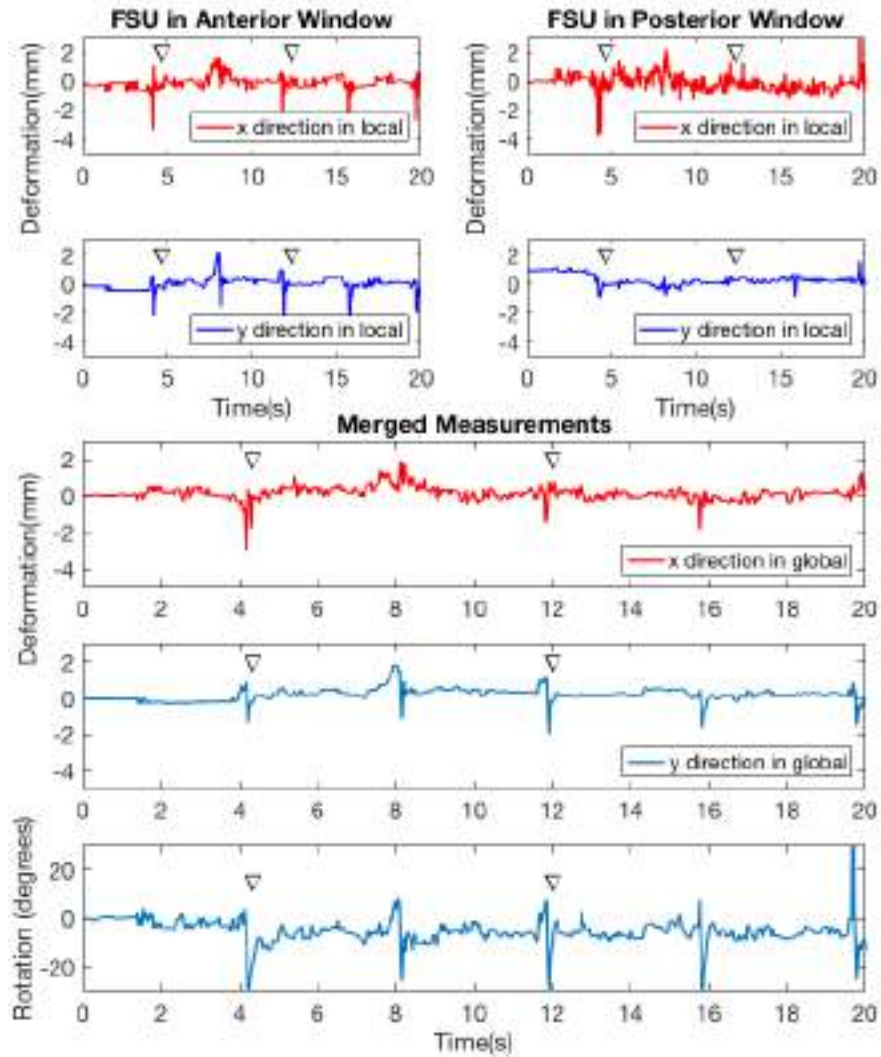


Figure 5-12: Merging the local dynamic images from anterior and posterior ultrasound transducers to derive kinematics of a male FSU in the mid sagittal plane. The "x/y direction in local" refers to the lateral/axial direction in the ultrasound image. The "x/y direction in global" refers to the superior-inferior / anterior-posterior direction in the anatomy plane. The positive and negative direction of rotation refer to extension and flexion of FSU. The triangles show the moments when the subject landed on ground.

E. C4-C5 FSU Deformation In-vivo vs. Muscle EMG Activities

Ultrasound measurements of the C4-C5 FSU deformation were calculated at the maximum compressive impulse amplitude for each jump and averaged over the same progress mark among the 3 trials during the course of the 4-minute jump test. The initial IVD height measured from the MRI scan of each subject was used to calculate the compressive strain. As shown in Figure 5-13, the additional 2.5-lb weight on the helmet significantly increased ($p < 0.05$) the IVD compressive strain from 22.3% to 43.6% during the course of the jump test at all times.

EMGs were used to measure the power of action potential applied from nerve system to innervate muscles. Data for all subjects are shown in Figure 5-14. When subjects were wearing an unweighted helmet, the signal power showed a small correlation with time ($R^2 < 0.1$). The

slight decrease of the power implies there is possibly muscle adaptation during the jumping over time. When an additional weight is added, the activities of the para-cervical muscles were much increased, showing muscle fatigue possibly occurs. This muscle fatigability differs from subject to subject. Two out of the ten subjects showed no significant increase in the muscle EMG power over time. This is possibly due to the individual difference in physical fitness. Among all of the subjects, the slope of linear regression result of EMG power with additional weight is larger than the slope of the group without additional weight.

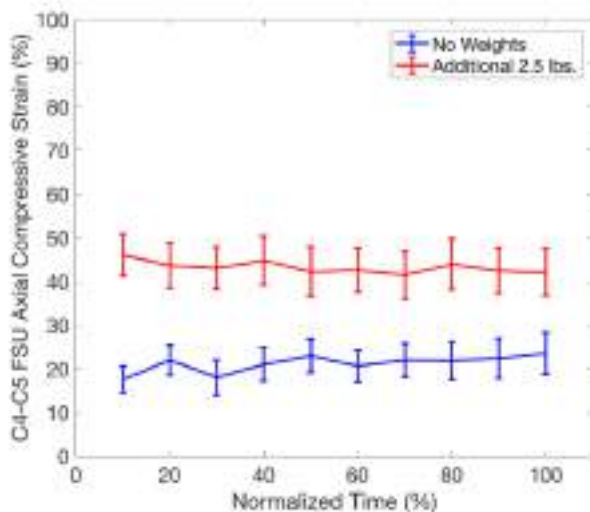


Figure 5-13: C4-C5 FSU strain of all human subjects wearing a helmet without additional gear weight (4.0 lbs) and a helmet with additional gear weight (6.5 lbs). Error bars show standard error.

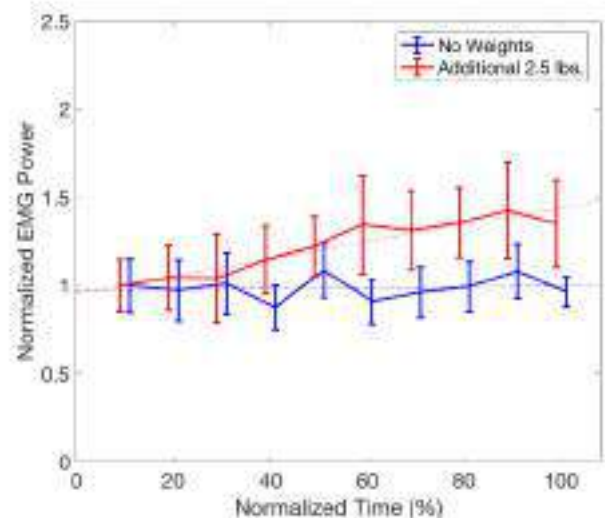


Figure 5-14: Trapezius muscle fatigue measured by EMG is compared between jumping with the unweighted helmet (4 lbs) and weighted helmet (6.5 lbs). Error bars show standard error.

Plotting the amplitudes of FSU strain as a function of muscle signal power activities for all subjects in shows a moderate correlation (Pearson Coefficient = 0.69) between FSU deformation and muscle activation when subjects are wearing unweighted helmet (Figure 5-15) and a weak correlation (Pearson Coefficient = 0.31) when subjects are wearing a weighted helmet (Figure 5-16). The correlation result in the unweighted group suggests in a normal range of strain, the FSU strain increases when the muscles are less capable of stiffening neck and dampening impacts. In the case when a larger impact is applied to the head and neck, there is a significant increase in the muscle fatigue and the FSU strain. However, the FSU strain is capped at 70%, possibly because the loading is transmitted to FSU flexion or further compression is limited by the facet joints. This implies overloading the disc in the high range of strain could possibly lead to damage to the disc as well as the formation of osteophytes.

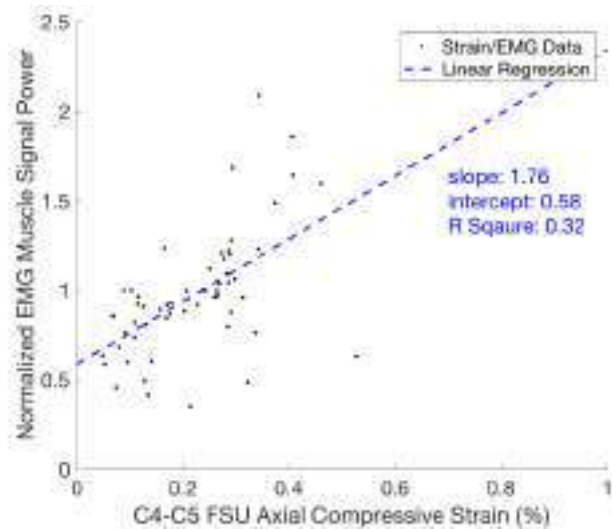


Figure 5-15: C4-C5 FSU strain vs. trapezius EMG power in the unweighted helmet (4 lbs) jump trial. Each data point represents the averaged FSU strain and EMG among the three-jumping trial at the same time for each subject.

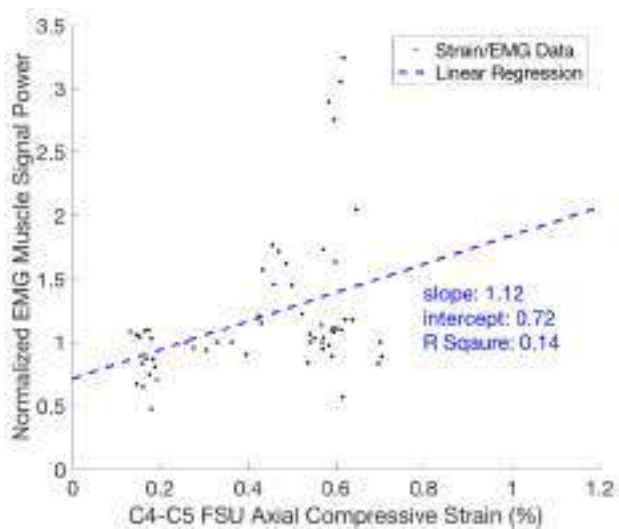


Figure 5-16: C4-C5 FSU strain vs. trapezius EMG in weighted helmet (6.5 lbs) jump trials. Each data point represents the averaged FSU strain and EMG among the three-jumping trial at the same time for each subject.

5.3 Ongoing Study of In-vivo Ultrasound Imaging of C-Spine in MARS

A. Research Design and Procedure

This study will have a repeated-measures ANOVA (MANOVA) with between subjects with two independent variables (helmet mass and mass offset configurations) and three dependent variable groups (Physiologic, Kinematic, and Subjective). Helmet configurations will have two levels (baseline condition and experimental configuration). The mass and center of mass (CM) offset chosen for each helmet configuration to be investigated was selected based on previous work performed at Beth Israel Deaconess Medical Center.

The study population will be healthy military and non-military personnel recruited from the general population of Ft. Rucker, Alabama. All participants must meet the inclusion/exclusion criteria. We are asking to recruit up to 90 volunteers. The total target N is 28 complete data sets.

Inclusion Criteria:

1. In self-reported good health
2. Males and females between the ages of 18-50

Exclusion Criteria:

1. Congenital abnormality of neck or cervical spine
2. Current or historical head, neck, or back injury, including vertebral fractures, degenerative disc disease, etc.
3. Self-reported history of neck or cervical spine pain
4. Volunteers with a contraindication to MRI examinations will be excluded from this study. Contraindications include:
 - Medically unstable
 - Cardiac pacemaker

- Intracranial clips, metal implants, or external clips within 10mm of the head and neck
 - Metal in the eyes
 - Claustrophobia
5. Self-reported pregnancy, per AR 40-501 7-9 d.6.
 6. Allergy to silver

Volunteer testing will occur over two days. One day will include simulated vehicular ride profiles under two head-supported mass (HSM) conditions while wearing a dual-ultrasound collar, while the remaining day will be allotted for obtaining an MRI scan of the volunteer's cervical spine. The order of these two days can be reversed, such that the MRI scan occurs on the first day, and the simulated ride profiles occur on the second. On the first day of testing, volunteers will review and sign an informed consent document.

If the volunteer is eligible and informed consent is obtained, basic demographic and anthropometry data will be collected from the volunteer including neck circumference, neck length, helmet size, height, age, and gender. All measurement standards will be those used in a U.S. Army anthropometric survey (Gordon, et al., 1989). Anthropometry data will be documented on a spreadsheet in Microsoft Excel.

After consenting, the participant will be scheduled to obtain a MRI scan (Siemens Verio Open-Bore 3T Scanner, Siemens Healthcare, Erlangen, Germany) of the cervical spine at the Auburn University MRI Research Center. The purpose of obtaining a cervical spine MRI is to feed participant-specific parameters, particularly anatomical geometries and tissue properties, into a custom computational script that analyzes the ultrasound data collected from each specific participant during the simulated ride profiles. On the day of testing, a member of the research team may escort the participant to the Auburn University MRI Research Center. The MRI technologists will review contraindications with the participant per standard clinical practice. At the same time, the participants will be asked questions pertaining to metal implants, pacemakers and other possible conditions which would disqualify them from participating in this study. The MRI will be performed and then read by a radiologist and researcher to assess the hydration condition of cervical IVDs using Pfirrmann grading.

At the start of the simulated exposures testing day, the participant will be asked to give a baseline rating for perceived neck pain using the neck rating scale (NRS-11). The NRS-11 uses 0 to represent no pain and 10 to represent the worst pain imaginable. Scores from 1 to 3 represent mild pain, 4 to 6 will represent moderate pain, and 7 to 10 will represent severe pain (Fejer et al., 2005). A researcher will review the NRS-11 with the participant to ensure full understanding of its use. If the baseline rating is not 0, the participant will be excused from further participation on that day. The PI will determine if the data collection period can be rescheduled, or if the participant needs to be dropped from the study.

Anthropometry: Basic anthropometry data will be collected from qualified participants including neck circumference, neck length, height, age, and gender. All measurement standards will be those used in a US Army anthropometric survey (Gordon, et al., 1989). Anthropometry data will be documented on a spreadsheet in Microsoft Excel.

Participant Clothing / Instrumentation: Participants will be given spandex long-sleeve shirts and pants to wear. Locations on the skin identified for marker and/or instrumentation placement will be prepared by shaving any excess hair to minimize electrode impedance and discomfort upon

marker or electrode removal. Prior to application, the skin locations will be cleaned with rubbing alcohol for at least five seconds.

At the start of each testing day, participants will be instrumented with disposable adhesive EMG electrodes (Blue Sensor N, Ambu, Denmark) placed on the left sternocleidomastoid, and upper trapezius muscles (Fraser, 2006). Either one wired (MyoWare Muscle Sensor, Advancer Technologies, Raleigh, NC) or one wireless (Delsys Trigno Mini Sensors, Delsys Inc., Natick, MA) EMG system will be employed, depending on instrumentation availability between concurrent research protocols. The EMG sensors will be attached via disposable adhesive electrodes (Figure 5-17). Due to sweating and dynamic movement, two additional steps may be taken to ensure the electrodes stay in place: 1) after cleaning the attachment area, a skin prep adhesive will be applied in the area under the disposable electrodes with care taken to ensure the skin prep adhesive does not interfere with the electrode/skin coupling; 2) a conformable transparent tape, designed for long-term wear and moisture permeability, will be applied over the electrodes and wiring.

The MyoWare sensors will be housed with the portable data acquisition unit secured in a pouch attached to a standard issue webbed belt that the participants will wear over the spandex clothing. The MyoWare sensors will be connected to the disposable surface EMG sensors via extended cables with snap-lead connectors. Internal testing verified that there was no decrease in data quality or loss in amplification with the sensor dislocated from the surface electrodes. The decision to dislocate the MyoWare sensors was made after feasibility testing demonstrated that the sensors were prone to popping off with the limited available surface area and the dynamic nature of the neck (Figure 5-17).

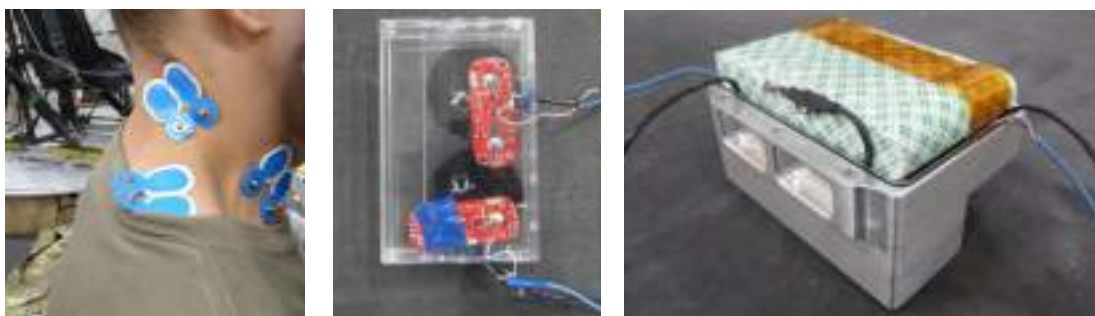


Figure 5-17: Disposable adhesive electrodes placed on the neck musculature (left); Casing for MyoWare sensors (middle); Casing attached to portable data acquisition unit (right).

Motion Capture Kinematics: The Vicon motion capture system (Vicon, Oxford, UK) allows for the collection of 3D motion data with sub-millimeter accuracy by surrounding a space with an array of near-infrared and digital video cameras. The system is controlled using the Vicon Nexus v2.5 software. The system is comprised of eight MX-T40/T40S cameras, and a reference digital video Basler camera with a 4.0 megapixel resolution. The cameras interface with the MX Giganet, which provides power, synchronization and data transfer for the MX cameras, digital reference video cameras and communication to the computer. The system also includes a 64 channel A/D box, through which the Delsys Trigno EMG and built-in accelerometer readings will be acquired in Vicon Nexus.

At the start of each testing day, retroreflective Vicon markers will be attached directly to the participant's skin using hypoallergenic toupee tape. The markers will be attached to any of the following locations to acquire kinematic data: the mastoid processes behind each ear, bridge of

the nose, spinous processes of C3 and C7 (if possible, depending on fit of the ultrasound collar), medial ends of the clavicles, acromion processes, and the anterior and posterior sacroiliac bones. Additional markers will be placed on the helmet, ultrasound device probes, chest, upper back, and lower back. In some locations, it may be necessary to use clusters of these markers; these clusters consist of multiple markers attached in a fixed array to a molded plastic piece (Figure 5-18). Marker clusters may be attached directly to the skin or on the clothing. Both markers and marker clusters may be further reinforced with self-adhesive stretch tape wrapped around the limb/joint to further prevent marker movement.



Figure 5-18: Example of a Vicon marker cluster.

B. Data Acquisition

A custom-built nine channel SLICE data acquisition system (DAQ) will be used to record data from the Myoware EMG sensors and any helmet-mounted instrumentation (such as accelerometers and angular rate sensors). The DAQ is a modular, high-speed data acquisition system that can record up to 1 million samples per second per channel with up to 200 kHz analog bandwidth. The DAQ will be secured in a pouch attached to the webbed belt. The wrapped cabling from the helmet-mounted sensors and the EMG sensors will be secured to the spandex clothing and in a pouch secured to the webbed belt using zip ties or Velcro to minimize snag hazards and/or motion impediment of the participant. The EMG and helmet-mounted data acquisition will be synchronized when the DAQ is initialized prior to testing.

Pre-Test Procedures: Once fully instrumented on the testing day, participants' baseline nerve function, neck strength, and range of motion (ROM) may be assessed. Timing and instrumentation availability constraints may force the pre-test data collection procedures to be trimmed to ensure we are not impeding throughput on concurrent research protocols. However, these metrics are only auxiliary to the validation of the dual-ultrasound technique.

Subjective Questionnaire: Four subjective measures will be recorded from each participant. After each dynamic exposure profile, participants will be asked to describe the following: 1) Current level of perceived neck fatigue, on a scale from 0-10, where 0 is non-existent and 10 is the maximum; 2) Current level of neck discomfort/pain, on a scale from 0-10, where 0 is non-existent and 10 is the maximum; 3) Current level of perceived exertion, on a scale from 6-20 (Borg Rating of Perceived Exertion, RPE) (Borg, 1985). After all dynamic exposure testing is completed with a particular HSM configuration, participants will be asked to give 4) a "user acceptance" rating of the ultrasound device collar, on a scale from 1-10, where 10 is very acceptable to wear on a regular basis and 0 is not acceptable at all. These subjective scales can be observed in Appendix B.

Nerve Function: Baseline nerve function will be measured via the Hoffmann Reflex (H-Reflex) using previously established techniques (Inglis et al., 2007; Shivers, 2012). Previous research has indicated that changes in HSM and head position may alter nerve function (Shivers, 2012). The

H-reflex will be evoked with a surface stimulus electrode placed proximal to the antecubital fossa over the median nerve (Sabbahi and Abdulwahab, 1999) and a dispersive electrode placed on the back of the arm above the elbow. A small amount of EEG paste will be applied to this electrode to aid in stimulus transmission. The stimulus and dispersive electrodes will be connected to one of two nerve stimulation systems with equivalent capability to deliver a single square-wave pulse for 0.5-1 ms: 1) Digitimer DS7A stimulator, or 2) Grass Telefactor constant current unit (CCU1), isolation unit (SIU5), and a stimulator control unit (S88). The recording electrode will be placed over the belly of the participant's right flexor carpi radialis. The belly of the muscle will be palpated and identified for electrode placement by having the participant flex and radially deviate the wrist while manual resistance is applied to the thenar eminence.

The participant will be seated in the test chair with the feet flat on the floor so that the knees and ankles are set at 90°. The arms will be relaxed at his/her sides with the forearms resting in his/her lap with the palms up. The participant will be instructed to remain as still as possible throughout the testing and to breathe normally. H-reflex maximum amplitude and M-wave maximum amplitude will be recorded at baseline. The M-wave is considered to be a measure of the percentage of the motoneuron pool being recruited through electrical stimulation. A maximum M-wave is indicative of all innervated muscle fibers being recruited. This is traditionally used as a method of normalization allowing for between participant comparisons (Palmieri et al., 2004). H-reflex stimulation typically occurs at a percentage of M-wave maximum (10-20%) which allows researchers to say that all participants were tested with a stimulus equivalent to "X"% of that needed to recruit all muscle fibers innervated by the median nerve. For the purposes of this study, we will record the H-reflex at a stimulation level of 20% of M-wave maximum (H20%). Ten amplitude and latency values will be measured. The ten values will be averaged and any individual values falling more than one standard deviation from the mean will be removed. The remaining values will be averaged, and this value will be set as the baseline value. H-reflex latency varies between individuals and is related to height and arm length. These two factors will be recorded for trend analysis.

Strength: Three-part neck strength assessments will be performed in the directions of flexion, extension, left/right rotation, left/right lateral flexion, and shoulder shrug using the BTE Primus RS dynamometer (BTE Technologies, Hanover, MD) with a contoured, padded variable-length lever attachment (Figure 5-19). The following general procedures will be used for strength testing: participants will be seated with their head in a neutral position; 1) neck flexors – the study investigator will position the dynamometer attachment on the middle of the forehead and the participant will move the head through cervical flexion (touch your chin to your chest); 2) neck extensors – the study investigator will position the dynamometer attachment against the occiput just above the nape strap of the helmet and the participant will move the head into cervical extension (look to the sky); 3) left/right lateral flexion – the study investigator will position the dynamometer attachment over the temple on the side of movement and the participant will move the head into left or right lateral flexion (touch your ear to your shoulder); 4) left/right rotation – the study investigator will position the dynamometer attachment over the temple on the side of movement and the participant will rotate the head left or right (look over your shoulder); 5) shoulder shrug – the study investigator will position the HHD just proximal to the Acromioclavicular joint and the participant will be instructed to shrug their shoulder (try to raise your shoulder to your ear). The participants will be instructed to move their head through

each range of motion while the dynamometer applies static resistance; therefore, the head will not actually move.

First, the participant will complete an isometric maximum voluntary contraction (MVC) in each direction by exerting his/her maximal strain against the head harness for up to four seconds. The participant will repeat this effort twice more with a 45 second rest period between efforts. A three-minute rest period will be allotted between each direction tested. The peak force values of the three trials for each direction will be recorded manually into a computer-based spreadsheet and will be used as the MVCs. From these tests, EMG will be normalized for each person using the average of the MVCs recorded during the strength assessments. This normalization will allow for between-participant comparisons and between run comparisons of EMG median power frequency (MPF) and EMG root mean square (RMS) data. This step will also be used to ensure that EMG electrodes are on and properly synched to the acquisition software through a live feed of the data.

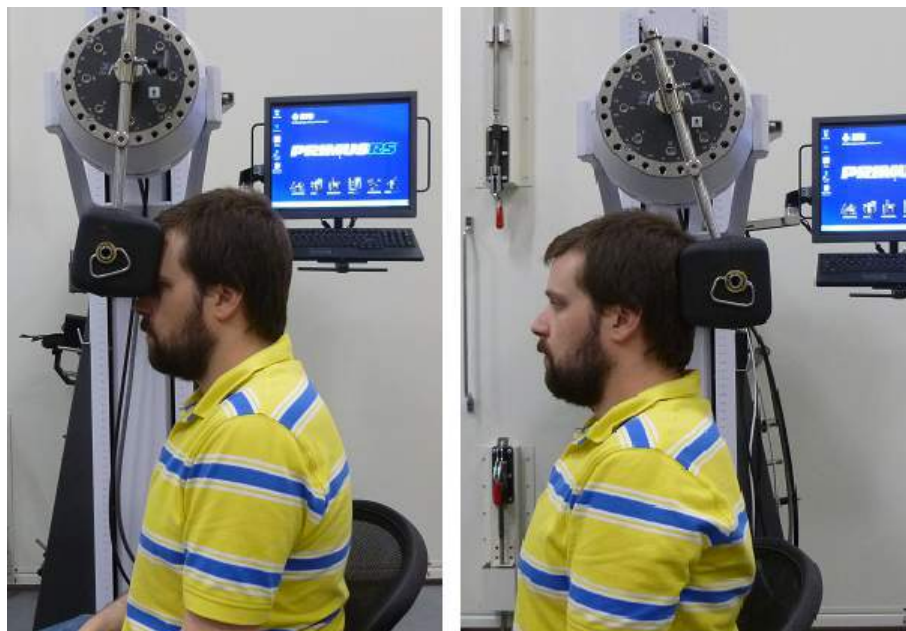


Figure 5-19: MVCs being conducted in the flexion (left) and extension (right) directions.

Next, the participant will exert a target force beginning at 0% MVC and increasing to 70% in 5% increments to calculate MVC-EMG calibration curves. The participants will ramp from 0 to 70% and then back down to 0% holding each target force for 2 sec. The software will show real-time feedback of the force being exerted and the target zone in the form of a sliding white bar on screen. The target zone will appear green. This process will be repeated for extension, flexion, left/right lateral flexion, and left/right rotation. A 3-min rest will be allowed between each direction.

Finally, the participants will exert a target force of 70% ($\pm 5\%$) MVC for as long as they are able to measure isometric endurance. An onscreen display will again show the target zone with the sliding white bar indicating the level of force being exerted. When the force exerted falls short of 70% for longer than 2 sec the software will automatically end the trial. The process will be repeated for extension, flexion, left lateral flexion, and right lateral flexion with a 5-min rest between directions.

Range of Motion (ROM): Baseline ROM will be measured immediately after the strength assessments. This will be done using the cervical range of motion (CROM) goniometers system (Performance Attainment Associates, Lindstrom, MN). The CROM will be used to determine the maximum angles for the different head positions with respect to the participant's anatomical zero (neutral) with the participant in a seated position. Neutral will be determined as the position where the participant's head is comfortably placed over the shoulders with the eyes looking straight ahead and the chin is level with the ground. From this position, participants will be asked to go to the end-point of their range of motion for flexion (touch your chin to your chest), extension (look up to the sky), left/right lateral flexion (touch your ear to your shoulder), and left/right rotation (look over your shoulder). Values recorded from the CROM will be manually recorded on the same spreadsheet as the MVC peak force data.

Helmet Configurations: Following the pre-test procedures, participants will be fitted with a Helmet Mass Simulation Device (HMSD) in one of two mass and center of mass (CM) configurations. The HMSD is based on the Skull Mounting System (**Error! Reference source not found.**) that has been modified to include an instrumentation package (three accelerometers, three angular rate sensors, and an InterSense inertia cube) on the "crown" of the helmet. The HMSD also features custom-built mounting bars and masses that allow simulation of multiple mass configurations. The Skull Mounting System (Ops-Core, Boston, MA) is a multi-adjustable helmet system, allowing a custom fit specific to the user's head size and shape, increasing stability. Previous internal testing demonstrated that dynamic retention, which is a measure of stability, was better in the HMSD than an ACH or HGU-56/P (Estep, 2016). Vicon markers will be attached to the front, back, and sides of the HMSD to capture helmet motions.



Figure 5-20: Skull Mounting System (left). HMSD configured with example rearward mass (right).

One of the two configurations will be the HMSD in a "null" or baseline configuration, featuring just the helmet and instrumentation package with no additional weight. The second configuration will be the HMSD in a configuration with a mass of X and a CM of Y, based on previous work performed at BIDMC. This configuration will be achieved by mounting additional masses at a specific location along the mounting bars. Mass properties will be recorded for both configurations to confirm the desired mass and system CM were met.

Ultrasound: The ultrasound device to be used is a dual-ultrasound system which consists of two Terason t3200 systems with a 15L4 linear transducer (**Error! Reference source not found.**) produced by Terason (Burlington, MA). Each t3200 system features a laptop platform with an ergonomically designed user console with Terason's patented System-on-a-Chip technology which provides high-performance imaging in a highly efficient portable package. The 15L4

transducer, operating between 4-15 MHz, was chosen for its superiority in musculoskeletal imaging. This device will be used to measure cervical spine stiffness, range of motion, and dynamic responses in real-time during controlled simulations of vehicular ride profiles.

During the study, participants will wear an adjustable cervical collar (produced by National Orthopedics and Prosthetics Corporation, Boston Children's Hospital, Boston, MA). The collar holds the ultrasound probes in set positions without restricting the movement of the participant's head or neck. The participant will experience light pressure from the probes being applied to: 1) the front of the neck between the trachea and the sternocleidomastoid muscle and 2) the back of the neck on the spinous process; however, the collar will not restrict breathing or circulation.

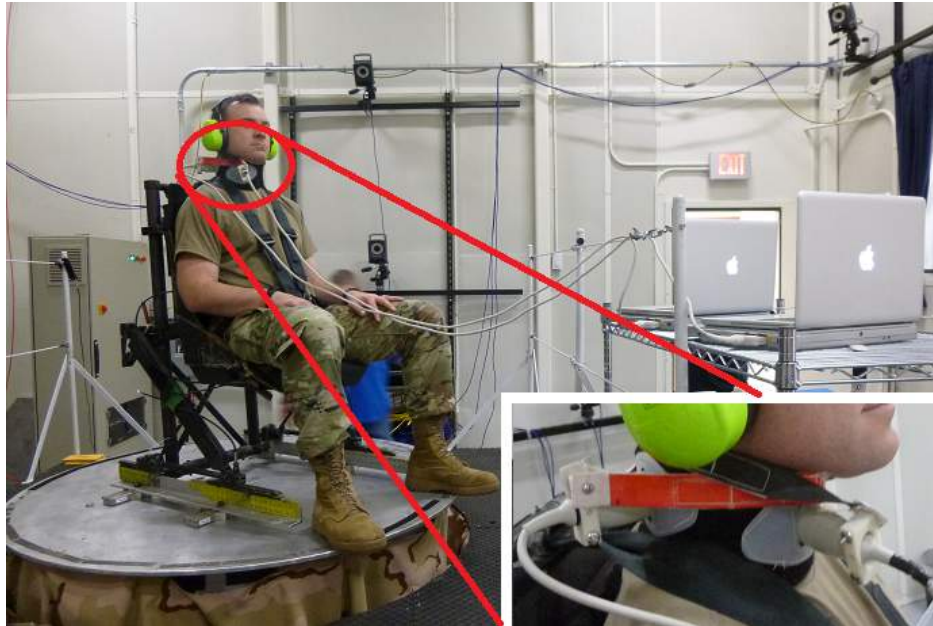


Figure 5-21: Dual-ultrasound system in use on the MARS platform. The two ultrasound probes are held in the correct orientation and position by the Velcro straps secured to the collar.

On the dynamic exposure testing day, participants will be tested while wearing the ultrasound device and each of the two HSM configurations on the MARS. The MARS (Figure 5-21) is a six degree-of-freedom Stewart-style motion platform that is driven by six linear actuators, with capabilities of 3D motion and rotation at frequencies up to 40 Hz and accelerations up to 3 G. The MARS platform is equipped with a generic seat that is mounted to the platform. The custom-built generic seat is adjustable to fit anthropometries ranging from 5th percentile female to 95th percentile male. Both the MARS platform and the seat will have accelerometers and Vicon markers attached. A ride pad with a tri-axial accelerometer will be positioned on the seat below the participant. The ride pad will provide information relating to transmissibility of the dynamic exposures through the platform, seat, and participant. Throughout testing, participants will have access to an emergency stop switch and can request the research team to stop testing at any time.

For each of the HSM configurations, participants will be seated and secured in a generic seat while being exposed to two ride signature sequences. The first sequence will be a short-term stepped-sine dynamic ride-signature exposure profile that will last approximately three minutes while the participant is wearing the ultrasound device. The stepped-sine exposure is composed of

integer frequencies between 2-35 Hz, dwelling at each frequency for approximately five seconds before briefly stopping and changing to the next frequency.

Following this sequence, there will be a 2-10 minute pause during which intermittent ROM and strength testing will be conducted using the HMSD-mounted inertia cube and a hand-held dynamometer (HHD). Interval strength assessments will be conducted using three manual muscle tests (MMT). MMTs will be performed in the directions of flexion, extension, and left/right lateral flexion using an HHD. The HHD (model 01163; Lafayette Instrument Company, Lafayette, IN, USA) will be programmed to measure the peak force in pounds during two seconds of muscle contraction. The HHD will indicate the start and the finish of the two-second duration by audible beeps (one for start and two successive for stop). The tests will be conducted in the following sequence: flexion, extension, left/right lateral flexion, and left/right rotation. The sequence will be repeated three times with approximately five seconds between sequences. The following general procedures will be used for testing: participants will be seated with their head in a neutral position; 1) neck flexors – the study investigator will position the HHD on the middle of the forehead and the participant will move the head through cervical flexion (chin to chest); 2) neck extensors – the study investigator will position the HHD against the occiput just above the nape strap of the helmet and the participant will move the head into cervical extension (look to the sky); 3) left/right lateral flexion – the study investigator will position the HHD over the temple on the side of movement and the participant will move the head into left or right lateral flexion (touch your ear to your shoulder); 4) left/right rotation – the study investigator will position the HHD over the temple on the side of movement and the participant will rotate the head left or right (look over your shoulder). The participants will be instructed to move their head through each range of motion while the study investigator applies static resistance (hand with HHD), therefore the head will not actually move. The peak force values for each direction will be recorded manually into a computer-based spreadsheet. From these tests, EMG will be normalized for each person using the average of the MVCs recorded during the MMTs. This normalization will allow for between-participant comparisons and between run comparisons of EMG MPF and EMG RMS data. MMT data will be documented on a spreadsheet in Microsoft Excel. The stepped-sine exposure will be given for each HSM configuration. The test order for the HSM configurations, as well as the frequency steps, will be randomized and balanced across participants to control for order effects. Head/neck kinematics will be recorded during the exposure profiles using a surrounding Vicon motion capture system in conjunction with the HMSD instrumentation.

After the step-sine exposure, participants will be exposed to a composite vibration signature representative of current military vehicle platforms. The dynamic exposure profiles may consist of energies associated with the low-level frequencies of fixed-wing platforms, predominant frequencies within UH-60 airframes, and/or frequencies of ground vehicles. These frequencies range from 11-32 Hz as reported in MIL-STD-810G. The amplitudes for the composite dynamic exposure profiles will fall within the safety standards described in the ISO 2631 series. The dynamic exposure testing will last for 30 minutes (six 5-minute segments). After each five-minute segment, participants will be tested for up to 10 minutes in repeated measures assessments (strength assessments, ROM, subjective questionnaire).

Post-Test Procedures: After the dynamic exposure profiles, participants will have their neck strength and ROM assessed again using the same techniques as in the pre-test procedures.

Table 5-1: Metrics to be collected and assessed in this protocol. Items highlighted in gray indicate metrics that may be collected if time and instrumentation availability constraints permit.

Data Element / Variable	Source	Dependent Variable Group
C-Spine Pathoanatomy / Hydration	MRI Scan	Physiologic / Biomechanical
Median Power Frequency (MPF) - Muscle Activation	Pre/During/Post-exposure electromyography (EMG); sternocleidomastoid, trapezius, splenius capitis	Physiologic / Biomechanical
Root Mean Square (RMS) - Muscle Fatigue	Pre/During/Post-exposure electromyography (EMG); sternocleidomastoid, trapezius, splenius capitis	Physiologic / Biomechanical
3D Motion – Helmet, Head, Body Position	During exposure; Vicon / ride pad; Helmet, head, neck, shoulders, arms, chest, hips, upper leg	Kinematic
C-Spine IVD - Deformation	During exposure; Terason dual-ultrasound collar device	Kinematic
Fatigue	Survey; Likert scale	Subjective
Discomfort	Survey; Likert scale	Subjective
User Acceptance	Survey; Likert scale	Subjective
Borg Rating of Perceived Exertion (RPE)	Survey; Likert scale	Subjective
Peak Force - Strength (Maximum Isometric Voluntary Contraction [MVC])	Pre/During/Post-exposure; Dynamometer	Physiologic / Biomechanical
Isometric Endurance	Pre/Post-exposure; Dynamometer	Physiologic / Biomechanical
Nerve Function	Pre/Post-exposure; Hoffmann Reflex	Physiologic / Biomechanical
Helmet Acceleration	Helmet-mounted instrumentation; tri-axial accelerometers	Kinematic
Helmet Angular Rotation	Helmet-mounted instrumentation; tri-axial angular rate sensors	Kinematic
Helmet Position / Orientation	Helmet-mounted instrumentation; Inertia Cube 3	Kinematic
Cervical Spine Range of Motion	Pre/Post-exposure CROM	Kinematic

Year 6: Standard operating procedure (SOP) for the dual US system and study protocol was developed for the research being conducted at USAARL, and a consent form and subject recruitment flyer were created. Mass properties of the helmet were evaluated for experiment replication at USAARL, and a mass attachment device for the helmet was developed to recreate vertical (z-axis) offset helmet configurations. Technology was also developed to image the spine using a single 3D US system to remove the need for dual US probes.

6.1 IRB Protocol for USAARL Subject Enrollment Center

Coordination efforts with Auburn University MRI Research Center are ongoing. We have discussed MRI scanner availability, volunteer coordination, as well as multi-site IRB protocol development, submission, and approval in order to acquire MRI cervical scan imaging data for eligible participants.




We have also identified military ground vehicle types that will be used in the composite vibration exposure. Tank and tracked-wheel vehicles will be targeted so that data collected can be used in support of current U.S. Army modernization priority efforts. Mock testing using an anthropometric test device (ATD) is being conducted to ensure proper placement of optical markers, US collar device, and other participant instrumentation during vibration exposure. The final composite vibration exposure profile will be developed and tested with the ATD concurrent to IRB review.





A. Standard Operating Procedure for Dual US System

Summary: The following SOP will describe the steps necessary to attach US transducers to image real-time image of human participant's C-spine and save the data to local drives.

Keywords: Ultrasound, C-spine

Table 6-1: List of materials.

Item Name	Item Picture	Quantity
Terason ultrasound systems with 2 15L4 transducers		2
Terason sync cable		1
Transducer back brackets with elastic bands		2 sets

Transducer front brackets (anterior)		1 set
Transducer front brackets (posterior)		1 set
Ultrasound C-spine collar		1
TENSIVE conductive adhesive gel		1
Masking tapes		1

Collar Preparation:

1. Examine the condition of the US transducer's case and cable connection. If any of the electronic wires is exposed, use electric tape for insulation and protection. The head of the transducer's marked by different shapes of groove (dot and line). **The dot groove should face superior (head)** when the transducer is being used (Figure 6-1). Clean the head of the transducer with alcohol wipes gently.
2. To aid in transducer fixation, install the back brackets on the US transducer. **The two elastic bands must be on the superior end**, or in other words, on the same side of the dot groove of the US transducer.
3. Examine the condition of US C-spine collar (hereinafter referred to as "collar") with gentle stretching. Avoid using the collar if it has any tears. Insert the transducers in the plastic openings on the collar. The best practice is the use the transducer from the "Master" label system in the anterior opening and the other transducer in the posterior opening.

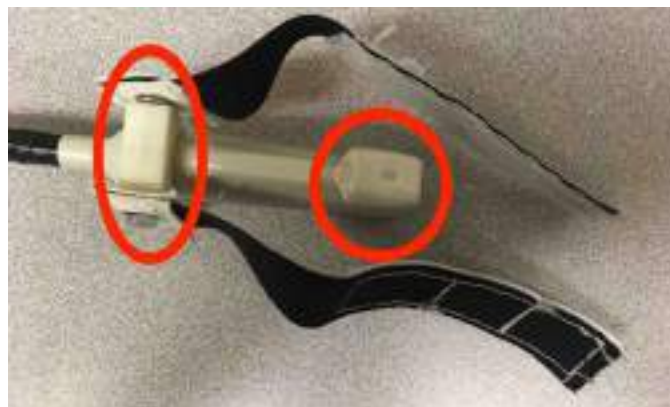


Figure 6-1: The dot groove of transducer is facing to the superior (head) side.

4. Install the front brackets on the anterior and posterior openings of the collar to facilitate local fixation (Figure 6-2). Wrap one layer of masking tape on the outer surface of the brackets and finish the collar preparation.

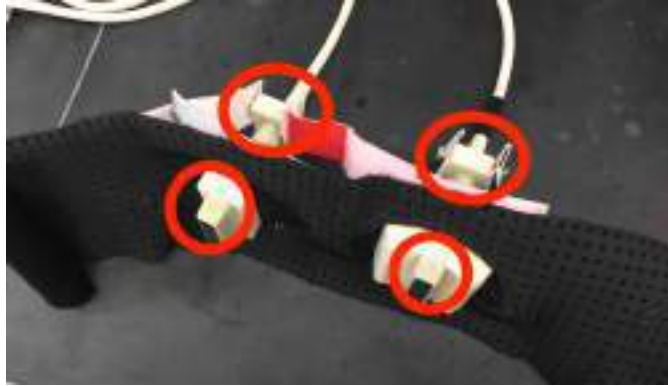


Figure 6-2: Proper installation of front brackets.

Imaging System Preparation:

1. Perform palpation on the subject's neck to identify the landmarks for imaging window.
Posterior: Identify the most prominent spinous process as C7, and then ask the subject to extend and flex his/her neck. Identify the last mobile spinous process as C6. Use masking tape to mark subject's skin.
Anterior: When the correct C-spine vertebral margin image is identified, slide the transducer to the superior side until it can't be moved further. The level seen in US image is C3.
2. Use the sync cable to connect the two Terason systems through EKG ports (Figure 6-3).

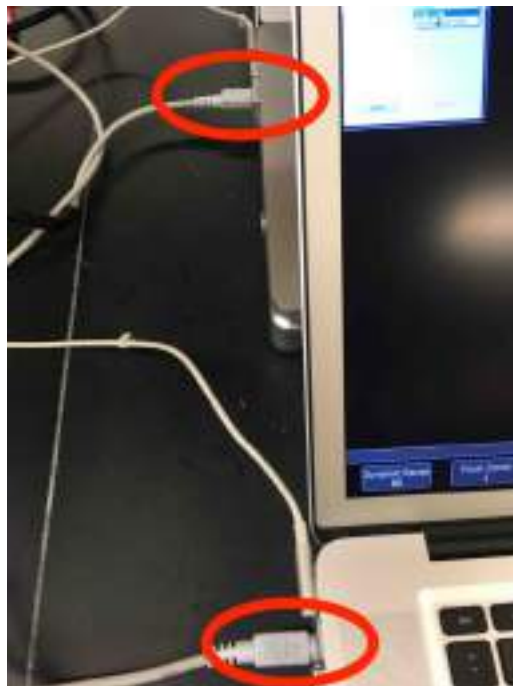


Figure 6-3: Terason systems connected by sync cable using EKG ports.

3. Connect the transducers to Terason system laptops. For consistency, the transducer on the anterior side of neck should be connected to the system labeled as “Master”. **Lock the connection by sliding the locking lever (Figure 6-4).**



Figure 6-4: Ultrasound transducer connected to Terason laptop.

4. Boot the Terason systems and run the Terason program on the desktop. After the program is loaded, it displays a live view of US imaging if the transducer is connected. **If no image is being displayed, check that the transducer is connected correctly. If the patient info view is prompted, click “close” on the bottom.**
5. Push the “Presets” button on the software interface and load the “BIDMC C-spine” preset under musculoskeletal exam to the system, or manually tune the scanning parameters shown in Table 6-2 to optimize image scan quality.

Table 6-2: Recommended settings for ultrasound parameters.

Parameters	Recommended Setting
View Mode	“Trap” (Trapezoidal)
Persistence	0
Scanning Depth	4 cm
Frequency	“M” (Medium)
Focal Zone	1
TV Level	Off
Map	A
Focal Range	Put the * mark on bone surface, typically 1.3~3 cm
OmniBeam Mode	On



Figure 6-5: Preset locations in Terason software.

6. Perform a pre-scan on human participant without enveloping the collar on his/her neck. Firstly, apply some TENSIVE conductive adhesive gel (hereinafter referred to as “gel”) over the head of anterior transducer. Secondly, start imaging the C-spine by placing the transducer on participant’s neck. Gently wipe the transducer to disperse gel on the skin, and then apply a small force to couple the transducer and skin. **Orient the transducers to obtain the anterior (left) and posterior (right) images shown in Figure 6-6.**

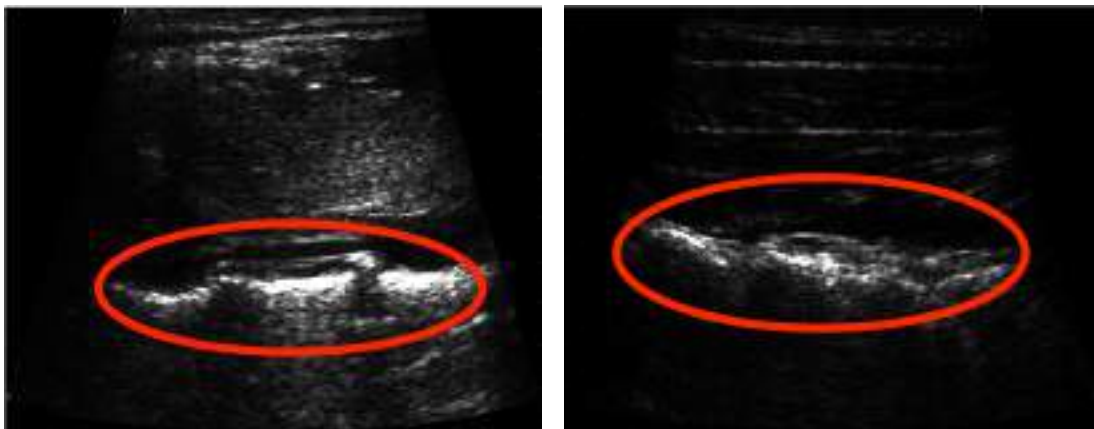


Figure 6-6: Anterior (left) and posterior (right) views of the C-spine.

7. After the desired US imaging windows are obtained, wrap the collar around the participant’s neck. Attach the elastic bands onto the collar to hold the transducers in place. Adjust the positions of the mating surfaces of the elastic bands to apply different amounts of pressure so that the anterior and posterior images are visible.

Test Imaging Quality: The Terason program should be running and displaying live images of the C-spine with the correct scanning parameters.

1. Run the Terason Recorder in taskbar (shortcut: WIN/CMD + 1)



Figure 6-7: Terason Recorder window.

2. Click “Preferences”-> “Target Folder”->“Select”. Create new data folder for the current participant and confirm. The program will automatically name the recording in a format UltrasoundStreamXXX.ust



Figure 6-8: Target folder settings.

3. Re-focus to the Terason program. Type: “ctrl+T” to call the control panel. Choose “periodic” in scanning mode and press the “Acquire” button. Both system displays should be frozen right now – if the subject moves their neck, the change of C-spine isn’t shown in the Terason program. The system is in a ready state to stream all radio-frequency data to local hard drives. Once it is triggered, the display will be live again.



Figure 6-9: Terason trigger menu.

4. Move the panel to the right to avoid display blocking.
5. Re-focus to the Terason Stream Recorder on both of the system and click “Start”. **Both systems should remain frozen and the number of frames in the recorder should be zero.** This isn’t a trigger signal but instead, allow the access of recorder to the write data to hard drive. If you navigate to the folder that is created, a new zero-byte .ust file can be seen.



Figure 6-10: After triggering the systems, press Start to initiate a .ust file.

6. On the “**master**” system, click “unsync” to switch its mode from unsynchronized state to synchronized mode. **This will trigger the recording of both systems.** The subject can start performing tests.
7. In the test end or when pause is needed, **click “sync” to switch the system from synched state to unsynched state.** This stops both of the systems from data streaming. Then, click “**stop**” on the system to complete the file writing process to hard drive.
8. Write the filename down in your test log notebook if necessary and repeat steps 3-5 for new recordings.
9. **Note:** the system sometimes stops running after a large quantity of recordings. The sign of the stop is that the program refuses to write data to local hard drive. Check if the “number of frames” status in the recorder every time unsync is clicked. If the number remains unchanged, and the entire system needs to closed and restarted.
10. **Strict steps to close the program must be followed,** otherwise it will create an idle “ultrasound.exe” process in the background which needs manual termination in Task Manager. Firstly, click “**Cancel**” on the control panel in the Terason program, so the system goes back to live status. Secondly, hit “**Close**” to close the Terason Recorder program. Finally close the Terason program itself. All the setting parameters will be reset after closing. **If it is a restart, please load the preset file or manually set the parameters again.**

Post-Test Maintenance:

1. Use alcohol wipes to completely clean the transducer head so that no gel adheres to the case and contact surface.
2. Soak the collar and front brackets in water and remove the gel.

3. Dry the collar and brackets on a paper towel out of sunlight. Sunlight may increase the deterioration of neoprene.
4. After the collar is clean and dry, slightly stretch it and roll it up for storage.

6.2 *Consent Form and Flyer for Subject Enrollment*



USAARL

U.S. Army Aeromedical Research Laboratory

Volunteers Needed!

The U.S. Army Aeromedical Research Laboratory is investigating whether ultrasound is useful when looking at the cervical spine. This study aims to determine if ultrasound is a useful tool for viewing the cervical spine motion during operating environment motion and transport. The results of the study will be used to develop methods to evaluate cervical spine disease and injury.



Eligibility Criteria:

- Males or females
- Between the ages of 18-40
- In self-reported good health
- No current profile limiting physical activity
- No personal history of nerve injury or degeneration
- No current or historical head, neck, or back injury, including vertebral fractures, degenerative disc disease, etc.
- Females must not be pregnant
- Ability to undergo MRI scan

You Will Be Asked To:

- Sit in a seat during different vibration sequences while wearing ultrasound cervical collar device and different simulated helmet configurations
- Test strength, range of motion, nerve function, and fatigue
- Get a MRI scan of the cervical spine

Time:

Participation will take from 3-6 hours per/day for two days.

Compensation:

- \$100 monetary gift(s) card at the end of data collection and debrief
- Reimbursement for meal and travel to MRI facility

If you are interested in participating, please call or e-mail:

Dr. Adrienne M. Madison: 334-255-6811,
adrienne.m.madison.ctr@mail.mil
 OR
Mr. Patrick Estep: 334-255-6811,
patrick.n.estep.ctr@mail.mil

<https://www.facebook.com/USAARL>
<https://www.linkedin.com/company/usaarl>
<https://twitter.com/usaarl>
<https://www.youtube.com/user/usaarl>



Scan to visit our website.

Version: 13 July 2017



6.3 *Consent Form for Subject Enrollment*

U.S. Army Aeromedical Research Laboratory

CONSENT TO PARTICIPATE IN RESEARCH

Title of Protocol: Evaluation of Ultrasound Assessment Technique to Measure In Vivo Dynamic Cervical Spine Intervertebral Disc Mechanics

Principal Investigator: Adrienne Madison, Ph.D., Biomechanical Engineer/Scientific Researcher

Co-Investigators: Patrick Estep, Bethany L. Shivers Ph.D., Brian Snyder MD Ph.D., Amin Mohamadi, MD MPH

Funding Source(s)/Sponsor: U.S. Army Medical Research and Materiel Command / Military Operational Medicine Research Program (MOMRP) – Project #18180

INTRODUCTION

You are asked to participate in a research study conducted at the U.S. Army Aeromedical Research Laboratory (USAARL) by Dr. Adrienne Madison, Mr. Patrick Estep, and Dr. Bethany Shivers, members of the USAARL Injury Biomechanics Division, and Dr. Brian Snyder and Dr. Amin Mohamadi from the Beth Israel Deaconess Medical Center (BIDMC). You are asked to participate in this research because you have no current or previous record of: (a) injury/disease related to the head, neck, back, and/or nerves and (b) symptoms or conditions that will prevent you from undergoing a MRI examination.

Your participation in this research is voluntary. It is important that you read what is written below and ask questions about anything you do not understand. You may want to talk with your family, friends, or others to help you decide if you want to be part of this study. When you feel that your questions have been answered, you will be asked if you agree to be part of the research or not. If you agree, you will be asked to sign this consent form. You will be given a copy of this form to keep.

WHY IS THIS RESEARCH BEING DONE?

The mass, or weight, and location of the weight of the helmets and helmet-mounted systems (i.e. head-supported mass or HSM) have been linked to decreased performance and increased risk of injury.

We are studying whether ultrasound is useful when looking at the portion of the spine in your neck known as the “cervical spine”. We will use ultrasound to take video pictures of the cervical spine (neck) while you sit in a seat on a simulator that recreates what it feels like to ride in military aircraft and/or ground vehicles. While seated on the simulator, you will wear two

different helmet conditions. We will also measure your head and neck motions during this simulated environment. This study is investigational because ultrasound has not been used in this way. However, ultrasound is often used by doctors when trying to diagnose and treat people with certain spine diseases and conditions. We do not yet know if it is useful or safe as a tool for viewing the cervical spine in motion.

The researchers need complete data sets from 28 volunteers for this study. Your participation will involve two test days. One testing day will take place at USARRL. The other will take place at USAARL and at the Auburn University MRI Research Center.

WHAT WILL HAPPEN DURING THIS RESEARCH?

A. The following steps will only occur on the first day of the study (today):

1. The principal investigator (PI) will determine if you are qualified to participate in this study based on your current health.
2. The PI will determine if you have a Hoffmann Reflex (H-reflex), which is a technique to measure changes in nerve function. Not everyone has an H-Reflex; however, its presence is important to our study. If you do not have a detectable H-reflex then this portion of the testing won't be used for the remainder of your testing. In order to measure the H-Reflex, we will instrument your arm with adhesive sensors and apply a weak electric stimulus (shock) to generate a muscle twitch. We will start at a very low-level intensity that you likely won't even feel. We will increase the intensity until we begin to see the response that we are looking for. As we increase the intensity, you will likely begin to feel a prickling sensation directly under the sensor, but it won't be painful – it will feel like a pin-prick. As the intensity increases further, you may feel the stimulus run down your forearm and into your fingers. You may also see your fingers or wrist move because of the muscle twitch. At the peak intensity, the stimulus will feel like a carpet shock. This may be uncomfortable, but most individuals do not find it painful enough to stop testing. This high-level intensity will only be used a few times (up to 10) to determine the maximum response. If the PI is able to identify an H-reflex, the baseline process will be repeated at the start of each test day because there can be small changes in your nerve response from day to day. If the PI cannot find an H-reflex on the first day, this process will not be repeated.
3. You will be scheduled for a Magnetic Resonance Imaging (MRI) scan at the Auburn University MRI Research Center in Auburn, Alabama. Depending on appointment availability, the scan may be scheduled for either the first or the second day of testing.

The MRI is only for research and is not meant to diagnose any medical conditions. MRI is a method of taking pictures of the brain and of the blood flow in the brain, using a large magnet and radio signals.

4. We will measure and record your age, height, weight, neck circumference, neck length, arm length, shoulder breadth, hip breadth, and leg length.
5. You will then watch a short video to explain the function and safety procedures for the simulator. If you have any additional questions that are not covered by the video, the research staff will be available to answer them for you.
6. You will be shown the ultrasound collar device and helmet which will be used during the study.
7. You will be sized and fit for spandex shirt and pants that you will wear during testing. The spandex clothing is required to ensure that reflective motion capture markers do not move during testing.
8. You will be sized and fit for a chest strap that holds a sensor in position. This sensor will measure your heart-rate, breathing-rate, and other metrics that will allow the researchers to monitor your response to the different research conditions.

B. The following steps will occur on the test day at USAARL:

9. You will change into spandex clothing, the chest strap, and appropriate footwear.
10. You will be instrumented with the chest sensor, adhesive electromyography (EMG) sensors, and reflective markers.
 - a. The chest sensor will be attached to the chest strap first and will be worn under your shirt (just below a sports bra for females).
 - b. The EMG sensors will allow us to record muscle activity from your neck muscles.
 - i. If necessary and with your consent, we may shave parts of your neck to remove excess hair. This will help with adhesion of the sensors and will minimize discomfort to you.
 - ii. We will clean your neck with an alcohol wipe to help with the adhesion of the sensors.
 - iii. If necessary, we may apply a sticky substance and/or medical tape to help with the adhesion of the sensors.
 - iv. We will place and secure sensors on various muscles of your neck. We will put sensors on one or both sides of your neck depending on sensor availability.
 - c. The reflective markers will allow us to monitor the movements of specific points on your body using video analysis.
 - i. If necessary and with your consent, we may shave parts of your body to remove excess hair. This will help with adhesion of the markers and will minimize discomfort to you.
 - ii. We will place and secure markers on your armor and helmet, on your head (behind your ears and on the bridge of your nose), on your upper torso

(collar bones and shoulders), on your arms (elbows and wrists), on your pelvis/hips, and on your upper legs (thigh).

11. Once you are fully outfitted and instrumented, we will collect the following pre-test measures from you before we begin testing:
 - a. Resting heart-rate and breathing rate.
 - b. Subjective Measures:
 - i. You will be asked to grade your neck fatigue, neck pain/discomfort, and level of exertion using a numeric scale (“On a scale from 0-10, how is your neck pain?”).
 - c. Hoffmann Reflex:
 - i. We will place two adhesive sensors on your elbow and produce a light electric shock (imagine static generated from carpet shock).
 - ii. We will follow the same procedure used today to establish your baseline. We will then record five repeated shock stimuli at the 20% level.
 - d. Neck Range of Motion:
 - i. Head/neck range of motion will be measured using a specialized device. You will be placed in a seated position and asked to move your head throughout your full range of motion; this will include touching your chin to your chest, looking up towards the sky, looking over each of your shoulders, and touching your ear to your shoulders.
 - e. Neck Strength:
 - i. Neck strength will be measured using another specialized device. You will be placed in a seated position and have your head placed against a padded surface. You will then be asked to exert varying levels of force against the padded surface for approximately five seconds at a time. This will be done in a similar manner to the range of motion tests. You will be given 45 seconds to 5 minutes of rest between each test.
12. You will be given a special helmet to wear. This helmet was designed to allow us to get a very secure fit. The helmet is also set up to allow us to place weights in different positions to simulate the helmet conditions used in the military.
 - a. You will wear 2 different helmet conditions. These conditions represent a range of helmets used in the military.
 - b. You will wear each helmet for a total time of approximately 1.5 hours.
13. You will climb the stairs to the ride simulator and sit down in a chair. A research technician will fit ultrasound collar device and probes around your neck. The probes will be attached to the ultrasound system located next to the simulator. The researcher will record images of your cervical spine to make sure the probes are in the proper location. This should take about 10 minutes.
14. A research technician will secure you to the chair with the appropriate restraint device. The ride simulator will be used to produce up and down motions of different

speeds and lengths. The ultrasound collar device will record images of your cervical spine during these motions. You will be given an emergency stop device in case you need to stop testing at any point in time.

15. You will complete two test series wearing each of the two helmet conditions:
 - a. You will be exposed to short segments of repeated up and down motions generated by the ride simulator. These motions will randomly increase or decrease at speeds within a pre-set range. This test will last for approximately three minutes.
 - i. This procedure will be repeated for each of the helmet conditions.
 - ii. You will be asked to complete neck range of motion and neck strength tests between each helmet condition.
 - b. You will be exposed to a simulated vibration environment based on current military aircraft and/or ground vehicles. Each simulation will last for approximately 30 minutes. There will be six total simulations, with approximately 10 minutes between each. You will be allowed to take breaks to use the restroom between the segments when needed.
 - i. This procedure will be repeated for each of the helmet conditions.
 - ii. Between each 30 minute exposure, you will complete a brief strength test, a range of motion test, and a subjective questionnaire (Section B. #11) while seated on the simulator.
 16. Following the test procedures, we will remove the helmet and body armor from you.
 17. We will collect post-test measures. These are the exact same as the pre-test measures and include the subjective questions, H-Reflex, range of motion, and neck strength assessments (Section B, #11).
 18. We will remove all EMG sensors and motion capture markers from you. This may leave some adhesive residue on your skin. We will clean all areas with a hypoallergenic cleanser that will remove all remaining residue. This process may induce some redness or irritation of the skin.
 19. Once all equipment and sensors have been removed, you will be allowed to change back into normal clothing and depart for the day. The USAARL testing day will last for approximately 3 hours.
- C. The following steps will occur on the MRI test day at Auburn University MRI Research Center:
20. You will report to the Auburn University MRI Research Center.
 21. You will first be asked screening questions to make sure it is safe for you to undergo an MRI scan.

22. You will change into surgical scrubs. If you are female, you will be asked to remove your bra if it contains a metal underwire or metal fasteners.
23. You will be asked to lie down on a platform that can slide into the magnet. An MRI imaging coil, which is made from special wires that are covered in plastic, will be placed around your head. Foam pads will be placed around your head to limit head movement during the scan.
24. You will be asked to lie still on your back for the duration of the scan.
25. Some MRI scans may require you to take a deep breath, blow it out, and then hold your breath for 25 seconds or less. You may be asked to repeat this exercise multiple times during the scan.
26. Multiple scans may be performed in a single session with approximately one minute of rest between scans.
27. You will hear a loud knocking or hammering noise while the MRI is taking pictures, but the process itself will be painless. Disposable earplugs will be given to you to help make the noise less noticeable.
28. During the procedure, you will be in constant contact with the MRI technologist through an intercom. If at any time during the scan you feel too uncomfortable to continue, the procedure will be immediately stopped and you will be removed from the scanner.
29. Once the scan is completed, you will be allowed to change back into normal clothing and depart for the day.
30. The scan is expected to take approximately 30 minutes. Your total testing time on the MRI test day will be approximately 1-2 hours.

WHAT ARE THE POTENTIAL RISKS AND DISCOMFORTS FROM BEING IN THIS RESEARCH?

You may experience motion sickness symptoms. The likelihood of severe motion sickness symptoms such as vomiting, extreme dizziness or vertigo is unlikely. You may experience dizziness, headaches, or minor fatigue. If all safety procedures are followed accordingly, the risks associated with participating in this study include, but are not limited to: general musculoskeletal soreness and/or fatigue related to the different helmet conditions, discomfort from the H-Reflex shock, discomfort from wearing the body armor and/or helmet, and redness or irritation around sites where the ultrasound collar device, sensors, or motion capture markers are placed.

The effects of vehicle vibration on developing cells, embryos and fetuses are not well-understood at this time. If there is any possibility that you may be pregnant, you are not permitted to participate in this study. Female volunteers will complete a urine pregnancy test after completing the consent process, but prior to any additional testing.

There are no documented risks associated with ultrasound. MRI is a safe and painless procedure for most people. However, it is not safe for people who have pacemakers, some ear implants, shrapnel injuries, or certain types of metal and/or electrical devices in their bodies. These individuals will not be allowed to participate in this study. You will be required to remove all metal from your metal objects from your clothing and pockets on the MRI testing day. For your safety, you will not be allowed to bring any metal objects into the metal room at any time.

You may experience a feeling of claustrophobia (fear of small, confined places) while lying in the MRI scanner. The sides and top of the scanner are very close to your face and body. If you suffer from claustrophobia, then we ask that you do not participate in the study.

WHAT ARE THE POSSIBLE BENEFITS FROM BEING IN THIS RESEARCH?

There is no direct benefit to you from participating in this study. Information obtained from this research may benefit other individuals in the future. The information that we learn in this research may help us develop methods to evaluate cervical spine disease and injury in environments where the body is exposed to constant vehicle motion.

WHAT ALTERNATIVE OPTIONS TO PARTICIPATION ARE AVAILABLE TO ME?

The only alternative is not to participate in the study.

WILL I HAVE TO PAY FOR ANYTHING IF I TAKE PART IN THIS RESEARCH?

Participants will be reimbursed for travel to Auburn University MRI Research Center or meal expenses during the two-day study period. This amount will not exceed \$105 for travel and \$30 for meals and incidentals.

WILL I BE PAID TO TAKE PART IN THIS RESEARCH?

Subjects who participate in the study will receive \$100 monetary gift(s) card (\$50 per test day) upon completion of the data collection and debrief. In order for Active Duty or National Guard members on orders to receive compensation, they must be in an off-duty status at the time of participation in the study. Any subject participating during duty hours will not be eligible for compensation and must have the consent of their cadre or supervisor. Subjects will be requested to self-report off-duty status during consent. A member of the research team will document confirmation of reported off-duty status in the study logbook.

WHAT HAPPENS IF I AM INJURED AS A RESULT OF TAKING PART IN THIS RESEARCH?

If at any time you believe you have suffered an injury or illness as a result of participating in this research, please contact the PI:

Dr. Adrienne Madison, Injury Biomechanics Division

Phone: (334) 255-6811

Address: 6902 Andrews Ave, Fort Rucker, AL 36362

If you are injured because of your participation in this research and you are a DoD healthcare beneficiary (e.g., active duty military, dependent of active duty military, retiree), you are entitled to medical care for your injury within the DoD healthcare system, as long as you remain a DoD healthcare beneficiary. This care includes, but is not limited to, free medical care at Army hospitals or clinics.

If you are injured because of your participation in this research and you are not a DoD healthcare beneficiary, you are entitled to medical care for your injury at an Army hospital or clinic; medical care charges for care at an Army hospital or clinic will be waived for your research-related injury. You are also entitled to care for your injury at other DoD (non-Army) hospitals or clinics, but care for your injury may be limited to a given time period, and your insurance may be billed. It cannot be determined in advance which Army or DoD hospital or clinic will provide care. If you obtain care for research-related injuries outside of an Army or DoD hospital or clinic; you or your insurance will be responsible for medical expenses.

For DoD healthcare beneficiaries and non-DoD healthcare beneficiaries: Transportation to and from hospitals or clinics will not be provided. No reimbursement is available if you incur medical expenses to treat research-related injuries. No compensation is available for research-related injuries. You are not waiving any legal rights. If you believe you have sustained a research-related injury, please contact the Principal Investigator (PI). If you have any questions, please contact the PI.

HOW WILL YOU PROTECT MY PRIVACY AND THE CONFIDENTIALITY OF RECORDS ABOUT ME?

The principal investigator will keep records of your participation in the research. To protect your privacy, any of your research-related records will be labeled or “coded” with an assigned research participant number that will not include your name or social security number. Dr. Bethany Shivers will keep the link between your identification number and your research records in a locked filing cabinet in Dr. Shivers’ office. The principal investigator or designated associate investigator is the only person who will be able to match your research identification number with any of your personal identifying information.

When the results of the research are published or discussed in conferences, no information will be included that would reveal your identity to others. Data may be used for future research,

presentations, and publications. If photographs, videos, or audio-tape recordings of you will be used for educational purposes, your identity will be protected or disguised.

Authorized representatives of the following groups may need to review your research and/or medical records as part of their responsibilities to protect research participants:

- U.S. Army Medical Research & Materiel Command Institutional Review Board
- U.S. Army Human Research Protections Office and other DOD offices charged with oversight of human research
- U.S. Army Aeromedical Research Laboratory Regulatory Compliance Office
- Beth Israel Deaconess Medical Center

Complete confidentiality cannot be promised for military personnel, because information bearing on your health may be required to be reported to appropriate medical or command authorities.

WHAT IF I DECIDE NOT TO PARTICIPATE IN THIS RESEARCH?

Your participation in this research is voluntary. You may decline to participate now or stop taking part in this research at any time without any penalty or loss of benefits to which you are entitled. Deciding not to participate now or withdrawing at a later time does not harm, or in any way affect, your medical care future relationships with USAARL.

Should you decide to stop taking part in this research before the completion of data collection, we will not be able to use your data in the study at all because it will be incomplete. Also, it should be noted that, if at some time after completion of the study you want us to remove your data from everyone else's data, we will not be able to do that because there will be no way to identify which data is yours because data will not be linked to any personal identification.

WHAT COULD END MY INVOLVEMENT IN THE RESEARCH?

The investigator may withdraw you from participating in this research if circumstances arise which warrant doing so, particularly sustaining any muscular or skeletal injury. The investigator will make the decision and let you know if it is not possible for you to continue. Your taking part in the study may be stopped without your consent if it is determined by the investigator that remaining in the study might be dangerous or harmful to you.

WHAT IF ANY NEW INFORMATION IS FOUND OUT?

During the course of the research, the investigators will tell you of any new findings that might cause you to change your mind about continuing in the study. If new information is provided to you, the investigators will obtain your consent to continue participating in this study.

WHO SHOULD I CALL IF I HAVE QUESTIONS OR CONCERNS ABOUT THIS RESEARCH?

If you have questions about the research at any time, you should contact one of the following individuals:

Name	Phone Number	Email
Adrienne Madison	(334) 255-6811	adrienne.m.madison.ctr@mail.mil
Bethany Shivers	(334) 255-6894	bethany.l.shivers.civ@mail.mil
Patrick Estep	(334) 255-6811	patrick.n.estep.ctr@mail.mil
Carol Chancey	(334) 255-6952	valeta.c.chancey.civ@mail.mil

If you have questions regarding your rights as a research participant, you may contact the USAARL Regulatory Compliance Office at (334) 255-6940 or (334) 255-6992, or you may contact the HQ USAMRMC IRB Office at 301-619-6240 or by email to usarmy.detrack.medcom-usamrmc.other.irb-office@mail.mil.

I agree to be contacted in the future about other research studies.

_____Yes _____No

Initial your choice

If you answered "Yes" to the previous statement, please provide the following information:

Name:

Phone Number:

Email Address:

I agree to the use of any pictures or video (used together or separately) taken/ recorded by or on behalf of USAARL in future research, briefings, proposals, technical reports, or presentations/papers in conferences or peer-reviewed papers

_____Yes _____No

Initial your choice

SIGNATURE OF RESEARCH PARTICIPANT
--

I have read the information provided above. I have been given an opportunity to ask questions and all of my questions have been answered to my satisfaction.

Printed Name of Participant

Signature of Participant

Date

ENROLLMENT CRITERIA CONFIRMATION:

A protocol representative (PI, AI, or research technician) has verified that the participant meets all inclusion criteria prior to enrollment in the study:

YES ☐

NO ☐

Printed Name of Protocol Representative

Signature of Protocol Representative

Date

6.4 Evaluation of Mass Properties of Helmet

Assessment of Mass Properties Instrument (MPI) helmet utilized in BIDMC experiments for designing similar experiments at USAARL [53]. MPI with a custom anatomical headform is shown in Figure 6-11 to measure the mass properties of head-borne systems. The center of gravity (CG) and moment of inertia (MOI) are determined using multiple orientations of the headform (Table 6-3).

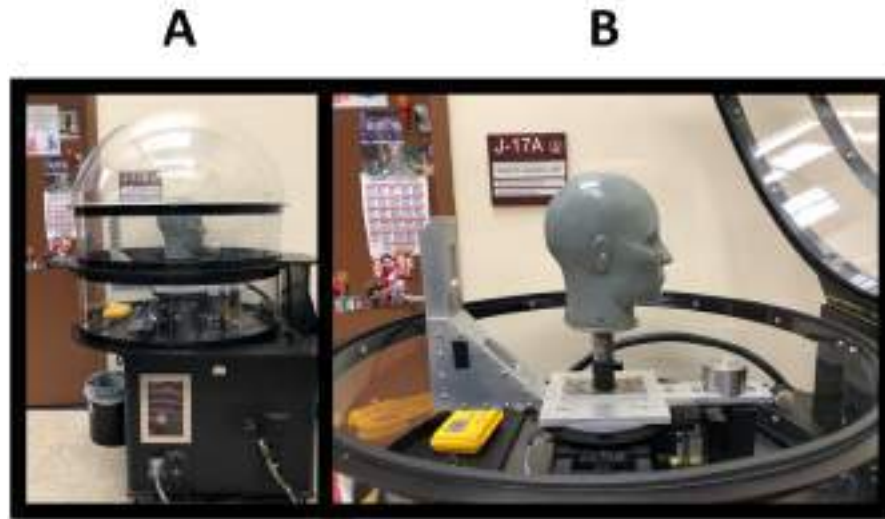








Figure 6-11: A) MPI apparatus; B) headform interface plate located inside MPI.

Table 6-3: Orientations used to determine CG (I_{zz} , I_{xx} , I_{yy}) and MOI (I_{zz} , I_{xx} , I_{yy} , I_{xz} , I_{xy} , I_{yz}).

Orientation	Headform base orientation relative to machine coordinate system	Headform orientation relative to headform base	Machine/global axis to headform/local axis
I_{zz} 	0	0	+X = +x +Y = +y
I_{xx} 	90	0	+X = +z +Y = -y

I_{yy}		90	90	$+X = +z$ $+Y = +x$
I_{xz}		45	0	N/A
I_{xy}		90	45	N/A
I_{yz}		45	90	N/A

USAARL conducted mass property assessments on the helmet provided by BIDMC (Figure 6-12). The mass and CG measurements obtained will be used to recreate the two helmet conditions, null and weighted, using a Helmet Mass Simulation Device (HSMD). These helmet conditions will be achieved by mounting additional masses at a specific location along the mounting bars. The HSMD in both recreated conditions will be worn by the participants in addition to the ultrasound cervical collar device during simulated exposures to vehicular ride profiles.

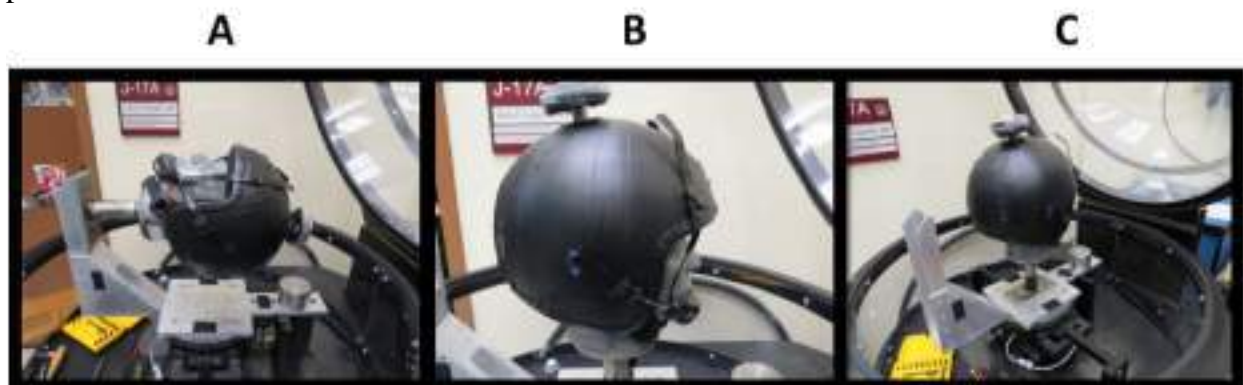


Figure 6-12: BIDMC helmet on the MPI apparatus in the I_{xx} (A) and I_{zz} (B-C) orientations.

Mass, CG, and MOI measurements were performed for each helmet condition (Table 6-4). The measurements were obtained in accordance with the procedures, methods, and theories outlined in USAARL Report No. 93-4 [53]. One technician was responsible for the fitting of the helmet during a test series to minimize positioning and retention adjustment variations that could possibly affect the results. A baseline test of the headform, fixture, and null helmet configuration was executed first. Testing of the weighted condition followed. In between runs, the helmet was completely removed from the headform and refitted prior to performing the next test.

Table 6-4: Mass property measurements of BIDMC helmet.

Results			CG Measurements (cm)				MOI Measurements (kg*cm ²)		
	Condition	Mass (kg)	X	Y	Z		Ixx	Iyy	Izz
	BIDMC US Helm - Null	1.8120	-2.256	0.146	9.577		226.623	231.463	180.627
	BIDMC US Helm - Weighted	3.0824	-2.785	-0.026	15.339		384.867	392.423	210.173

6.5 Development of Mass Attachment Device to Recreate Vertical (z-axis) Offset Helmet Configurations

The proposed testing procedures, helmet configurations, and participant instrumentation are being revamped due to lessons learned from previous lab-based data collections conducted by USAARL research personnel. Throughout this process, we have identified ways to better streamline and sync data collected from multiple devices as well as potentially shorten participant testing time in the lab. The introduction of wireless EMG capabilities and Man-Rated Multi-Axis Ride Simulator (MARS) chair-mounted devices for intermittent strength assessments will assist with this effort. In addition to ensuring operational relevancy, we are working to select helmet configurations representative of current and future fielded helmet systems. A second helmet mass attachment apparatus have been fabricated to assist us in the recreation of operational military helmets (Figure 6-13).



Figure 6-12: Helmet mass attachment device to recreate vertical (z-axis) offset helmet configurations.

The apparatus will be used to recreate helmet configurations with a vertical offset; this apparatus system will be used separately from the custom built side bars and masses used to recreate helmet configurations with forward and aft longitudinal offsets (Figure 6-14).

Additionally, we are exploring the option of placing participants in one of two groups for testing. Group A would wear a baseline generic helmet (Figure 6-15) and a helmet configuration with a vertical offset, while Group B would wear the baseline generic helmet and helmet configuration with longitudinal offset. This grouping would allow us to determine if and how cervical motion is affected by mass offset. Potential helmet configurations are being finalized. The protocol will be updated to include changes to testing procedures, instrumentation, and helmet configuration selection prior to IRB submission.



Figure 6-14: Helmet mass attachment device to recreate longitudinal (x-axis) offset helmet configurations.



Figure 6-15: Baseline generic helmet configuration to be worn by all participants.

6.6 Technology to Image Spine Using Single 3D US System

We developed a novel method of using 3D US images “stitched together” to create a volumetric representation of the entire spine that can be analyzed in multiple dimensions. This will allow us to use a single US transducer to evaluate entire spine without need for dual US probes. Specifically, we imaged the thoracic spine, the anatomic location of most adolescent idiopathic scoliosis (AIS) and were able to determine the frontal plane Cobb angle used to clinically describe the lateral curvature of the spine. In addition, we demonstrated 3D US technology to characterize axial torsion of spine in AIS model. While 3D US is able to measure frontal plane Cobb angle [54] as well as axial torsion of spine, it has the potential for automatic or semi-automatic analysis of lateral sagittal plane displacement and torsional deformity of individual vertebrae.

The extent and location of the lateral curvature of the spine associated with adolescent idiopathic scoliosis (AIS) is characterized by the projected deformity onto frontal plane

radiographs measured by the Cobb angle [54]. AIS patients undergo serial radiographic evaluations to assess progression of the spinal deformity and/or treatment response [55]. US is a low cost, radiation-free, portable modality capable of assessing spinal deformity. The purpose of this feasibility study is to demonstrate the ability of a novel 3D US transducer to characterize the 3D spinal deformity associated with AIS.

Methods: A biomimetic plastic spine model was contorted to simulate a 30° Lenke 1A scoliosis [56]. The spine was submerged in a water bath to simulate the soft tissue envelope and imaged using a 3D US transducer translated incrementally over the spine from C6 to T8 using a robotic arm. 3D US surface volume images of the vertebrae (Figure 6-16a) were generated from sequential, parallel, trans-axial linear US scans (Figure 6-16b) concatenated to generate a 3D volumetric surface rendition of the thoracic spine (Figure 6-16c) using a custom MATLAB program. Based on trigonometric equivalencies, the Cobb angle was estimated by doubling the lateral displacement angle between the central vertical spine axis and the maximum lateral displacement of the spine at T6 (Figure 6-16d). Additionally, the transverse plane axial rotation of each vertebra can be measured, and maximum torsional deformity calculated using following formulae:

$$\begin{aligned}\theta &= \theta_{T6} + \theta_{C6} \\ \theta_{T6} &= \tan^{-1} \left(\frac{\Delta x_{T6}}{\Delta z_{T6}} \right) = \tan^{-1} \left(\frac{|x_o - x_{T6}|}{|z_o - z_{T6}|} \right) \\ \theta_{C6} &= \tan^{-1} \left(\frac{\Delta x_{C6}}{\Delta z_{C6}} \right) = \tan^{-1} \left(\frac{|x_o - x_{C6}|}{|z_o - z_{C6}|} \right)\end{aligned}$$

Results: The maximum lateral displacement between the spinous processes of C7 and T6 was 43 mm, analogous to a lateral displacement angle of 15.3°, which corresponds to Cobb angle of 30.6°, which was equivalent to the prescribed 30° scoliosis. The maximum axial torsion was 62° (Figure 6-17).

Conclusion: We have demonstrated the feasibility of using 3D US images “stitched together” to create a volumetric representation of the entire spine that can be used to analyze spinal deformity in multiple dimensions without the cost of MRI and radiation exposure of CT. We imaged the thoracic spine, a common location for AIS, to determine the Cobb angle based on the maximum lateral deviation of the spine. Axial torsion can also be characterized. Limitations of this study include the use of a homogeneous spine model devoid of soft tissues and the absence of the rib cage.

Significance: This feasibility study indicates that 3D US can be used to characterize 3D spine deformity. The portability of this technology may facilitate screening programs and frequent examinations of high-risk patients without radiation exposure.

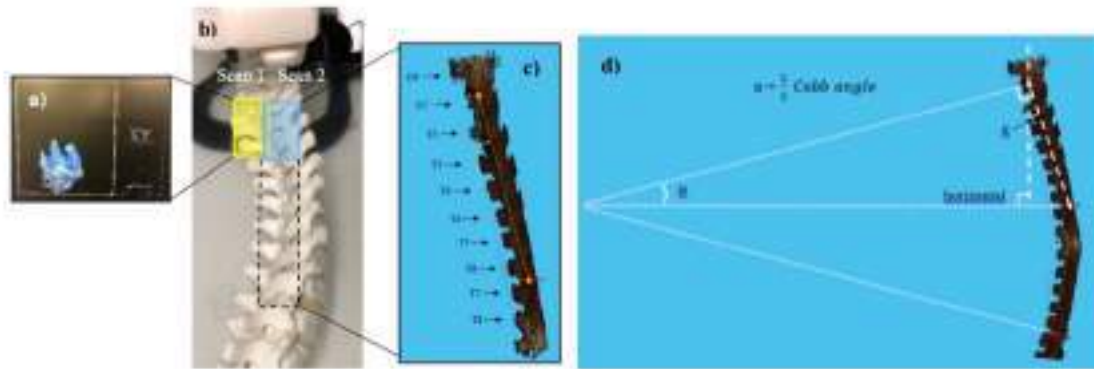


Figure 6-16: a) Spine model and overlay of imaging method. b) 3D US image using XL14-3 transducer. c) Stitched image of spine volume. d) Trigonometric equivalencies demonstrating calculation of Cobb angle. Red lines extrapolate angle between first angled vertebra and horizontal intersecting the point of maximum lateral deflection. Yellow dashed lines indicate vectors used to determine Cobb angle.

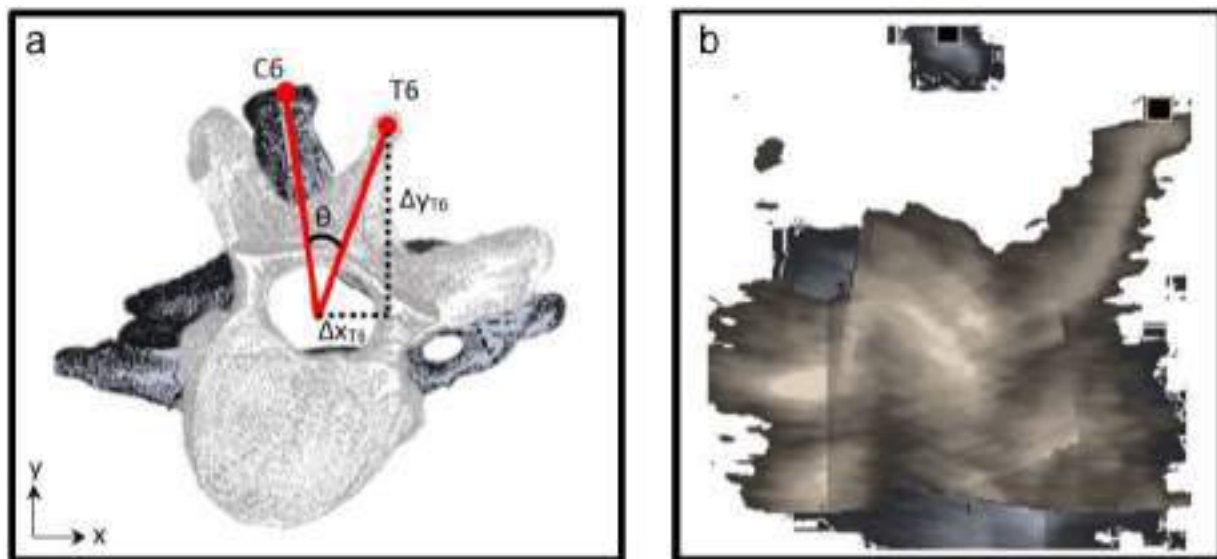


Figure 6-17: a) Torsion angle was calculated between the spinal processes of C6 and T6. The x- and y-displacements of the processes were determined using image slices of the constructed volume, and a maximum angle of 61° was determined through basic trigonometric functions. b) Ultrasound images of C6 and T6 vertebrae overlaid to demonstrate torsion.

Conclusion: We demonstrated that dual B-mode US provides low cost, portable, non-ionizing radiation imaging system capable of accurately measuring real time dynamic FSU deformation in simulated work environments. B-mode US can accurately track vertebral motion under clinically relevant physiologic conditions and can characterize dynamic behavior of C-spine FSU at higher frame rates than MRI and CT. We have also shown that dynamic material properties measured by US can be related to anatomy and IVD integrity and hydration. Some limitations to our study include small sample sizes in both *ex-vivo* and *in-vivo* experiments, 2D FSU deformation was measured only in the sagittal plane, and that *ex-vivo* validation studies may not correspond to *in-vivo* accuracy. From this study, we conclude that para-cervical muscles serve to dampen loads applied to the C-spine, thereby protecting IVD from excessive deformation. As muscles fatigue,

this protective effect lost, and resulting deformation may contribute IVD “fatigue failure” over repetitive loading in extreme environments. This work provides insight on improving procedures for physical laborers as well as developing exercise regimens to strengthen muscles to protect C-spine from excessive loading in different tasks and dynamic environments.

5. Conclusion

We have achieved all of the goals proposed on the statement of work except for the second part of aim two that was subcontracted to be done at Ft. Rucker by USAARL. Owing to the rigorous requirements of IRB for protection of our troops, USAARL have not been able to obtain IRB approval to use our dual US device on troops performing simulated combat activities on the MARS. Grant money has been sequestered so that USAARL can recruit human subjects at Ft. Rucker, once IRB approval is granted so that they can fulfill their subcontract. However, we have developed Standard Operating System, transferred the knowledge and technology of how to use the dual US system to USAARL and we are actively working on an agreement with USAARL to fulfill the final remaining parts of the proposed work.

6. Publications, Abstracts, and Presentations

Publications

Zheng M, Shiuan K, Masoudi A, Buckland D, Szabo T, Snyder B. Dynamic ultrasound imaging of cervical spine intervertebral discs, Ultrasonics Symposium (IUS), 2013 IEEE International, Page(s): 836-839

Zheng M, Masoudi A, Buckland D, Stemper B, Yoganandan N, Szabo T, Snyder B. Dynamic ultrasound imaging of cervical spine intervertebral discs, Ultrasonics Symposium (IUS), 2014 IEEE International, Page(s): 448-451

Arun MW, Yoganandan N, Stemper BD, Zheng M, Masoudi A, Snyder B. Sensitivity and stability analysis of a nonlinear material model of cervical intervertebral disc under cyclic loads using the finite element method. Biomedical sciences instrumentation. 2014;50:19-30.

Masoudi A, Fama D, Yoganandan N, Snyder B. Methodology to Calibrate Disc Degeneration in the Cervical Spine During Cyclic Fatigue Loading. Biomedical sciences instrumentation. 2015; 51:222-9.

Zheng M, Mohamadi A, Szabo T, Snyder BD. In-vivo Cervical Spine FSU Dynamic Motion Measured by Dual Ultrasound: The Effect of Muscle Activation, 2016 IEEE Ultrasound Symposium Proceedings:1-4

Stemper BD, Yoganandan N, Zheng M, Snyder B. Fatigue in the Cervical Spine Intervertebral Disc with Repetitive Axial Compression. The Spine Journal. 2016.1;16(10):S362.

Umale S, Yoganandan N, Curry W, Stemper B, Snyder BD. Responses of the cervical disc under cyclic loading: data for finite element models. Rocky Mountain Bio mechanics Symposium 2016.

Yoganandan N, Umale S, Stemper B, Snyder B. Fatigue responses of the human cervical spine intervertebral discs. Journal of the mechanical behavior of biomedical materials. 2017 May 1;69:30-8.

Zheng M, Mohamadi A, Szabo T, Snyder B. Evaluation of In-vivo Kinematics of Cervical Spines by Co-Registering Dynamic Ultrasound with MRI. IEEE International Ultrasonics Symposium, IUS, 2017, vol. 2017–September, pp. 1–4.

Zheng M, Mohamadi A, Szabo T, Snyder B. Long-term movement analysis of cervical vertebrae with normalized cross-correlation and subsample estimation. IEEE International Ultrasonics Symposium, IUS, 2017, vol. 2017–September, pp. 1–4.

Umale S, Yoganandan N. Mechanisms of Cervical Spine Disc Injury under Cyclic Loading. Asian spine journal. 2018 Oct;12(5):910.

Zheng M, Szabo T, Mohamadi A, Snyder B. Long Duration Tracking of Cervical Spine Kinematics with Ultrasound accepted at IEEE Transactions on Ultrasonics, Ferroelectrics, and Frequency Control. 2019

Conference Abstracts

1. Shiuan K.S, Zheng M, Buckland D.M, Snyder B.D. Ultrasound Can Measure Dynamic Motion of Cervical Spine Intervertebral Disc. Orthopedic Research Society (ORS) 2013 Annual Meeting. San Antonio, TX, Jan 26 - 29, 2013.
2. Shiuan K.S, Zheng M, Buckland D.M, Snyder B.D. Clinical Ultrasound Can Measure Dynamic Intervertebral Disc Deformation In-vivo. Orthopedic Research Society (ORS) 2013 Annual Meeting. San Antonio, TX, Jan 26 - 29, 2013.
3. Zheng M, Arun M, Masoudi A, Buckland D, Yoganandan N, Stemper B, Snyder B. Real Time Ultrasound Can Measure Dynamic Properties of Cervical Spine Intervertebral Disc. Orthopedic Research Society (ORS) 2014 Annual Meeting. New Orleans, LA, Mar 15 - 18, 2014
4. Zheng M, Masoudi A, Buckland D, Yoganandan N, Stemper B, Szabo T, Snyder B. Ultrasound Imaging of Cervical Spine Intervertebral Discs. World Congress of Biomechanics 2014 Annual Meeting. Boston, MA, Jul 6 -11, 2014.
5. Zheng M, Masoudi A, Buckland D, Yoganandan N, Stemper B, Szabo T, Snyder B. Dynamic ultrasound imaging of cervical spine intervertebral discs. World Congress of Biomechanics, Boston, MA, July 6-11, 2014.
6. Zheng M, Masoudi A, Buckland D, Stemper B, Yoganandan N, Szabo T, Snyder B: Dynamic ultrasound imaging of cervical spine intervertebral discs, Ultrasonics Symposium (IUS), 2014 IEEE International: 448-451 doi: 10.1109/ULTSYM.2014.0111
7. Zheng M, Masoudi A, Buckland D, Szabo T, Snyder B. Use of Portable Ultrasound to Measure Dynamic Motion of Cervical Spine Ex-Vivo and In-Vivo, Biomedical Engineering Society 2014 Annual Meeting. San Antonio TX, Oct 22-25, 2014
8. Umale S, Stemper BD, Zheng M, Masoudi A, Fama D, Yoganandan N, Snyder B. Progressive changes in cervical spine intervertebral disc properties during cyclic compressive fatigue loading. American Society of Mechanical Engineers (ASME) Summer Biomechanics, Bioengineering, and Biotransport Conference, Snowbird Resort, Utah, Jun 17-20, 2015.
9. Zheng M, Masoudi A, Umale S, Buckland D, Yoganandan N, Stemper B, Szabo T, Snyder B. Dual Ultrasound Can Measure Kinematic Motion and Intervertebral Disc Deformation of Cervical Spine. Orthopedic Research Society (ORS) 2015 Annual Meeting, Las Vegas, NV, Mar 28-31, 2015.
10. Stemper BD, Yoganandan N, Zheng M, Snyder BD. Fatigue in the Cervical Spine Intervertebral Disc with Repetitive Axial Compression. North American Spine Society 31st Annual Meeting, Boston, MA, Oct 26-29, 2016.
11. Zheng M, Mohamadi A, Szabo T, Snyder B. In-vivo cervical spine FSU dynamic motion measured by dual ultrasound: The effect of muscle activation. Ultrasonics Symposium (IUS), 2016 IEEE International: DOI: 10.1109/ULTSYM.2016.7728863

12. Umale S, Yoganandan N, Arun M, Stemper B, Snyder B: Mechanisms of cervical spine disc injury under cyclic loading: experimental and finite element analysis. American Society of Mechanical Engineers (ASME) Summer Biomechanics, Bioengineering, and Biotransport Conference (SB3C), National Harbor, MD, Jun 29-Jul 2, 2016.
13. Stemper BD, Shah AS, Yoganandan N, Zheng M, Snyder B: Changes in cervical spine intervertebral disc properties with repetitive axial loading. American Society of Mechanical Engineers (ASME) Summer Biomechanics, Bioengineering, and Biotransport Conference (SB3C), National Harbor, MD, Jun 29-Jul 2, 2016.
14. Zheng M, Masoudi A, Buckland D, Szabo T, Snyder B. In-vivo Cervical Spine FSU Dynamic Motion Measured by Dual Ultrasound: the Effect of Muscle Activation, Orthopedic Research Society (ORS) 2016 Annual Meeting. Orlando, FL, Mar 5-8 2016
15. Zheng M, Mohamadi A, Szabo T, Snyder B. Real Time In-vivo Cervical Functional Spine Unit Kinematics Evaluated by Merging Static MRI with Dynamic Ultrasound Images. Orthopedic Research Society (ORS) 2017 Annual Meeting. San Diego, CA, Mar 17-22, 2017.
16. Mohamadi A, Zheng M, Szabo T, Snyder B. Ultrasound is a Reliable Modality for Measuring Cervical Spine Intervertebral Disk Height. Orthopedic Research Society (ORS) 2017 Annual Meeting. San Diego, CA, Mar 17-22, 2017.
17. Zheng M, Mohamadi A, Szabo T, Snyder B. Evaluation of in-vivo kinematics of cervical spines by co-registering dynamic ultrasound with MRI. Ultrasonics Symposium (IUS), 2017 IEEE International: DOI: 10.1109/ULTSYM.2017.8092502
18. Zheng M, Mohamadi A, Szabo T, Snyder B. Long-term movement analysis of cervical vertebrae with normalized cross-correlation and subsample estimation. Ultrasonics Symposium (IUS), 2017 IEEE International: DOI: 10.1109/ULTSYM.2017.8092558
19. Zheng M, Mohamadi A, Szabo T, Snyder B. Effects of Motion Blurring and Tissue Artifacts on Accuracy of Bone Motion Analysis Using Ultrasound. Orthopedic Research Society (ORS) 2018 Annual Meeting. New Orleans, LA, Mar 10-13, 2018.
20. Zheng M, Mohamadi A, Szabo T, Snyder B. Cervical Spine Kinematics from Dynamic Ultrasound Images Co-Registered to Patient-specific 3D MRI. Orthopedic Research Society (ORS) 2018 Annual Meeting. New Orleans, LA, Mar 10-13, 2018.
21. Aiello A, Mohamadi A, Szabo T, Snyder B. 3D Ultrasonography Is Capable of Measuring Three-Dimensional Spinal Deformity. Orthopedic Research Society (ORS) 2019 Annual Meeting. Austin, TX, Feb 2-5, 2019.

Conference Presentations

Ultrasound Can Measure Dynamic Motion of Cervical Spine Intervertebral Disc, Orthopaedics Research Society 2013 (Poster)

Clinical Ultrasound Can Measure Dynamic Intervertebral Disc Deformation In-vivo, Orthopaedics Research Society 2013 (Poster)

Real-Time Ultrasound Can Measure Dynamic Properties of Cervical Spine Intervertebral Disc, Orthopaedics Research Society 2014 (Poster)

3D Kinematics Using Dual Ultrasound Stereographic Imaging of Human Cervical Spine, Aerospace Medical Association (Oral Presentation)

Ultrasound Imaging of Cervical Spine Intervertebral Discs, 2014 World Congress of Biomechanics (Poster)

Use of Portable Ultrasound to Measure Dynamic Motion of Cervical Spine Ex-Vivo and In-Vivo, Biomedical Engineering Society 2014 (Oral Presentation)

Dual Ultrasound Can Measure Kinematic Motion and Intervertebral Disc Deformation of Cervical Spine, Orthopaedics Research Society 2015 (Poster)

Dynamic Ultrasound Imaging of Cervical Spine Intervertebral Discs, 2013 IEEE International Ultrasonics Symposium (Poster)

Dynamic Ultrasound Imaging of Cervical Spine Intervertebral Discs, 2014 IEEE International Ultrasonics Symposium (Oral Presentation)

Muscle Fatigue Affects Functional Spinal Units Deformation Measured by Dual Ultrasound, Orthopaedics Research Society 2016 (Poster)

Correlating Cervical Magnetic Resonance and Ultrasound Image to Reconstruct Kinematics in-vivo, Orthopedics Research Society 2016 (Poster)

Measurement of C-Spine Kinematics during Simulated Work Conditions using Dual Ultrasound; Oral presentation at 2018 Philadelphia Spine Research Symposium (Oral Presentation)

Dissertations

Daniel A. Buckland, MD, Ph.D. Dissertation, Massachusetts Institute of Technology in Aeronautics and Astronautics (2011) M.D., Harvard Medical School (2014). Ultrasound imaging of cervical spine motion for extreme acceleration environments.

Mingxin Zheng Ph.D. Dissertation, Boston University, College of Engineering. (2018) Development of ultrasound to measure deformation of functional spinal units in cervical spine.

7. Inventions, Patents and Licenses

Provisional Patent Claim

Imaging of Multiple Projection Ultrasound System to measure structural kinematics in human

An ultrasound system complex, comprising:

1. Multiple ultrasound systems synchronized for simultaneous acoustic imaging data acquisition

2. Stereoscopic transducer positioning through mechanical means and/or positioning sensors
3. Dynamic displacement tracking in 3D (3 coordinates) of imaged objects based on raw radio frequency data from each imaging system
4. High resolution long term tracking low error achieved through specialized tracking algorithms

8. Reportable Outcomes

The outcomes were published and presented in several publications, national and international conferences and the multiframe-tracking algorithm were developed operating on Radio Frequency data. The technology were developed and standard operating procedure prepared for transferring the technology to the new testing environments.

9. Other Achievements

Two doctoral dissertations were completed and defended:

Daniel A. Buckland, MD, Ph.D. Dissertation, Massachusetts Institute of Technology in Aeronautics and Astronautics (2011) M.D., Harvard Medical School (2014). Ultrasound imaging of cervical spine motion for extreme acceleration environments.

Mingxin Zheng Ph.D. Dissertation, Boston University, College of Engineering. (2018)
Development of ultrasound to measure deformation of functional spinal units in cervical spine.

One Post-doctoral research fellowship were awarded to Dr. Amin Mohamadi MD, MPH at the Center for Advanced Orthopedic Studies, Beth Israel Deaconess Medical Center and Harvard Medical School

Capstone research project was completed at Boston University School of Biomedical Engineering by Ashlyn Aiello.

10. References

- [1] D. G. Hoy, M. Protani, R. De, and R. Buchbinder, "The epidemiology of neck pain," *Best Pract. Res. Clin. Rheumatol.*, vol. 24, no. 6, pp. 783–792, 2010.
- [2] H. Yang, S. Haldeman, A. Nakata, B. Choi, L. Delp, and D. Baker, "Work-Related Risk Factors for Neck Pain in the US Working Population," *Spine (Phila. Pa. 1976)*, vol. 40, no. 3, pp. 184–192, Feb. 2015.
- [3] H. S. An, K. Masuda, and N. Inoue, "Intervertebral disc degeneration: Biological and biomechanical factors," in *Journal of Orthopaedic Science*, 2006, vol. 11, no. 5, pp. 541–552.
- [4] N. K. Kittusamy and B. Buchholz, "Whole-body vibration and postural stress among operators of construction equipment: A literature review," *Journal of Safety Research*, vol. 35, no. 3, pp. 255–261, 2004.
- [5] J. R. Ledsome, V. Lessoway, L. E. Susak, F. A. Gagnon, R. Gagnon, and P. C. Wing, "Diurnal changes in lumbar intervertebral distance, measured using ultrasound," *Spine (Phila Pa 1976)*, vol. 21, no. 14, pp. 1671–1675, 1996.
- [6] Y. L. Leung, A. L. Roshier, S. Johnson, R. Kerslake, and D. S. McNally, "Demonstration of the appearance of the paraspinal musculoligamentous structures of the cervical spine using ultrasound," *Clin. Anat.*, vol. 18, no. 2, pp. 96–103, 2005.
- [7] D. S. McNally, C. Naish, and M. Halliwell, "Intervertebral disc structure: observation by a novel use of ultrasound imaging," *Ultrasound Med. Biol.*, vol. 26, no. 5, pp. 751–758, 2000.
- [8] C. Naish, R. Mitchell, J. Innes, M. Halliwell, and D. McNally, "Ultrasound Imaging of the Intervertebral Disc," *Spine (Phila. Pa. 1976)*, vol. 28, no. 2, pp. 107–113, 2003.
- [9] M. Kurutz, "In vivo deformability of human lumbar spine segments in pure centric tension, measured during traction bath therapy," *Acta Bioeng. Biomech.*, vol. 4, pp. 219–220, 2003.
- [10] M. Kurutz, "Age-sensitivity of time-related in vivo deformability of human lumbar motion segments and discs in pure centric tension," *J. Biomech.*, vol. 39, no. 1, pp. 147–157, 2006.
- [11] A. Leardini, L. Chiari, U. Della Croce, and A. Cappozzo, "Human movement analysis using stereophotogrammetry," *Gait Posture*, vol. 21, no. 2, pp. 212–225, Feb. 2005.
- [12] M. S. Andersen, D. L. Benoit, M. Damsgaard, D. K. Ramsey, and J. Rasmussen, "Do kinematic models reduce the effects of soft tissue artefacts in skin marker-based motion analysis? An in vivo study of knee kinematics," *J. Biomech.*, vol. 43, no. 2, pp. 268–273, 2010.
- [13] A. Cereatti, U. Della Croce, and A. Cappozzo, "Reconstruction of skeletal movement using skin markers: comparative assessment of bone pose estimators," *J. Neuroeng. Rehabil.*, vol. 3, no. 1, p. 7, Mar. 2006.
- [14] Rahimi A, Morency L-P. 2001. "Reducing drift in parametric motion tracking." Computer Vision, 2001. ICCV 2001. Proceedings. Eighth IEEE International Conference on. Vol. 1.
- [15] Qasim, Muhammad, Raghu N. Natarajan, Howard S. An, and Gunnar B.J. Andersson. 2012. "Initiation and Progression of Mechanical Damage in the Intervertebral Disc under Cyclic Loading Using Continuum Damage Mechanics Methodology: A Finite Element Study." *Journal of Biomechanics* 45 (11): 1934–40.

- [16] Qasim, Muhammad, Raghu N. Natarajan, Howard S. An, and Gunnar B.J. Andersson. 2014. "Damage Accumulation Location under Cyclic Loading in the Lumbar Disc Shifts from Inner Annulus Lamellae to Peripheral Annulus with Increasing Disc Degeneration." *Journal of Biomechanics* 47 (1): 24–31.
- [17] Wheeldon, John A., Frank A. Pintar, Stephanie Knowles, and Narayan Yoganandan. 2006. "Experimental Flexion/extension Data Corridors for Validation of Finite Element Models of the Young, Normal Cervical Spine." *Journal of Biomechanics* 39 (2): 375–80.
- [18] Abramowitch, Steven D. 2004. "An Improved Method to Analyze the Stress Relaxation of Ligaments Following a Finite Ramp Time Based on the Quasi-Linear Viscoelastic Theory." *Journal of Biomechanical Engineering* 126 (1): 92.
- [19] Toms, Stephanie R., Greg J. Dakin, Jack E. Lemons, and Alan W. Eberhardt. 2002. "Quasi-Linear Viscoelastic Behavior of the Human Periodontal Ligament." *Journal of Biomechanics* 35 (10): 1411–15.
- [20] Stemper, Brian D., Jamie L. Baisden, Narayan Yoganandan, Barry S. Shender, and Dennis J. Maiman. 2014. "Mechanical Yield of the Lumbar Annulus: A Possible Contributor to Instability: Laboratory Investigation." *Journal of Neurosurgery: Spine* 21 (4): 608–13.
- [21] M. Zheng, A. Masoudi, D. Buckland, B. Stemper, N. Yoganandan, T. Szabo, and B. Snyder, "Dynamic ultrasound imaging of cervical spine intervertebral discs," *IEEE Int. Ultrason. Symp. IUS*, pp. 448–451, 2014.
- [22] W. Goldberg, C. Mueller, E. Panacek, S. Tigges, J. R. Hoffman, and W. R. Mower, "Distribution and patterns of blunt traumatic cervical spine injury," *Ann. Emerg. Med.*, vol. 38, no. 1, pp. 17–21, 2001.
- [23] A. Masoudi, D. Fama, N. Yoganandan, and B. Snyder, "Methodology to Calibrate Disc Degeneration in the Cervical Spine During Cyclic Fatigue Loading.," *Biomed. Sci. Instrum.*, vol. 51, pp. 222–229, 2015.
- [24] T. R. Derrick, D. Dereu, and S. P. Mclean, "Impacts and kinematic adjustments during an exhaustive run," *Med. Sci. Sport. Exerc.*, vol. 34, no. 6, pp. 998–1002, 2002.
- [25] J. Hamill, T. R. Derrick, and K. G. Holt, "Shock attenuation and stride frequency during running," *Hum. Mov. Sci.*, vol. 14, no. 1, pp. 45–60, 1995.
- [26] L. T. Muftuler, J. P. Jarman, H. J. Yu, V. O. Gardner, D. J. Maiman, and V. E. Arpinar, "Association between intervertebral disc degeneration and endplate perfusion studied by DCE-MRI," *Eur. Spine J.*, vol. 24, no. 4, pp. 679–685, 2015.
- [27] T. L. Bredbenner, T. D. Eliason, W. L. Francis, J. M. McFarland, A. C. Merkle, and D. P. Nicolella, "Development and validation of a statistical shape modeling-based finite element model of the cervical spine under low-level multiple direction loading conditions," *Front. Bioeng. Biotechnol.*, vol. 2, no. November, p. 58, 2014.
- [28] M. B. Panzer and U. of W. D. of M. Engineering, "Numerical Modelling of the Human Cervical Spine in Frontal Impact," p. 263, 2006.
- [29] M. M. Panjabi and A. A. 3rd White, "Clinical biomechanics of the spine," *Clin. Biomech. spine*, 1990.
- [30] N. Yoganandan, S. Kumaresan, L. Voo, and F. A. Pintar, "Finite element applications in human cervical spine modeling.," *Spine (Phila. Pa. 1976)*, vol. 21, pp. 1824–1834, 1996.
- [31] H. W. Ng and E. C. Teo, "Nonlinear finite-element analysis of the lower cervical spine (C4-C6) under axial loading.," *J. Spinal Disord.*, vol. 14, no. 3, pp. 201–10, 2001.
- [32] M. Qasim, R. N. Natarajan, H. S. An, and G. B. J. Andersson, "Damage accumulation location under cyclic loading in the lumbar disc shifts from inner annulus lamellae to

- peripheral annulus with increasing disc degeneration,” *J. Biomech.*, vol. 47, no. 1, pp. 24–31, Jan. 2014.
- [33] A. C. Jones and R. K. Wilcox, “Finite element analysis of the spine: Towards a framework of verification, validation and sensitivity analysis,” *Med. Eng. Phys.*, vol. 30, no. 10, pp. 1287–1304, Dec. 2008.
 - [34] M. B. Panzer and D. S. Cronin, “C4–C5 segment finite element model development, validation, and load-sharing investigation,” *J. Biomech.*, vol. 42, no. 4, pp. 480–490, 2009.
 - [35] T. Pitzén, B. Schmitz, T. Georg, D. Barbier, T. Beuter, W. I. Steudel, and W. Reith, “Variation of endplate thickness in the cervical spine,” *Eur. Spine J.*, vol. 13, no. 3, pp. 235–40, May 2004.
 - [36] J. Noailly, H.-J. Wilke, J. A. Planell, and D. Lacroix, “How does the geometry affect the internal biomechanics of a lumbar spine bi-segment finite element model? Consequences on the validation process,” *J. Biomech.*, vol. 40, no. 11, pp. 2414–2425, 2007.
 - [37] M. Bayer and T. J. Hall, “Variance and covariance of accumulated displacement estimates,” *Ultrason Imaging*, vol. 35, no. 2, pp. 90–108, 2013.
 - [38] M. Bayer, T. J. Hall, L. P. Neves, and A. A. O. Carneiro, “Two-Dimensional Simulations of Displacement Accumulation Incorporating Shear Strain,” *Ultrason. Imaging*, vol. 36, no. 1, pp. 55–73, 2014.
 - [39] T. Benz, M. Kowarschik, and N. Navab, “Kernel-based Tracking in Ultrasound Sequences of Liver,” 2014.
 - [40] T. P. O’Shea, J. C. Bamber, and E. J. Harris, “Temporal regularization of ultrasound-based liver motion estimation for image-guided radiation therapy,” *Med. Phys.*, vol. 43, no. 1, pp. 455–464, 2016.
 - [41] R. Zahiri-azar and S. Salcudean, “Motion Estimation in Ultrasound Images Using Time Domain Cross Correlation With Prior Estimates,” *IEEE Trans. BME*, vol. vol, no. 10, p. 53pp1990-, 2006.
 - [42] H. Rivaz, E. M. Boctor, M. A. Choti, and G. D. Hager, “Ultrasound elastography using multiple images,” *Med. Image Anal.*, vol. 18, no. 2, pp. 314–329, 2014.
 - [43] a. Rahimi, L.-P. Morency, and T. Darrell, “Reducing drift in parametric motion tracking,” *Proc. Eighth IEEE Int. Conf. Comput. Vision. ICCV 2001*, vol. 1, pp. 315–322, 2001.
 - [44] A. Rahimi, L. P. Morency, and T. Darrell, “Reducing drift in differential tracking,” *Comput. Vis. Image Underst.*, vol. 109, no. 2, pp. 97–111, 2008.
 - [45] G. Marini, G. Huber, K. P??schel, and S. J. Ferguson, “Nonlinear dynamics of the human lumbar intervertebral disc,” *J. Biomech.*, vol. 48, no. 3, pp. 479–488, 2015.
 - [46] S. Umale, B. Stemper, M. Zheng, A. Masoudi, D. Fama, N. Yoganandan, and B. Snyder, “Methodology to Calibrate Disc Degeneration in the Cervical Spine During Cyclic Fatigue Loading,” *Biomed. Sci. Instrum.*, vol. 51, pp. 222–229, 2015.
 - [47] J. Village, J. B. Morrison, and D. K. Leong, “Whole-body vibration in underground load-haul-dump vehicles,” *Ergonomics*, vol. 32, no. 10, pp. 1167–1183, 1989.
 - [48] J. H. van Dieën, M. Creemers, I. Draisma, H. M. Toussaint, and I. Kingma, “Repetitive lifting and spinal shrinkage, effects of age and lifting technique,” *Clin. Biomech.*, vol. 9, no. 6, pp. 367–374, Nov. 1994.
 - [49] S. J. Manoogian, E. A. Kennedy, and S. M. Duma, “A Literature Review of Musculoskeletal Injuries to the Human Neck and the Effects of Head-Supported Mass Worn by Soldier,” 2005.

- [50] S. J. Manoogian, E. A. Kennedy, K. A. Wilson, S. M. Duma, and N. M. Alem, "Predicting neck injuries due to head-supported mass," *Aviat. Sp. Environ. Med.*, vol. 77, no. 5, pp. 509–514, May 2006.
- [51] M. A. M. Bandpei, N. Rahmani, B. Majdoleslam, I. Abdollahi, S. S. Ali, and A. Ahmad, "Reliability of surface electromyography in the assessment of paraspinal muscle fatigue: An updated systematic review," *J. Manipulative Physiol. Ther.*, vol. 37, no. 7, pp. 510–521, 2014.
- [52] S. Ostojic, M. Cifrek, V. Medved, and S. Tonkovic, "Clinical Biomechanics Surface EMG based muscle fatigue evaluation in biomechanics," vol. 24, pp. 327–340, 2009.
- [53] Deavers, Michael B., and B. J. McEntire. (1992). An automated method for determining mass properties. USAARL Report No. 93-4. Fort Rucker, AL.
- [54] Cobb JR. Outline for the study of scoliosis. The American Academy of Orthopedic Surgeons Instructional Course Lectures. Vol. 5. Ann Arbor, MI: Edwards; 1948.
- [55] Rigo M. Patient evaluation in idiopathic scoliosis: radiographic assessment, trunk deformity and back asymmetry. *Physiotherapy theory and practice*. 2011 Jan 1;27(1):7-25.
- [56] Lenke LG, Edwards CC, Bridwell KH. The Lenke classification of adolescent idiopathic scoliosis: how it organizes curve patterns as a template to perform selective fusions of the spine. *Spine*. 2003 Oct 15;28(20S):S199-207.

11.Appendices

Full text of publications



Fatigue responses of the human cervical spine intervertebral discs

Narayan Yoganandan^{a,b,*}, Sagar Umale^b, Brain Stemper^b, Bryan Snyder^c

^a Department of Neurosurgery, Medical College of Wisconsin, Milwaukee, WI, United States

^b Department of Orthopaedic Surgery Medical College of Wisconsin, Milwaukee, WI, United States

^c Center for Advance Orthopaedics Studies, Beth Israel Deaconess Medical Center, Boston, MA, United States



ARTICLE INFO

Keywords:

Cyclic loading
Finite element model
Human cervical spine
Internal mechanics
Disc
Viscoelastic response

ABSTRACT

Numerous studies have been conducted since more than fifty years to understand the behavior of the human lumbar spine under fatigue loading. Applications have been largely driven by low back pain and human body vibration problems. The human neck also sustains fatigue loading in certain type of civilian occupational and military operational activities, and research is very limited in this area. Being a visco-elastic structure, it is important to determine the stress-relaxation properties of the human cervical spine intervertebral discs to enable accurate simulations of these structures in stress-analysis models. While finite element models have the ability to incorporate viscoelastic material definitions, data specific to the cervical spine are limited. The present study was conducted to determine these properties and understand the responses of the human lower cervical spine discs under large number of cyclic loads in the axial compression mode. Eight disc segments consisting of the adjacent vertebral bodies along with the longitudinal ligaments were subjected to compression, followed by 10,000 cycles of loading at 2 or 4 Hz frequency by limiting the axial load to approximately 150 N, and subsequent to resting period, subjected to compression to extract the stress-relaxation properties using the quasi-linear viscoelastic (QLV) material model. The coefficients of the model and disc displacements as a function of cycles and loading frequency are presented. The disc responses demonstrated a plateauing effect after the first 2000 to 4000 cycles, which were highly nonlinear. The paper compares these responses with the “work hardening” phenomenon proposed in clinical literature for the lumbar spine to explain the fatigue behavior of the discs. The quantitative results in terms of QLV coefficients can serve as inputs to complex finite element models of the cervical spine to delineate the local and internal load-sharing responses of the disc segment.

1. Introduction

External mechanical loads on the human spinal column can be broadly classified into physiological and traumatic or injury-producing loads. Physiological loading from head-neck perspectives include flexion, extension, lateral bending, and axial rotation bending moments applied in a quasi-static mode (Clark and Benzel, 2005). Rate or time of application of the load vector is not a factor under this mode. The eccentric location of the human head with respect to the sub-axial cervical column consisting of the discs, uncovertebral joints, uncinate type of vertebrae, and facet joints adds the cranial axial compressive force component to the neck (Yoganandan et al., 2009). A considerable majority of biomechanical studies has reported moment-angulation and force-deflection responses of cervical spines under single cycle loads (Clark and Benzel, 2005; Cusick et al., 1988). These studies have assisted in the understanding the responses of normal, diseased, injured, iatrogenically altered, and stabilized spines mimicking surgi-

cal treatments. Traumatic loading of the head-neck complex, in contrast, is associated with the application of acute dynamic forces, i.e., incorporation of the short time factor from a biomechanical perspective. Studies in this area have produced information in the form of peak axial forces and bending moments for the structural failure of the osteoligamentous column (Yoganandan et al., 2014). Injury risk curves have also been derived (Pintar et al., 1998). Tolerance-based studies have assisted in the development of human injury criteria for assessing safety in environments such as motor vehicle crashes, aviation incidents, and underbody blast loads (DeWesse et al., 2007; FMVSS-208, 2001; Yoganandan et al., 2016).

A third mode often encountered in certain civilian occupations such as industrial workplace duties and military operational activities involves cyclic or fatigue loading (Ang and Harms-Ringdahl, 2006; Balasubramanian et al., 2011; Cohen et al., 2012; Cote et al., 2009; Dolan and Adams, 1998; Hardy et al., 1958; Huber et al., 2010; Jones et al., 2000). Numerous cyclic loading studies have been conducted

* Correspondence to: Biomedical Engineering Department of Neurosurgery, Medical College of Wisconsin, Milwaukee, WI 53226, United States.
E-mail address: yoga@mcw.edu (N. Yoganandan).

Table 1
Summary of some literature data from fatigue tests.

First author	Year	Rate (Hz)	Max # of cycles	Load amplitude	Loading mode	Specimen description
Brown	1957	18.3	1000	70 N	axial and eccentric	Lumbar disc segments
Hardy	1958	2.0	1,290,000	400 to 3500 N	compression	Lumbar column
Farfan	1970	0.83	< 144,000 ^a	1, 2, 3, 5, 10 deg	torsion	Lumbar FSU
Cyron	1978	1.7	54,543	380 to 760 N	oblique loading	L3, L4, L5 neural arch
Adams	1983	0.7	9600	1500 to 6000 N	flexion	Lumbar FSU
Liu	1983	0.5	10,000	37 to 80% Failure load	axial	Lumbar FSU
McElhaney	1983	20.0	150	0.7 cm	axial	Base of skull to C5, 6, 7 or T1
Liu	1985	0.5	10,000	1.5°	torsion	Lumbar FSU
McElhaney	1988	1.0	~50	0.7 cm	axial-eccentric	Base of skull or C1 to T1
Gordon	1991	1.5	37,260	combined	flex-rot-compr.	L1-L5 FSU
Yoganandan	1994	0.5	4000	250 N	axial	Lumbar spinal column
Gallagher	2005	0.3	10,020	1000 to 3000 N	axial	Lumbar FSU
Huber	2010	5.0	300,000	0 to 2000 N	axial	L4-L5 FSU

^a Out of 11 specimens, nine were tested up to 3000, one up to 72,000 and the other up to 144,000 cycles.

using human cadaver lumbar spine vertebrae, functional units, and osteoligamentous spinal columns (Adams and Hutton, 1983; Brown et al., 1957; Cyron and Hutton, 1978; Hardy et al., 1958; Lafferty et al., 1977; Liu et al., 1985; Liu et al., 1983; Yoganandan et al., 1994). They have been primarily targeted to low back pain and vibration-related issues. A non-inclusive summary is given (Table 1). Intervertebral joint components, including discs and endplates, susceptible to injury under axial and eccentric loads have been identified in these studies. However, this type of external insult to the cervical spine is the one of the least researched topics in biomechanics. The present study is focused on this type of insult.

With reference to the cervical spine, human cadaver specimens have been tested to “approximately 50 cycles” of compressive displacements in one and 150 cycles in another experimental series (McElhaney et al., 1988, 1983). Moment versus cycle curves, cyclic modulus and relaxation stiffness data were reported. These tests were done in conjunction with failure tests, and the authors also reported preliminary injury tolerances. However, studies better characterizing the viscoelastic responses are sparse and with large number of cycles, which occur in civilian and military operational environments. The present study further focuses on large cyclic load applications.

It is well known that the human spinal intervertebral disc is the major load transferring medium between the various subaxial vertebrae in the osteoligamentous column (Pal and Routal, 1986). It is also known to be viscoelastic (Virgin, 1951). Consequently, it is important to first investigate fatigue properties of intervertebral discs before determining the cyclic responses of functional units and osteoligamentous cervical column. Thus, the objective of this study is to determine the fatigue loading properties of the human cervical spine intervertebral discs. Responses are characterized in terms of pre- and post-cycle stress-relaxation, and disc displacements patterns.

2. Methods

Post mortem human subjects were approved by the Institutional Review Board (IRB) for this study. Cervical spinal columns were procured, and x-rays and computed tomography scans were obtained at 0.625 mm intervals. The spinal columns were isolated to excise the C4-C5 and C6-C7 functional spinal units. The pedicles were transected to obtain adjacent vertebral bodies and the intervening disc, along with the anterior and posterior longitudinal ligaments. The caudal and rostral vertebrae were embedded in poly-methyl-methacrylate. The specimens were placed on an x-y cross table. The entire preparation including the x-y cross table was mounted in a sealed environment chamber, completely immersing the specimen in a heated saline bath at 37° C. A schematic of the experimental setup is shown (Fig. 1). The specimens were allowed to acclimatize in the chamber for approximately one hour before testing. They were pre-conditioned, x-rays were

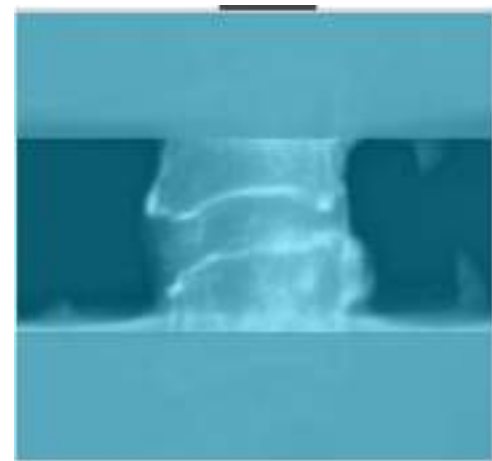


Fig. 1. Radiograph of a disc segment showing the disc and the adjacent vertebrae embedded in PMMA at the ends. The specimen was submerged in a heated bath, shown in blue tint.

taken, and compressed to determine the stress-relaxation properties. Relaxation tests used ramp and hold command signals consisting of five second rise time and maintaining at ten percent strain for 1800 s. Following 15 min of settling time, compressive cyclic loads were applied at a frequency of 2 Hz or 4 Hz for 10,000 cycles. The shape of the loading pulse was one-half sinusoidal waveform. The applied force was limited to approximately 150 N. Viscoelastic tests were repeated following cyclic loading tests. The applied load and displacement signals were recorded using a uniaxial load cell and a linear variable differential transducer, both attached in-series to the electro-hydraulic piston of the testing device (model 359, MTS corp., Eden Prairie, MN). The configuration of the device was such that the piston applied the load from the top crosshead. The axial force and displacement signals were recorded using a digital data acquisition system (DTS Corp., Seal Beach, CA) at the rate of 100 samples per second. The displacement of the specimen as a function of the number of cycles was extracted from the fatigue/cyclic loading tests. The loss of height of the disc following the cyclic loading process was determined. Viscoelastic properties of the disc segment before and after the cyclic load application were derived. The quasi-linear viscoelastic (QLV) material model was used to fit the stress-relaxation data, and the material property constants were compared for each disc level and frequency. The material model estimated the response of the specimen as a stress-relaxation function in terms of various coefficients, described by the QLV formulation.

A quasi-linear viscoelastic material model was used to fit the stress relaxation data and the material parameters were obtained (Toms

et al., 2002). The QLV theory models the viscoelastic response of a material based on a stress relaxation function and the instantaneous stress resulting from a ramp strain and is given as:

$$\sigma(t) = G(t) \times \sigma^e(\epsilon) \quad (1)$$

where $\sigma(t)$ is the stress at any time t , $\sigma^e(\epsilon)$ is the stress corresponding to an instantaneous strain, is $G(t)$ the reduced relaxation function representing the stress of the material divided by the stress after the initial ramp strain. Applying convolution integral over the complete stress history over time, substituting Gas the reduced relaxation function and integrating from t_0 (time at peak strain) to t (end of stress relaxation curve) one obtains the following relationship [12],

$$\sigma(t > t_0) = AB\gamma \left[\frac{ae^{-bt}e^{(b+B\gamma)t_0}}{b+B\gamma} + \frac{ce^{-dt}e^{(d+B\gamma)t_0}}{d+B\gamma} + \frac{ge^{-ht}e^{(h+B\gamma)t_0}}{h+B\gamma} \right] - AB \left[\frac{ae^{-bt}}{b+B\gamma} + \frac{ce^{-dt}}{d+B\gamma} + \frac{ge^{-ht}}{h+B\gamma} \right] \quad (2)$$

Where a , b , c , d , g , h are constants for reduced stress relaxation function and A , B are constants representing instantaneous stress response. This analytical form shown in Eq. (2) was used in this study to optimize the QLV material parameters in Matlab (The Mathworks Inc., Natick, MA) software. The parameters were optimized with the experimental curve using the Matlab function *fminsearch*.

Pre-test x-rays were used to measure disc heights. Posttest x-rays were obtained immediately after taking the specimen out of device. An experienced observer made all measurements. The consistency was estimated using the coefficient of repeatability metric. The coefficient of repeatability was 0.65 across all measurements.

3. Results

The mean age, total body mass, stature and body mass index of seven post mortem human subjects were 52.7 ± 11.7 years, 82.4 ± 31.2 kg, 166.2 ± 10.6 cm, 20.2 ± 8.4 kg/m², respectively. The cervical spinal columns and excised segments were of normal curvature for the age and without the formation of bridging osteophytes at subaxial levels. The sample size consisted of two specimens each for disc segment at each cyclic loading frequency. Tables 2 and 3 show the disc geometry details for C4-C5 and C6-C7 specimens.

Table 2
Summary of data for C4-C5 disc segments.

ID/ frequency Hz	Pre-test disc height (mm)					
	Anterior	Posterior	Middle	Anterior middle	Posterior middle	Mean
1/2	5.48	4.26	7.21	6.26	5.61	5.76
2/4	5.21	3.15	5.54	5.57	5.12	5.34
3/2	5.60	2.99	4.87	4.63	5.34	4.80
4/2	5.29	5.21	6.36	5.43	6.07	5.18
Ave	5.40	3.90	6.00	5.47	5.54	5.27
SD	0.18	1.04	1.01	0.67	0.41	0.40
Mean 4 Hz	5.35	3.71	6.38	5.92	5.37	5.55
SD 4 Hz	0.19	0.78	1.18	0.49	0.35	0.30
Mean 2 Hz	5.45	4.10	5.62	5.03	5.71	4.99
SD 2 Hz	0.22	1.57	1.05	0.57	0.52	0.27
Posttest disc height (mm)						
1/2	5.30	3.88	6.87	6.31	5.12	5.50
2/4	4.99	3.13	5.57	5.77	4.71	4.83
3/2	5.54	2.59	4.80	4.41	4.62	4.39
4/2	5.15	4.07	6.13	4.87	5.66	5.18
Ave	5.25	3.42	5.84	5.34	5.03	4.97
SD	0.23	0.68	0.88	0.86	0.47	0.47
Mean 4 Hz	5.15	3.51	6.22	6.04	4.92	5.17
SD 4 Hz	0.22	0.53	0.92	0.38	0.29	0.47
Mean 2 Hz	5.35	3.33	5.47	4.64	5.14	4.78
SD 2 Hz	0.28	1.05	0.94	0.33	0.74	0.55

Table 3
Summary of data for C6-C7 disc segments.

ID/ frequency Hz	Pre-test disc height (mm)					
	Anterior	Posterior	Middle	Anterior middle	Posterior middle	Mean
1/2	4.15	3.89	4.55	3.49	4.01	4.02
2/4	4.20	3.47	6.53	5.95	5.73	5.18
3/2	5.06	3.20	4.98	3.85	4.35	4.29
4/2	5.29	3.56	6.70	4.96	6.16	5.33
Ave	4.68	3.53	5.69	4.56	5.06	4.70
SD	0.59	0.28	1.08	1.12	1.04	0.65
Mean 4 Hz	4.18	3.68	5.54	4.72	4.87	4.60
SD 4 Hz	0.04	0.30	1.40	1.74	1.22	0.82
Mean 2 Hz	5.18	3.38	5.84	4.41	5.26	4.81
SD 2 Hz	0.16	0.25	1.22	0.78	1.28	0.74
Posttest disc height (mm)						
1/2	4.09	3.71	4.30	3.21	3.61	3.78
2/4	4.05	3.35	6.33	5.86	6.14	5.15
3/2	5.14	1.74	4.39	2.63	3.61	3.50
4/2	5.09	3.51	6.64	4.67	6.14	5.21
Ave	4.59	3.08	5.42	4.09	4.88	4.41
SD	0.60	0.90	1.24	1.46	1.46	0.89
Mean 4 Hz	4.07	3.53	5.32	4.54	4.88	4.47
SD 4 Hz	0.03	0.25	1.44	1.87	1.79	0.96
Mean 2 Hz	5.12	2.63	5.52	3.65	4.88	4.36
SD 2 Hz	0.04	1.25	1.59	1.44	1.79	1.21

The decrease in disc heights post cyclic loading for the C4-C5 and C6-C7 disc segments are given (Table 4). Fig. 2 and Fig. 3 show the applied force and obtained displacement during cyclic loadings at 2 Hz and 4 Hz respectively. Fig. 4 shows the nonlinear variation of the intervertebral disc height compression as a function of the number of cycles. Fig. 5a and b demonstrate pre- and post-cyclic force and displacement data at 2 Hz. Similarly Fig. 7a and b demonstrate these data, applied to segments tested at 4 Hz pre- and post-cyclic tests. Stress-relaxation curves comparing the pre- and post-cyclic loading tests are shown (Figs. 6 and 8). Viscoelastic property data defining the response via six coefficients of the QLV model are tabulated for pre- and post-cyclic loading tests (Table 5).

4. Discussion

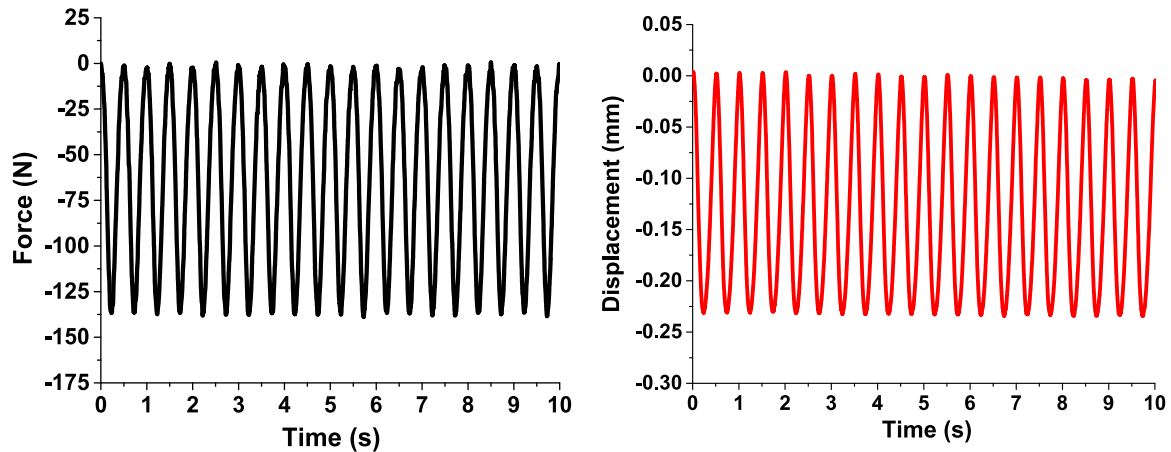
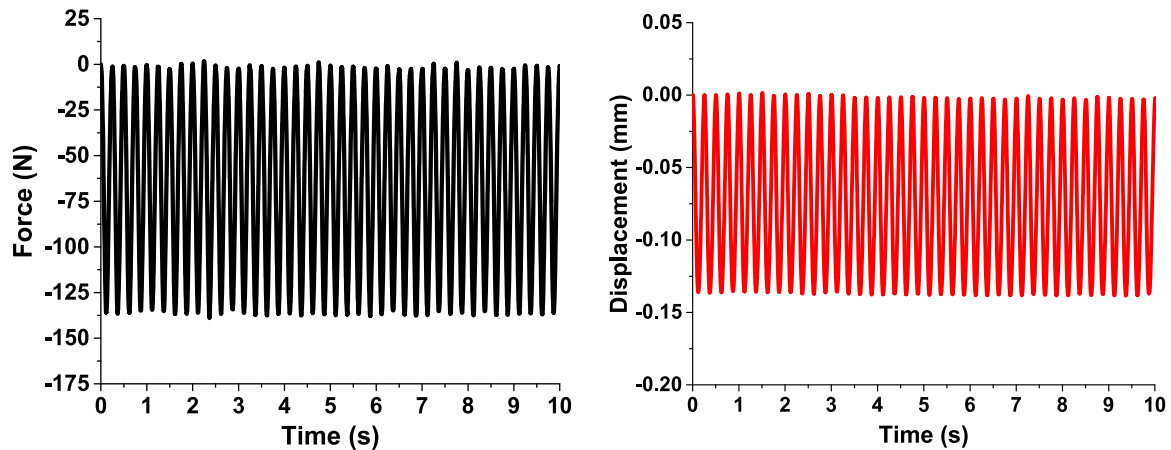
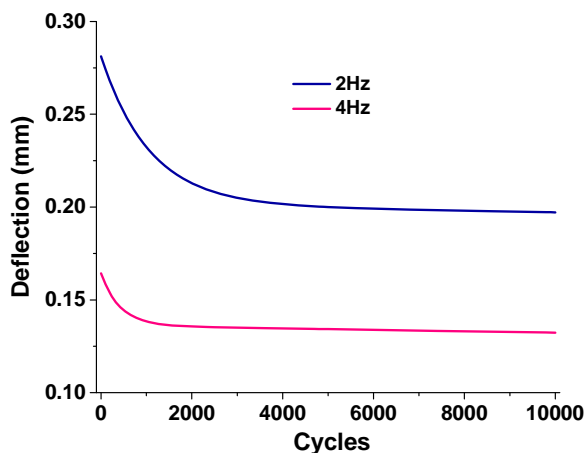
4.1. General

As stated in the introduction, the objective of this study was to determine the fatigue properties of human cervical spine intervertebral discs for civilian occupation- and military operation-related applications. Axial forces were applied to the preparation, as this mode of loading exists in vivo, although sagittal bending moments also act on the human cervical osteoligamentous column. The present results are therefore, applicable only to the axial mode. While lumbar spine tests have largely used functional spinal units, in the present study, the posterior complex was excised for testing the disc segment. The superior-to-inferior facet joint orientations in the lumbar spine are different from the superior-to-medial orientation in the cervical spine, i.e., sagittal versus transverse (Clark and Benz, 2005). Inclusion of these joints along with the posterior vertebral components complicates the experimental design. Fixations of the caudal and rostral vertebrae in PMMA to ensure that the disc and facet joints are unconstrained pose challenges, as the cervical spine structural and geometrical anatomy is smaller than the lumbar spine. More importantly, it is difficult to extract the fatigue mechanical/structural properties of the disc from a functional spinal unit experimental model. From this perspective, the present results are directly applicable to the disc joint of the intervertebral unit. As facet joints also resist and contribute to the load carrying capacity of the spine, it is necessary to determine their

Table 4

Decrease in disc height (%) due to fatigue loading.

Level/frequency	Anterior	Posterior	Middle	Anterior middle	Posterior middle	Mean
C4-C5/both Hz	2.8	12.4	2.5	2.4	9.2	5.6
C4-C5/4 Hz	3.7	5.4	2.4	-2.1	8.4	7.0
C4-C5/2 Hz	1.8	18.8	2.7	7.8	9.9	4.1
C6-C7/both Hz	1.8	12.8	4.8	10.3	3.7	6.2
C6-C7/4 Hz	2.5	4.1	4.1	3.9	-0.1	2.9
C6-C7/2 Hz	1.2	22.3	5.6	17.1	7.2	9.5

**Fig. 2.** Force and displacement plots for cyclic tests at 2 Hz.**Fig. 3.** Force and displacement plots for cyclic tests at 4 Hz.**Fig. 4.** Variation of disc height with loading cycles at the two frequencies.

role in resisting cyclic loads across the entire intervertebral joint (Pal and Routal, 1986). This is the next research study.

4.2. Loading

Studies have assumed that 74–80 N of axial compressive force acts on the lower cervical spine under physiologic conditions (Kumaresan et al., 2001; Moroney et al., 1988). The weight of the head and neck is approximately 77 N (Plagenhoef et al., 1983). Studies have reported that the mean weight of the human head is 46 ± 7 N, peak weight 64 N (Yoganandan et al., 2009). The weight of the visor and communications combo varies from 11 to 20 N, medium size army combat helmet weighs 15 N, and PVS systems weigh from 17 to 23 N (Jones et al., 2000). The load acting on the C2-C3 disc with the head-helmet system is reported to be approximately 138 N (Motiwale et al., 2016). Thus, the compressive force of 150 N (loading across the entire cycles 148 ± 4.6 N) used for applying the compressive fatigue load and the ensuing results are in-line and applicable to the military populations. However,

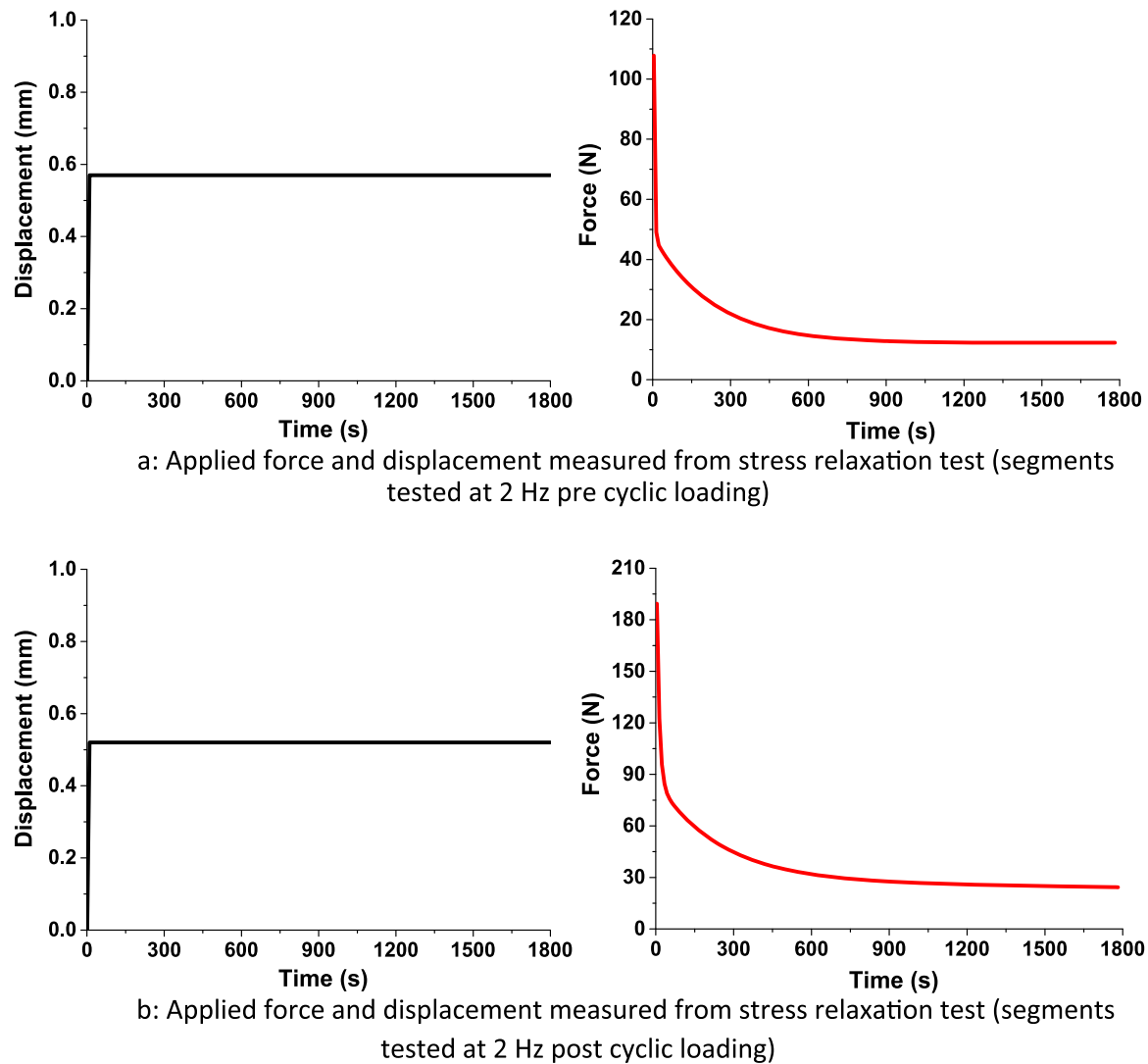


Fig. 5. a: Applied force and displacement measured from stress relaxation test (segments tested at 2 Hz pre cyclic loading) b: Applied force and displacement measured from stress relaxation test (segments tested at 2 Hz post cyclic loading).

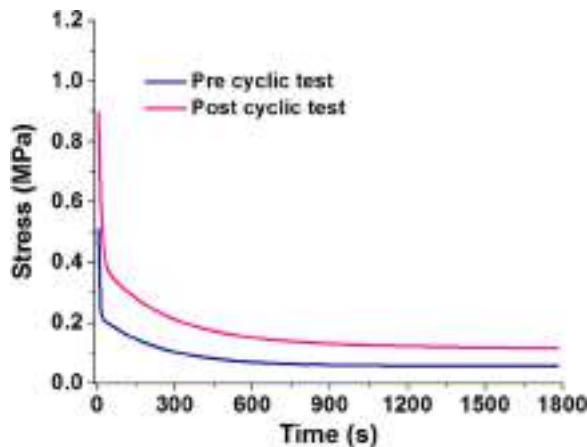


Fig. 6. Stress-relaxation data at 2 Hz.

they can also be considered to be appropriate for certain occupational activities in the civilian domain. Based on the typical length of a loaded march required to gain the Expert Infantryman Badge and assuming a helmeted soldier to walk 19 km, the estimated number of cycles is reported to be 11,000 (Motiwale et al., 2016). The use of 10,000 cycles is in line with this finding.

4.3. Environment

Previous studies have generally used the same type of environment for single cycle and fatigue loading tests. While it is necessary and generally sufficient to keep the specimen moist in the former loading paradigm, it is inadequate in the latter because of the longer time factor involved in conducting fatigue tests (Yoganandan et al., 1988). As described in the introduction (and Table 1, not all inclusive list), testing periods for specimens of the lumbar spine have extended up to 48 h (Farfan et al., 1970; Huber et al., 2010). In the present study, it was deemed necessary to keep the specimen continuously hydrated over the entire fatigue loading process. The hydration was at body temperature simulating in vivo conditions. Thus, the model is more physiologic with the acknowledgment that the specimens were excised from human cadavers, the only scaling independent human anatomic experimental model to determine properties reported in this study (Race et al., 2000) (Fig. 7).

4.4. Response

A comparison of the disc height loss due to cyclic loading indicated greater nonlinearity at the lower frequency, as demonstrated by the delayed plateauing effect (Figs. 6 and 8). This is typical of biological materials, although the specific response demonstrating delay is some-

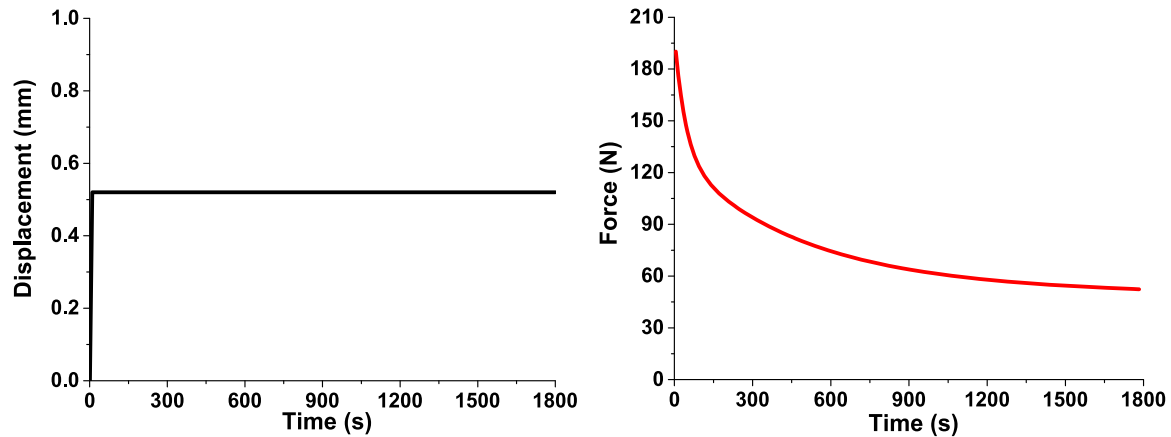
Table 5
QLV model coefficients.

Description	A	B	a	b	c	d	g	h
C4-C5 pre	1.079E-02	4.516E+00	2.063E-01	1.289E-01	1.472E-01	4.122E-03	7.966E-02	2.784E-05
C6-C7 pre	2.122E-02	4.023E+00	1.743E-01	4.058E-02	1.482E-01	2.349E-03	8.355E-02	6.177E-05
C4-C5 2 Hz	2.076E-02	4.294E+00	2.137E-01	1.108E-01	1.137E-01	4.806E-03	5.871E-02	4.715E-05
C6-C7 2 Hz	4.413E-02	3.230E+00	3.081E-01	6.190E-02	2.659E-01	3.184E-03	8.516E-02	-7.980E-05
C4-C5 4 Hz	4.393E-03	7.860E+00	1.587E-01	4.244E-02	1.610E-01	3.313E-03	6.651E-02	5.660E-05
C6-C7 4 Hz	1.789E-02	4.897E+00	1.262E-01	1.066E-01	1.017E-01	4.926E-03	7.631E-02	7.035E-05
variance	0.65	0.28	0.35	0.66	0.52	0.36	0.49	0.15

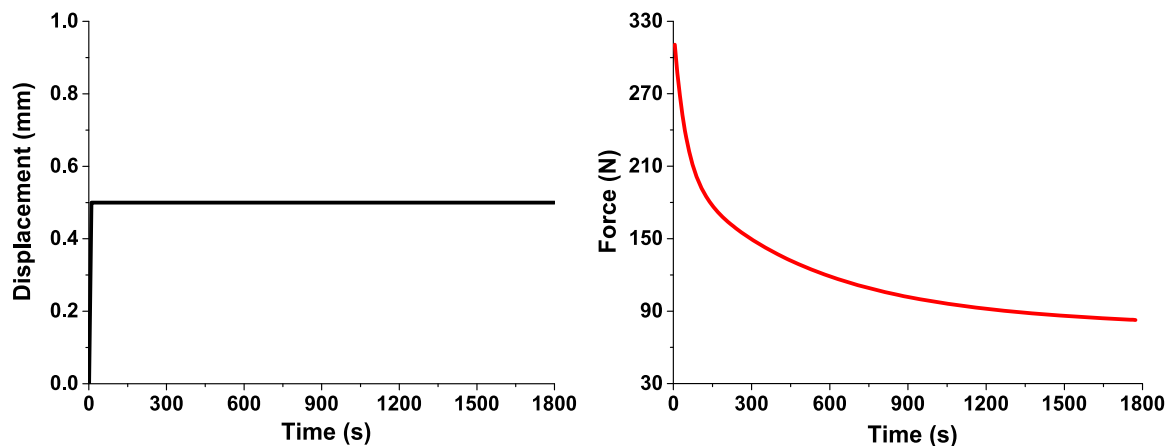
what atypical (discussed later). In general, the viscoelastic response was highly non-linear in the initial stages of cyclic loading, showing stabilization between 2000 and 4000 cycles. A similar plateauing effect early in the cyclic loading period is also observed in the human cadaver lumbar spine experiments, suggesting a commonality in the regional intervertebral fatigue response. For example, an earlier study reported that lumbar intervertebral joints under axial twist response stabilizes during the first 1500 to 3000 cycles (Farfan et al., 1970). Another study showed that stabilization occurs within 3000 cycles (Liu et al., 1985). A study using entire lumbar columns reported plateauing effects to occur between 1000 and 2000 cycles (Yoganandan et al., 1994). The authors

found that the axial stiffness was statistically significantly greater in the first 2000 cycles. The varying nature of the plateauing effect may be attributed to the differing cycles, loading magnitude, experimental model, and spinal regional anatomy and structure, i.e., lumbar versus cervical spine.

In the present cervical spine disc segment study, the initial considerable drop off or increased loss of disc height followed by a more plateauing with continued cycles of loading indicates the strain hardening of the disc itself, with the acknowledgement that the anterior and posterior ligaments are silent under compression because of their uniaxial responsive nature. The plateauing represents the initial, slow,



a: Applied force and displacement measured from stress relaxation test (segments tested at 4 Hz pre cyclic loading)



b: Applied force and displacement measured from stress relaxation test (segments tested at 4 Hz post cyclic loading)

Fig. 7. a: Applied force and displacement measured from stress relaxation test (segments tested at 4 Hz pre cyclic loading) b: Applied force and displacement measured from stress relaxation test (segments tested at 4 Hz post cyclic loading).

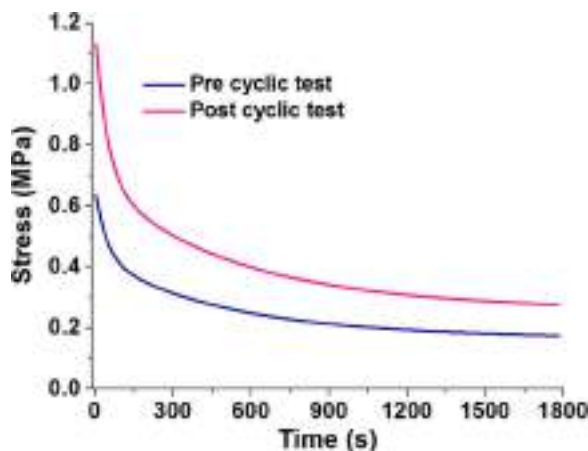


Fig. 8. Stress-relaxation data at 4 Hz.

cumulative alterations to the annulus, nucleus, and endplates, although their integrity was maintained. With compressive loading, the annulus fibers bulge outward while the nucleus exerts pressures on the inner fibers and adjacent endplates. With increasing cycles up to the plateauing region, this phenomenon continues to develop resulting in the decrease in displacement, and after stabilization, the decrease rate tends to be slower. The plateauing phenomenon was also reported in the lumbar spine functional units (decrease in torque with increasing cycles) under torsional cyclic loads. This phenomenon was termed as “work hardening” in clinical literature (Farfan et al., 1970). From this perspective, the current results have shown that the fatigue response follows similar mechanics principles between the two spinal regions and loading modes. Because of sample size limitations, it is not appropriate to comment on the statistical significance and the exact level of the plateauing effect. Factors such as disc health/degeneration quality, bone mineral density, curvature of the column, and sex of the subject may also play a role. It is known that the structural anatomy of the female spine is different from the male, and in addition, biomechanical responses under single cycle loading are also different between men and women from segmental kinematics perspectives (Cusick et al., 2001; Katz et al., 1975; Liguoro et al., 1994; Stemper et al., 2003; Stemper et al., 2008; Yoganandan et al., 2001; Yoganandan et al., 2006a; Yoganandan et al., 2006b). Thus, additional experiments are needed to determine the role of these issues on the fatigue properties of the human cervical spine. The present results have laid a foundation to explore this line of research. With the increasing female population in the military and recognizing that head protective devices have differing effects on men and women, it is necessary to conduct experiments using female-only spines to delineate their fatigue loading-related characteristics.

Post cyclic test images showed no evidence of fracture, indicating that the specimen resisted the fatigue load without failure, i.e., stable from a clinical perspective. These findings parallel those observed in lumbar functional unit studies under axial loading, wherein stable specimens sustained 12,000 cycles of loading (Liu et al., 1983). Thus it can be concluded that the PMHS cervical spine segments subjected to axial fatigue loading at 150 N compressive force in a hydrated chamber can sustain 10,000 cycles without loss of integrity. Failure may occur at higher cycles, which should be determined in future studies to delineate responses focused on tolerance investigations. Advancements have been made in imaging technologies to measure in vivo spine geometry (van Eerd et al., 2014). Studies have shown that the ultrasound can capture disc heights in an academic laboratory setting with human research volunteers performing cyclic loading exercises (Zheng et al., 2016). It is possible to use such techniques to examine the disc height subsequent to military operational maneuvers as subject recruitments can be confined to military personnel, volun-

teers are relatively younger and healthier, and discs are normally fully desiccated. Correlations of in vivo measurements (pre- and post-operations) with current PMHS data and perhaps finite element modeling efforts may lead to safety improvements in these environments. This is a likely application of the present investigation from clinical perspectives.

4.5. QLV relationships and potential applications

The QLV parameters represent the entire disc structure. The viscoelastic model chosen in this study to describe the material properties of the disc is widely used in biomechanics (Fung, 1981). The model coefficients in the QLV formulation represent the elastic and time-varying parameters of the tissue under consideration. All the reported coefficients from the model can be incorporated into finite element commercial software such as LS DYNA and ABAQUS. LS DYNA software has inbuilt quasi linear viscoelastic material (MAT_176, LS-DYNA manual) formulation developed for soft biological tissues, which reads the instantaneous stress relaxation response or uses the material parameters in Section 3 of the “material card.” Although other material models in LS DYNA use the QLV parameters in conjunction with other material formulations, their use is limited in spine applications (Untaroiu et al., 2012). Similarly, the viscoelastic module in ABAQUS also reads in the instantaneous stress relaxation response in time domain and generates the material coefficients. A custom material formulation can be developed in finite element solvers based on the formulation provided in Eq. (2). From this perspective, the present results on the coefficients of the model are valuable to future finite element modelers of the cervical spine. Once the formulation with the described constants are implemented in a solver, it would be possible to determine the stress-analysis responses of the cervical spine by incorporating the viscoelastic properties specific to cervical discs extracted from cervical spine experiments. Thus, this effort may be considered as the availability of fundamental material property data for future finite element models.

Although finite element modeling of the cervical spine has been an area of research for more than two decades, it has not been fully extended to the fatigue loading domain, regardless of the application, civilian or military (Yoganandan et al., 1996a). This is perhaps due to the lack of characterization cervical spine-specific properties. Cervical spine models have traditionally adopted disc geometry and/or material properties from lumbar spine and simulated the disc as a solid structure with varying details (Kumaresan et al., 2001; Kumaresan et al., 1997b; Osth et al., 2016; Panzer and Cronin, 2009; Teo and Ng, 2001; Voo et al., 1997; Yoganandan et al., 1996a, 1997, 1996b). The present results can be used to determine the internal responses of cervical spines, obviating the need to use lumbar spine data. Poroelastic models accounting for the fluid phase are being reported for lumbar spine responses, although full range of data does not exist to exercise these models (Natarajan et al., 2008). Comparisons have not been made between visco- and poroelastic responses with loading frequency, although research is done in other areas (McGarry et al., 2015). As described in the lumbar literatures, and acknowledging the paucity of published cervical spine poroelastic models, the next step would be to determine cervical spine-specific data for poroelastic models. Combining present time-dependent results with a poroelastic material formulation would be another step. In the meantime, the gross disc properties from this study can be used as a first step to understand the solid-phase of the cervical response through modeling.

The annular layer arrangements of the human cervical spine discs are different from the lumbar spine, and in addition, the location of the nucleus pulposus is different between the two regions of the human vertebral column (Browne, 2010; Mercer and Bogduk, 1999). The presence of uncovertebral joints, only present in the cervical spine, alters the stress distribution and load-paths within the neck disc (Clausen et al., 1997; Hall, 1965; Kumaresan et al., 1997a). The

Sharpey's fibers are also different between the two regions, and very few studies have examined these fibers in the cervical spine. Further, finite element models have not traditionally used the viscoelastic/QLV formulation for inputting the mechanical properties for the cervical intervertebral disc (Yoganandan et al., 1996a). The global human body model consortium has also used simplified definitions for the disc (Panzer and Cronin, 2009; Schwartz et al., 2015). While all these issues are not addressed herein as it is outside the scope of this investigation, the viscoelastic coefficients reported in the results section can be easily incorporated in future finite element models, a principal outcome of the study. Because spinal disorders such as herniation, radiculopathy, and myelopathy are generally focused at the lower cervical vertebral levels, and as tests were done at these levels, data from the current study can be used in stress-analysis modeling of the cervical spine under fatigue loading. This study provides mechanical property data from pre- and sub-injury post-cyclic loadings. The threshold of head supported mass resulting in injuries is not known. Additional studies are needed with increasing cycles to determine injury thresholds, and such data may help the designer of the head supported mass and or personnel in charge of administering training or combat activities.

4.6. Stiffness comparison

Indentation tests were done using 93 C3-T1 discs in a study, wherein reduced relaxation coefficients were given for G_4 and G_∞ parameters (Lucas et al., 2006). Axial loads were applied in a study to the skull base to C4-T1 preparations at 20 Hz for 150 cycles (McElhaney et al., 1983). The initial stiffness was 320 N/mm for one specimen. The stiffness at 150 cycles ranged from 128 to 225 N/mm for all samples. Another study tested functional units and disc segments from C2 to T1 (Moroney et al., 1988). The mean quasistatic compressive stiffness for the disc segment was 492 ± 472 N/mm. The mean stiffness of the disc joint was 37% of the functional unit. A separate study tested functional units under axial loading (Yoganandan et al., 1985). The mean stiffness was 665 N/mm. Using the above conversion factor, the stiffness of the disc joint is estimated to be 250 N/mm. The initial stiffness of (396 ± 103 N/mm) in this study compares favorably with previous data. The final stiffness cannot be compared as specimens in previous studies were not subjected to the same number of cycles.

While the present study provides valuable mechanical property data on cervical spinal discs, it is only a first step in the understanding of the complex and multi-dimensional responses of the spine. Future studies should include factors such as multi-axis loading paradigms and anisotropic properties.

Acknowledgments

This material is the result of work supported with resources and use of facilities at the Zablocki VA Medical Center (ZVAMC), Milwaukee, Wisconsin, the Department of Neurosurgery at the Medical College of Wisconsin (MCW), and the U.S. Army Medical Research and Materiel Command Fort Detrick, Maryland, W81XWH-16-1-0010 and W81XWH-13-1-0050 (experiments). The MCW authors are part time employees of the ZVAMC. Any views expressed in this article are those of the authors and not necessarily representative of the funding organizations.

References

Adams, M.A., Hutton, W.C., 1983. The effect of fatigue on the lumbar intervertebral disc. *J. Bone Jt. Surg. Br.* 65, 199–203.
 Ang, B., Harms-Ringdahl, K., 2006. Neck pain and related disability in helicopter pilots: a survey of prevalence and risk factors. *Aviat. Space Environ. Med.* 77, 713–719.
 Balasubramanian, V., Dutt, A., Rai, S., 2011. Analysis of muscle fatigue in helicopter pilots. *Appl. Ergon.* 42, 913–918.
 Brown, T., Hansen, R.J., Yorra, A.J., 1957. Some mechanical tests on the lumbosacral

spine with particular reference to the intervertebral discs; a preliminary report. *J. Bone Jt. Surg. Am.* 39A, 1135–1164.
 Browne, K.M., 2010. The anatomy, spatial relationships, and role of uncovertebral articulations as the source of posterolateral cervical cartilage sequestrations. *J. Neurosurg. Spine* 12, 270–274.
 Clark, C.R., Benz, E.C., 2005. *The Cervical Spine*. Lippincott Williams & Wilkins, MD.
 Clausen, J.D., Goel, V.K., Traynelis, V.C., Scifert, J., 1997. Uncinate processes and Luschka joints influence the biomechanics of the cervical spine: quantification using a finite element model of the C5–C6 segment. *J. Orthop. Res.: Off. Publ. Orthop. Res. Soc.* 15, 342–347.
 Cohen, S.P., Gallagher, R.M., Davis, S.A., Griffith, S.R., Carragee, E.J., 2012. Spine-area pain in military personnel: a review of epidemiology, etiology, diagnosis, and treatment. *The spine journal: official journal of the North American Spine Society* 22, 833–842.
 Cote, P., van der Velde, G., Cassidy, J.D., Carroll, L.J., Hogg-Johnson, S., Holm, L.W., Carragee, E.J., Haldeman, S., Nordin, M., Hurwitz, E.L., Guzman, J., Peloso, P.M., 2009. The burden and determinants of neck pain in workers: results of the Bone and Joint Decade 2000–2010 Task Force on Neck Pain and Its Associated Disorders. *J. Manip. Physiol. Ther.* 32, S70–S86.
 Cusick, J.F., Pintar, F.A., Yoganandan, N., 2001. Whiplash syndrome: kinematic factors influencing pain patterns. *Spine* 26, 1252–1258.
 Cusick, J.F., Yoganandan, N., Pintar, F., Myklebust, J., Hussain, H., 1988. Biomechanics of cervical spine facetectomy and fixation techniques. *Spine* 13, 808–812.
 Cyron, B.M., Hutton, W.C., 1978. The fatigue strength of the lumbar neural arch in spondylolysis. *J. Bone Jt. Surg. Br.* 60B, 234–238.
 DeWesse, R., Moorcraft, D., Green, T., 2007. Assessment of injury potential in side facing seats using the ES-2 anthropomorphic test dummy, DOT/FAA/AM-07/13, Office of Aerospace Medicine, Washington, DC 20591.
 Dolan, P., Adams, M.A., 1998. Repetitive lifting tasks fatigue the back muscles and increase the bending moment acting on the lumbar spine. *J. Biomech.* 31, 713–721.
 Farfan, H.F., Cossette, J.W., Robertson, G.H., Wells, R.V., Kraus, H., 1970. The effects of torsion on the lumbar intervertebral joints: the role of torsion in the production of disc degeneration. *J. Bone Jt. Surg. Am.* 52, 468–497.
 FMVSS-208, 2001. Federal Motor Vehicle Safety Standards. US Government, Washington, DC USA, (<https://www.gpo.gov/fdsys/granule/CFR-2011-title49-vol6/CFR-2011-title49-vol6-sec571-208>).
 Fung, Y.C., 1981. *Biomechanics: Mechanical Properties of Living Tissues*. Springer, New York.
 Hall, M.C., 1965. *Luschka's Joint*. Springfield, Thomas.
 Hardy, W.G., Lissner, H.R., Webster, J.E., Gurdjian, E.S., 1958. Repeated loading tests of the lumbar spine; a preliminary report. *Surg. forum* 9, 690–695.
 Huber, G., Skrzypiec, D.M., Klein, A., Puschel, K., Morlock, M.M., 2010. High cycle fatigue behaviour of functional spinal units. *Ind. health* 48, 550–556.
 Jones, J.A., Hart, S.F., Baskin, D.S., Effenhauser, R., Johnson, S.L., Novas, M.A., Jennings, R., Davis, J., 2000. Human and behavioral factors contributing to spine-based neurological cockpit injuries in pilots of high-performance aircraft: recommendations for management and prevention. *Mil. Med.* 165, 6–12.
 Katz, P.R., Reynolds, H.M., Foust, D.R., Baum, J.K., 1975. Mid-sagittal dimensions of cervical vertebral bodies. *Am. J. Phys. Anthropol.* 43, 319–326.
 Kumaresan, S., Yoganandan, N., Pintar, F., 1997a. Methodology to quantify human cervical spine uncovertebral joint anatomy. *J. Musculoskelet. Res.* 1, 131–139.
 Kumaresan, S., Yoganandan, N., Pintar, F.A., Maiman, D.J., Goel, V.K., 2001. Contribution of disc degeneration to osteophyte formation in the cervical spine: a biomechanical investigation. *J. Orthop. Res.: Off. Publ. Orthop. Res. Soc.* 19, 977–984.
 Kumaresan, S., Yoganandan, N., Pintar, F.A., Voo, L.M., Cusick, J.F., Larson, S.J., 1997b. Finite element modeling of cervical laminectomy with graded facetectomy. *J. Spinal Disord.* 10, 40–46.
 Lafferty, J.F., Winter, W.G., Gambaro, S.A., 1977. Fatigue characteristics of posterior elements of vertebrae. *J. Bone Jt. Surg. Am.* 59, 154–158.
 Liguoro, D., Vandermeersch, B., Guerin, J., 1994. Dimensions of cervical vertebral bodies according to age and sex. *Surg. Radiol. Anat.: SRA* 16, 149–155.
 Liu, Y.K., Njus, G., Buckwalter, J., Wakano, K., 1983. Fatigue response of lumbar intervertebral joints under axial cyclic loading. *Spine* 8, 857–865.
 Liu, Y.K., Goel, V.K., Dejong, A., Njus, G., Nishiyama, K., Buckwalter, J., 1985. Torsional fatigue of the lumbar intervertebral joints. *Spine* 10, 894–900.
 Lucas, S., Bass, C., Salzar, R., Shender, B., Paskoff, G., 2006. High rate properties of human cervical spine intervertebral discs. *Am. Soc. Biomech.*, 1–2.
 McElhaney, J.H., Paver, J.G., McCrackin, H.J., Maxwell, G.M., 1983. Cervical spine compression responses, Stapp Car Crash Conf, San Diego, CA, 163–177.
 McElhaney, J.H., Dougherty, B.J., Paver, J.G., Myers, B.S., Gray, L., 1988. Combined bending and axial responses of the human cervical spine, Stapp Car Crash Conf. Atlanta GA, 21–28.
 McGarry, M.D., Johnson, C.L., Sutton, B.P., Georgiadis, J.G., Van Houten, E.E., Pattison, A.J., Weaver, J.B., Paulsen, K.D., 2015. Suitability of poroelastic and viscoelastic mechanical models for high and low frequency MR elastography. *Med. Phys.* 42, 947–957.
 Mercer, S., Bogduk, N., 1999. The ligaments and annulus fibrosus of human adult cervical intervertebral discs. *Spine* 24, 619–626, [discussion 627–618].
 Moroney, S.P., Schultz, A.B., Miller, J.A., Andersson, G.B., 1988. Load-displacement properties of lower cervical spine motion segments. *J. Biomech.* 21, 769–779.
 Motiwale, S., Subramani, A.V., Zhou, Z., Kraft, R., 2016. Damage prediction for a cervical spine intervertebral disc IMECE, Phoenix, AZ.
 Natarajan, R.N., Williams, J.R., Lavender, S.A., An, H.S., Anderson, G.B., 2008. Relationship between disc injury and manual lifting: a poroelastic finite element model study. *Proc. Inst. Mech. Eng. Part H J. Eng. Med.* 222, 195–207.

- Osth, J., Brolin, K., Svensson, M.Y., Linder, A., 2016. A female ligamentous cervical spine finite element model validated for physiological loads. *J. Biomech. Eng.* 138, 061005.
- Pal, G.P., Routal, R.V., 1986. A study of weight transmission through the cervical and upper thoracic regions of the vertebral column in man. *J. Anat.* 148, 245–261.
- Panzer, M.B., Cronin, D.S., 2009. C4–C5 segment finite element model development, validation, and load-sharing investigation. *J. Biomech.* 42, 480–490.
- Pintar, F.A., Yoganandan, N., Voo, L., 1998. Effect of age and loading rate on human cervical spine injury threshold. *Spine* 23, 1957–1962.
- Plagenhoef, S., Evans, F., Abdelnour, T., 1983. Anatomical data for analyzing human motion. *Res. Q. Exerc. Sport* 54, 169–178.
- Race, A., Broom, N.D., Robertson, P., 2000. Effect of loading rate and hydration on the mechanical properties of the disc. *Spine* 25, 662–669.
- Schwartz, D., Guleyupoglu, B., Koya, B., Stitzel, J.D., Gayzik, F.S., 2015. Development of a computationally efficient full human body finite element model. *Traffic Inj. Prev.* 16 (Suppl 1), S49–S56.
- Stemper, B.D., Yoganandan, N., Pintar, F.A., 2003. Gender dependent cervical spine segmental kinematics during whiplash. *J. Biomech.* 36, 1281–1289.
- Stemper, B.D., Yoganandan, N., Pintar, F.A., Maiman, D.J., Meyer, M.A., DeRosia, J., Shender, B.S., Paskoff, G., 2008. Anatomical gender differences in cervical vertebrae of size-matched volunteers. *Spine* 33, E44–E49.
- Teo, E.C., Ng, H.W., 2001. Evaluation of the role of ligaments, facets and disc nucleus in lower cervical spine under compression and sagittal moments using finite element method. *Med. Eng. Phys.* 23, 155–164.
- Toms, S.R., Dakin, G.J., Lemons, J.E., Eberhardt, A.W., 2002. Quasi-linear viscoelastic behavior of the human periodontal ligament. *J. Biomech.* 35, 1411–1415.
- Untaroiu, C., Shin, J.S., Yue, N., Kim, Y., Eberhardt, A.W., 2012. A finite element model of the pelvis and lower limb for automotive impact applications. In: *Proceedings of the 12th International LS-DYNA users conference*.
- van Eerd, M., Patijn, J., Sieben, J.M., Sommer, M., Van Zundert, J., van Kleef, M., Lataster, A., 2014. Ultrasonography of the cervical spine: an in vitro anatomical validation model. *Anesthesiology* 120, 86–96.
- Virgin, W.J., 1951. Experimental investigations into the physical properties of the intervertebral disc. *J. Bone Jt. Surg. Br.* 33, 607–611.
- Voo, L.M., Kumaresan, S., Yoganandan, N., Pintar, F.A., Cusick, J.F., 1997. Finite element analysis of cervical facetectomy. *Spine* 22, 964–969.
- Yoganandan, N., Nahum, A.M., Melvin, J.W., 2014. *Accidental Injury: Biomechanics and Prevention*. Springer, NY, 851.
- Yoganandan, N., Kumaresan, S., Voo, L., Pintar, F.A., 1996a. Finite element applications in human cervical spine modeling. *Spine* 21, 1824–1834.
- Yoganandan, N., Kumaresan, S., Voo, L., Pintar, F.A., 1997. Finite element model of the human lower cervical spine: parametric analysis of the C4–C6 unit. *J. Biomech. Eng.* 119, 87–92.
- Yoganandan, N., Cusick, J.F., Pintar, F.A., Rao, R.D., 2001. Whiplash injury determination with conventional spine imaging and cryomicrotomy. *Spine* 26, 2443–2448.
- Yoganandan, N., Pintar, F.A., Zhang, J., Baisden, J.L., 2009. Physical properties of the human head: mass, center of gravity and moment of inertia. *J. Biomech.* 42, 1177–1192.
- Yoganandan, N., Cusick, J.F., Pintar, F.A., Droese, K., Reinartz, J., 1994. Cyclic compression-flexion loading of the human lumbar spine. *Spine* 19, 784–790, [discussion 791].
- Yoganandan, N., Kumaresan, S.C., Voo, L., Pintar, F.A., Larson, S.J., 1996b. Finite element modeling of the C4–C6 cervical spine unit. *Med. Eng. Phys.* 18, 569–574.
- Yoganandan, N., Pintar, F., Myklebust, J., Maiman, D.J., Sances, A., Jr., Larson, S.J., 1985. Initiation of injury in cervical spine segments. *Cerv. Spine Res. Soc.*, 1–2.
- Yoganandan, N., Pintar, F.A., Humm, J.R., Maiman, D.J., Voo, L., Merkle, A., 2016. Cervical spine injuries, mechanisms, stability and AIS scores from vertical loading applied to military environments. *European Spine Journal: Official Publication of the European Spine Society, the European Spinal Deformity Society, and the European Section of the Cervical Spine Research Society*.
- Yoganandan, N., Maiman, D.J., Pintar, F., Ray, G., Myklebust, J.B., Sances, A., Jr., Larson, S.J., 1988. Microtrauma in the lumbar spine: a cause of low back pain. *Neurosurgery* 23, 162–168.
- Yoganandan, N., Pintar, F.A., Stemper, B.D., Baisden, J.L., Aktay, R., Shender, B.S., Paskoff, G., 2006a. Bone mineral density of human female cervical and lumbar spines from quantitative computed tomography. *Spine* 31, 73–76.
- Yoganandan, N., Pintar, F.A., Stemper, B.D., Baisden, J.L., Aktay, R., Shender, B.S., Paskoff, G., Laud, P., 2006b. Trabecular bone density of male human cervical and lumbar vertebrae. *Bone* 39, 336–344.
- Zheng, M., Masoudi, A., Buckland, D., Szabo, T., Snyder, B., 2016. In-vivo Cervical Spine FSU Dynamic Motion Measured by Dual Ultrasound: the Effect of Muscle Activation, Orthopedic Research Society.

Evaluation of *In-vivo* Kinematics of Cervical Spines by Co-Registering Dynamic Ultrasound with MRI

^{1,2}Mingxin Zheng, ²Amin Mohamadi, ¹Thomas Szabo, ^{1,2,3}Brian Snyder

¹Department of Biomedical Engineering, Boston University, Boston, MA

²Center for Advanced Orthopaedics Studies, Beth Israel Deaconess Medical Center, Boston, MA

³Boston Children's Hospital, Boston, MA

Abstract—Workers who are repeatedly exposed to high cyclic loading are at high risk for degenerative cervical spine disease. Standard methods to evaluate spine motion using optical tracking or dual fluoroscopy are impractical for imaging patients in the work environment. Portable ultrasound can image cervical spine kinematics in real time, and may be able to detect abnormal spine function not apparent by static imaging of the spine pathoanatomy. We have developed a novel technique to merge dynamic real-time 2D ultrasound analysis of cervical spine kinematics with 3D static MRI images. Dynamic 2D ultrasound image profiles of the cervical spine were spatially co-registered with 3D MRI models of cervical functional spinal units. Using this approach we were able to measure the vectorial response of the cervical spine to applied loads in real time.

Index Terms—spine; MRI; tracking; kinematics; ultrasound

I. INTRODUCTION

Neck pain associated with cervical spine intervertebral disc (IVD) degeneration instigated by acute or chronic injury sustained in the work place is a common occupational health complaint [1], [2]. Laborers exposed to repetitive loads and vibrations are at highest risk [2]–[4]. Structural defects such as disc herniation or endplate fracture can be revealed by traditional static imaging technologies such as plain radiography, computed tomography (CT) and magnetic resonance imaging (MRI). However, understanding the pathophysiology of acute and chronic degenerative IVD disease induced by repetitive load scenarios encountered in the work environment remains a challenge since the etiology of these injuries are not evident in static images or pathoanatomic grading systems [5]–[7]. Current methods to evaluate cervical spine kinematics include optical tracking systems and dual fluoroscopy. However these methods are limited by inaccuracies associated with skin motion, risk of radiation exposure, or large equipment size and power requirements.

B-mode, clinical ultrasound can provide a portable, low-cost, real-time, non-ionizing imaging to evaluate dynamic spine motion based on exploiting the differences in acoustic impedance among the soft tissues comprising the IVD, ligaments, paraspinal muscles and bone comprising the vertebra. Previously we reported the ability of ultrasound imaging to accurately track the dynamic motion of cervical functional spine units (FSU) and to measure the deformation of the

interposed IVD *ex-vivo* and *in-vivo* [8]–[10]. However, using 2D ultrasound to directly track spinal motion is compromised by the lack of 3D structural information and a limited 2D view of the complex 3D vertebral anatomy. Our goal was to derive a method using clinical ultrasound to provide correct spatially oriented kinematic measurements of dynamic C-spine motion by combining dynamic 2D ultrasound image profiles of the vertebrae with a 3D model of the C-spine derived from *in-vivo* MRI of the neck and C-spine.

II. METHODS

A. Overview

Our approach incorporates the following steps identified in Fig. 1: Step 1 - develop 3D model for specific vertebra to be imaged. A generic model of the cervical vertebra was created by editing digitized CT scans of the selected vertebra. Step 2 - the generic cervical vertebra model was deformed and scaled to match a specific human subject's cervical spine anatomy imaged by MRI. This generated the 3D spatial surfaces corresponding to the patient specific vertebral anatomy. Step 3 - a bone surface segmentation algorithm was applied to extract bony profiles from ultrasound images of the vertebra. Step 4 - ultrasound bone profiles were co-registered to the individualized 3D vertebral model. Real time vertebral motion can be derived from dynamic ultrasound images projected onto the 3D MRI based vertebral model.

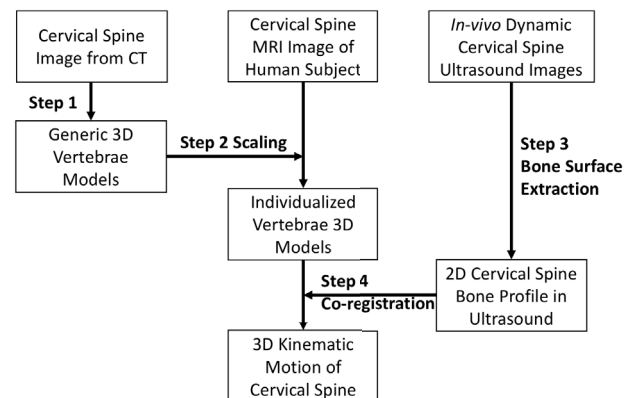


Fig. 1. Workflow of C-spine kinematics evaluation by co-registering ultrasound and MRI with generic cervical vertebrae models.

This work was supported by the U.S. Army Medical Research and Materiel Command Fort Detrick, Maryland (01026018, Contract No. W81XWH-13-1-0050).

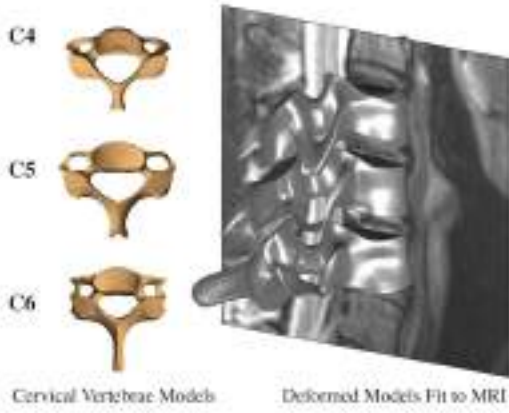


Fig. 2. Generic vertebrae models were scaled and fit to the 3D MRI scans of a human subject.

B. Individualized MRI Cervical Spine Model

C-spine MRI images were obtained from human subjects (IRB approved), the size of voxel is $0.4492\text{mm} \times 0.4492\text{mm} \times 0.8\text{mm}$. Since bone segmentation is difficult using MRI based images owing to the low image contrast of bone relative to the soft tissues, generic vertebral models obtained from CT scans of human vertebrae (Fig. 2 left) containing more than 100,000 triangular facets were transformed to emulate the exact bony surfaces corresponding to patient-specific MRI scans using anatomic landmark registration (Fig. 2 right). Selected anatomic landmarks were the endplates of the anterior vertebral body, spinal canal and spinous processes.

C. Bone Surface Extraction by Ultrasound

Bone surface recognition is complicated by the spatial impulse response [11]. The pulse response function (PSF) creates a spatially variant depiction of the actual 3D bone surface. Haines [12] proposed a model to simulate the response of planar surfaces and a method to manage non-analytical surfaces. The reflection response of complex 3D vertebral surface anatomy illuminated by a 3D focused ultrasound beam can be modeled if the PSF of a flat planar surface is given. The model was revised into the form expressed as:

$$\phi(t) = \phi_0(t) * \int_z \int_{A'} N(z, \sigma|t) * F(A'(z)|t) dA dz \quad (1)$$

ϕ_0 and ϕ are the impulse response of the surface and the actual response of the surface, respectively. (*) is convolution operation. $N(z, \sigma|t)$ is the roughness response of a planar surface that Gaussian distributed around depth z with standard deviation depending on surface of the roughness. $F(A'(z)|t)$ is smooth surface response as a function of the projected surface area A' . As a simplified example, Fig. 3 illustrates a cylindricallyshaped ultrasound beam incident on a 3D surface approximated by triangulation.

Since the impulse response is dependent on material properties, and the surface roughness is unknown, simulating the bone response using the surface model is difficult. Therefore,

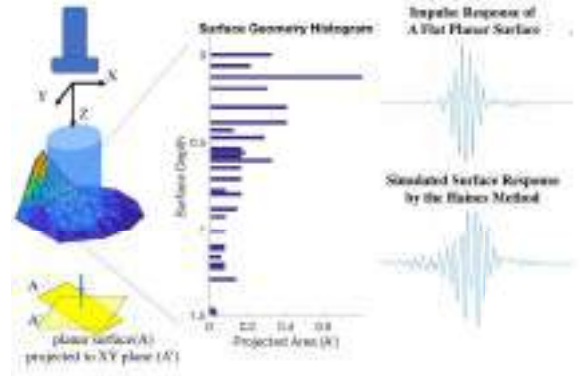


Fig. 3. A cylindrical ultrasound beam incident on a 3D surface, and the approximation of its surface response.

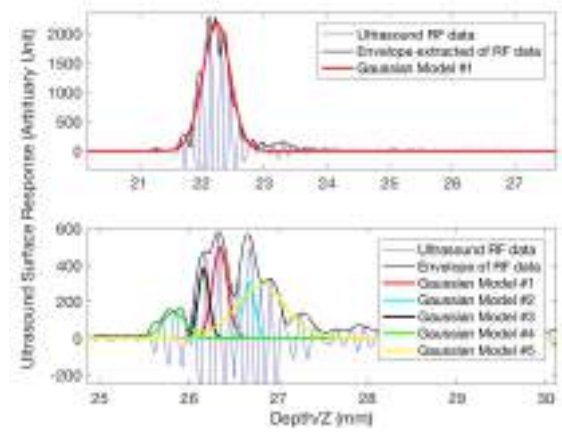


Fig. 4. RF responses of different surfaces on a plastic vertebrae model. The upper graph demonstrates the surface response on a flat surface. The lower graphs demonstrates the surface response of a curved surface inclined ≈ 45 degrees.

a mixture of Gaussian models was proposed to analyze the envelope of ultrasound radio frequency pulse echo data and extract the key surface reflections (Fig. 4). When the incident beam is vertical to the surface, we can extract one surface response in which the mean of the Gaussian distribution represents the location of the perpendicular plane in the axial direction. When the surface structure is complicated, a mixture of surface reflections introduces different signal delays and amplitudes, so that the temporal extent of the reflection signal response is altered and lengthened. Several Gaussian models were used to find the location of key components in the responses, and the mean of each distribution was considered a surface reflection at that location in ultrasound RF pulse echo response.

D. Co-Registration of Bone Surface in Ultrasound and 3D Vertebra Model

To spatially align the MRI C-spine model with bone surface points detected by ultrasound, the Iterative Closest Point (ICP)

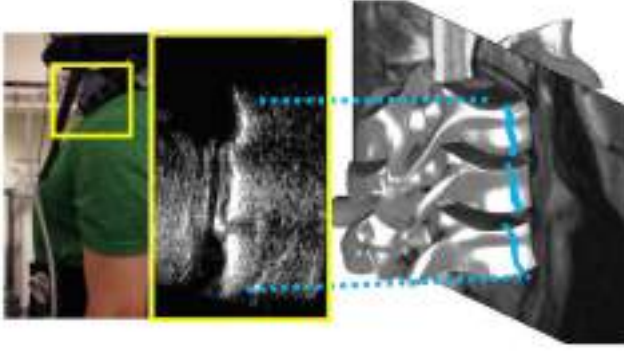


Fig. 5. Ultrasound profile was co-registered with 3D static MRI based model by minimizing point the mapping function between the profile and the model.

algorithm[13] was modified and applied to solve the 2D-3D co-registration problem. ICP is commonly used to register two 3D point clouds P and Q , by finding the optimal point-to-point mapping through minimizing the distance function. For each point Q_i in point cloud Q , the algorithm searches for a point in P , P_j , that has the minimum distance to Q_i :

$$j = \arg \min_j \|Q_i - P_j\| \quad (2)$$

and this process is repeated iteratively until the sum of distances of point mapping converges to its minimum. However, being an iterative method, ICP requires appropriate initiation points, otherwise it can become trapped in local minima. Furthermore, because the ultrasound image only provides 2D point sets, the solution point-map may not be unique.

To apply ICP to our ultrasound image and MRI registration problem, we modified the distance function to account for the projected area of planar surfaces on the model (Fig. 3 lower left) as:

$$j = \arg \min_j (\|Q_i - P_j\| - \lambda \vec{A}_i \cdot \vec{n}_{ij}) \quad (3)$$

The projected surface area $\vec{A}_i \cdot \vec{n}_{ij}$ is based on the applied rotation, and computed by the dot product of surface and unit vector of the beam orientation with a positive impact factor λ . The value of λ depends on the 3D model resolution and physical units of point clouds and the area; we set λ to be 0.2 in our model. To minimize effects of local minima, the modified ICP was applied 10,000 times to find the optimal mapping with different random initiation points.

E. Experiments

Plastic Vertebra Phantom Validation: the generic model from a CT scan of a vertebra was printed by Form2 Desktop Stereolithography (SLA) 3D Printer (FormsLab, Boston, MA). The model was mounted to an alignment coupler device, which measured the relative position between ultrasound transducer and the model. The bone surface was imaged with ultrasound at 18 different angles and compared to the actual anatomic surface data.

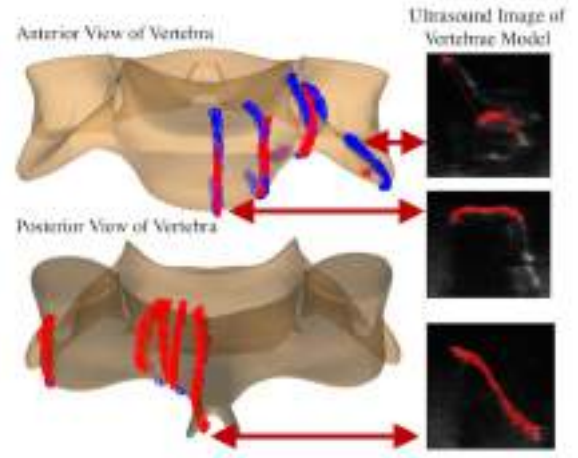


Fig. 6. Bone profiles (red) extracted from ultrasound image are registered to 3D vertebra model. They are compared to the ground truth data (blue) which are measured by displacement and rotation calculation.

In-vivo Experiment: After IRB approval, a static MRI 3D scan of a human cervical spine was used to rescale the cervical spine model. Human volunteers performed repetitive jump test on/off a 0.8 ft. step with and without weight applied to the head and neck. Ultrasound probe was maintained in set positions relative to the cervical spine using a neoprene cervical collar (Fig. 5 left). ultrasound images of vertebrae profile were registered on the model to show deformation and flexion angles were derived from sequential ultrasound Images with tracked vertebrae positions (Fig. 5 right).

III. RESULTS

A. Plastic Vertebra Phantom Validation

Fig. 6 shows the experimental results of co-registering ultrasound bone profiles on the plastic vertebra model. The Root Mean Square Error (RMSE) of registration is 0.624 ± 0.151 mm. Vertebra surfaces in the anterior and posterior regions (anterior vertebral bodies, facet, and lamina) have a higher contrast in ultrasound due to their smooth surface geometry; therefore they provided better bone matching results with more surface points identified.

B. In-vivo Experiment

Sequential ultrasound images of C4-5 and C5-6 portrayed the relative displacements and flexion angles of the FSU calculated by matching the dynamic ultrasound images to the static 3D model. Fig. 7 shows the synchronized measurements of subject jumping with ultrasound transducers over 1s. The impact force indicated the landing impact when the load measured by grounded force plate reached its maximum. Para-cervical muscles were activated to dampen inertial forces, as measured by EMG waveforms. FSU deformation, measured by translational motion of vertebra, showed the compression and relaxation of IVDs during and after landing. C4-C5 and C5-C6 FSU flexion angles was measured by vertebra rotation, which implies the change of the C-spine curvature of cervical spine.

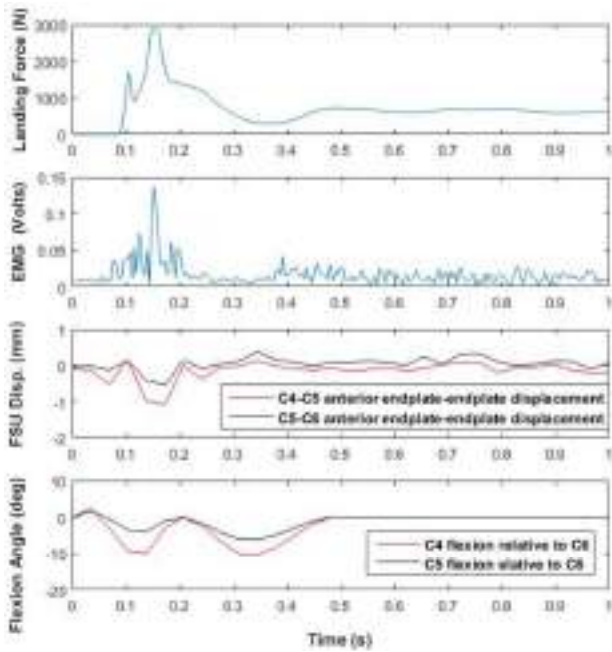


Fig. 7. C4-5-6 kinematics calculated from ultrasound data from a subject who jumped off 0.8 foot high step.

IV. DISCUSSION

We present a co-registration method to solve the problem of merging MRI and ultrasound imaging to determine in-vivo kinematics of the C-spine during simulated work activities. Since the vertebra is a rigid body, its kinematic motion can be theoretically re-constructed from 5 points on calibrated views. Due to limited field of view and the nature of 2D ultrasound imaging, only a limited number of points from the vertebra on a 2D plane can be extracted from a single ultrasound image. Therefore, apriori information about the anatomic structure of the vertebra, i.e. a generic 3D model, is required to facilitate co-registration of the ultrasound 2D image and the 3D MRI derived model to calculate the relative vertebral motion.

2D-3D registration is an ill-posed problem because there usually exist more than one possible solution to map 2D curves on a 3D surface. We introduced the projected surface area as an additional parameter to confine the scope of possible mapping, based on the assumption that the ultrasound signal intensity is dependent on the surface projection area in the acoustic beam. For validation, we applied this method to co-register a plastic vertebra model with known anatomic data. Nonetheless, other feature extraction methods of ultrasound can also be applied. In our validation, we demonstrated that smooth surfaces gave better results than surfaces with a complicated structure. These findings suggested that certain anatomical landmarks, e.g. vertebral bodies and lamina can be selected for better matching and co-registration of C-spine ultrasound imaging with 3D MRI.

V. CONCLUSION

We proposed a method to co-register 2D ultrasound surface image profiles to a 3D cervical vertebra model, which can be individualized to a subject specific MRI scan. We validated this method using a plastic vertebral model and then applied it to measure the real time *in-vivo* kinematics of the cervical spine using human MRI cervical spine images from subjects performing a jump test with the resultant C-spine motion monitored using ultrasound probe directed towards the vertebrae.

REFERENCES

- [1] M. D. Grossman, P. M. Reilly, and T. Gillett, et al, National Survey of the Incidence of Cervical Spine Injury and Approach to Cervical Spine Clearance in US Trauma Centers," J Trauma., 1999.
- [2] H. Yang, S. Haldeman, A. Nakata, B. Choi, L. Delp, and D. Baker, Work-Related Risk Factors for Neck Pain in the US Working Population, Spine (Phila. Pa. 1976)., vol. 40, no. 3, pp. 184192, Feb. 2015.
- [3] M. Qasim, R. N. Natarajan, H. S. An, and G. B. J. Andersson, Damage accumulation location under cyclic loading in the lumbar disc shifts from inner annulus lamellae to peripheral annulus with increasing disc degeneration, J. Biomech., vol. 47, no. 1, pp. 2431, Jan. 2014.
- [4] J. Village, J. B. Morrison, and D. K. Leong, Whole-body vibration in underground load-haul-dump vehicles., Ergonomics, vol. 32, no. 10, pp. 11671183, 1989.
- [5] J. F. Holmes and R. Akkinipalli, Computed tomography versus plain radiography to screen for cervical spine injury: a meta-analysis., J. Trauma, vol. 58, no. 5, pp. 9025, 2005.
- [6] A. Kettler and H. J. Wilke, Review of existing grading systems for cervical or lumbar disc and facet joint degeneration, Eur. Spine J., vol. 15, no. 6, pp. 705718, 2006.
- [7] D. Volkheimer, M. Malakoutian, T. R. Oxland, and H.-J. Wilke, Limitations of current in vitro test protocols for investigation of instrumented adjacent segment biomechanics: critical analysis of the literature, Eur. Spine J., vol. 24, no. 9, pp. 18821892, Sep. 2015.
- [8] M. Zheng, K. Shiuan, A. Masoudi, D. Buckland, T. Szabo, and B. Snyder, Dynamic Ultrasound Imaging of Cervical Spine Intervertebral Discs, IEEE Trans. Ultrason. Ferroelectr. Freq. Control, pp. 836839, 2013.
- [9] M. Zheng, A. Masoudi, D. Buckland, B. Stemper, N. Yoganandan, T. Szabo, and B. Snyder, Dynamic ultrasound imaging of cervical spine intervertebral discs, IEEE Int. Ultrason. Symp. IUS, pp. 448451, Jul. 2014.
- [10] M. Zheng, A. Mohamodi, T. Szabo, and B. Snyder, In-vivo cervical spine FSU dynamic motion measured by dual ultrasound: The effect of muscle activation, in IEEE International Ultrasonics Symposium, IUS, 2016, vol. 2016Novem, pp. 14.
- [11] T. L. Szabo, Diagnostic ultrasound imaging: inside out. Second edition. ed. Elsevier, Amsterdam ; Boston, 2014, pp 209-215.
- [12] N. F. Haines and D. B. Langston, The reflection of ultrasonic pulses from surfaces, J. Acoust. Soc. Am., vol. 67, no. 5, pp. 14431454, 1980.
- [13] P. Besl and N. McKay, A Method for Registration of 3-D Shapes, IEEE Transactions on Pattern Analysis and Machine Intelligence, vol. 14, no. 2, pp. 239256, 1992.

Long-term Movement Analysis of Cervical Vertebrae with Normalized Cross-Correlation and Subsample Estimation

^{1,2}Mingxin Zheng, ²Amin Mohamadi, ¹Thomas Szabo, ^{1,2,3}Brian Snyder

¹Department of Biomedical Engineering, Boston University, Boston, MA

²Center for Advanced Orthopaedics Studies, Beth Israel Deaconess Medical Center, Boston, MA

³Boston Children's Hospital, Boston, MA

Abstract—Cervical spine pathoanatomy is typically evaluated by static radiographs, CT or MRI; however, these modalities are unable to directly measure the dynamic performance of the spine that account for its functionality. We have developed an ultrasound based technique that provides a non-invasive, real-time, quantitative, textititn-vivo image of the C-spine that allows for assessment of the dynamic motion of contiguous functional spinal units. The purpose of this work was to develop a multi-frame method that enables accurate tracking of the motion of vertebra from ultrasound radio-frequency data. The tracking method was validated using a vertebra phantom and 6 human cadaveric specimens subjected to cyclic displacement. Ultrasound was capable of accurately tracking vertebral motion when using the multi-frame method compared to the traditional frame-by-frame, or multi-compression methods.

Index Terms—orthopedics, cervical spine, ultrasound, long-term tracking

I. INTRODUCTION

The motion of spine *in-vivo* is difficult to measure by traditional imaging techniques, such as X-ray, Computed Tomography, and Magnetic Resonance Imaging. Evidence has emerged recently indicating that *ex-vivo* spine models are insufficient to replicate *in-vivo* kinematics and may not predict the injury mechanics and assess the effect of surgical instrumentation [1]. Therefore, imaged-based motion analysis of human musculoskeletal system has become a growing area of interest in spine evaluation. Ultrasound imaging can image bone profiles by identifying the acoustic impedance difference between soft tissues and cortical bone. Intraoperative ultrasound has been used to guide needle injection in lumbar epidural anesthesia [2]–[4]. In recent years, ultrasound has been proposed to image the anatomy of lumbar spines [5], [6] and cervical spine [7], [8] *in-vivo*.

High frame rate (>30Hz) and long exposure times (>1 minute) are requisite for analyzing *in-vivo* spine kinematics during activities such as running or jumping, which leads to the question of how to track large movements in hundreds of frames in ultrasound imaging. Traditionally, large strains were tracked by the multi-compression method, which breaks

a large deformation into smaller steps. However for frame-by-frame motion tracking, summing error and error variance increase inherently over time, and can accumulate infinitely [9], [10]. In this study, we present and validate a multi-frame tracking algorithm to analyze ultrasound radio frequency (RF) data of long-term, large motion of vertebrae, using a cervical vertebra phantom and human cadaver vertebrae.

II. METHODS

A. Tracking Framework

Traditional two-dimensional frame-to-frame tracking is a temporally sequential method in which displacements are formed by comparing points in a current frame with those in a previous frame or frames. In order to introduce our multi-frame approach in which we use spatially collocated frames, we define terms used for comparison of these methods. The position of a vertebra at the frame t in the ultrasound RF data sequence I_t is expressed as a 2-dimensional (2D) vector x_t^* , and the estimated position is denoted as x_t . The goal of deriving an accurate tracking algorithm is to minimize the error between the true position of vertebra and its estimated position, $x_t^* - x_t$.

Conventionally, to find the position x_t , vertebra is tracked as rigid body by computing displacements between tempo-

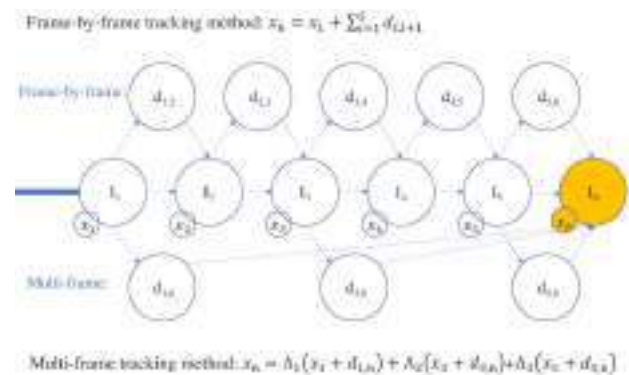


Fig. 1. The multi frame tracking method compared to the frame-by-frame tracking method. To estimate the position of vertebra in ultrasound image I_6 , the frame-by-frame method uses all the displacement estimations and accumulates the results, while the multi frame method uses 3 prior estimations.

This work was supported by the U.S. Army Medical Research and Materiel Command Fort Detrick, Maryland (01026018, Contract No. W81XWH-13-1-0050).

rally adjacent frames, and then is calculated by summing all previous displacements frame-by-frame (Fig. 1 top). The true 2D translational displacement of a vertebra between two RF frames I_s and I_t , noted as $d_{s,t}^*$, is the difference of true positions as in:

$$d_{s,t}^* = x_s^* - x_t^* \quad (1)$$

The displacement estimation computed by image correlation or other technique is a noisy version of $d_{s,t}^*$ with noise $\epsilon_{s,t}$:

$$d_{s,t} = d_{s,t}^* + \epsilon_{s,t} \quad (2)$$

The traditional framework only compares the current frame with a previous frame. Provided that the initial true position and its estimation are the same, in this frame-by-frame framework, position estimation was obtained by summing displacements of adjacent frames. The error ϵ is the summation of noise over all frame pairs, as in:

$$\epsilon_T = x_T^* - x_T = \sum_{i=2}^T d_{i-1,i}^* - \sum_{i=2}^T d_{i-1,i} = \sum_{i=2}^T \epsilon_{i-1,i} \quad (3)$$

We assume the error accumulates linearly over time if only one previous frame is selected for comparison.

To solve the problem of error accumulation, Rahimi et al. has proposed a method that evaluates multiple previous video frames, instead of only the adjacent previous frame, to estimate current position of an object [11], [12]. For each current frame number T , the historical trajectory of motion was used to select a set of K frames, $C(k, t)$ (Fig. 1 bottom). The estimated position of vertebra in frame T is the sum of previous estimates and displacements with weighted by Λ , as in:

$$x_T = \sum_{k=1}^K \Lambda_{C(k,T)} (x_{C(k,T)} + d_{C(k,T)}) \quad (4)$$

For all time 1 to T , there are T linear equations, which can be reformed in matrix form and solved to find optimal solution.

While sufficient information exists to solve all $x_t (t = 1..T)$ uniquely in the frame-by-frame analysis, when multiple frames

are chosen, redundant displacement estimates can be used to minimize the position error and improve tracking accuracy. In our multi-frame analysis, we chose $K = 4$; $C(k, t)$ is defined by searching the 4 spatially closest image frames corresponding to the objects prior trajectory. Λ is determined by the sum of image gradient of the RF data.

B. Displacement Estimation

As in the frame-by-frame method, the multi-frame method requires displacement estimations between spatially collated RF data frames. We chose Normalized Cross-Correlation (NCC) to estimate translational displacement, with parabolic fitting subsample estimation for the lateral translation since ultrasound resolution in the lateral direction is limited to the beam width and is considered less accurate than axial measurements.

The vertebra was manually outlined as a box region in the first frame of the ultrasound image sequence. A moving average blur filter was applied to segment the vertebral surface define a Region of Interest (ROI) that corresponded to the vertebral body, and excluded regions that had low RF responses. The kernel of NCC was 3 lateral RF samples by 15 axial RF samples. No data reduction or skipping was applied.

C. Experiment Setup

A 3D printed phantom of an isolated human cervical vertebra and 6 human cadaver cervical vertebrae with soft tissue retained were mounted in a servohydraulic material testing system that accurately controlled vertical piston displacement, (Fig. 2). The phantom provided high quality US images of the cervical spine surface profile. The ultrasound images of cadaveric specimens were affected by the soft tissue attachments to the bone surface that induced signal distortion (Fig. 3). A series of vertical sinusoidal displacements (amplitude: 1-4mm, frequency: 1-10Hz) were imaged using a Terason t3200 US probe (Teratech, MA, USA) with a 7.5 MHz linear transducer 8IOL4. Each series of sinusoidal displacements were repeated over 18 different imaging angles of the phantom and 5 different imaging angles for the 6 cadaveric specimens.

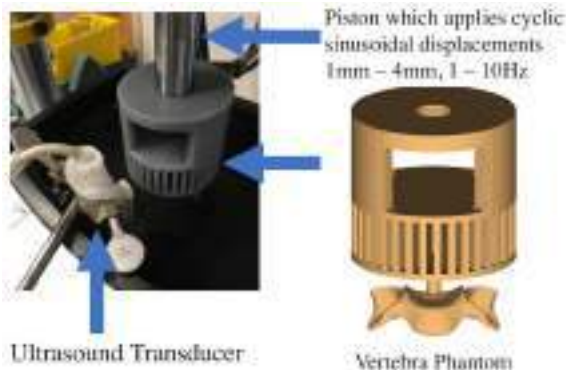


Fig. 2. Experimental setup for plastic vertebral phantom imaging and motion tracking. The 3D printed model was mounted to a servo hydraulic actuator capable of high-accuracy and precision displacements. The US transducer imaged the applied displacement in a water bath, and the RF data was recorded for offline data analysis.

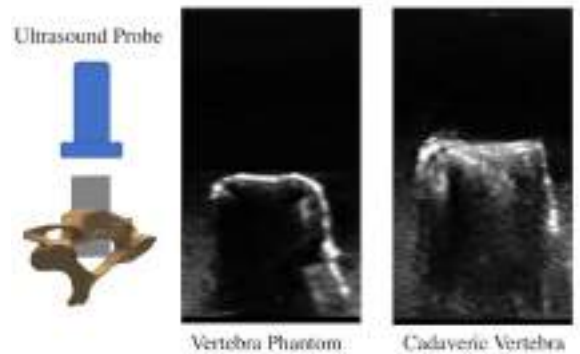


Fig. 3. The ultrasound images of vertebra phantom and cadaveric vertebra were compared. The bone profile on vertebra phantom on the imaging plane was sharp while the real vertebra has a broad ridge.

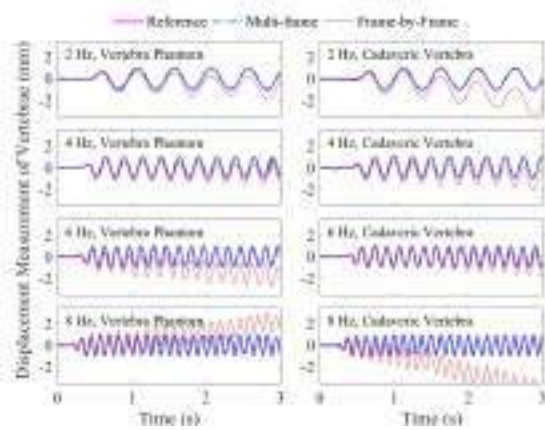


Fig. 4. Representative vertebral displacement derived from ultrasound RF data using multi-frame and frame-by-frame algorithms for phantom and cadaveric vertebra for different applied displacement. The applied amplitude is 1mm and the imaging plane is oriented at 5 degrees from the sagittal plane. The multi-frame derived displacements were highly correlated with the reference data, while the frame-by-frame derived displacements drifted after a few cycles.

III. RESULTS

A. Displacement Errors over Time

Axial vertebral motion derived using the multi-frame and frame-by-frame algorithms were compared to the known applied sinusoidal axial displacement for the vertebra phantom and cadaveric vertebrae (Fig. 4). There was significant drift that accumulated over time for all vertebral displacements tracked using the frame-by-frame method. Higher applied displacement frequency induced more drift over the same number of frames. The frame-to-frame displacement error increased linearly over time, but the slope of the increase was random and unpredictable. In contrast, vertebral displacement derived from ultrasound RF data using the multi-frame algorithm was highly correlated with the known applied displacement for both the vertebra phantom and cadaveric specimens. The increase of error was negligible over duration of the test (>600 frames).

B. Error Variance over Time

The variance of error is a metric to statistically evaluate the distribution of accumulated displacement error over time. Error variance was calculated for all image sequences (18 for the phantom, 30 for cadaveric specimens) subjected to the same testing protocol (identical frequency and amplitude) for the frame-by-frame and multi-frame tracking algorithm (Fig. 5). Using the traditional frame-by-frame algorithm, the error variance of the vertebral model increased over time. While the error variance using the multi-frame algorithm increased initially at the beginning of the cyclic motion test, the variance stabilized over time and was 2-3 magnitudes lower compared to the frame by frame algorithm. Similarly, error variances were observed using the multi-frame algorithm to track cadaveric vertebrae, which were 1-2 magnitudes lower than those using frame-by-frame tracking algorithm (Fig. 6). Since an increase in error variance over time indicates a

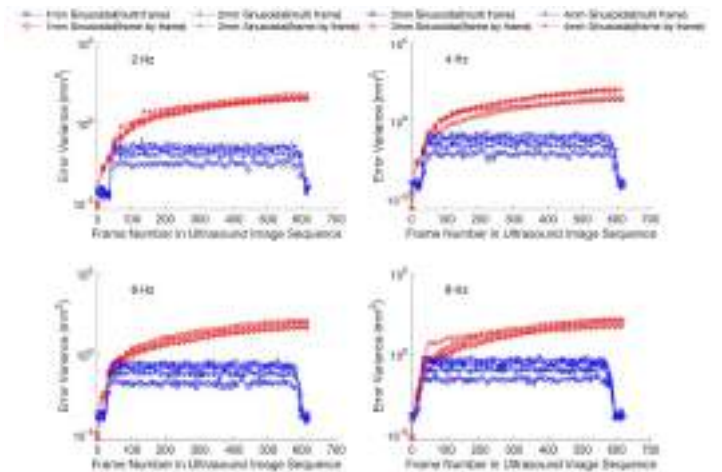


Fig. 5. Error variance for the two tracking methods as a function of number of frames in vertebra phantom cyclic sinusoidal experiment. Only 4 out of the 10 frequencies are illustrated because of space limits. Marker type represents different amplitudes of the sinusoidal wave.

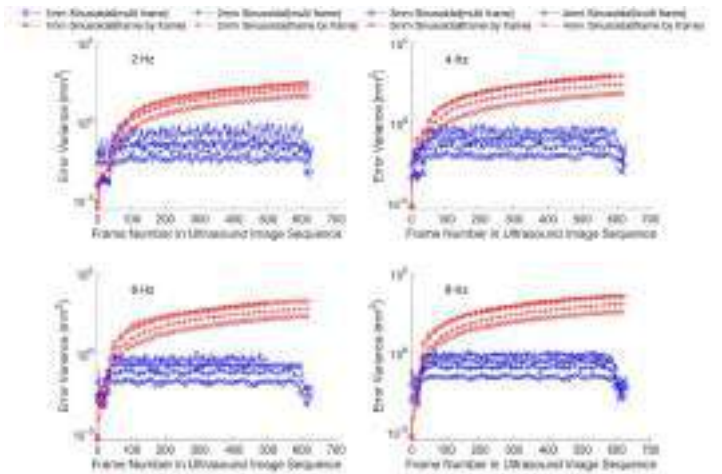


Fig. 6. Error variance for the two tracking methods as a function of number of frames in cadaveric vertebra subjected to cyclic sinusoidal motion. Each marker type represents a specific amplitude of the sinusoidal wave.

decrease in the precision of the US measured displacement, these results suggest that using the multi-frame algorithm has statistically significant advantages for tracking spine kinematics over long duration testing.

Both frequency and amplitude affect the tracking accuracy and precision. Since the motion of larger displacement and frequency had larger displacement error and error variance, it is implied that the presence of motion blurring may also affect tracking precision in ultrasound RF sequence. Tracking the motion of the cadaveric vertebrae had a higher error and error variance than tracking the motion of the vertebra phantom under the similar testing conditions. The major difference between the cadaveric vertebrae and the phantom is that the retained soft tissues covering the cadaveric bone surface altered the imaging of the bone surface.

IV. DISCUSSION

We demonstrated that using the multi-frame tracking method improved the accuracy of determining real time, dynamic cervical spine motion derived from ultrasound RF data sequences. Specifically, we compared the accuracy and accumulated error for cervical spine motion simulated by the application of known cyclic axial displacement evaluated by B-mode US and post-processed using multi-frame and conventional multi-compression frame-by-frame tracking algorithms. The multi-frame method requires multiple operations to estimate the displacement of the vertebra in each image frame, and thus increases the computation time. Further optimization can be made on accelerated NCC computation by using general-purpose graphics processing units (GPU) or by replacing NCC with other correlation methods, such as Sum of Square Difference (SSD). In our experiment, implementing SSD reduced the time consumed by correlation to 1/8 of that using NCC, with an error increase of less than 10%.

V. CONCLUSION

Our study demonstrated that ultrasound derived kinematic analysis of dynamic spine motion deduced using multi-frame analysis improves the accuracy and precision of the measured displacement, compared to the traditional frame-by-frame multi-compression method over long duration testing. Motion analysis of cadaveric specimens has a higher error due to the presence of soft tissues which alters the imaging of the bone surface. However, ultrasound can provide a portable, low cost imaging modality capable of quantifying dynamic cervical spine motion over prolonged time durations.

REFERENCES

- [1] D. Volkheimer, M. Malakoutian, T. R. Oxland, and H.-J. Wilke, Limitations of current in vitro test protocols for investigation of instrumented adjacent segment biomechanics: critical analysis of the literature, *Eur. Spine J.*, vol. 24, no. 9, pp. 18821892, Sep. 2015.
- [2] T. Grau, R. W. Leipold, S. Fatehi, E. Martin, and J. Motsch, Real-time ultrasonic observation of combined spinal-epidural anaesthesia, *Eur. J. Anaesthesiol.*, vol. 21, no. 1, pp. 2531, 2004.
- [3] D. Tran, A. A. Kamani, V. A. Lessoway, C. Peterson, K. W. Hor, and R. N. Rohling, Preinsertion paramedian ultrasound guidance for epidural anesthesia, *Anesth. Analg.*, vol. 109, no. 2, pp. 661667, 2009.
- [4] C. Arzola, S. Davies, A. Rofaeel, and J. C. A. Carvalho, Ultrasound using the transverse approach to the lumbar spine provides reliable landmarks for labor epidurals, *Anesth. Analg.*, vol. 104, no. 5, pp. 11881192, 2007.
- [5] D. Tran and R. N. Rohling, Automatic detection of lumbar anatomy in ultrasound images of human subjects., *IEEE Trans. Biomed. Eng.*, vol. 57, no. 9, pp. 22482256, 2010.
- [6] S. Gill, P. Abolmaesumi, G. Fichtinger, J. Boisvert, D. Pichora, D. Borshneck, and P. Mousavi, Biomechanically constrained groupwise ultrasound to CT registration of the lumbar spine, *Med. Image Anal.*, vol. 16, no. 3, pp. 662674, 2012.
- [7] M. Zheng, A. Masoudi, D. Buckland, B. Stemper, N. Yoganandan, T. Szabo, and B. Snyder, Dynamic ultrasound imaging of cervical spine intervertebral discs, *IEEE Int. Ultrason. Symp. IUS*, pp. 448451, Jul. 2014.
- [8] M. Zheng, A. Mohamodi, T. Szabo, and B. Snyder, In-vivo cervical spine FSU dynamic motion measured by dual ultrasound: The effect of muscle activation, in *IEEE International Ultrasonics Symposium, IUS*, 2016, vol. 2016Novem, pp. 14.
- [9] M. Bayer and T. J. Hall, Variance and covariance of accumulated displacement estimates., *Ultrason Imaging*, vol. 35, no. 2, pp. 90108, 2013.
- [10] M. Bayer, T. J. Hall, L. P. Neves, and A. A. O. Carneiro, Two-Dimensional Simulations of Displacement Accumulation Incorporating Shear Strain, *Ultrason. Imaging*, vol. 36, no. 1, pp. 5573, 2014.
- [11] a. Rahimi, L.-P. Morency, and T. Darrell, Reducing drift in parametric motion tracking, *Proc. Eighth IEEE Int. Conf. Comput. Vision. ICCV 2001*, vol. 1, pp. 315322, 2001.
- [12] A. Rahimi, L. P. Morency, and T. Darrell, Reducing drift in differential tracking, *Comput. Vis. Image Underst.*, vol. 109, no. 2, pp. 97111, 2008.

Mechanisms of Cervical Spine Disc Injury under Cyclic Loading

Sagar Umale¹, Narayan Yoganandan^{1,2,3}

¹Department of Neurosurgery, Medical College of Wisconsin, Milwaukee, WI, USA

²Department of Orthopaedic Surgery, Medical College of Wisconsin, Milwaukee, WI, USA

³Center for NeuroTrauma Research, Department of Neurosurgery, Medical College of Wisconsin, Milwaukee, WI, USA

Study Design: Determination of human cervical spine disc response under cyclic loading.

Purpose: To explain the potential mechanisms of intervertebral disc injury caused by cyclic loading.

Overview of Literature: Certain occupational environments in civilian and military populations may affect the cervical spine of individuals by cyclic loading. Research on this mechanism is scarce.

Methods: Here, we developed a finite element model of the human C4–C5 disc. It comprised endplates, five layers of fibers, a nucleus, and an annulus ground substance. The endplates, ground substance, and annular fibers were modeled with elastic, hyper-viscoelastic, and hyper-elastic materials, respectively. We subjected the disc to compressive loading (150 N) for 10,000 cycles at frequencies of 2 Hz (low) and 4 Hz (high). We measured disc displacements over the entire loading period. We obtained maximum and minimum principal stress and strain and von Mises stress distributions at both frequencies for all components. Further, we used contours to infer potential mechanisms of internal load transfer within the disc components.

Results: The points of the model disc displacement versus the loading cycles were within the experimental corridors for both frequencies. The principal stresses were higher in the ground matrix, maximum stress was higher in the anterior and posterior annular regions, and minimum stress was higher along the superior and inferior peripheries. The maximum principal strains were radially directed, whereas the minimum principal strains were axially/obliquely directed. The stresses in the fibers were greater and concentrated in the posterolateral regions in the innermost layer.

Conclusions: Disc displacement was lower at high frequency, thus exhibiting strain rate stiffening and explaining stress accumulation at superior and interior peripheries. Greater stresses and strains at the boundaries explain disc injuries, such as delamination. The greater development of stresses in the innermost annular fiber layer (migrating toward the posterolateral regions) explains disc prolapse.

Keywords: Fatigue; Finite element analyses; Intervertebral disc; Neck pain

Introduction

Biomechanical studies of the human spine help determine external and internal responses to day-to-day activities,

such as those occurring in occupational environments [1]. Clinical, experimental, and computational models are used to investigate the behavior of the spine. Clinical models are used to obtain *in vivo* data, whereas ex-

Received Nov 17, 2017; Revised Jan 27, 2018; Accepted Mar 19, 2018

Corresponding author: Narayan Yoganandan

Department of Neurosurgery, Medical College of Wisconsin, Milwaukee, WI 53226, USA

Tel: +1-414-805-5430, Fax: +1-414-955-0115, E-mail: yoga@mcw.edu

perimental models using human cadavers are used to determine external responses of the spine, such as the range of motion. A majority of experimental studies have focused on physiological models, particularly under pure moment-based, quasi-static or static, flexion, extension, lateral bending, and axial rotation loads [1]. Such modalities continue to drive developments for newer applications, such as cervical and lumbar spine artificial discs, in the field of spine biomechanics. In physiological models, the load application to the spine predominantly belongs to the single-cycle type.

Other studies have focused on traumatic models by delivering loads to the spine via contact or non-contact forces; contact loading to the head is applied to simulate automotive and sporting events. These studies have determined fracture loads and described human neck injury tolerances [2]. Inertial or non-contact loading is applicable to automotive rear impacts. Research in this area is mainly aimed at understanding whiplash-associated disorders. Tests using human cadaver models have delineated the role of demographic factors based on differences in intervertebral space and segmental kinematics [3]. The insult is applied to the spine in one cycle in these traumatic loading events.

From an occupational perspective, certain civilian and military occupations subject the human spine to repeated loading. Exposure to whole body vibrations from industrial workplace duties have long been recognized as a mechanical cause, further predisposing to long-term complications, such as lower-back pain, stemming from radicular symptoms, and disc-related issues involving annular fibers and endplates. Over the past five decades,

studies have been conducted using cadaver lumbar spinal columns and segments to understand the cyclic loading response [4]. Injuries in cadavers can be used to search for correlations with *in vivo* lesions caused by repeated loading activities in civilian populations.

From a military perspective, certain operational activities, such as specific personnel training, can induce cyclic loading on the neck [5]. The prevalence of neck pain in helicopter pilots exposed to repeated load ranges from 29% to 57% [5-8]. The helmet worn adds its mass to the natural *in vivo* head weight. Devices, such as night vision goggles, visor, and communications combo, also add to the physical properties of the helmet and head. The increased mass, moment of inertia, and center of gravity shift due to helmet- and head-mounted devices place additional loads on the cervical spine during normal military training and operational activities. Because such activity-based loads in the military are cyclic and because vertebral fractures are uncommon, the most susceptible regions for potential injury or weakening of the spine are the disc and/or the endplates. The axial load on the cervical spine column caused by the head-supported mass has not been completely investigated under cyclic loading conditions. An investigation regarding internal responses, such as stresses and strains and their distributions, is needed to better understand the biomechanics of helmet-wearing situations. Therefore, here, we aimed to use a simplified finite element (FE) model of the human cervical disc and apply axial cyclic loading similar to the head-supported mass sustained by military personnel wearing helmets. We used internal response outputs to offer explanations for clinical disc disorders of the human cervical spine.

Table 1. Material properties of the disc components

Component	Material	Material properties	References
Bony endplates	Elastic	$E=5,600 \text{ MPa}$, $\mu=0.3$	
Cartilaginous endplates	Elastic	$E=24 \text{ MPa}$, $\mu=0.4$	
Nucleus	Elastic	$E=1 \text{ MPa}$, $\mu=0.45$	[16]
Annulus ground matrix	Arruda-Boyce hyper-viscoelastic	$\mu_0=0.35 \text{ MPa}$, $\lambda_m=7.00$, $D=1.2$, $G_0=0.45$, $G_\infty=0.38$, $\beta=12.8$	[8]
Annular fibers (innermost)	Arruda-Boyce hyper-elastic	$\mu_0=4.5 \times 10^{-02} \text{ MPa}$, $\lambda_m=7.00$, $D=14.8$	
Annular fibers (second from inner)		$\mu_0=3.85 \times 10^{-02} \text{ MPa}$, $\lambda_m=7.00$, $D=17.3$	
Annular fibers (third from inner)		$\mu_0=7.49 \times 10^{-03} \text{ MPa}$, $\lambda_m=7.00$, $D=87.9$	
Annular fibers (forth from inner)		$\mu_0=7.68 \times 10^{-03} \text{ MPa}$, $\lambda_m=7.00$, $D=85.65$	
Annular fibers (outermost)		$\mu_0=7.95 \times 10^{-03} \text{ MPa}$, $\lambda_m=7.00$, $D=82.87$	

E, elastic modulus; μ , Poisson's ratio; ρ , density; G_0 , instantaneous shear modulus; G_∞ , shear modulus at infinite time; β , decay in shear; μ_0 , λ_m , D , Arruda-Boyce model coefficients.

Materials and Methods

We developed the FE model of the human C4–C5 disc using computed tomography images imported into commercial software. We performed vertebral segmentation using bone threshold frequency. We exported the segmented images in a stereo-lithographic format for further processing in the Altair Hypermesh software. We selected the vertices surrounding the endplate locations based on the adjacent vertebral bodies. The chosen vertices on the vertebral bodies defined the bony endplate boundaries of the disc. The cartilaginous and bony endplates were meshed with quadratic elements, and we developed a hexahedral mesh of the disc annulus and nucleus using the superior and inferior endplates as references (Fig. 1).

We modeled the nucleus pulposus and annulus ground substance using solid hexahedral elements; the annular fibers were modeled with five pairs of concentric quadratic shell layers embedded in the ground substance. The rationale for using the five pairs of layers is described later. We modeled the superior and inferior cartilaginous and bony endplates using shell elements. The element size for the model was 0.5 mm, and the model contained 8,740 solid hexahedral and 18,636 quadratic shell elements.

We obtained the material properties for the ground substance from experimental data [4]. Properties of the endplates, nucleus, and annular fiber components of the disc were obtained from literature studies (Table 1).

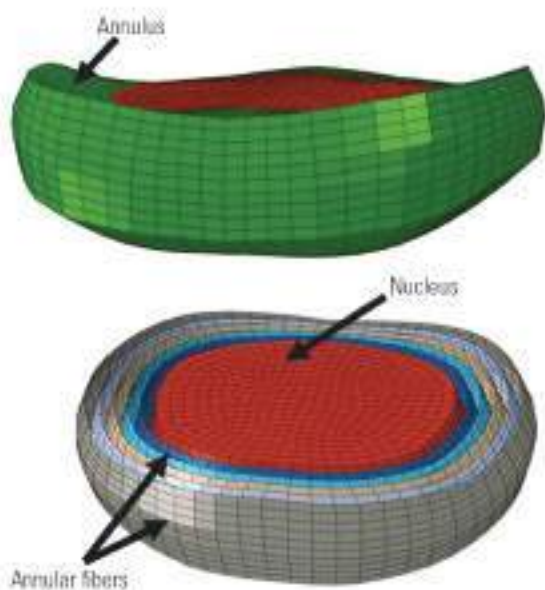


Fig. 1. The model showing the disc with annulus, nucleus, and annular fibers embedded in the annular ground matrix.

The annular ground substance was modeled as a hyper-viscoelastic material. We obtained the elastic properties for the annulus from tension–compression experiments and the viscous properties from stress–relaxation tests. We exported the curves from the experiments into the Abaqus software. The stress–strain data from the tension–compression experiments and stress–relaxation data were directly used as inputs into the Abaqus software for the Aruda–Boyce hyper-elastic material. The nucleus was modeled using an incompressible elastic material with a modulus of 1 MPa and a Poisson's ratio of 0.45 [9,10]. The annular fibers were modeled as hyper-elastic materials, and tension-only material properties varied from the innermost to the outermost layer. We used a value of 0.4 for the Poisson's ratio for the ground substance [11,12]. We included the gradual change in the fiber angle with the radial position in the model: fiber angles $\pm 25^\circ$ in the outer layers to $\pm 45^\circ$ in the inner layers; the elastic modulus and Poisson's ratio of the bony endplates were 5,600 MPa and 0.3, respectively [13]. These values for the cartilaginous endplates were 24 MPa and 0.4, respectively.

The inferior bony endplate was constrained at all degrees-of-freedom. We applied a uniform load of 150 N at 2 and 4 Hz (low and high frequency) to the superior endplate for 10,000 cycles. The model results were outputted as displacements of the superior endplate over the entire cyclic loading, and we compared them with the corresponding experimental data for validation purposes [4]. We obtained residual stresses and strains in the annulus, nucleus, and annular fibers at the end of cyclic loading. We used the stress–strain profiles to infer the potential mechanisms of load transfer and disc injury from cyclic loading.

Results

We compared the displacement of the superior endplate during the entire cyclic loading period with the experimental data at both low and high frequencies (Fig. 2). The model-predicted displacements were within the mean ± 1 standard deviation corridors of the test data. The displacement was greater during the initiation of the loading process and reduced exponentially in the first 2,000 cycles for the lower frequency and 1,000 cycles for the higher frequency. The displacement magnitudes were lower at the high frequency.

At the low frequency, the maximum (tensile) and mini-

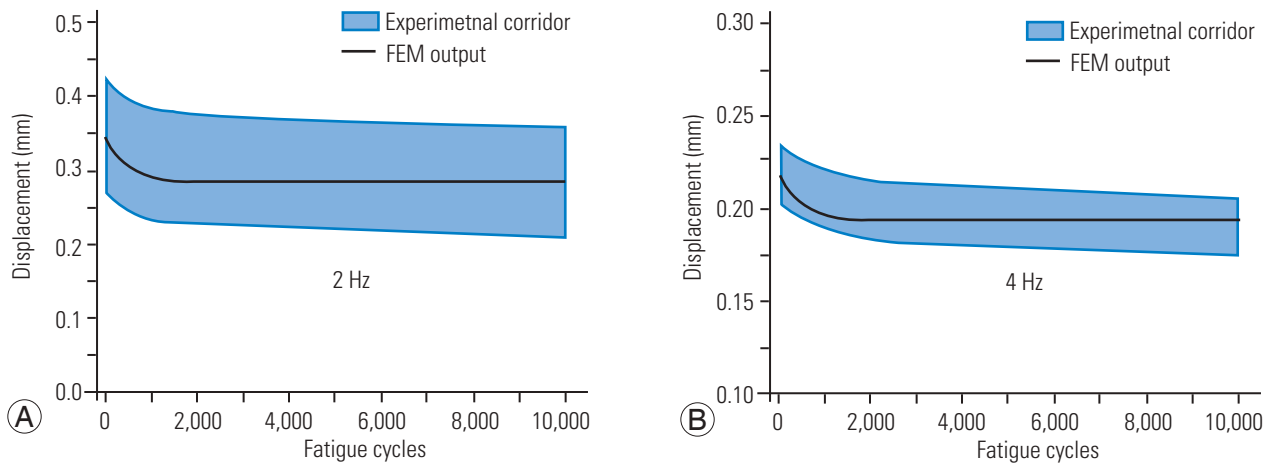
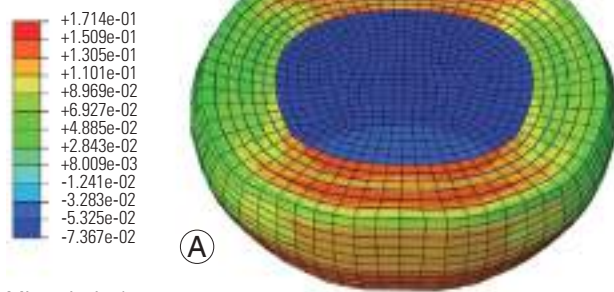


Fig. 2. Comparison of the model-predicted cyclic loading response (curve) with experimental corridors (shaded) at low (A) and high (B) frequency loadings. FEM, finite element method.

Max. principal
Fraction=-1.0 (Avg: 75%)



Min. principal
Fraction=-1.0 (Avg: 75%)

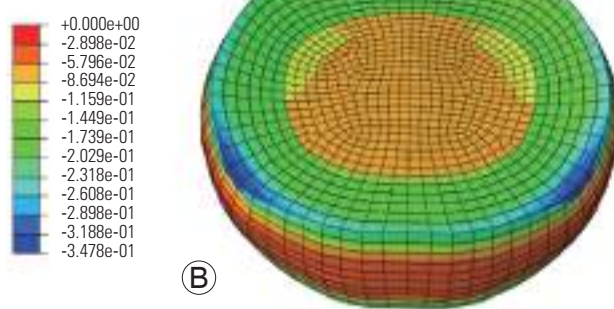
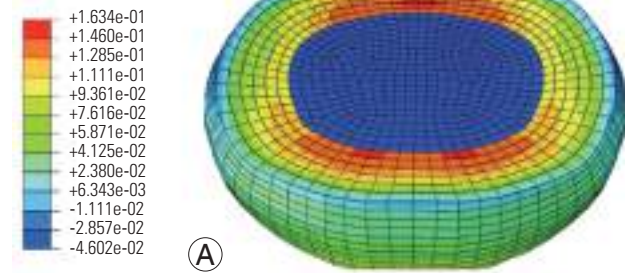


Fig. 3. Maximum (A) and minimum (B) principal stress distributions in the disc at the low frequency loading. Avg, average.

Max. principal
Fraction=-1.0 (Avg: 75%)



Min. principal
Fraction=-1.0 (Avg: 75%)

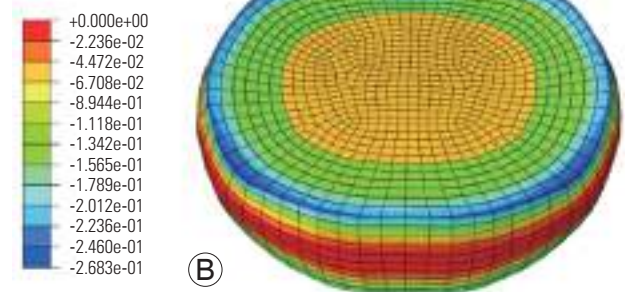


Fig. 4. Maximum (A) and minimum (B) principal stress distributions in the disc at the high frequency loading. Avg, average.

imum (compressive) principal stresses were higher in the annulus ground matrix than in the nucleus and annular fibers (Fig. 3). The maximum stress was higher in the anterior and posterior annular regions (regions toward the red color, Fig. 3). Further, the minimum stress was higher along the superior (blue color, Fig. 3) and inferior periphery of the disc. The pattern was similar at the high frequency, with lower amplitudes (Fig. 4). The compressive stresses were higher than the tensile stresses at both

frequencies.

At both frequencies, the maximum principal strains were radially directed, whereas the minimum principal strains (Figs. 5, 6) were axially and/or obliquely directed. The tensile and compressive strain vector amplitudes were higher at the low loading frequency (Fig. 5) than at the high loading frequency (Fig. 6).

At the low frequency, the von Mises stress distributions were transmitted across the cross-section of the annulus

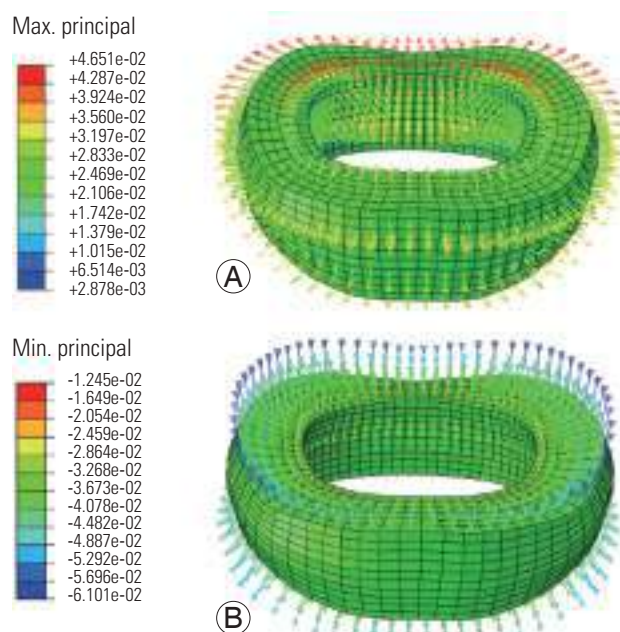


Fig. 5. Maximum (A) and minimum (B) principal strain distributions in the disc simulated at the low frequency loading.

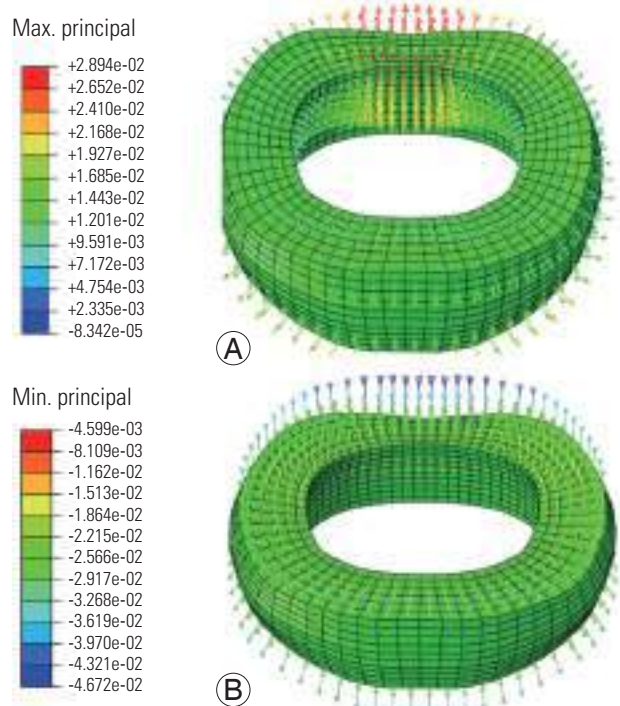


Fig. 6. Maximum (A) and minimum (B) principal strain distributions in the disc simulated at the high frequency loading.

(Fig. 7); however, at the high frequency, they were concentrated at the superior and inferior boundaries (Fig. 8). At both frequencies, the stresses in the annular fibers were greater in the posterior regions in the innermost layer and

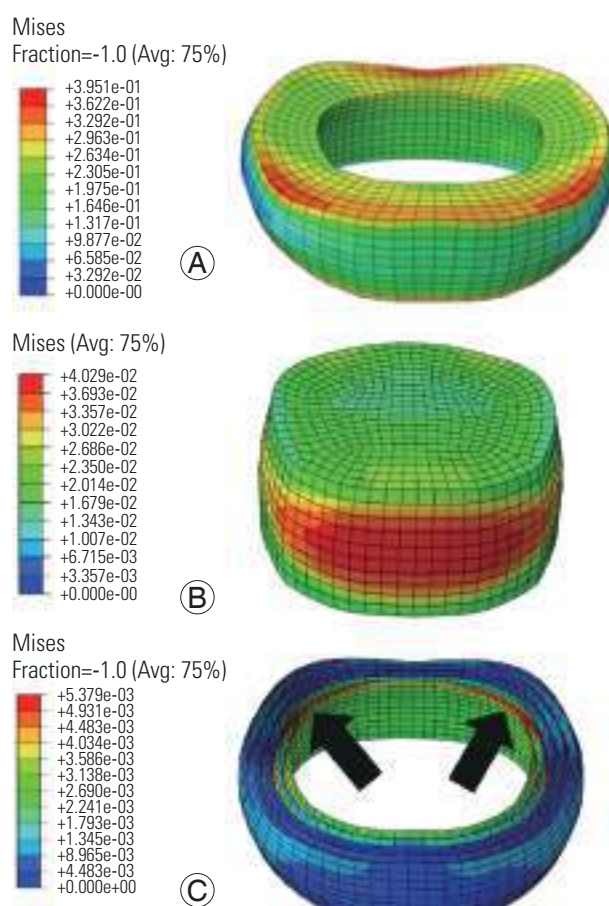


Fig. 7. Von Mises stress distribution in the annulus (A), nucleus (B), and annular fibers (C) at the low frequency loading. Red regions indicate largest magnitudes. Blue shows the smallest magnitudes. Arrows show the posterolateral regions with the largest stresses. Avg, average.

were concentrated near the posterolateral region of the disc (Figs. 7, 8). At both frequencies, the stress distributions in the nucleus were greater in the anterior and posterior directions; however, the stress was distributed in a larger area at the low frequency.

Discussion

Cyclic loading of the neck occurs in civilian and military occupational environments; however, individuals in military environments are subject to specific variables that render them more prone to suffering neck injuries from cyclic loading (e.g., head-supported masses, i.e., wearing of military helmets and their devices for longer periods) [14,15]. While the etiology of neck pain is multifactorial, biomechanical loading has been identified as a major external stress factor causing long-term changes, including

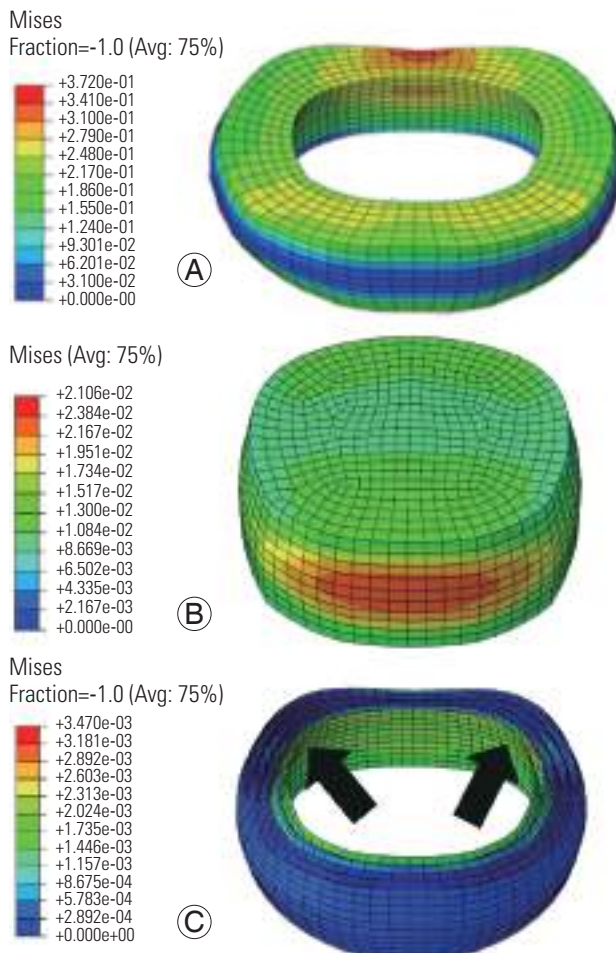


Fig. 8. Von Mises stress distribution in the annulus (A), nucleus (B), and annular fibers (C) at the high frequency loading. Red regions indicate largest magnitudes. Blue shows the smallest magnitudes. Avg, average.

cervical spondylosis. The identified pathways in civilian cases begin with biomechanical loads resulting in internal and physiological responses, causing mechanical strain and fatigue, thus leading to pain, discomfort, and impairment; loading repetitiveness is an important risk factor. Operating or driving of vibrating equipment has been positively associated with prolapsed discs in civilian environments. Changes in muscular activities caused by prolonged use of head-supported masses alter the muscular activity, as in low-velocity impacts, and result in pain [16]. In patients with known mechanisms of injury, 14% used Kevlar helmets, and noncombat operations accounted for 96% of all neck pains in a military-specific study [14]. Longer wearing periods of such helmets that are heavier than those used by civilians and carrying heavy backpacks were attributed as reasons for the predis-

position of military personnel to neck pain. The number of hours and repeated exposure accelerations and the use of head-mounted devices, such as night vision goggles, helmets, and oxygen masks, were identified in the etiology of flight-related neck pain in military pilots and airmen [17-21]. Extreme vibration was also considered a risk factor [8]. Although brief, these studies indicate that cyclic loading of the human head-neck occurs in both civilian occupational and military fields, with the head-supported mass acting as an added contributing factor in the military environments.

We aimed to explain clinical observations of disc disorders based on internal responses using a disc FE model. The loading magnitude represented the axial compressive forces sustained by the disc in military situations with head-supported masses, i.e., the helmet used in training and operational activities [22]. The model responses, expressed as disc displacement over the entire loading period, were within the experimental corridors. This validation process has been accepted in spine biomechanics studies with quasi-static and dynamic loadings [23-25].

Lower displacements at the high frequency indicate a strain rate-stiffening phenomenon (Fig. 2) associated with the disc responding to increasing loading rates with increased stiffness. This phenomenon has also been reported for lumbar discs. From this perspective, cyclic responses of the two regions of the spine are similar. While the experiments and present modeling results show a plateau of the response after 1,000–2,000 cycles of loading, the stress analysis outputs revealed additional insights into the internal mechanics of the disc components and assisted us in drawing clinical correlations.

The viscoelastic behavior of the annulus (simulated as a hyperviscoelastic material) contributed to the exponential reduction of disc displacement. A viscoelastic material is represented with a spring and a dashpot system, with the former representing elasticity and the latter representing the viscous behaviors. After applying the external force, the elastic and viscous components shared the strain in the annulus. With the removal of the force during the unloading phase, the strain in the elastic part instantaneously recovered, whereas the strain in the viscous component took time to recover. However, the next compression loading cycle started before the full recovery of the strain. The residual strain from the previous cycle caused the force to reach 150 N with lesser displacement. This phenomenon resulted in the exponential reduction in response over the

number of cycles.

The greater magnitude of the minimum principal stress and its concentration around the annulus periphery indicates an internal mechanism of load transfer. The lower magnitudes of the compressive stresses at the high frequency indicate that the cervical disc does not get time to react to the applied axial loading. This process may result in the accumulation of stress concentration in the superior and inferior boundaries of the disc, thus leading to local failures at the interface between the annulus and the endplates at the high frequency. The radial development of tensile strain and axial/oblique development of compressive strain shows that disc response is multimodal, although the loading is uniaxial. Therefore, we used von Mises stresses to understand the multimodal effects.

The distribution of the von Mises stresses over the thickness of the disc at the low frequency and their localization near the boundaries at the high frequency indicate the following: with increasing loading rates, the time required to transmit the stresses along the cross-section is reduced, thereby resulting in stress accumulation at the boundaries. This pattern may be clinically relevant. Asymmetric distributions in the stress patterns between the two frequencies, along with differences in the stress concentration patterns (higher at the boundaries and lesser stress concentration area with increases in frequency) indicate the likelihood of disc injury at the high frequency. The stress concentration at the posterior boundaries may lead to delamination of the annulus and endplates emanating from the posterior region (Figs. 7, 8). The development of gradients due to localized stresses is a risk factor for the delamination in lumbar spine aging-related disc and degeneration studies. Clinical studies in the area (not cited due to limitations in the number of references) have also implicated vibration/cyclic loading in accelerated disc degeneration leading to delamination. Studies concerning the cervical spine with repeated loading simulating military environments are few; however, based on the prevalence of neck pain in this population and the similarities between the lumbar and cervical disc components, it is reasonable to infer that the cervical discs are also susceptible to delamination. In addition, the cervical intervertebral discs also degenerate with increasing age (similar to lumbar discs), further supporting this idea.

The greater nucleus stresses in the anterior and posterior directions indicate that under axial loading, the incompressible nucleus attempts to move preferentially

along these directions. This movement is constrained by the innermost fiber layer, thus resulting in greater stresses in the posterolateral region. The stress concentration in the posterolateral regions of annular fibers may explain disc prolapse. In addition, these observations suggest that the mechanism of disc prolapse originates from the greatest stresses sustained by the innermost annular fibers transmitted to the outer layers. Cervical prolapse and disc herniation has been reported in civilian and military studies (not cited due to constraints in the number of references). From these perspectives, our study has provided additional insights into the internal mechanics of the disc and has offered an explanation for disc delamination and the propensity to initiate prolapse in the posterolateral regions, which are clinically relevant in both civilian and military populations.

Cervical disc herniation has been classified into central, para-central, posterolateral and lateral types [26-28]. One study reported a review of 745 cases of disc lesions, out of which lateral disc accounted for 607 (82%, soft type) and 95 (13%, hard type) of the cases, central spondylosis for 32 (4.3%), and central soft disc herniation for eight (1.0%) [29]. In a follow-up study involving surgical patients, data were reported from 296 cases: 246 (83%) from lateral soft and hard discs, 39 (13.2%) from spondylosis, and 11 (3.7%) from central/para-central soft discs [27]. Of those 11, there were seven cases of central and four cases of para-central herniation [27]. Other studies have reported greater numbers of para-central than posterolateral cases: from eight cases, five were para-central and three were posterolateral [30], and from 34 cases, 22 were para-central and 12 were posterolateral [28]. While the results from our study explain the posterolateral mechanism, other loading modes, such as flexion-extension may have to be considered to explain the para-central mechanism.

The present study used compressive loading; however, *in vivo*, the human cervical spine sustains complex loading including flexion and extension. We used compression for our cyclic loading experiments. However, to include other modes, it would be necessary to first conduct cyclic loading tests under those modes, use test data to validate the FE model, and then use its outputs, such as stresses, to delineate the injury mechanisms. In principle, this may be achieved using the same process used in the present investigation; however, we focused on the compression mode in our FE model. Another limitation is that our model applies only to the cervical spine and excludes the

lumbar spine where disc injuries are common. We limited our study to two frequencies, because of the availability of experimental data. Additional studies are warranted to relax these limitations and achieve wider applications for other spinal regions, loading modes, and frequencies.

Conclusions

We developed a FE model of the human C4–C5 disc; it comprised five layers of annulus fibers, a nucleus pulposus, ground substance, and endplates with appropriate material and element definitions. We validated the model using experimental data from C4–C5 disc segments under a compressive loading of 150 N for 10,000 cycles at two frequencies. Disc displacement was lower at high frequency, thus exhibiting strain rate stiffening and explaining stress accumulation at superior and inferior peripheries. Greater stresses and strains at the boundaries may explain disc injuries, such as delamination. The greater development of stresses in the innermost annular fiber layer migrating toward the posterolateral regions may explain disc prolapse.

Conflict of Interest

No potential conflict of interest relevant to this article was reported.

Acknowledgments

This material is the result of work supported with resources and use of facilities at the Zablocki Veterans Administration Medical Center (ZVAMC), Milwaukee, Wisconsin, the Department of Neurosurgery at the Medical College of Wisconsin (MCW), and the U.S. Army Medical Research and Materiel Command, Fort Detrick, Maryland, W81XWH-16-1-0010. The MCW authors are part time employees of the ZVAMC. Any views expressed in this article are those of the authors and not necessarily representative of the funding organizations.

References

1. Cervical Spine Research Society Editorial Committee, Clark CR, Benzel EC, et al. The cervical spine. 4th ed. Philadelphia (PA): Lippincott Williams &

- Wilkins; 2005.
2. Nightingale RW, Myers BS, Yoganandan N. Neck injury biomechanics. In: Yoganandan N, Nahum AM, Melvin JW, editors. Accidental injury: biomechanics and prevention. 3rd ed. New York (NY): Springer; 2015. p. 259-308.
3. Stemper BD, Yoganandan N, Pintar FA. Gender dependent cervical spine segmental kinematics during whiplash. *J Biomech* 2003;36:1281-9.
4. Yoganandan N, Umale S, Stemper B, Snyder B. Fatigue responses of the human cervical spine intervertebral discs. *J Mech Behav Biomed Mater* 2017;69:30-8.
5. Ang B, Harms-Ringdahl K. Neck pain and related disability in helicopter pilots: a survey of prevalence and risk factors. *Aviat Space Environ Med* 2006;77:713-9.
6. Balasubramanian V, Dutt A, Rai S. Analysis of muscle fatigue in helicopter pilots. *Appl Ergon* 2011;42:913-8.
7. Bridger RS, Groom MR, Jones H, Pethybridge RJ, Pullinger N. Task and postural factors are related to back pain in helicopter pilots. *Aviat Space Environ Med* 2002;73:805-11.
8. Cohen SP, Gallagher RM, Davis SA, Griffith SR, Carragee EJ. Spine-area pain in military personnel: a review of epidemiology, etiology, diagnosis, and treatment. *Spine J* 2012;12:833-42.
9. Jones JA, Hart SE, Baskin DS, et al. Human and behavioral factors contributing to spine-based neurological cockpit injuries in pilots of high-performance aircraft: recommendations for management and prevention. *Mil Med* 2000;165:6-12.
10. Qasim M, Natarajan RN, An HS, Andersson GB. Damage accumulation location under cyclic loading in the lumbar disc shifts from inner annulus lamellae to peripheral annulus with increasing disc degeneration. *J Biomech* 2014;47:24-31.
11. Ng HW, Teo EC. Nonlinear finite-element analysis of the lower cervical spine (C4-C6) under axial loading. *J Spinal Disord* 2001;14:201-10.
12. Yoganandan N, Kumaresan S, Voo L, Pintar FA. Finite element applications in human cervical spine modeling. *Spine (Phila Pa 1976)* 1996;21:1824-34.
13. Pitzen T, Schmitz B, Georg T, et al. Variation of endplate thickness in the cervical spine. *Eur Spine J* 2004;13:235-40.

14. Cohen SP, Kapoor SG, Nguyen C, et al. Neck pain during combat operations: an epidemiological study analyzing clinical and prognostic factors. *Spine (Phila Pa 1976)* 2010;35:758-63.
15. Bongers PM, Ijmker S, van den Heuvel S, Blatter BM. Epidemiology of work related neck and upper limb problems: psychosocial and personal risk factors (part I) and effective interventions from a bio behavioural perspective (part II). *J Occup Rehabil* 2006;16:279-302.
16. Kumar S, Narayan Y, Prasad N, Shuaib A, Siddiqi ZA. Cervical electromyogram profile differences between patients of neck pain and control. *Spine (Phila Pa 1976)* 2007;32:E246-53.
17. Andersen HT. Neck injury sustained during exposure to high-G forces in the F16B. *Aviat Space Environ Med* 1988;59:356-8.
18. Green ND. Acute soft tissue neck injury from unexpected acceleration. *Aviat Space Environ Med* 2003;74:1085-90.
19. Hamalainen O, Vanharanta H, Bloigu R. Determinants of +Gz-related neck pain: a preliminary survey. *Aviat Space Environ Med* 1993;64:651-2.
20. De Loose V, van den Oord M, Burnotte F, et al. Individual, work-, and flight-related issues in F-16 pilots reporting neck pain. *Aviat Space Environ Med* 2008;79:779-83.
21. Van den Oord MH, de Loose V, Meeuwssen T, Sluiter JK, Frings-Dresen MH. Neck pain in military helicopter pilots: prevalence and associated factors. *Mil Med* 2010;175:55-60.
22. Motiwale S, Subramani AV, Zhou Z, et al. Damage prediction for a cervical spine intervertebral disc. *Proceedings of the International Mechanical Engineering Congress & Exposition*; 2016 Nov 13-17; Phoenix, USA.
23. Kumaresan S, Yoganandan N, Pintar FA, Maiman DJ. Finite element modeling of the cervical spine: role of intervertebral disc under axial and eccentric loads. *Med Eng Phys* 1999;21:689-700.
24. Kumaresan S, Yoganandan N, Pintar FA, Maiman DJ, Goel VK. Contribution of disc degeneration to osteophyte formation in the cervical spine: a biomechanical investigation. *J Orthop Res* 2001;19:977-84.
25. Yoganandan N, Kumaresan S, Voo L, Pintar FA. Finite element model of the human lower cervical spine: parametric analysis of the C4-C6 unit. *J Biomech Eng* 1997;119:87-92.
26. Aronson N, Filtzer DL, Bagan M. Anterior cervical fusion by the smith-robinson approach. *J Neurosurg* 1968;29:396-404.
27. Scoville WB, Dohrmann GJ, Corkill G. Late results of cervical disc surgery. *J Neurosurg* 1976;45:203-10.
28. Yamano Y. Soft disc herniation of the cervical spine. *Int Orthop* 1985;9:19-27.
29. Scoville WB. Types of cervical disk lesions and their surgical approaches. *JAMA* 1966;196:479-81.
30. Yamano Y. Disc herniation of cervical spine. *Arch Orthop Trauma Surg* 1980;96:271-7.

Long Duration Tracking of Cervical Spine Kinematics with Ultrasound

Mingxin Zheng, Thomas L. Szabo, *Senior Life Member, IEEE*, Amin Mohamadi, and Brian D. Snyder

Abstract—Cervical-spine (C-spine) pathoanatomy is commonly evaluated by plane radiographs, CT or MRI; however, these modalities are unable to directly measure the dynamic mechanical properties of the functional spinal units (FSU) comprising the C-spine that account for its functional performance. We have developed an ultrasound-based technique that provides a non-invasive, real-time, quantitative, *in-vivo* assessment of C-spine kinematics and FSU viscoelastic properties. The fidelity of the derived measurements is predicated on accurate tracking of vertebral motion over a prolonged time duration. The purpose of this work was to present a bundle adjustment method that enables accurate tracking of the relative motion of contiguous cervical vertebrae from ultrasound radio-frequency data. The tracking method was validated using both a plastic anatomical model of a cervical vertebra undergoing prescribed displacements, and also human cadaveric C-spine specimens subjected to physiologically relevant loading configurations. While the velocity of motion and thickness of the surrounding soft tissue envelope affected accuracy, using the bundle adjustment method, B-mode ultrasound was capable of accurately tracking vertebral motion under clinically relevant physiologic conditions. Therefore, B-mode ultrasound can be used to evaluate *in-vivo* real-time C-spine kinematics and FSU mechanical properties in environments where radiographs, CT or MRI cannot be used.

Index Terms—ultrasound, spine, speckle tracking, tissue characterization

I. INTRODUCTION

NECK pain, a common occupational complaint [1], [2], is often instigated by chronic, repetitive loading or whole body vibrations encountered in the work environment [3]–[5]. Evaluation of C-spine pathoanatomy is assessed by physical examination and imaging studies that typically include multiple-planar radiographs, Computed Tomography (CT) or Magnetic Resonance Imaging (MRI) [6]. However recent research suggests that these diagnostic studies may be insufficient to reveal the mechanical etiology of C-spine degeneration [7], [8]. The static or quasi-static images acquired using these modalities fail to replicate the dynamic behavior of the C-spine encountered in the workplace during extreme or repetitive loading conditions. Less clinically accessible measurement techniques to evaluate C-spine kinematics such as optical

tracking systems [9] and dual fluoroscopy [10] are limited by radiation exposure, equipment size, power requirements and/or inaccuracies introduced by skin motion artifacts [11].

B-mode clinical ultrasound may provide a low-cost, non-invasive, non-radiative, portable diagnostic imaging method that can be employed in actual workplace environments. Image enhancement and segmentation algorithms have been developed to facilitate the identification of spinal landmarks by ultrasound [12]–[14]. Ultrasound imaging has been previously used to identify spinal anatomy during needle insertion for epidural anesthesia, nerve root or facet blocks and intrathecal administration of medications. Sequential ultrasound images have also been applied to measure changes in intervertebral disc height in response to applied spinal loads [15]–[19].

Acquisition of spine images by ultrasound requires an experienced sonographer to properly position the ultrasound transducer to visualize the desired anatomy. However, to measure dynamic vertebral motion *in-vivo* requires 1) the prolonged positioning of an ultrasound transducer in a consistent orientation and 2) an algorithm that corrects for small changes in the position of the transducer relative to the spinal anatomy unrelated to the dynamic motion of the vertebrae. To address the first problem, our group has developed a soft cervical collar that stabilizes the ultrasound transducer in a fixed orientation relative to the anterior structures of the subjects neck, such that the real-time motion of cervical functional spinal units (FSU, contiguous vertebral bodies with interposed intervertebral disc) could be imaged while the subject performed activities such as running and jumping [20]. To address the second problem, the development of an algorithm to correct for changes in the position of the transducer and motion artifact, is the subject of the current work.

The suitability of an ultrasound system to track the motion of vertebrae depends on the frame rate and exposure time of the imaging system [21]. Frame rates of current imaging systems range from 30 Hz (dual fluoroscopy) to 250 Hz (infrared optical tracking cameras); exposure times range from several seconds to minutes. To apply ultrasound to measure real time spine kinematics requires the acquisition of hundreds to thousands of image frames for each sequence. The frame-by-frame, multi-compression method employed by ultrasound elastography for long-term tracking tasks [22], [23] breaks large displacements into small incremental steps and sums the estimated displacements of each step. However, this approach leads to measurement drift and error accumulation since inherent measurement error and error variance will inexorably increase over time if displacements are summed in a step-by-step fashion. Several methods have been proposed to reduce

M. Zheng was with the Department of Biomedical Engineering, Boston University, Boston, MA 02215 USA, and also with Beth Israel Deaconess Medical Center, Boston, MA 02215 USA (e-mail:rogge@bu.edu)

T. L. Szabo is with the Department of Biomedical Engineering, Boston University, Boston, MA 02215 USA

A. Mohamadi is with Beth Israel Deaconess Medical Center, Boston, MA 02215 USA

B. D. Snyder is with the Department of Biomedical Engineering, Boston University, Boston, MA 02215 USA, Beth Israel Deaconess Medical Center, Boston, MA 02215 USA, and also Boston Children's Hospital, Boston, MA 02115 USA

measurement drift associated with the step-by-step summing approach: use larger incremental steps [24], self-correction [25], [26], or basing displacement estimates on an empirical model predicated on observed tissue biomechanics [27]. Bundle adjustment methods address the issue of object position reconstruction from different camera poses by solving a large sparse geometric parameteric estimation problem. Conversely, this same method can also be used to track the motion of a rigid body. By constructing a similar parametric estimation problem for ultrasound speckle tracking, we aimed to apply and validate a drift reducing bundle adjustment framework [28] that enables prolonged ultrasound tracking of dynamic vertebral motion.

II. METHODS

A bundle adjustment algorithm was developed to track rigid body motion using long-duration, ultrasound radio frequency (RF) data sequences. Implementation of the algorithm was validated by applying known, physiologically relevant, cyclic, lateral displacements that simulated cephalad-caudal spinal motions to a homogeneous plastic model of a cervical vertebra and then to human cadaveric cervical vertebrae, with soft tissue attachments. From knowledge of the true lateral displacement profiles applied over time, the accuracy of the displacement profiles was derived by comparing long duration, radio frequency (RF) data sequences using the bundle adjustment tracking algorithm to that derived using a standard frame-by-frame tracking technique.

A. Ultrasound RF Tracking Bundle Adjustment

The goal of deriving an accurate tracking algorithm is to minimize the error between the true position of the object and its estimated position in sequential ultrasound frames. Vertebrae are tracked as rigid bodies in the ultrasound RF sequence $\{I(p)\}$ where p is a single data sample in a region of interest (ROI) P . The current frame I_m is the m^{th} data frame in the sequence. The true position of the vertebra in I_m is expressed as a 2-dimensional (2D) vector x_m^* , extending from the image origin to a data point in the imaging plane. Its estimated position is denoted as x_m . When the vertebra moves, the RF signal pattern changes because the vertebra changes its position within the field of view (FOV) of the ultrasound transducer.

In typical ultrasound tracking applications [29]–[31], displacements between a 2D object and the transducer are calculated by comparing the position of the object over temporally sequential frames and summing to establish the new position of the object in the current frame. Motion estimation techniques, such as the template-based block-matching and optical flow tracking, compute the 2D displacement of the object between frames. However, the portrayal of the object in one frame may be an inaccurate template to compare the object in another frame. Therefore, the measured 2D displacement $d_{m,n}$ of an object between frame I_m and I_n is a noisy version of the difference between the true position of the

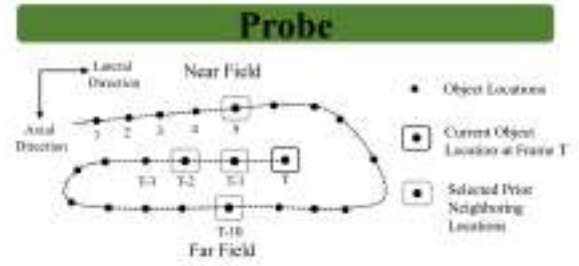


Fig. 1. Incremental object trajectory over time. Black dots represent object locations over time. The solid frame dot is the current object location at frame T . Four prior frames in which the object was in the neighborhood of the current location are selected from an image frame set K following this criteria: firstly, among all the historical frames from 1 to $T-1$, the immediate previous frame $T-1$ is selected; secondly, based on the computed displacements, K also includes the three previous frames in which the object locations were closest to the object location at $T-1$. Finally, object displacements are estimated between each of the four neighboring frames with the current frame I_m .

body in corresponding frames x_m^* and x_n^* , respectively, with measurement error $e_{m,n}^*$ (1).

$$e_{m,n}^* = x_m^* - x_n^* - d_{m,n} \quad (1)$$

The disadvantage of conventional frame-by-frame tracking routines is that errors accumulate over time if displacements are calculated by comparing the position of an object in the current frame relative to the position of the object in immediately adjacent previous frame (2). Representing the true initial position of an object x_1^* and its estimate x_1 as zero vectors, the estimated position x_m is obtained by summing displacements over all serially adjacent frames. The error e_m between x_m^* and its estimate x_m in the current frame, is the summation of noise e derived from each sequential frame pair (3), indicating that error will accumulate infinitely if only one reference frame is selected for comparison.

$$x_m = \sum_{i=2}^m d_{i,i-1} \quad (2)$$

$$e_m \stackrel{\text{def}}{=} x_m^* - x_m = \sum_{i=2}^m (x_i^* - x_{i-1}^* - d_{i,i-1}) = \sum_{i=2}^m e_{i,i-1}^* \quad (3)$$

To solve this problem, bundle adjustment method evaluates multiple previous spatially collocated frames, instead of the temporally adjacent previous frame, to better estimate the position change of the object and reduce progressive error accumulation. For the current frame I_m , the preceding frame positions comprising the objects trajectory of motion are used to select a set of former frame locations K that neighbor the current location (shaded region, Fig. 1). Displacements $d_{m,n}$ are estimated between the current frame I_m and each prior frame I_n , $1 \leq n < m$, in set K . The objective is to minimize the sum of displacement error between the selected frame pairs [32], which is a least square problem(4):

$$\min_{x_m} \sum_{n \in K_m} (e_{m,n}^T \Lambda_{m,n}^{-1} e_{m,n} + e_{n,m}^T \Lambda_{n,m}^{-1} e_{n,m}) \quad (4)$$

where: $e_{m,n}$ is the estimation of displacement measurement error (5) and $\Lambda_{m,n}$ is the covariance matrix of the estimated

object position between frame I_m and I_n . $\Lambda_{m,n}$ represents how reliable the pair-wise estimation is. The approximation of $\Lambda_{m,n}$ was previously derived [28] as (6), where N_P is the number of data samples representing object P in each frame.

$$e_{m,n} = x_m - x_n - d_{m,n} \quad (5)$$

$$\Lambda_{m,n} = \frac{1}{N_P} \sum_{p \in P} [I_n(p + d_{m,n}(p)) - I_m(p)]^2 \nabla I_m(p)^T \nabla I_m(p) \quad (6)$$

In our implementation of the algorithm, we solve the least square problem represented by (4) recursively for the current location relative to each of four previous neighboring frames. In the neighboring frames, the appearance and the location of object are similar to those in the current frame. This selected set of frames K is deduced from the prior trajectory (Fig.1): firstly, the immediate previous frame is selected; secondly, based on the computed displacements, K also includes the three previous frames in which the object locations were closest to the object location in the immediate previous frame. As suggested by the literature [28], size of K is set to four to balance the cost of the computation time and algorithm performance. The estimated positions of the object are derived from these multiple redundant displacement estimates to improve the robustness of tracking results.

B. Displacement Estimation

In our algorithm implementation, we used a 2D normalized cross-correlation (NCC) with subsample estimates to compute the displacement of the object $d_{m,n}$. The profile of the object (i.e. vertebra) was manually outlined as the ROI in the initial frame of the ultrasound RF data set. Given the bony surface of the vertebra has higher echogenicity than that of the surrounding soft tissues and the ambient environment, the acoustic signal of the vertebra was further localized by thresholding a 2D moving averaged filter image of the ROI. Since the measured vertebral motion was acquired low-resolution in the lateral direction of the ultrasound image, quadratic fitting subsample estimation method [33] was applied. The tracking

kernel contained 3 lateral and 15 axial RF data samples. As the vertebra is a rigid body with distinct bony surface geometry, the displacement estimate is derived by averaging over all the kernels for which the normalized correlation coefficient is greater than 0.85. For the purpose of fully validating the accuracy of the derived object displacements, no data point reduction was used in our experiments. The algorithm to calculate the 2D translational displacement of the vertebra was implemented using MATLAB 2016b (MathWorks, Natick, MA).

C. Validation Methods

The accuracy of the ultrasound displacement tracking algorithm was evaluated by applying known, cyclic, lateral displacements to a homogeneous plastic model of a cervical vertebra and then to human cadaveric cervical vertebrae, replete with soft tissue attachments. The specimens were subjected to lateral displacements that simulated *in-vivo* cephalad-caudal spinal motion [3], [5]. Sinusoidal and saw-tooth cyclic waveforms were applied at different frequencies and amplitudes to mimic the active functional motion of human subjects during repetitive activities [20], [34].

Test specimens were mounted onto the linear actuator piston of a servo-hydraulic material testing system (Instron 8511, Norwood, MA) and immersed in a water tank (Fig. 2). Lateral displacement was applied to the specimens by the servo hydraulic actuator under displacement control measured by an internal linear voltage displacement transformer (LVDT) at a sampling rate of 1000 Hz. The LVDT displacement data, considered to be ground truth, was compared to the displacement data derived from ultrasound RF data.

Ultrasound RF data was acquired using a Terason T3200 ultrasonic system (Terason Corp, Burlington, MA) with a Vernon 8IOL4 linear array (128 elements, center frequency: 3.6 MHz). The transmit focus length and imaging depth was set to 20mm and 40mm, respectively, at a imaging frame rate of 54 Hz. Time gain compensation (TGC) was set to the same intermediate value. The ultrasound projection angle was calculated by minimizing the square error between the

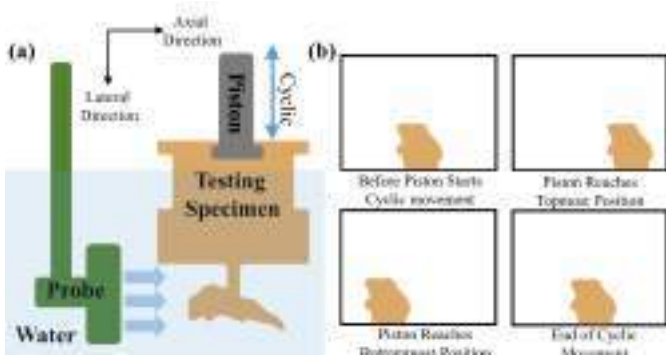


Fig. 2. (a) Test specimen and alignment jig mounted to the Instron linear actuator. The actuator translated the specimen in a cyclic lateral direction in the ultrasound image, monitored and controlled by the internal LVDT. The displacement of the specimen was measured by the ultrasound probe in a water tank. (b) Illustrations of different specimen positions in ultrasound images.

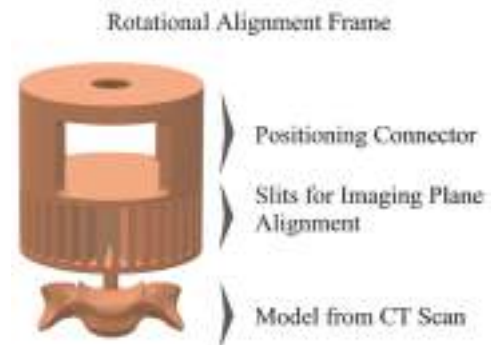


Fig. 3. Rotational alignment assembly: a circularly symmetric positioning frame consisting of a positioning connector with alignment slits attached to a plastic model of a human C4 vertebra. The positioning frame is used to align ultrasound probe with the phantom so that the out-of-plane specimen motion is minimized during the piston actuation. The piston is connected to the hole in the top of the frame. The vertebra model is attached in the bottom.

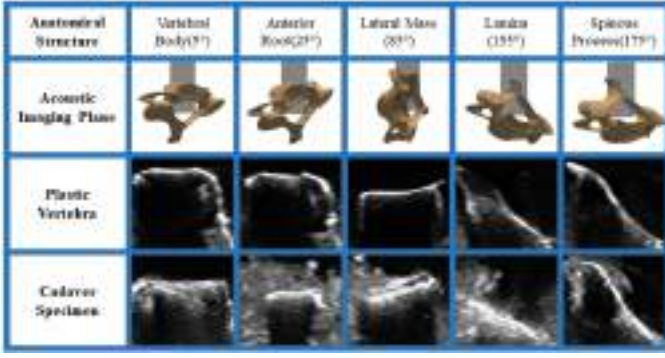


Fig. 4. Acoustic imaging plane and B-mode ultrasound images of corresponding surface profiles of the plastic vertebra and the cadaver specimen: acoustic imaging plane (grey) of the vertebra relative to different rotations of the vertebra reflect the different bone surface profiles generated by specific anatomical structures (vertebral body, anterior root, lateral mass, lamina and spinous process). Note RF speckle pattern noise induced by the overlaying soft tissue envelope in the cadaver specimen.

vertical displacement vector measured by the LVDT and the 2D displacement vector measured by the projected acoustic plane wave transmitted by the ultrasound transducer array. Data acquisition was synchronized between the LVDT and the ultrasound system.

1) *Plastic Vertebral Model*: A homogeneous plastic cervical spine vertebral model was created from a segmented CT scan of a human C4 cadaveric vertebra. The plastic vertebra was printed using a Form2 Desktop Stereolithography (SLA) 3D Printer (FormLabs, Boston, MA) attached to a specimen alignment assembly (Fig. 3). The alignment assembly was comprised of 36 circumferential vertical slits, spaced 10° apart, emanating radially from the central axis of the servo hydraulic piston, which served as a reference for determining the image angle between the ultrasound wave generated by the transducer and the mid-sagittal plane of the vertebra. This reference assembly was used to generate the range of ultrasound RF surface profiles representing the highly variable surface geometry of the vertebral structural anatomy as the specimen was rotated in 10° increments and imaged over 18 different acoustic wave projection angles from 0° to 180° (Fig. 4).

The plastic vertebral model was subjected to 40 combinations of sinusoidal displacement: integer value combinations of vibrational frequency (1-10 Hz) and amplitude (1-4 mm) over 10 seconds. This pattern was repeated for each of the 18 acoustic wave projection angles to evaluate the effect of using different RF surface profiles to evaluate different rotational alignments of the vertebra. Each slit provided a unique position for precisely aligning the transducer for each angle. The width and depth of each slit were designed based on an analysis of the beam and image plane sizes [35] so that the walls of the slit were invisible when the image plane was precisely aligned.

To describe the overall speed of motion in one cycle of the piston, we calculated the absolute velocity $|v|$ averaged over a cycle $\frac{1}{f}$, where A and f are the amplitude and frequency of an applied sinusoid as a function of time t :

$$|v| \stackrel{\text{def}}{=} f \int_0^{\frac{1}{f}} \left| \frac{d(A \cos(2\pi ft))}{dt} \right| dt = 4Af \quad (7)$$

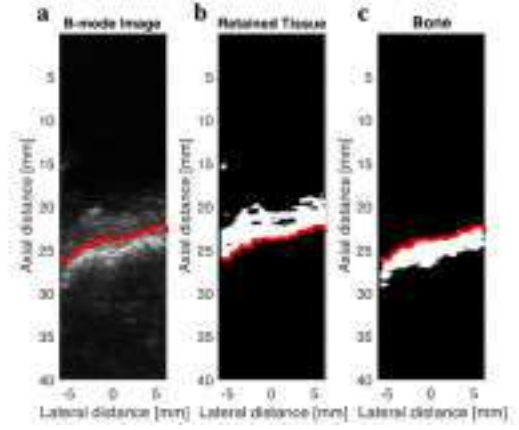


Fig. 5. (a) A typical B-mode ultrasound image of cadaveric vertebra at one angle. Tissue-bone boundary indicated by red curve. (b) Segmentation of soft tissue envelope above bone is highlighted by masking white. (c) Bone ROI below boundary is highlighted by binary masking white.

The displacement profiles of the plastic vertebra, estimated over time by the conventional frame-by-frame tracking method and the bundle adjustment tracking method, were compared to the true LVDT displacement profiles over time. The accumulated errors in estimating the displacement profiles during prolonged ultrasound imaging were statistically compared for each tracking method as a function of the applied amplitude, frequency and average velocity of cyclic motion.

2) *Ex-vivo Cadaveric Vertebrae*: Six fresh frozen vertebrae (C4, C5, and C6) were obtained from 2 human cadaveric cervical spines. These vertebral levels were chosen because they are most frequently involved in cervical spine degeneration and ultrasound can easily image these vertebra *in-vivo*. After defrosting at 4°C, the excised vertebrae were isolated, preserving the enveloping soft tissues to mimic conditions during *in-vivo* imaging applications. A vertebral screw anchor was inserted through the top of the vertebral body, co-axial with the centroid, to attach the vertebra to the rotational alignment assembly. The servo hydraulic piston served as a reference for determining each image angle between the acoustic wave generated by the ultrasound transducer and the applied displacement vector. RF ultrasound data were acquired for 5 different rotations of the vertebra (5°, 25°, 85°, 155° and 175°, the orientation of the acoustic wave relative to the mid-sagittal plane of the vertebrae) to generate different bone surface profiles evident when the specimen is imaged over a representative range of ultrasound transducer orientations (Fig. 4) that reflect bone surface contour shapes corresponding to specific anatomic structures (vertebral body, anterior root, lateral mass, lamina and spinous process).

Ultrasound tracking was based on the assumption that vertebrae were rigid bodies and they provided a consistent RF speckle pattern. The confounding effect of the soft tissue envelope was evaluated by segmenting the bone surface from the soft tissue envelope by thresholding the intensity of RF data (Fig. 5). The segmented regions of soft tissue and bone are shown individually as binary (white) masked regions in Fig. 5b and 5c. We calculated the tissue layer thickness in the ROI from the segmentation of tissue layer from the length

of each axial RF line in the ROI. Since the dimension of each pixel is known from the imaging system, we calculated the thickness of tissue for each data line and averaged them over all the RF lines in ROI to obtain a mean value of tissue layer thickness. The thicknesses of the soft tissue ROI were used as a metric to estimate the volume of tissue on the bone surface. Rigid body motion was derived both by excluding the soft tissues ROI from the bone ROI, thereby avoiding the incorporation of kernels contained within the surrounding soft tissue envelope into the derived ultrasound estimates of vertebral displacement. Each vertebra was subjected to 40 iterations of sinusoidal lateral displacements (amplitude range: 1-4 mm, frequency range: 1-10 Hz) for 10 seconds.

The displacement profiles over time of the cadaveric vertebrae were estimated by the conventional frame-by-frame tracking method and the bundle adjustment tracking algorithm and compared to the true LVDT displacement profiles over time. The accumulated errors in estimating the displacements of the vertebrae over time during prolonged ultrasound imaging were statistically compared for each tracking method as a function of the applied amplitude, frequency and average velocity of cyclic motion as well as errors induced in the bone RF speckle pattern due to incorporation of the retained soft tissue layer.

D. Statistical Analysis

Data acquisition from the LVDT and ultrasound imaging were synchronized, but the LVDT sampling rate (1000 Hz) was much higher than the imaging frame rate (54 Hz). Thus ultrasound displacements were mapped to the LVDT data at corresponding time points in error analysis. Ultrasound displacement measurement errors were computed by subtracting the estimated displacements for the frame-by-frame method and the bundle adjustment method from the actual applied displacement measured by the LVDT. Two statistical metrics: mean square error (MSE, σ^2) and error variance were used to identify and compare sources of error for the displacement estimates derived from the ultrasound RF data for the frame-

by-frame and bundle adjustment tracking methods for both the plastic vertebral model and cadaveric C-spine specimens.

MSE provided an overall assessment of measurement error for ultrasound RF derived displacement estimates compared to the true applied displacements portrayed by the LVDT data. We assumed that the confounding effects of motion artifact, $e_{v,i}$, related to the amplitude, frequency and average velocity of the cyclically applied displacements, affected the estimated displacements for both the plastic vertebra and the cadaveric vertebrae, while imaging artifacts, related to the volume of the retained soft tissue envelope in the ROI, $e_{tis,i}$, only affected the estimated displacement of the cadaveric vertebrae. These were considered to be independent sources of error affecting the displacement estimates (8). The MSE for displacement measured by ultrasound RF for the cadaveric vertebrae includes the MSE contributed by the soft tissue layer, σ_{tis}^2 and that contributed by motion artifact, σ_v^2 . The MSE related to the soft tissue layer can be determined by decomposing the MSE for the displacement data from the cadaveric vertebrae, by assuming that the MSE contributed by motion artifact only is represented by the plastic vertebral model displacement.

$$\begin{aligned}\sigma^2 &= \frac{1}{N} \sum_{i=1}^N e_i^2 = \frac{1}{N} \sum_{i=1}^N (e_{v,i} + e_{tis,i})^2 \\ &= \frac{1}{N} \sum_{i=1}^N (e_{v,i}^2 + e_{tis,i}^2) = \sigma_v^2 + \sigma_{tis}^2\end{aligned}\quad (8)$$

Error variance provides a time-dependent assessment of error accumulation and was used to compare the accumulated displacement error [22], [23] between the frame-by-frame and bundle adjustment displacement algorithms for the plastic vertebra over time for all 40 iterations of applied cyclic sinusoidal motion. An increase in error variance over time indicates a decrease in measurement accuracy over prolonged observation intervals.

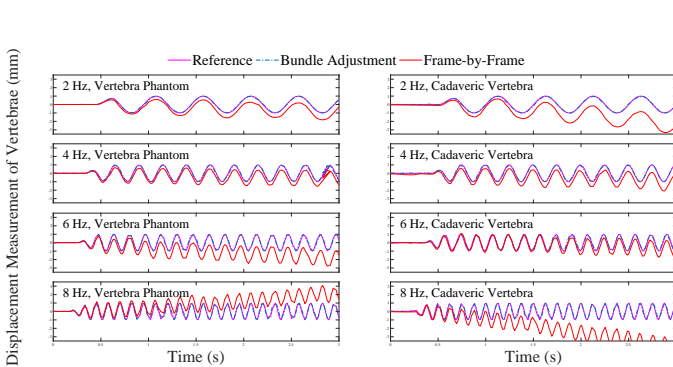


Fig. 6. Representative example of cyclic lateral displacement over time using ultrasound RF estimates derived by bundle adjustment algorithm (violet) and frame-by-frame method (red) for frequencies 2Hz, 4Hz, 6Hz and 8Hz compared to applied displacement (blue). The applied amplitude is 1mm; the imaging plane is oriented at 5 degrees to the mid-sagittal plane of the vertebra. Displacement estimates using the bundle adjustment algorithm are highly correlated with the reference data, while displacement estimates using the frame-by-frame method drift with increasing time duration.

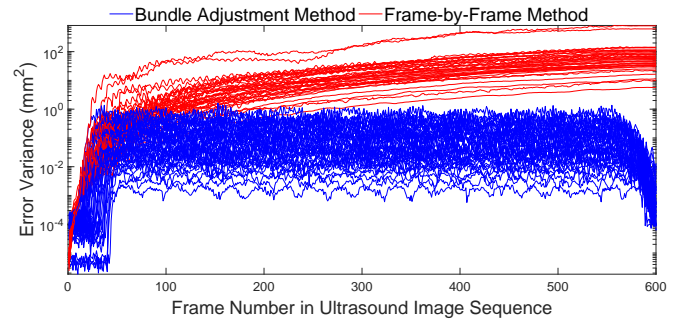


Fig. 7. Error variance viewed error accumulation from a time-dependent perspective and was used to compare the accumulated displacement error between the frame-by-frame (red) and bundle adjustment (blue) algorithms for the 40 iterations of cyclic sinusoidal motion applied to the plastic vertebra. Individual curves represent the error variance over time at a specific amplitude and frequency combination. The ascent and descent of the blue curves reflect the initiation and completion of the loading cycle, with 10 seconds of cyclic loading in between. At the end of each test, the error variance of bundle adjustment method dropped after the actuation stops, which suggests this method is less prone in accumulating error over time.

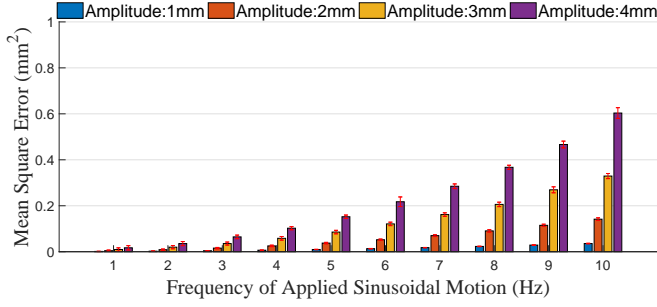


Fig. 8. MSE for ultrasound RF displacement estimates derived using the bundle adjustment tracking algorithm for plastic vertebra depends on both the frequency and the amplitude of the applied sinusoidal displacement. Each bar represents average MSE of 18 independent image sequences; error bars show standard deviations of MSE, which ranged from $7.33 \times 10^{-4} \text{ mm}^2$ (1Hz, 1mm) to $2.33 \times 10^{-2} \text{ mm}^2$ (10Hz, 4mm). The lowest MSE of $1.31 \times 10^{-3} \text{ mm}^2$ corresponds to an applied displacement amplitude of 1mm at a frequency of 1Hz; 3.6% error (approximated by RMSE divided by amplitude). The largest MSE of $6.03 \times 10 \text{ mm}^{-1} \text{ mm}^2$ corresponds to an applied displacement amplitude of 4mm at a frequency of 10 Hz; 19.4% error.

III. RESULTS

A. Bundle Adjustment vs. Frame-by-frame Tracking

For the plastic vertebra model and the cadaver vertebra, comparison of the ultrasound RF displacement estimates derived using the frame-by-frame method versus the bundle adjustment algorithm matched to the applied displacement demonstrate progressive error accumulation with increasing time duration of observation for the frame-by-frame method (Fig. 6). In particular, the speed of error accumulation speed in the frame-by-frame method is uncertain and difficult to correct by methods such as low-pass filters. This is in distinct contrast to the relatively stable and consistent displacement estimates derived using the bundle adjustment algorithm, which correlated highly (correlation ratio > 0.95) with the applied displacements and were less affected by the magnitude and frequency of the applied displacements or time duration of observation.

Comparison of the error variances for ultrasound RF displacement estimates derived using the bundle adjustment algorithm versus the frame-by-frame method (Fig. 7) indicate a progressive increase in error variance over time for the frame-by-frame method for observation intervals exceeding 100 frames, whereas the corresponding error variance plateaus at 1 mm^2 for the bundle adjustment algorithm; for observation intervals exceeding 200 frames, the error variance is 1-2 orders of magnitude smaller than the frame-by-frame method.

B. Bundle Adjustment Accuracy Analysis: Motion Artifacts

The MSE for the plastic vertebra model depended on both the amplitude and frequency of the applied displacement (Fig. 8): at each frequency, the larger the amplitude of applied displacement, the greater the MSE and for the same amplitude of applied displacement, the greater the frequency of applied displacement, the greater the MSE.

The average absolute velocity portrays the integrated product of the frequency of motion and amplitude of the applied displacement. For ultrasound RF displacement derived using

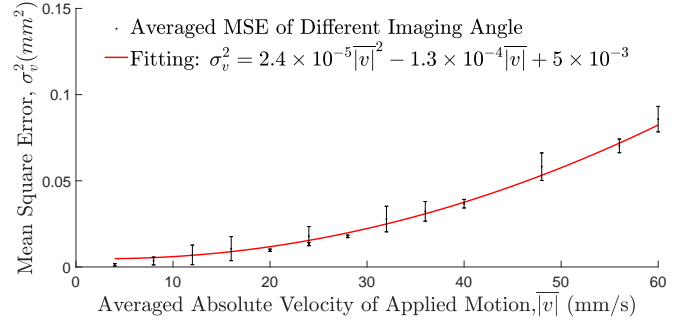


Fig. 9. The MSE for ultrasound RF displacement derived using the bundle adjustment tracking algorithm is a quadratic function of the average absolute velocity of the applied sinusoidal displacement, $R^2 = 0.96$.

the bundle adjustment tracking algorithm, the MSE varies as a quadratic function of the average absolute velocity ($R^2 = 0.96$; Fig. 9). This implies that the bundle adjustment tracking algorithm is robust for tracking rigid body motion at low speeds, but at higher speeds, motion artifact increases the frame-to-frame variability such that RF signal cross-correlation is decreased for sequential frames.

C. Bundle Adjustment Accuracy Analysis: Soft Tissue

The MSE for the cadaveric vertebrae was similar to that of the plastic vertebral model, affected both by the amplitude and frequency of the applied displacement: at each frequency, the larger the amplitude of applied displacement, the greater the MSE, and for the same amplitude of applied displacement, the greater the frequency of applied displacement, the greater the MSE (Fig. 10). However, the average MSE for ultrasound RF estimated displacements for the cadaveric vertebra was 28% greater than that for the plastic vertebra and the average standard deviation increased 620%. Even though soft tissue was excluded from the kernels evaluated in the ROI, so that only movement of the bone surface was tracked, inertial forces attributed to water in the soft tissues probably affected the RF signal pattern of the bone surface. The nonuniform thickness of the tissue layer may also have contributed to the error. Thus the increased error can be attributed to motion blurring induced by the retained soft tissue envelope and inconsistent geometric surface profiles related to anatomic variability among individuals.

Based on the assumption that motion and soft tissue artifacts affecting the displacement profiles for cadaveric vertebrae tracked by ultrasound RF were independent, the MSE attributed to the soft tissue envelope was derived by subtracting the MSE attributed solely to motion induced artifact, as represented by the quadratic function of the absolute velocity for the plastic vertebra (Fig. 9), from the total MSE for the cadaveric vertebrae. The resulting MSE varies as a quadratic function of the average thickness of the retained soft tissue layer ($R^2 = 0.69$; Fig. 11). The retained soft tissues affected the bone surface speckle pattern and degraded the cross-correlation among subsequent ultrasound RF frames.

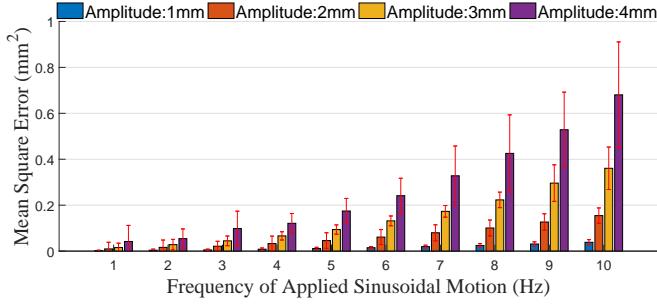


Fig. 10. MSE for ultrasound RF displacement estimates derived using the bundle adjustment tracking algorithm for cadaveric vertebrae is affected by both the frequency and the amplitude of the applied sinusoidal displacement. Each bar represents average MSE over 5 independent image profiles projections; error bars show standard deviations which range from $1.87 \times 10^{-3} \text{ mm}^2$ (1Hz, 1mm) to $2.30 \times 10^{-1} \text{ mm}^2$ (10Hz, 4mm). Using the bundle adjustment algorithm to track cadaveric vertebral motion, the MSE ranges between $1.87 \times 10^{-3} \text{ mm}^2$, error 4.32% for an applied frequency of 1Hz, 1mm displacement amplitude; to $6.80 \times 10^{-3} \text{ mm}^2$, error 20.6% at an applied frequency of 10Hz, 4mm displacement amplitude.

IV. DISCUSSION AND CONCLUSION

Frame-by-frame, multi-compression methods have been previously employed in ultrasound elastography for long-term tracking tasks. However in 1- and 2-D ultrasound elastography simulations Bayer et al [22], [23] demonstrated that while initially the variance was constant for an applied strain, as strain magnitudes accumulated over time, the variance rapidly increased. Several methods have been proposed to reduce measurement drift associated with a step-by-step summing approach: use larger incremental steps [24], self-correction [25], [26], or basing displacement estimates on an empirical model predicated on observed tissue biomechanics [27]. Normalized crosscorrelation (NCC) based template matching and subsample analysis of lateral displacement estimates can improve the long-term tracking of objects by ultrasound. Focusing the ultrasound beam width and the pitch of the acoustic elements improves the noise and reliability of object displacements estimated in the lateral direction for ultrasound elastography [36], [37]. Subsample estimation methods can also improve the accuracy of lateral displacement ultrasound measurements [26], [33], [37], [38]. In our analysis, since the majority of object displacement is lateral, the bundle adjustment tracking algorithm uses a simplified 2D quadratic fit to a subsample of ultrasound frames to estimate lateral displacement. Multi-dimensional 2-D polynomial fitting methods [33] may provide better estimates, but were not explored in our study.

For *in-vivo* ultrasound imaging, the dynamic motion of the vertebra will not necessarily be 2D, and the tissue deformation will be asynchronous, owing to different dynamic material tissue properties. Though there are previous studies using signal decorrelation or deep learning algorithms to analyze the complex motion in a 2D transducer, recovering 3D motion with a 2D imaging device is essentially an ill-posed problem. Furthermore, while we assume rigid body motion of the vertebrae, elastic and viscoelastic deformation of the surrounding soft tissue envelope and IVD can introduce artifacts, as highlighted by comparing the MSE of the plastic vertebral model to the cadaveric vertebrae. Previous studies have reviewed factors

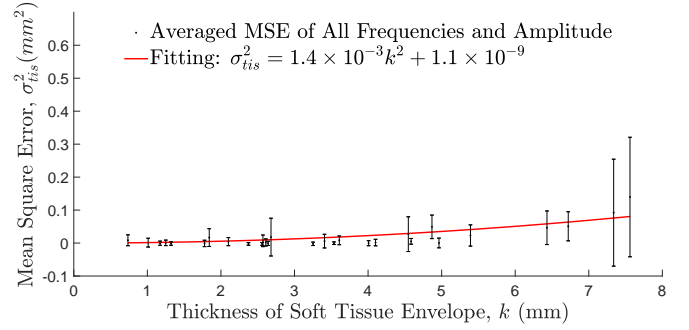


Fig. 11. MSE varies as quadratic function of the retained soft tissue thickness for the cadaveric vertebrae ($R^2 = 0.69$). Each data point represents the MSE for a specific orientation profile for each cadaveric vertebra averaged over 4 amplitudes and 10 frequencies. The MSE contributed by soft tissue thickness less than 4 mm is close to zero, but increases dramatically for specimens with greater retained soft tissue volumes.

that degrade ultrasound image profiles such as signal intensity variation and non-rigid body motion attributed to elastic and inelastic soft tissue deformation that affect speckle tracking accuracy [39], [40]. Our work only accounts for 2D planar motion of a rigid body, and out of plane motion is not expected in our validation experiments. To apply such an algorithm in a clinical setup, fixation of the ultrasound probe to the anatomy needs to be well-designed to minimize out-of-plane motion. We have used this tracking approach successfully for jumping and other motion experiments described elsewhere [20]. In addition, our current method bundles sets of frames with similarity in object location. To address 3D motion, the appearance of object of interest would also be important to consider in the process of frame set bundling.

The bundle adjustment tracking algorithm presented here enables ultrasound RF tracking of rigid body motion over a prolonged time interval of observation, with less accumulated error compared to conventional frame-by-frame tracking methods. The bundle adjustment algorithm uses the profile of retrospective tracking frames and redundant information to reduce accumulated error, but at an added computational cost proportional to the number of redundant frame points engaged by the algorithm. This model-free algorithm does not require prior knowledge of the dynamic material properties of the FSU or anticipation of the trajectory of the rigid body motion, required for other accumulated error reduction techniques. Cyclic displacement tests using both a plastic vertebral model and human cadaveric vertebrae validated that the algorithm can be applied to clinical B-mode ultrasound to track cervical spine motion over extended time intervals. Furthermore, they are sufficient to provide non-invasive, real-time, quantitative, assessment of C-spine kinematics and FSU viscoelastic properties over a range of frequencies and amplitudes relevant to studying repetitive occupational exposures associated with acute and chronic cervical spine injuries. The precision and accuracy of the estimated vertebral displacements deduced using the bundle adjustment algorithm applied to ultrasound RF tracking frames were dependent on the sonic reflective surface geometry of the vertebral anatomy relative to the orientation of the ultrasonic transducer, the velocity of the moving

vertebrae, and the thickness of soft tissue envelope surrounding the bone surface. Shallow anatomic surfaces with larger radii of curvature improved the reliability of ultrasonic tracking, thus ultrasound projections of anterior spinal anatomy that included the vertebral body and interposed intervertebral discs provided the most consistently identifiable RF profiles of the FSU to track over time. Based on the quadratic relationship between MSE and relative velocity, the expected MSE will be less than 5% when tracking an applied FSU-IVD strain of 50% at 5 Hz or an applied FSU-IVD strain of 25% at 10 Hz. Compared to the posterior aspect of the C-spine where multiple para-cervical muscles insert onto specific posterior anatomic elements, there are few direct muscle attachments directly onto the anterior anatomic surfaces of the cervical spine, thus the soft tissues immediately adjacent to the anterior aspect of the cervical vertebrae are relatively thin, decreasing the MSE attributable to the attached soft tissue envelope.

As indicated in (Fig. 8-10), and the accompanying text, MSE rose with the square of the frequency. The maximum frequency we measured, 10 Hz, was determined by the frame rate of our portable delay and sum imaging system and was sufficient for the clinical studies we undertook [20] which involved two synchronized imaging systems. Limitations of access to the software of the system prevented us from other options, for example, plane wave imaging [41] which could significantly increase our frame rate as well as the amount of data generated. However, more data would also significantly increase the computational time and the error accumulation over time. To the best of our knowledge, due to drifts in tracking, acceleration of motion is considered a more appropriate measurement in bone imaging with a high frame rate system [42]. Future work can address ways of reducing the computation time required for tracking; once solutions are available, other options such as plane wave imaging become more feasible.

The work presented here establishes the methods for using B-mode ultrasound as a portable means to measure C-spine kinematics in subjects performing workplace activities and to provide a noninvasive method to evaluate the mechanical performance of the C-spine that can be correlated with clinical symptoms and pathologic changes.

ACKNOWLEDGMENT

We appreciate funding support from the U.S. Army Medical Research and Materiel Command Fort Detrick, Maryland (01026018, Contract No. W81XWH-13-1-0050).

REFERENCES

- [1] M. D. Grossman, P. M. Reilly, T. Gillett, and D. Gillett, "National survey of the incidence of cervical spine injury and approach to cervical spine clearance in us trauma centers," *Journal of Trauma and Acute Care Surgery*, vol. 47, no. 4, pp. 684–690, 1999.
- [2] H. Yang, S. Haldeman, A. Nakata, B. Choi, L. Delp, and D. Baker, "Work-related risk factors for neck pain in the us working population," *Spine*, vol. 40, no. 3, pp. 184–192, 2015.
- [3] N. K. Kittusamy and B. Buchholz, "Whole-body vibration and postural stress among operators of construction equipment: a literature review," *Journal of safety research*, vol. 35, no. 3, pp. 255–261, 2004.
- [4] M. Qasim, R. N. Natarajan, H. S. An, and G. B. Andersson, "Damage accumulation location under cyclic loading in the lumbar disc shifts from inner annulus lamellae to peripheral annulus with increasing disc degeneration," *Journal of Biomechanics*, vol. 47, no. 1, pp. 24–31, 2014.
- [5] J. Village, J. B. Morrison, and D. K. N. Leong, "Whole-body vibration in underground load-haul-dump vehicles," *Ergonomics*, vol. 32, no. 10, pp. 1167–1183, 1989.
- [6] L. Ombregt, "6 - clinical examination of the cervical spine," in *A System of Orthopaedic Medicine (Third Edition)*. Churchill Livingstone, 2013, vol. 1, pp. 119–133.
- [7] J. F. Holmes and R. Akkinepalli, "Computed tomography versus plain radiography to screen for cervical spine injury: a meta-analysis," *Journal of Trauma and Acute Care Surgery*, vol. 58, no. 5, pp. 902–905, 2005.
- [8] A. Kettler and H.-J. Wilke, "Review of existing grading systems for cervical or lumbar disc and facet joint degeneration," *European Spine Journal*, vol. 15, no. 6, pp. 705–718, 2006.
- [9] N. R. Evans, G. Hooper, R. Edwards, G. Whatling, V. Sparkes, C. Holt, and S. Ahuja, "A 3d motion analysis study comparing the effectiveness of cervical spine orthoses at restricting spinal motion through physiological ranges," *European Spine Journal*, vol. 22, no. 1, pp. 10–15, 2013.
- [10] W. J. Anderst, E. Baillargeon, W. F. Donaldson III, J. Y. Lee, and J. D. Kang, "Validation of a non-invasive technique to precisely measure in vivo three-dimensional cervical spine movement," *Spine*, vol. 36, no. 6, p. E393, 2011.
- [11] R. Shultz, A. E. Kedgley, and T. R. Jenkyn, "Quantifying skin motion artifact error of the hindfoot and forefoot marker clusters with the optical tracking of a multi-segment foot model using single-plane fluoroscopy," *Gait & posture*, vol. 34, no. 1, pp. 44–48, 2011.
- [12] D. Tran and R. N. Rohling, "Automatic detection of lumbar anatomy in ultrasound images of human subjects," *IEEE Transactions on Biomedical Engineering*, vol. 57, no. 9, pp. 2248–2256, 2010.
- [13] S. Mehdizadeh, S. Muller, T. F. Johansen, and S. Holm, "Application of eigen-spaced beamformers for imaging lamina of vertebral arch," in *2012 IEEE International Ultrasonics Symposium*. IEEE, 2012, pp. 2238–2241.
- [14] S. Yu, K. K. Tan, B. L. Sng, S. Li, and A. T. H. Sia, "Feature extraction and classification for ultrasound images of lumbar spine with support vector machine," in *2014 36th Annual International Conference of the IEEE Engineering in Medicine and Biology Society*. IEEE, 2014, pp. 4659–4662.
- [15] C. Arzola, S. Davies, A. Rofaeel, and J. C. Carvalho, "Ultrasound using the transverse approach to the lumbar spine provides reliable landmarks for labor epidurals," *Anesthesia & Analgesia*, vol. 104, no. 5, pp. 1188–1192, 2007.
- [16] G. N. Kawchuk, A. M. K. Holm, L. Ekström, T. Hansson, and S. H. Holm, "Bulging of the inner and outer annulus during in vivo axial loading of normal and degenerated discs," *Clinical Spine Surgery*, vol. 22, no. 3, pp. 214–218, 2009.
- [17] T. H. Marshburn, C. A. Hadfield, A. E. Sargsyan, K. Garcia, D. Ebert, and S. A. Dulchavsky, "New heights in ultrasound: first report of spinal ultrasound from the international space station," *The Journal of emergency medicine*, vol. 46, no. 1, pp. 61–70, 2014.
- [18] W. van den Hoorn, M. W. Coppieters, J. H. van Dieën, and P. W. Hodges, "Development and validation of a method to measure lumbosacral motion using ultrasound imaging," *Ultrasound in medicine & biology*, vol. 42, no. 5, pp. 1221–1229, 2016.
- [19] C. D. McKinnon and J. P. Callaghan, "Validation of an ultrasound protocol to measure intervertebral axial twist during functional twisting movements in isolated functional spinal units," *Ultrasound in medicine & biology*, vol. 45, no. 3, pp. 642–649, 2019.
- [20] M. Zheng, A. Mohamodi, T. Szabo, and B. Snyder, "In-vivo cervical spine fsu dynamic motion measured by dual ultrasound: The effect of muscle activation," in *2016 IEEE International Ultrasonics Symposium (IUS)*, Sep. 2016, pp. 1–4.
- [21] G. Li, S. K. Van de Velde, and J. T. Bingham, "Validation of a non-invasive fluoroscopic imaging technique for the measurement of dynamic knee joint motion," *Journal of biomechanics*, vol. 41, no. 7, pp. 1616–1622, 2008.
- [22] M. Bayer and T. J. Hall, "Variance and covariance of accumulated displacement estimates," *Ultrasonic imaging*, vol. 35, no. 2, pp. 90–108, 2013.
- [23] M. Bayer, T. J. Hall, L. P. Neves, and A. Carneiro, "Two-dimensional simulations of displacement accumulation incorporating shear strain," *Ultrasonic imaging*, vol. 36, no. 1, pp. 55–73, 2014.

- [24] T. Benz, M. Kowarschik, and N. Navab, "Kernel-based tracking in ultrasound sequences of liver," in *Proceedings of challenge on liver ultrasound tracking, MICCAI workshop*, 2014, pp. 21–28.
- [25] T. P. O'shea, J. C. Bamber, and E. J. Harris, "Temporal regularization of ultrasound-based liver motion estimation for image-guided radiation therapy," *Medical physics*, vol. 43, no. 1, pp. 455–464, 2016.
- [26] R. Zahr-Azar and S. E. Salcudean, "Motion estimation in ultrasound images using time domain cross correlation with prior estimates," *IEEE Transactions on Biomedical Engineering*, vol. 53, no. 10, pp. 1990–2000, 2006.
- [27] H. Rivaz, E. M. Bector, M. A. Choti, and G. D. Hager, "Ultrasound elastography using multiple images," *Medical image analysis*, vol. 18, no. 2, pp. 314–329, 2014.
- [28] A. Rahimi, L.-P. Morency, and T. Darrell, "Reducing drift in differential tracking," *Computer Vision and Image Understanding*, vol. 109, no. 2, pp. 97–111, 2008.
- [29] A. Hsu, N. Miller, P. Evans, J. Bamber, and S. Webb, "Feasibility of using ultrasound for real-time tracking during radiotherapy," *Medical physics*, vol. 32, no. 6Part1, pp. 1500–1512, 2005.
- [30] M. Larsson, P. Verbrugghe, M. Smoljkić, J. Verhoeven, B. Heyde, N. Famaey, P. Herijgers, and J. Dhooze, "Strain assessment in the carotid artery wall using ultrasound speckle tracking: validation in a sheep model," *Physics in Medicine & Biology*, vol. 60, no. 3, p. 1107, 2015.
- [31] R. Prevost, M. Salehi, S. Jagoda, N. Kumar, J. Sprung, A. Ladikos, R. Bauer, O. Zettinig, and W. Wein, "3d freehand ultrasound without external tracking using deep learning," *Medical image analysis*, vol. 48, pp. 187–202, 2018.
- [32] B. Triggs, P. F. McLauchlan, R. I. Hartley, and A. W. Fitzgibbon, "Bundle adjustment modern synthesis," in *International workshop on vision algorithms*. Springer, 1999, pp. 298–372.
- [33] R. Z. Azar, O. Goksel, and S. E. Salcudean, "Sub-sample displacement estimation from digitized ultrasound rf signals using multi-dimensional polynomial fitting of the cross-correlation function," *IEEE transactions on ultrasonics, ferroelectrics, and frequency control*, vol. 57, no. 11, pp. 2403–2420, 2010.
- [34] J. H. v an Dieen, M. Creemers, I. Draisma, H. Toussaint, and I. Kingma, "Repetitive lifting and spinal shrinkage, effects of age and lifting technique," *Clinical Biomechanics*, vol. 9, no. 6, pp. 367–374, 1994.
- [35] T. L. Szabo, "Chapter 6- beamforming," in *Diagnostic Ultrasound Imaging: Inside Out*. Academic Press, 2014, pp. 167–207.
- [36] R. Righetti, S. Srinivasan, A. T. Kumar, J. Ophir, and T. A. Krouskop, "Assessing image quality in effective poisson's ratio elastography and poroelastography: I," *Physics in Medicine & Biology*, vol. 52, no. 5, p. 1303, 2007.
- [37] J. Jiang and T. J. Hall, "A coupled subsample displacement estimation method for ultrasound-based strain elastography," *Physics in Medicine & Biology*, vol. 60, no. 21, p. 8347, 2015.
- [38] B. J. Geiman, L. N. Bohs, M. E. Anderson, S. M. Breit, and G. E. Trahey, "A novel interpolation strategy for estimating subsample speckle motion," *Physics in Medicine & Biology*, vol. 45, no. 6, p. 1541, 2000.
- [39] T. Liang, L. Yung, and W. Yu, "On feature motion decorrelation in ultrasound speckle tracking," *IEEE transactions on medical imaging*, vol. 32, no. 2, pp. 435–448, 2013.
- [40] S. K. Alam and J. Ophir, "Reduction of signal decorrelation from mechanical compression of tissues by temporal stretching: Applications to elastography," *Ultrasound in medicine & biology*, vol. 23, no. 1, pp. 95–105, 1997.
- [41] G. Montaldo, M. Tanter, J. Bercoff, N. Benech, and M. Fink, "Coherent plane-wave compounding for very high frame rate ultrasonography and transient elastography," *IEEE Transactions on Ultrasonics, Ferroelectrics, and Frequency Control*, vol. 56, no. 3, pp. 489–506, March 2009.
- [42] T. Kaddoura, A. Au, G. Kawchuk, R. Uwiera, R. Fox, and R. Zemp, "Non-invasive spinal vibration testing using ultrafast ultrasound imaging: A new way to measure spine function," *Scientific reports*, vol. 8, no. 1, p. 9611, 2018.



Mingxin Zheng, Ph.D. Mingxin Zheng received the B.S. degree in microelectronics from the Peking University, Beijing, China in 2011 and the Ph.D. degree in biomedical engineering from Boston University, Boston, Massachusetts, United States in 2018.

From 2012 to 2018, he was a Research Assistant and Postdoctoral Fellow in the Center of Advanced Orthopaedics Studies in Beth Israel Deaconess Medical Center, Boston. Currently he is a Research Scientist in the Ultrasound Intervention and Intervention

Department in Philips Research North America. His research interests include motion tracking and pattern recognition in ultrasound imaging.



Thomas L. Szabo (M'72-SM'99-LSM'09) received the B.S. in electrical engineering from the University of Virginia, Charlottesville, VA in 1966, the M.S.EE from the University of Rochester, Rochester, NY in 1968, and the Ph.D. in Physics from the University of Bath, Bath, U.K. in 1993.

From 1970–1981, he was a Research Scientist at Air Force Cambridge Research Laboratories (later Rome Air Development Center) doing basic research on surface acoustic wave devices and nondestructive evaluation. For 1979–1980, he was on the staff, School of Engineering Sciences, Oxford University, UK. During 1981–2000, as a Senior R&D Engineer, he conducted research and development on diagnostic ultrasound imaging systems at Hewlett Packard and Agilent Technologies in Andover, MA. Since 2001, he has been a Research Professor with the Biomedical and Mechanical Engineering Departments at Boston University, Boston, MA. He is author of *Diagnostic Ultrasound Imaging: Inside Out* as well as over 100 papers and twelve book chapters, and holds four patents. He is a leader of international and U.S. technical and standards committees. His wide range of interests include ultrasound tissue and spine characterization, wave equations, novel imaging systems, therapeutic ultrasound, nonlinear phenomena and geophysical exploration.

Dr. Szabo is a Fellow of the American Institute of Ultrasound in Medicine (2007) and the Acoustical Society of America (2000). He has been a U.S. delegate to the International Electrotechnical Commission (IEC), Technical Committee 87, since 1986 and a Convenor of working Group 6 on high intensity therapeutic ultrasound and focusing since 1988. He was a recipient of a 1973 U. S. Meritorious Service Medal, a Hewlett Packard Fellowship and the 1974 best paper award in the IEEE Transactions on Sonics and Ultrasonics.



Amin Mohamadi, M.D., M.PH. was born in Arak, Iran in 1985 and received his MD-MPH degree from Tehran University of Medical Sciences in Tehran, Iran in 2013.

He joined Professor Snyders lab at the Center for Advanced Orthopaedic Studies at Beth Israel Medical Center with joint appointment at Harvard Medical School in Boston, Massachusetts, USA as postdoctoral research fellow in 2016. He has published more than 30 peer-reviewed articles in the field of musculoskeletal injury and bone regeneration

and serves as an ad hoc peer-reviewer for several journals.

Dr. Mohamadis current research interests include clinical and translational research in the field of musculoskeletal injury and as well as studying spine structure and dynamic mechanical behavior using clinical ultrasound.



Brian D. Snyder, M.D., Ph.D. received B.Sc. and M.Sc. in bioengineering from University of Pennsylvania, Philadelphia, PA, USA. He then finished his Medical Doctorate and Ph.D. at University of Pennsylvania School of Medicine, Philadelphia, PA in 1986.

He is a Professor of Orthopaedic Surgery at Harvard Medical School and Research Professor of Bioengineering at Boston University, Department of Bioengineering. As an attending orthopaedic surgeon at Boston Childrens Hospital, he directs the Cerebral Palsy program; his clinical practice focuses on congenital and acquired deformities about the hip and spine related to neuromuscular conditions as well as pediatric trauma. Professor Snyder is a clinician-scientist funded by NIH, DoD and OREF, and his translational research focuses on improving the practice of orthopaedic surgery by applying engineering principles to solve clinical problems. Using principles of structural engineering to analyze computed tomographic images of skeletal metastases; he developed a non-invasive method to accurately predict pathological fractures in cancer patients, thereby providing a mechanical assay of bone health that is now being used to optimize orthopaedic treatment in clinical trials. In recognition for this work, Dr. Snyder received a Kappa Delta Award from the American Academy of Orthopaedic Surgeons.

Ultrasound Can Measure Dynamic Motion of Cervical Spine Intervertebral Disc

^{1,2}Shiuan, KS; ^{1,2}Zheng, M; ^{1,3,4}Buckland, DM; ^{1,4,5}Snyder, BD

¹Beth Israel Deaconess Medical Center, Boston, MA, USA, ²Boston University, Boston, MA, USA, ³Massachusetts Institute of Technology, Cambridge, MA, USA, ⁴Harvard Medical School, Boston, MA, USA, ⁵Children's Hospital Boston, Boston, MA, USA

Introduction: Neck pain, a common occupational health complaint, is strongly associated with cervical spine disease, the result of acute or chronic injury that produces degeneration of the intervertebral disc (IVD). Laborers exposed to repetitive loads and vibrations in extreme work environments are at highest risk. Currently there are no imaging protocols to assess cervical spine motion and IVD strain in personnel while operating in extreme work environments. Attempts to evaluate the anatomy and dynamic motion of the cervical spine during exposure to these extreme environments are hampered by the large equipment size and power required by traditional medical imaging technologies such as radiography, computed tomography (CT) and Magnetic Resonance Imaging (MRI). We hypothesize that clinical Ultrasound (US) can provide a portable imaging modality capable of quantifying cervical spine IVD displacement and the mechanical compliance of a functional spinal unit (FSU) in response to applied forces. The purpose of this study is to demonstrate that US can determine the mechanical behavior of human, cadaveric, cervical spine FSU's in response to statically or dynamically applied loads.

Methods: Specimen Preparation: After defrosting, the trachea, esophagus, and skin were removed from four contiguous human cadaveric, fresh frozen, cervical spines, C2-C7, ages 53-81 yrs (Medcare, Portland, OR). The surrounding paracervical muscles and adipose tissue were retained.

Static Analysis: Each spine was subjected to static compressive and distractive loads ranging from -20 to +20 lbs. in 5 lbs. increments using a servo-hydraulic material testing machine (Instron, Norwood, MA). B-mode US images were captured during the load application (Terason t3000, 12L5 linear array; Teratech, Burlington, MA). A consistent anatomic landmark was identified on each of the imaged vertebrae to standardize FSU/IVD displacement measurements. The overall compliance for each FSU (C4-C5, C5-C6) was calculated from the slope (displacement vs. applied load) using General Linear Model. Analysis of covariance (ANCOVA) was used to determine effect of disc level and age.

Dynamic Analysis: Sinusoidal amplitudes of 1 mm were applied to each spine at frequencies of 1, 2, 4, 6 and 8 Hz. The 3D kinematics of C4, C5 and C6 in the anatomical coordinate system were measured using an optical tracking system (Qualisys, Gothenburg, Sweden) and compared to the change of C4-C5 and C5-C6 IVD displacements measured by US.

Results: Static Analysis: Mechanical compliance curves were plotted for C4-C5 and C5-C6 from the four cadaveric cervical spines (Figure 1a). The C5-C6 IVD was more compliant than C4-C5 for the specimens obtained from the younger individuals, but with increasing age, the C5-C6 IVD became stiffer (Figure 1b).

Dynamic Analysis: Dynamic IVD height measured by US was consistent with the data from the mechanical tracking system (Figure 2). The coefficients of determination for these linear regressions were plotted as a function of the applied frequency (Figure 3). The IVD displacement measured by US accounted for 60-95% of the variability of the cervical spine kinematics measured directly for frequencies < 6 Hz. However, measurements of dynamic IVD displacement become less reliable at 8 Hz as the Nyquist limit of the measurement system was approached. For applied frequencies less than 8 Hz, the overall error (root mean squared error) was ± 0.148 mm.

Discussion: As this was conducted as a feasibility study, the number of samples analyzed was low and our preliminary findings must be viewed with some caution. Analysis of additional samples will allow us to validate our preliminary results. Nonetheless, we have established the capability of US to measure the overall static compliance of cervical spine FSU's. The cadaveric FSU's showed a significant decrease in C5-C6 compliance (i.e. increase in stiffness) with age, compared to the C4-C5 FSU, which did not show any variation with age. This suggests the possibility that compliance of the FSU may vary at different spine levels. While many more specimens must be evaluated to support this preliminary finding, a possible explanation of the apparent difference in compliance between C5-C6 and C4-C5 is that the C5-C6 level experiences different loading as a consequence of cervical lordosis. This is further supported by the observation that c-spine IVD degeneration occurs most frequently at the C5-C6 and C6-C7 levels.

Further, we have demonstrated the ability of clinical US to capture the real time motion of human cadaveric vertebrae at frequencies < 6 Hz with an overall error of ± 0.148 mm. Although the Nyquist limit was not fully attained, the accuracy of the US to measure IVD deformation deteriorated at frequencies > 6 Hz. A primary reason for the lower accuracy of US measurements is due to blurring artifact. For the US system evaluated, the images are obtained at 30 frames/sec, (i.e. 33ms/image), so that at current frame rates there is 0.2mm of displacement at 6 Hz, approaching the root mean squared error of 0.148 mm for our system.

Significance: We demonstrate that clinical US can provide a portable, low cost imaging modality capable of quantifying cervical spine IVD displacement and the mechanical compliance of a FSU in response to applied forces. It appears feasible to further develop this technology to evaluate cervical spine mechanical behavior in-vivo in dynamic environments where MRI and CT cannot be used.

Acknowledgements: This work was supported by the MRMC-AARL: Aero-medical Research Laboratory (Carol Chancey) under the auspices of the U.S. Army Research Office Scientific Services Program administered by Battelle (Delivery Order 0081, Contract No. W911NF-11-D-0001).

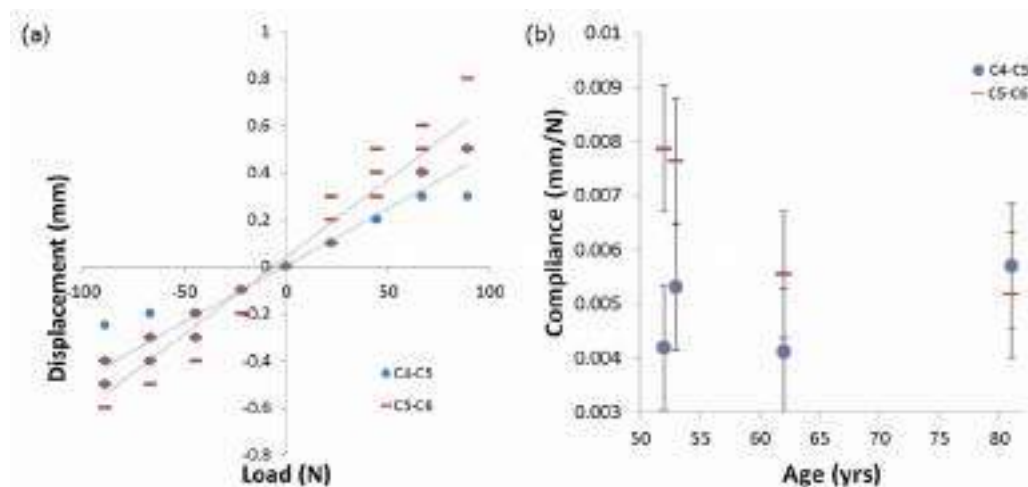


Fig. 1: (a) Compliance of C4-C5 and C5-C6 FSU

for all samples. ANCOVA indicated that the slopes, or compliance, of C4-C5 and C5-C6 were not quite statistically different ($p=0.07$) for the entire group, but were different among the younger aged specimens ($p=0.001$) when the older aged specimens were removed from the analysis. (b) Compliance measures for C4-C5 and C5-C6 as function of age. Error Bars = standard errors in compliance calculated from uncertainties of the US and load-cell measurements. C5-C6 tended to be more compliant than C4-C6 in younger age specimens, but in older age specimens the difference was not evident.

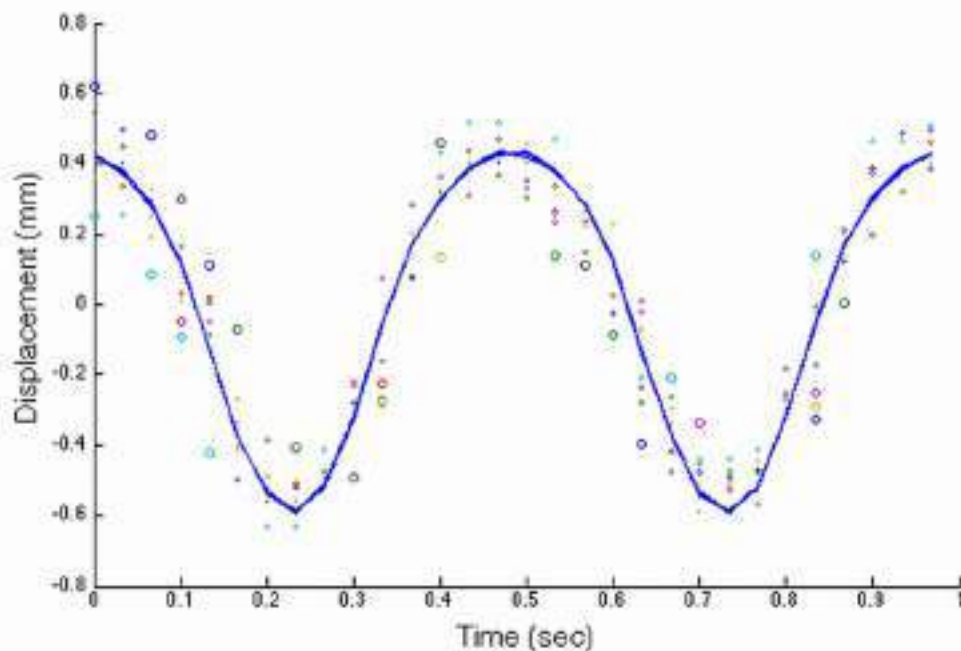


Fig. 2: Representative displacement C4 relative to C6 for 2 Hz sine wave with 1 mm amplitude. Seven seconds of data are overlapped to illustrate precision. The solid blue line represents the C4-C6 displacement measured using optical tracking system. The multi-colored circles represent the same displacements measured using US. Each color represents one second of data. The diameters are proportional to the error.

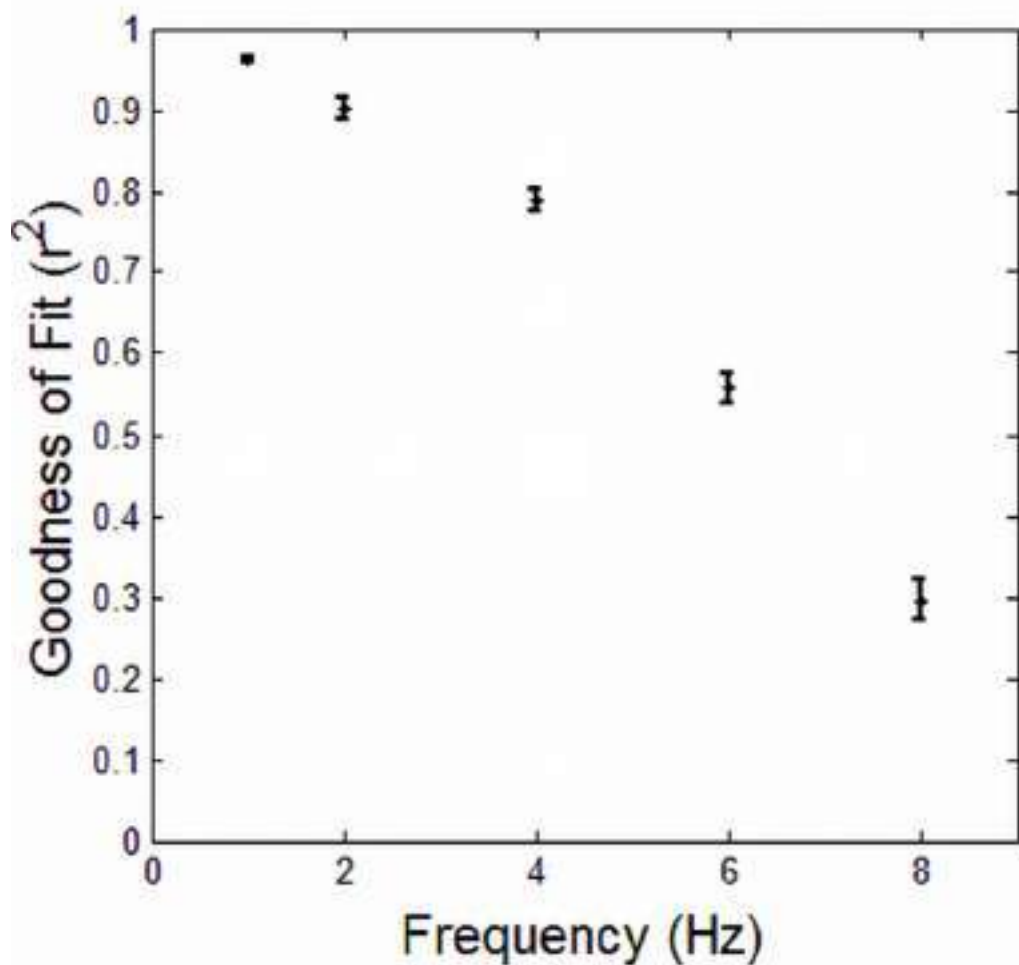


Fig. 3: Coefficients of determination (r^2) for US measurements of cervical spine FSU motion vs. that measured by optical tracking system at different loading rates. Error bars represent the standard error. The applied loading rate affected the reliability of the measured displacement ($p < 0.001$). US measurements > 6 Hz were less reliable.

ORS 2013 Annual Meeting

Real Time Ultrasound Can Measure Dynamic Properties of Cervical Spine Intervertebral Disc

Mingxin Zheng^{1,2}, Mike Arun³, Aidin Masoudi¹, Daniel Buckland, MD/PhD^{1,4}, Narayan Yoganandan³, Brian Stemper³, Brian Snyder, MD/PhD^{5,6}.

¹Beth Israel Deaconess Medical Center - Harvard Medical School, Boston, MA, USA, ²Boston University, Boston, MA, USA,

³Medical College of Wisconsin, Milwaukee, WI, USA, ⁴Massachusetts Institute of Technology, Cambridge, MA, USA, ⁵Beth Israel Deaconess Medical Center – Harvard Medical School, Boston, MA, USA, ⁶Children's Hospital Boston, Boston, MA, USA.

Disclosures:

M. Zheng: None. **M. Arun:** None. **A. Masoudi:** None. **D. Buckland:** None. **N. Yoganandan:** None. **B. Stemper:** None. **B. Snyder:** None.

Introduction: Neck pain is a common occupational health complaint associated with cervical spine inter-vertebral disc (IVD) degeneration, the result of acute and/or chronic injury sustained in the work place. Laborers exposed to repetitive loads and vibrations are at highest risk. Currently there are no methods to evaluate the dynamic motion of the cervical spine in individuals working in extreme environments. Imaging technologies such as plain radiography, computed tomography and Magnetic Resonance Imaging are limited by the large size and power requirements of the equipment. The purpose of this study is to demonstrate that clinical ultrasound (US) can provide a portable imaging modality capable of quantifying cervical spine IVD motion in individuals working in extreme environments. We have previously validated that US can provide a portable imaging modality capable of quantifying real time cervical spine IVD motion in human cadavers at frequencies <6 Hz with an overall error of ± 0.148 mm. The purpose of current study is to demonstrate that clinical US can quantify the elastic and viscoelastic properties of cadaveric human cervical spine functional spinal units (FSU) in response to linearly or dynamically applied loads.

Methods: Specimen Preparation and Testing: The skin, trachea and esophagus were removed from contiguous C2-C7 fresh frozen human cadaveric cervical spines (N=4, Age 72-91, Medcure, Portland, OR), retaining the surrounding paracervical muscles and adipose tissue. After the vertebrae were aligned along the central longitudinal axis of the neural canal, the upper (C2) and lower (C7) vertebrae were potted in Polymethylmethacrylate to allow consistent mounting of the specimen in the servo-hydraulic testing machine load frame (Instron, Norwood, MA). A cyclic, sinusoidal axial displacement of 1 mm @ 1Hz was applied to C2 while the resultant axial load was measured at C7 via the in-line load cell. The US transducer, positioned just anterior to the sternocleidomastoid muscle, was sonically coupled to the spine using a hydrogel (standard clinical protocol); the trajectory of the US pulse oriented toward the midline of the vertebral bodies, anatomically similar to the surgical window to the anterior cervical spine. Since the C4-C5 IVD is most commonly affected by degenerative disease, continuous, real-time, B-mode US images (Terason t3000, 12L5 linear array; Teratech, Burlington, MA) of the C4-5 FSU were captured during the cyclic load test. Video US images were exported in AVI format to image analysis software (Mocha, Imagineer Systems, Guildford, UK) where a region of interest corresponding to the mid-sagittal plane profile of the anterior cortical shell of the vertebral body intersecting the endplate adjacent to the IVD were defined manually on the first image frame and then that signature profile tracked throughout the rest of the images. The C4-5 IVD deformation calculated from these landmarks was correlated with corresponding measured load.

Linear Model: The overall linear compliance of the C4-C5 FSU was calculated as the slope of the resultant deformation of the IVD in response to applied compressive/distractive load to the entire spine using a general linear regression. The work loss during the stress loading cycle, indicative of the hysteresis effect, was calculated by computing the area of cycle. Coefficient of determination (R^2) was used to evaluate the goodness of fit.

Dynamic Model: A three-network model developed by Bergström and Boyce [2] was used to capture the complex hysteretic and fatigable behavior of IVDs during cyclic loading. The three network model consists of three parts acting in parallel: the first part captures the elastic and viscoplastic response of IVD; the second part captures the time-varied viscoelastic response of the structure; the third part captures the hyperelastic non-linear material response.

Results: Real time US was able to capture the dynamic IVD deformation of the C4-5 FSU induced by the axial load applied to C2-C7 (Figure 1). While the overall compliance of the C4-C5 FSU calculated by linear regression (0.0016 mm/N) accounted for 72% of the variation in the experimental data ($R^2 = 0.72$), it does not reflect the differential behavior of the FSU in tension and compression (Figure 2). The C4-C5 FSU exhibits a differential hysteric viscoelastic response during cyclic loading that incorporates both applied tensile and compressive forces (Figure 3). The unloading path does not follow the loading path, consistent with Mullin's effect [1]. The three-network model which computed the shear modulus and resistance of each structural and time-varied component (Table 1) accounted for 93% of the variation ($R^2 = 0.983$) of the experiment data (Figure 4).

Discussion: This feasibility study helps to establish the capability of clinical US to measure the overall linear compliance and to model the dynamic elasticity and non-linear properties of the cervical spine FSU as a result of applied cyclic loads. The linear

compliance provides a simple and direct method to examine the elastic properties of FSU, but the three-network model better portrays the complex non-linear viscoplastic and viscoelastic properties of the FSU since it accounts for time-varied affects. As the testing time was short (less than 10s), the loss of stiffness was not computationally characterized by the experimental data. Longer duration testing will be necessary to characterize the loss of stiffness (damage accumulation) during prolonged cyclic loading.

We are currently designing a system to apply low amplitude traction and compressive cyclic loads to the head/neck *in-vivo* while measuring the resultant deformations of the cervical spine FSU’s by US to deduce the static and dynamic mechanical properties of the FSU. This system will allow assessment of the mechanical performance of the cervical spine *in-vivo* without the radiation exposure risk of conventional imaging modalities.

Significance: We demonstrate that clinical US can provide a portable, low cost imaging modality capable of quantifying cervical spine IVD displacement and the dynamic mechanical behavior of an FSU in response to applied forces. It is feasible to further develop this technology to evaluate cervical spine mechanical behavior *in-vivo* in dynamic environments where MRI and CT cannot be used.

Acknowledgments: This work was supported by the The U.S. Army Medical Research Acquisition Activity (Contract No. W81XWH-13-1-0050).

References: [1] Diani, J., et al. (2009). "A review on the Mullins effect." European Polymer Journal 45(3): 601-612.
[2] Bergström, J. S. and M. C. Boyce (2000). "Large strain time-dependent behavior of filled elastomers." Mechanics of Materials 32(11): 627-644.

Table 1. Representative material properties values in three-model network for C4-5 IVD			
Description	Value	Description	Value
Shear modulus of network A(structural network)	768 MPa	Initial shear modulus of network B(time varied network)	297 MPa
Locking stretch	4.6	Final shear modulus of network B	97 MPa
Bulk Modulus	2000 MPa	Evolution rate of shear modulus	4
Resistance of network A	3.0 MPa	Resistance of network B	48 MPa
Pressure dependence factor	2.1	Stress exponential of network B	1.1
Stress exponential of network A	3	Shear modulus of network C(hyperelastic network)	51 MPa

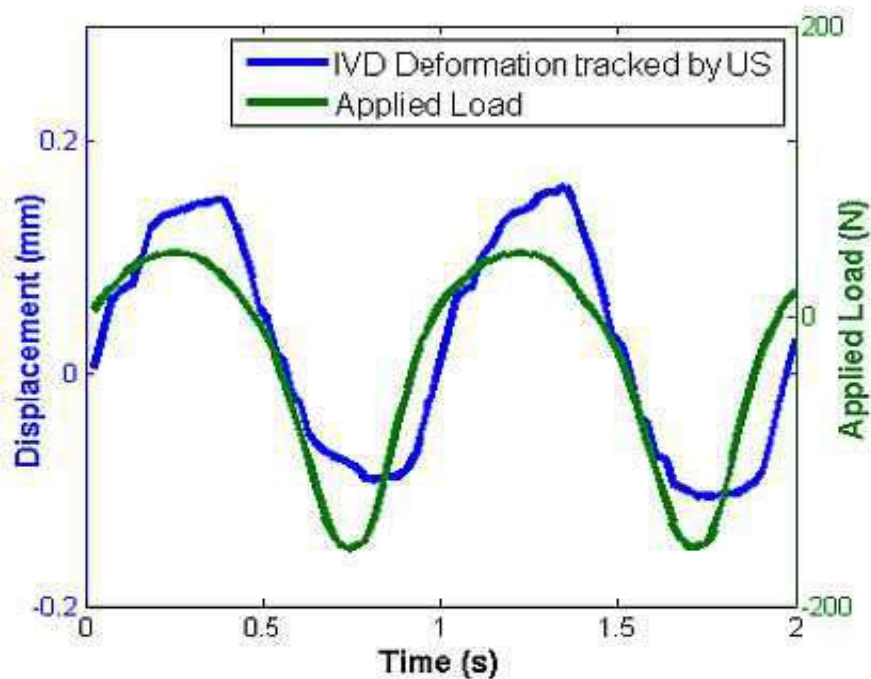


Fig.1 US captures the IVD deformation induced by applied load

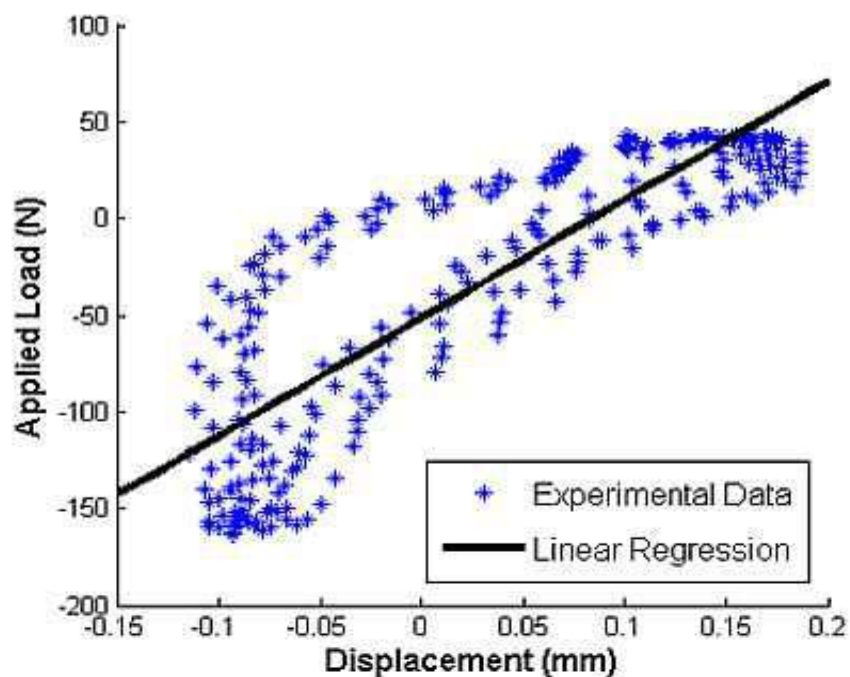
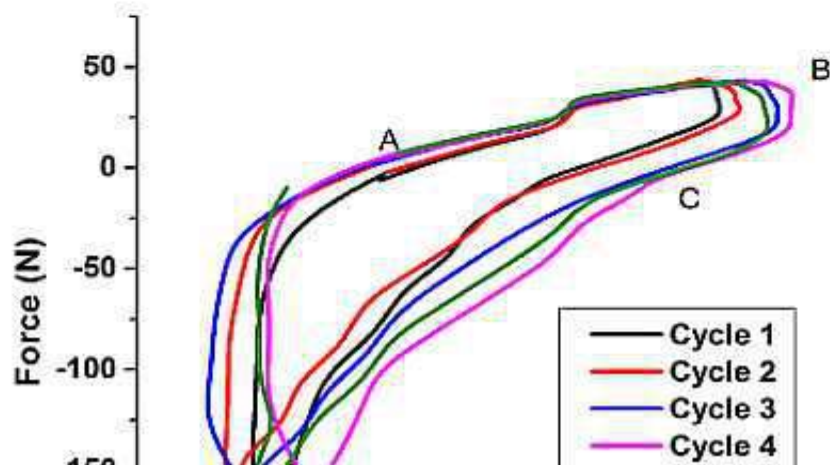


Fig. 2 Slope (Compliance of IVD) calculated from linear regression of dynamic loading data is 0.0016 mm/N ($R^2 = 0.72$)



Clinical Ultrasound Can Measure Dynamic Intervertebral Disc Deformation *In-vivo*1.²Shiuan, KS; 1.²Zheng, M; 1.^{3,4}Buckland, DM; 1.^{4,5}Snyder, BD¹Beth Israel Deaconess Medical Center, Boston, MA, USA, ²Boston University, Boston, MA, USA, ³Massachusetts Institute of Technology, Cambridge, MA, USA, ⁴Harvard Medical School, Boston, MA, USA, ⁵Children's Hospital Boston, Boston, MA, USA
ks4ors@gmail.com

Introduction: Neck and back pain have become increasingly prevalent among military personnel. Cervical spine injuries result in pain, disability and increased medical expenses as well as the loss of experienced Warriors. Difficulty measuring *in-vivo* spine kinematics during operational maneuvers has limited a complete understanding of the etiology of cervical spine injuries in military personnel. Due to large size and power requirements, traditional medical imaging technologies such as plain radiography, computed tomography (CT), and magnetic resonance imaging (MRI) cannot be used to evaluate the dynamic motion of the cervical spine during operational conditions. We have previously demonstrated the ability of US to measure dynamic cervical spine motion in animal and human cadaveric specimens. The purpose of this feasibility study is to demonstrate the capability of clinical ultrasound (US) to image real-time cervical spine intervertebral discs (IVD) deformation and dynamic vertebral motion in young male volunteers jumping off a 1.5 foot bench with and without a weighted standard issue Army helmet.

Methods: After obtaining approval by the Committee on Clinical Investigation at Beth Israel Deaconess Medical Center (BIDMC), five male subjects (age 20-30 yrs) volunteered to participate in the study. The subjects donned a motocross EVS RC-Evolution vest (Rancho Dominguez, CA) with Velcro straps that was optimized to fit for different body types and an integrated cervical collar to hold the US probe in a set position relative to the trunk and cervical spine (National Orthotics and Prosthetics Corporation, Boston, MA). Subjects jumped off a 1.5 ft. stool while maintaining upright posture and landed on both feet while instructed to not dampen impact by bending their knees. The vest and collar did not limit the motion of the subject's head or neck during the performance of jumping activity. A Vicon Motion Capture System (Oxford, UK) utilizing 8 cameras was used to measure the external displacement of the head relative to the top of the torso (1st thoracic vertebra). To evaluate the effect of wearing an Army helmet with night vision goggles on the dynamic performance of the cervical spine while jumping from a height, the aforementioned task was executed in a similar manner with the volunteers wearing a standard issue Army helmet with a 2.5 lbs. weight attached to the front of the helmet to mimic night vision goggle (Figure 1).

Results: The external displacement of the head relative to T1 was compared to the dynamic IVD displacement measured by US at C4-C5 in the time domain (Figure 2a) and frequency domain (Figure 2b). The profile of the amplitude-time curves demonstrated that the IVD displacement at C4-C5 positively correlated with the vertical displacement of the head relative to T1, with significant attenuation of the displacement applied to the head occurring at C4-C5 IVD. The frequency domain analysis indicated that the measured amplitudes were heavily weighted to the lower frequencies, with more than 50% of the power spectra (area under the curve) for frequencies <5 Hz. We evaluated the initial impulse applied to the head/neck upon landing on the ground after jumping 1.5 feet. The amplitude of the initial impulse was defined as the first significant compressive displacement of the head and neck relative to the torso (T1). The C4-C5 IVD attenuation coefficient was calculated as the ratio of the C4-C5 IVD displacement measured by US divided by the total displacement of the head relative to T1 measured by the Vicon Motion Capture System. The attenuation coefficient of the C4-C5 IVD was significantly increased ($p<0.001$) by the additional weight of the Army helmet (Figure 3).

Discussion: This feasibility study demonstrates the ability of clinical US to measure dynamic cervical spine motion and IVD deformation during simulated military maneuvers. While preliminary, this data suggests that a larger fraction of the compressive impulse is transmitted to the C4-C5 IVD when a subject wears weighted head gear compared to when the subject is not wearing weighted head gear while jumping from a controlled height. There was considerable variability between and within subjects in consistently performing the jumping task. The total c-spine displacement and frequency response of the head and neck during landing fluctuated from trial to trial. However, from the frequency analysis, the total displacement of the head relative to the torso and the resultant C4-C5 IVD deformation incurred upon landing demonstrated that most of the compressive impulse wave occurred at frequencies <5 Hz, which is within the dynamic range of the US system. (In a separate validation experiment conducted in *ex-vivo* human cadaveric cervical spines, we demonstrated that dynamic cervical spine IVD deformation measured by US accounted for 75-95% of the variability in dynamic IVD displacement measured directly for applied frequencies < 6 Hz.) These results suggest that reflexive contraction of the paracervical muscles may help to dampen the forces transmitted to the cervical spine, but prolonged and recurrent jumping may result in muscle fatigue, which increases the fraction of the load transmitted to the IVD.

Significance: In this feasibility study, the ability of clinical US to image real-time cervical spine IVD deformation and dynamic vertebral motion in young male volunteers jumping off a 1.5 foot bench with and without a weighted standard issue Army helmet was demonstrated. Such knowledge could fundamentally change design requirements for helmets to limit dynamic exposures and repeated shock impacts.

Acknowledgements: The authors would like to thank Leia Stirling from the Wyss Institute at Harvard University for her valuable help. This work was supported by the MRMCAARL: Aero-medical Research Laboratory (Carol Chancy) under the auspices of the U.S. Army Research Office Scientific Services Program administered by Battelle (Delivery Order 0081, Contract No. W911NF-11-D-0001).

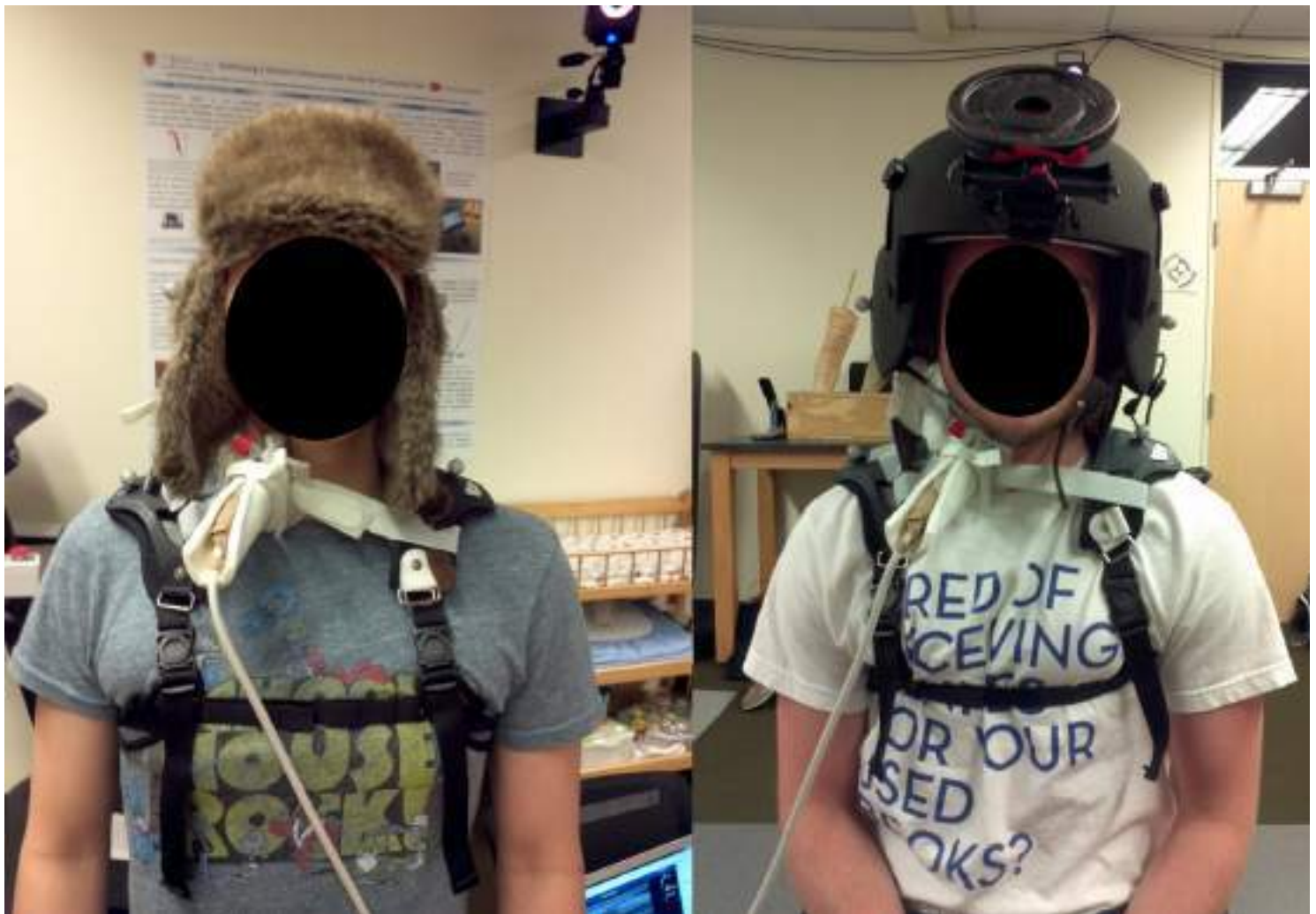


Fig. 1: Vest and ultrasound probe coupled to subjects' necks. Subject on left with tight-fitting cap mounted with optical tracking spheres. Subject on the right wearing standard Army issued helmet with 2.5 lbs. weight attached to mimic night vision gear.

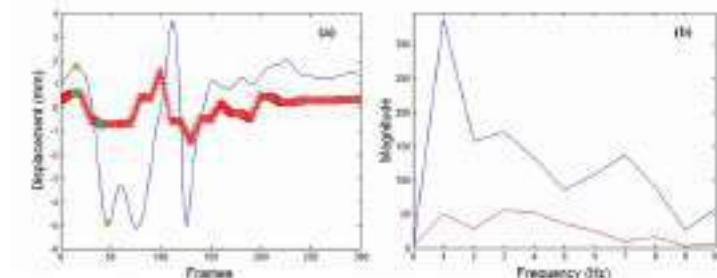


Fig. 2: Representative time-domain measurement (a) and frequency response (b) of displacement head relative to torso measured by optical tracking system (blue) and C4-C5 IVD deformation measured by US (red). Errors bars (a) represent ± 0.148 mm uncertainty in US measurements. Green dots reflect time points at which initial compressive impulse amplitude was measured. Discrete Fourier transform of time-domain signal (b) indicates that major contribution to power spectra were frequencies <5 Hz.

[Print this Page](#)

Presentation Abstract

Session: Tuesday General Poster Session

Presentation: Dynamic Ultrasound Imaging of Cervical Spine Intervertebral Discs

Presentation Time: Tuesday, Jul 08, 2014, 9:00 AM - 5:00 PM

Abstract: **Background**

The diagnoses of C-spine injury and degenerative intervertebral disc (IVD) disease are challenging because these conditions are more evident under dynamic loading conditions. This measurement requirement rules out CT and MRI for evaluation of C-spine kinematics in work environments. Ultrasound imaging, though not usually applied to bone imaging, can be used to track the movement of vertebrae and IVDs under dynamic conditions. The aim of this study was to demonstrate the ability of portable ultrasound to: 1) accurately measure IVD deformation and mechanical compliance *ex-vivo*; 2) provide real-time images of IVDs and dynamic vertebral motion *in-vivo* during simulated tasks.

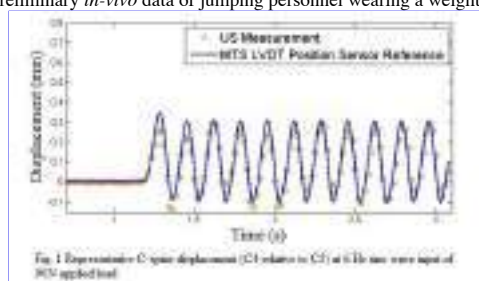
Methods

The feasibility of the approach was evaluated by tracking the movement of *ex-vivo* human spines subjected to compressive/distractive dynamic sinusoidal applied load (90N @ 1-8 Hz). A 7.5 MHz linear array was used to capture a sequence of images during loading. Radio Frequency (RF) data-derived movement of IVD displacements versus time was simultaneously measured with a Linear Variable Differential Transformer (LVDT) system. For the initial *in-vivo* experiments, an ultrasound probe was worn by young male volunteers; each one wore a weighted helmet to simulate a loading condition and jumped repetitively from a 1.5 ft. stool. Movement of vertebrae C4-5 was determined from US measurements and related to the displacements of the head relative to the torso as measured by optical tracking system.

Results/Discussion

Ex-vivo: Dynamic IVD displacements of vertebrae C4-5 measured by US were consistent with LVDT data (Figure 1). For motion frequencies up to 8Hz, US accounted for 77-96% of the true IVD displacements.

In-vivo: Amplitude-time curves of IVD deformation measured by US correlated with the vertical displacement of the head relative to torso. Spectral analysis demonstrated that most deformation occurred at frequencies < 6Hz. Wearing a weighted helmet during jumping significantly increased ($p < 0.001$) the proportion of inertial head displacement transmitted to vertebrae C4-5. Portable US provides a low cost means of accurately measuring dynamic vertebral motion and C-spine IVD displacement during simulated tasks. Preliminary *in-vivo* data of jumping personnel wearing a weighted helmet demonstrates that portable ultrasound can be used to



monitor the effects of transient loading.

For technical inquiries, [click here](#) to contact OASIS Helpdesk or call 217-398-1792.

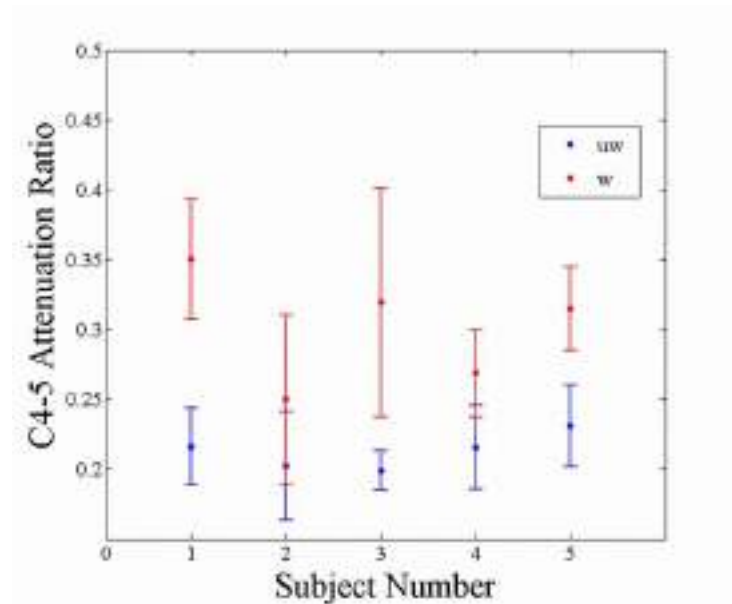


Fig. 3: C4-5 IVD attenuation ratio (ratio of C4-C5 displacement relative to total displacement of head relative to torso) at time of initial compressive impulse during landing from 1.5 foot height for all subjects. UW (blue) = unweighted, W (red) = weighted wearing helmet. Error bars = standard error. The attenuation ratio significantly increases with the added weight of the helmet ($p<0.001$).
ORS 2013 Annual Meeting
Poster No: 1982

Use of Portable Ultrasound to Measure Dynamic Motion of Cervical Spine Ex-Vivo and In-Vivo

M. Zheng^{1,2}, A. Masoudi², D. Buckland^{2,3}, T. Szabo¹, and B. Snyder^{2,4}

¹Boston University, Boston, MA, ²Beth Israel Deaconess Medical Center, Boston, MA, ³Massachusetts Institute of Technology, Cambridge, MA, ⁴Boston Children's Hospital, Boston, MA

Introduction:

Neck pain from cervical spine intervertebral disc (IVD) pathology is a common occupational health problem, especially among military troops. Currently there is no method to assess the static and dynamic properties of the IVD in subjects while performing duties in the work place. The aim of this study was to demonstrate the ability of portable ultrasound (US) to: 1) accurately measure IVD deformation and mechanical compliance *ex-vivo*; 2) measure dynamic vertebral motion *in-vivo* during simulated combat conditions. The compactness and portability of clinical US systems will facilitate the development of preventative strategies in occupational health by allowing real time evaluation of cervical spine kinematics in work place environments where MRI and CT cannot be used.

Material and Methods:

Ex-vivo: Cadaveric human cervical C6-7 functional spinal units (FSU) were submerged in 0.9% saline @ 37°C to replicate physiological conditions. Each FSU was subjected to sinusoidal compressive/distractive loads (90N @ 1-8Hz) and imaged by US (4 MHz linear array @ 50 frames/s). The vertebrae were modeled as rigid bodies, attributing the motion of the FSU to deformation of the IVD. Regions of interest (ROI) corresponding to distinct bony vertebral landmarks were specified by the user on the initial B-mode image and subsequently tracked automatically using a block matching operation on the radio frequency (RF) US image data generated during dynamic loading. The dynamic motion of the FSU derived using this US algorithm was compared to direct measurements using a linear variable differential transformer (LVDT).

In-vivo: After receiving IRB approval, a custom cervical-thoracic orthotic was used to mount an US probe to the neck of 12 young male volunteers, just anterior to the sternocleidomastoid muscle, providing a sonic window to cervical spine FSUs C3-C6. Each subject jumped repetitively from a 1.5 ft. stool with and without a weighted helmet simulating combat conditions. The dynamic motion of the C4-5 FSU was measured in real time by US and related to the displacements of the head relative to the torso measured by an optical tracking system.

Results and Discussion:

Ex-vivo: C6-7 IVD deformation derived from US image data using the RF algorithm accounted for ~92% of the variation in IVD motion measured directly for frequencies ≤ 6 Hz and 77% of the variability at 8Hz ($R^2 = 0.77$). This established the feasibility of using clinical US to measure dynamic IVD deformation in response to applied loads.

In-vivo: Amplitude-time curves of C4-5 FSU motion measured by US correlated with the vertical displacement of the head relative to torso. Spectral analysis demonstrated that most deformation occurred at frequencies < 6 Hz. Wearing a weighted helmet during jumping significantly increased ($p < 0.001$) the proportion of the inertial load from the head transmitted to C4-5, resulting in increased IVD deformation.

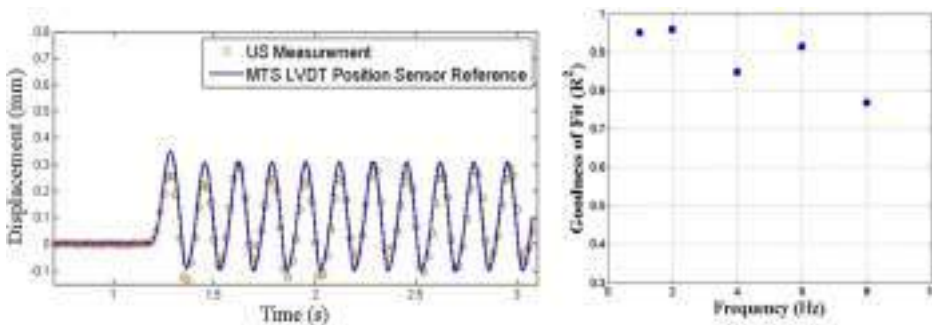


Figure 1. (a) Representative C6-7 IVD deformation deduced by RF compared to deformation measured directly by in-line LVDT for applied -90N to +90N sinusoidal force @ 6Hz. Blue line is LVDT displacement measurements and red circles are displacements deduced from US. (b) The coefficient of determination for US vs. LVDT measurements of IVD deformation plotted as function of applied frequency.

Conclusions:

Clinical US can provide a portable, low cost method to accurately measure dynamic cervical spine vertebral motion and IVD displacement during simulated tasks in the work place. This technique will allow the non-invasive assessment of the mechanical properties of cervical spine FSUs in health and disease and the ability to monitor the efficacy of treatments designed to reconstitute the mechanical properties of the IVD.

Acknowledgements:

This work was supported by DoD award W81XWH-13-1-0050.

PROGRESSIVE CHANGES IN CERVICAL SPINE INTERVERTEBRAL DISC PROPERTIES DURING CYCLIC COMPRESSIVE FATIGUE LOADING

Sagar Umale (1), Brian D. Stemper (1,2), Mingxin Zheng (3), Aidin Masoudi (3), Daniel Fama (1,2), Narayan Yoganandan (1,2) Brian Snyder (3,4,5)

(1) Department of Neurosurgery, Medical College
of Wisconsin, Milwaukee, WI

(2) Clement J. Zablocki VA Medical Center,
Milwaukee, WI Department

(3) Beth Israel Deaconess Medical Center,
Boston, MA

(4) Harvard Medical School, Boston, MA

(5) Cerebral Palsy Clinic Children's
Hospital, Boston, MA

INTRODUCTION

Prolonged exposure to whole body vibration in environments such as, helicopters, fast boats, and land-based vehicles can contribute to neck, back, and shoulder pain in military personnel [1,2]. Prior experimental studies have shown that repetitive loading of spinal units may cause bony injuries such as endplate and cortical fractures [3,4], and clinical hypotheses have included development of intervertebral disc herniation [2]. However, due to fatigue, changes in disc material properties can alter the mechanical response of the spinal column, change segmental load sharing resulting in increased injury risk to other tissues, and may become permanent with continued repetitive loading. To our best knowledge, progressive changes in soft tissue properties have not been reported for compressive fatigue in cervical spine segments. Therefore, it is important to characterize these changes due to vibrational environment and by progressive loading and determining the changes during fatigue and compare pre and post fatigue changes. The purpose of this study was to characterize changes in mechanical properties of cervical spine disc due to low magnitude compressive fatigue loading.

METHODS

Four cervical bone disc bone spine motion segments without posterior elements obtained from post-mortem human subjects (mean age: 58.2±3.2 yr) were fixed at cranial and caudal extents using polymethylmethacrylate. Specimens were exposed to a protocol that included fatigue loading for 5 sets of 10,000 cycles with tension compression and viscoelastic assessments prior to the first and after each fatigue set. Fatigue testing was performed with specimens submerged in a physiologic saline bath with temperature maintained at 34 deg C and consisted of repetitive compression applied using the piston of an electrohydraulic testing device (MTS Systems, Eden

Prairie, MN) between 0 and 150 N at 2 Hz using a sine wave function. Tension compression tests were performed at a static speed of 0.1 mm/s to 10% strain. The viscoelastic test involved compressing the specimen to 10% strain and allowing it to relax under the constant deformation. Disc height was measured from x-rays obtained after each fatigue set and an average of three readings was measured as disc height. Axial force was measured at 100 Hz during the entire test using a uniaxial load cell attached to the piston. After each test the segment was allowed to settle for 15 minutes in the saline bath and then the next test was performed.

RESULTS

Cycle-by-cycle intervertebral disc height during each fatigue set is plotted in Figure 1. Disc height loss was greater during the first and second fatigue sets. The disc regained some height during the inter-set relaxation period. The average decrease in disc height during fatigue loading was observed to be 16.5±6.5%, 12.5±5.8%, 9.7±3.4%, 6.9±1.8% and 5.9±3.1% from fatigue set 1 to fatigue set 5 respectively, whereas about 10% height was recovered after first two fatigue sets and about 5% was recovered after later three. The average decrease in disc height was calculated as 15% for all the four segments over 50,000 cycles. The stress relaxation curves for segment 4 are plotted in Figure 2. Segments demonstrated the most flexible behavior during the first and second fatigue sets and became progressively stiffer for subsequent fatigue sets. The curves for pre fatigue and post first and second fatigue test shows similar viscoelastic behavior whereas post third, fourth, and fifth fatigue the stiffness of the disc can be observed to be increased, as the stress required for same strain is increased. This observation is also illustrated in Figure 3, in which average stiffness for all the segments during fatigue is plotted. It can be observed that during first three sets there was not much change in

stiffness of the disc, whereas fourth and fifth sets showed a high increase in stiffness. The tension and compression tests showed that after fatigue the disc was less stiff in tension, whereas stiffer in compression. The viscoelastic test demonstrated decrease in viscous properties of the disc. The relaxation time was observed to be lesser for disc with increase in fatigue.

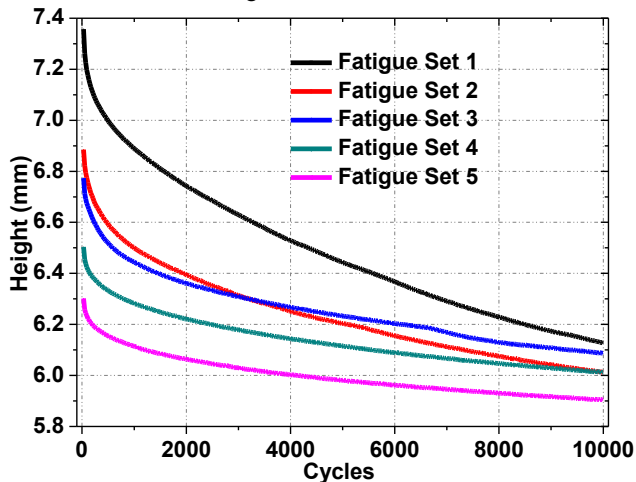


Figure 1. Average disc height loss during each fatigue set.

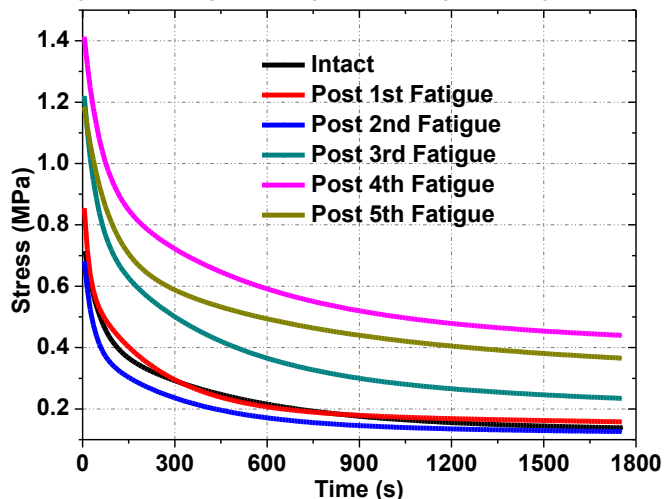


Figure 2. Stress relaxation curves for segment 4 post fatigue.

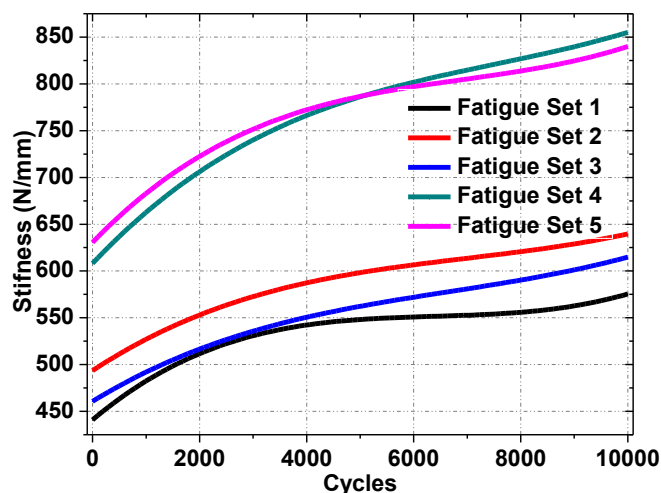


Figure 3. Average stiffness during each fatigue set.

DISCUSSION

The disc height was observed to be reduced after each fatigue set for each segment. It can also be observed from Figure 1 that the curve profile for first two fatigue sets is similar and the curve profile for next three fatigue sets is similar. It shows that for the first two fatigue sets the disc demonstrates viscoelastic properties, whereas for the next three sets the disc shows only elastic response with decrease in height. It can be observed from Figure 2 that the initial stiffness of the disc increased up to 65% between intact segment and post fifth fatigue set. Thus there was a gradual decrease in viscous response and a gradual increase in stiffness of the disc. If the curves from Figure 2 and Figure 3 are grouped during the first three fatigue sets the stiffness of the specimens was relatively less as compared to the following two fatigue sets. This behavior is observed due to decrease in disc height and loss in viscous behavior. Loss in viscosity can also lead to ore fractional losses and thus failure of the soft tissue.

The tension compression tests however showed that the stiffness of the segments was decreased in tension. Progressive disc height loss can contribute to pain-related conditions including intervertebral foraminal stenosis. These changes also contribute to altered loading sharing of the intervertebral segment that can contribute to elevated loading of adjacent structures such as the facet joints, eventually resulting in an accelerated degenerative process. Understanding these mechanisms and the transition from acute to chronic changes is a key to the development of exposure limits for repetitive axial loading environments that will be used to limit the onset of neck and low back pain symptoms for military personnel. Given inter-personal differences in spinal biomechanics based on gender, age, and loading history, among other factors, it is conceivable that these changes could be assessed using non-invasive techniques such as multiplanar ultrasound under controlled loading inputs to the cervical spine [5]. This remains an ongoing focus of the current line of investigation.

ACKNOWLEDGEMENTS

This work was supported by the U.S. Army Medical Research and Materiel Command Fort Detrick, Maryland (01026018, Contract No. W81XWH-13-1-0050), and the Department of Veterans Affairs Medical Research.

REFERENCES

1. Harrison MF, et al. (2012). A predictive logistic regression equation for neck pain in helicopter aircrew. *Aviat Space Envir Med.* 83, 6, 604-8.
2. Pope MH, Magnusson M, Wilder DG. (1998). Low back pain and whole body vibration. *Clin Orthop Relat Res.*(354):241-8.
3. Goel, V.K., et al. (1987). Response of the Ligamentous Lumbar Spine to Cyclic Bending Loads, in: *Second Annual Meeting of the North American Spine Society.* Banff, Alberta, Canada., pp. 294-300.
4. Adams M & Hutton W (1980). The effect of posture on the role of the apophysial joints in resisting intervertebral compressive forces. *JBJS B62:* 358-62.
5. Z. Mingxin, M. Aidin, S. Umale, D. Buckland, N. Yoganandan, B. Stemper, T. Szabo, and B. Snyder, "Dual Ultrasound Can Measure Kinematic Motion and Intervertebral Disc Deformation of Cervical Spine.," presented at the ORS 2015 Annual Meeting, Las Vegas, Nevada, March 2015., 2015, p. 1096.

Dual Ultrasound Can Measure Kinematic Motion and Intervertebral Disc Deformation of Cervical Spine

Mingxin Zheng^{1,2}, Aidin Masoudi, MD¹, Sagar Umale³, Daniel Buckland⁴, Narayan Yoganandan³, Brian Stemper³, Thomas Szabo², Brian Snyder, MD/PhD^{1,5}.

¹Beth Israel Deaconess Medical Center, Boston, MA, USA, ²Boston University, Boston, MA, USA, ³Medical College of Wisconsin, Milwaukee, WI, USA, ⁴Massachusetts Institute of Technology, Cambridge, MA, USA, ⁵Children's Hospital Boston, Boston, MA, USA.

Disclosures: **M. Zheng:** None. **A. Masoudi:** None. **S. Umale:** None. **D. Buckland:** None. **N. Yoganandan:** None. **B. Stemper:** None. **T. Szabo:** None. **B. Snyder:** None.

Introduction: Neck pain is a common occupational health complaint associated with cervical spine intervertebral disc (IVD) degeneration, the result of acute and/or chronic injury sustained in the work place. Laborers exposed to repetitive loads and vibrations are at highest risk. Currently there are no methods to evaluate the dynamic motion of the cervical spine in individuals working in extreme environments. Imaging technologies such as plain radiography, computed tomography and Magnetic Resonance Imaging are limited by the large size and power requirements of the equipment. Our overarching goal is to demonstrate that clinical ultrasound (US) can provide a portable imaging modality capable of quantifying cervical spine IVD motion in individuals working in extreme environments. In our previous work, we validated that clinical ultrasound (US) is capable of quantifying cervical spine IVD deformation in human cadaveric vertebrae at frequencies <6 Hz with an overall error of ± 0.148 mm. The purpose of current study is to develop a dual US system capable of measuring C-spine kinematics stereographically. This system hardware and software were validated using PMMA phantoms at frequencies 1-8 Hz and *ex vivo* using human cadaveric C-spine.

Methods: PMMA Phantom Tracking Validation: The precision of US tracking software was validated using phantom tests to track rigid body motion over a range of frequencies. We developed a least sum of square difference (LSSD), error-correcting, acoustic signal tracker with subsample estimation. To validate the tracking algorithm, a PMMA cylinder acoustic phantom was manufactured and known displacements applied which were then compared to the displacements measured using the dual US system.

Cadaveric Dynamic Validation: 5 Human cervical C6-C7 FSUs were submerged in 0.9% saline at 37°C physiological conditions. Each FSU was subjected to sinusoidal compressive/distractive loads from -90N to 90N at frequencies ranging 1-8Hz. Continuous, real-time, synchronized B-mode US acoustic signals were captured during load application using a custom designed dual US system (Terason T3200, 15L4 linear array, 50 frames per second; Teratech, Burlington, MA). Consistent anatomic landmarks were identified on each of the imaged vertebrae to standardize C6-7 FSU kinematics and IVD displacement measurements in response to the applied load (Figure 1). The vertebrae were modeled as rigid bodies, attributing the motion of the FSU to deformation of the IVD. Regions of interest (ROI) corresponding to distinct vertebral landmarks were specified by the user on the initial B-mode US image and subsequently tracked automatically using a block matching operation on the radio frequency (RF) image data

generated during dynamic loading. The dynamic motion of the FSU derived using this US algorithm was compared to direct measurements using a linear variable differential transformer (LVDT).

Cadaveric Mechanical Creep Test: After defrosting, the trachea, esophagus, and skin were removed from 5 contiguous human cadaveric, fresh frozen, cervical spines, C2-T1, ages 54 - 67 years (Medcure, Portland, OR). The surrounding paracervical muscles and adipose tissue were retained. Each spine was subjected to 150N compressive creep test. Using minimally invasive technique, uniaxial, 5 mm diam. titanium pedicle screws were placed into the vertebral bodies under fluoroscopic guidance. Steel rods were used to fix C2-C4 FSUs and C5-T1 FSUs. Change in the height of the C4-C5 IVD measured by US was correlated with the real-time load measurement. C4-C5 level is commonly affected by degenerative disease, presumptively as a consequence of chronic overloading. Stiffness and damping coefficient of C4-C5 FSU were derived from standard Voigt model and compared to IVD hydration level in MRI Images.

Results: Phantom Validation: For applied frequencies from 1 - 8 Hz, the mean absolute error (MAE) between US tracking and LVDT measurements for each frequency ranged from 0.0227 to 0.0508 mm. The overall average MAE of US measurements was ± 0.041 mm.

Cadaveric Validation: Dynamic IVD deformation measured by US was consistent with the IVD deformation measured directly by the LVDT. Coefficients of determination for linear regressions between the IVD deformations measured by US vs that measured directly were plotted as a function of the applied frequency (Figure 2). C6-7 IVD deformation derived from US using the RF algorithm accounted for ~92% of the variation in FSU motion compared to that measured directly using the LVDT for frequencies up to 6Hz and 77% at 8Hz ($R^2 = 0.77$).

Mechanical Behavior of C4-C5: In compressive creep test, the stiffness of a specimen was affected its Pfirrmann Grade while the damping coefficient was not (Table 1). Younger specimens with integral disc tends to be more compliant in creep test analysis compared to older specimens.

Discussion: The phantom study quantified the technical limits of our US based system for measuring cervical spine kinematics and IVD deformation. In cadaveric specimen tests, the accuracy of US tracking accounted for >90% of the variation in IVD deformation at frequencies ≤ 6 Hz. At high frequency of FSU motion, the accuracy is lower (77%) at 8Hz possibly due to the irregular shape of bone-tissue boundary (compared to a cylinder phantom) which may distort the sound echo at higher rates of motion. As this was conducted as a feasibility study, the number of samples analyzed was low and our preliminary findings must be viewed with some caution. Analysis of additional samples will allow us to validate our preliminary results. But the correlation between stiffness and IVD hydration is consistent with the observation that the “health” and integrity of the IVD affects the mechanical performance of the FSU. Our US system may provide a cost-effective clinical tool to evaluate the integrity and performance of the IVD by applying low amplitude traction and compressive loads to the head and neck *in-vivo*.

Significance: We demonstrate that clinical ultrasound can provide a portable, low cost imaging modality capable of quantifying cervical spine IVD displacement and the mechanical compliance of a functional spinal unit in response to applied forces. Our study establishes the feasibility of using two synchronized clinical US to stereographically measure dynamic FSU motion in response to applied loads in real time up to 8 Hz. This technology allows the *in-vivo* evaluation of cervical spine mechanical behavior in dynamic environments where MRI and CT cannot be used. As treatments to reconstitute degenerated IVD

become available, quantitative analysis of IVD mechanics will be necessary to determine which patients will be appropriate for these treatments and to monitor their response.

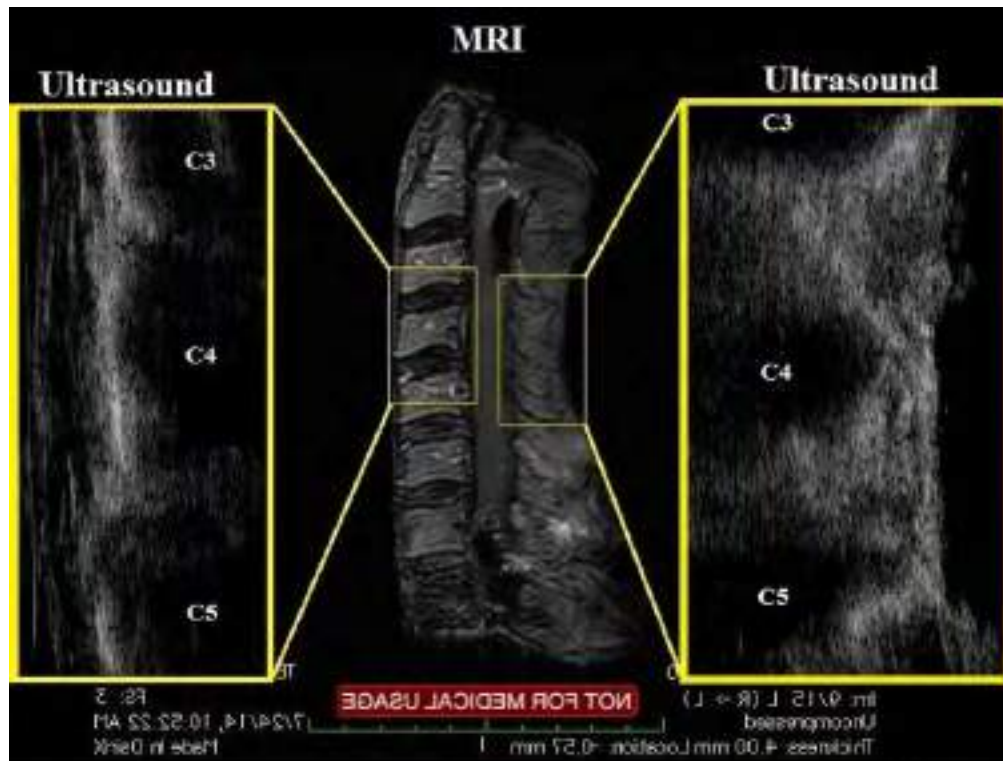


Fig. 1 B-mode Ultrasound provides a magnified window of Functional Spinal Units. One US acquired anterior vertebrae body and the other imaged posterior spinal processes

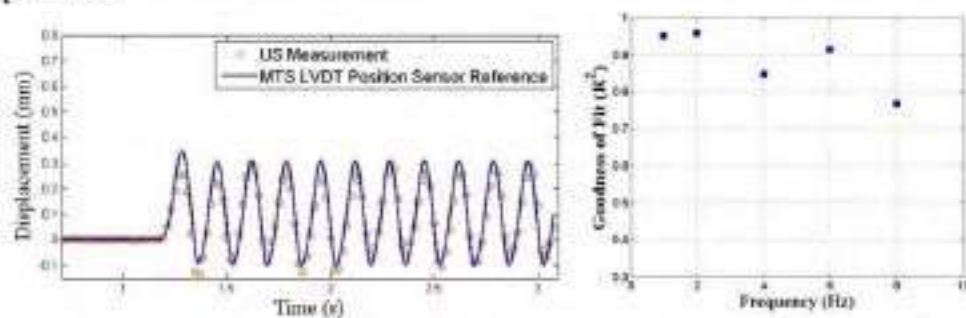


Fig. 2 Representative C6-7 FSU motion measured by US compared to deformation measured directly by in-line LVDV for applied -90N to +90N sinusoidal force @ 6Hz. Blue line is LVDV displacement measurement and red circles are displacements deduced from US images. The coefficient of determination for US vs. LVDV measurements of FSU motion plotted as function of applied frequency. The US tracking are highly consistent with reference measurements <= 6Hz motion.

Compliance and damping coefficient derived for C4-5 FSU levels from each specimen

Specimen#	1	2	3	4	5
Stiffness (N/mm)	117.3	203.3	258.3	264.2	312.5
Damp Coefficient (N•s/mm)	1420	1497	1045	1534	1110

Pfirrmann Grading of IVD	2	3	3	3	4
Age (yrs)	54	58	63	58	67

ORS 2015 Annual Meeting

Poster No: 1096

RESULTS: For C5–C6, the intact ROM (12.2 ± 2.2 deg) was split into three zones: extension high stiffness zone (2.5 ± 2.4 deg), HFZ (6.7 ± 2.9 deg) and flexion high stiffness zone (3.0 ± 1.8 deg). The HFZ covers $23 \pm 5\%$ (0.7 ± 0.1 Nm) of the applied FE moment, but contributes $54 \pm 17\%$ of the total segmental ROM. At C6–C7, the intact ROM (10.0 ± 2.9 deg) yielded: extension high stiffness zone (1.9 ± 0.4 deg), HFZ (4.6 ± 1.1 deg) and flexion high stiffness zone (3.5 ± 3.2 deg). The HFZ covers $23 \pm 4\%$ (0.7 ± 0.1 Nm) of the applied FE moment, but contributes $49 \pm 13\%$ of the total segmental ROM. The change in location of the C5–C6 HFZ-COR between intact and TDA averaged 1.0 ± 1.1 mm posteriorly ($n=8$, $p<.05$) and 0.6 ± 1.4 mm caudally ($n=8$, $p=.3$). At C6–C7 the change in C6–C7 HFZ-COR between intact and TDA averaged 1.4 ± 0.8 mm posteriorly ($n=7$, $p<.01$) and 0.3 ± 2.0 mm cranially ($n=7$, $p=.7$).

CONCLUSIONS: Each individual spinal motion segment has a unique COR depending on its bony and soft tissue anatomy. Fixed center of rotation arthroplasty designs force a nonphysiologic COR upon implanted motion segments. This fixed COR may cause abnormal quantity and quality of motion resulting in altered facet loading and degenerative changes. The facet joints and ligamentous structures have a significant effect on COR location. Activities of daily living occur primarily in the HFZ making traditional measures of COR from full extension to full flexion an inaccurate representation of COR location. A new COR measure has been presented to measure COR in the high flexibility zone where it is less affected by the facets and tensioned soft tissues. The results of this study show that the investigated TDA device allowed individual motion segments to maintain their COR position in the anteroposterior direction within 1.2 ± 1.0 mm ($p=.00$) and in the cranial-caudal direction to 0.2 ± 1.7 mm ($p=.70$) of the intact COR location.

FDA DEVICE/DRUG STATUS: Triadyme-C, Dymicron, Inc., UT (Not approved for this indication).

<http://dx.doi.org/10.1016/j.spinee.2016.07.295>

261. Fatigue in the Cervical Spine Intervertebral Disc with Repetitive Axial Compression

Brian D. Stemper, PhD¹, Narayan Yoganandan, PhD², Mingxin Zheng, PhD³, Brian Snyder, MD, PhD⁴, ¹Medical College of Wisconsin, Milwaukee, WI, USA; ²Milwaukee VA Medical Center, Milwaukee, WI, USA; ³Beth Israel Deaconess Medical Center, Boston, MA, USA; ⁴Children's Hospital/Orthopaedic Surgery, Boston, MA, USA

BACKGROUND CONTEXT: Axial vibration is common in workplace environments such as heavy machinery operators, truck drivers, and military personnel. Long duration and repetitive axial vibration have been associated with cervical spine-based pain syndromes, likely associated with progressive changes soft tissue mechanics over time.

PURPOSE: Determine changes in cervical spine intervertebral disc properties during repetitive axial loading.

STUDY DESIGN/SETTING: An experimental biomechanical study with cervical segments repeatedly exposed to 10,000 cycles of axial loading followed by a rest period to characterize intervertebral disc fatigue-related height loss and unloaded disc height restitution, accounting for differences by spinal level and loading rate.

PATIENT SAMPLE: Twenty-one cervical spine intervertebral disc segments (C2–3, C4–5, or C6–7) obtained from cadaveric specimens (55 ± 11 yrs) were exposed to the experimental protocol.

OUTCOME MEASURES: Cycle-by-cycle stiffness was calculated based on axial force and compressive displacement during compressive testing. Intervertebral disc height loss was calculated as the mean disc height (across five locations on lateral X-ray) measured before and immediately after each 10,000 cycle set. Disc height recovery was calculated as change in disc height after a 15 min rest period.

METHODS: Specimens were exposed to five sets of 10,000 axial compressive cycles (0–150 N) at either 2 or 4 Hz in a physiologic saline bath maintained at 37°C using an electrohydraulic testing device, and allowed a 60-min rest period between sets. Repeated measures ANOVA analysis was used to determine statistically significant differences ($p<.05$) in compressive stiffness, disc height loss, and disc height recovery as a function of set number, cyclic compression rate, and spinal level.

stiffness, disc height loss, and disc height recovery as a function of set number, cyclic compression rate, and spinal level.

RESULTS: Mean compressive stiffness increased during each 10,000-cycle set ($p<.05$), and generally increased from the first to the fifth sets ($p<.05$). Intervertebral disc height loss and restitution were significantly dependent upon set number and cyclic compression rate. Height loss was also dependent on spinal level. Height loss was greatest during the first set (29%) and decreased dramatically for the second through fifth sets, greater at lower cervical levels (C4/5 and C6/7), and greater for testing conducted at 2 Hz. Disc height recovery was generally greatest during following the first set (23%) and decreased dramatically for later sets, was greater at lower cervical levels (C4/5 and C6/7), and was greater for 2-Hz tests.

CONCLUSIONS: Results of this experimental study demonstrated changes in cervical spine intervertebral disc properties under vibrational loading that were dependent on cyclic compression rate and spinal region. Specifically, the loading paradigm had a greater effect on the lower cervical spine and at lower frequencies. These findings have significant real-world implication in that the intervertebral disc had lost approximately 29% of its pre-test height over the first 10,000 cycles and had not recovered to pre-test levels after a 15-min relaxation period. However, rate dependence indicates that changes in disc properties during vibrational loading will likely depend on the specific environment and, therefore, occupational exposure limits to prevent chronic changes should be based on the characteristics of the environment. These data can be used to develop and validate predictive models for changes in disc properties under a variety of different loading paradigms.

FDA DEVICE/DRUG STATUS: This abstract does not discuss or include any applicable devices or drugs.

<http://dx.doi.org/10.1016/j.spinee.2016.07.296>

262. Direct Measure of Cervical Interbody Forces in Vivo: Load Reversal after Plating

Eric H. Ledet, PhD¹, Josh Peterson¹, Rebecca A. Wachs, MS¹, Mary Beth M. Grabowsky, PhD¹, Joseph Glennon², Darryl J. DiRisio, MD³, ¹Rensselaer Polytechnic Institute, Troy, NY, USA; ²Capital District Veterinary Surgical Associates, Pattersonville, NY, USA; ³Albany Medical College, Albany, NY, USA

BACKGROUND CONTEXT: Biomechanics play an important role in spine fusion, but the in vivo biomechanics of the cervical spine are not well characterized and the in vivo biomechanics after spinal arthrodesis have never been studied. Load sharing facilitates fusion, but overloading of interbody implants can lead to subsidence and failure. In vitro studies have demonstrated that anterior plating significantly alters mechanical loading in the cervical spine. The instantaneous axis of rotation is shifted anteriorly and loading is reversed relative to an uninstrumented spine; the interbody space is compressed during extension and unloaded during flexion. However, this has never been tested in vivo and the magnitude of loads in the instrumented and uninstrumented cervical spine are unknown.

PURPOSE: The purpose of this study was to use a novel force-sensing implant to directly measure interbody loading in the cervical spine in real time in vivo in a large animal model following instrumented or uninstrumented arthrodesis.

STUDY DESIGN/SETTING: In vivo biomechanical loading following anterior cervical discectomy and fusion (ACDF) in goats.

OUTCOME MEASURES: Real time in vivo interbody forces and kinematic motion data during flexion/extension exercises after interbody arthrodesis in the goat cervical spine.

METHODS: A custom interbody implant/load cell was developed to measure real time forces in the interbody space of the goat cervical spine. The implants incorporated a wired button load cell (Futek, Irvine, CA) between implant endplates. The implant/load cells were calibrated and sterilized. After IACUC approval, under general anesthesia, and using standard clinical technique, a discectomy was performed at C4–5 in three skeletally mature goats. In each animal, an interbody implant/load cell was placed in the disc space and the lead wires were tunneled submuscularly to exit percutaneously on the dorsal surface of the neck. In two animals, a PEEK washer was at-

MECHANISMS OF CERVICAL SPINE DISC INJURY UNDER CYCLIC LOADING: EXPERIMENTS AND FINITE ELEMENT ANALYSIS

Sagar Umale (1), Narayan Yoganandan (1), Mike Arun (1), Brian Stemper (1), Brian Snyder (2)

(1) Department of Neurosurgery,
Medical College of Wisconsin,
Milwaukee, WI, USA

(2) Beth Israel Deaconess Medical Center,
Harvard Medical School,
Cerebral Palsy Clinic Children's Hospital,
Boston, MA, USA

INTRODUCTION

Military helicopter pilots, soldiers, heavy duty vehicle drivers and others working in vibratory environments sustain cyclic loading as a part of their activities [1]–[3]. Many studies have been conducted to understand the mechanical response of the lumbar spine under cyclic loading, with a primary focus on experiments from human cadaver spines [4]–[6]. While finite element modeling (FEM) to understand the internal responses of disc components have primarily concentrated on acute loading of lumbar and cervical spines [7], some repeated loading simulations are also published on the lumbar spine [8]. However, cyclic loading studies on the human cervical spine combining experimental data and FEM are limited. The objective of this study is to develop and validate a three-dimensional FEM of the human C4-C5 intervertebral disc using in-house experiments and determine the stress strain distributions within its components in an attempt to explain the potential mechanisms of disc injury.

METHODS

The finite element model of the C4-C5 disc with the associated superior and inferior end plates was developed from CT images. The nucleus pulposus and annulus ground substance were modeled using solid hexahedral elements. The annular fibers were modeled with five pairs of concentric quadratic shell layers embedded in the ground substance [7]. The superior and inferior cartilaginous and bony endplates were modeled using shell elements. The element size was 0.5 mm, and the model was composed of 8,740 solid hexahedral elements and 18,636 quadratic shell elements. The geometry represented the average area and disc height of the C4-C5 disc segments tested at 2 Hz for 10,000 cycles. The material properties for the ground substance were obtained from in-house experiments, performed on disc segments before cyclic loading, described later.

The material properties for the endplates, nucleus and annular fiber components were obtained from literature [7]–[9]. The annular ground substance was modeled as a hyper-viscoelastic material. The nucleus was modeled with an elastic modulus of 1 MPa and a Poisson's ratio of 0.45. The annular fibers were modeled as hyper-elastic (Aruda-Boyce) material, and tension-only material properties were varied from the inner most layer to the outer most layer. The bony endplates were modeled with an elastic modulus of 5,600 MPa and a Poisson's ratio of 0.3, and uniform thickness of 1 mm. The cartilaginous endplates were modeled with an elastic modulus of 24 MPa and a Poisson's ratio of 0.4, and uniform thickness of 0.8 mm. The cyclic loading was applied in two steps: (1) a uniform load of 150 N at 2 Hz was applied to the superior end plate, and (2) a direct cyclic step simulating 10,000 compression cycles based on the previous step history.

The model was validated by conducting experiments with two female (mean age 47±23 years) C4-C5 disc segments. Pre-test antero-posterior and lateral radiographs and computed tomography (CT) scans of the spinal columns were obtained. All tests were done in a physiologic chamber by maintaining the specimen in a heated water bath during the entire loading period. Tension-compression and viscoelastic tests were conducted, and this was followed by subjecting the specimens to 150 N of compressive force at a frequency of 2 Hz for 10,000 cycles. Tension-compression and viscoelastic tests were repeated after the cyclic loading. The specimens were x-rayed after the loading period.

The initial output of the FEM was used to extract displacement-time responses and compare with the experimental corridors, expressed as mean and plus and minus one standard deviation. Stress analysis outputs consisted of determining profiles of maximum and minimum principal stresses and strains, vector directions, and Von Mises stresses

in the constituents of the disc and endplates. Patterns of these internal distributions were used to infer the potential mechanisms of load transfer within the disc components under cyclic loading.

RESULTS

The displacement-cycle responses from the model were within the experimental mean plus minus one standard deviation corridors (Figure 1). The displacement was greater during the initiation of the loading process and reduced exponentially in the first 2,000 cycles, followed by a plateau showing the effect of viscoelasticity in this first 2,000 cycle period. The Von Mises stress distribution in the disc at the end of the step 2, that is, 10,000 cycles is shown (Figure 2). The residual stress was maximum in the annulus and concentrated along the periphery. The residual Von Mises stress in the nucleus was approximately one-tenth of the annulus and was concentrated along the outer circumference. As expected, the annular fibers had the least residual stress, concentrated in the innermost layer.

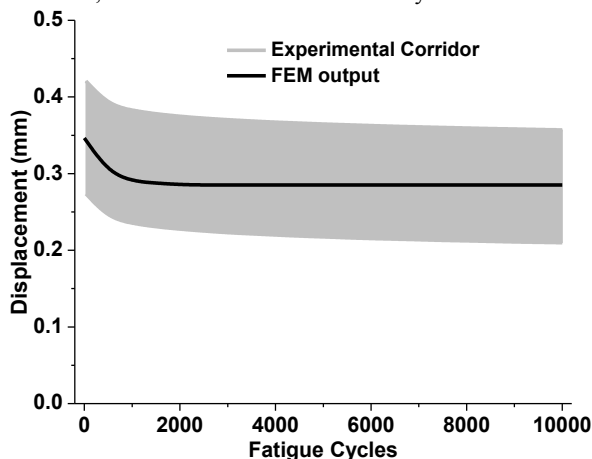


Figure 1: Comparison of the cyclic response from FEM with experimental corridor (Shaded region)

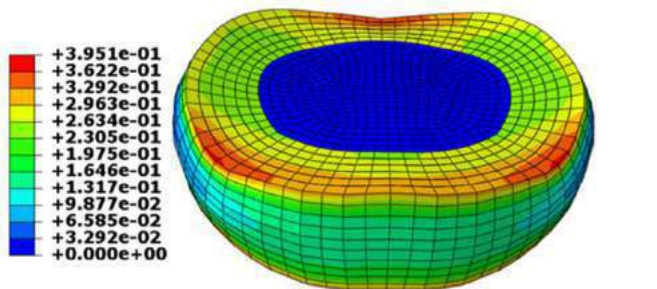


Figure 2: Von Mises stress distribution

The principal stresses were considerably lower than the Von Mises stresses, indicating the development of the shear stress during the cyclic loading process. This was also evident from the direction vectors of the principal stresses. The principal strains were found to be maximum in the annulus ground substance and fibers. The tensile stresses and strains occurred in the radial direction, whereas the compressive stresses and strains occurred in the axial direction.

DISCUSSION

This is the first study to conduct cyclic loading experiments simulating physiological situations and use its inputs and outputs to develop and validate a three-dimensional FEM of the C4-C5 disc. Following validation, the internal responses of the components of the discs were extracted from stress analysis. Although the external cyclic

loading was axial, the response of the cervical disc was multi-modal: compressive and shear stresses were developed due to anisotropy. The concentration of the minimum principal stresses at the annulus nucleus boundary along the anterior and posterior direction can lead to circumferential tears, and the maximum principal stresses concentrated at the annulus and cartilaginous endplate boundary can lead to radial tears in the disc, thus explaining a mechanism of internal disc failure due to cyclic loading and correlating with clinical observations of radial and circumferential tears [10]. The development of the shear stresses in association with the peak principal stresses may lead to delamination of the disc under cyclic loading in human cervical spines. It is known that the posterior annulus is supplied by the sinuvertebral nerves, and the anterior and lateral regions are supplied by autonomic nerves [11]. The compression of the annulus and the presence of the nerves in these regions may elicit discogenic pain in patients sustaining cyclic loading from occupational and military activities. The present study offers an explanation for these clinical phenomena.

ACKNOWLEDGEMENTS

This work was supported in part by the U.S. Army Medical Research and Materiel Command Fort Detrick, Maryland (01026018, Contract No. W81XWH-13-1-0050). This material is a result of work supported with resources and use of facilities at the Zablocki VA Medical Center, Milwaukee, Wisconsin. NY and BDS are part-time employees of the Zablocki VA Medical Center, Milwaukee, Wisconsin. The content included in this work does not necessarily reflect the position or policy of the U.S. Government.

REFERENCES

- [1] S. P. Cohen et. al., "Spine-area pain in military personnel: a review of epidemiology, etiology, diagnosis, and treatment," *Spine J.*, vol. 12, no. 9, pp. 833–842, 2012.
- [2] V. De Loose et. al., "Individual, work-, and flight-related issues in F-16 pilots reporting neck pain," *Aviat. Space Environ. Med.*, vol. 79, no. 8, pp. 779–783, 2008.
- [3] M. Mangnusson et. al., "Are occupational drivers at an increased risk for developing musculoskeletal disorders," *Spine*, vol. 21, pp. 710–7, 1996.
- [4] J. McElhaney et. al., "Cervical Spine Compression Responses," in *STAPP car crash conference*, 1983.
- [5] M. A. Adams and W. C. Hutton, "The effect of fatigue on the lumbar intervertebral disc," *J. Bone Joint Surg. Br.*, vol. 65, no. 2, pp. 199–203, 1983.
- [6] C. E. Gooyers et. al., "The Impact of Posture and Prolonged Cyclic Compressive Loading on Vertebral Joint Mechanics," *Spine*, vol. 37, no. 17, pp. E1023–E1029, 2012.
- [7] M. B. Panzer and D. S. Cronin, "C4–C5 segment finite element model development, validation, and load-sharing investigation," *J. Biomech.*, vol. 42, no. 4, pp. 480–490, 2009.
- [8] M. Qasim et. al., "Initiation and progression of mechanical damage in the intervertebral disc under cyclic loading using continuum damage mechanics methodology: A finite element study," *J. Biomech.*, vol. 45, no. 11, pp. 1934–1940, 2012.
- [9] T. Pitzen et. al., "Variation of endplate thickness in the cervical spine," *Eur. Spine J.*, vol. 13, no. 3, pp. 235–240, 2004.
- [10] M. A. Adams and P. J. Roughley, "What is intervertebral disc degeneration, and what causes it?," *Spine*, vol. 31, no. 18, pp. 2151–2161, 2006.
- [11] N. Bogduk et. al., "The nerve supply to the human lumbar intervertebral discs," *J. Anat.*, vol. 132, no. Pt 1, p. 39, 1981.

CHANGES IN CERVICAL SPINE INTERVETEBRAL DISC PROPERTIES WITH REPETITIVE AXIAL LOADING

**Brian D. Stemper, PhD (1,2), Alok S. Shah, MS (1,2), Narayan Yoganandan, PhD (1,2),
Mingxin Zheng, MS (3,4) Brian Snyder, MD, PhD (3,4)**

(1) Department of Neurosurgery
Medical College of Wisconsin
Milwaukee, Wisconsin, USA

(2) Research Service
Zablocki Veterans Affairs Medical Center
Milwaukee, Wisconsin, USA

(3) Beth Israel Deaconess Medical Center
Boston, Massachusetts, USA

(4) Harvard Medical School
Harvard University
Cambridge, Massachusetts, USA

INTRODUCTION

High rates of neck pain in military personnel may be attributable to vibrational environments that can subject the cervical spine to repetitive axial loading. Those types of environments can be experienced in military helicopters, fixed-wing aircraft, and fast boats. For example, the rate of recurrent neck pain in military helicopter pilots was reported to be approximately 30% [1], compared to 14% in the general population [2]. Additionally, the effect of axial vibration can be exaggerated with the use of helmets and helmet-mounted instrumentation that can increase the inertial load on the cervical spine. Non-specific neck pain could be attributed to progressive subfailure changes in cervical spine biomechanics associated with fatigue of the spinal soft tissues. Characterizing these changes is important for the development of environment-specific exposure limits. However, previous efforts to determine the fatigue response of spinal tissues have focused on the onset of tissue failure [3] or characterizing the effect of spinal implants [4]. Therefore, the objective of the current study was to characterize the effect of repetitive compressive loading on cervical spine biomechanics in an experimental study incorporating Post-Mortem Human Subjects (PMHS), focusing on the influence of spinal level and loading rate.

METHODS

Cervical spine intervertebral disc segments were used to quantify the progressive change in compressive stiffness during repetitive loading. Cervical spines were obtained from fresh/frozen PMHS with mean age of 55±11 years and sectioned into C2/3, C4/5, and C6/7 motion segments. The posterior elements were then removed at the pedicle, resulting in intervertebral disc segments that consisted of adjacent vertebral bodies, the intervertebral disc, and the anterior and posterior longitudinal ligaments. The cranial and caudal aspects of the

specimens were potted in polymethylmethacrylate (PMMA) to facilitate fixation to the loading apparatus.

Each specimen was subjected to five sets of 10,000 compression cycles (total 50,000 cycles) between 0 and 150 N using a sine wave function. All testing was conducted in a physiologic saline bath at 37 deg C to simulate in vivo conditions. Cyclic compressive loading was applied to the specimen using an electrohydraulic testing device (MTS Systems Corporation, Eden Prairie, MN). The protocol consisted of five consecutive sets of 10,000 cycles separated by an approximately 60-minute rest period between sets. Cyclic compression testing was conducted at either 2 or 4 Hz.

Axial force was measured at 100 Hz using a uniaxial load cell mounted to the piston of the electrohydraulic testing device. Piston displacement was measured at 100 Hz using a linear variable differential transducer (LVDT). Displacement of the piston was quantified for each 150-N cycle and slope of the force versus displacement trace was used to compute compressive stiffness. Stiffness magnitudes were then compared between spinal levels, cycles, and loading rates using multiple factor repeated measures Analysis of Variance (ANOVA). Pairwise comparisons were conducted for significant main effects using Bonferroni adjustment to account for multiple comparisons.

RESULTS

Twenty-one cervical spine intervertebral disc segments (8 C2/3, 6 C4/5, 7 C6/7) obtained from 12 PMHS were subjected to 50,000 cycles of compressive loading. Eleven specimens were tested at 2 Hz and 10 specimens were tested at 4 Hz. Stiffness progressively increased throughout the testing period, with consistent set-to-set behavior characterized by a sharp increase in stiffness during the first 1,000 cycles followed by a more gradual increase for the remaining

9,000 cycles of each set (Figures 1, 2). Multi-factor ANOVA revealed that compressive stiffness was significantly dependent upon loading rate ($p<0.0001$), cycle ($p<0.0001$), and spinal level ($p<0.0001$). Post hoc analysis revealed that each spinal level demonstrated significantly different stiffness profiles compared to every other spinal level ($p<0.001$). The C6/7 spinal level demonstrated the greatest stiffness and the C2/3 level generally demonstrated the lowest stiffness. Post hoc analysis of cycle-by-cycle stiffness demonstrated that stiffness magnitudes during the first 10,000 cycles were significantly different from all other sets ($p<0.01$) and that stiffness during the last 10,000 cycles was significantly different than the first 30,000 cycles ($p<0.05$). In general, stiffness values during the first set were lower than the subsequent sets.

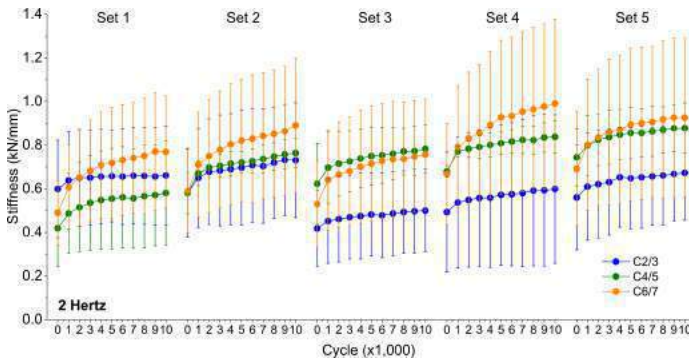


Figure 1: Compressive stiffness of intervertebral disc segments during 2 Hz repetitive loading.

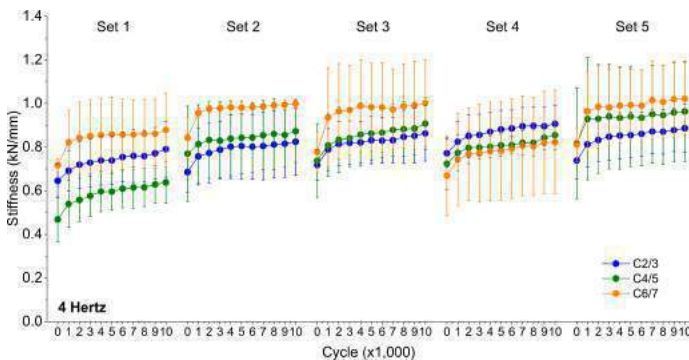


Figure 2: Compressive stiffness of intervertebral disc segments during 4 Hz repetitive loading.

The change in stiffness (N/mm/cycle) for each 10,000-cycle set was mathematically modeled using a bilinear approximation, with the first regression characterizing the slope of increasing stiffness for cycles 1 to 1,000 and the second regression characterizing the slope of increasing stiffness for cycles 1,001 to 10,000. ANOVA analysis demonstrated that the slope of stiffness change during the first 1,000 cycles was significantly dependent on spinal level ($p<0.05$) but not cyclic testing rate, with a greater increase in compressive stiffness occurring at the C6/7 spinal level than the other tested levels (Figure 3). However, the slope of stiffness change during the last 9,000 cycles was significantly dependent on both spinal level and cyclic testing rate (Figure 4). Statistically significant increases in stiffness for both spinal level and cyclic loading rate were driven primarily by the large increase in C6/7 stiffness during the last 9,000 cycles for the 2-Hz cyclic loading rate.

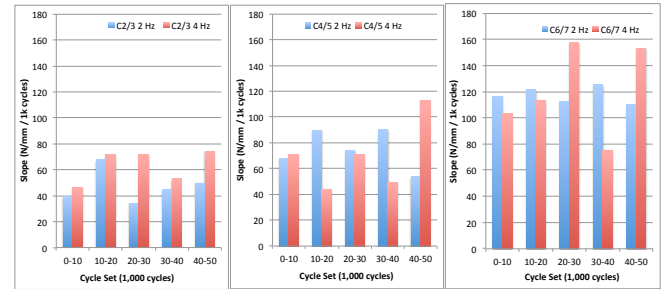


Figure 3: Slope of increasing stiffness during the first 1,000 cycles of each set of cyclic compressive loading.

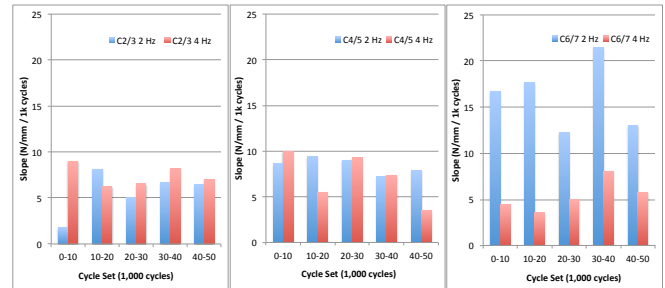


Figure 4: Slope of increasing stiffness during the last 9,000 cycles of each set of cyclic compressive loading.

DISCUSSION

Results of this study characterized the change in compressive stiffness of the cervical intervertebral disc during cyclic loading designed to mimic the types of inertial loading experienced in vibrational environments. Although testing was conducted below the threshold for injury, level-based differences may imply a greater likelihood for injury at the C6/7 level compared to other tested levels due to greater initial stiffness and a greater effect of cyclic loading evident by the increased slope of the regression fit over the last 9,000 cycles of each set. Increased propensity for lower cervical spine injury is consistent with studies quantifying injury in automotive environments [5] and may focus future analyses of exposure limits to vibrational environments. Another important factor not accounted for in this analysis may be an effect of gender, wherein prior studies have indicated significantly different mechanical response of spinal disc segments between men and women [6]. Given an increased combat role for females in the military, delineation of possible gender effects in fatigue response of the spine remains of focus of this ongoing research. Future research in this area will also focus on characterizing the effect of loading rate/duration and increased helmet mass on the fatigue response of the cervical spine intervertebral disc.

ACKNOWLEDGEMENTS

This work was supported by the U.S. Army Medical Research and Materiel Command Fort Detrick, Maryland (01026018, Contract No. W81XWH-13-1-0050), and the Department of Veterans Affairs Medical Research.

REFERENCES

- [1] Ang, B et al., *Aviat Space Environ Med* 77(7): 713-19, 2006.
- [2] Bovim, G et al. *Spine* 19(12): 1307-09, 1994.
- [3] Hansson, TH et al., *J Orthop Res* 5: 479-87, 1987.
- [4] Ordway, NR et al., *J Orthop Res* 30(4): 587-92, 2012.
- [5] Yoganandan, N et al., *J Clin Eng* 15(6), 505-12.
- [6] Stemper, BD et al., *J Craniovert Jun Spine* 1(1): 18-22.

In-vivo Cervical Spine FSU Dynamic Motion Measured by Dual Ultrasound: the Effect of Muscle Activation

Mingxin Zheng^{1,2}, Aidin Masoudi¹, Dan Buckland^{1,3}, Thomas Szabo², Brian Snyder^{1,2,4}

¹Center for Advance Orthopaedics Studies, Beth Israel Deaconess Medical Center, Boston, MA, ²Boston University, Boston, MA

³Massachusetts Institute of Technology, Cambridge, MA 02139 ⁴Boston Children's Hospital, Boston, MA 02115

Disclosures: Mingxin Zheng (N), Aidin Masoudi (N), Dan Buckland (N), Thomas Szabo (N), Brian Snyder (N)

INTRODUCTION: Neck pain, instigated by acute or chronic injury sustained in the work place, is a common occupational health complaint associated with cervical spine inter-vertebral disc (IVD) degeneration. Laborers and Army troops exposed to repetitive loads and vibrations are at highest risk. Currently there are no methods to measure the dynamic motion and mechanical properties of the cervical spine IVD in at-risk individuals while working in these environments. Imaging technologies such as plain radiography, computed tomography and Magnetic Resonance Imaging are limited by large size and power requirements. In previous studies we reported the development of a dual ultrasound system (US) to study the kinematics, static and dynamic mechanical properties of cervical spine functional spinal units (FSU) *ex-vivo*. The aim of the current study is to apply this novel dual US system to measure the deformation of FSU *in-vivo* and evaluate the effect of paracervical muscle activation on the dynamic properties of the FSU during repetitive jumping.

METHODS: With IRB approval, subjects repetitively jumped on and off a 0.8 foot step for 4 minutes while wearing a helmet to simulate typical Army troop activities. The load applied to the head/neck during impact was measured by an interposed load cell inside the helmet; the load applied to the feet at landing was measured by a force plate. A Motion Capture system was used to measure the 3D motion of the subject's head relative to the torso. Para-cervical muscle (SCM, upper trapezius) activity was measured by surface EMG. Since the C4-C5 IVD is most commonly affected by degenerative disease, continuous, real-time, B-mode US images of the C4-5 FSU were captured during the jump test. A custom neck collar maintained the dual US probes in fixed orientation, sonically coupled to the spine by an adhesive hydrogel. Two projections of the FSU were imaged: the wave trajectory of the anterior US probe, positioned just anterior to the sternocleidomastoid muscle, imaged the midline profile of the vertebral bodies and IVD; the wave trajectory of the posterior US probe, positioned adjacent to the spinous processes, imaged the profile of the corresponding facet joints and spinous processes. A block-matching algorithm validated in cyclic load cadaveric experiment was used to analyze the dynamic US radio frequency data and calculate FSU motion.

RESULTS: During the jump tests, the C4-C5 FSU was repetitively compressed and then recovered after each landing (Fig 1). Paracervical muscle activation dynamically stiffened the FSU (dampened IVD deformation). The difference between minimum and maximum FSU displacements was used to characterize the amplitude of IVD deformation sequentially over time. A subject who did weight training program had greater paracervical muscle activation signal compared to a subject who did endurance training (Fig. 2: A/B vs. D/E). However, muscle fatigue appeared sooner in the weight training subject (EMG decreases over time, slope = -0.17 s^{-1}) compared to the endurance training subject (EMG remains relatively constant, slope = -0.012 s^{-1} , Fig. 2: C vs. F). The decrease in para-cervical muscle EMG amplitude over time, and corresponding increase in the amplitude of IVD deformation implies that muscle fatigue may decrease the protective effect of paracervical muscle activation that serves to dampen the effect of loads applied to the FSU (Fig. 3).

DISCUSSION: While the sample size is small and the data needs to be viewed with caution, in this first of its kind study, we demonstrate the capability of dual US to measure FSU motion and IVD deformation *in-vivo* in subjects performing real life, work place activities. Specifically we revealed that para-cervical muscle activation affects the dynamic stiffness of the FSU and serves to dampen IVD deformation during repetitive tasks. However, with sustained jumping, muscle fatigue is noted, and the para-cervical muscles are less capable of dampening transmitted loads so that IVD deformations rise, potentially contributing to increased IVD wear and risk of degeneration. While paracervical muscle activation was greater in a subject that strength trained, muscle fatigue ensued sooner than a subject who endurance trained, suggesting that proper training may help prevent neck injuries for workers performing tasks where loads are applied repetitively to the head and neck.

SIGNIFICANCE: We demonstrate that US can provide a portable, low cost imaging modality capable of quantifying cervical spine IVD deformation and the compliance of cervical spine FSUs in response to applied loads. In particular the *in-vivo* evaluation of cervical spine mechanical behavior during the performance of repetitive loading of the head and neck revealed that para-cervical muscle activation affects the dynamic stiffness of the FSU and serves to dampen IVD deformation thereby suggesting that proper training may help prevent neck injuries for workers engaged in these activities.

ACKNOWLEDGEMENTS: This work was supported by the U.S. Army Medical Research and Materiel Command Fort Detrick, Maryland.

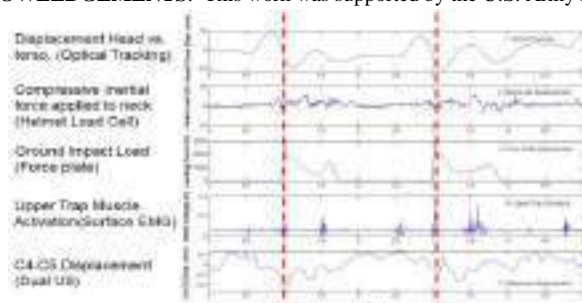


Figure 1. C4-C5 FSU compression - recovery during the jump tests

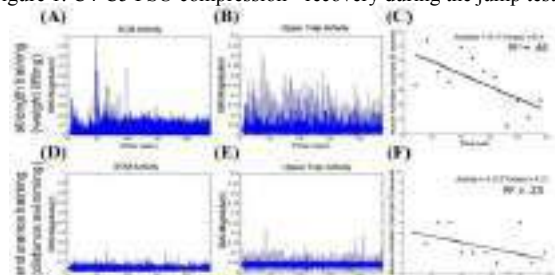


Figure 2. Muscle activities for volunteers (strength vs. endurance)

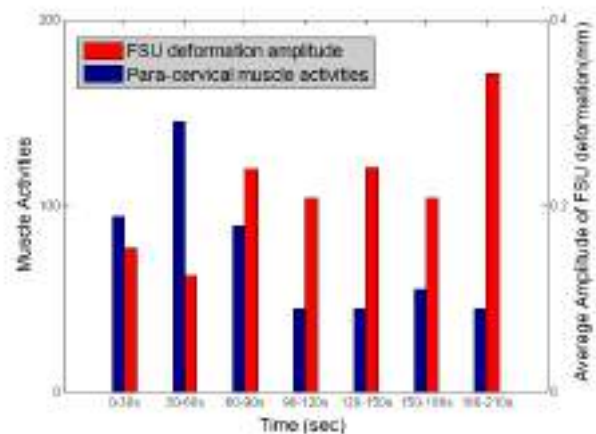


Figure 3. Every 30s, muscle activities were summed and compared to the mean of FSU deformation amplitudes in the same period. Muscle fatigued over time, which may be less able to dampen the load transmitted to IVD.

Real Time *In-vivo* Cervical Functional Spine Unit Kinematics Evaluated by Merging Static MRI with Dynamic Ultrasound Images

Mingxin Zheng^{1,2}, Amin Mohamadi¹, Thomas Szabo², Brian Snyder^{1,2,3}

¹Center for Advanced Orthopaedics Studies, Beth Israel Deaconess Medical Center, Boston, MA, ²Boston University, Boston, MA

³Boston Children's Hospital, Boston, MA

Disclosures: Mingxin Zheng (N), Amin Mohamadi (N), Thomas Szabo (N), Brian Snyder (N)

INTRODUCTION: Neck pain, instigated by acute or chronic injury sustained in the work place, is a common occupational health complaint associated with cervical spine inter-vertebral disc (IVD) degeneration. Laborers and military personnel exposed to repetitive loads and vibrations are at highest risk. Currently there are no methods to measure the dynamic motion of the cervical spine IVD in at-risk individuals while working in these extreme environments. Imaging technologies such as computed tomography and Magnetic Resonance Imaging (MRI) are limited by large size and power requirements. In previous studies we reported the development of a dual ultrasound system (US) to measure the real-time, *in-vivo* deformation of cervical functional spinal units (FSU) in human subjects performing a repetitive jump test. The aim of the current study is to develop a methodology for calculating real-time *in-vivo* C4-5-6 FSU kinematics by merging static MRI images of each individual's cervical spine with serial dynamic dual US image profiles of C4-5-6 during the jump test.

METHODS: With IRB approval, cervical MRI scan were obtained from 12 subjects (21 – 45 yrs, 9 males and 3 females). Vertebral body profiles were manually segmented by using the reversed Cervical MR images (Fig. 1). Each subject repetitively jumped on and off a 0.8 feet step for 4 minutes while wearing a helmet to simulate typical troop activities running/jumping through a field. The load applied to the feet at landing was measured by a force plate. Paracervical muscle (SCM, upper trapezius) activity was measured by surface electromyography (EMG). Since the C4-5 and C5-6 IVD are most commonly affected by degenerative disease, continuous, real-time, B-mode US images of the C4-5 and C5-6 FSU were captured during the jump test. Dual US probes supported by a cervical collar in fixed orientations imaged the anterior and posterior profiles of the C4-5-6 FSUs. The specific trans-sagittal cervical spine image profile visualized by the US probe was co-registered with the matching MRI image profile generated from the 3D MRI data set by finding the trans-sagittal profile that minimized residuals between the matched vertebral body profiles (Figure 1). A block-matching algorithm, validated in human cadaveric C-spine specimens subjected to cyclic loading, was used to analyze the dynamic US images and calculate FSU kinematics. By assuming that the vertebrae behave as rigid bodies, we created point-to-point matching between coincident US and MR profiles to calculate C4-5-6 FSU displacements and flexion angles *in-vivo*.

RESULTS: Representative FSU kinematic motion over 1 second is shown in Figure 2: landing impulse and recovery during the jump measured by force plate (Fig. 2a). Para-cervical muscles activated during landing are activated to dampen the inertial forces generated by the head and impact load transmitted by the helmet (Fig. 2b). Sequential US images of C4-5 and C5-6 portray the vertebral body translation (Fig 2c) and flexion angle of the FSUs (Fig. 2d) calculated by matching the profiles of the segmented sagittal MR static images to the dynamic US images (Fig. 2e).

DISCUSSION: This technique merges real-time, *in-vivo* US profiles of C4-5-6 cervical spine FSUs obtained during conditions simulating combat conditions to matching, static, subject specific, image profiles generated from 3D MRI scans to calculate FSU translation, rotation and IVD deformation. The attenuation of load during impact imparted by activation of the paracervical muscles helps to protect the cervical spine from injury, but muscle fatigue over sequential jumps diminish this protective effect, indicating that troops are at increased risk for cervical spine injury during missions that expose them to repetitive exposures over prolonged time. Additionally this displacement and force data can be imported as boundary conditions into a finite element model to calculate the fatigue properties of the IVD.

SIGNIFICANCE: We demonstrate that US can provide a low-cost, non-invasive measurements of dynamic cervical spine kinematics in real time enhanced by co-registration of US image profiles matched to static MRI sagittal images.

ACKNOWLEDGEMENTS: This work was supported by the DoD and U.S. Army Medical Research and Materiel Command Fort Detrick, Maryland (Grant#: W81XWH-13-1-0050).

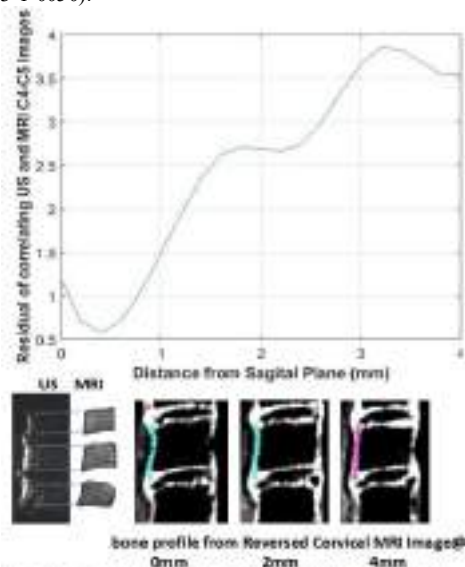


Fig. 1 Co-register MR and US profile by calculating minimal residual. US images at the plane 0.4mm from mid sagittal plane in the representative data. For better segmentation result, reverse MR image was used for outlining profile (cyan).

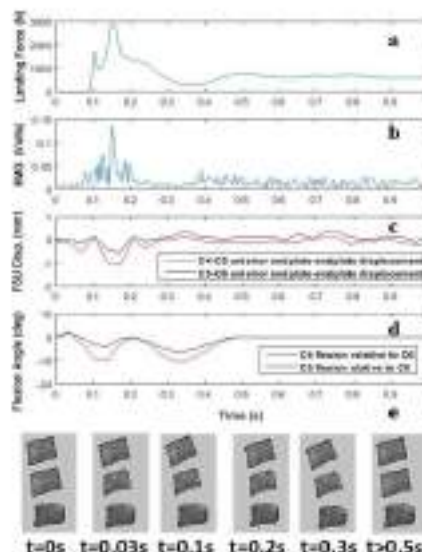


Fig. 2. Subject jumped off 0.8 feet step and landed (1s). US measured the kinematics of FSU (translational and rotational motion), and provided information for reconstruction.

Ultrasound is a Reliable Modality for Measuring Cervical Spine Intervertebral Disk Height

Amin Mohamadi MD, MPH ^{1,2}, Mingxin Zheng, BSc ^{1,4}, Brian Snyder, MD, PhD ^{1,2,3}

1. Center for Advanced Orthopaedic Studies, Beth Israel Deaconess Medical Center, Boston, MA
2. Department of orthopedic surgery, Harvard medical school, Boston, MA
3. Department of Orthopaedic Surgery, Boston Children's Hospital, Harvard Medical School, Boston, MA
4. Department of biomedical engineering Boston University, Boston, MA

Disclosures: None.

INTRODUCTION:

Neck pain, instigated by acute or chronic injury sustained in the work place, is a common occupational health complaint associated with cervical spine inter-vertebral disc (IVD) degeneration. Evaluating the deformation of the cervical spine IVD in response to applied loads is important to understanding the mechanical behavior of cervical spine functional units during various tasks. Imaging technologies such as computed tomography and Magnetic Resonance Imaging (MRI) are limited by large size and power requirements. β -mode ultrasound (US) can provide portable, low-cost, non-invasive imaging of the cervical spine IVD and can be used to evaluate the biomechanical behavior of the IVD *in-vivo* (1). Accurate measurement of dynamic changes in IVD height is particularly important to assess IVD strain. Therefore the aim of this study was to determine the reliability of clinical β -mode US for measuring cervical spine IVD height compared to MRI.

METHODS:

After approval from Beth Israel Deaconess Medical Center and Harvard Medical School Institutional Review Board, nine adult subjects (age range of 21 – 45 years, 7 males and 2 females) gave written consent to participate in this study. Sagittal T1-weighted images of the cervical spine using a 3-Tesla MRI were obtained for each subject. β -mode clinical US was used to measure the height of C4-C5 and C5-C6 IVDs by placing the US probe along the anterior triangle of the neck, bounded infero-laterally by the clavicular head of the sternocleidomastoid muscle, supero-laterally by the omohyoid and strap muscles and medially by the lateral border of the trachea (Figure 1). The trajectory of US probe was aimed towards the anterior margins of cervical vertebrae C4 to C6. IVD height for C4-C5 and C5-C6 disk were measured from both MRI and US images using ImageJ software (Wayne Rasband, National Institute of Mental Health). US images visualize only the anterior profile of the IVD, while MRI demonstrates the entire disk, which is non-uniform in height extending from the anterior to posterior margin of the vertebral body (Figure 2). Therefore the IVD was measured at the anterior, middle and posterior aspects of the mid-sagittal MRI image of the cervical spine. Paired t-test was used to compare IVD height measured by US vs. MRI for all subjects. Linear regression models were generated to assess the correlation of US derived IVD height with that derived from MRI. The coefficient of determination R^2 was used to assess the goodness of fit. P-value less than 0.05 was considered statistically significant.

RESULTS:

The mid-sagittal MRI images of the cervical spine demonstrated significant variability in IVD height from anterior to posterior: mean C4-C5 IVD height @ anterior border = 4.67 mm (SD = 0.99), @ midline = 5.68 mm (SD = 0.86), @ posterior border = 3.72 mm (SD = 0.69). These mean C4-C5 IVD height measured by US = 4.72 mm (SD = 0.95). The C5-C6 IVD height measured by MRI was similar to C4-C5, mean IVD height @ anterior border = 4.75 mm (SD = 1.02), @ midline = 6.17 mm (SD = 0.52), @ posterior border = 3.75 (SD = 1.54). The mean IVD C5-C6 height measured by US = 4.84 mm (SD = 1.03). The mean of US derived IVD heights did not differ from those measured by MRI at the anterior or posterior borders, but US derived IVD heights were significantly smaller than the IVD measured at the midline on MRI. US measures of cervical IVD height were more highly correlated with that measured at the anterior border of the MRI images for C4-C5 IVD ($R^2 = 0.52$) than C5-C6 IVD ($R^2 = 0.32$) and for the averaged value of all three MRI IVD heights (Graph 1).

DISCUSSION:

The purpose of this study was to evaluate the accuracy of US to measure cervical spine IVD height compared to MRI. Given that the height of the IVD varies along the mid-sagittal plane from anterior to posterior, US imaging was better at measuring IVD height at the anterior margin. Furthermore US imaging of the C4-C5 IVD was more accurate than the C5-C6 IVD, perhaps reflecting some distortion induced by increasing soft tissue mass at the base of the neck as well as a higher incidence of C5-C6 IVD dehydration.

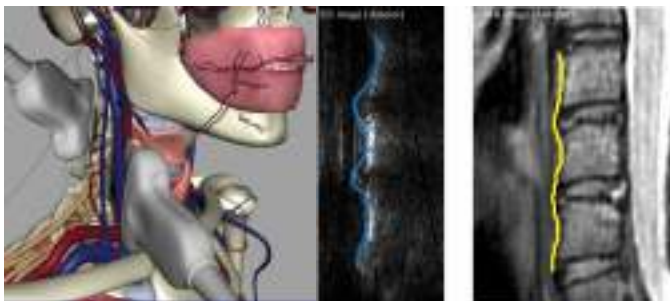
SIGNIFICANCE:

1. We have shown that clinical US may provide a useful tool for measuring the IVD height under static conditions.
2. We believe that the US technique described here may be further developed to evaluate cervical spine kinematics in dynamic environments where MRI and CT cannot be used.

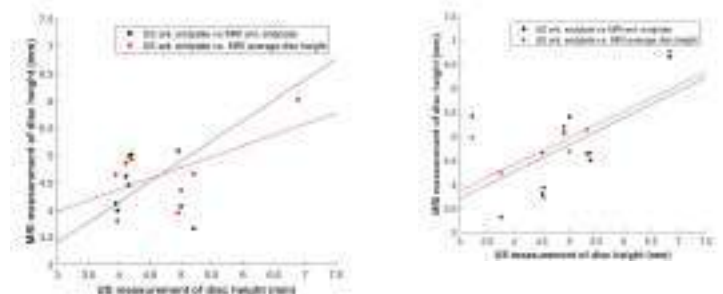
ACKNOWLEDGEMENTS: This study was supported by DoD grant W81XWH-13-1-0050

Figure 1. a. Position of US probe,

b) Anterior margin of vertebral body shown on US or MRI



Graph 1: Correlation of US measure of IVD height with anterior IVD height or mean IVD height using MRI. A) C4-C5 IVD, b) C5-C6 IVD



Cervical Spine Kinematics from Dynamic Ultrasound Images Co-Registered to Patient-specific 3D MRI

Mingxin Zheng^{1,2}, Amin Mohamadi¹, Thomas L. Szabo¹, Brian D. Snyder^{1,2,3}

¹Beth Israel Deaconess Medical Center, Boston, MA, ²Boston University, Boston, MA, ³Boston Children's Hospital, Boston, MA
Email of Presenting Author zmx.pku@gmail.com

Disclosures: Mingxin Zheng (N), Amin Mohamadi (N) Thomas L. Szabo (N), Brian D. Snyder(N)

INTRODUCTION: Understanding the pathophysiology of acute and chronic degenerative intervertebral disc (IVD) disease induced by repetitive load scenarios encountered in the work environment remains a challenge since the etiology of these injuries are not evident in static X-ray, CT, or MRI imaging or pathoanatomic grading systems. Current methods to evaluate cervical spine kinematics include optical tracking systems and dual fluoroscopy. However, these methods are limited by inaccuracies associated with skin motion, risk of radiation exposure, or large equipment size and power requirements. Previously we demonstrated B-mode ultrasound(US) imaging to accurately track the dynamic motion of cervical functional spine units (FSU) and to measure the deformation of the interposed IVD ex-vivo and in-vivo. However, using 2D US to directly track 4D spinal motion is compromised by the lack of 3D structural information and a limited 2D window of the complex 3D vertebral anatomy. Our goal was to derive a method to combine dynamic 2D US image profiles of cervical vertebrae with a 3D model of the C-spine derived from *in-vivo* MRI of the neck and C-spine.

METHODS: Step 1 - develop 3D model for specific vertebra to be imaged. A generic model of cervical vertebrae was created by editing digitized CT scans of cadaveric C-spines. Step 2 - by matching anatomical landmarks, the generic cervical vertebral model was deformed and scaled to match a specific human subject's cervical spine anatomy imaged by MRI. This generated the 3D spatial surfaces corresponding to the patient specific vertebral anatomy. Step 3 - a bone surface segmentation algorithm was applied to extract bony profiles from US images of the vertebra. Step 4 - US bone profiles were co-registered to the individualized 3D vertebral model, by matching the 2D US point set to the 3D model and accounting for the maximum projected area of surfaces (Fig. 1). Real time vertebral motion can be derived from dynamic US images projected onto patient specific 3D MRI vertebral model.

Plastic Vertebra Model Validation: the generic model from a CT scan of a vertebra was 3D printed and mounted to a coupler device, which measured the relative position between US transducer and the model. The bone surface was imaged with US at 18 different angles and compared to the actual anatomic surface data.

In-vivo Experiment: After IRB approval, a static MRI 3D scan of a human cervical spine was used to rescale the cervical spine model. Human volunteers performed repetitive jump test on/off a 0.8 ft. step with and without weight applied to the head and neck. Two US probes were maintained in set positions relative to the cervical spine using a neoprene cervical collar. Real time in-vivo US images of vertebrae profile were registered on the model to show deformation and flexion angles derived from sequential US imaged of the cervical spine FSUs C4-5-6.

RESULTS SECTION: The Root Mean Square Error (RMSE) of co-registering the US bone profiles on the plastic vertebra model was 0.624 ± 0.151 mm (Fig. 2). Anatomic surfaces forming the anterior and posterior regions (vertebral body, facets, and lamina) have a higher contrast in US imaging due to their "smooth" surface geometry; therefore they provide better bone surface matching with more planar points to reflect sound waves. Sequential US images of C4-5 and C5-6 portrayed the relative displacements and flexion angles of the FSUs calculated by matching the dynamic real time US images to the static 3D model. IVD deformation, measured by axial translation of contiguous vertebrae revealed cyclic compression & relaxation during and after impact on landing as well as corresponding C4-C5 and C5-C6 FSU flexion measured by vertebral rotation (Fig. 3).

DISCUSSION: 2D to 3D image registration can be an ill-posed problem because mapping 2D image profiles onto a 3D surface may not represent a unique solution. We confined the scope of possible projections by assuming that the US signal intensity depends on the orientation of the projected 3D surface relative to that of the acoustic beam (Fig 1). This approach was validated by mapping 18 (every 20 deg.) sequential 2D US image profiles of a plastic cervical vertebral model and comparing to the known 3D structural anatomy. Anatomic regions with planar or simple curvilinear surfaces (i.e. large radius of curvature) gave better RF signal patterns than anatomic regions with complex surface anatomy. This implies that certain anatomical landmarks, e.g. anterior vertebral body and lamina should be selected for matching and co-registering 2D real time dynamic US images with static 3D MRI images of the C-spine to derive C-spine kinematics and IVD strain.

SIGNIFICANCE/CLINICAL RELEVANCE: (1-2 sentences): We have developed a reliable in-vivo technique using real time B-Mode US to image specific anatomic landmarks on cervical vertebrae related to a 3D vertebral model to evaluate the dynamic motion of the cervical spine during simulated work place conditions where current radiographic, CT or MRI based imaging cannot be used.

ACKNOWLEDGEMENTS: This work was supported by the U.S. Army Medical Research and Materiel Command Fort Detrick, Maryland (01026018, Contract No. W81XWH-13-1-0050).

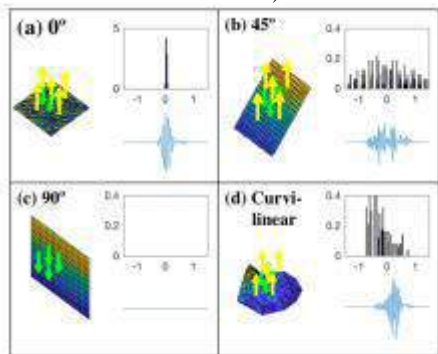


Fig. 1: US RF signal pattern depends on angle of incidence between the acoustic wave and projected surface. (A) It is maximum for a surface normal to the principal trajectory of the acoustic wave and (C) minimum for a surface parallel to the wave trajectory. The signal pattern is Gaussian for (B) oblique and (D) curvilinear surfaces.

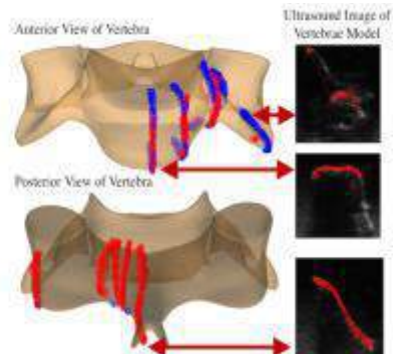


Fig. 2: Bone profiles extracted from ultrasound image (red) are registered to 3D vertebra model. They are compared to the reference(blue) that are measured by displacement and rotation calculation.

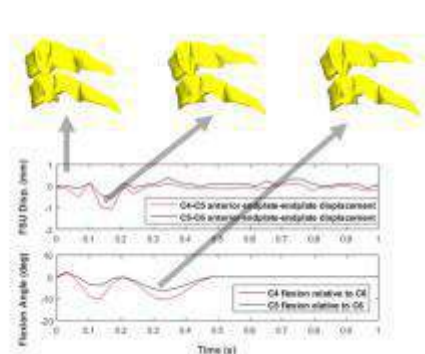


Fig. 3: Human subject jumped off 0.8 foot step. Top: the simulated 3D model showed C4-5 FSU motion before and at impact loading; Bottom: C4-5 IVD strain and flexion angle over course of 1 jump.

Effects of Motion Blurring and Tissue Artifacts on Accuracy of Bone Motion Analysis Using Ultrasound

Mingxin Zheng^{1,2}, Amin Mohamadi¹, Thomas L. Szabo¹, Brian D. Snyder^{1,2,3}

¹Beth Israel Deaconess Medical Center, Boston, MA, ²Boston University, Boston, MA, ³Boston Children's Hospital, Boston, MA
Email of Presenting Author zmx.pku@gmail.com

Disclosures: Mingxin Zheng (N), Amin Mohamadi (N) Thomas L. Szabo (N), Brian D. Snyder(N)

INTRODUCTION: Cervical spine pathoanatomy is typically evaluated by static radiographs, CT or MRI; however, these modalities are unable to directly measure the dynamic performance of the C-spine in-vivo that account for its functionality. *Ex-vivo* spine models may be insufficient to replicate *in-vivo* kinematics, predict acute/chronic injury mechanics or assess the effect of surgical instrumentation on *in-vivo* spine kinematics. We have previously illustrated the ability of B-mode ultrasound (US) to image cervical vertebrae in-vivo in real time by identifying the acoustic impedance differences between the bony surfaces forming the vertebral body and adjacent soft tissue structures (intervertebral disc, muscle, ligaments and facet joint capsule). The goal of this study is to analyze the effects of motion blurring and tissue artifacts on the measured C-spine kinematics analyzed by US.

METHODS: A 3D printed plastic anatomical model of an isolated human cervical vertebra and 6 human cadaver cervical vertebrae (give age and sex) with soft tissues retained were mounted in a servohydraulic material testing system that accurately controlled axial displacement. The plastic anatomical model provided high quality US image profiles of the 3D cervical spine "bony" surface anatomy. In comparison, soft tissue attachments to the cadaveric vertebrae distorted the US radio frequency (RF) signal pattern. Using US image segmentation, we measured the thickness of soft tissue retained on the vertebral bone surface to analyze the effect of soft tissue artifacts on tracking dynamic vertebral motion.

A series of axial sinusoidal vertical displacements applied over a physiological range of average velocities (4-120 mm/s) were imaged using a Terason t3200 US probe (Teratech, MA, USA) with a 7.5 MHz linear transducer 8IOL4. Each series of sinusoidal displacements were repeated over 18 different US transducer imaging angles for the plastic anatomical model and 5 different imaging angles for the 6 cadaveric specimens. Tracking accuracy was measured by mean square error (MSE). We then evaluated the effect of motion artifacts, which existed for both the plastic model and cadaveric vertebrae, and soft tissue artifact, which existed only for the cadaveric vertebrae, on the accuracy of US measurements of vertebral motion.

RESULTS SECTION: For motion artifact, the MSE of the plastic vertebral model varied as a quadratic function of the average absolute velocity, accounting for 96% of the variation in MSE (Fig.1). This indicates that US tracking of real time cervical spine motion is robust and accurate at lower velocities but at higher speeds, motion artifact blurs the image (speckle pattern) such that there is a progressive loss of RF signal correlation between sequential US image frames.

For soft tissue artifact, from motion analysis of the cadaveric vertebrae it was assumed that artifacts introduced by motion and soft tissue attachments contributed independently to the overall error in US tracking of dynamic vertebral motion. Thus the proportion of error attributed to soft tissue attachments was calculated by subtracting the MSE attributed to motion artifact from the total MSE of US tracking cadaveric vertebral motion. The resulting MSE varied as a quadratic function of the average thickness of attached soft tissues to the bony surfaces of the vertebrae, accounting for 69% of the variance in MSE (Fig. 2). Therefore anatomic sites such as the vertebral body with relatively little fixed soft tissue attachments are less prone to tracking errors by US than regions with thicker soft tissue attachments such as the spinous processes and lamina. Compared to tracking vertebral model, tracking cadaveric vertebrae at different angles increased the standard deviation of MSE by 520%, which suggested changing the imaging orientation or specimens has a much larger effect on the error in tracking cadaveric vertebrae.

DISCUSSION: Our study reveals that the accuracy and precision of dynamic vertebral motion measured by real time US depends on the velocity of vertebral spine motion and the volume of soft tissue attached to the region of the vertebra being tracked. Retained soft tissue inconsistently changed the RF signal pattern of the vertebrae so it is advantageous to image and track anatomical regions of cervical vertebra that have little soft tissue attachments, e.g. anterior vertebral body. However the accuracy of measuring vertebral kinematics using B-Mode US is affected by the velocity of motion, incurring significant blurring artifacts at large amplitude or high frequency.

SIGNIFICANCE/CLINICAL RELEVANCE: (1-2 sentences): Clinical US is capable of accurately tracking vertebral motion in real time at low frequency or small amplitude. Anatomic landmarks on the cervical vertebrae most conducive to tracking include the anterior vertebral body where attached soft tissues interfere less with perturbing the RF signal pattern.

ACKNOWLEDGEMENTS: This work was supported by the U.S. Army Medical Research and Materiel Command Fort Detrick, Maryland (01026018, Contract No. W81XWH-13-1-0050).

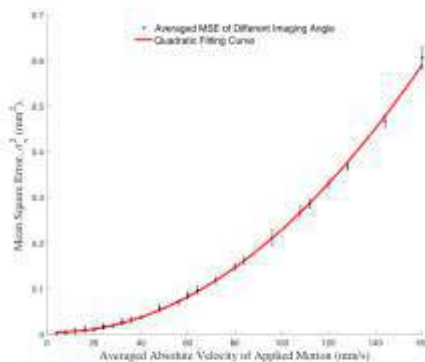


Fig. 1. The MSE of tracking a rigid phantom is plotted as a function of the average absolute velocity of applied sinusoidal movement, denoted as v . Motion speed leads to larger motion between frame to frame and introduced tracking errors. The R^2 of quadratic fitting model ($\sigma_{\text{fit}}^2 = 2.34 \times 10^{-5} v^2 - 1.3580 \times 10^{-4} v + 0.005$) is 0.96.

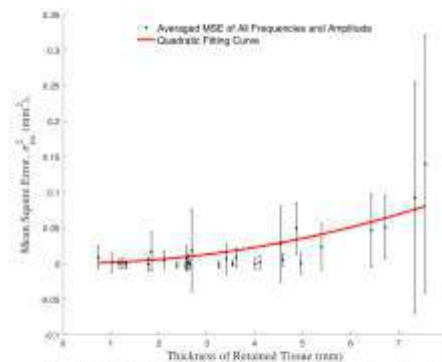


Fig. 2. MSE introduced by tissue plotted as function of tissue thickness, denoted as k . Each data sets represents the MSE of one specific image orientation of cadaver specimen averaged over all 4 amplitudes and 10 frequencies. The R^2 of the quadratic fitting model ($\sigma_{\text{fit}}^2 = 1.41 \times 10^{-3} k^2 + 1.11 \times 10^{-9}$) is 0.69.

3D Ultrasonography Is Capable of Measuring Three-Dimensional Spinal Deformity

Ashlyn J. M. Aiello^{1,2}, Amin Mohamadi², Thomas L. Szabo¹, Brian D. Snyder^{1,2,3}

¹Department of Biomedical Engineering, Boston University, Boston, MA, ²Center for Advanced Orthopaedic Studies, Beth Israel Deaconess Medical Center, Harvard Medical School, Boston, MA, ³Boston Children's Hospital, Harvard Medical School, Boston, MA
Email: aaiello2@bidmc.harvard.edu

Disclosures: None

INTRODUCTION: Adolescent idiopathic scoliosis (AIS) is a common spinal disease characterized by lateral curvature of the spine greater than 10 degrees. AIS comprises roughly 80% of all scoliosis cases and affects 2-4% of predominantly female adolescents between ages 10 and 16. Patients with AIS undergo serial radiographic evaluations of the entire spine every 4 to 6 months until skeletal maturity is reached to assess progression of spinal deformity or regression with brace treatment. Due to concerns of repetitive radiation exposures by serial radiographic examinations over several years, efforts to decrease radiation exposure for the monitoring of scoliosis progression and treatment response over time have been pursued. Currently, EOS is the preferred medical imaging system to provide frontal and lateral radiographic images at significantly limited absorbed X-ray dose predicated on the use of a multi-wire chamber, high sensitivity detector. However this system is rather large and expensive, limiting its availability to large volume centers and academic institutions. Ultrasound imaging is potentially a low cost, radiation-free, widely available modality that may be developed for assessing scoliosis and spinal deformity. Previously we have shown that B-mode ultrasound can provide accurate assessment of cervical spine kinematics and intervertebral disk dynamics. The objective of this study is to demonstrate that 3D ultrasound is capable of visualizing spinal deformity in three dimensions. We present proof of this concept using a plastic spine model and the “stitching together” of serial transaxial 3D ultrasound images of the surfaces of sequential vertebrae to measure spinal deformity typical of AIS.

METHODS: We used a full-spine synthetic bone model (model 323-40, Pacific Research Laboratories) to evaluate the deformed spinal anatomy typical of AIS. The flexible plastic model features soft intervertebral discs thereby allowing manipulation of the model to simulate mild scoliosis with Cobb angle of approximately 30 degrees. The entire spine was submerged in a water bath and imaged using 3D ultrasound (EpiQ 7, Philips Ultrasound). The transducer was translated along the length of the spine in 5mm increments from C6 to T8 using a robotic arm (UR5, Universal Robot). Sequential 3D surface ultrasonic volume images (Figure 1a) were generated by sequential parallel trans-axial linear US scans taken 40mm apart (Figure 1b) and concatenated using a custom program written in MATLAB (Mathworks Inc.) to generate a 3D volumetric surface rendition of the deformed thoracic spine (Figure 1c). The program extracted volume intensity information from 3D ultrasound DICOM files and stitched together the individual volumes into a larger model by taking the average of overlapping pixels. This complete model was visualized in 3D using Volume Viewer (Mathworks Inc.). Cobb angle was estimated using ImageJ by doubling the angle between the central axis and that of the greatest lateral displacement, T6 (Figure 2).

RESULTS: The 3D spine model displayed in Figure 1c was generated from the concatenated three-dimensional ultrasound images of more than 40 trans-axial images acquired over two linear scans paths from C6 to T8. The maximum lateral displacement between spinous processes was 43 mm, corresponding to vertebrae C7 and T6. The frontal plane spinal deformity angle measured by 3D US was 15.3 degrees. Trigonometry equivalencies demonstrate that twice this angle is equal to the Cobb angle measured on frontal plane radiographs, therefore the 3D US estimated Cobb angle of 30.6 degrees was nearly equivalent to the 30 degrees scoliosis induced in the plastic spine model and within the 5 degree uncertainty of Cobb angle measured on radiographs.

DISCUSSION: We have demonstrated a novel method of using 3D ultrasound images “stitched together” to create a volumetric representation of the entire spine that can be analyzed in multiple dimensions. We imaged the thoracic spine, the anatomic location of most AIS, and were able to determine the frontal plane Cobb angle used to clinically describe the lateral curvature of the spine. Limitations of this study include the use of a homogeneous spine model devoid of soft tissues and the absence of the rib cage. Further studies will address these deficiencies by using cadaveric specimens and animal models to refine this technique across a range of body habitus and spinal deformities. While 3D ultrasound is able to measure frontal plane Cobb angle, it has the potential for automatic or semi-automatic analysis of lateral sagittal plane displacement and torsional deformity of individual vertebrae.

SIGNIFICANCE/CLINICAL RELEVANCE: This feasibility study indicates that 3D ultrasound images can be “stitched together” to visualize spine deformity and determine Cobb angle. The use of ultrasound, a non-radiation based modality, for the diagnosis and monitoring of spinal deformity may substantially facilitate standard school screening programs by permitting frequent, minimally-invasive examinations without additional radiation exposure in children and adolescents with this condition.

ACKNOWLEDGEMENTS: We appreciate the funding support from the U.S. Army Medical Research and Materiel Command Fort Detrick, Maryland (01026018, Contract No. W81XWH-13-1-0050). We also acknowledge Philip Research North America for assisting with the imaging process.

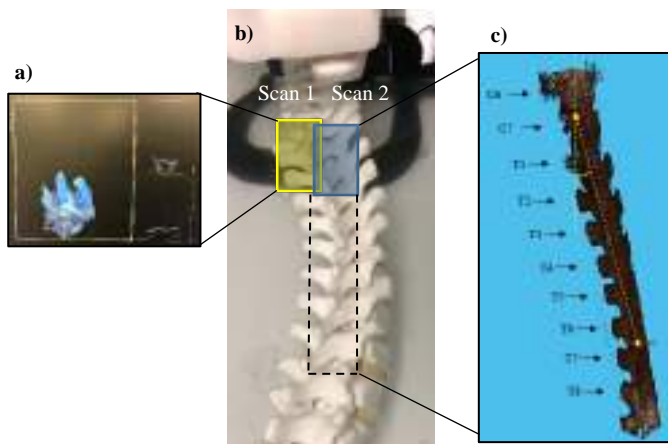


Figure 1: a) Spine model and overlay of imaging method. b) 3D ultrasound image using XL14-3 transducer. c) Stitched image of spine volume.

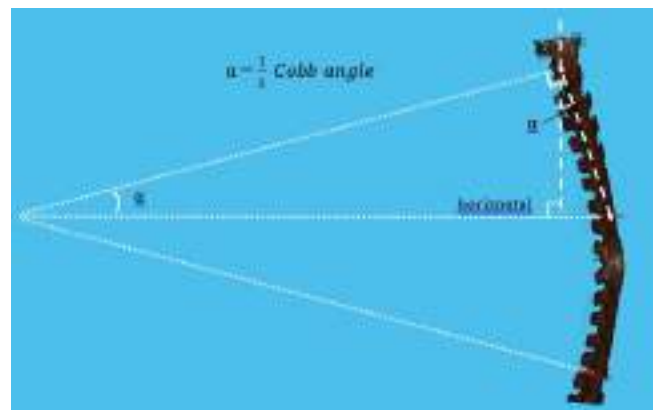


Figure 2: Trigonometric equivalencies demonstrating calculation of Cobb angle. Red lines extrapolate angle between first angled vertebra and horizontal intersecting the point of maximum lateral deflection. Yellow dashed lines indicate vectors used to determine Cobb angle.